materials

Special Issue Reprint

Testing of Materials and Elements in Civil Engineering (3rd Edition)

Edited by
Krzysztof Schabowicz

mdpi.com/journal/materials

MDPI

Testing of Materials and Elements in Civil Engineering (3rd Edition)

Testing of Materials and Elements in Civil Engineering (3rd Edition)

Editor

Krzysztof Schabowicz

MDPI

Basel • Beijing • Wuhan • Barcelona • Belgrade • Novi Sad • Cluj • Manchester

Editor
Krzysztof Schabowicz
Wrocław University of Science and Technology
Wroclaw
Poland

Editorial Office
MDPI
St. Alban-Anlage 66
4052 Basel, Switzerland

This is a reprint of articles from the Special Issue published online in the open access journal *Materials* (ISSN 1996-1944) (available at: https://www.mdpi.com/journal/materials/special_issues/365B2984NJ).

For citation purposes, cite each article independently as indicated on the article page online and as indicated below:

Lastname, A.A.; Lastname, B.B. Article Title. *Journal Name* **Year**, *Volume Number*, Page Range.

ISBN 978-3-7258-0381-1 (Hbk)
ISBN 978-3-7258-0382-8 (PDF)
doi.org/10.3390/books978-3-7258-0382-8

Contents

About the Editor

Krzysztof Schabowicz

Krzysztof Schabowicz is the author and co-author of seven books, over 300 publications, and 10 patents. He has more than 1000 citations in the Web of Science database. He serves as an Editor of *Materials* (MDPI) and is an Editorial Board Member of *Civil Engineering and Architecture* (HRPUB) and *Nondestructive Testing and Diagnostics* (SIMP). He has developed more than 300 reviews of journal and conference articles. He is the co-author of 10 patents and 1 patent application. He is also a member of the Polish Association of Civil Engineers and Technicians (PZITB) and the Polish Association of Building Mycology (PSMB). His research interests include concrete, fiber cement, ultrasonic tomography, impact-echo testing, impulse response, GPR, and other nondestructive tests, as well as artificial intelligence.

Preface

Last year, we ran a successful Special Issue titled "Testing of Materials and Elements in Civil Engineering (2nd Edition)" (https://www.mdpi.com/journal/materials/special_issues/testing_civil_engineering), with over 50 papers published. The field of material testing in civil engineering is very broad and interesting from both engineering and scientific perspectives. Therefore, we have decided to assemble a third edition dedicated to this topic.

This new Special Issue is proposed and organized as a means to present recent developments in the field of material testing in civil engineering. The articles highlighted in this Issue should relate to different aspects of the testing of different materials in civil engineering, from building materials and elements to building structures. The current trend in the development of material testing in civil engineering is mainly concerned with the detection of flaws and defects in elements and structures using destructive, semidestructive, and nondestructive testing.

Topics of interest include, but are not limited to, the following:

- Testing of materials and elements in civil engineering;
- Testing of structures made of novel materials;
- Condition assessment of civil materials and elements;
- Detecting defects that are invisible on the surface;
- Damage detection and damage imaging;
- Diagnostics of cultural heritage monuments;
- Structural health monitoring systems;
- Modeling and numerical analysis;
- Nondestructive testing methods;
- Advanced signal processing for nondestructive testing.

Krzysztof Schabowicz
Editor

materials

MDPI

Article

The Multi-Objective Optimization Design and Hydrothermal Performance Evaluation of Anhydrous Calcium Sulfate Whisker and Polyester Fiber Compound Modified Asphalt Mixture in Hot-Humid Areas

Taotao Fan [1,2], Qiuping Song [3], Chundi Si [1,2,*] and Songkai Han [1,2]

[1] School of Traffic and Transportation, Shijiazhuang Tiedao University, Shijiazhuang 050043, China; fantaotao@stdu.edu.cn (T.F.); han18533099477@163.com (S.H.)
[2] State Key Laboratory of Mechanical Behavior and System Safety of Traffic Engineering Structures, Shijiazhuang Tiedao University, Shijiazhuang 050043, China
[3] Hebei Provincial Communications Planning, Design and Research Institute Co., Ltd, Shijiazhuang 050200, China; sqp900618@126.com
* Correspondence: sichundi@stdu.edu.cn

Abstract: In hot and humid climates, asphalt pavements frequently encounter environmental factors such as elevated temperatures and rainfall, leading to rutting deformations and potholes, which can affect pavement performance. The primary objective of this study was to enhance the hydrothermal characteristics of asphalt mixtures through an investigation into the impact of anhydrous calcium sulfate whisker (ACSW) and polyester fiber (PF) on the hydrothermal properties of asphalt mixtures. In this paper, a central composite concatenation design (CCC) was employed to determine the optimal combination of ACSW and PF contents, as well as the asphalt aggregate ratio (AAR). Each influencing factor was assigned three levels for analysis. The evaluation indexes included dynamic stability, retained Marshall stability, and tensile strength ratio. Using the analysis methods of variance and gray correlation degree analysis, the hydrothermal properties of the asphalt mixture were examined in relation to the contents of ACSW, PF, and AAR based on the CCC results. Consequently, the optimal mix design parameters for composite modified asphalt mixture incorporating ACSW and PF were determined. The results indicated that the asphalt mixtures with hydrothermal qualities exhibited optimal performance in terms of 4.1% ARR, 11.84% ACSW, and 0.4% PF. The interaction between AAR and ACSW content had a greater effect on the dynamic stability and tensile strength ratio of the asphalt mixture, whereas the incorporation of ACSW and PF had a greater effect on the retained Marshall stability of the asphalt mixture. Among the three contributing factors, AAR exhibited the strongest relationship with the hydrothermal characteristics of the asphalt mixture, followed by the ACSW content; the correlation of PF content was the lowest. Therefore, to enhance the hydrothermal characteristics of the asphalt mixture, it is important to conduct a full evaluation of the constituents of ACSW and PF, along with the AAR in hot–humid regions.

Keywords: anhydrous calcium sulfate whisker; polyester fiber; asphalt mixture; central composite circumscribed design; gray correlation grade analysis; hydrothermal performance

Citation: Fan, T.; Song, Q.; Si, C.; Han, S. The Multi-Objective Optimization Design and Hydrothermal Performance Evaluation of Anhydrous Calcium Sulfate Whisker and Polyester Fiber Compound Modified Asphalt Mixture in Hot-Humid Areas. *Materials* **2023**, *16*, 6662. https://doi.org/10.3390/ma16206662

Academic Editor: Krzysztof Schabowicz

Received: 7 September 2023
Revised: 2 October 2023
Accepted: 4 October 2023
Published: 12 October 2023

1. Introduction

Asphalt pavements in different climatic regions have various performance requirements for asphalt mixtures [1–4]. In order to comprehensively analyze the performance of asphalt mixtures, it is important to have a thorough comprehension of the meteorological attributes pertaining to the specific geographical region in which the road is situated. Asphalt pavements in hot–humid areas are often influenced by high temperatures, rain, and other natural conditions and are prone to rutting, and potholes in the process of use, which result in the overall functionality and durability of the asphalt pavements being significantly

compromised. Therefore, researchers have occasion to conduct research on methods that would enhance the properties of asphalt pavements to be suitable for hot–humid areas.

Current research shows that there is a certain correlation between the roadway effectiveness of modified asphalt mixtures and the proportion parameters (externally modified amount and asphalt aggregate ratio). The results presented by Hong R.B. showed that when the polyester fiber (PF) content was 0.4% and the gangue powder replacement rate was 50%, the interaction between asphalt, PF, and gangue powder caused asphalt mixtures to exhibit excellent low-temperature anti-cracking properties [5]. Zhao X.W. studied the effect of Sasobit and Deurex on the characteristics of crystalline tetra-alpha-ethylene-modifying asphalt mixes and found that 4% Sasobit +2% Deurex was the optimal amount for asphalt mixtures, and they had better mechanical properties and economic benefits [6]. P. Ahmedzade found that when the asphalt content was 5.3%, asphalt mixtures made from 8% tall oil bitumen and 6% styrene–butadiene–styrene had the best physical and mechanical properties [7]. Yang B. found that the best performance of large-particle-size-modified asphalt mixtures was achieved at elevated temperatures when the asphalt aggregate ratio was 3.23% and the rock asphalt content was 20% [8]. Zhai R.X. showed that 5% nano-$CaCO_3$ and 4% SBR exhibited exceptional resistance to rutting deformation under elevated temperatures [9]. In the study conducted by Gong Y.F., it was observed that the composite-modified asphalt mixtures retained their pore properties in optimal water stability even after undergoing freeze–thaw cycles with a 3.9% basalt fiber, 5.1% nano-TiO_2/$CaCO_3$ content, and 5.67% asphalt aggregate ratio [10]. Yan K.ZH. found that 15% waste tire rubber and 4% amorphous polyolefin was the optimal content for achieving the best performance for asphalt mixtures [11]. Zhang H.T. concluded that asphalt mixtures modified using 4% SBS and 15% rubber were appropriate for asphalt pavements located in high-temperature, heavy traffic regions, and asphalt mixtures containing 4% SBS and 3% SBR were deemed suitable for cold–humid regions [12]. Cheng Y.CH. found that diatomite and basalt-fiber-composite-modified asphalt mixtures were more resistant to seasonal permafrost than the base asphalt mixtures in areas with freeze–thaw cycle damage [13]. Zhe H. demonstrated that a 2% thermoplastic polyurethane and 6% amorphous poly-alpha-olefin-modified asphalt mixtures had better rutting and moisture resistance than base asphalt mixtures [14]. Therefore, optimizing the mix design of modified asphalt mixtures to adapt to the climatic conditions in hot–humid regions has a beneficial impact on the enhancement of asphalt pavements' resistance to high temperature and water damage.

A common method for creating a mix ratio design for externally mixed and modified asphalt is to first determine the optimum asphalt aggregate ratio of asphalt mixtures under different externally mixed mixtures using the Marshall test, and then to carry out mixture performance tests such as the wheel tracking test, low bending test, immersed Marshall test, and freeze–thaw cycle test. Asphalt mixture proportion parameters with better overall performance are then obtained according to the results of the various performance tests for asphalt mixtures under different external mixing amounts. Nevertheless, this method usually requires a large amount of experimentation, resulting in the squandering of both resources and time. Thus, researchers have conducted relevant research on convenient methods applicable to the optimization of the design parameters of asphalt mixture ratios, such as response surface design and multifactorial orthogonal design. Fan T.T. used the central composite circumscribed design (CCC) method, a type of response surface design, to optimize the design parameters of polyester fiber and anhydrous calcium sulfate whisker composite modified asphalt mixtures with better low-temperature properties [15]. Ahmed I. Nassar utilized response surface design to optimize the mixing ratio of an emulsified asphalt mixture [16]. Taher B.M. used response surface design to optimize the content of asphalt and polyethylene terephthalate in asphalt mixtures, and the results showed that the Marshall properties of the modified asphalt mixture achieved the best performance after adding 5.88% asphalt and 0.18% polyethylene terephthalate [17]. Wei Y. revealed the relationship between the bone glue/polyurethane content and the properties of an asphalt binder using response surface design, and the optimal contents were 6.848% bone

glue and 2.759% polyurethane [18]. Cheng Y.CH conducted a comprehensive study on the optimization design and testing of a diatomite- and basalt-fiber-compound-modified asphalt mixture. Through the application of grey correlation grade analysis, the ideal mixing scheme was determined. The experimental findings indicated that the incorporation of 14% diatomite, 0.32% basalt fibers, and 5.45% asphalt aggregate resulted in the improved high- and low-temperature performance of the asphalt mixture [19]. Du J.CH. studied an approach for conducting grey relational regression analysis on hot-mix asphalt [20]. Lyu ZH.H. conducted an analysis of the performance of cold recycled mixtures. Additionally, an objective theory was optimized for the material content based on a multi-index-weighted grey methodology [21]. Slebi Acevedo, C.J. used multi-standard decision-making technology to study the functional and mechanical properties of polyolefin-aramid fiber and hydrated-lime-modified porous asphalt mixtures [22,23].

Therefore, this article conducts a study on the optimization of mix proportion design and hydrothermal-performance-influencing factors of the asphalt mixture with the addition of ACSW and PF. Three mix ratio design parameters (namely, ACSW content, PF content, and asphalt aggregate ratio) and three hydrothermal performance evaluation indexes (namely, dynamic stability, retained Marshall stability, and tensile strength ratio) were selected. The central composite circumscribed design (CCC) and grey correlation grade analysis (GCGA) were used to perfect the mix ratio design characteristics of modified asphalt mixtures in hot–humid areas. The effects of the design parameters on the hydrothermal performance of the asphalt mixtures were explored; meanwhile, the correlation degree between the design parameters and the hydrothermal performance indexes was evaluated using GCGA.

2. Materials and Methods

2.1. Materials

SK-90# asphalt (penetration grade 80/100) was used, and its properties are shown in Table 1. The aggregate was generated in Xianyang City, Shaanxi Province. According to Chinese standard JTG E20-2011 [24], 20 sets of asphalt mixtures were prepared with an aggregate particle size characterized by a nominal maximum of 19 mm, as shown in Tables 2 and 3. The characteristics of ACSW and PF are listed in Tables 4 and 5, respectively.

Table 1. Basic characteristics of SK-90# asphalt.

Properties	Value	Standard Value
Penetration (25 °C, 0.1 mm)	85.9	80–100
Softening point (°C)	46.5	≥45
Ductility (15 °C, cm)	>100	≥100
Viscosity (135 °C, Pa.s)	0.344	-

Table 2. Passing rate and physical characteristics of aggregates.

Sieve Size (mm)	19	16	13.2	9.5	4.75	2.36	1.18	0.6	0.3	0.15	0.075
Passing rate (%)	97.5	88.5	75.5	55.5	33.5	23.0	17.3	12.0	8.0	6.3	4.0
Apparent specific gravity	2.705	2.719	2.715	2.729	2.718	2.743	2.644	2.719	2.725	2.744	2.584
Bulk volume relative density	2.686	2.678	2.691	2.701	2.689	2.707	2.556	2.503	2.593	2.504	2.444
Water absorption (%)	0.263	0.555	0.335	0.380	0.400	0.489	1.314	2.746	1.866	3.502	2.222

Table 3. Physical characteristics of mineral powder.

Index		Results
Apparent specific gravity		2.710
Water absorption (%)		0.300
Passing rate of sieve size	<0.6 mm	100
	<0.15 mm	99.1
	<0.075 mm	90.4

Table 4. Properties of ACSW.

Index	Bulk Density (g/cm^3)	Length (μm)	Diameter (μm)	Aspect Ratio	Melting Point (°C)
Value	0.1–0.4	10–200	1–4	40–100	1450

Table 5. Properties of PF.

Index	Diameter (μm)	Tensile Strength (MPa)	Specific Gravity (g/cm^3)	Melting Point (°C)	Length (mm)	Elongation (%)
Value	19–21	591	1.38	259	6	10.8

2.2. Experimental Methods

2.2.1. Rutting Test

The rutting test is a commonly employed technique for assessing the durability of asphalt mixtures in terms of their ability to withstand permanent deformation when subjected to repetitive loading at elevated temperatures. According to Chinese standard T0719, the evaluation of the anti-deformation of asphalt mixtures under high temperatures was conducted using the rutting test. Specimens of 300 × 300 × 50 mm were made using the wheel-rolling method according to Chinese standard T0703. Before testing, the samples were placed in an oven at 60 °C for 5 h. Then, the rutting test was conducted under 0.7 MPa rubber wheel pressure, a 42 times/min loading rate, and a test temperature of 60 °C. The value of dynamic stability (DS) was calculated based on Equation (1).

$$\mathrm{DS} = \frac{N \times (t_1 - t_2)}{d_1 - d_2} \times c_1 \times c_2 \quad (1)$$

where N is the loading speed, 42 times/min; t_1 and t_2 are the test times, usually 45 min and 60 min, respectively; d_1 and d_2 are the surface rut depth of the asphalt mixture specimens in correspondence with the test times t_1 and t_2, mm; and c_1 and c_2 are the test parameters, and their values are 1.0, respectively.

2.2.2. Immersed Marshall Test

The immersed Marshall test is the main method employed for ascertaining the moisture sensitivity of asphalt mixtures under high-temperature immersion. The test was carried out according to Chinese standard T0709. Eight samples were generated for each mixture using the Marshall method, and these samples were evenly divided into two groups. The first group of specimens should be soaked in water at 60 °C for 30 min and tested for the stability value MS_0. The second group of specimens should be soaked in water at 60 °C for 48 h and tested for the stability value MS_1. The assessment of moisture stability in the asphalt mixtures was conducted by obtaining the retained Marshall stability (RMS), as shown in Equation (2).

$$\mathrm{RMS} = \frac{MS_1}{MS_0} \times 100\% \quad (2)$$

2.2.3. Freeze–Thaw Splitting Test

The moisture stability of the titanium combination was assessed using a frozen splitting test, conducted in line with Chinese standard T0729. A total of eight samples were generated using the Marshall approach and subsequently separated into two groups, resulting in an equal distribution. A single group of samples was subjected to ambient temperatures ranging from around 20 to 25 °C. An additional set of samples underwent a freezing process for 16 h at −18 °C after water saturation. These samples were subsequently immersed in a solution at 60 °C for 24 h. Following this, the two sets of specimens were immersed in water at a temperature of 25 °C for 2 h. Subsequently, an indirect tensile test was conducted, employing an indirect tensile load with a loading rate of 50 mm/min. The tensile strength ratio (TSR) is determined by calculating the average split stretch strength before (S_{before}) and after the freeze–thaw cycle (S_{after}), as demonstrated in Equation (3).

$$\text{TSR} = \frac{S_{after}}{S_{before}} \times 100\% \tag{3}$$

2.2.4. Grey Correlation Grade Analysis

To ascertain the most suitable composition of ACSW and PF in the asphalt mixture, the CCC results were examined using GCGA [25]. The grey correlation coefficient pertaining to the reference sequence $g_0 = (g_0(1), g_0(2), g_0(3))$ and the comparison sequence $g_i = (g_i(1), g_i(2), g_i(3))$, $\xi_i(m)$ are defined as Equation (4).

$$\xi_i(m) = \frac{\min\limits_i \min\limits_m |g_0(m) - g_i(m)| + 0.5 \times \max\limits_i \max\limits_m |g_0(m) - g_i(m)|}{|g_0(m) - g_i(m)| + 0.5 \times \max\limits_i \max\limits_m |g_0(m) - g_i(m)|} \tag{4}$$

where $\xi_i(m)$ is the correlation coefficient between the m-th evaluation index of the i-th comparison group and the associated reference group. $\max\limits_i \max\limits_m |x_0(m) - x_i(m)|$ is the maximum difference between the reference and comparison series. $\max\limits_i \max\limits_m |x_0(m) - x_i(m)|$ is the minimum difference value between the reference sequence and comparative sequences.

Then, the grey correlation grade λ_i is derived by calculating the weighted sum of the grey correlation coefficients, as outlined in Equation (5).

$$\lambda_i = Z_D \xi_i(m) + Z_R \xi_i(m) + Z_T \xi_i(m) \tag{5}$$

$$Z_D + Z_R + Z_T = 1 \tag{6}$$

where Z_D, Z_R, and Z_T represent the weighting of DS, RMS, and TSR, respectively.

2.3. Experimental Design

CCC, a type of response surface design, is used to assess the interaction between independent and response variables within the context of an experiment. In the CCC technique, at least two numerical inputs are required and are varied in the range of alpha (α) to five ($-\alpha$, -1, 0, $+1$, $+\alpha$) ($\alpha > 1$) phases. The CCC method offers the benefit of incorporating both sequential and rotational aspects within the framework of experimental design. In this paper, CCC was chosen to evaluate the association between the independent and response variables with the aim of identifying the most suitable experimental formulation. The number of test times can be expressed as ($2^m + 2m + n$), where m represents the count of independent variables and n is the number of center points. The value of α can be determined by $2^{m/4}$.

The experimental design employed in this study necessitates the execution of 20 experimental trials. It encompassed eight factorial points, six star points, and six center points, all of which were conducted at five levels. The design parameters were as follows: $m = 3$, $n = 6$, and $\alpha = 1.682$. The decision to establish six center points was made in order to account for

potential experimental errors by the inclusion of additional replications. Three independent variables were the asphalt aggregate ratio (AAR), ACSW content (related to asphalt-binding mass ratio), and PF content (relative to asphalt mix mass ratio), as presented in Table 6. Three response variables, DS, RMS, and TSR, were chosen to optimize the content of ACSW and PF, and the AAR of the asphalt mixture. Table 7 presents the experimental design and corresponding outcomes.

Table 6. Experimental factors and levels of CCC.

	Experimental Factors	**Unit**	**Levels**				
			−1.682	**−1**	**0**	**1**	**1.682**
F_1	Asphalt aggregate ratio (AAR)	%	3.16	3.5	4	4.5	4.84
F_2	ACSW content (ACC)	%	7.64	9	11	13	14.36
F_3	PF content (PFC)	%	0.23	0.3	0.4	0.5	0.57

Table 7. Results of CCC.

No.	**Experimental Variables**			**Response Variables**		
	F_1 **(%)**	F_2 **(%)**	F_3 **(%)**	**DS** R_1 **(Times/mm)**	**RMS** R_2 **(%)**	**TSR** R_3 **(%)**
1	3.5	13	0.3	1610.1	94.25	97.02
2	4.5	9	0.5	2460.9	91.57	106.54
3	3.5	13	0.5	1123.5	93.93	93.12
4	4.0	11	0.4	2137.3	94.06	104.26
5	3.5	9	0.3	1461.7	91.59	82.02
6	4.0	11	0.4	2460.9	93.37	106.52
7	4.0	11	0.4	2113.4	93.64	101.13
8	4.0	11	0.23	1903.3	89.47	90.47
9	4.0	14.36	0.4	1862.2	95.42	93.39
10	4.0	11	0.4	2472.9	94.59	102.24
11	3.5	9	0.5	905.2	87.77	89.96
12	4.5	13	0.5	1716.6	94.77	93.35
13	4.84	11	0.4	1039.6	95.63	103.86
14	4.5	9	0.3	1707.3	92.28	96.28
15	4.0	11	0.57	2045.5	90.78	94.96
16	4.0	11	0.4	2344.8	94.35	103.33
17	3.16	11	0.4	851.4	96.20	87.23
18	4.5	13	0.3	1202.3	93.66	86.47
19	4.0	7.64	0.4	1916.8	90.65	101.96
20	4.0	11	0.4	2106.5	94.47	100.38

Design-Expert 10.0 software was used to perform a response model (as shown in Equation (7)) and statistical regression analysis of the experimental program to determine the best combination of independent variable levels.

$$R = \mu_0 + \sum_{i=1}^{3} \mu_i F_i + \sum_{i=1}^{2} \sum_{j=i+1}^{3} \mu_{ij} F_i F_j + \sum_{i=1}^{3} \mu_{ii} F_i^2 + \eta \quad (7)$$

where the response variable is denoted by R. The coded independent parameters are represented by F_i and F_j. The coefficients for the constant, primary, interaction, and quadratic terms are denoted by μ_0, μ_i, μ_{ij}, and μ_{ii}, respectively. The random error is denoted by η.

3. Results and Discussion

3.1. Statistical Modeling

To study the interaction between different independent variables and their impact on the responsive variable, analysis of variance (ANOVA) was used. When the p-value was

less than 0.05, there was a significant difference between the model and the factor variable. The results of the ANOVA are presented in Tables 8 and 9, respectively.

Table 8. ANOVA results of CCC.

Responses		*R*-Squared	Adj. *R*-Squared	Adeq. Precision	*F*-Value	*p*-Value	Significant
F_1	*DS*	0.9389	0.8839	13.292	17.07	<0.0001	yes
F_2	*RMS*	0.9252	0.8579	12.223	13.75	0.0002	yes
F_3	*TSR*	0.9167	0.8418	12.643	12.23	0.0003	yes

Table 9. ANOVA results for experimental variables.

Responses	Factors	Sum of Squares	Degree of Freedom	Mean Square	*F*-Value	*p*-Value	Significant
DS	F_1	3.884×10^5	1	3.884×10^5	12.08	0.0060	yes
	F_2	6.953×10^4	1	6.953×10^4	2.16	0.1722	no
	F_3	1.576×10^4	1	1.576×10^4	0.49	0.4998	no
	F_1F_2	3.264×10^5	1	3.264×10^5	10.15	0.0097	yes
	F_1F_3	6.676×10^5	1	6.676×10^5	20.77	0.0010	yes
	F_2F_3	3587.04	1	3587.04	0.11	0.7453	no
	${F_1}^2$	3.285×10^6	1	3.285×10^6	102.19	<0.0001	yes
	${F_2}^2$	2.976×10^5	1	2.976×10^5	9.26	0.0124	yes
	${F_3}^2$	1.863×10^5	1	1.863×10^5	5.79	0.0369	yes
	Lack of Fit	1.695×10^5	5	3.389×10^4	1.11	0.4540	no
RMS	F_1	1.05	1	1.05	1.53	0.2449	no
	F_2	33.60	1	33.60	48.99	<0.0001	yes
	F_3	0.17	1	0.17	0.25	0.6264	no
	F_1F_2	2.25	1	2.25	3.28	0.1004	no
	F_1F_3	2.58	1	2.58	3.76	0.0813	no
	F_2F_3	3.54	1	3.54	5.16	0.0465	yes
	${F_1}^2$	4.31	1	4.31	6.28	0.0311	yes
	${F_2}^2$	3.20	1	3.20	4.67	0.0560	no
	${F_3}^2$	32.44	1	32.44	47.30	<0.0001	yes
	Lack of Fit	5.68	5	1.14	4.80	0.0552	no
TSR	F_1	172.16	1	172.16	21.32	0.0010	yes
	F_2	27.14	1	27.14	3.36	0.0966	no
	F_3	60.44	1	60.44	7.49	0.0210	yes
	F_1F_2	211.77	1	211.77	26.23	0.0004	yes
	F_1F_3	21.45	1	21.45	2.66	0.1342	no
	F_2F_3	28.96	1	28.96	3.59	0.0875	no
	${F_1}^2$	129.45	1	129.45	16.03	0.0025	yes
	${F_2}^2$	72.57	1	72.57	8.99	0.0134	yes
	${F_3}^2$	230.32	1	230.32	28.52	0.0003	yes
	Lack of Fit	55.72	5	11.14	2.23	0.2001	no

The ANOVA results for the quadratic model of the DS are presented in the first row of Table 8. The *R*-squared value of 0.9389 and the adjusted *R*-squared value of 0.8839 indicated that the fit of the DS model was strong. Furthermore, Adeq.precision was adopted to evaluate the signal-to-noise ratio of the response model. It is worth noting that the regression model was considered optimal when the Adeq.precision value exceeded 4. Based on the findings shown in Table 8, it can be observed that the Adeq.precision of the DS model was 13.292, suggesting the favorable match of the model. The statistical significance of the DS model is supported by the *p*-value, which is less than 0.0001. The ANOVA results in Table 8 demonstrate that the models for RMS and TSR exhibited a good fit.

The significance of Lack of Fit is used to evaluate the model fit. The *p*-values of the Lack of Fit for the DS, RMS, and TSR models, as presented in Table 9, were 0.4540, 0.0552, and 0.2001, respectively, which suggests that all models were well fitted.

According to the findings presented in Table 9, the DS model revealed several statistically significant terms, which included F_1, F_1F_2, F_1F_3, $(F_1)^2$, $(F_2)^2$ and $(F_3)^2$. The significant terms of the RMS model included F_2, F_2F_3, $(F_1)^2$, and $(F_3)^2$, and that of the TSR model consists of the significant terms F_1, F_3, F_1F_2, $(F_1)^2$, $(F_2)^2$, and $(F_3)^2$. After eliminating the insignificant terms, the relation between the design parameters and response variables was represented by Equations (8)–(10).

$$R_1 = 2273.89 + 168.64F_1 - 202.0F_1F_2 + 288.88F_1F_3 - 477.46F_1^2 - 143.70F_2^2 - 113.69F_3^2 \quad (8)$$

$$R_2 = 93.71 + 1.57F_2 + 0.67F_2F_3 + 0.59F_1^2 - 1.45F_3^2 \quad (9)$$

$$R_3 = 103.03 + 3.55F_1 + 2.10F_3 - 5.14F_1F_2 - 3.00F_1^2 - 2.24F_2^2 - 4.00F_3^2 \quad (10)$$

3.2. Muti-Objective Optimization

3.2.1. Optimization Results Based on CCC

For the hot–humid area, the target values listed in Table 10 were chosen based on Chinese standard JTG F40-2004 [26]. The larger the values of response variables, the better the anti-deformation and anti-water damage of the asphalt mixture.

Table 10. Target values of response variables.

Response	DS (R_1)	RMS (R_2)	TSR (R_3)
Unit	times/mm	%	%
Target value	Maximize	Maximize	Maximize

The most suitable values of the layout parameters were determined by calculating Equations (8)–(10). The ramps of CCC analysis are depicted in Figure 1. Each ramp is associated with a specific point that represents the intended aim for both the independent and dependent variables. The meaning of the red dot in Figure 1 is the value of the ideal design parameters of asphalt mixture, and the blue dot is the value of the predicted values of hydrothermal performance of asphalt mixture. Based on the data presented in Figure 1, it can be observed that the ideal design parameters for the ACSW and PF compound-modified asphalt mixture were 4.1% AAR, 11.84% ACC, and 0.42% PFC.

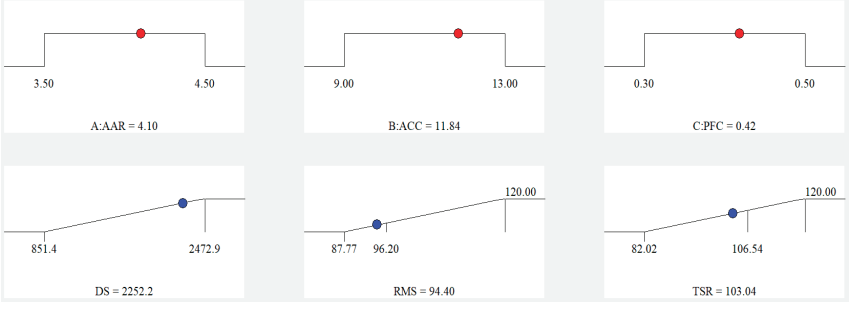

Figure 1. Analysis ramps of CCC.

Table 11 shows the optimal predicted values and laboratory values of response variables of the asphalt mixtures. The laboratory tests were conducted three times. The assess-

ment of the deviation rate between the predicted and laboratory results was conducted using Equation (11).

$$\text{Deviation rate } (\%) = \frac{V_{Laboratory} - V_{Predicted}}{V_{Laboratory}} \times 100\% \quad (11)$$

Table 11. Validation laboratory results of CCC.

Response	Unit	Predicted Values	Laboratory Values	Deviation Rate (%)
AAR (F_1)	%	4.10	4.10	
ACC (F_2)	%	11.84	11.84	
PFC (F_3)	%	0.42	0.42	
DS (R_1)	times/mm	2252.2	2255.9	0.16%
RMS (R_2)	%	94.40	93.53	−0.93%
TSR (R_3)	%	103.04	101.25	−1.77%

In Table 11, the deviation rates of all three response variables were lower than 2%, which showed that there was no discernible distinction between the predicted values and laboratory values. This demonstrated that it was feasible to enhance the hydrothermal characteristics of the modified asphalt mixture by optimizing its mix proportion using the CCC-RSM approach.

3.2.2. Optimization Results Based on GCGA

The GCGA is a scientific methodology utilized to evaluate the correlation between components by analyzing the similarity in their developmental tendencies. This approach holds significant potential as a viable answer for research programs focused on multi-objective optimal design. The challenges in drawing accurate findings when making comparisons arise from the varying physical interpretations of the measured indicators and the lack of standardization in data dimensions.

Typically, to obtain better hydrothermal properties of the asphalt mixture, the index values of high-temperature performance and water stability are needed to reach the maximum. In GCGA, the reference series and the comparative series need to be established first. The maximum values of DS, RMS, and TSR are defined as reference series; the values of DS, RMS, and TSR are set to 2500 times/mm, 100%, and 100%, respectively. The results of 20 schemes are defined as comparative series. Secondly, the numerical dimensionless test is carried out using Equation (12), and the dimensionless results are shown in Table 12.

$$x_n = \frac{f_n}{average(f_1, f_1, \cdots, f_{20})} \quad (12)$$

where x_n represents the dimensionless result of the n-th group, n = 1, 2, …, 20; and f_n represents the test result of group n.

$\xi_i(m)$ of the dimensionless test results is computed based on Equation (4), as presented in Table 12. In the proportion design of the asphalt mixture in hot and humid regions, the high-temperature performance index and water stability index of the asphalt mixture are equally important. Consequently, the performance indicators are assigned equal weights in order to derive the most ideal contents of ACSW and PF, as well as the optimal asphalt aggregate ratio. The weights assigned to the performance indicators are determined as follows: Z_D = 0.5, Z_R = 0.25, and Z_T = 0.25. The λ is calculated using Equation (5), as presented in Table 12. Table 13 displays the average correlation grade associated with each evaluation and level.

Table 12. Analysis results of grey correlation degree.

No.	Non-Dimensional			Grey Correlation Degree			
	DS	RMS	TSR	DS	RMS	TSR	λ
1	0.891	1.009	0.997	0.497	0.910	0.799	0.676
2	1.362	0.980	1.094	0.986	0.862	0.958	0.948
3	0.622	1.005	0.956	0.387	0.904	0.748	0.607
4	1.183	1.007	1.071	0.717	0.907	0.915	0.814
5	0.809	0.980	0.842	0.457	0.863	0.634	0.603
6	1.362	0.999	1.094	0.986	0.894	0.958	0.956
7	1.170	1.002	1.039	0.703	0.899	0.861	0.792
8	1.053	0.957	0.929	0.599	0.828	0.717	0.686
9	1.031	1.021	0.959	0.582	0.933	0.752	0.712
10	1.369	1.012	1.050	1.000	0.917	0.879	0.949
11	0.501	0.939	0.924	0.352	0.803	0.712	0.555
12	0.950	1.014	0.959	0.530	0.920	0.751	0.683
13	0.575	1.023	1.067	0.373	0.937	0.907	0.648
14	0.945	0.987	0.989	0.527	0.875	0.789	0.680
15	1.132	0.971	0.975	0.666	0.849	0.772	0.738
16	1.298	1.010	1.031	0.869	0.912	0.898	0.887
17	0.471	1.029	0.896	0.344	0.948	0.683	0.580
18	0.665	1.002	0.888	0.401	0.899	0.675	0.594
19	1.061	0.970	1.047	0.605	0.847	0.875	0.733
20	1.166	1.011	1.031	0.699	0.914	0.849	0.790

Table 13. Average relational between levels of each factor and response.

ACC (%)	Relational	PFC (%)	Relational	AAR (%)	Relational
7.64	0.733	0.23	0.686	3.16	0.580
9.0	0.697	0.3	0.638	3.5	0.610
11.0	0.784	0.4	0.786	4.0	0.806
13.0	0.640	0.5	0.698	4.5	0.726
14.36	0.712	0.57	0.738	4.84	0.648

In the GCGA algorithm, as per its specifications, the greater the correlation rank, the closer the corresponding factor level is to the optimal value. As can be seen from Table 13, the factors correspond to the optimal ratios of ACC = 11%, PFC = 0.4%, and AAR = 4.0%. Hence, in accordance with the multi-objective results of CCC, modified asphalt mixture performs better at high temperature and has greater moisture susceptibility when the ACSW content is 11%, the PF content is 0.4%, and the asphalt aggregate ratio is 4.0%.

In addition, compared with the results of CCC and GCGA, as shown in Table 14, the deviation rates of the optimal design parameters of the modified asphalt mixtures were smaller than 7%, which revealed that it was feasible to carry out the multi-objective optimized design of asphalt mixtures using the GCGA method.

Table 14. Deviation rate of CCC and GCGA results.

Factors	Results of CCC (%)	Results of GCGA (%)	Deviation Rate (%)
AAR	4.1	4.0	2.44
ACC	11.8	11.0	6.78
PFC	0.42	0.4	4.76

3.3. Hydrothermal Property Analysis

3.3.1. High-Temperature Performance

Dynamic stability (DS) was adopted to evaluate the high-temperature performance of the asphalt mixture, and the larger the DS value, the better its high-temperature perfor-

mance. The DS results of the ACSW- and PF-compound-modified asphalt mixture (APCRA) at different AAR, ACC, and PFC are shown in Figure 2.

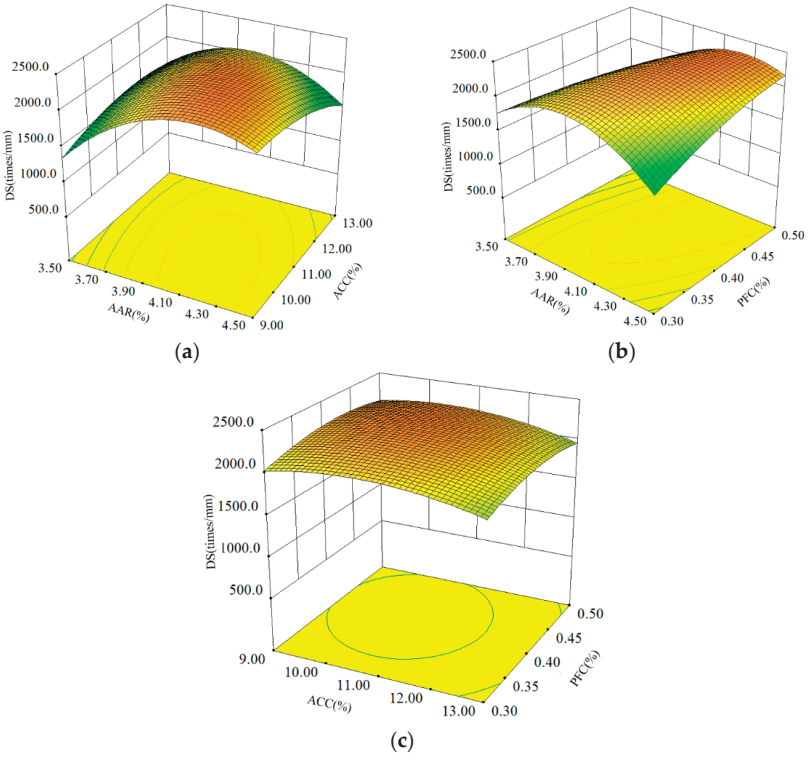

Figure 2. Influence of three factors on DS: (**a**) AAR and ACC; (**b**) ARR and PFC; and (**c**) ACC and PFC.

Figure 2 shows that the coupling effects of AAR and ACC, as well as AAR and PFC, exhibited more significant effects on the DS values of APCRA than the interaction between ACC and PFC, which is in accordance with the findings in Table 9. In Figure 2a,c, the DS values of APCRA first increased as the ACSW content increased from a lower level (9.0%) to a higher level (13.0%), and then stabilized with a further increase in the AAR, reaching a maximum value when the AAR was 4.1%. When the AAR was constant, the DS value of APCRA was less affected by the ACSW content. In Figure 2b, the DS value of APCRA first increased at constant PFC and then increased with AAR, and this pattern of change became more pronounced when the PFC was at a low level (0.3%) compared to a high level (0.5%).

3.3.2. Moisture Susceptibility

The evaluation of moisture sensitivity in APCRA was conducted using two parameters: residual Marshall stability (RMS) and tensile strength ratio (TSR). The larger the RMS or TSR value, the better the moisture damage resistance of APCRA.

RMS

Figure 3 shows the RMS results of APCRA at different AAR, ACC, and PFC. The coupling effect of ACC and PFC on the RMS values of APCRA was more significant than the effect of AAR and ACC or AAR and PFC on the RMS values of APC. As shown in Figure 3a,c, when the AAR or PFC was kept constant, the RMS values of APCRA increased with the increase in ACC. When the value of ACC was kept constant, the RMS values of

APCRA increased and then decreased with the increase in PFC. In addition, an increase in AAR did not result in a significant change in the RMS values of APCRA.

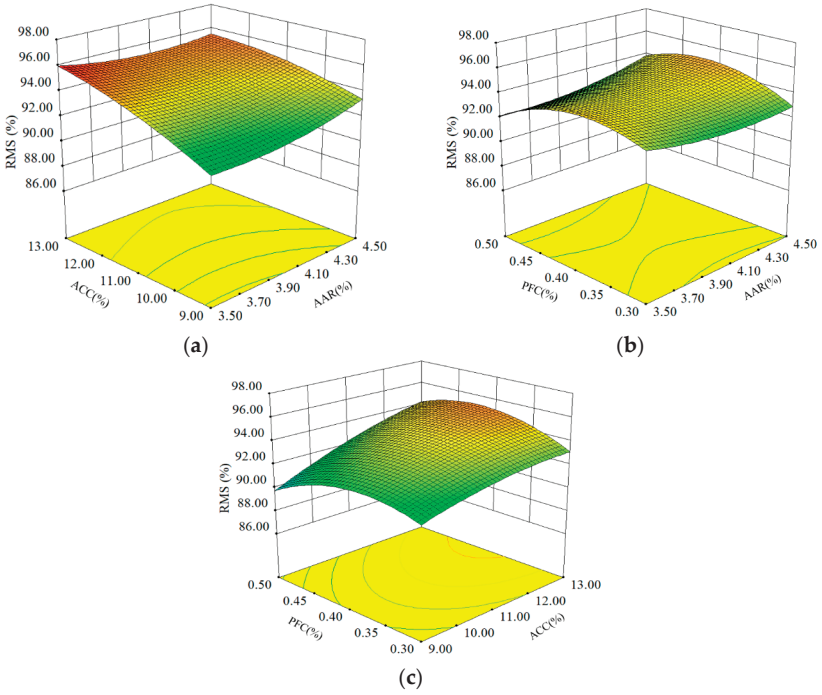

Figure 3. Influence of three factors on RMS: (**a**) AAR and ACC; (**b**) ARR and PFC; and (**c**) ACC and PFC.

From Figure 3a,b, the RMS values of APCRA did not change significantly with the increase in AAR at the same PFC. Meanwhile, at the same AAR, the RMS values of APCRA increased and then decreased with the increase in PFC. The RMS values of APRA reached a relative maximum when the PFC was at a medium level (0.4%) and the AAR was at a high level (4.5%).

TSR

The TSR results of APCRA at different AAR, ACC, and PFC content levels are shown in Figure 4. Figure 4a shows that the coupling relationship between ACC and AAR had a significant effect on the TSR values of APCRA. When the ACC value was at a low level (9.88%), the TSR values gradually increased with the increase in AAR, and when the ACC value was at a high level (13.88%), the TSR values gradually decreased with the increase in AAR. In addition, when the coupling values of ACC and AAR changed from 9.88% (ACC) and 3.7% (AAR) to 13.88% (ACC) and 4.7% (AAR), the TSR values increased first and then decreased.

Figure 4b shows that the TSR values of APCRA gradually increased when the coupling values of AAR and PFC changed from 0.3% (PFC) and 3.7% (AAR) to 0.5% (PFC) and 4.7% (AAR). Figure 4c illustrates that when the value of PFC was lower than 0.4%, the TSR values of APCRA increased with the increase in ACC, whereas when the value of PFC was higher than 0.4%, the TSR values of APC gradually decreased with the increase in ACC.

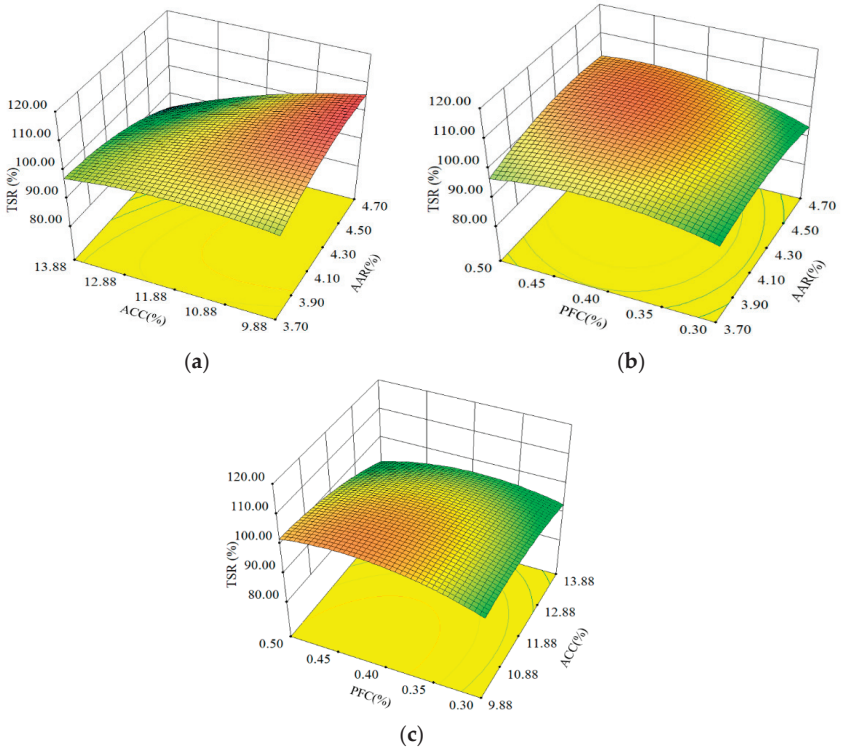

Figure 4. Influence of three factors on TSR: (**a**) AAR and ACC; (**b**) ARR and PFC; and (**c**) ACC and PFC.

3.3.3. Effect Degree of Factors on Performance Indexes

In this paper, GCGA was used to evaluate the correlation rank of the influencing factors with the performance indexes. The AAR, ACC, and PFC values were selected as comparison sequences, while the DS, RMS, and TSR results were adopted as reference sequences. Using Equations (4) and (12), the dimensionless results and $\xi_i(m)$ were calculated as shown in Tables 15 and 16.

From Table 16, it can be observed that the grey correlation degrees of the different factors on various performance indicators were different. The grey correlation degrees of DS were as follows: AAR (0.660) > PFC (0.614) > ACC (0.593); on RMS: AAR (0.788) > ACC (0.748) > PFC (0.696); and on TSR: AAR (0.810) > ACC (0.710) > PFC (0.683). This indicates that the effect of AAR on the high-temperature and moisture sensitivity of the asphalt mixtures was more significant than that of ACC and PFC. In addition, ACC mainly affected the moisture sensitivity of the asphalt mixture, while PFC mainly affected the high-temperature performance of the asphalt mixture.

Table 15. Dimensionless results.

No.	Non-Dimensional					
	AAR	**ACC**	**PFC**	**DS**	**RMS**	**TSR**
1	0.875	1.182	0.750	0.909	1.012	1.003
2	1.125	0.818	1.250	1.389	0.983	1.101
3	0.875	1.182	1.250	0.634	1.009	0.963
4	1.000	1.000	1.000	1.206	1.010	1.078
5	0.875	0.818	0.750	0.825	0.984	0.848

Table 15. *Cont.*

No.	Non-Dimensional					
	AAR	**ACC**	**PFC**	**DS**	**RMS**	**TSR**
6	1.000	1.000	1.000	1.389	1.003	1.101
7	1.000	1.000	1.000	1.193	1.006	1.046
8	1.000	1.000	0.575	1.074	0.961	0.935
9	1.000	1.305	1.000	1.051	1.025	0.966
10	1.000	1.000	1.000	1.395	1.016	1.057
11	0.875	0.818	1.250	0.511	0.943	0.930
12	1.125	1.182	1.250	0.969	1.018	0.965
13	1.210	1.000	1.000	0.587	1.027	1.074
14	1.125	0.818	0.750	0.963	0.991	0.995
15	1.000	1.000	1.425	1.154	0.975	0.982
16	1.000	1.000	1.000	1.323	1.013	1.068
17	0.790	1.000	1.000	0.480	1.033	0.902
18	1.125	1.182	0.750	0.678	1.006	0.894
19	1.000	0.695	1.000	1.082	0.973	1.054
20	1.000	1.000	1.000	1.189	1.014	1.038

Table 16. Analysis results of grey correlation degree.

No.	DS			RMS			TSR		
	AAR	**ACC**	**PFC**	**AAR**	**ACC**	**PFC**	**AAR**	**ACC**	**PFC**
1	0.934	0.586	0.713	0.629	0.577	0.467	0.686	0.599	0.505
2	0.595	0.401	0.741	0.621	0.584	0.463	0.978	0.475	0.648
3	0.617	0.410	0.382	0.635	0.572	0.488	0.775	0.544	0.471
4	0.654	0.654	0.654	0.968	0.968	0.968	0.801	0.801	0.801
5	0.897	1.001	0.847	0.683	0.583	0.496	0.964	0.954	0.750
6	0.497	0.497	0.497	1.000	1.000	1.000	0.743	0.743	0.743
7	0.670	0.670	0.670	0.987	0.987	0.987	0.898	0.898	0.898
8	0.849	0.849	0.433	0.862	0.862	0.373	0.838	0.838	0.412
9	0.896	0.603	0.896	0.912	0.450	0.912	0.936	0.427	0.936
10	0.492	0.492	0.492	0.946	0.946	0.946	0.861	0.861	0.861
11	0.513	0.556	0.340	0.778	0.652	0.428	0.867	0.719	0.443
12	0.716	0.646	0.578	0.685	0.585	0.498	0.628	0.547	0.473
13	0.379	0.481	0.481	0.558	0.904	0.904	0.670	0.812	0.812
14	0.709	0.731	0.646	0.634	0.572	0.489	0.683	0.601	0.513
15	0.719	0.719	0.588	0.910	0.910	0.337	1.000	1.000	0.361
16	0.544	0.544	0.544	0.956	0.956	0.956	0.827	0.827	0.827
17	0.554	0.423	0.423	0.486	0.882	0.882	0.719	0.750	0.750
18	0.461	0.431	0.854	0.661	0.568	0.474	0.530	0.471	0.656
19	0.835	0.498	0.835	0.905	0.452	0.905	0.870	0.413	0.870
20	0.674	0.674	0.674	0.951	0.951	0.951	0.924	0.924	0.924
Average values	0.660	0.593	0.614	0.788	0.748	0.696	0.810	0.710	0.683

4. Conclusions

In this article, a multi-objective optimal proportioning design of an anhydrous calcium sulfate whisker and polyester fiber composite modified asphalt mixture was carried out using the central composite concatenation design and grey correlation grade analysis methods. The effects of anhydrous calcium sulfate whisker content, polyester fiber content, and asphalt aggregate ratio on the hydrothermal properties of the asphalt mixture were investigated using rutting tests, retained Marshall tests, and freeze–thaw splitting tests. The conclusions are as follows:

(1) The central composite concatenation design and grey correlation grade analysis methods are suitable for the quantitative study of the optimum mix ratio design of

anhydrous calcium sulfate whisker and polyester fiber compound modified asphalt mixtures in hot–humid areas.

(2) The proportions of 11.8% anhydrous calcium sulfate whisker, 0.42% polyester fiber, and 4.1% asphalt aggregate can produce an asphalt mixture with better hydrothermal performance.

(3) The asphalt aggregate ratio has a greater influence on the hydrothermal performance, polyester fibers mainly affect the moisture susceptibility, and anhydrous calcium sulfate whiskers mainly affect the high-temperature properties of the asphalt mixture.

Recommendations: Feasibility research on the application of calcium sulfate whiskers as a renewable solid-waste resource in pavement materials has just begun. This paper studied the influence of calcium sulfate whiskers on the high-temperature deformation resistance and water damage resistance of an asphalt mixture and puts forward an optimization method for the mix ratio design of a modified asphalt mixture based on hygrothermal performance. However, the influence and mechanism of calcium sulfate whiskers on the low-temperature crack resistance and durability of asphalt mixtures, as well as the optimization method of the mix ratio design of modified asphalt mixtures considering physical and mechanical properties and road performance, need to be further studied.

Author Contributions: Conceptualization, T.F. and C.S.; formal analysis, T.F. and Q.S.; funding acquisition, C.S.; writing-original draft, T.F.; writing—review and editing, C.S. and S.H. All authors have read and agreed to the published version of the manuscript.

Funding: This study was funded by the National Natural Science Foundation of China, grant numbers 11972237 and 52378455; the Key R&D Project of Hebei Province, grant number 21373801D; and the Science and Technology Project of Hebei Education Department, grant number QN2023178.

Institutional Review Board Statement: Not applicable.

Informed Consent Statement: Not applicable.

Data Availability Statement: Data sharing not applicable. No new data were created or analyzed in this study.

Conflicts of Interest: The authors declare no conflict of interest.

References

1. Slebi-Acevedo, C.J.; Lastra-Gonzalez, P.; Pascual-Munoz, P.; Castro-Fresno, D. Mechanical performance of fibers in hot mix asphalt: A review. *Constr. Build. Mater.* **2019**, *200*, 756–769.
2. Wu, J.R.; Niu, Z.X.; Chen, H.Y. Effect of aging on low-temperature crack resistance and water stability of polyester fiber asphalt mixture. *Mater. Res. Express* **2022**, *9*, 015101. [CrossRef]
3. Zhang, K.; Luo, Y.F.; Li, Z.H.; Zhao, Y.L.; Zhao, Y. Evaluation of performance deterioration characteristics of asphalt mixture in corrosion environment formed by snow-melting agents. *J. Mater. Civ. Eng.* **2022**, *34*, 04021481. [CrossRef]
4. Behbahani, H.; Hamedi, G.H.; Gilani, V.N.M. Evaluating the surface free energy and moisture susceptibility of modified asphalt mixtures with nano hydrated lime under saturated conditions with deicer materials and distilled water. *J. Indian Chem. Soc.* **2020**, *97*, 791–798.
5. Hong, R.B.; Wu, J.R.; Cai, H.B. Low-temperature crack resistance of coal gangue powder and polyester fibre asphalt mixture. *Constr. Build. Mater.* **2020**, *238*, 117678. [CrossRef]
6. Zhao, X.W.; Yan, K.Z.; Yang, S.; Peng, H.Y. Laboratory Research on the Properties of Warm Amorphous Poly Alpha Olefin–Modified Asphalt Mixture Using Sasobit and Deurex. *J. Mater. Civ. Eng.* **2018**, *30*, 04018076. [CrossRef]
7. Ahmedzade, P.; Tigdemir, M.; Kalynocuoglu, S.F. Laboratory investigation of the properties of asphalt concrete mixtures modified with TOP-SBS. *Constr. Build. Mater.* **2007**, *21*, 626–633. [CrossRef]
8. Yang, B.; Liang, P.; Xie, J.; Zen, X. Study on mechanical property of large particle size modified asphalt mixture with multipore. *Mater. Res. Innov.* **2014**, *18*, 811–815. [CrossRef]
9. Zhai, R.X.; Ge, L.B.; Li, Y. The effect of nano-$CaCO_3$/styrene-butadiene rubber (SBR) on fundamental characteristic of hot mix asphalt. *Road Mater. Pavement Des.* **2018**, *2018*, 1006–1026. [CrossRef]
10. Gong, Y.F.; Bi, H.P.; Liang, C.Y.; Wang, S.R. Microstructure analysis of modified asphalt mixtures under freeze-thaw cycles based on CT scanning technology. *Appl. Sci.* **2018**, *8*, 2191. [CrossRef]
11. Yan, K.Z.; Wang, S.Q.; Ge, D.D.; Chen, J.H.; Tian, S.; Sun, H. Laboratory performance of asphalt mixture with waste tyre rubber and APAO modified asphalt binder. *Int. J. Pavement Eng.* **2022**, *23*, 59–69. [CrossRef]

12. Zhang, H.T.; Gong, M.Y. Study on durability of composite-modified asphalt mixture based on inherent and improved performance. *Constr. Build. Mater.* **2018**, *179*, 539–552. [CrossRef]
13. Cheng, Y.C.; Yu, D.; Gong, Y.F.; Zhu, C.F.; Tao, J.L.; Wang, W.S. Laboratory evaluation on performance of eco-friendly basalt fiber and diatomite compound modified asphalt mixture. *Materials* **2018**, *10*, 2400. [CrossRef]
14. Hong, Z.; Yan, K.Z.; Wang, M.; Yuan, J.; Ge, D.D.; Liu, J. The laboratory performance of asphalt mixture with thermoplastic polyurethane (TPU) and amorphous poly alpha olefin (APAO) compound modified asphalt binder. *Constr. Build. Mater.* **2022**, *349*, 128742. [CrossRef]
15. Fan, T.T.; Si, C.D.; Zhang, Y.; Zhu, Y.F.; Li, S. Optimization design of asphalt mixture composite reinforced with calcium sulfate anhydrous whisker and polyester fiber based on response surface methodology. *Materials* **2023**, *16*, 594. [CrossRef] [PubMed]
16. Ahmed, I.N.; Nicholas, T.; Tony, P. Optimizing the mix design of cold bitumen emulsion mixtures using response surface methodology. *Constr. Build. Mater.* **2016**, *104*, 216–229.
17. Moghaddam, T.B.; Soltani, M.; Karim, M.R.; Baaj, H. Optimization of asphalt and modifier contents for polyethylene terephthalate modified asphalt mixtures using response surface methodology. *Measurement* **2015**, *74*, 159–169. [CrossRef]
18. Yan, W.; Ou, Y.J.; Xie, J.; Huang, T.; Peng, X.H. Study on properties of bone Glue/polyurethane composite modified asphalt and its mixture. *Materials* **2021**, *14*, 3769. [CrossRef]
19. Cheng, Y.C.; Li, L.D.; Zhou, P.L.; Zhang, Y.W.; Liu, H.B. Multi-objective optimization design and test of compound diatomite and basalt fiber asphalt mixture. *Materials* **2019**, *12*, 1461. [CrossRef]
20. Du, J.C.; Kuo, M.F. Grey relational-regression analysis for hot mix asphalt design. *Constr. Build. Mater.* **2011**, *25*, 2627–2634. [CrossRef]
21. Lyu, Z.H.; Shen, A.Q.; Qin, X.; Yang, X.L.; Li, Y. Grey target optimization and the mechanism of cold recycled asphalt mixture with comprehensive performance. *Constr. Build. Mater.* **2019**, *198*, 269–277. [CrossRef]
22. Slebi-Acevedo, C.J.; Pascual-Munoz, P.; Lastra-Gonzalez, P.; Castro-Fresno, D. Multi-response optimization of porous asphalt mixtures reinforced with aramid and polyolefin fibers employing the CRITIC-TOPSIS based on Taguchi methodology. *Materials* **2019**, *12*, 3789. [CrossRef] [PubMed]
23. Slebi-Acevedo, C.J.; Lastra-Gonzalez, P.; Calzada-Perez, M.A.; Castro-Fresno, D. Effect of synthetic fibers and hydrated lime in porous asphalt mixture using multi-criteria decision-marking techniques. *Materials* **2020**, *13*, 675. [CrossRef] [PubMed]
24. *JTG E20*; Standard Test Methods of Bitumen and Bituminous Mixtures for Highway Engineering. Highway Science Research Institute, Ministry of Transport: Beijing, China, 2011. (In Chinese)
25. Wang, Z.J.; Wang, Q.; Ai, T. Comparative study on effects of binders and curing ages on properties of cement emulsified asphalt mixture using gray correlation entropy analysis. *Constr. Build. Mater.* **2014**, *54*, 615–622. [CrossRef]
26. *JTG F40*; Technical Specification for Construction of Highway Asphalt Pavements. Highway Science Research Institute, Ministry of Transport: Beijing, China, 2004. (In Chinese)

materials

MDPI

Review

Advanced Geopolymer-Based Composites for Antimicrobial Application

Gabriel Furtos [1,*], Doina Prodan [1,*], Codruta Sarosi [1], Marioara Moldovan [1], Michał Łach [2], Mykola Melnychuk [3] and Kinga Korniejenko [2,*]

[1] "Raluca Ripan" Institute for Research in Chemistry, Babes-Bolyai University, 30 Fantanele Street, 400294 Cluj-Napoca, Romania; codruta.sarosi@gmail.com (C.S.); mmarioara2004@yahoo.com (M.M.)
[2] Department of Materials Engineering, Faculty of Materials Engineering and Physics, Cracow University of Technology, 37 Jana Pawła II Av., 31-864 Cracow, Poland; michal.lach@pk.edu.pl
[3] Department of Materials Science, Lutsk National University, 75 Lvivska, 43000 Lutsk, Ukraine; m.melnychuk@lntu.edu.ua
* Correspondence: gfurtos@yahoo.co.uk (G.F.); doina.prodan@ubbcluj.ro (D.P.); kinga.korniejenko@pk.edu.pl (K.K.)

Abstract: In most studies about geopolymeric materials used in construction, the antibacterial properties of the building materials are treated as secondary features. Today, antimicrobial properties are a key feature in many building applications. The main objective of this article is to summarize the state-of-the-art in the area of design, development, and applications of nanoparticles as additives to geopolymer composites used in construction to improve their physical mechanical properties and induce a potential antibacterial effect, protecting them against alkali-resistant bacteria. On the basis of the literature and authors' experience, the most important methods of obtaining especially the porous geopolymers, of nanomaterials used as additives, with potential antibacterial effect but also the potential mechanism of action against bacterial development were presented. The main findings show that using graphene oxide (GO) in geopolymer composites, but also other nanoparticles such as silver (Ag), zinc oxide (ZnO), silica (SiO_2), titanium dioxide (TiO_2), copper (Cu) as additives, is an effective way to induce a potential antibacterial effect and to improve the physical and mechanical properties in building materials.

Keywords: nanoparticles; geopolymers; graphene oxide; antibacterial; building materials

Citation: Furtos, G.; Prodan, D.; Sarosi, C.; Moldovan, M.; Łach, M.; Melnychuk, M.; Korniejenko, K. Advanced Geopolymer-Based Composites for Antimicrobial Application. *Materials* **2023**, *16*, 7414. https://doi.org/10.3390/ma16237414

Academic Editor: Daniela Caschera

Received: 16 October 2023
Revised: 14 November 2023
Accepted: 21 November 2023
Published: 29 November 2023

1. Introduction

Geopolymers are inorganic polymers obtained by the polycondensation of precursors based on silicon dioxide and aluminum oxide, in a strongly alkaline environment [1]. Although, in the beginning, natural precursors (kaolin, metakaolin, silica fume, and calcined clays) were used to obtain geopolymers, after a while, industrial residues also started being used (fly ash, clay-based slag, etc.). Geopolymers are obtained through the ionic interaction that takes place following the dissolution of Al, Si, and oxygen from the precursors in an alkaline environment by breaking the covalent bond between their atoms. The negatively charged Al (III) attracts alkaline cations (Na^+, Ca^{2+}, K^+, etc.), followed by the processes of condensation, coagulation, gelation, and polycondensation in three-dimensional networks of silicon and aluminum. The properties of the geopolymer depend on the composition and reactivity of the precursors and, respectively, on the Si/Al ratio of the hydrolyzed species. When reactive Si is predominant, it leads to a larger amount of alkaline aluminosilicate gel, and the Al content contributes to the formation of the network and the chemical structure of the geopolymer [2].

Geopolymers with dense structures have emerged as an alternative to Portland cement, for minimizing or eliminating greenhouse gases. They give building materials high early mechanical strength and good resistance to aggressive atmospheres [3]. Geopolymers with

porous structures are materials that can be subjected, especially in a humid environment, to microbial degradation. In dry environments, geopolymers have some antimicrobial protection due to the alkali metal ions in their composition. However, high humidity raises serious problems, contributing to the degradation of geopolymer surfaces or geopolymer concrete by providing a favorable environment for the development of alkali-resistant bacteria, such as those that use sulfur oxidation as a source of energy [4].

The porous geopolymers facilitate antibacterial protection, thanks to the ion exchange of free alkalis in their network, but they can also contribute, depending on the added components, to obtaining a photoactive effect and taming the pH by releasing hydroxyl ions. The properties of porous geopolymer materials can be optimized by adding filler particles, reinforcing components, or those with antibacterial potential, leading to hybrid materials with a synergistic effect by combining the properties of the added components [5].

There is a growing interest in the development of geopolymer materials with antimicrobial protection, both to ensure their durability over time and also due to the possibility of their use in environments with high humidity. The addition of antimicrobial additives can be carried out either by directly adding them to the composition (paste) of the materials (mortar, cement, concrete) or by covering their surfaces. The nature of antimicrobial additives can be both inorganic and organic. Inorganic additives (Ag, ZnO, CuO, etc.) can be added in the form of nanoparticles, ensuring antimicrobial protection against a significant number of microorganisms [6]. Figure 1 highlights the different modalities of the nanoparticles from the surface of the materials to fight the bacteria.

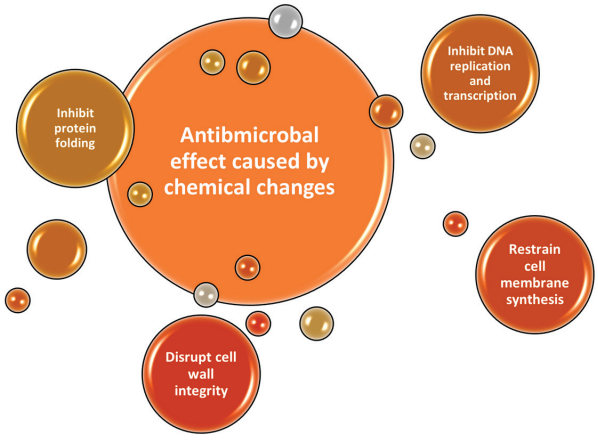

Figure 1. Schematic image of antimicrobial mechanism at surface of materials, caused by ion exchange.

Due to their high surface-volume ratio and small dimensions, nanoparticles can be added to the geopolymer matrix, creeping into the pores that form between the larger particles of the majority precursor, providing a filling effect with the help of the alkaline activator [7,8]. Several studies have evaluated the influence of nanomaterials on the properties of geopolymer-based mortars and concretes, both fresh and hardened, in different conditions [9,10]. Most of the reported data are focused on the evaluation of the mechanical properties of building materials based on geopolymers, cured at ambient temperatures [11]. Some authors [12] have investigated the antibacterial effect of a metakaolin-based geopolymer with zinc oxide (ZnO) nanoparticles mixed with sodium hydroxide (NaOH), reporting high mechanical resistance and antibacterial effect. Apart from ZnO, the addition of silver (Ag), titanium oxide (TiO_2), or copper oxide (CuO_2) nanoparticles can induce a potential antibacterial and antifungal effect [13,14]. Although these nanoparticles alone can induce an antibacterial effect, several studies have demonstrated that combining them with a geopolymer or with graphene oxide [15] can contribute to synergistic antibacterial activity. The recovery of industrial waste, along with metal oxides or graphene, by including them

in the composition of construction materials, can represent a sustainable and cheap alternative way to obtain durable construction materials with improved mechanical properties and potential antibacterial effects. The aims of this review refer to the obtaining methods of nanoparticles, the factors that can influence the obtaining methods, the influence of the added quantities on the properties of the formulated materials, and the potential antibacterial mechanism that nanoparticles can introduce into the materials to which they are added.

2. Methods of Obtaining Geopolymers

The denser structure of geopolymers is generally linked to a higher silica content. The abundant silica in the geopolymeric matrix leads to the formation of a denser network, with low porosity and smaller pore size. Therefore, this structure leads to low permeability and an increase in compression resistance. The addition of cellulose or cotton fibers to the composition of geopolymers can also have a good influence on their properties, increasing the mechanical resistance even more [11]. Geopolymers have the ability to stabilize or immobilize certain pollutants or heavy metals and to filter water. Moreover, their adsorption properties help them to stabilize nanoparticles with antimicrobial potential when added to their composition. The geopolymer formulation with a potential antimicrobial effect can prevent the deposition of microorganisms on their surface, preventing microbial degradation [4]. Zhang et al. [5] developed a synthesis of the literature regarding the methods of obtaining other types of geopolymers, with a porous structure. However, porosity and water absorption can lead to a decrease in mechanical resistance and predispose the material to bacterial degradation. Certain inconveniences can be easily solved by adding reinforcing particles or other additives, for example, hydrophobic or antibacterial additives, depending on the scope of application and the expected characteristics. The methods of obtaining porous geopolymers have been classified into two groups: traditional methods and new methods under development. Known traditional methods are: direct foaming and the addition of light or porous filling. One of the most advantageous methods is the use of 3D printing technology due to the possibility of obtaining porous geopolymers with adapted shapes and controlled pore sizes and also due to its flexibility and low costs. Another method of obtaining porous geopolymers is through suspension solidification in order to obtain porous geopolymeric spheres with metakaolin and fly ash for pH buffering applications. The study reports that a higher content of fly ash in geopolymers leads to higher alkaline leaching. The innovative character of these spheres is that they can be handled and collected easily, ensuring gradual and prolonged leaching that no longer requires the addition of hydroxide for continuous pH regulation. This fact could also lead to antibacterial protection including in anaerobic environments [16]. Over time, other methods have also been developed, such as post-grafting, used for the functionalization of porous geopolymers, or the combination of zeolites with porous geopolymers, obtaining superior properties such as an increase in mechanical properties, a large specific surface area, porosity, etc. Other methods are based on the introduction of various fibers (basalt, PVA, polypropylene, cotton, cellulose, etc.) into the composition of porous geopolymers, which can lead to the improvement of mechanical properties [5].

3. Nanoparticles Used as Additives in Geopolymers

The use of nanoparticles as additives aims to improve some characteristics of geopolymeric materials. In order to obtain the expected effect, it is very important that these nanoparticles are dispersed uniformly in the mass of the material to avoid agglomerations that could lead to the deterioration of the material's properties. The most widely used dispersion techniques are ultrasonication, mechanical stirring, or ball milling. Water is a known dispersion medium for the uniform distribution of additives in the material. To increase the homogeneity of the additives by avoiding the formation of agglomerates, surfactants and organic additives can be added to the additives. In order to improve the dispersion of nanoparticles used as additives, it is important that there is a sufficient num-

ber of hydrophilic groups in the mixture. These lead to a decrease in the surface tension of water, preventing the formation of agglomerates. From the literature, it appears that certain surfactants used to improve the dispersion can have a negative influence on some additives, namely, on the hydration kinetics of the geopolymer. In this sense, a more appropriate choice is the use of superplasticizers to improve dispersion. It was reported that the 10:1 wt.% ratio of dispersant/nanomaterial led to a reduction in the amount of water used in that study [17]. For this study, we referred to graphene oxide, Ag, Cu, silica, and ZnO, tracking which proportion is more effective. We also find which factors of the method of obtaining can contribute to providing a potential antibacterial effect and to improving the mechanical properties or other properties in the materials in which they are introduced.

3.1. Graphene Oxide (GO)

Graphene oxide is a versatile material with useful properties for many applications. It is extremely light, having a large specific surface area and good electrical and thermal conductivity. Due to the large specific surface area, GO covers a large contact area with cementing materials, forming a strong network within the cement matrix and ensuring strong adhesion and a dense structure [18]. There are many methods used to obtain GO, which have improved over time. However, each of them has certain advantages and disadvantages. Hummers' method, e.g., which is based on the use of strong oxidants such as $KMnO_4$ and $NaNO_3$ to oxidize graphite in an acidic environment, has limited homogeneity. Another method is chemical exfoliation in which graphite layers are separated by oxidation or with the help of solvents. The disadvantage is the toxicity of hydrazine, the most commonly used in this method. The electrochemical exfoliation: uses graphite as a sacrificial electrode, together with exfoliating electrolytes such as: HBr, HCl, HNO_3, and H_2SO_4. The disadvantage of this method is that the obtained graphene has many defects. This method was improved by adding KOH to H_2SO_4 (slower oxidation) and combining electrochemical exfoliation with spark plasma sintering (voltage below 10 V), adding surfactants; this has the advantage of being able to obtain graphene on an industrial scale, low price, efficient, environmentally friendly. The arc discharge method has the advantage of large-scale production, graphene has fewer defects, and it is a simple and cheap method [19]. Due to the functional groups with oxygen (hydroxy, epoxy, carboxy) present on the edges and on the surface of the graphene sheets, they can be easily synthesized by chemical oxidation and graphite exfoliation, and they can also be easily functionalized with CuO [20], fly ash, silver, or ZnO [21] Figure 2.

In another study, experimental mortars with potential use in the rehabilitation of heritage buildings were used as additives as 5% GO powder mixtures with ZnO and TiO_2, and 5% GO powder mixtures with fly ash and Ag. The best antibacterial effect was reported for the mortar with the GO powder mixture with ZnO and TiO_2 as additives. This result is due to the fact that the concentration of Ag in the additive was much lower than that of Zn and Ti. However, the result was very encouraging, with the values of the diameter of the bacterial inhibition zone being very close in both cases [22]. The photonic properties of GO can improve the photocatalytic properties of other materials [23]. Long et al. [24] added different percentages of GO (0.05 wt.%, 0.1 wt.%, and 0.2 wt.%) to cement using a water-cement ratio (W/C) of 0.66. After 28 days, the measured flexural strength of the mortar samples was higher with 16 wt.%, 27 wt.%, and 41 wt.% compared to the mortar without GO. Moreover, the compressive strength increased by approximately 7%, 10%, and 10%, respectively. In another study, Wang et al. [25] reported that a cement paste with a W/C ratio of 0.40 in which different wt.% percentages of GO were added (0.02 wt.%, 0.04 wt.%, 0.06 wt.%, and 0.08 wt.%) increased the values of the compressive and bending strengths after 1, 3, 7, and 28 days. By adding 0.02 wt.% GO, the strengths were only slightly higher compared to the sample without GO. By adding 0.04 wt.% GO, after 28 days, the compressive and flexural strengths increased by 20% and 23%, and for 0.08 wt.% GO, increases of 16% and 27 wt.% were recorded.

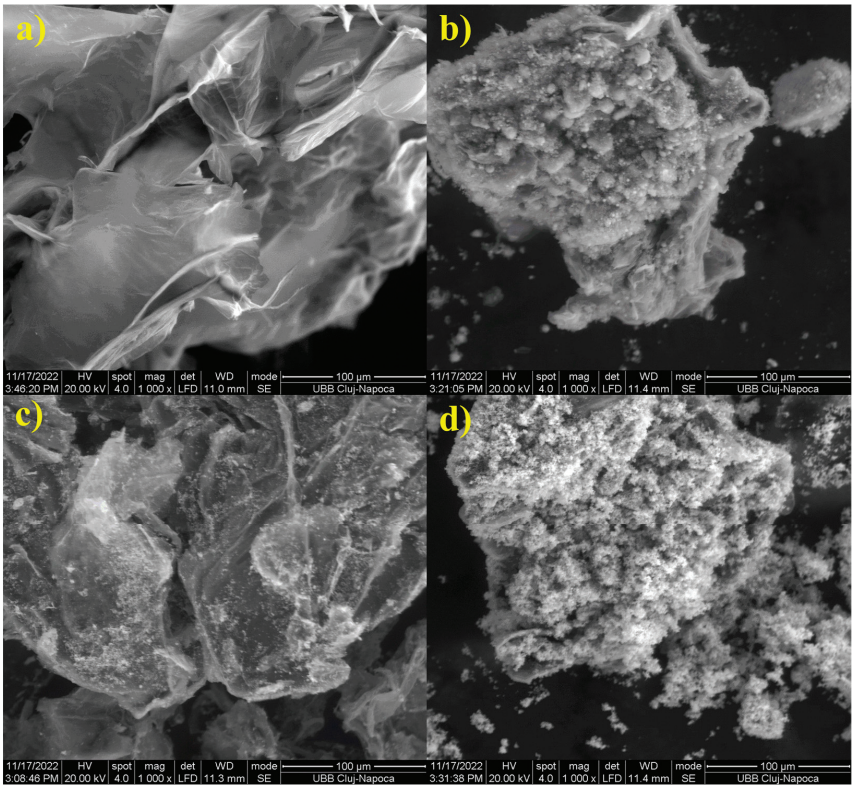

Figure 2. SEM images of the GO: (**a**) GO; (**b**) GO with fly ash; (**c**) GO with silver; (**d**) GO with ZnO at ×1000 magnifications.

3.2. Silver (Ag)

The antibacterial effect of Ag nanoparticles has been known since ancient times. This effect is due to silver ions (Ag+), which once released, prevent the formation of an enzyme like adenosine triphosphate (ATP) through energy storage, but also through the replication of bacterial DNA, thus inducing bacterial death [14]. There are several physical, chemical, or biological methods to obtain Ag nanoparticles. By ball milling, laser ablation, or sputtering [26], large quantities of nanoparticles can be obtained, but depending on the chosen technique, the obtained nanoparticles can show a higher purity. The disadvantages of this method include high energy consumption, expensive equipment and high pressure and temperature [27]. Electrochemical reduction, the sol-gel method, or chemical reduction, besides being considered cheap methods, require only a metal precursor, a reducing agent, and a stabilizing agent. They are simple to perform, but also controllable, leading to the obtaining of spherical nanoparticles [28]. The disadvantage of these chemical methods would be the pollution generated from the use of toxic reagents or solvents [29]. Most often, nanoparticles are obtained by the sol-gel method. In the first stage, the goal is to obtain a stable metal precursor through hydrolysis. The condensation leads to obtaining a metal hydroxide network. These stages are influenced by a series of parameters like type of solvent, pH, temperature, catalyst, additives, etc. Finally, very fine particles with the desired crystallinity are obtained by drying and heating [30]. The syntheses that use natural extracts as reagents [31] to obtain Ag nanoparticles ensure high yield and stability [32] and have low costs due to the variety of natural products.

Geopolymer nanocomposites can also be used for water treatment. The addition of 0.05 wt.% silver nanoparticles and hydrogen peroxide foam to a composite based on

aluminosilicate (bentonite) for water filters against bacteria had a low efficiency against coliphages. However, the efficiency increased against *E. coli* and *enterococci* bacteria [4]. Some characteristics of porous geopolymers with Ag or Cu additives (0.05 wt.%) were compared and introduced, using several methods, into geopolymers, with the aim of obtaining water filters with potential disinfectant or catalytic properties. The compressive strength values for the samples obtained by three different methods were: 16 MPa (by 3D printing), 1 MPa (by direct foam), and 10 MPa (granulation). The amount, state of oxidation, and stability of the additives were influenced by both the filter preparation method and the additive impregnation method. The largest amount of Ag was obtained by the granulation method in which Ag was introduced by immersing the filter in a colloidal Ag solution, compared to adding it to the fresh paste [33].

3.3. Zinc Oxide

Synthesis of ZnO nanoparticles by the sol-gel technique has the advantage of low cost and diverse applicability, improving the properties of many polymers [34]. Like Ag, Zn nanoparticles can also be obtained by biological methods which are more environmentally friendly. Bhuyan et al. [35] obtained spherical nanoparticles of ZnO, using *Azadirachta indica* (Neem) leaf extract, which showed good antimicrobial activity against *Staphylococcus aureus*, *Streptococcus pyogenes*, and *Escherichia coli*. In general, the production of nanoparticles is observed by the changing color of the reaction mixture [36] and can be confirmed by Fourier Transform Infrared Spectroscopy (FTIR), identifying the biomolecules involved in the reaction [37]. In their study, Singh et al. [38] evaluated the antimicrobial effect of cement with additions of 0.5, 10, and 15 wt.% ZnO against *Escherichia coli*, *Bacillus subtilis*, and *Aspergillus niger*. It was observed that the antibacterial and antifungal effects of cement increased with the increase in ZnO concentration and were enhanced by sunlight. Wang et al. [39] investigated the antimicrobial effect of high-performance concrete with ZnO addition and found that the antibacterial effect was 100% against *Escherichia coli* and 54.61% and 99.12%, respectively, against *Staphylococcus aureus*. In the literature, there are reports about the addition of supplements with antimicrobial properties to building materials (concrete, mortar, bricks, etc.), which do not significantly affect the essential properties of the materials [40].

3.4. Silica Nanoparticles and Silica Fume

Silica nanoparticles can be obtained by dry or wet methods. In the dry method category, the gas phase method and the arc method can be mentioned. Some wet methods include precipitation, sol-gel, microemulsion, and high-gravity reaction [41]. Stefanidou and Karazou [42] tested bricks treated with linseed oil, silane/siloxane, and alcosiloxane modified with 1–1.5 wt.% silica nanoparticles and demonstrated that the alcosiloxane and silica nanoparticles protect the bricks, providing a high resistance to water absorption and an increase in their durability. Zhang et al. [43] studied the influence of different nanoparticles introduced into the mortar and investigated the resistance and hydration mechanism for the cement mortar. It was reported that the added nanoparticles, formed bonds with the matrix, leading to an increase in the strength of the samples and a decrease in the initial and final setting time of the matrix. Comparing nano-silica with silica fume, a study reported that only 75 wt.% of silica fume was consumed after 90 days [43], while nano-silica, due to its high specific surface, can play a nucleation role in the process of cement hydration, accelerating this process and improving early strength [41]. By adding nano-silica, a denser microstructure can be obtained, due to the penetration of nanoparticles into the pores of the material making it possible to effectively control the release of calcium hydroxide, which can influence the corrosion of concrete, thus increasing its strength and durability [43,44]. Wang et al. [45] believed that the graphene nanosheets can accelerate the hydration process with the formation of a compact microstructure.

3.5. Copper

As in the case of Ag or Zn, Cu nanoparticles can be obtained by physical, chemical, or biological methods. The major problem is that the Cu particles tend to oxidize in the air, resulting in an agglomeration of the particles. To avoid this shortcoming, the Cu nanoparticles are obtained in an inert gas atmosphere [46]. Moreover, to avoid oxidation, protective polymers or surfactants can be used [47].

Using chemical methods, the size and shape of the particles can be controlled by adjusting the pH and the ratio between the electrolyte and the surfactant with the help of a protective agent, varying the type of solvent, etc. However, obtaining large quantities is not possible. An alternative to this method is needed, which should require cheaper reagents and an easier reaction condition. Therefore, biological methods can be considered a safer alternative, based on bio-organisms or plants requiring ecological reagents [48]. They are considered to be the most convenient methods because, in addition to plant extracts, they use bacteria, fungi and algae, and phytochemicals from plants, which act both as reducing agents and as stabilizers [46]. In the case of mortar mixed with copper powder, the compressive and flexural strengths were higher than those of the reference mortar [48]. Table 1 shows the most used methods of obtaining nanoparticles used as additives in geopolymers and the effect they have on some properties of the geopolymers in which they are introduced.

Table 1. The most used methods of obtaining nanoparticles; nanoparticles' effect on geopolymer properties.

NPs	Obtaining Methods	Sources	Effects on Geopolymers	Sources
GO	Hummers' method Chemical exfoliation Electrochemical Exfoliation Arc discharge	[19]	Strong adhesion and a dense structure Improve the photocatalytic properties Induce an antibacterial effect Increasing flexural and compression resistance	[18] [23] [22] [24,25]
Ag	Ball milling Electrochemical reduction Sol-gel method, Chemical reduction	[26,28]	Antibacterial properties against *E. coli* and *enterococci bacteria* The mechanical strengths depend on the NP addition mode	[4] [33]
ZnO	Sol-gel technique Biological method	[34,35]	Antimicrobial effect against *Escherichia coli*, *Bacillus subtilis*, *Aspergillus niger* and *Staphylococcus aureus*	[35,38,39]
Silica NPs and silica fume	Gas phase method Arc method Precipitation Sol–gel method Microemulsion, High-gravity reaction	[41]	Resistance to the water absorption of the bricks Decrease in the initial and final setting time of the matrix Preventing corrosion and increasing strength and durability of concrete	[42] [43] [43,44]
Cu	Physical methods Chemical methods Biological methods	[46,48]	Increasing compression and flexural resistances	[48]

4. The Antibacterial Mechanism of Nanoparticles Used as Additives in Building Materials

The addition of Ag, Cu, TiO_2, ZnO, or GO nanoparticles in the geopolymer matrix can lead to an increase in resistance to compression, dehumidification, and a potential antibacterial effect. Bacteria develop on the surface of any material if they have favorable conditions such as a suitable temperature, a source of nutrients that can be absorbed and decomposed by enzymes to provide the energy necessary for bacterial growth, a suitable pH, and a gaseous environment. At a pH value between 12 and 13, bacteria will not grow

on the surface of the freshly prepared material. However, there are environments, such as sewage, where, after a while, an increased concentration of H_2S accumulates. In the case of sewer pipes, it was found that sulfate ions deposited on the material in an anaerobic environment. These are reduced by sulfate-reducing bacteria, leading to the formation of H_2S. In contact with the pipe walls, H_2S is oxidized to H_2SO_4 by sulfur-oxidizing bacteria in the air. Figure 3 presents a case of a porous geopolymer, with graphene oxide as an additive used for sewage, which, in a closed environment, suffered an acid attack. Especially in the case of sewers where there is water and the bacteria have a large amount of nutrients, concrete corrosion is more serious. The nutrients of sulfur-oxidizing bacteria are provided by heterotrophic fungi that break down organic substances with sulfur even in a large pH range. Through the action of microorganisms, other acids can be produced, such as HNO_3, acetic acid, or oxalic acid, which can also lead to concrete corrosion. When the pH inside drops below 9, microorganisms multiply. These microorganisms will provide acid, and the pH can drop even more [49]. Around a pH of 4, there is a massive bacterial proliferation, leading to the worsening of concrete corrosion. The advantage of geopolymer concrete compared to plain concrete is that the microorganisms have a larger volume than the pore size, the material being more compact, and the acid metabolism takes place only on the surface of the material, making the corrosion process more difficult [50]. Data from the literature report that physical contact can cause the destruction of bacteria, through the ion exchange mechanism. The divalent cations in the outer wall of the cell membrane can be dislocated by the cations on the surface of the material loaded with antimicrobial additives, leading to cell death. The authors are of the opinion that the sharp tips that come out of the surface of a material (for example, graphene oxide has sharp edges) can pierce the cell wall, causing the leakage of the cytoplasm and finally cell death [51]. The mechanism of inducing the antibacterial effect depends on the type, shape, and size of the added nanoparticles and is explained below.

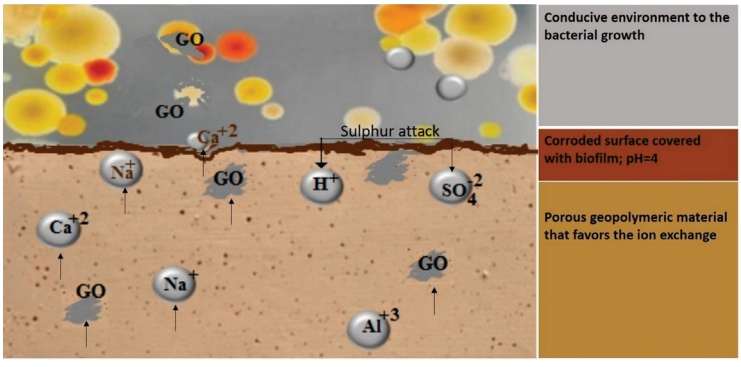

Figure 3. Schematic representation of the surface of the geopolymeric material after acid attack followed by microbial action and the potential antibacterial mechanism of the graphene oxide nanosheets.

4.1. Graphene Oxide

It is supposed that one of the mechanisms for the antibacterial effect is of a mechanical nature. Due to the shapes of the graphene nanosheets, the "sharp" edges, could section the cell membrane, leading to the leakage of the intracellular matrix, and finally, to its death. Another explanation could be that larger sheets of GO can wrap the bacteria, preventing their proliferation. A study proposes, that the antibacterial activity is not due to reactive oxygen species (ROS) but to the transfer of electrons between the bacterial membrane and the graphene surface [52]. It is believed that oxidative stress does not depend on ROS because graphene acts as an electron acceptor and its surface is important in inducing the antibacterial effect and not its edges. Therefore, GO does not kill the bacteria but inactivates them [53]. However, there could be some doubts: the possibility that the GO sheets are too

thick and their edges could not penetrate the bacterial membrane or if the rigidity of the nanosheets does not allow them to wrap the bacteria. For this, an experiment was carried out in which the Langmuir–Blodgett technique was used [54]. The GO sheets, including the edges, were immobilized on a substrate, and then the antimicrobial test was performed. It was concluded that the antimicrobial mechanism of GO depended on the surface of the GO sheets, which can lead to bacterial inactivation in different ways, and does not depend at all on their edges [55].

There are studies that have demonstrated the antibacterial effect of graphene oxide [21]. Figure 4 shows the antibacterial effect of different graphene powders: GO, GO-Ag, GO-Zn, GO-APTES, GO-Ag-APTES, and GO-Zn-APTES against five bacterial strains (*Streptococcus mutans* ATCC 25175, *Porphyromonas gingivalis* ATCC 33277, *Enterococcus faecalis* ATCC 29212, *Escherichia coli* ATCC 25922, and *Staphylococcus aureus* ATCC 25923) by measuring the zone of inhibition after 18–24 h incubation at 37 °C.

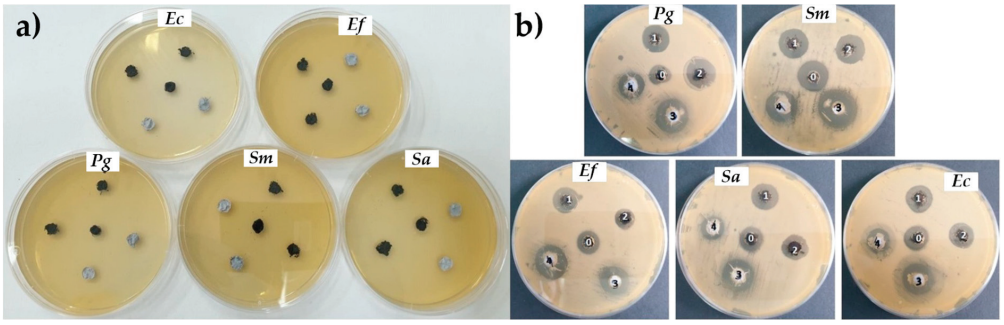

Figure 4. Disk diffusion assay on *Porphyromonas gingivalis* (Pg), *Streptococcus mutans* (Sm), *Staphylococcus aureus* (Sa) and *Escherichia coli* (Ec) for the GO powders [21].

4.2. Silver

The opinion of some authors is that Ag can induce an antibacterial effect in three ways. It is supposed that the Ag nanoparticles can penetrate the outer membrane and then surround the inner membrane, increasing its permeability favoring the leakage of the cell content and then death [56]. On the other hand, the Ag nanoparticles can cause damage due to interactions with sulfur proteins, located in the cell wall, leading to the rupture of the cell wall. Another possibility of inducing the antibacterial effect is that the Ag nanoparticles can penetrate and cross the cell membrane, entering the cell, where they could interact with the DNA and the proteins, disturbing the structure and functions of the cell. On the other hand, Ag nanoparticles can interact with enzymes through thiol groups, inducing reactive oxygen species, leading to the impairment of intracellular functions, and inducing apoptosis. The third way can appear at the same time as the other two and refers to the release of ions from Ag nanoparticles. Ag ions can interact with cellular components affecting cellular metabolism and genetic material [57]. Silver nanoparticles are also used by combining with carbon fibers against bacteria and other harmful microorganisms [58]. This composition is sometimes enriched with organic compounds, such as antibiotics (gentamicin) to improve antimicrobial properties. One of the popular antibacterial additives is also silver salts, especially silver nitrate [58]. One study [33] reported adding a composite foam prepared with 0.05% silver nanoparticles as an additive, to geopolymers based on bentonite for the purpose of water disinfection. In time, the effect against *coliphages* decreased, but against *E. coli* and *enterococci* bacteria, it was significant.

4.3. Zinc Oxide (ZnO)

For zinc, the most accepted antibacterial theory is based on the generating of reactive oxygen species (ROS). Active oxygen occurs from reducing oxygen O^{2+} $e^{-} \rightarrow {}^{*}O^{2-}$ and the most common ROS are peroxides, hydroxyl radicals, and singlet oxygen. Because OH-

cannot penetrate the cell membrane; is placed on its walls, disrupting cellular functions by destroying the membrane. Hydrogen peroxide (H_2O_2) can penetrate the cell membrane, causing its destruction and the destruction of DNA, which has a bactericidal role [59]. By releasing it from ZnO, Zn^{2+} can destroy the cell membrane leading to the inhibition of cell proliferation due to the denaturation of proteins and the disruption of the cellular energy mechanism by disturbing the electron transport. Although there are numerous reports in the literature attributing the potential antibacterial effect of Zn after catalysis, it was demonstrated that a strong antibacterial effect was also obtained in dark conditions [60]. The opinion of some researchers is that the antibacterial effect of Zn does not increase with the rise in Zn^{2+} concentration. It can be assumed that the destruction of bacteria can take place due to electrostatic attraction between positively charged Zn^{2+} and the surface of the cell membrane, which is negatively charged, by disturbing the charge balance of the membrane surface [61].

4.4. Silica (SiO_2)

In order to find an alternative for Portland cement in concrete, a geopolymer based on fly ash was proposed, improved by the addition of ZnO nanopowder (rods) covered with spherical silica nanoparticles in order to protect against corrosion, to improve mechanical resistance, and to fight against: *E. coli*, *S. aureus* and *A. niger*. The tests showed that the geopolymer with Zn-SiO_2 nanohybrid powder has a bactericidal action rather than a bacteriostatic one. The cells that were treated with the Zn-SiO_2 nanohybrid generated an approximately four times higher ROS level compared to the reference for the microbial strains. Although the effect against microbial species was mainly due to Zn, it has been proven that the combination of the proposed nanohybrid is successful both for protection against chemical corrosion and against biological corrosion. High mechanical strengths were also recorded [62].

4.5. Copper (CuO)

Like Ag, the Cu ions from nanoparticles can interact with the DNA and proteins, disrupting the cellular biochemical structure and process. A study [63] proposed the obtaining of cement mortars for the treatment of waste water and for the inhibition of bacterial growth. They obtained Cu-Ti alloys in atomic ratios: 35:65, 50:50 and 65:35 by ball grinding. The authors of this study investigated the influence of different concentrations of amorphous Cu-Ti alloy (from 0.3 to 0.9 wt.%) added to mortars, together with 0.5% superplasticizer. The Cu-Ti alloy (35:65) has the finest particles, leading to an increase in the mechanical properties of the mortar. The mortar with 0.9 wt.% Cu-Ti alloy (50:50) recorded the best antibacterial effect. Another study [64] showed that cell filamentation is caused by membrane depolarization, under the influence of Cu nanoparticles, more precisely under the influence of Cu^{2+} ions, resulting from the oxidation of the metallic Cu atoms of the nanoparticles. The destruction of cells is caused by the production of ROS under the action of nanoparticles, leading to DNA degradation, together with lipid peroxidation and protein oxidation. Table 2, there are shortly summarizes the most popular theories about the antimicrobial effects of selected nanoparticles.

Table 2. The main antibacterial mechanism for selected nanoparticles.

Nanoparticle	Main Antibacterial Mechanism	Sources
GO	Larger sheets of GO can wrap the bacteria; "sharp" edges, could destroy the cell membrane.	[52,53,55]
Ag	Distorting the cellular membrane; Interaction with the DNA and proteins, especially sulfur proteins.	[56,57]
ZnO	Generating of reactive oxygen species.	[59–61]
SiO_2	Zn-SiO_2 nanohybrid generating reactive oxygen species	[62]
Cu	Interaction with the DNA and proteins.	[63,64]

5. Trends in Geopolymer Nanocomposites Applications as Building Materials

The use of nanomaterials in the building industry become more and more popular [65,66] but the most obvious application is the antimicrobial application in the infrastructure dedicated to health care [27,32]. By combining the carbon fibers with silver nanoparticles or silver nitrate additives [67] a new area of application in the design of health infrastructure with aseptic properties was opened. Due to the absorption properties of porous geopolymers, they can offer real potential in medical applications for the adsorption of specific biomolecules. In recent years, the human organism has become increasingly resistant to the action of antibiotics. An alternative method to avoid dependence on the consumption of antibiotics would be to obtain porous geopolymers, with controlled porosity, capable of removing the pathogenic material and having a preventive role to avoid infections in hospitals. The area of applicability of these materials could be extensive, to avoid potential infections in poultry farms, in aquaculture, in agriculture, and even for the delivery of medicines [68]. The other application is connected with the functionalization of materials to provide antimicrobial properties for vulnerable materials to microbially-induced degradation in specific environments allowing for protection of the materials against bio-corrosion or control the material colonization [4,22]. Zhang et al. [69] obtained hybrid materials, based on geopolymers with metakaolin, functionalized with (3-aminopropyl) triethoxysilane (APTES) for surface protection and for improving the workability of mortars. It was found that APTES slow down the geopolymerization reaction and in their opinion there is a slow decomposition of the geopolymer network that recombines with the silane forming a more homogeneous network and much more resistant to compression. The functionalization of porous geopolymers with hydrophobic agents, such as polydimethylsiloxane, for the protection of their surfaces against moisture, also represents another direction of their use [4]. Alkali-activated foams based on coal gangue used as porous pH regulators, having high porosity and high resistance, also have a great perspective. In addition to the fast method of obtaining and the possibility of recycling the waste, it also offers anti-corrosion protection. They could also have antibacterial potential due to the gradual and prolonged alkali leaching [70].

6. Conclusions

The use of GO in building materials implies the achievement of cleaner production and the support of "green technologies". It can be considered as the best option to protect the environment and reuse current resources, as abundantly available precursors. This study is a review of the opportunity of using GO and graphene oxide in building materials, but also other nanoparticles such as Ag, ZnO, SiO_2, and Cu as additives, in order to induce a potential antibacterial effect. The methods of obtaining these nanoparticles are briefly presented, as the influence of different quantities of nanoparticles on some material properties, as well as examples of characterization techniques that can highlight the presence of these additives in building materials. Also, the mechanism of achieving antibacterial properties is briefly presented and correlated with the used nanoparticles. These nanoparticles can be included in the building materials, as additives, alone or together with GO and/or geopolymers. Due to the small size of nanoparticles, there is a risk of their release from the network of the geopolymer material into the environment, which should be considered and monitored for each material before application.

Author Contributions: Conceptualization, G.F., D.P. and K.K.; methodology, G.F. and D.P.; validation, M.Ł. and M.M. (Mykola Melnychuk); formal analysis, G.F. and D.P.; investigation, G.F., D.P. and K.K.; resources, M.Ł.; data curation, G.F. and D.P.; writing—original draft preparation, G.F., D.P. and K.K.; writing—review and editing, M.M. (Mykola Melnychuk) and M.Ł; visualization, G.F., C.S. and M.M. (Marioara Moldovan); supervision, G.F.; project administration, G.F., C.S., M.M. (Marioara Moldovan) and M.Ł. All authors have read and agreed to the published version of the manuscript.

Funding: This research was supported by a grant of the Ministry of Research, Innovation and Digitization, CNCS/CCCDI-UEFISCDI, project number COFUND-M-ERANET-3-GEOSUMAT, 314/2022,

within PNCDI III and by the project called the "Materials for circular economy—industrial waste based geopolymer composites with hybrid reinforcement" under the M-ERA.NET 3 program by the Polish National Centre for Research and Development, grant number M-ERA.NET3/2021/70/GEOSUMAT/2022. The authors thank the COST Action CA21103 and CA21121 for COST meeting support.

Institutional Review Board Statement: Not applicable.

Informed Consent Statement: Not applicable.

Data Availability Statement: The data that support the findings of this study are contained within the article.

Acknowledgments: This work was supported by a grant of the Ministry of Research, Innovation and Digitization, CNCS/CCCDI-UEFISCDI, project number COFUND-M-ERANET-3-GEOSUMAT, 314/2022, within PNCDI III and by the Polish National Centre for Research and Development, grant number M-ERA.NET3/2021/70/GEOSUMAT/2022. The authors thank COST Action CA21103 and CA21121 for COST meeting.

Conflicts of Interest: The authors declare no conflict of interest. The funders had no role in the design of the study; in the collection, analyses, or interpretation of data; in the writing of the manuscript; or in the decision to publish the results.

References

1. Davidovits, J. Geopolymers and geopolymeric materials. *J. Therm. Anal.* **1989**, *35*, 429–441. [CrossRef]
2. Farhan, K.Z.; Johari, M.A.M.; Demirboğa, R. Assessment of important parameters involved in the synthesis of geopolymer composites: A review. *Constr. Build. Mater.* **2020**, *264*, 120276. [CrossRef]
3. Singh, N.B.; Middendorf, B. Geopolymers as an alternative to Portland cement: An overview. *Constr. Build. Mater.* **2020**, *237*, 117455. [CrossRef]
4. Růžek, V.; Novosád, J.; Buczkowska, K.E. Geopolymer Antimicrobial and Hydrophobic Modifications: A Review. *Ceramics.* **2023**, *6*, 1749–1764. [CrossRef]
5. Zhang, X.; Bai, C.; Qiao, Y.; Wang, X.; Jia, D.; Li, H.; Colombo, P. Porous geopolymer composites: A review. *Composites* **2021**, *150*, 106629. [CrossRef]
6. Ortega-Nieto, C.; Losada-García, N.; Prodan, D.; Furtos, G.; Palomo, J.M. Recent advances on the design and applications of antimicrobial materials. *Nanomaterials* **2023**, *13*, 2406. [CrossRef] [PubMed]
7. Huseien, G.F.; Hamzah, H.K.; Sam, A.R.M.; Khalid, N.H.A.; Shah, K.W.; Deogrescu, D.P.; Mirza, J. Alkali-activated mortars blended with glass bottle waste nano powder: Environmental benefit and sustainability. *J. Clean. Prod.* **2020**, *243*, 118636. [CrossRef]
8. Zhang, P.; Ling, Y.; Wang, J.; Shi, Y. Bending resistance of PVA fiber reinforced cementitious composites containing nano-SiO_2. *Nanotechnol. Rev.* **2019**, *8*, 690–698. [CrossRef]
9. Jindal, B.B.; Sharma, R. The effect of nanomaterials on properties of geopolymers derived from industrial by-products: A state-of-the-art review. *Constr. Build. Mater.* **2020**, *252*, 119028. [CrossRef]
10. Zidi, Z.; Ltifi, M.; Ayadi, Z.B.; Mir, L.E.; Nóvoa, X.R. Effect of nano-ZnO on mechanical and thermal properties of geopolymer. *J. Asian Ceram. Soc.* **2020**, *8*, 1–9. [CrossRef]
11. Nawaz, M.; Heitor, A.; Sivakumar, M. Geopolymers in construction-recent developments. *Constr. Build. Mater.* **2020**, *260*, 120472. [CrossRef]
12. Nur, Q.A.; Sari, N.U. Development of geopolymers composite based on metakaolin-nano ZnO for antibacterial application. *IOP Conf. Ser. Mater. Sci. Eng.* **2017**, *180*, 012289. [CrossRef]
13. Qiu, L.; Dong, S.; Ashour, A.; Han, B. Antimicrobial concrete for smart and durable infrastructures: A review. *Constr. Build. Mater.* **2020**, *260*, 120456. [CrossRef]
14. Li, H.; Zou, Y.; Jiang, J. Synthesis of Ag@ CuO nanohybrids and their photo-enhanced bactericidal effect through concerted Ag ion release and reactive oxygen species generation. *Dalton Trans.* **2020**, *49*, 9274–9281. [CrossRef] [PubMed]
15. Zhong, L.; Liu, H.; Samal, M.; Yun, K. Synthesis of ZnO nanoparticles-decorated spindle-shaped graphene oxide for application in synergistic antibacterial activity. *J. Photochem. Photobiol. B Biol.* **2018**, *183*, 293–301. [CrossRef] [PubMed]
16. Novais, R.M.; Seabra, M.P.; Labrincha, J.A. Porous geopolymer spheres as novel pH buffering materials. *J. Clean. Prod.* **2017**, *143*, 1114–1122. [CrossRef]
17. Zhao, L.; Guo, X.; Liu, Y. Hydration kinetics, pore structure, 3D network calcium silicate hydrate, and mechanical behavior of graphene oxide reinforced cement composites. *Constr. Build. Mater.* **2018**, *190*, 150–163. [CrossRef]
18. Paul, S.C.; Van Rooyen, A.S.; van Zijl, G.P.; Petrik, L.F. Properties of cement-based composites using nanoparticles: A comprehensive review. *Constr. Build. Mater.* **2018**, *189*, 1019–1034. [CrossRef]

19. Farjadian, F.; Abbaspour, S.; Sadatlu, M.A.A.; Mirkiani, S.; Ghasemi, A.; Hoseini-Ghahfarokhi, M.; Hamblin, M.R. Recent developments in graphene and graphene oxide: Properties, synthesis, and modifications: A review. *ChemistrySelect* **2020**, *5*, 10200–10219. [CrossRef]
20. Lertcumfu, N.; Jaita, P.; Thammarong, S.; Lamkhao, S.; Tandorn, S.; Randorn, C.; Tunkasiri, T.; Rujijanagul, G. Influence of graphene oxide additive on physical, microstructure, adsorption, and photocatalytic properties of calcined kaolinite-based geopolymer ceramic composites. *Colloids Surf. A Physicochem. Eng. Asp.* **2020**, *602*, 125080. [CrossRef]
21. Prodan, D.; Moldovan, M.; Furtos, G.; Saroși, C.; Filip, M.; Perhaița, I.; Carpa, R.; Popa, M.; Cuc Varvara, S.; Popa, D. Synthesis and characterization of some graphene oxide powders used as additives in hydraulic Mortars. *Appl. Sci.* **2021**, *11*, 11330. [CrossRef]
22. Kırgız, M.S.; Mirza, J.; Cuc, S.; Prodan, D.; Saroşi, C.; Perhaiţă, I.; Popa, M. Physico-Antibacterial Feature and SEM Morphology of Bio-Hydraulic Lime Mortars In-corporating Nano-Graphene Oxide and Binary Combination of Nano-Graphene Oxide with Nano Silver, Fly Ash, Zinc, and Titanium Powders. *Buildings* **2023**, *13*, 172. [CrossRef]
23. Falah, M.; MacKenzie, K.J.D. Photocatalytic Nanocomposite Materials Based on Inorganic Polymers (Geopolymers): A Review. *Catalysts* **2020**, *10*, 1158. [CrossRef]
24. Long, W.J.; Wei, J.J.; Ma, H.; Xin, F. Dynamic mechanical properties and microstructure of graphene oxide nanosheets reinforced cement composites. *Nanomaterials* **2017**, *7*, 407. [CrossRef] [PubMed]
25. Wang, L.; Zhang, S.; Zheng, D.; Yang, H.; Cui, H.; Tang, W.; Li, D. Effect of graphene oxide (GO) on the morphology and microstructure of cement hydration products. *Nanomaterials* **2017**, *7*, 429. [CrossRef]
26. Tran, Q.H.; Nguyen, V.Q.; Le, A. Silver nanoparticles: Synthesis, properties, toxicology, applications and perspectives. Adv. Nat. Sci. Nanosci. *Nanotechnology* **2013**, *4*, 033001.
27. Zhang, X.F.; Liu, Z.G.; Shen, W.; Gurunathan, S. Silver nanoparticles: Synthesis, characterization, properties, applications, and therapeutic approaches. *Int. J. Mol. Sci.* **2016**, *17*, 1534. [CrossRef] [PubMed]
28. Yaqoob, A.A.; Umar, K.; Ibrahim, M.N.M. Silver nanoparticles: Various methods of synthesis, size affecting factors and their potential applications—A review. *Appl. Nanosci.* **2020**, *10*, 1369–1378. [CrossRef]
29. Sharma, D.; Gulati, S.S.; Sharma, N.; Chaudhary, A. Sustainable synthesis of silver nanoparticles using various biological sources and waste materials: A review. *Emergent Mater.* **2022**, *5*, 1649–1678. [CrossRef]
30. Kalpana, V.N.; Rajeswari, D.V. Biosynthesis of metal and metal oxide nanoparticles for food packaging and preservation: A green expertise. *Food Biosynth.* **2017**, 293–316. [CrossRef]
31. Flieger, J.; Franus, W.; Panek, R.; Szymańska-Chargot, M.; Flieger, W.; Flieger, M.; Kołodziej, P. Green synthesis of silver nanoparticles using natural extracts with proven antioxidant activity. *Molecules* **2021**, *26*, 4986. [CrossRef]
32. Chung, I.M.; Park, I.; Seung-Hyun, K.; Thiruvengadam, M.; Rajakumar, G. Plant-Mediated Synthesis of Silver Nanoparticles: Their Characteristic Properties and Therapeutic Applications. *Nanoscale Res. Lett.* **2016**, *11*, 1–14. [CrossRef]
33. Luukkonen, T.; Yliniemi, J.; Sreenivasan, H.; Ohenoja, K.; Finnilä, M.; Franchin, G. Ag- or Cu-modified geopolymer filters for water treatment manufactured by 3D printing, direct foaming, or granulation. *Sci. Rep.* **2020**, *10*, 7233. [CrossRef]
34. Raj, R.S.; Arulraj, G.P.; Anand, N.; Kanagaraj, B.; Lubloy, E.; Naser, M.Z. Nanomaterials in geopolymer composites: A review. *DIBE* **2022**, *13*, 100114. [CrossRef]
35. Bhuyan, T.; Mishra, K.; Khanuja, M.; Prasad, R.; Varma, A. Biosynthesis of zinc oxide nanoparticles from *Azadirachta indica* for antibacterial and photocatalytic applications. *Mat. Sci. iSemicon. Proc.* **2015**, *32*, 55–61. [CrossRef]
36. Pirtarighat, S.; Ghannadnia, M.; Baghshahi, S. Green synthesis of silver nanoparticles using the plant extract of *Salvia spinosa* grown in vitro and their antibacterial activity assessment. *J. Nanostruct. Chem.* **2018**, *9*, 1–9. [CrossRef]
37. Vijayakumar, S.; Krishnakumar, C.; Arulmozhi, P.; Mahadevan, S.; Parameswari, N. Biosynthesis, characterization and antimicrobial activities of zinc oxide nanoparticles from leaf extract of *Glycosmis pentaphylla* (Retz.) DC. *Microb. Pathogen.* **2018**, *116*, 44–48. [CrossRef] [PubMed]
38. Singh, V.P.; Sandeep, K.; Kushwaha, H.S.; Powar, S.; Vaish, R. Photocatalytic, hydrophobic and antimicrobial characteristics of ZnO nano needle embedded cement composites. *Constr. Build. Mater.* **2018**, *158*, 285–294. [CrossRef]
39. Bica, B.O.; Staub de Melo, J.V. Concrete blocks nano-modified with zinc oxide (ZnO) for photocatalytic paving: Performance comparison with titanium dioxide (TiO_2). *Constr. Build. Mater.* **2020**, *252*, 119120. [CrossRef]
40. Ślosarczyk, A.; Klapiszewska, I.; Parus, A.; Lubianiec, O.; Klapiszewski, Ł. Alkali-Activated Materials Doped with ZnO: Physicomechanical and Antibacterial Properties. *Materials* **2023**, *16*, 6224. [CrossRef] [PubMed]
41. Zhao, Z.; Qi, T.; Zhou, W.; Hui, D.; Xiao, C.; Qi, J.; Zheng, Z.; Zhao, Z. A review on the properties, reinforcing effects, and commercialization of nanomaterials for cement-based materials. *Nanotechnol. Rev.* **2020**, *9*, 303–322. [CrossRef]
42. Stefanidou, M.; Karozou, A. Testing the effectiveness of protective coatings on traditional bricks. *Constr. Build. Mater.* **2016**, *111*, 482–487. [CrossRef]
43. Zhang, A.; Ge, Y.; Yang, W.; Cai, X.; Du, Y. Comparative study on the effects of nano-SiO_2, nano-Fe_2O_3 and nano-NiO on hydration and microscopic properties of white cement. *Constr. Build. Mater.* **2019**, *228*, 116767. [CrossRef]
44. Tabish, M.; Zaheer, M.M.; Baqi, A. Effect of nano-silica on mechanical, microstructural and durability properties of cement-based materials: A review. *J. Build. Eng.* **2022**, *65*, 105676. [CrossRef]
45. Wang, B.; Shuang, D. Effect of graphene nanoplatelets on the properties, pore structure and microstructure of cement composites. *Mater. Express* **2018**, *8*, 407–416. [CrossRef]

46. Bhagat, M.; Anand, R.; Sharma, P.; Rajput, P.; Sharma, N.; Singh, K. Multifunctional copper nanoparticles: Synthesis and applications. *ECS J. Solid State Sci. Technol.* **2021**, *10*, 063011. [CrossRef]
47. Khodaei, M.M.; Karegar, M. Synthesis and characterization of copper nanoparticles stabilized with polyvinyl pyrrolidone and its performance on the conductivity and stability of polyindole. *J. Iran. Chem. Soc.* **2021**, *18*, 863–872. [CrossRef]
48. Kim, I.S.; Choi, S.Y.; Yang, E.I. Comparison of fundamental properties and durability of mortar mixed with antibacterial functional materials. *Mag. Concr. Res.* **2023**, 1–13. [CrossRef]
49. Li, X.; Kappler, U.; Jiang, G.; Bond, P.L. The ecology of acidophilic microorganisms in the corroding concrete sewer environment. *Front. Microbiol.* **2017**, *8*, 683. [CrossRef]
50. Kong, L.; Zhao, W.; Xuan, D.; Wang, X.; Liu, Y. Application potential of alkali-activated concrete for antimicrobial induced corrosion: A review. *Constr. Build. Mater.* **2022**, *317*, 126169. [CrossRef]
51. Kirthika, S.K.; Goel, G.; Matthews, A.; Goel, S. Review of the untapped potentials of antimicrobial materials in the construction sector. *Prog. Mater. Sci.* **2022**, *133*, 101065. [CrossRef]
52. Li, J.; Wang, G.; Zhu, H.; Zhang, M.; Zheng, X.; Di, Z.; Wang, X. Antibacterial activity of large-area monolayer graphene film manipulated by charge transfer. *Sci. Rep.* **2014**, *4*, 4359. [CrossRef] [PubMed]
53. Hui, L.; Piao, J.G.; Auletta, J.; Hu, K.; Zhu, Y.; Meyer, T.; Liu, H.; Yang, L. Availability of the basal planes of graphene oxide determines whether it is antibacterial. *ACS Appl. Mater. Interfaces* **2014**, *6*, 13183–13190. [CrossRef] [PubMed]
54. Mallick, A.; Haldar, N.; Nandy, S.; Ghosh, C.K. Fabrication of Graphene, Graphene Oxide, Reduced Graphene Oxide, Fullerene (C60) and Carbon Nanotube Thin Film by Langmuir–Blodgett Method. In *Handbook of Porous Carbon Materials*; Springer Nature: Singapore, 2023; pp. 21–38.
55. Mangadlao, J.D.; Santos, C.M.; Felipe, M.J.L.; de Leon, A.C.C.; Rodrigues, D.F.; Advincula, R.C. On the antibacterial mechanism of graphene oxide (GO) Langmuir–Blodgett films. *Chem. Commun.* **2015**, *51*, 2886–2889. [CrossRef] [PubMed]
56. Qing, Y.; Cheng, L.; Li, R.; Liu, G.; Zhang, Y.; Tang, X.; Wang, J.; Liu, H.; Qin, Y. Potential antibacterial mechanism of silver nanoparticles and the optimization of orthopedic implants by advanced modification technologies. *Int. J. Nanomed.* **2018**, *13*, 3311–3327. [CrossRef] [PubMed]
57. Gomaa, E.Z. Silver nanoparticles as an antimicrobial agent: A case study on Staphylococcus aureus and Escherichia coli as models for Gram-positive and Gram-negative bacteria. *J. Gen. Appl. Microbiol.* **2017**, *63*, 36–43. [CrossRef] [PubMed]
58. Jiang, L.; Jia, Z.; Xu, X.; Chen, Y.; Peng, W.; Zhang, J.; Wang, H.; Li, S.; Wen, J. Preparation of antimicrobial activated carbon fiber for adsorption. *J. Porous Mater.* **2022**, *29*, 1071–1081. [CrossRef]
59. Kumar, R.; Umar, A.; Kumar, G.; Nalwa, H.S. Antimicrobial properties of ZnO nanomaterials: A review. *Ceram. Intern.* **2017**, *43*, 3940–3961. [CrossRef]
60. Liu, X.; Yang, Z.; Li, K.; Briseghella, B.; Marano, G.C.; Xu, J. Visible light antibacterial potential of cement mortar incorporating Cu-ZnO/gC_3N_4 nanocomposites. *RSC Adv.* **2023**, *13*, 9448–9456. [CrossRef]
61. Sawai, J. Quantitative evaluation of antibacterial activities of metallic oxide powders (ZnO, MgO and CaO) by conductimetric assay. *J. Microbiol. Methods* **2003**, *54*, 177–182. [CrossRef] [PubMed]
62. Sarkar, M.; Maiti, M.; Akbar Malik, M.; Xu, S. Development of anti-bio deteriorate sustainable geopolymer by SiO_2 NPs decorated ZnO NRs. *Adv. Mater. Lett.* **2019**, *10*, 128–131. [CrossRef]
63. Xie, J.; Chu, H.; Wang, L.; Fang, Y.; Xu, Y.; Liu, D.; Jiang, L. Influences of Cu-Ti amorphous alloy on the properties of mortar: Wastewater treatment and bacteria inactivation. *Constr. Build. Mater.* **2023**, *377*, 131099. [CrossRef]
64. Chatterjee, A.K.; Chakraborty, R.; Basu, T. Mechanism of antibacterial activity of copper nanoparticles. *Nanotechnology* **2014**, *25*, 135101. [CrossRef] [PubMed]
65. Buczkowska, K.E.; Ruzek, V.; Louda, P.; Bousa, M.; Yalcinkaya, B. Biological Activities on Geopolymeric and Ordinary Concretes. *J. Biomed. Res. Environ. Sci.* **2022**, *3*, 748–757. [CrossRef]
66. Jędrzejczak, P.; Parus, A.; Balicki, S.; Kornaus, K.; Janczarek, M.; Wilk, K.A.; Klapiszewski, Ł. The influence of various forms of titanium dioxide on the performance of resultant cement composites with photocatalytic and antibacterial functions. *Mater. Res. Bull.* **2023**, *160*, 112139. [CrossRef]
67. Armayani, M.; Pratama, M.; Subaer, S. The Properties of Nano Silver (Ag)-Geopolymer as Antibacterial Composite for Functional Surface Materials. *MATEC Web Conf.* **2017**, *97*, 01010. [CrossRef]
68. Popovich, J.; Chen, S.; Iannuzo, N.; Ganser, C.; Seo, D.K.; Haydel, S.E. Synthesized geopolymers adsorb bacterial proteins, toxins, and cells. *Front. Bioeng. Biotechn.* **2020**, *8*, 527. [CrossRef]
69. Zhang, C.; Hu, Z.; Zhu, H.; Wang, X.; Gao, J. Effects of silane on reaction process and microstructure of metakaolin-based geopolymer composites. *J. Build. Eng.* **2020**, *32*, 101695. [CrossRef]
70. Li, X.; Zheng, J.; Zheng, K.; Su, F.; Zhao, Z.; Bai, C.; Colombo, P. Rapid fabrication of coal gangue-based alkali activated foams and application as pH regulators. *Mater. Lett.* **2023**, *338*, 134020. [CrossRef]

materials

MDPI

Article

Long-Term Prestress Loss Calculation Considering the Interaction of Concrete Shrinkage, Concrete Creep, and Stress Relaxation

Weiwei Han [1,2], Panpan Tian [2], Yigang Lv [3,*], Chaosheng Zou [3] and Tao Liu [3]

[1] National Engineering Research Center of Highway Maintenance Technology, Changsha University of Science & Technology, Changsha 410114, China
[2] School of Traffic & Transportation Engineering, Changsha University of Science & Technology, Changsha 410114, China
[3] School of Civil Engineering, Changsha University of Science & Technology, Changsha 410114, China
* Correspondence: andrew@csust.edu.cn

Abstract: In order to accurately calculate the long-term prestress losses of prestressed tendons, a time-varying model of long-term prestress loss considering the interaction between concrete shrinkage, creep, and the stress relaxation of prestressed tendons was constructed. Then, a method for calculating the long-term prestress losses of concrete structures was developed. A long-term prestress loss test of a prestressed concrete T-beam in a long-term field test environment was carried out. The measured values of long-term prestress losses are compared with the calculated results of JTG 3362-2018, AASHTO LRFD-2007, and the time-varying law model. The results show that the long-term effective tension of the T-beam decreases gradually with the increase in the load holding time. At the beginning of loading, the tensile force changes rapidly and then gradually slows down. The later the tensile age or the higher the initial loading stress level, the smaller the long-term prestress losses of the prestressed tendons. The long-term prestress loss values calculated by JTG 3362-2018, AASHTO LRFD-2007, and the time-varying law model increase with the increase in the load holding time. In the early stage of loading, the rate of change slows down and tends to be stable. The calculated results of JTG 3362-2018 and AASHTO LRFD-2007 are significantly different from the measured values. However, the calculated results of the time-varying law model are in good agreement with the measured values. The average coefficients of variation of the long-term prestress loss calculated by JTG 3362-2018, AASHTO LRFD-2007, and the time-varying law model are 17%, 10%, and 5%, respectively. The time-varying law model of the long-term prestress losses of prestressed tendons is accurate, and the long-term prestress loss of prestressed reinforcement can be predicted effectively.

Keywords: loss of prestress; field test; creep by contraction; relaxation of stress; time-varying; law model

Citation: Han, W.; Tian, P.; Lv, Y.; Zou, C.; Liu, T. Long-Term Prestress Loss Calculation Considering the Interaction of Concrete Shrinkage, Concrete Creep, and Stress Relaxation. *Materials* **2023**, *16*, 2452. https://doi.org/10.3390/ma16062452

Academic Editor: Krzysztof Schabowicz

Received: 19 February 2023
Revised: 13 March 2023
Accepted: 18 March 2023
Published: 19 March 2023

1. Introduction

Prestress loss is the key factor affecting the cracking of prestressed concrete bridges under torsion; it can be divided into short-term prestress loss and long-term prestress loss. Short-term prestress loss mainly includes the prestress loss caused by the friction between the prestressed bar and the pipe wall, anchor deformation, retraction of the steel bar, etc., which is easy to measure and calculate because it is independent of time [1–4]. The long-term prestress loss caused by prestressed rib relaxation, concrete shrinkage, and concrete creep is time-sensitive and difficult to calculate [5–10]. Long-term prestress loss accounts for more than 30% of the total prestress loss, and it has a great influence on the long-term performance of concrete bridge structures [11–14]. Therefore, determining how to accurately calculate the long-term prestress losses of prestressed tendons is of great significance.

Scholars at home and abroad have conducted some theoretical and experimental studies on the long-term prestress losses of concrete structures. Lu et al. [15] developed a long-term prestress loss calculation method for concrete structures based on the Latin hypercube sampling method. The effective modulus method was adjusted by age based on accurate and rapid sampling. It was also applied to the calculation of the prestress loss of a C50 concrete test beam, and the measured value of the long-term prestress loss of the test beam was located in the middle of the confidence interval of the prestress loss calculated using this method. Pablo M. Páez et al. [16] proposed a simplified equation for improving the prediction of the long-term prestress loss of unbonded prestressed concrete components considering concrete shrinkage creep, the stress relaxation of prestressed ribs, and the influence of bonded non-prestressed ribs. Compared with the simplified existing model, the proposed equation can fully predict the prestress loss with higher accuracy. Guo et al. [17] used load cells, vibrating line strain gauges (VWSG), and elastic magnetic (EM) sensors to measure prestress losses due to the creep and shrinkage of concrete, as well as the total prestress losses. After obtaining the long-term prestress loss of post-tensioned concrete beams, an improved model for predicting time-varying prestress loss is proposed. Compared with the existing model, the accuracy of the results is improved, and the maximum difference between the test results and the predicted results is within 10%. Based on their test results and for ease of calculation, Cao et al. [18] used the least squares method to fit the long-term prestress losses. Samer et al. [19], using equilibrium and compatibility principles based on solid mechanics, presented an analytical method for predicting the long-term prestress losses of precast, pre-tensioned, or post-tensioned concrete members. It can be used for multi-stage loading and prestressing. Yang et al. [20] used the median integral theorem based on the shrinkage creep models of FIB MC 2010 and AASHTO-LRFD 2014 to create a refined method for estimating the time-varying prestress loss. Compared with the numerical results obtained by the step-by-step method, it has good accuracy. Zhang et al. [21] established a finite element analysis (FEA) model based on the long-term prestress loss test of prestressed concrete beams and used the ABAQUS UMAT software to establish and calibrate it. Combined with an artificial neural network (ANN), a long-term prestress loss prediction model is proposed. Compared with the measured results, the prediction model is more accurate and efficient in the long-term prestress loss assessment of a prestressed concrete cylinder structure. The Chinese JTG 3362-2018 specification [22] adopts the itemized overlay method. Specifically, the losses caused by shrinkage and creep and the losses caused by the prestressed tendon stress relaxation of concrete are calculated separately and then added together to obtain the total loss. The US AASHTO-LRFD 2007 specification [23] considers the interactions between long-term prestress losses. The losses caused by time-dependent concrete shrinkage and creep, as well as the stress relaxation of prestressed tendons, are calculated separately. Finally, the total losses are obtained by adding them together.

The long-term prestress losses caused by concrete shrinkage and creep, as well as prestressed rib stress relaxation, have a mutual influence, as well as time-varying and uncertain changes over time [24–26]. In the calculation of prestress loss, the total effect of the interaction between concrete shrinkage, creep, and prestressed rib stress relaxation is compared with the effect considering their influences alone. The deviation value is generally large and cannot be ignored. At present, there are few studies on the calculation method of long-term prestress loss considering the interaction between the two in the design codes and the literature. As a result, the calculation results are quite different from the actual situation [27–30]. The long-term performance of concrete structures is an uncertain variable associated with the environment. However, most of the relevant experimental studies were carried out indoors, which is quite different from the complex natural environments in which concrete structures are located [31,32]. To accurately calculate the long-term prestress losses of concrete structures, a long-term time-varying model of prestress loss considering the interaction between concrete shrinkage, creep, and the stress relaxation of prestressed tendons is proposed. In addition, a long-term prestress loss test of a prestressed concrete

T-beam in a long-term field test environment was carried out, and a long-term prestress loss calculation method for concrete structures was formed for test verification. It made the calculation of the long-term prestress loss of the structure safer and more reliable.

2. Calculation Method of Long-Term Prestress Loss Considering the Interaction of Shrinkage, Creep, and Stress Relaxation

2.1. Basic Assumptions

In the process of deducing the formula of long-term prestress loss, the following basic assumptions are satisfied [33–35]:

1. At any time, the elastic stress and elasticity of concrete should become linear;
2. The assumption of flat section deformation of the beam body is valid;
3. The creep deformation is linear, satisfying the superposition principle;
4. Ordinary reinforcement and prestressed reinforcement are completely bonded to the concrete without slip;
5. There is no cracking phenomenon in the concrete section.

2.2. Relaxation of Prestressed Reinforcement

When calculating the instar (t_i) moment, the inherent relaxation loss ($\sigma_\chi(t_i)$) of prestressed reinforcement is calculated as follows [33]:

$$\sigma_\chi(t_i) = \frac{\sigma_{p0}}{10} \cdot \left(\frac{\sigma_{p0}}{C \cdot f_{py}} - 0.55 \right) \cdot log(t_i - t_p + 1) \quad (1)$$

where t_p is the tensile age of the prestressed tendons (d); σ_{p0} is the effective prestress of the force transmission anchorage; f_{py} is the standard value of the tensile strength of the prestressed tendons; and C is the constant related to steel (0.85 for general steel and 0.90 for low-slack steel).

During the loading period from t_0 to t_i, the variation in the natural relaxation loss of prestressed tendons ($\sigma_l(t_i, t_0)$) is

$$\sigma_l(t_i, t_0) = \sigma_\chi(t_i) - \sigma_\chi(t_0) \quad (2)$$

When t_0=t_p, $\sigma_\chi(t_0) = 0$.

In the actual prestressed concrete structure, there is no constant strain. Using inherent relaxation as stress loss would overestimate the loss. In the concrete unit, due to the influence of concrete shrinkage and creep, the relaxation of prestressed tendons is less than their inherent relaxation. Therefore, the reduction in the relaxation loss of prestressed tendons must be used in the design calculation ($\overline{\sigma_l}(t_i, t_0)$):

$$\overline{\sigma_l}(t_i, t_0) = \lambda(t_i)\sigma_l(t_i, t_0) \quad (3)$$

where $\lambda(t_i)$ is the stress relaxation reduction coefficient from t_0 to t_i, considering the effects of shrinkage and creep.

2.3. Time-Varying Law Model of Long-Term Prestress Loss

When calculating the long-term prestress loss of the prestressed reinforcement of a prestressed concrete beam under the interactive influences of shrinkage, creep, and prestress relaxation, the interaction of the precompression zone and the pre-tension zone is ignored [36–39]. A calculation diagram of the prestress loss of a concrete beam is shown in Figure 1.

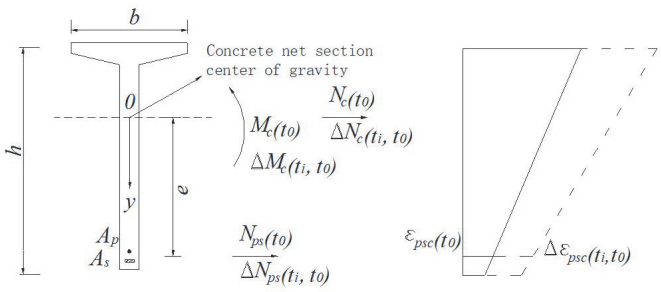

Figure 1. Calculation of prestress losses of prestressed concrete beams.

In Figure 1, the areas of non-prestressed and prestressed tendons are A_s and A_p; the distance between the center of gravity and the center of gravity of the net section of concrete is e; the net area and the net moment of inertia of the concrete section are A_n and I_n; at the loading age t_0, the normal force and bending moment of the concrete section on the section are $N_c(t_0)$ and $M_c(t_0)$; the normal force of the rebar is $N_{ps}(t_0)$; and the concrete strain at the center of the rebar is $\varepsilon_{psc}(t_0)$.

During the period from t_0 to t_i, the external load does not change. In order to simplify the calculation, the centers of gravity of prestressed reinforcement and non-prestressed reinforcement in the prestressed zone (or pre-stretching zone) are approximately concentrated on the two centers of gravity. Then,

$$\begin{cases} \Delta\varepsilon_p(t_i, t_0) = \Delta\varepsilon_{psc}(t_i, t_0) \\ \Delta\varepsilon_s(t_i, t_0) = \Delta\varepsilon_{psc}(t_i, t_0) \end{cases} \tag{4}$$

where $\Delta\varepsilon_{psc}(t_i, t_0)$, $\Delta\varepsilon_p(t_i, t_0)$, and $\Delta\varepsilon_s(t_i, t_0)$, respectively, represent the strain increment of concrete, prestressed reinforcement, and non-prestressed reinforcement at the center of gravity of reinforcement during the period from t_0 to t_i.

Considering the inherent relaxation of the reinforcement without strain change, the relationship between the stress increment and the strain increment of each reinforcement is as follows:

$$\begin{cases} \Delta\sigma_p(t_i, t_0) = E_p\Delta\varepsilon_p(t_i, t_0) + \lambda(t_i)\sigma_l(t_i, t_0) \\ \Delta\sigma_s(t_i, t_0) = E_s\Delta\varepsilon_s(t_i, t_0) \end{cases} \tag{5}$$

where $\Delta\sigma_s(t_i, t_0)$ and $\Delta\sigma_p(t_i, t_0)$ are the stress increment of non-prestressed reinforcement and prestressed reinforcement, respectively, and E_s and E_p are the elastic moduli of non-prestressed and prestressed tendons, respectively.

According to Equations (4) and (5), the internal force change ($\Delta N_{ps}(t_i, t_0)$) of prestressed reinforcement and non-prestressed reinforcement in the period from t_0 to t_i is

$$\Delta N_{ps}(t_i, t_0) = \left(A_p + \frac{E_s}{E_p}A_s\right)E_p\Delta\varepsilon_{psc}(t_i, t_0) + \lambda(t_i)\sigma_l(t_i, t_0)A_p \tag{6}$$

Within the period from t_0 to t_i, the increment in the normal force ($\Delta N_c(t_i, t_0)$) on the concrete part of the section and the increment in the bending moment ($\Delta M_c(t_i, t_0)$) on the barycenter axis of the net section of the concrete are

$$\begin{cases} \Delta N_c(t_i, t_0) = -\Delta N_{ps}(t_i, t_0) \\ \Delta M_c(t_i, t_0) = \Delta N_c(t_i, t_0) \cdot e \end{cases} \tag{7}$$

The concrete stress increment ($\Delta\sigma_{psc}(t_i,t_0)$) at the center of gravity of reinforcement ($\rho_s = A_s/A_n$, $\rho_p = A_p/A_n$, $r_n = \sqrt{I_n/A_n}$, and $\rho_{ps} = 1 + e^2/r_n^2$) is

$$\begin{aligned}\Delta\sigma_{psc}(t_i,t_0) &= \tfrac{\Delta N_c(t_i,t_0)}{A_n} + \tfrac{\Delta M_c(t_i,t_0)}{I_n}\cdot e \\ &= -\left[\left(\rho_p + \tfrac{E_s}{E_p}\rho_s\right)\cdot E_p\Delta\varepsilon_{psc}(t_i,t_0) + \rho_p\lambda(t_i)\sigma_l(t_i,t_0)\right]\cdot\rho_{ps}\end{aligned} \tag{8}$$

According to the principle of linear superposition, under a constant load, the concrete strain increment ($\Delta\varepsilon_{psc}(t_i,t_0)$) at the center of gravity of reinforcement is as follows when it is loaded for a longer time than t_0 ($t_i > t_0$):

$$\begin{aligned}\Delta\varepsilon_{psc}(t_i,t_0) &= \tfrac{\sigma_{psc}(t_0)\cdot\phi(t_i,t_0)}{E_c(t_0)} + \tfrac{\Delta\sigma_{psc}(t_i,t_0)\cdot[1+\chi(t_i,t_0)\cdot\phi(t_i,t_0)]}{E_c(t_0)} + \varepsilon_{sh}(t_i,t_0) \\ &= \tfrac{\sigma_{psc}(t_0)\cdot\phi(t_i,t_0)}{E_c(t_0)} - n_p\rho_{ps}\left(\rho_p + \tfrac{E_s}{E_p}\rho_s\right)\cdot[1+\chi(t_i,t_0)\cdot\phi(t_i,t_0)]\Delta\varepsilon_{psc}(t_i,t_0) \\ &\quad - \tfrac{\rho_p\rho_{ps}[1+\chi(t_i,t_0)\cdot\phi(t_i,t_0)]\lambda(t_i)\sigma_l(t_i,t_0)}{E_c(t_0)} + \varepsilon_{sh}(t_i,t_0)\end{aligned} \tag{9}$$

where $E_c(t_0)$ and $\sigma_{psc}(t_0)$ are, respectively, the elastic modulus and the initial stress of the concrete at time t_0; $\phi(t_i,t_0)$ refers to the creep coefficient with a loading age of t_0 and calculating the creep coefficient with a loading age of t_i; $\chi(t_i,t_0)$ is the aging coefficient; $\varepsilon_{sh}(t_i,t_0)sh$ is the shrinkage strain of the concrete beam at time t_i; and $n_p = E_p/E_c(t_0)$. Among them, $\phi(t_i,t_0)$ and $\varepsilon_{sh}(t_i,t_0)sh$ were calculated according to reference [40].

According to Equations (4) and (9), we can obtain

$$\begin{aligned}\Delta\varepsilon_p(t_i,t_0) &= 1/\left\{1 + n_p\rho_{ps}\left(\rho_p + \tfrac{E_s}{E_p}\rho_s\right)\cdot[1+\chi(t_i,t_0)\cdot\phi(t_i,t_0)]\right\} \\ &\cdot\left\{\tfrac{\sigma_{psc}(t_0)\cdot\phi(t_i,t_0)}{E_c(t_0)} - \tfrac{\rho_p\rho_{ps}[1+\chi(t_i,t_0)\cdot\phi(t_i,t_0)]\lambda(t_i)\sigma_l(t_i,t_0)}{E_c(t_0)} + \varepsilon_{sh}(t_i,t_0)\right\}\end{aligned} \tag{10}$$

From t_0 to t_i, the time-varying law model of the long-term prestress loss ($\Delta\sigma_p(t_i,t_0)$) of prestressed tendons is

$$\begin{aligned}\Delta\sigma_p(t_i,t_0) &= E_p\Delta\varepsilon_p(t_i,t_0) + \lambda(t_i)\sigma_l(t_i,t_0) \\ &= \left\{n_p\sigma_{psc}(t_0)\phi(t_i,t_0) + E_p\varepsilon_{sh}(t_i,t_0) + \left\{1 + n_s\rho_s\rho_{ps}[1+\chi(t_i,t_0)\cdot\phi(t_i,t_0)]\right\}\cdot\lambda(t_i)\sigma_l(t_i,t_0)\right\} \\ &\quad/\left\{1 + n_p\rho_{ps}\left(\rho_p + \tfrac{E_s}{E_p}\rho_s\right)\cdot[1+\chi(t_i,t_0)\cdot\phi(t_i,t_0)]\right\}\end{aligned} \tag{11}$$

where it is equal to $n_s = E_s/E_c(t_0)$.

In the common range of prestressed concrete structures, $E_s \approx E_p$ can be approximated; the common range of the aging coefficient ($\chi(t_i,t_0)$) is 0.6~0.9, while 0.82 is generally preferable; and the stress relaxation reduction coefficient ($\lambda(t_i)$) generally varies from 0.5 to 0.9. Generally, 0.75 is taken. The simplified time-varying law model of $\Delta\sigma_p(t_i,t_0)$ is

$$\begin{aligned}\Delta\sigma_p(t_i,t_0) &= \left[n_p\sigma_{psc}(t_0)\phi(t_i,t_0) + E_p\varepsilon_{sh}(t_i,t_0)\right]/\left\{1 + n_p[1+0.82\phi(t_i,t_0)]\rho\rho_{ps}\right\} \\ &+\left\{0.75\left\{1 + n_s\rho_s\rho_{ps}[1+0.82\phi(t_i,t_0)]\right\}\sigma_l(t_i,t_0)\right\}/\left\{1 + n_p[1+0.82\phi(t_i,t_0)]\rho\rho_{ps}\right\}\end{aligned} \tag{12}$$

where it is equal to $\rho = (A_s + A_p)/A_n$.

3. Long-Term Field Test

3.1. Experimental Materials

The cement in the raw material of the test concrete is ordinary Portland cement with a strength of 52.5 MPa, produced by China Gezhouba Group Cement Co., Ltd. The aggregate is produced from 5~25 mm basalt crushed stone from the Lianhuaqiao crushing field in Changsha County and river sand from Dongting Lake, and the steel bars and strands are produced by Hunan Valin Lianyuan Iron and Steel Co., Ltd. In order to ensure the accuracy

of the test and reduce the interference of unfavorable factors in the test results, the aqueous states of the aggregates used in this test are all dry after natural air drying.

3.2. Test Setup

A field test station was established in the living environment of the general structure, and a long-term prestress loss test of a prestressed concrete T-beam was carried out. A total of four pieces of bonded prestressed concrete T-beams with 6.0 m lengths were produced. Their numbers were B1#~B4#. The calculated span of the T-beams was 5.8 m, the beam height was 0.32 m, the flange plate width was 0.40 m, and the T-rib width was 0.11 m. The cement was 52.5# ordinary Portland cement, and the concrete mix ratio was cement/sand/gravel/water/water-reducing agent = 460:585:1175:232.5:3.68. The lower edge was equipped with two HRB335 longitudinal steel bars with diameters of 14 mm and one low-relaxation prestressed steel strand with a diameter of 15.24. The upper edge was equipped with six vertical R235 steel bars with diameters of 6 mm, as shown in Figure 2. The tensioned control stress (σ_{con}) of each beam was 1395 and was single-end tensioned. The tensioned age (t_p) of B1# and B2# was 7 d, and the tensioned age (t_p) of beams B3# and B4# was 28 d. The test T-beam was placed in the field test station for natural maintenance, as shown in Figure 3. The cubic compressive strength and elastic modulus of the concrete at an age of 28 d were 57.0 MPa and 36.7 GPa, respectively. Taking the average value of the previous 365 d as the annual average temperature and annual average humidity, the measured annual average temperature was approximately 23.80 °C, and the measured annual average relative humidity was approximately 64.2%.

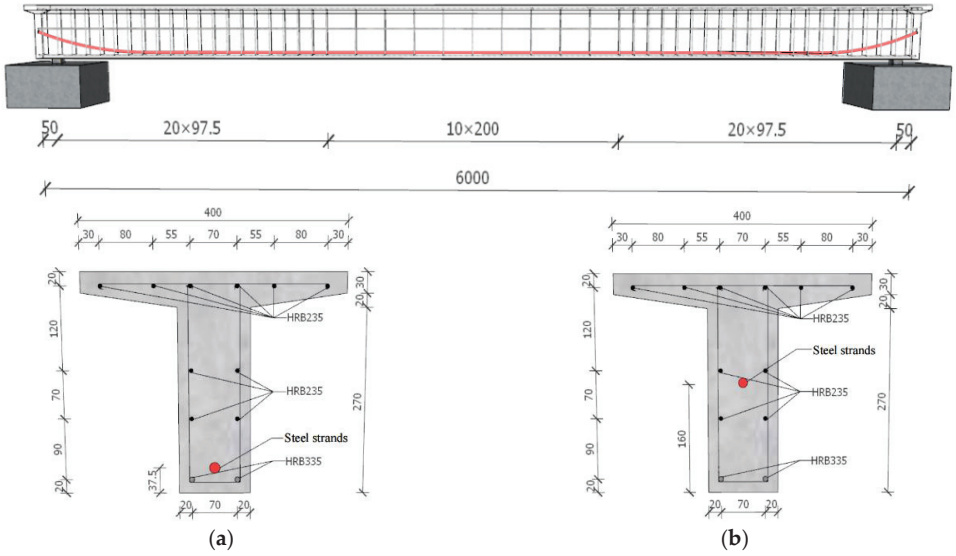

Figure 2. Size and reinforcement of T-beam (unit: mm): (**a**) mid-span section and (**b**) fulcrum cross-section.

3.3. Loading and Testing

In the test, standard concrete blocks were locally uniformly loaded. The mechanical property parameters after loading are shown in Table 1. The loading mode of the test T-beam is shown in Figure 4. A vibrating wire strain gauge was embedded at one end of each test T-beam to test the effective prestress of the prestressed steel strand.

Figure 3. Natural maintenance of T-beam field test station.

Table 1. Mechanical property parameters of the secondary loading of the T-beam.

Number of Beam	Locally Uniformly Distributed Load		Dead Weight + Local Uniform Load + Prestress	
	Value of Load (kN/m)	Tensile Age (t_0/d)	Upper-Edge Concrete Stress (MPa)	Lower-Edge Concrete Stress (MPa)
B1#	5.31	7	2.64	4.84
B2#	9.74	7	6.34	−0.42
B3#	5.31	28	2.64	4.84
B4#	9.74	28	6.34	−0.42

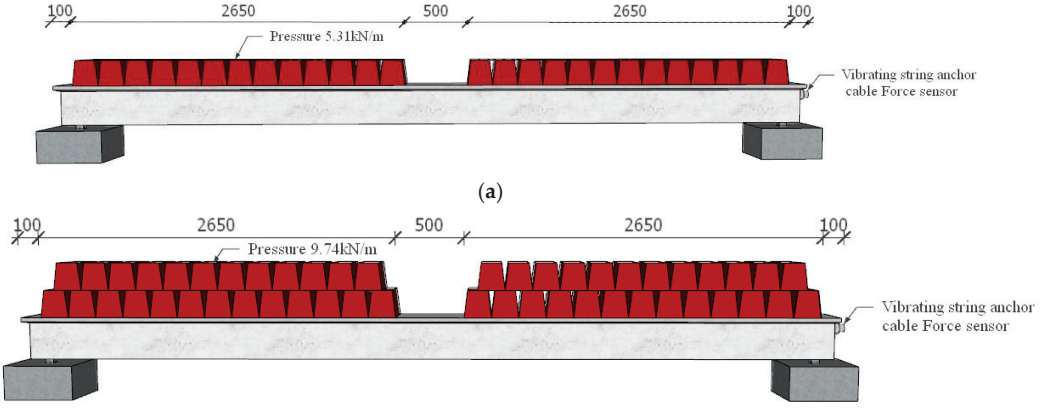

Figure 4. Loading of T-beam (unit: mm): (**a**) loading status of B1# and B3#; (**b**) loading status of B2# and B4#.

4. Results and Discussion

4.1. Long-Term Effective Tensile Test Results and Analysis

Taking the loading age t_0 as the starting time, the vibrating wire strain gauge embedded in the test T-beam was used to test the long-term effective tension of the prestressed tendons of B1#~B4# in the field test environment. The long-term effective tensile force values of the prestressed tendons of the T-beam varied in all tests with the load holding time (t), as shown in Figure 5.

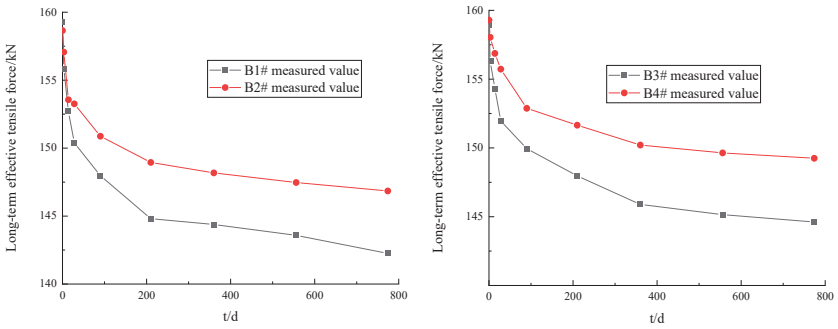

Figure 5. Results of long-term effective tensile test of test T-beam: (**a**) loading age = 7 d; (**b**) loading age = 28 d.

As can be seen in Figure 5, the development trend of the long-term effective tensile force of the prestressed tendons of the T-beam was essentially the same in all tests. With an increase in the load holding time (t), the long-term effective tensile force gradually decreased. The tensile force changed rapidly in the initial stage of loading and gradually slowed down in the later stage. When the load holding time (t) was 774 d, the long-term tensile loss (ΔP) values of the prestressed tendons of B1#~B4# were 16.74 kN, 11.8 kN, 14.32 kN, and 10.04 kN, respectively. When the load holding time (t) was 90 days, the tensile loss values of the prestressed tendons of B1#~B4# were 66%, 65%, 62%, and 63% of those of ΔP, respectively. When the load holding time (t) increased from 90 d to 360 d, the tensile loss values of the prestressed tendons of B1#~B4# were 84%, 86%, 89%, and 89% of those of ΔP, respectively.

4.2. Analysis of Influence of Tensile Age and Initial Loading Stress Level

(1) Tensile age

The same initial loading stress level was maintained. Then, the long-term prestress loss values of prestressed tendons corresponding to B1# and B3#, and B2# and B4#, were compared at different tensile ages (t_p), as shown in Figure 6.

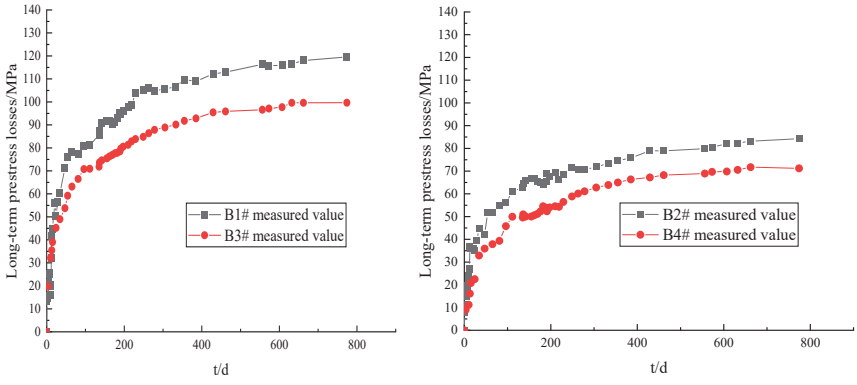

Figure 6. Comparison of long-term prestress losses at different tension ages.

As can be seen in Figure 6, the long-term prestress losses of the prestressed tendons of each test T-beam at different tensile ages gradually increased with the holding time. The early stage of development was relatively fast, and the later stage tended to gradually flatten. When the load holding time (t) was 774 d, the ratio of the long-term prestress

losses of B1# and B3# was 1.169, and that of B2# and B4# was 1.175. The results show that, with the same initial loading stress level, the later the tensile age (t_p), the smaller the influence of concrete shrinkage and creep and the smaller the long-term prestress loss of the prestressed tendons.

(2) Initial loading stress level

The same tensile age (t_p) was maintained, and the long-term prestress losses of the prestressed tendons corresponding to B1# and B2#, and B3# and B4#, at different initial loading stress levels were compared, as shown in Figure 7.

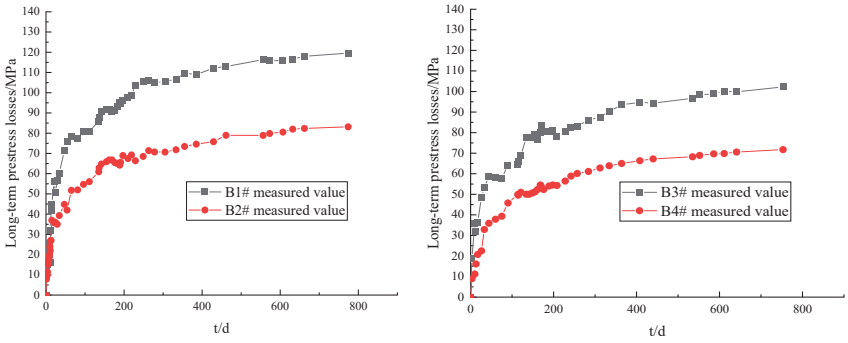

Figure 7. Comparison of long-term prestress loss values at different initial loading stress levels.

As can be seen in Figure 7, the long-term prestress loss values of the prestressed tendons of each test T-beam with different initial loading stress levels gradually increased with the holding time. The early stage of development was relatively fast, and the later stage tended to gradually flatten. When the load holding time (t) was 774 d, the ratio of the long-term prestress losses of B1# and B2# was 1.418, and that of B3# and B4# was 1.425. The results show that, with the same loading age (t_p), the higher the initial loading stress level of the test beam, the smaller the long-term prestress loss of the prestressed tendons.

4.3. Comparison and Verification of the Measured Values and Calculated Results

Taking the loading age of t_0 as the starting time, the long-term prestress losses of the prestressed tendons of beams 1#~4# in the field test environment were calculated using the JTG 3362-2018 specification [21], the AASHTO LRFD-2007 specification [22], and the long-term prestress loss time-varying law model of this paper.

The calculation process of the JTG 3362-2018 specification is as follows.

(1) Prestress loss caused by relaxation of prestressed ribs:

$$\sigma_{l5} = \psi \cdot \zeta \cdot \left(0.52\frac{\sigma_{pe}}{f_{py}} - 0.26\right) \cdot \sigma_{pe} \tag{13}$$

where ψ is the tension coefficient; ψ = 1.0 with one tension; ψ = 0.9 with an over tensile state; ζ is the steel bar relaxation coefficient; for level I relaxation (ordinary relaxation), ζ = 1.0; for level II relaxation (low relaxation), ζ = 0.3; σ_{pe} is the rebar stress (MPa) during anchoring.

(2) Prestress loss caused by concrete shrinkage creep:

$$\sigma_{l6}(t) = \frac{0.9\left[E_p\varepsilon_{cs}(t,t_0) + \alpha_{Ep}\sigma_{pc}\phi(t,t_0)\right]}{1 + 12\rho\rho_{ps}} \tag{14}$$

where $\sigma_{l6}(t)$ is the prestress loss (MPa) caused by concrete shrinkage and creep at the center of gravity of the longitudinal rebar section; σ_{pc} is the normal stress of concrete (minus the first loss) generated by the prestress of the center of gravity of all longitudinal rebar

sections (MPa); E_p is the modulus of elasticity (MPa) of the prestressed rebar; α_{Ep} is the ratio of the elastic modulus of prestressed steel bars to the elastic modulus of concrete; ρ is the longitudinal reinforcement ratio of the component; $\varepsilon_{cs}(t, t_0)$ is the concrete shrinkage strain at the computed age t, when the age of the transmitting of forces and anchorage of prestressed reinforcement is assumed as t_0; $\phi(t, t_0)$ is the creep coefficient when the loading age is t_0, and the computed age is t. ρ_{ps} is the parameter related to the radius of rotation of the section i and the distance e_{ps} from the cross section gravity of prestressed reinforcement and non-prestressed rebar in the tensioning zone for members to the gravity axis of the cross section of members.

Long-term prestress loss:

$$\sigma_{l11} = \sigma_{l5} + \sigma_{l6}(t) \tag{15}$$

The calculation process of the AASHTO LRFD-2007 specification is as follows.

(1) Prestress loss caused by relaxation of prestressed ribs:

$$\Delta f_{pR1} = \frac{f_{pt}}{K_L}\left(\frac{f_{pt}}{f_{py}} - 0.55\right) \tag{16}$$

where f_{pt} is the stress of the prestressed steel strand after the anchor is transmitted, and the value is not less than $0.55f_{py}$ (MPa); if K_L does not have more accurate factory data, we take 30 for a low-relaxation steel strand, and 7 for other prestressed steel bars.

(2) Prestress loss due to concrete shrinkage:

$$\Delta f_{pSD} = \frac{\varepsilon_{bdf} E_p}{1 + \frac{E_p A_{ps}}{E_{ci} A_c}\left(1 + \frac{A_c e_{pc}^2}{I_c}\right)\left[1 + 0.7\psi_b\left(t_f, t_i\right)\right]} \tag{17}$$

where ε_{bdf} is the shrinkage strain of concrete from the moment of plate installation to the final moment; e_{pc} is the eccentricity (mm) of the prestress shape of the combined section; A_c is the cross-sectional area (mm^2); I_c is the cross-sectional moment of inertia (mm^4). A_{ps} is the area of prestressing steel. E_{ci} is concrete bullet mold. $\psi_b\left(t_f, t_i\right)$ is girder creep coefficient at final time due to loading introduced. t_f is final age (days). t_i is age at transfer (days).

(3) Prestress loss caused by concrete creep:

$$\Delta f_{pCD} = \frac{E_p}{E_{ci}} f_{cgp}\left[\psi_b\left(t_f, t_i\right) - \psi_b(t_d, t_i)\right] K_{df} + \frac{E_p}{E_c}\Delta f_{cd}\psi_b\left(t_f, t_d\right) K_{df} \tag{18}$$

where Δf_{cd} is the change in concrete stress at the center of the steel strand caused by long-term stress loss during the installation of the anchor to the plate, and the self-weight and applied load (MPa) of the plate are considered. $\psi_b\left(t_f, t_d\right)$ is the creep coefficient of the final time component. f_{cgp} is sum of concrete stresses at the center of gravity of prestressing tendons due to the prestressing force after jacking and the self-weight of the member at the sections of maximum moment(MPa). K_{df} is transformed section coefficient that accounts for time-dependent interaction between concrete and bonded steel in the section being considered for time period between deck placement and final time. $\psi_b(t_d, t_i)$ is girder creep coefficient at time of deck placement due to loading introduced. t_d is age at deck placement (days).

Long-term prestress loss:

$$\Delta f_{pLT} = \Delta f_{pSD} + \Delta f_{pCD} + \Delta f_{pR1} \tag{19}$$

The comparison between the measured values and the calculated results of the long-term prestress losses of the prestressed tendons of the T-beam in each test at different load holding times (t) is shown in Figure 8.

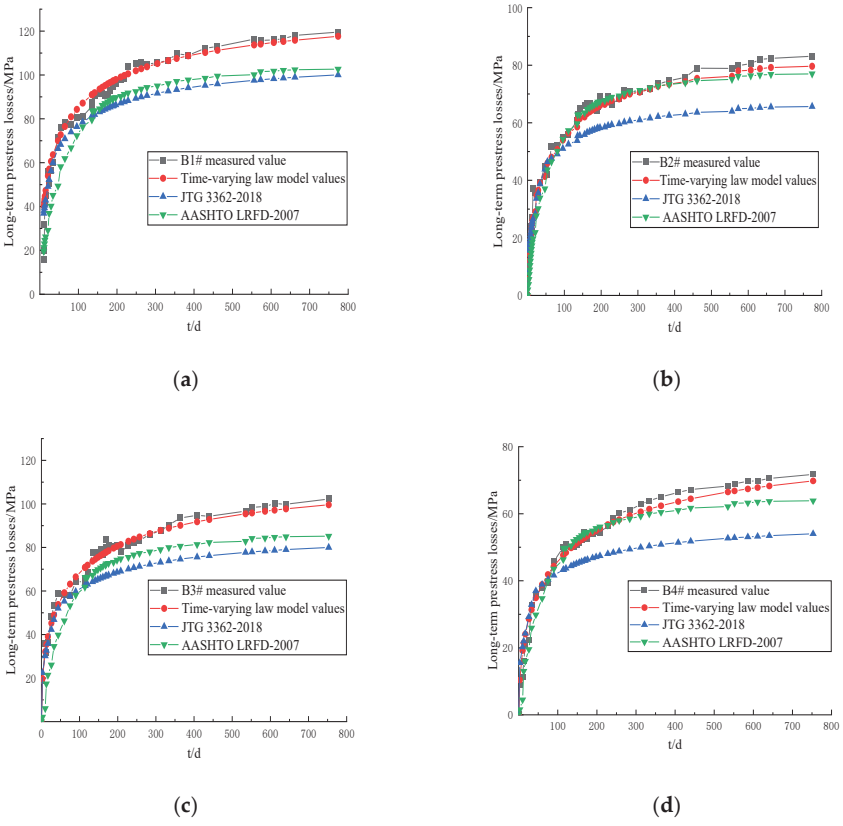

Figure 8. Comparison of the measured values of the long-term prestress losses of the test T-beams and the calculation results: (**a**) B1#; (**b**) B2#; (**c**) B3#; (**d**) B4#.

As can be seen in Figure 8, the calculated results of the long-term prestress losses of the prestressed tendons using the JTG 3362-2018 specification, the AASHTO LFD-2007 specification, and the time-varying law model were essentially consistent with the development trend of the measured values. With an increase in the load holding time (t), the long-term prestress losses gradually increased. The long-term prestress losses developed rapidly in the initial loading stage. In the later period, the rate of change gradually slowed down and tended to be stable. When the load holding time (t) was less than 100 d, the calculated results of the three models were in good agreement with the measured values. However, as the load holding time (t) continued to increase, the differences between the calculated results of JTG 3362-2018 and AASHTO LFD-2007 and the measured values became larger and larger. When the load holding time (t) was 774 d, the relative errors of long-term prestress loss calculated by JTG 3362-2018 for B1#~B4# were 1.198, 1.272, 1.281, and 1.327, respectively. The relative errors of long-term prestress loss calculated by the AASHTO LRFD-2007 code were 1.164, 1.094, 1.200, and 1.072, respectively. The relative errors of long-term prestress loss calculated by the time-dependent law model were 1.017, 1.039, 1.027, and 1.027, respectively. The error between JTG 3362-2018 and AASHTO LRFD-2007 was large. The calculated results of the long-term prestress losses of the prestressed tendons using the time-varying law model were in good agreement with the measured values.

The calculated results of the long-term prestress losses of the prestressed tendons using JTG 3362-2018, AASHTO LRFD-2007, and the time-varying law model had variation coefficients (ϑ) relative to the measured values of each test T-beam, as shown in Table 2.

Table 2. The coefficient (ϑ) of variation of each predictive model relative to the measured values (unit: %).

Model of Prediction	B1#	B2#	B3#	B4#	Mean Coefficient of Variation
JTG 3362-2018	15.69	17.27	17.93	20.15	17
AASHTO LRFD	12.56	8.73	10.54	9.34	10
Time-varying law model	9.10	4.88	4.12	4.98	6

Remarks: $\vartheta = \sqrt{\frac{1}{n-1}\sum_{i=1}^{n}\left(\Delta\sigma'_{p,i} - \Delta\sigma_{p,i}\right)^2}/\overline{\Delta\sigma_p}$, $\overline{\Delta\sigma_p} = \sum_{i=1}^{n}\Delta\sigma_{p,i}/n$, and $\overline{\vartheta} = \sqrt{\frac{1}{n}\sum_{j}\vartheta^2}$. $\Delta\sigma'_{p,i}$ is the calculated value of the long-term prestress loss (i); $\Delta\sigma_{p,i}$ is the measured value of the long-term prestress loss (i); ϑ is the j group of the variation coefficient, and $\overline{\vartheta}$ is the coefficient of variation relative to all the data.

As can be seen in Table 2, the average coefficients of variation of JTG 3362-2018, AASHTO LRFD-2007, and the time-varying law model were 17%, 10%, and 5%, respectively. The results show that the interaction of concrete shrinkage, concrete creep, and stress relaxation is considered in the theoretical derivation, and more accurate calculation results are obtained.

5. Conclusions

- The interaction between concrete shrinkage, creep, and the stress relaxation of prestressed reinforcement was considered. A time-varying model of the long-term prestress losses of prestressed concrete beams was established. A calculation method for the long-term prestress losses of concrete structures was developed. The calculation results of the long-term prestress loss of a structure were more secure and reliable.
- A long-term prestress loss test of a prestressed concrete T-beam in a long-term field test environment was carried out. The development trend of the long-term effective tensile force of the prestressed tendons of the T-beam was essentially the same in all tests. With an increase in the load holding time, the long-term effective tensile force gradually decreased. The tensile force changed rapidly in the initial stage of loading and gradually slowed down in the later stage. When the load holding time was 774 d, the long-term tensile losses of the prestressed tendons of B1#~B4# were 10.52%, 7.44%, 9.01%, and 6.30%, respectively.
- The influence of the tensile age and the initial loading stress level on the long-term prestress losses of prestressed concrete T-beams was analyzed. When the holding time was 774 d, the ratios of the long-term prestress losses of beams 1# and 3# and beams 2# and 4# were 1.169 and 1.175, respectively. This shows that the later the tensile age, the smaller the long-term prestress loss of the prestressed tendons. The ratios of the long-term prestress losses of beams 1# and 2# and beams 3# and 4# were 1.418 and 1.425, respectively. This indicates that the higher the initial loading stress level, the smaller the long-term prestress loss of the prestressed tendons.
- The measured values of the long-term prestress losses of the prestressed concrete T-beams were compared with the calculated results of the JTG 3362-2018 specification, the AASHTO LRFD-2007 specification, and the time-varying law model. The calculated results of the long-term prestress losses of the three theoretical models were essentially consistent with the development trend of the measured values. When the load holding time was less than 100 d, the calculated results of the three models were in good agreement with the measured values. However, as the load holding time continued to increase, the differences between the calculated results of JTG 3362-2018 and AASHTO LRFD-2007 and the measured values became larger and larger. The average coefficients of variation of the long-term prestress loss calculation results of JTG 3362-2018, AASHTO LRFD-2007, and the time-varying law model were 17.23%, 10.29%, and 5.64%, respectively. This shows that the time-varying law model of the

long-term prestress losses of prestressed tendons established in this study has good accuracy and can better predict the long-term prestress losses of prestressed tendons.

In this paper, a long-term time-varying model of prestress loss considering the interaction of concrete shrinkage, concrete creep, and stress relaxation is proposed. The long-term prestress loss test of a prestressed T-beam under a long-term exposure test environment was carried out for test verification. A long-term prestress loss calculation method for concrete structures was formed, which makes the calculation of the internal forces of bridge structures safer and more reliable.

Author Contributions: Conceptualization, W.H.; data curation, P.T. and C.Z.; formal analysis, P.T.; investigation, W.H.; methodology, Y.L.; supervision, Y.L.; writing—original draft, T.L. and C.Z.; writing—review and editing, T.L. All authors have read and agreed to the published version of the manuscript.

Funding: The work was supported by the Open Fund of the National Engineering Research Center of Highway Maintenance Technology (Changsha University of Science & Technology) (Grant No. kfj210102); the Natural Science Foundation of Hunan Province (Grant No. 2022JJ30600); the Natural Science Foundation of Changsha (Grant No. kq2202208); and the Open Fund of Scientific Research and Innovation Platform of the Education Department of Hunan Province (Grant No. 20K005).

Institutional Review Board Statement: Not applicable.

Informed Consent Statement: Not applicable.

Data Availability Statement: Data are contained within the article.

Conflicts of Interest: The authors declare no conflict of interest.

References

1. Pavlović, A.; Donchev, T.; Petkova, D.; Limbachiya, M. Short- and Long-Term Prestress Losses in Basalt FRP Prestressed Concrete Beams under Sustained Loading. *J. Compos. Constr.* **2022**, *26*, 56–63. [CrossRef]
2. Xu, Q.; Zeng, B.; Xu, X.D.; Wang, X.F. Distribution Characteristics and Estimation Method of Prestress in Concrete Structures Based on Gaussian Mixture Model. *J. Archit. Struct.* **2022**, *43*, 60–67.
3. Zheng, X.; He, M.; Lam, F.; Sun, X.; Liang, F.; Li, Z. Experimental and Numerical Investigation of Long-Term Loss of Prestressing Force in Posttensioned Timber Joints with Different Structural Details. *J. Struct. Eng.* **2022**, *148*, 97–105. [CrossRef]
4. Shokoohfar, A.; Rahai, A. Prediction model of long-term prestress loss interaction for prestressed concrete containment vessels. *Arch. Civ. Mech. Eng.* **2017**, *17*, 132–144. [CrossRef]
5. Moravčík, M.; Kraľovanec, J. Determination of Prestress Losses in Existing Pre-Tensioned Structures Using Bayesian Approach. *Materials* **2022**, *15*, 3548. [CrossRef] [PubMed]
6. Tahsiri, H.; Belarbi, A. Evaluation of prestress relaxation loss and harping characteristics of prestressing CFRP systems. *Constr. Build. Mater.* **2022**, *331*, 127339. [CrossRef]
7. Gao, X.; Jia, J.; Mei, G.; Bao, X.; Zhang, L.; Liao, X. A New Prestress Loss Calculation Model of Anchor Cable in Pile–Anchor Structure. *Mathematics* **2022**, *10*, 1260. [CrossRef]
8. Biswal, S.; Ramaswamy, A. Uncertainty based model averaging for prediction of long-time prestress losses in concrete structures. *Constr. Build. Mater.* **2017**, *153*, 469–480. [CrossRef]
9. Sun, G.; Li, Z.; Wu, J.; Qu, X.; Ren, J. Investigation into the Prestress Loss and Thermal Expansion Performance of Steel Cables at High Temperature. *Int. J. Steel Struct.* **2022**, *22*, 1–17. [CrossRef]
10. Lee, S.; Lee, C. Bonding Time and Prestress Loss in Precast Pretensioned Concrete during Steam Curing. *J. Struct. Eng.* **2022**, *148*, 04022002. [CrossRef]
11. Kim, S.H.; Park, S.Y.; Kim, S.T.; Jeon, S.J. Analysis of Short-Term Prestress Losses in Post-tensioned Structures Using Smart Strands. *Int. J. Concr. Struct. Mater.* **2022**, *16*, 1–15. [CrossRef]
12. Kim, S.T.; Park, Y.S.; Yoo, C.H.; Shin, S.; Park, Y.H. Analysis of Long-Term Prestress Loss in Prestressed Concrete (PC) Structures Using Fiber Bragg Grating (FBG) Sensor-Embedded PC Strands. *Appl. Sci.* **2021**, *11*, 12153. [CrossRef]
13. Abdel-Jaber, H.; Glisic, B. Monitoring of long-term prestress losses in prestressed concrete structures using fiber optic sensors. *Struct. Health Monit.* **2019**, *18*, 254–269. [CrossRef]
14. Bonopera, M.; Chang, K.C.; Lee, Z.K. State-of-the-art review on determining prestress losses in prestressed concrete girders. *Appl. Sci.* **2020**, *10*, 7257. [CrossRef]
15. Lu, Z.F.; Liu, M.Y. A Calculation Method for Long-term Prestress Loss of Concrete Structures. *J. Wuhan Univ. Technol.* **2011**, *33*, 83–87.

16. Páez, P.M.; Sensale, B. Improved prediction of long-term prestress loss in unbonded prestressed concrete members. *Eng. Struct.* **2018**, *174*, 111–125. [CrossRef]
17. Guo, T.; Chen, Z.; Lu, S.; Yao, R. Monitoring and analysis of long-term prestress losses in post-tensioned concrete beams. *Measurement* **2018**, *122*, 573–581. [CrossRef]
18. Cao, G.; Zhang, W.; Hu, J.; Zhang, K. Experimental study on the long-term behaviour of RBPC T-beams. *Int. J. Civ. Eng.* **2018**, *16*, 887–895. [CrossRef]
19. Samer, A.; Youakim, A.G.; Hida, S.E. Prediction of long-term prestress losses. *PCI J.* **2007**, *52*, 116–130.
20. Yang, M.; Gong, J.; Yang, X. Refined calculation of time-dependent prestress losses in prestressed concrete girders. *Struct. Infrastruct. Eng.* **2020**, *16*, 1430–1446. [CrossRef]
21. Zhang, H.; Guo, Q.; Xu, L.Y. Prediction of long-term prestress loss for prestressed concrete cylinder structures using machine learning. *Eng. Struct.* **2023**, *279*, 115577. [CrossRef]
22. CCCC Highway Consultants Co, Ltd. *Code for Design of Highway Reinforced Concrete and Prestressed Concrete Bridges and Culverts: JTG 3362-2018*; Communications Press: Beijing, China, 2018.
23. *AASHTO LRED Bridge Design Soecifications (2007)*; American Association of State Highway and Transportion Officiais: Washington, DC, USA, 2009.
24. Pan, Z.F.; Lv, Z.T.; Liu, Z. Uncertainty Analysis of Shrinkage and creep Effect of Continuous Rigid Frame on Sutong Bridge. *Eng. Mech.* **2009**, *26*, 67–73. [CrossRef]
25. Bazant, Z.P. Prediction of concrete creep effects using age-adjusted effective modulus method. *ACI J.* **1972**, *69*, 212–217.
26. Bažant, Z.P. Concrete fracture models: Testing and practice. *Eng Fract Mech.* **2002**, *69*, 165–205. [CrossRef]
27. Alghazali, H.; Myers, J. Time-dependent prestress loss behavior of girders in Missouri bridge A7957 compared with a US data set of high-performance concrete bridge girders. *PCI J.* **2017**, *62*, 76–87. [CrossRef]
28. Guo, T.; Ping, Z.; De, L.; Tian, Z. Study on short-term prestress loss of bridge reinforced with large diameter carbon fiber bars. *IOP Conf. Ser. Earth Environ. Sci.* **2021**, *820*, 012001. [CrossRef]
29. Shi, K.; Wu, X.; Tian, Y.; Xie, X. Analysis of Re-Tensioning Time of Anchor Cable Based on New Prestress Loss Model. *Mathematics* **2021**, *9*, 1094. [CrossRef]
30. Li, X.; Deng, J.; Wang, Y.; Xie, Y.; Liu, T.; Rashid, K. RC beams strengthened by prestressed CFRP plate subjected to sustained loading and continuous wetting condition: Time-dependent prestress loss. *Constr. Build. Mater.* **2021**, *275*, 122187. [CrossRef]
31. Bellendir, E.N.; Rubin, O.D.; Lisichkin, S.E.; Zyuzina, O.V. Experimental Study into Prestress Losses of Basalt Composite Reinforcement Used in the Composition of Concrete Elements. *Power Technol. Eng.* **2021**, *54*, 605–608. [CrossRef]
32. Yue, S.; Chu, Q. Prestress Loss Analysis and Overload Early Warning Research of Simply Supported Girder Bridge Based on Embedded Computer and Fiber Grating Sensing Technology. *J. Phys. Conf. Ser.* **2020**, *1648*, 032037. [CrossRef]
33. Kamatchi, R.; Rao, K.B.; Dhayalini, B.; Saibabu, S.; Parivallal, S.; Ravisankar, K.; Iyer, N. R Long-Term Prestress Loss and Camber of Box-Girder Bridge. *ACI Struct. J.* **2014**, *111*, 1297–1306. [CrossRef]
34. Li, G.; Wu, J.T. Stress relaxation characteristics of prestressed GFRP anchor under erosion conditions. *Chin. J. Rock Mech. Eng.* **2022**, *39*, 877–886.
35. Xu, F.; Li, D.; Zhang, Z.; Zhang, Q.T.; Kang, L.; Wei, Y. Comparison of Concrete Creep-Induced Structural Prestress Loss Calculated by Codes from Different Countries. *J. Highw. Transp. Res. Dev.* **2019**, *13*, 23–34. [CrossRef]
36. Shi, J.; Wang, X.; Wu, Z.; Wei, X.; Ma, X. Long-term mechanical behaviors of uncracked concrete beams prestressed with external basalt fiber-reinforced polymer tendons. *Eng. Struct.* **2022**, *262*, 114309. [CrossRef]
37. Sung, D.; Hong, S. Experimental study on long-term behavior of prestressed steel I-beam-concrete composite beams. *Steel Compos. Struct.* **2022**, *42*, 671–683.
38. Dai, L.; Bian, H.; Wang, L.; Potier-Ferry, M.; Zhang, J. Prestress loss diagnostics in pretensioned concrete structures with corrosive cracking. *J. Struct. Eng.* **2020**, *146*, 04020013. [CrossRef]
39. Chai, S.; Guo, T.; Chen, Z.; Yang, J. Monitoring and simulation of long-term performance of precast concrete segmental box girders with dry joints. *J. Bridge Eng.* **2019**, *24*, 04019043. [CrossRef]
40. Han, W.; Lü, Y. Experimental research on prediction model of concrete shrinkage and creep. *J. Cent. South Univ. (Sci. Technol.)* **2016**, *47*, 3515–3522.

materials

MDPI

Article

Effect of Vibration Procedure on Particle Distribution of Cement Paste

Jia Ke [1,2], Zhonghe Shui [2,3,4], Xu Gao [3,5,*], Xibo Qi [2,5], Zihang Zheng [2,5] and Shaolin Zhang [6]

[1] International School of Materials Science and Engineering, Wuhan University of Technology, Wuhan 430070, China
[2] State Key Laboratory of Silicate Materials for Architectures, Wuhan University of Technology, Wuhan 430070, China
[3] Wuhan University of Technology Advanced Engineering Technology Research Institute of Zhongshan, Xiangxing Road 6, Zhongshan 528400, China
[4] School of Materials Science and Engineering, Wuhan University of Technology, Wuhan 430070, China
[5] School of Civil Engineering and Architecture, Wuhan University of Technology, Wuhan 430070, China
[6] China Construction Third Bureau First Engineering Co., Wuhan 430070, China
* Correspondence: x.gao@whut.edu.cn

Abstract: Vibration procedures significantly affect the performances of cement-based materials. However, studies on the distribution of certain particles within cement-based materials are limited due to the complexity and difficulty of identifying each specific particle. This paper presents a new method for simulating and quantifying the movements of particles within cement paste through the use of "tagged materials". By separating the tagged particles from the cement paste after vibration, the distribution of the particles in the cement paste can be calculated statistically. The effect of the vibration time and frequency, fresh behavior, and powder characteristics of cement paste on particle motions are investigated. The results demonstrate that when the vibration exceeds 1800 s, it induces a significant uneven dispersion of microparticles. This effect is more pronounced at low viscosities (<1 Pa·s) of cement paste or high vibration frequencies (>200 Hz). Larger and denser particles exhibit greater dispersion. This method provides a valuable tool for investigating the theory of particle motion in cement paste, which is crucial for understanding the influence of vibration on the properties of cement-based materials.

Keywords: vibration procedure; particle distribution; tagged materials; cement paste

Citation: Ke, J.; Shui, Z.; Gao, X.; Qi, X.; Zheng, Z.; Zhang, S. Effect of Vibration Procedure on Particle Distribution of Cement Paste. *Materials* **2023**, *16*, 2600. https://doi.org/10.3390/ma16072600

Academic Editor: Krzysztof Schabowicz

Received: 21 February 2023
Revised: 15 March 2023
Accepted: 22 March 2023
Published: 24 March 2023

1. Introduction

Cement-based materials are most widely used as concrete structures, dominating in buildings and infrastructure [1]. During casting, vibration is frequently used to maintain the ideal dispersion and density of cement-based materials, as vibration eliminates air bubbles and rearranges the particle composition in concrete [2]. Construction guides and specifications, such as the ACI Material Journal, have shown how vibration should be performed to achieve dense concrete [3]. However, the vibration process is usually designed based on previous experiences. These vibration procedures are different for different conditions and projects. Moreover, it should be noted that inappropriate vibration can cause a reduction in the strength and durability of cement-based materials [4].

The impact of mechanical vibration on the performance of cement-based materials has been extensively studied, as it is the most commonly encountered type of vibration during construction and directly affects the quality and service life of concrete structures [5,6]. Vibration is a macroscopic physical process, and the microstructure of cement-based materials is altered during this process [7]. Understanding how the structure and hydration mechanisms of cement-based materials change during vibration is crucial for comprehending the changes in their properties [8,9].

It has been concluded that in cement-based materials, vibration accelerates the hydration and dissolution of cementitious particles, leading to the rapid formation of the cement matrix. This process enhances the strength of cement-based materials but may also result in the formation of microcracks. More specifically, vibration can readily influence microstructure development and increase the possibility of microdefects [2,7,10]. Another widely accepted viewpoint is that the yield stress of cement-based materials significantly decreases upon vibration as a result of the breaking of the interlocking of coarse aggregates due to the movement of cement-based materials in response to vibration, which disrupts the attraction between the cement and other microscopic particles and reduces the internal friction of the cement paste [4]. The improvement of mechanical properties by vibration is often attributed to the rearrangement of particles within cement-based materials. It is widely accepted that the composition and structure of a material dictate its properties [11,12]. Particularly for the particle distribution characteristics of cement-based materials under vibration, particle rearrangement greatly determines the performance of cement-based materials [13]. The improvement in the compactness of cement-based materials can be confirmed by detecting the porosity of cement-based materials after vibration treatment, typically tested using mercury intrusion porosimetry (MIP) [14].

Currently, it is still a challenging issue to visually observe the changes of particle distribution in cement-based materials after vibration. Many scholars have studied the movement characteristics of the aggregates and fiber in cement-based materials during vibration. In steel-fiber-reinforced concrete (SFRC), researchers usually evaluate the fiber distribution by statistically analyzing the area, orientation, or count of fibers in different cross-sectional regions [15,16]. By washing out different parts of the coarse aggregate of concrete after vibration for weighing and statistical calculations, Mohammad derived the distribution characteristics of coarse aggregate at different vibration intensities and viscosities of concrete and proposed a vibration strategy to control fresh high-fluidity concrete to maintain homogeneity and workability [17,18]. Petrou used radioactive metal spheres as tagged aggregates and used a scintillation camera to track their position in a concrete mix under vibration, simulating the movement of aggregates in concrete-based materials under vibration in real time [4].

Compared to coarse aggregates and fibers, cement particles are much smaller, and it is more challenging to characterize their distribution. Due to limitations in testing methods and detection means, the distribution changes of small-sized particles such as cement particles and mineral admixtures in cement-based materials after vibration are often overlooked. By examining the strength, porosity, and elemental distribution of the various layers of cement test blocks, Ling was able to detect and characterize the inhomogeneous distribution of various microparticles and confirmed that this inhomogeneity is related to the mechanical properties of hardened cement paste [2]. This means that the distribution of microparticles is important to the properties of cement-based materials. At the current stage, numerical computer simulations are often unable to fully simulate actual operating conditions or experimental conditions, and the use of isotopic labeling is costly. There is a need for a simple and quantifiable method to characterize the motion of particles in cement-based materials under vibration.

In this paper, "tagged" materials are used to simulate cement particles and other particles in the paste [4]. These materials are insoluble in water and have a similar particle size as cement particles. After vibration, the tagged materials are separated from different parts of the cement block by washing with water and screening, allowing us to observe the particle distribution in the cement paste. The feasibility of using tagged materials to explore the distribution and movement patterns of cement particles under vibration is evaluated, and the correlation between the vibration procedure (time and frequency) and the properties of the cement paste are discussed, which is essential for optimizing the design and performance of cement-based materials.

2. Materials and Methods

Portland cement type I 42.5 according to Chinese National Standard GB 175-2007 was used as the binder. The water consumption of the cement was 26.1% [19]. The following were used to produce the paste samples: Fe powder with a particle size between 25 and 100 μm and a density of about 7.85 gr/cm^3; C powder with a particle size distribution of 25–100 μm and a density of about 1.60 gr/cm^3. The following were used as tag materials: silicon carbide powder with a particle size of 25–100 μm and a density of about 3.23 gr/cm^3; boron carbide (B_4C, a ceramic material composed of boron and carbon atoms that has good chemical resistance and does not interact with water or cement) powder with a particle size of 25–100 μm and a density of about 2.52 gr/cm^3. A polycarboxylic ether-based superplasticizer (SP) was used to adjust the workability. The SP had a solid content of about 20% and a water-reducing rate of more than 30% [20,21].

A method aimed at quantifying the trend and distribution of particles in cement-based materials under vibration is proposed. The experimental procedure is depicted in Figure 1. Solid particles of a similar size to cement particles were selected to simulate the motion of cement particles in the cement paste. These particles exhibit excellent chemical resistance, and they are not soluble in water. Therefore, they can be separated from different parts of the cement paste by sieving through a mesh with a smaller pore size than the particles. A four-degrees-of-freedom vibration table was used to provide different vibration conditions, with an iron vertical triple mold fixed on the vibration table. The mold size was 40 × 40 × 160 mm (height), with a thickness of 10 mm for the long side and 7 mm for the short side. After the tagged particles were screened through a 25 μm sieve, they were mixed into the cement paste according to the designed proportions and poured into the mold [22]. The vibration process was completed by adjusting the vibration table. Before the cement paste hardened, the mold was removed from the shaking table, and the long-side plate was taken off. The cement paste was then divided into four parts using 0.1 mm thick metal sheets, to allow for subsequent testing of different parts of the paste. The mass of each part was recorded as "m". Each part was rinsed with running water, and the cement paste was sieved through a 25 μm sieve to collect the particles that remained on the sieve. After drying under vacuum, the mass of these particles was weighed and recorded as "d" for further analysis. The ratio of d to m was defined as DR, and $\overline{DR}$ was defined as the ratio of the total mass of the dopant material to the total mass of the cement paste (as illustrated in Equations (1) and (2)) [17,23]:

$$DR = d/m = \frac{\text{weight of dopant materials of the layer}}{\text{weight of total mass of the layer}} \quad (1)$$

$$\overline{DR} = d_{total}/m_{\ total} = \frac{\text{total weight of dopant materials}}{\text{total weight of the cement paste}} \quad (2)$$

To quantitatively characterize the movement and migration of tagged materials in cement-based materials under different conditions, a calculation method has been defined. This method assigns discrete significance to the specific gravity of the DR for different layers and defines it as DF. The DF is used to measure the degree of dispersion of the tagged materials in each group (as illustrated in Equation (3)) [15,17]:

$$DF = \sqrt{\frac{\sum_{i=1}^{i=n}(1-x_i)^2}{n}} \ (x_i = \frac{DR_i}{(\overline{DR})}) \quad (3)$$

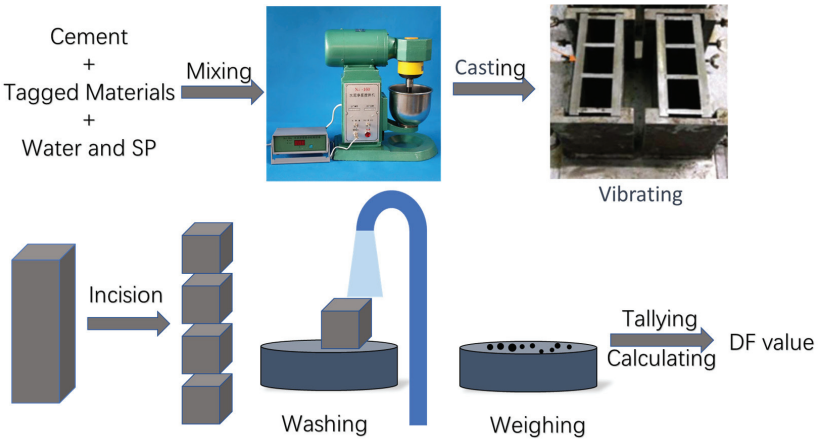

Figure 1. Schematic diagram of main experimental procedures.

The mix proportions used in this study for each section are listed in Table 1.

Table 1. Mix ratio of cement paste in this study.

Experiments	W/C	Dopant in Ratio to Cement				Size (μm)	Sp (%)
		SiC	Fe	B_4C	C		
Feasibility Study	0.33	0.1	0.1	0.1	0.1	Original size	/
Effect of Vibration Time	0.3	0.1	/	/	/	Original size	0.8
Influence of Viscosity of Cement Paste	0.30	0.10	/	/	/	Original size	1
	0.25	0.11	/	/	/		2
	0.35	0.10	/	/	/		0.5
	0.30	0.12	/	/	/		0.8
	0.25	0.09	/	/	/		1.6
	0.25	0.09	/	/	/		1.2
Influence of Flowability of Cement Paste	0.25	0.09	/	/	/	Original size	0.9
	0.30	0.11	/	/	/		0.8
	0.35	0.12	/	/	/		0.6
	0.40	0.11	/	/	/		0.4
	0.50	0.09	/	/	/		0
Significance of Particle Size and Density	0.30	0.1				75	0.8
	0.33	0.1				25	0.9
	0.32		0.1			75	0.8
	0.33		0.1			25	0.8
	0.35			0.1		75	1
	0.36			0.1		25	0.8
	0.49				0.1	75	1
	0.52				0.1	25	1
Effect of Vibration Frequency	0.30	0.1	/	/	/	75	0.8
	0.33	0.1	/	/	/	25	0.9

3. Results and Discussion

3.1. Validation of the Proposed Method

For the method used to quantitatively characterize the trend of particle distribution in cement-based materials under vibration, the following experiment is designed to illustrate its feasibility and reliability. All kinds of tagged particles were mixed and sifted through a screen with a 25-micron pore size. The mixture was weighed and subsequently added to the cement paste, which was then thoroughly mixed. After that, the cement paste, as well as the mixing container, was slowly rinsed through the same screen with running water. The mass of the particles collected through the sieve residue is weighed and compared to the mixture of tagged particles. The composition of the mixture is given in Table 1. Figure 2 shows the XRD results of the tagged material mixture with the sieve residue.

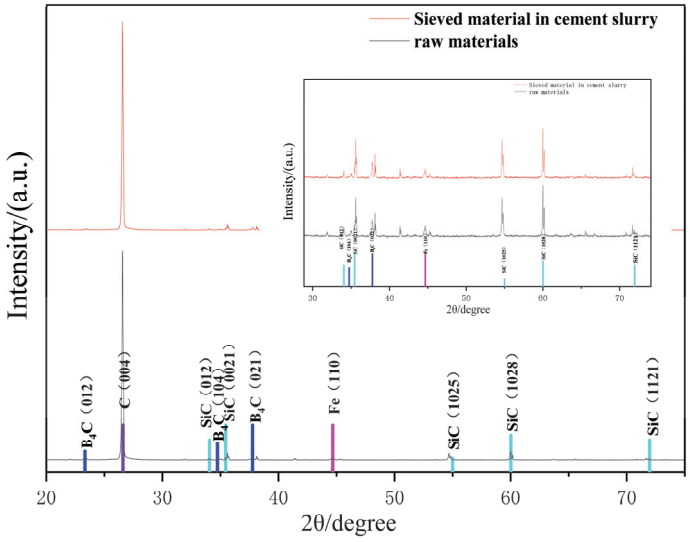

Figure 2. XRD results of the tagged material mixture with the sieve residue.

As a result, the mass of the tagged particles recovered was 93.2% of the original mass, by means of sieving, as water and cement particles reacted and combined to form a suspension. They adhered to each other. It could be flushed from the screen point with the flowing water, and other insoluble materials were left on the screen, as the materials used were not chemically or physically reactive with water, most of the tagged particles can be collected. The XRD plots of the original sample and the sample rinsed and sieved from the paste showed that the rinsed sample had basically the same XRD spectrum as the original sample. The (004) crystalline surface of the toner had a meritocratic orientation. Strong diffraction peaks appeared and showed high absorption values in XRD, and the peak intensity of the rest of the material is basically the same, indicating that the basic composition of the material obtained after the test process was the same as the raw material. The tagged materials selected for this experiment were easy to separate from the cement paste and maintain their original physical properties. It means that the tagged particles collected from different parts of the cement slurry can be considered representative of all tagged particles in certain parts. The feasibility of using flushing sieve residuals to quantify how much tagged material is available for different portions of cement-based materials was verified.

3.2. Effect of Vibration Duration

The relationship between vibration time and the distribution of the tagged particles is investigated. The materials ratios used in this phase of the experiment are shown in Table 1. The selected fundamental frequency of 200 Hz and the gravitational acceleration of 5G (average displacement—0.06 mm) and vibration times are selected as 0 s, 30 s, 90 s, 180 s, 360 s, 1080 s, 2160 s, 3600 s, and 5400 s.

Figure 3 shows the graph of DF values changing with vibration time, it can be seen that with the increase in vibration duration, the overall DF calculation value gradually increases. The DF value is used to characterize the dispersion of the distribution of tagged particles between the different layers. At this time, because of the occurrence of vibration, the yield stress of the cement paste decreased, and the particles were subjected to gravity to settle in the paste, resulting in a certain uneven distribution within the paste, and the result shows that the DF increases with time. When the vibration time was 0, the calculated DF value was very close to 0, which was in accordance with the expected result. When the cement paste was not subject to vibration, it possessed a certain yield stress. According to the research of Petrous et al. [4], even in the absence of vibration, it was difficult for high-quality aggregate or materials with higher densities than the aggregate to induce motion, even when their volume was the same. The added material was uniformly distributed in the paste at the vibration time of 0. As time went on, the rate at which the discrete distribution of marked particles increased gradually slowed down as the settle range of particles was limited, and the internal structure of the cement paste changed, causing a gradual change in yield stress and a gradual slowdown in the trend of the movement of material particles. These factors all contributed to the gradual decline in the growth rate of the DF value. The use of tagged particles has allowed researchers to discover that small particles with similar size and density to cement particles can move within cement paste when subjected to vibration. Even short periods of vibration, less than 180 s, can cause these particles to move vertically in a directional manner, although this may not be easily observable. However, after prolonged vibration for 2000 s or longer, this directional motion becomes more apparent, resulting in phenomena such as bleeding and bubble discharge in the cement substrate [9,24]. This suggests that long-term vertical vibration can cause the distribution of substances other than solid particles to become oriented.

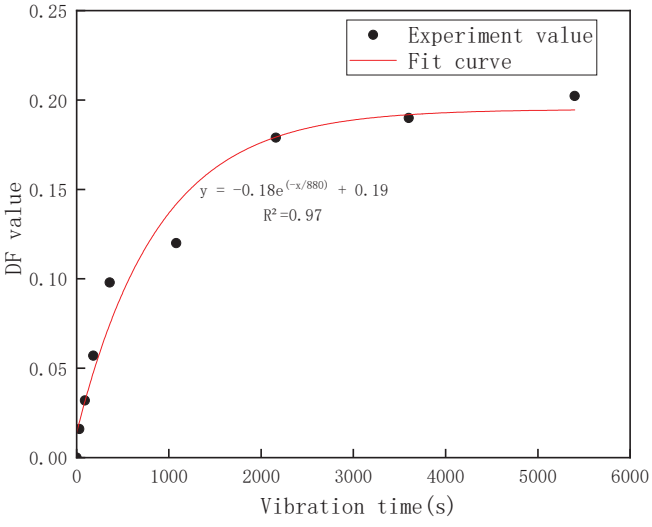

Figure 3. Variation of DF value with vibration time.

In this experiment, the movement of particles similar in size to the cement and mineral admixture particles in the cement paste by using tagged particles is studied. It was found that the particles within the cement slurry underwent continuous directional migration upon exposure to vibration; however, the trend of dispersion of particle distribution due to this migration gradually slowed down over time. The result demonstrates the feasibility of this method for simulating and quantifying the motion of particles similar in size to cement and provides a solid experimental foundation for further experiments

3.3. Influence of Paste Flowability and Viscosity

Based on the above experiments, the method shown in Figure 1 is used to evaluate the relationship between the fluidity of cement paste and the viscosity and particle distribution in the vibrating state. The distribution ratio of the tagged particles in different parts of the cement paste block is obtained. Different viscosities and fluidities were applied by adjusting the water–cement ratio and the Sp content. The viscosity of the cement paste was determined through the utilization of a rotational viscometer, while the fluidity of the cement paste was obtained through the utilization of the flow table test. When exploring the relationship between the viscosity of the slurry and particle movement, the fluidity of the slurry was controlled within the range of 300 ± 15 mm, while the viscosity of the cement paste was within the range of 0.2~1.2 Pa·s. In order to investigate the relationship between the flowability of the slurry and particle movement, the viscosity of the cement paste was then controlled within the range of 0.8 ± 0.1 Pa·s, while the fluidity of the cement paste was within the range of 160~320 mm, the vibration frequency was 200 Hz and the gravitational acceleration was set to 5G (average displacement—0.06 mm), and the vibration time was set to 2160 s. A relatively long period of time is used to increase the trend of particle movement. By controlling the fluidity, the relationship between viscosity and particle distribution trend can be obtained, the mixing ratios are listed in Table 1, then obtaining the relationship between the fluidity and the trend of particle distribution by controlling the viscosity, and the different mixing ratios are listed in Table 1.

In terms of the particles themselves, the particles are subjected to varying viscous forces during their movement in different cement paste environments. Therefore, at this stage the relationship between the rheology of the cement paste itself and the motion of the particles within the paste to obtain universal laws. Therefore the movement of particles in cement paste at different viscosities is studied, while the movement of particles in cement paste with different flowability was also tested.

As can be seen from Figure 4, the degree of dispersion of the tagged particles presents a negative power function of the natural base with the viscosity. When the viscosity was 0.2 Pa·s, the value of the particle distribution dispersion degree (DF) was 0.29, indicating that there was a significant unevenness in the distribution of the tagged particles at this time, suggesting that the particles had undergone large-scale motion within the cement paste during this period, and as the viscosity increased, the DF value gradually decreased, indicating that particles became increasingly difficult to move in the higher viscosity environment. The ease of motion of the tagged particles is related to the viscosity of the cement paste. Previous research [11] has demonstrated that moving particles in non-coagulated cement paste experience friction. The strength of the adhesion between particles determines their ability to impede the flow of cement paste and results in a greater frictional force on particle movement. This adhesive property is known as viscosity. When subjected to vibration, the yield stress of cement paste decreases, making the motion of tagged particles easier. This motion is facilitated by a combination of factors, including the mixing action, gravity, frictional forces, and the viscosity of cement paste. The greater the frictional force on the tagged particles, the more challenging their motion becomes [25]. This is similar to the research conclusions drawn by previous scholars on the movement of aggregates and fibers, indicating that the primary mechanism of solid phase movement in cement-based slurries is similar [18,26,27].

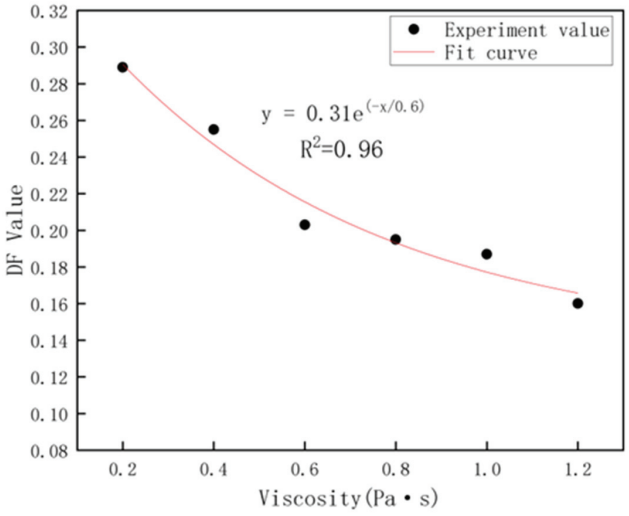

Figure 4. Relations between DF value and viscosity.

The relationship between the DF value and the flowability of the cement paste can be seen in Figure 5, where all the data are around a horizontal straight line, which means that in the case of similar viscosity of the cement paste, even if there is a large difference in the flowability of the cement paste, the ease of movement of the marked particles in it is comparable in the vibrating state. The presence of a large number of hydrophilic groups on the surface of the composite particles and the strong ability of the hydrophilic groups to adsorb water molecules made the movement of the tagged particles in the cement paste easier as some of the particles in the cement paste became the bigger particles with a surface covered with water molecules. It leads to easier movement of the tagged particles in the cement paste in the low viscosity state, exhibiting a more uneven distribution of the tagged particles.

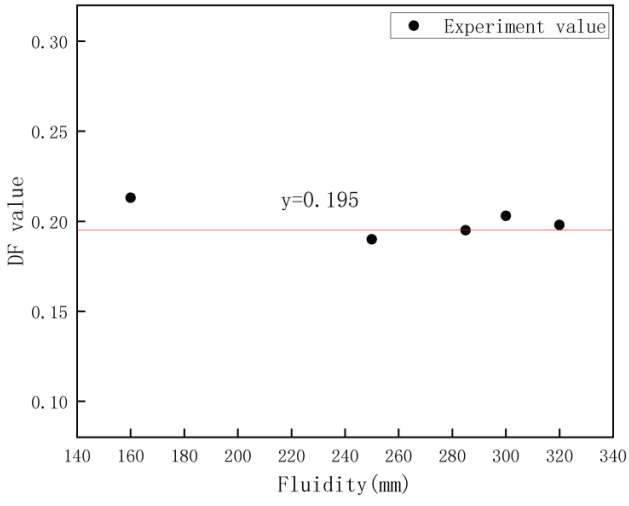

Figure 5. Relationship between DF value and the fluidity of cement paste after vibration.

As a result, during the movement of the particles in the cement paste, the particles are obviously affected by the viscosity of the cement paste, especially when the viscosity is <1 Pa·s, the particles in the cement paste will move substantially when the cement paste is vibrated. Therefore, it is possible to control the viscosity of the cement paste to ensure that it can reduce the tendency of the cement paste to segregate even if it is subjected to different vibration conditions.

3.4. Significance of Particle Size and Density

The distribution trend of tagged particles with different densities and particle sizes in the cement slurry after vibration was studied in this section. Materials with different densities, which are characterized by their insolubility in water or non-reactivity with water, were used. Experiments were carried out in the same process as shown in Figure 1. Materials of different densities were divided into 75 μm ± 2 μm and 25 μm ± 2 μm through different sieves. The vibration frequency was 200 Hz, the gravitational acceleration was set to 5G (average displacement—0.06 mm), and the vibration time was set to 2160 s. The different materials ratios used in this stage are listed in Table 1. The proportion of tagged material in each group was controlled to 10% of the cement mass.

Figure 6 shows the results of the distribution of tagged particles in the cement paste under vibration, as demonstrated by the different particle sizes and densities of the tagged material groups. It can be seen that in the case of using the same tagged material, the group with a large particle size showed a greater DF value compared to the group with a small size because the mass of the particles in the group with large-sized particles was greater compared to the group with small-sized particles. When the cement paste was vibrated, the raw material particles started to vibrate by the action of vibration. As the friction between the particles and the yield stress of the slurry started to drop, the tagged particles were subjected to the action of gravity and started to move. The particles of a larger size had stronger driving forces driving them to move at a higher speed. Therefore, a larger DF value is finally presented.

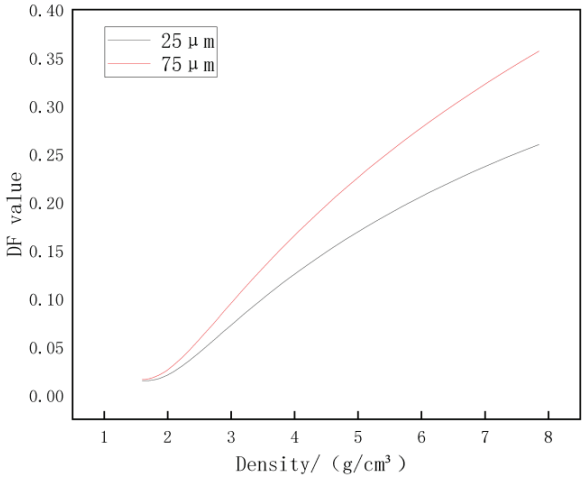

Figure 6. Effect of particle size and density on particle distribution under vibration.

As for the density factor, for the groups with the same particle size, the denser material also had a higher mass, thus such a group also had a greater dispersion of tagged particles. By combining the relationship between dispersion and density at different particle sizes of the tagged materials and the movement of the tagged materials with different particle sizes, it was inferred that the dispersion of the tagged materials in the cement paste was closely related to their mass. In addition, it was observed that when the density of the

tagged materials was less than 3 gr/cm^3, a very small dispersion of the tagged particle distribution was observed. This was because, in low-density materials, the self-weight of the material and the effect of the driving force on the low-mass object could not overcome the effect of the frictional force due to the viscosity within the cement paste, resulting in a very low dispersion of the materials. It was widely recognized that cement-based materials with the addition of various fine powders had high strength and durability. From the perspective of the conclusion of this stage, the low-mass powder was tenaciously fixed in the cement paste and evenly distributed to fill the pores in the cement-based material, and this structure was difficult to be destroyed by external disturbances. As a result, this cement-based material had a more reliable compactness and exhibited great mechanical properties and durability. Furthermore, it can be seen from the results that even if the effect of the chemical reaction between the cementitious particles and water was not considered, there were still directional movements in the vibrating cement paste, which may have been related to the stronger water-secretion effect that occurred in the vibrated cement paste. Additionally, the solid–liquid mixture in the cement paste was separated due to the great density and mass differences between the gas phase and the solid–liquid mixture, so it was easy to understand that after vibration the cement-based material usually exhibited good particle buildup and better porosity [12].

In general, the method displayed can differentiate the distribution discreteness of particles with different densities and grain sizes in cement slurry, and the effect of these movements was related to the mass of the particles. The larger the mass, the stronger the movement dispersion effect would be. In addition, for these movements to occur, the particles needed to be larger than a certain density value of about 3 gr/cm^3.

3.5. Effect of Vibration Frequency

In engineering practice, cement-based materials are subjected to vibrations over a wide frequency range, from several hertz to several hundred hertz [28,29]. Investigating the effects of different vibration frequencies on cement-based materials is crucial for understanding the underlying mechanisms of performance variations under dynamic conditions. Based on the above conclusions, the method mentioned above was used to evaluate the state of motion distribution of the particles at different frequencies. The different materials ratios are listed in Table 1. According to the conclusions of the above section, the viscosity of the different groups of cement slurries was regulated at the same level. The size of the particles of the tagged material used was controlled within the range of 25 ± 2 μm and 75 ± 2 μm by means of a sieve. Two size range groups were used to explore the differences between the different sizes of particles subjected to vibration in the cement paste. Different vibration frequencies are used to investigate the movement of particles in cement paste at different vibration frequencies. The frequencies were 1, 5, 35, 50, 100, 200, 500, 600, and 800 Hz. Vibration time was set to 2160 s.

From Figure 7, it can be found that the DF values are slowly increasing at increasing vibration frequencies, which means that at higher frequencies, the particles in the cement paste produced more motion when subjected to vibration, leading to an increase in the inhomogeneity of the particle distribution, considering that vibration is an external influence factor on the cement paste and does not apply directly on the particles in the cement-based material, the process of vibration to which the tagged particles are subjected in the cement paste can be considered as a damped forced vibration model, while the externally applied vibration load is a simple harmonic load. In this stage, we investigate the effect of vibration frequency as a variable factor on the degree of particle dispersion in the cement-based material. For this process, the equation of motion for the damped forced vibration of the particles is in Equation (4):

$$\ddot{y} = 2\xi\omega\dot{y} + \omega^2 y = \frac{F}{m}\sin\theta t, \tag{4}$$

y represents the displacement of the forced motion of the particle, ξ is the damping ratio of the cement paste, ω is the self-oscillation frequency of the particle, $Fsin\theta t$ represents the magnitude of the simple harmonic force, and m represents the mass size of the object subjected to the forced vibration.

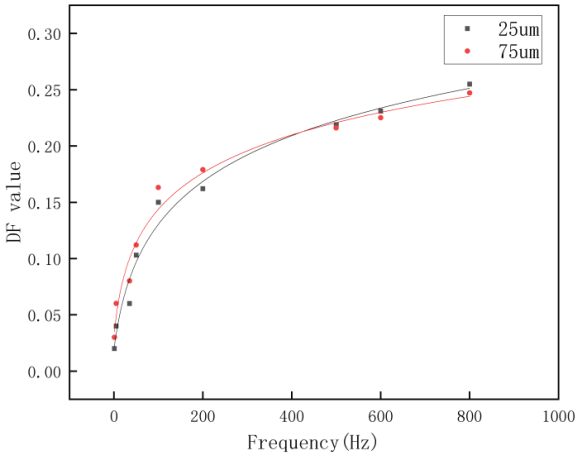

Figure 7. Effect of vibration frequency on particle distribution in vibration.

The solution of this equation is in Equations (5)–(7):

$$y = \frac{F}{m\omega^2} \times \frac{1}{\left(1-\frac{\theta^2}{\omega^2}\right)^2 + \left(\frac{2\xi\theta}{\omega}\right)^2}\left[\left(1-\frac{\theta^2}{\omega^2}\right)\sin\theta t - \left(\frac{2\xi\theta}{\omega}\right)\cos\theta t\right], \quad (5)$$

Set:

$$a = \sqrt{\left(1-\frac{\theta^2}{\omega^2}\right)^2 + \left(\frac{2\xi\theta}{\omega}\right)^2},\ \tan\alpha = \frac{\frac{2\xi\theta}{\omega}}{\left(1-\frac{\theta^2}{\omega^2}\right)},\ \beta = \frac{1}{a}, \quad (6)$$

Obtain:

$$y = \frac{F}{m\omega^2} \times \beta\sin(\theta t - \alpha) \quad (7)$$

The observed increase in DF can be explained by the fact that below the resonant frequency, the dynamic coefficient tends to increase as the frequency increases. Furthermore, higher frequencies meant that in this vibration condition, the mixed phase followed to make higher frequency movements, the friction between particles drops lower, and the higher frequency vibration also meant that the motion of particles would be higher in frequency. That is to say that there will be more chance of movement in the cement paste, which explains why there is an elevated particle dispersion at higher frequencies. At vibration frequencies below 200 Hz, even though the distribution of the movement of larger particles and smaller particles in the cement paste after being subjected to vibration was relatively close, it can be seen that the dispersion of the larger-sized particles was still greater than that of the smaller particles, and with the increase in frequency, the dispersion of the smaller size tagged particles increased significantly and even surpassed that of the cement paste mixed with the larger-size tagged particles. Although the results were relatively similar for different-sized particle sizes in different groups, the repeated experiments showed the same pattern. This is that under the action of low frequency, the system vibrated very slowly, the displacement was synchronized with the load, the inertia and damping forces

were small, and the dynamic load was mainly balanced by the elastic force (as illustrated in Equation (8)):

$$\frac{F}{m\omega^2} = \frac{F}{K_{11}} \qquad K_{11} \text{ is the stiffness coefficient of the material} \tag{8}$$

when the vibration frequency of the system was increasing, the stiffness coefficient of the system increased accordingly, the stiffness coefficient of the smaller-sized particles was smaller than that of the larger particle system, and the smaller size of the tagged material produced a larger deflection so that its degree of dispersion of distribution was increasing. It is predictable that the largest values of displacement excursions occur for both particles near the resonant frequency. The vibration frequency of the system keeps increasing, the dynamic coefficient of the system increases accordingly, the system starts to have a larger vibration, and the tagged materials produce a larger deflection so that the deflection coefficient DF keeps increasing. In a certain frequency from 500 to 800 Hz, the effect of the dynamic coefficient on the DF value is weaker than the effect of the stiffness coefficient on the DF value, and the lower particle size produces a larger displacement offset, making the lower particle size tagged materials exhibit a larger offset and show a larger DF value.

Based on the experimental results above, by using tagged particles, the motion patterns of cement particles under vibration were simulated. This method avoids the use of isotope labeling and large instruments, making it relatively cost-effective. The results can be quantified by weighing the particles compared to the visual tracer approach. Compared to using ping-pong balls, the tagged particles can be selected to match the size and density of cement particles, providing a more accurate reflection of the movement of cement particles in the slurry. By investigating the motion of microparticles in the vibrating cement slurry, this method allows us to explore the changes in the structure and mechanical properties of cement-based materials from the distribution of cement particles, which is more informative than investigating the distribution of fibers or aggregates. This is because the hydration products of cement particles are the most important part that supports the structure and strength of the entire cement-based material.

4. Conclusions

In this study, we developed a simulation method to analyze the movement of microparticles in vibrated cement paste, which is crucial for understanding the behavior of cement-based materials. This method provides a valuable tool for investigating the theory of particle motion in cement paste and complements previous research on the motion of microparticles in vibrated cement paste. Based on the results of the research process, the following conclusions can be obtained:

1. The proposed method shows the ideal feasibility of effectively simulating and quantifying the distribution of cement particles in cement slurry after vibration, which allows us to understand the distribution of the movement of the particles in cement slurry after vibration, and it is easy to implement, ensuring consistency between the collected material and the original added material.
2. The proposed method is able to quantify the discreteness in the distribution of particles between different densities and grain materials by the DF value, and it shows that during the vibration process, particles similar in size to cement particles maintain moving in a direction, but this trend gradually slows down. In order to ensure optimal handling of cement slurries subjected to prolonged vibration, it is necessary to carefully consider the selection of a slurry with appropriate viscosity.
3. The paste flowability alone does not contribute to the distribution pattern. The motion of cement particles of similar size in a vibrated cement slurry is limited by the viscosity of the slurry. The viscosity of the slurry and the dispersion degree of the tagged particles show a negative exponential change pattern. Maintaining high viscosity can well preserve the uniformity of the cement slurry.

4. The increase in frequency leads to a more pronounced degree of dispersion of the particles in the cement slurry. When utilizing vibration for processing cementitious materials with complex components, it is imperative to evaluate the impact of the vibration frequency on the homogeneity of the material.

Author Contributions: Conceptualization, J.K. and Z.S.; methodology, formal analysis, J.K. and S.Z.; validation, J.K.; writing original draft preparation, J.K. and X.G.; investigation, Z.Z.; resources, project administration, funding acquisition, Z.S.; writing—review and editing, X.G. and Z.S.; supervision, data curation, X.Q. All authors have read and agreed to the published version of the manuscript.

Funding: This research is financially supported by the open research project of the Advanced Engineering Technology Research Institute of Wuhan University of Technology in Zhongshan City (WUT202004).

Acknowledgments: The authors acknowledge the financial support from the State Key Laboratory of Silicate Materials for Architectures (Wuhan University of Technology).

Conflicts of Interest: The authors declare that they have no known competing financial interests or personal relationships that could have appeared to influence the work reported in this paper.

References

1. Hemalatha, T.; Ramaswamy, A. A review on fly ash characteristics—Towards promoting high volume utilization in developing sustainable concrete. *J. Clean. Prod.* **2017**, *147*, 546–559. [CrossRef]
2. Ling, G.; Shui, Z.H. Particle Distribution Characteristics and Hydration Mechanism of Cement-Based Paste Subjected to Mechanical Vibrations. *J. Mater. Civ. Eng.* **2022**, *34*, 04021393. [CrossRef]
3. Gong, J.; Yu, Y. Real-time tracking of concrete vibration effort for intelligent concrete consolidation. *Autom. Constr.* **2015**, *54*, 12–24. [CrossRef]
4. Petrou, M.F.; Harries, K.A. A unique experimental method for monitoring aggregate settlement in concrete. *Cem. Concr. Res.* **2000**, *305*, 809–816. [CrossRef]
5. Kwan, A.K.H.; Zheng, W.; Ng, I.Y.T. Effects of shock vibration on concrete. *ACI Mater. J.* **2005**, *1026*, 405–413.
6. Fernandes, J.F.; Bittencourt, T.N.; Helene, P. Concreto submetido a vibrações nas primeiras idades. *Rev. IBRACON Estrut. Mater.* **2011**, *44*, 592–609. [CrossRef]
7. Suk, J.H.; Kim, M.S. Strength Characteristics of Concrete Subjected to Vertical Continuous Vibration during Initial Curing Period. *J. Korean Constr. Inst.* **2005**, *172*, 273–279.
8. Hong, S.; Park, S.K. Effect of vehicle-induced vibrations on early-age concrete during bridge widening. *Constr. Build. Mater.* **2015**, *77*, 179–186. [CrossRef]
9. Gao, X.; Zhang, J.; Su, Y. Influence of vibration-induced segregation on mechanical property and chloride ion permeability of concrete with variable rheological performance. *Constr. Build. Mater.* **2019**, *194*, 32–41. [CrossRef]
10. Li, Z.; Cao, G. Rheological behaviors and model of fresh concrete in vibrated state. *Cem. Concr. Res.* **2019**, *120*, 217–226. [CrossRef]
11. Domone, P.L. Self-compacting concrete: An analysis of 11 years of case studies. *Cem. Concr. Compos.* **2006**, *282*, 197–208. [CrossRef]
12. Cao, G.D.; Li, Z.G.; Destech Publicat, I. Rheological Model of Fresh Concrete in Vibrated State. In Proceedings of the Conferences of International Conference on Materials Science and Engineering Application (ICMSEA)/International Conference on Mechanics, Civil Engineering and Building Materials (MCEBM), Nanjing, China, 21 April 2017.
13. Wang, X.P.; Yu, R. Optimized design of ultra-high performance concrete (UHPC) with a high wet packing density. *Cem. Concr. Res.* **2019**, *126*, 105921. [CrossRef]
14. Keulen, A.; Yu, Q.L. Effect of admixture on the pore structure refinement and enhanced performance of alkali-activated fly ash-slag concrete. *Constr. Build. Mater.* **2018**, *162*, 27–36. [CrossRef]
15. Dupont, D.; Vandewalle, L. Distribution of steel fibres in rectangular sections. *Cem. Concr. Compos.* **2005**, *273*, 391–398. [CrossRef]
16. Zhao, M.L.; Li, J.; Xie, Y.M. Effect of vibration time on steel fibre distribution and flexural behaviours of steel fibre reinforced concrete with different flowability. *Case Stud. Constr. Mater.* **2022**, *16*, e01114. [CrossRef]
17. Safawi, M.I.; Iwaki, I.; Miura, T. The segregation tendency in the vibration of high fluidity concrete. *Cem. Concr. Res.* **2004**, *342*, 219–226. [CrossRef]
18. Safawi, M.I.; Iwaki, I.; Miura, T. A study on the applicability of vibration in fresh high fluidity concrete. *Cem. Concr. Res.* **2005**, *359*, 1834–1845. [CrossRef]
19. *GB 1752007*; Common Portland Cement. Standardization Administration: Beijing, China, 2007.
20. Zhang, J.J.; Yu, R. Hydration kinetics and microstructure development of Ultra-High Performance Concrete (UHPC) subjected to microwave pre-curing. *Cem. Concr. Compos.* **2022**, *129*, 104484. [CrossRef]
21. Wang, Z.Y.; Shui, Z.H. Recycling utilization of phosphogypsum in eco excess-sulphate cement: Synergistic effects of metakaolin and slag additives on hydration, strength and microstructure. *J. Clean. Prod.* **2022**, *358*, 131901. [CrossRef]

22. Han, F.; Pu, S. Effect of ultrafine mineral admixtures on the rheological properties of fresh cement paste: A review. *J. Build. Eng.* **2022**, *51*, 104313. [CrossRef]
23. Yu, R.; Xu, L.L. Dynamic behaviors assessment of steel fibres in fresh Ultra-High Performance Concrete (UHPC): Experiments and numerical simulations. *J. Build. Eng.* **2022**, *59*, 105084. [CrossRef]
24. Zheng, Y.; Zhou, Y. Study on performance improvement of ultra-high performance concrete by vibration mixing. *Constr. Build. Mater.* **2022**, *327*, 126823. [CrossRef]
25. Han, D.; Lee, G.-C. Viscosity influence on rising behavior of model air bubbles in fresh mortar. *Constr. Build. Mater.* **2015**, *76*, 10–15. [CrossRef]
26. Spangenberg, J.; Roussel, N. Patterns of gravity induced aggregate migration during casting of fluid concretes. *Cem. Concr. Res.* **2012**, *4212*, 1571–1578. [CrossRef]
27. Spangenberg, J.; Roussel, N. Flow induced particle migration in fresh concrete: Theoretical frame, numerical simulations and experimental results on model fluids. *Cem. Concr. Res.* **2012**, *424*, 633–641. [CrossRef]
28. Zheng, Y.; Yang, J. Investigation on the concrete strength performance of underlying tunnel structure subjected to train-induced dynamic loads at an early age. *Constr. Build. Mater.* **2022**, *337*, 127622. [CrossRef]
29. Wang, H.; Zhang, C. Vibration characteristics and isolation in vibration-sensitive areas under moving vehicle load. *Soil Dyn. Earthq. Eng.* **2022**, *153*, 107077. [CrossRef]

materials

MDPI

Article

Experiments on the Dynamic Behavior of Curved Glass Panes Subjected to Low-Velocity Impact

Marcin Kozłowski * and Kinga Zemła

Department of Structural Engineering, Silesian University of Technology, Akademicka 5, 44-100 Gliwice, Poland; kinga.zemla@polsl.pl
* Correspondence: marcin.kozlowski@polsl.pl

Abstract: Curved glass enables designers to achieve unparalleled innovation in creating modern and undulating shapes for building enclosures. However, the curvature of panes changes the static and especially the dynamic behavior of the panes under loading. Studies on low-velocity impacts on curved glass have been limited and have primarily involved numerical studies. This paper experimentally investigates the dynamic response of cylindrically curved glass panes under a low-velocity impact. A flat, 5 mm thick, single-pane geometry with three curvature radii and the lack or presence of movement restraint is considered. Special attention is also paid to the variations caused by impacting bodies involving different stiffness, mass, and geometry parameters. It was found that flat plates have a lower capacity to dampen oscillations, resulting in longer decay times compared to curved panes. For impactors with a lower stiffness, the glass panes experience uneven oscillations at the moment of impact, followed by a chaotic period of transient vibrations before reaching a stationary state. This contrasts bodies with greater deformability in which the main dynamic behavior follows a more predictable pattern.

Keywords: curved glass; impact loading; dynamic; experiments

Citation: Kozłowski, M.; Zemła, K. Experiments on the Dynamic Behavior of Curved Glass Panes Subjected to Low-Velocity Impact. *Materials* **2023**, *16*, 7335. https://doi.org/10.3390/ma16237335

Academic Editor: Krzysztof Schabowicz

Received: 2 November 2023
Revised: 20 November 2023
Accepted: 22 November 2023
Published: 25 November 2023

1. Introduction

Glass has been a popular material for building use for many decades. Its transparency has long been a key feature that has inspired designers to find innovative ways to incorporate it into architectural designs [1]. Today, glass is being used more and more frequently in construction, even as a load-bearing element in the form of glass roofs, facades, and balustrades, as well as glass beams and stairs [2]. The reason behind this, in addition to esthetic features, is the growing trend of maximizing natural sunlight in buildings, which has a positive impact on people who live and work indoors [3].

The rise of free-form architectural structures has led to the development and advancement of curved glass as a component of geometrically intricate building facades [4]. In this way, utilizing curved glass enables designers to achieve unparalleled innovation in creating modern and undulating shapes for building enclosures.

There is a significant difference in the structural behavior of flat and curved sheets as demonstrated by Pini et al. [5]. The curvature particularly stiffens spatially thin sheets and changes their static and especially dynamic behavior [6]. In the case of Insulating Glass Units (IGUs), the curvature of the panes can result in unexpected structural responses to static and climatic loads due to their increased spatial stiffness [7,8].

An aspect that is crucial and often underestimated in the design process is dynamic loads. These actions usually govern the final thickness of the glass and should not be overlooked. Even after physical contact between an impactor and a glass element has ended, the glass may continue to react dynamically for a significant period [9]. As a result, the glass may experience critical stresses much later than the initial impact [10]. This is especially apparent in glass elements with intricate shapes or in slender glass panes with

openings in which the maximum stresses may occur during the later stages of a dynamic event [11].

Although curved elements have been extensively utilized in various applications, there has been limited research on low-velocity impact on shells. Ramkumar and Thaker [12] utilized Donnell's approximations for thin shells and the Fourier series method to predict the transient response of a curved, laminated plate under low-velocity transverse impacts by a rigid object. Similarly, Christoforou and Swanson [13] employed the Fourier series method to derive a closed-form solution for the problem of simply supported orthotropic cylindrical shells. Lin and Lee [14] conducted experimental and numerical studies on the impact damage of laminated plates and cylindrical panels, finding that shell structures are more vulnerable to damage than plates when exposed to the same impact velocity conditions. The study by Palazotto et al. [15] shed more light on the utilization of nonlinear shell theory to obtain the impact response of cylindrical panels, predicting deflections and stresses by experimental means. Kim et al.'s results contribute to our understanding of the dynamic behavior of curved laminated composite structures [16]. Numerical computations were carried out to show the effects of curvature and stacking sequence on the impact response of cylindrical composite shells. It was found that the curvature significantly affects the dynamic behavior; in particular, the contact force exerted on a cylindrical composite shell increases with the curvature.

The topic of the dynamic response of curved shells to low-velocity impact has indeed been addressed in the literature; however, it pertained to other materials such as steel, composites, and various honeycomb structures [17,18]. Glass is an entirely different material with different Young's modulus and damping properties, which influence its specific dynamic response. There are likely no strictly experimental research examples in the literature. It is probably caused by the fact that performing experimental studies is costly and challenging due to the fragility and smooth surface of the glass, which significantly limits the possibilities for the use of experimental equipment [19]. The novelty of the research results published in this article probably pertains to some of the initial studies of such structures made of glass. Another novelty lies in the analysis of various types of impactors involving different stiffness, mass, and geometry parameters.

In the case of glass, studies on low-velocity impact loads on curved glass have been limited and primarily involved performing numerical studies. Galuppi and Royer-Carfagni [20] analytically examined the effect of curvature on the shear coupling of glass plies through the interlayer using the traditional approach developed by Newmark. It was found that the response of a curved structure is greatly influenced by the axial force it undergoes, and such internal action is mainly governed, for fixed applied loads, by the boundary conditions at the extremities.

Sukhanova et al. performed a numerical analysis of the dynamic state of shallow shell laminated glasses [21]. Their work aimed to investigate the dependence of laminated glass's dynamic deformation on the glass curvature. The laminated glass model with a dimension of 305×305 mm^2 consisted of two glass panes with a thickness of 5 mm, laminated together with a PVB interlayer with a thickness of 1.52 mm. The curved samples were subjected to impact through contact with the 83 mm diameter smooth solid steel ball (2.3 kg). The results showed that the distribution of the maximum magnitude of the displacement vector and intensity strain could be traced with an increasing curvature parameter. The authors concluded that the maximum magnitude of the displacement vector decreases with increasing curvature parameters, but with a high curvature parameter, it can increase slightly. Moreover, the intensity stress increases with increasing curvature parameter until about 45 mm and then decreases. Sukhanova and Larin [19] studied the numerical dynamics of laminated glass panes with different curvatures (a curvature parameter ranging from 0 mm to 250 mm). Their work studied the influence of the curvature parameter on the frequencies and modes of composite panes involving the propagation of elastic waves in the linear state. It was found that, with a threshold value of the curvature

parameter of 48.88 mm, the first natural frequency increased by more than 330% and then decreased.

In the current paper, the authors empirically investigate the dynamic response of cylindrically curved glass panes under low-velocity impact. A 5 mm thick, single-pane geometry with different radii of curvature and the lack or presence of movement restraint is considered. Special attention is also paid to the variations caused by an impactor involving different stiffness, mass, and geometry parameters.

2. Materials and Methods

2.1. Test Specimens

Plates with dimensions of 1000 × 1000 mm^2 and a thickness of 5 mm, were made of soda-lime-silica glass. The length of the arc determined the dimension of the curved sheet. For all samples, fully tempered (toughened) glass was used. Before the heat treatment process, the edges were ground and polished.

Four glass plates were investigated: one was flat, while the other three had varying bending radii: 2821 mm, 1444 mm, and 1000 mm, which corresponds to an arch height of approx. 29, 57, and 86 mm, respectively. The minimum radius (1000 mm) was determined by production limitations for the glass thickness of 5 mm, while the others resulted from the division of the arch height of 86 mm (for the curved sample with a 1000 mm bending radius) into three parts.

2.2. Impacting Bodies

For the tests, impacting bodies with varying characteristics were selected, which involved different stiffness, mass, and geometry parameters, see Figure 1. A practically undeformable steel ball, a basketball (with a pressure equal to 0.62 bar), a rubber ball filled with sand, and a fabric bag filled with peas (beanbag) were used. A 7 mm thick rubber pad with dimensions of 300 × 300 mm^2 was used with the steel ball to ensure safety and that the pane would not be damaged during the tests. It should be noted that this setup resulted in a semi-hard-body impact.

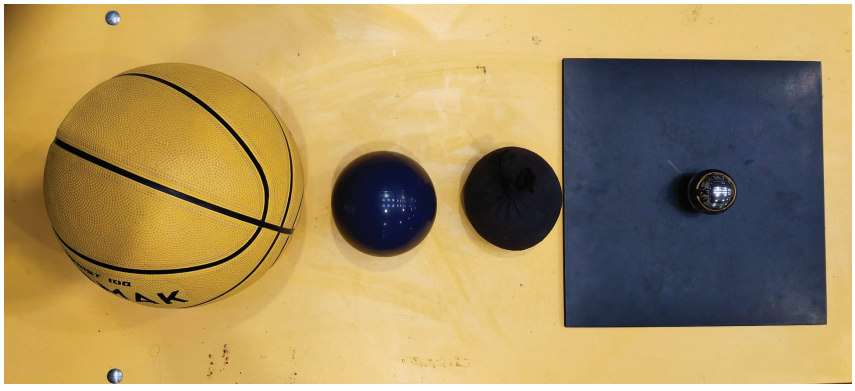

Figure 1. Impact bodies used in the study from the left: basketball ball, sand-filled rubber ball, fabric bag filled with peas (beanbag), steel ball on a rubber pad.

The parameters of the impacting bodies are summarized in Table 1.

Table 1. Parameters of impact bodies.

Impactor	Mass of Impactor [g]	% of Glass Weight	Diameter [mm]
Steel ball	510.25	4.08	50
Basketball	483.35	3.87	220
Rubber ball filled with sand	891.24	7.13	107
Fabric bag filled with peas	506.24	4.05	104/120 [1]

[1] Measured in a hanging position/resting on a flat surface.

2.3. Experimental Setup

The test stand is presented in Figures 2 and 3. It consists of four wooden beams on which Teflon flat bars, glass panes, and steel racks were placed to form a framework to attach the measuring tools that determine the height of the body drop. Figure 4 illustrates the plate locking elements required for two types of tests: simply supported slabs and those with restrained sliding (outside) perpendicular to the line of supports. Additional Teflon strips were used for wedging the plates. In addition, Teflon tubes were fitted in the corner zones of the sample to prevent the plates from moving horizontally in parallel directions to the support lines (as shown in Figure 4). It should be noted that the horizontal restraints only worked for the curved panes, while, for the flat panels, they were inactive. This occurred because, during impact, the curved sample flattens; its straight edges move to the outsides (the sample opens up), and horizontal reactions occur. However, the flat sample behaves differently during the impact; it deflects in the opposite direction of the impact, and its edges move closer to the center of the sample (chord shortening). Thus, restraining the movement of the flat sample was not effective, as it did not have a horizontal reaction on the supports during impact.

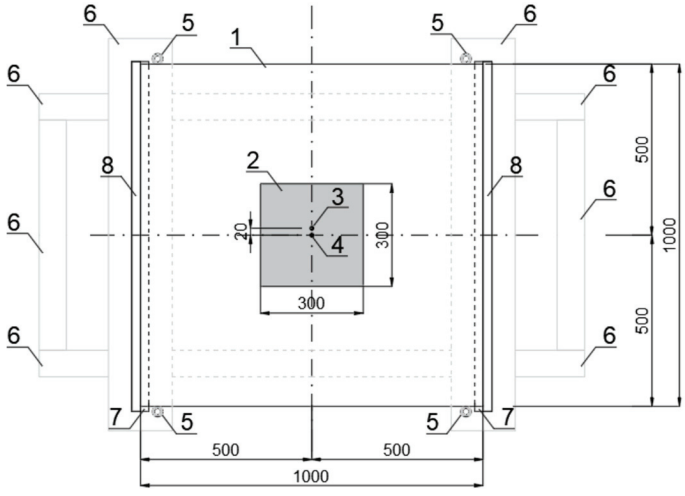

Figure 2. Top view of the test stand scheme: (1) glass plate, (2) rubber pad (used for steel ball impact), (3) bottom accelerometer, (4) inductive displacement sensor mounted from the bottom, (5) Teflon tubes that block movement in the direction parallel to the edge of the supports, (6) wooden frame, (7) Teflon strips on which the pane rests, and (8) additional Teflon strips (used in the variant with locked horizontal sliding).

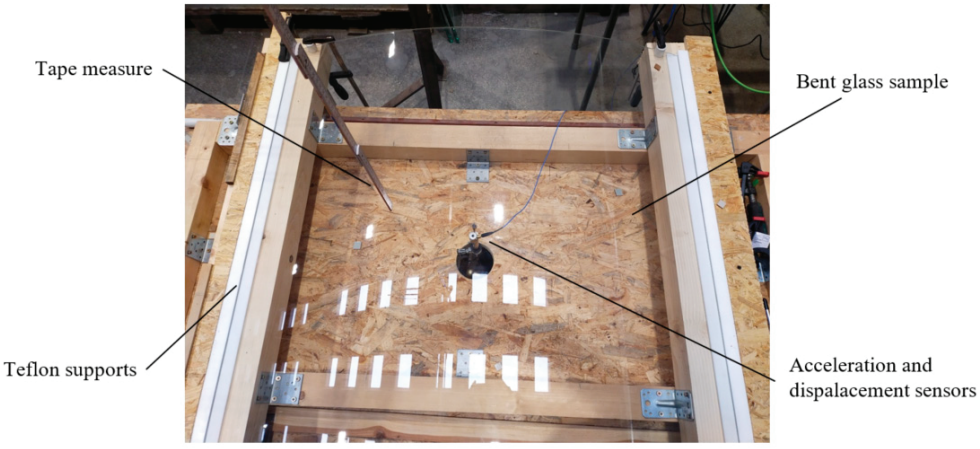

Figure 3. Test stand (top view).

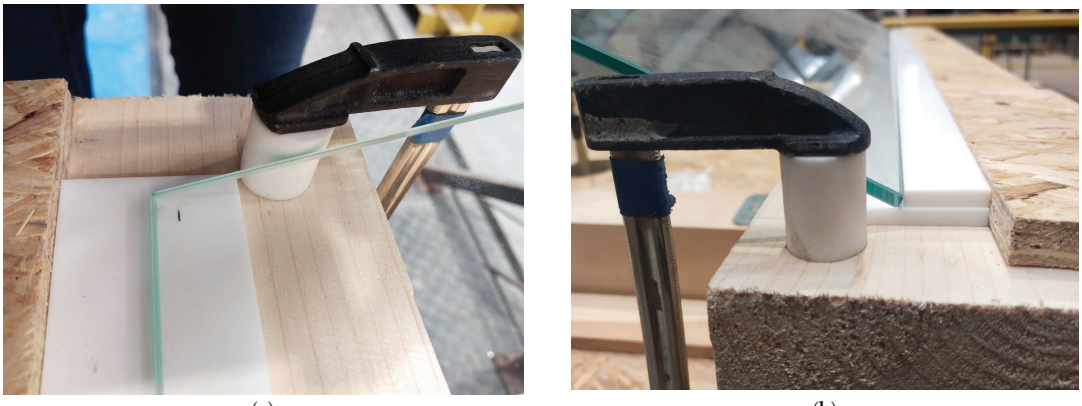

(**a**) (**b**)

Figure 4. Detailed support arrangement of the test stand: (**a**) simple support; (**b**) restrained movement.

The sensors were attached to the pane and then connected to two measurement devices: Alitec™ QACQ, Alitec, Łódź, Poland [22] and QuantumX - MX840B, HBM, Poznań, Poland [23]. The first recorded the acceleration of a selected point on the surface using an accelerometer weighing 10.5 g, with a maximum measuring range of $\pm$4900 m/s^2 and a frequency range of 1 to 5000 Hz $\pm$ 5%. This type of accelerometer was chosen due to its relatively small size and low mass to minimize its influence on the dynamic behavior of thin plates and the measured values. The latter was a Linear Variable Differential Transformer (LVDT) to collect displacement data.

To carry out this research, two highly specialized measuring devices were necessary. The Catman® 5.6.1 [24] software was used to collect displacement sensor data, while VIDIA® [25] was used to gather data from a QACQ device (acceleration). The measurement systems used in this research allowed for the independent recording of results. The QACQ device was able to sample at a frequency of 64,000 Hz, while the HBM QuantumX device was able to sample at 19,200 Hz. Figure 5 presents the sensors that were attached to the pane—the displacement sensor was attached at the center point of the pane, while the acceleration sensor was shifted 20 mm in the direction of the unsupported edge from the center point. Both the LVDT and the accelerometer were securely placed on the bottom surface of the glass sample. Details of the experimental campaign can be found in a master's

degree thesis devoted to the dynamical response of the curved glass pane subjected to impact [26].

Figure 5. Sensors attached to the sample.

2.4. Experimental Methodology

Four types of experiments were carried out using the impact bodies mentioned in Section 2.2 to investigate the dynamic behavior of curved glass panes under low-velocity impact. Each body was dropped from a different height, ensuring it impacted the panes with the same kinetic energy of 2.5 J according to EAD 210005-00-0505 [27]. The calculations were based on the potential energy equation, which indicates that a heavier body must fall from a lower height to achieve the same energy as a lighter body. The drop heights derived analytically for the individual bodies are presented in Table 2. However, it should be noted that achieving this precision during experiments was practically impossible, and this could affect the measured values and their scatter.

Table 2. Parameters of impacts.

Impactor	Mass [g]	Drop Height Derived Analytically [m]
Steel ball	510.25	0.499
Basketball	483.35	0.545
Rubber ball filled with sand	891.24	0.287
Fabric bag filled with peas	506.24	0.510

The glass panes were directly impacted at the center point. The objects were directly dropped on the glass pane, except the steel ball, which had a rubber pad of dimensions 300×300 mm^2 and thickness of 7 mm placed on it. The initial stage involved analyzing a flat reference sheet by subjecting it to six impacts with each object. Subsequently, curved sheets were tested in two variations. The first variation involved restraining the horizontal movement of the sample with Teflon flat bars, while the second was a simply supported scheme without an additional restraint (see Figure 4). Similar to the testing of the reference samples, curved glasses were subjected to six impacts. Regular checking of the displacement sensor was critical during the experiments as the vibrations from the impact could fall off the sensor from the tested samples. It is worth emphasizing that each of the impactors, except for a fabric bag filled with peas (beanbag), was caught after the first drop (after the first impact on the glass pane) to avoid a second impact. After dropping on the sample, only the beanbag was allowed to remain on it until the measurements were completed. Moreover, in each attempt, the beanbag hit the sample with a different shape due to its irregular structure. The above-mentioned facts could affect the final results due to the increased weight of the element.

3. Results and Discussion

To comprehensively study how glass panes react to low-velocity impact, the experimental results were analyzed by examining the displacement history of the glass panes, the decay time, and the maximum accelerations over time.

3.1. Displacement Response

Figures 6–9 show the displacement histories measured in the center of the glass panes during the tests for all impact bodies for flat and curved panes. The figures also show the difference in the dynamic behavior under two boundary conditions: simply supported and restrained movement. To maintain clarity, only one randomly chosen analysis result within each series is shown. To gain a deeper understanding of the subject of this research, the histories of the displacement for the centers of the panes have also been compiled separately for each impactor, considering different bending radii, see Figures 10–13. Table 3 presents detailed data in the form of tables regarding the mean values with coefficients of variation.

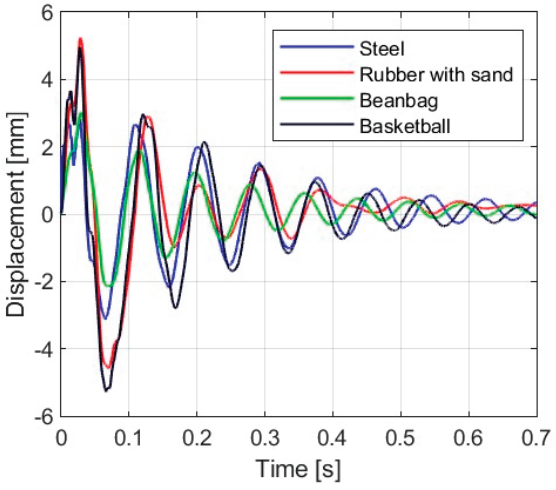

Figure 6. Results of experiments for the flat glass pane (simply supported).

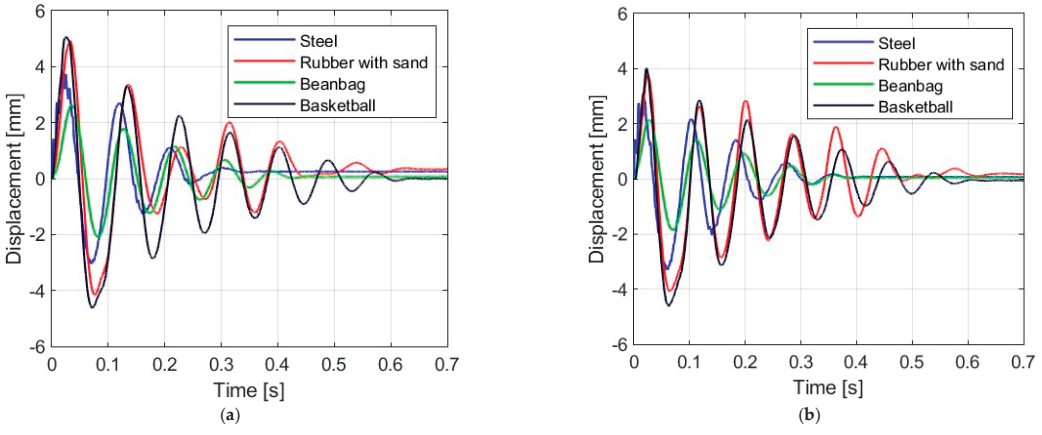

Figure 7. Results of experiments for the glass pane with radius R = 2821 mm: (**a**) simply supported, (**b**) restrained movement.

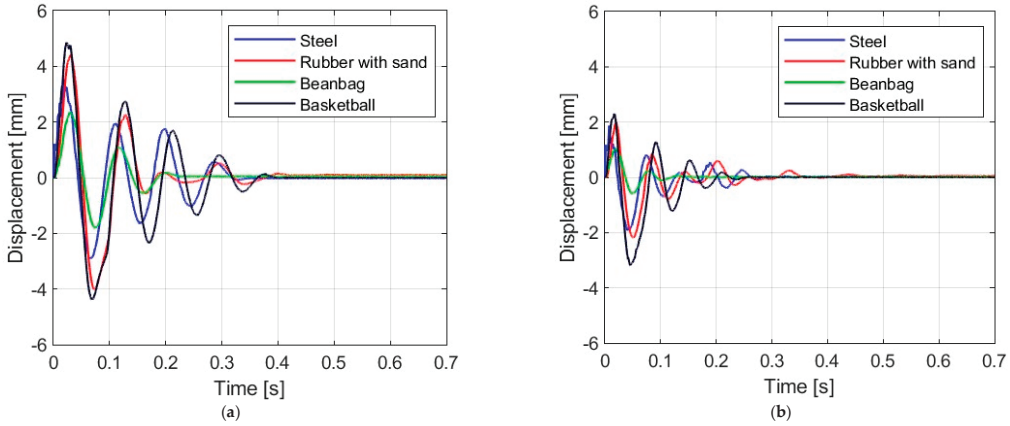

Figure 8. Results of experiments for the glass pane with radius R = 1444 mm: (**a**) simply supported, (**b**) restrained movement.

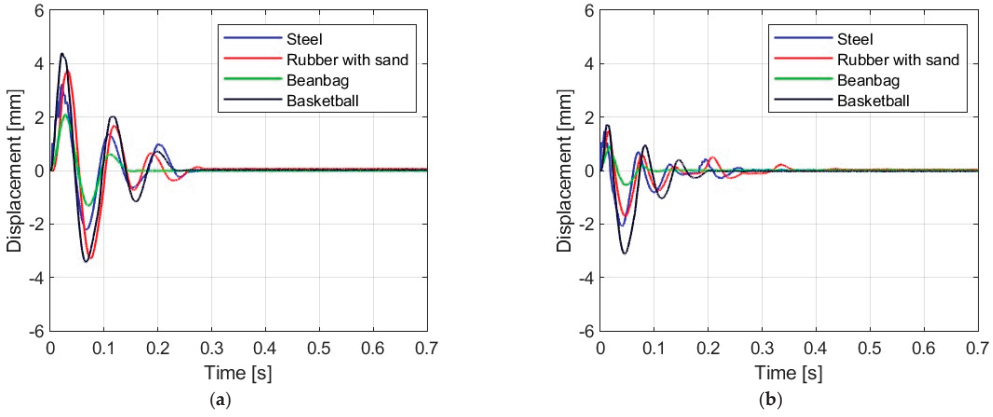

Figure 9. Results of experiments for the glass pane with radius R = 1000 mm: (**a**) simply supported, (**b**) restrained movement.

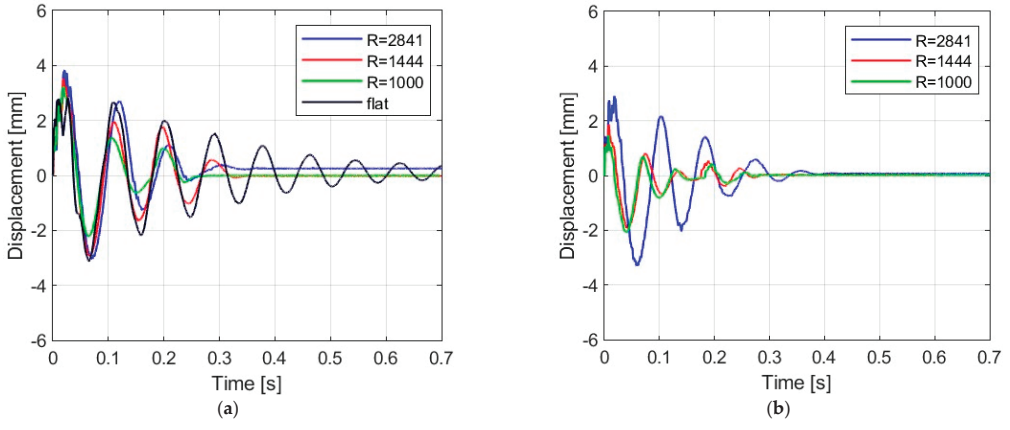

Figure 10. Results of experiments with steel ball: (**a**) simply supported, (**b**) restrained movement.

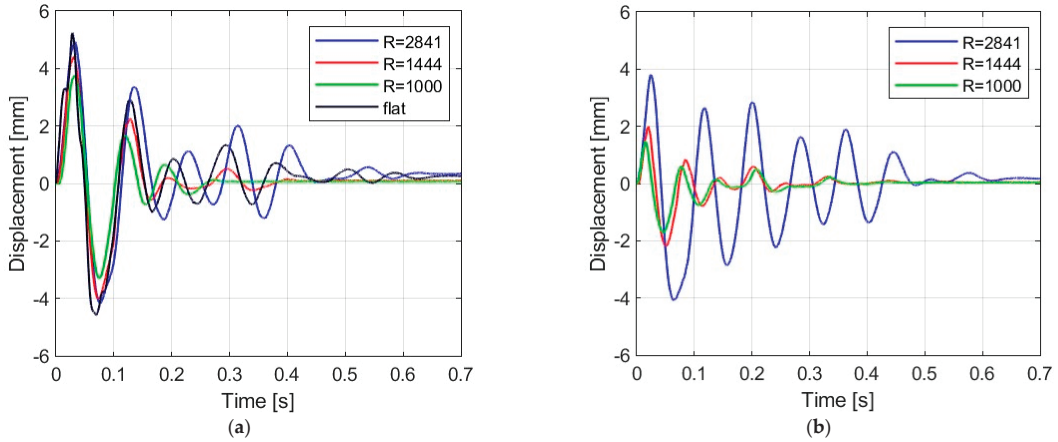

Figure 11. Results of experiments with rubber ball filled with sand: (**a**) simply supported, (**b**) restrained movement.

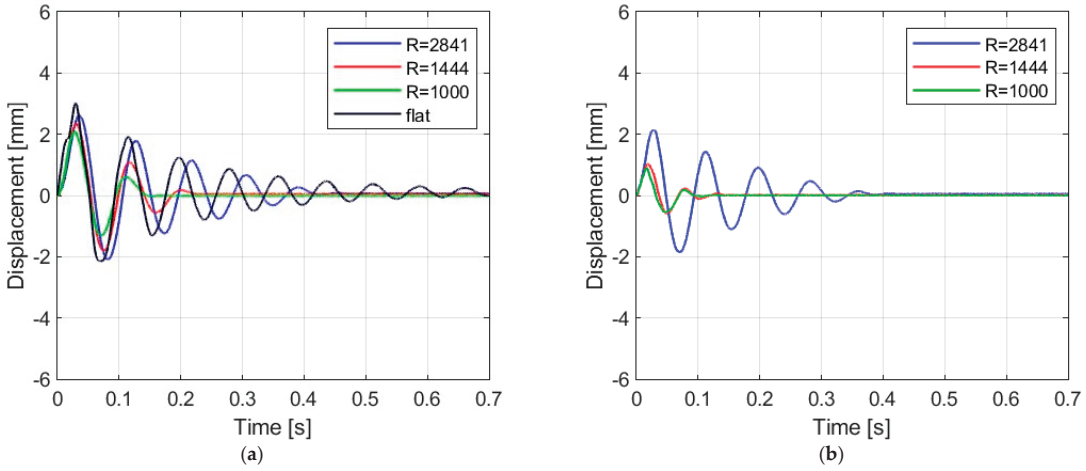

Figure 12. Results of experiments with fabric bag filled with peas: (**a**) simply supported, (**b**) restrained movement.

Comparing Figures 6, 7a, 8a, 9a and 10a showing the results for simply supported conditions, it can be noticed that the impactor significantly affects the dynamic behavior of the glass panes, and several observations can be made. The results indicate that the flat sheet has a lower capacity for energy dissipation, and its oscillation amplitudes decline exponentially with time. This is in contrast to the curved sheets, which experienced fewer oscillations. The curved plate (2821 mm) also exhibited a similar pattern of decreasing vibration amplitude in time for both support conditions. However, the damping for the curved plates (1444 mm and 1000 mm) was more erratic, with vibration amplitudes not decreasing exponentially. The damping waveforms for the plates were very similar, but there was a noticeable difference in the value of the first peak displacement. A common observation in all plots was the presence of noise in the first displacement peak, which was most likely due to the ball hitting the rubber pad first. Although a 2821 mm curved plate had a greater maximum displacement when simply supported, its damping time was comparable to that of a restrained pane. The ability to dissipate energy decreased as the bending radius increased. This ability was further demonstrated when comparing a

2821 mm slab with 1444 mm and 1000 mm panes. The results confirmed that 1444 mm and 1000 mm panes with restricted movement exhibited a similar course of displacements in time. The impact that resulted in a chaotic change in displacements over time was in the case of the rubber ball filled with sand. The trend of a flat sheet having a longer vibration damping time remained consistent. Similar to the damping course for a steel ball, the damping courses for sheets with a bending radius of 1444 mm and 1000 mm were comparable. For the beanbag, it was observed that the damping of the 1444 mm and 1000 mm panes were very similar. However, comparing them to the 2821 mm surface, it can be concluded that energy dissipation occurred much faster in more-curved sheets. Similarly, comparing panes with the same bending radii but different support methods, it was found that panes with locked travel tended to dampen vibrations quicker. The flat plate and the 2821 mm curved pane exhibited an exponential decrease in vibration amplitude. For the fabric bag filled with peas (beanbag), the values of minimal displacement were significantly smaller than the maximal (positive) ones. This can be caused by an impactor that remained on the sample after the impact. For restrained movement support, the minimal (negative) value of displacement was greater than the positive values (except for beanbag impact).

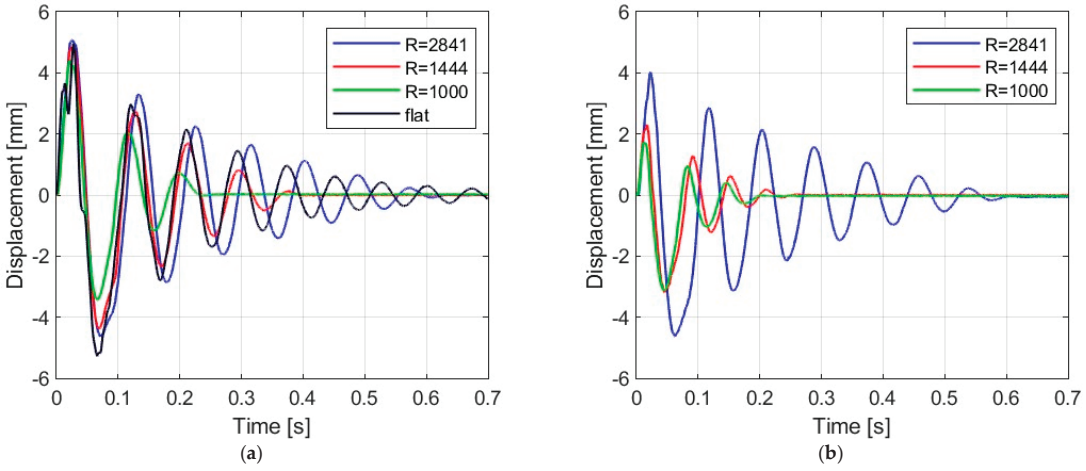

Figure 13. Results of experiments with basketball: (**a**) simply supported, (**b**) restrained movement.

Table 3. Values of maximal and minimal displacements for impactors and four radii of the panes.

Impacting Body		Flat Pane	SS [1]	RM [2]	SS	RM	SS	RM
Steel ball	Max.	2.82 ± 0.02	3.85 ± 0.02	2.91 ± 0.01	3.52 ± 0.02	1.87 ± 0.01	3.25 ± 0.02	1.46 ± 0.02
	Min.	−3.09 ± 0.03	−3.03 ± 0.02	−3.32 ± 0.03	−2.89 ± 0.02	−1.93 ± 0.02	−2.26 ± 0.04	−2.07 ± 0.02
Rubber ball filled with sand	Max.	5.29 ± 0.05	4.93 ± 0.07	3.82 ± 0.03	4.34 ± 0.06	1.97 ± 0.02	3.74 ± 0.04	1.47 ± 0.02
	Min.	−4.62 ± 0.05	−4.31 ± 0.11	−4.10 ± 0.03	−3.93 ± 0.09	−2.13 ± 0.05	−3.21 ± 0.07	−1.67 ± 0.05
Fabric bag filled with peas	Max.	2.95 ± 0.06	2.21 ± 0.04	2.12 ± 0.01	2.33 ± 0.02	1.06 ± 0.02	2.07 ± 0.03	0.91 ± 0.01
	Min.	−2.10 ± 0.05	−2.07 ± 0.05	−1.83 ± 0.02	−1.78 ± 0.02	−0.61 ± 0.02	−1.31 ± 0.02	−0.55 ± 0.01
Basketball	Max.	4.97 ± 0.02	5.11 ± 0.05	4.04 ± 0.03	4.81 ± 0.06	2.29 ± 0.01	4.47 ± 0.12	1.73 ± 0.01
	Min.	−5.25 ± 0.02	−4.60 ± 0.04	−4.63 ± 0.02	−4.31 ± 0.05	−3.16 ± 0.02	−3.54 ± 0.12	−3.11 ± 0.01

[1] SS stands for simply supported. [2] RM stands for restrained movement.

3.2. Decay Time

Figures 14 and 15 show the decay times for all impact bodies for the flat and curved panes. The figures also show the differences between two boundary conditions: simply supported and restrained movement. Table 4 presents detailed data in the form of a table regarding the mean values and coefficients of variation.

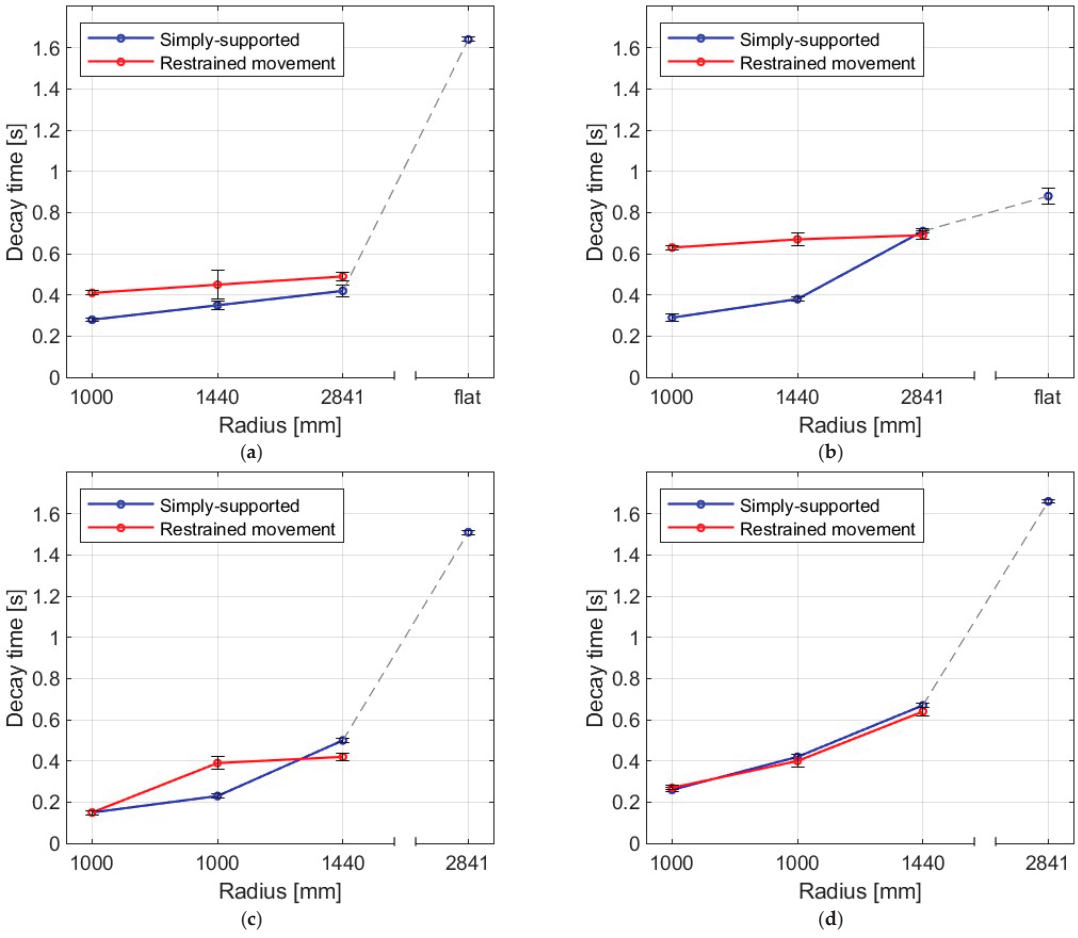

Figure 14. Mean decay time of the plates as a result of impact by (**a**) steel ball, (**b**) rubber ball filled with sand, (**c**) fabric bag filled with peas, (**d**) basketball.

Table 4. Values of maximal and minimal displacements for different impactors and four radii of the panes.

Impacting Body	Flat Pane	R = 2821 mm		R = 1444 mm		R = 1000 mm	
		SS [1]	RM [2]	SS	RM	SS	RM
Steel ball	1.64 ± 0.01	0.42 ± 0.03	0.49 ± 0.02	0.35 ± 0.02	0.45 ± 0.07	0.28 ± 0.01	0.41 ± 0.01
Rubber ball filled with sand	0.88 ± 0.04	0.71 ± 0.01	0.69 ± 0.02	0.38 ± 0.01	0.67 ± 0.03	0.29 ± 0.02	0.63 ± 0.01
Fabric bag filled with peas	1.51 ± 0.01	0.50 ± 0.01	0.42 ± 0.01	0.23 ± 0.01	0.39 ± 0.03	0.15 ± 0.01	0.15 ± 0.01
Basketball	1.66 ± 0.01	0.67 ± 0.01	0.64 ± 0.01	0.42 ± 0.01	0.43 ± 0.03	0.26 ± 0.01	0.27 ± 0.01

[1] SS stands for simply supported. [2] RM stands for restrained movement.

It was observed that the larger the bending radius, the lower the energy dissipation ability and the longer the decay time. For flat panes in a simply supported arrangement, this effect was significant. For the simply supported arrangement, it can be noted that the values for the fabric bag filled with peas (beanbag) for smaller radii were the smallest of all, whereas, for greater radii (2821 and flat), they were greater than for the steel ball and the rubber ball with sand, respectively. This unexpected outcome could be explained by the fact that, for the impact series with a fabric bag with peas, the impactor was not removed

after the first impact. This results in increasing the oscillatory period; thus, the decay time also increases.

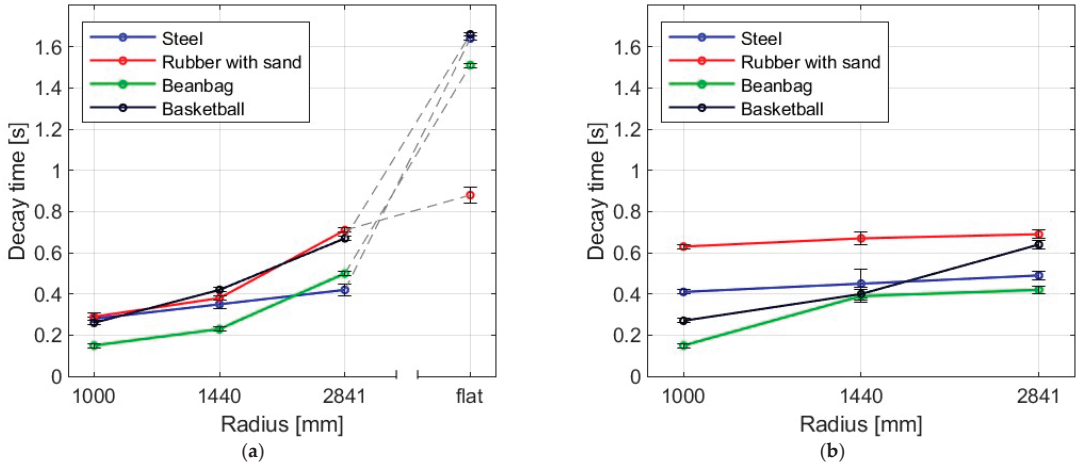

Figure 15. Mean values of decay time for four impactors in (**a**) simply supported, (**b**) restrained movement supports.

3.3. Maximum Acceleration

The results of testing glass plates with varying bending radii, both freely supported and locked with sliding outside the arc and struck with four different bodies are presented in this section. Figures 16 and 17 and Table 5 provide a summary of the average maximum acceleration values, including their standard deviation.

Table 5. Mean maximal values of the acceleration of the sample during tests.

Impacting Body	Flat Pane	R = 2821 mm		R = 1444 mm		R = 1000 mm	
		SS [1]	RM [2]	SS	RM	SS	RM
Steel ball	2476 ± 88	2934 ± 99	2506 ± 293	2241 ± 47	2122 ± 31	2650 ± 363	2552 ± 390
Rubber ball filled with sand	311 ± 30	162 ± 13	308 ± 47	202 ± 10	228 ± 8	226 ± 3	261 ± 22
Fabric bag filled with peas	640 ± 195	706 ± 111	940 ± 58	515 ± 33	440 ± 29	871 ± 141	1052 ± 157
Basketball	776 ± 24	321 ± 86	510 ± 122	213 ± 12	501 ± 41	449 ± 104	593 ± 75

[1] SS stands for simply supported. [2] RM stands for restrained movement.

The highest values of mean acceleration of the sample were observed to be achieved by the steel ball impact, whereas the smallest values were obtained for a rubber ball with sand. Moreover, for most impactors, it can be seen that, for samples with a radius of 1444 mm, the accelerations were the lowest. After analyzing the data presented, it can be inferred that the steel ball resulted in the highest accelerations. On the other hand, the rubber ball filled with sand caused the least acceleration. However, the results do not offer a definite conclusion on how the bending radius of the slab and its support method affect the impulse load acceleration. Accelerations and similar quantities are highly prone to aliasing errors [28]. This is also reflected in the values of the coefficients of variation.

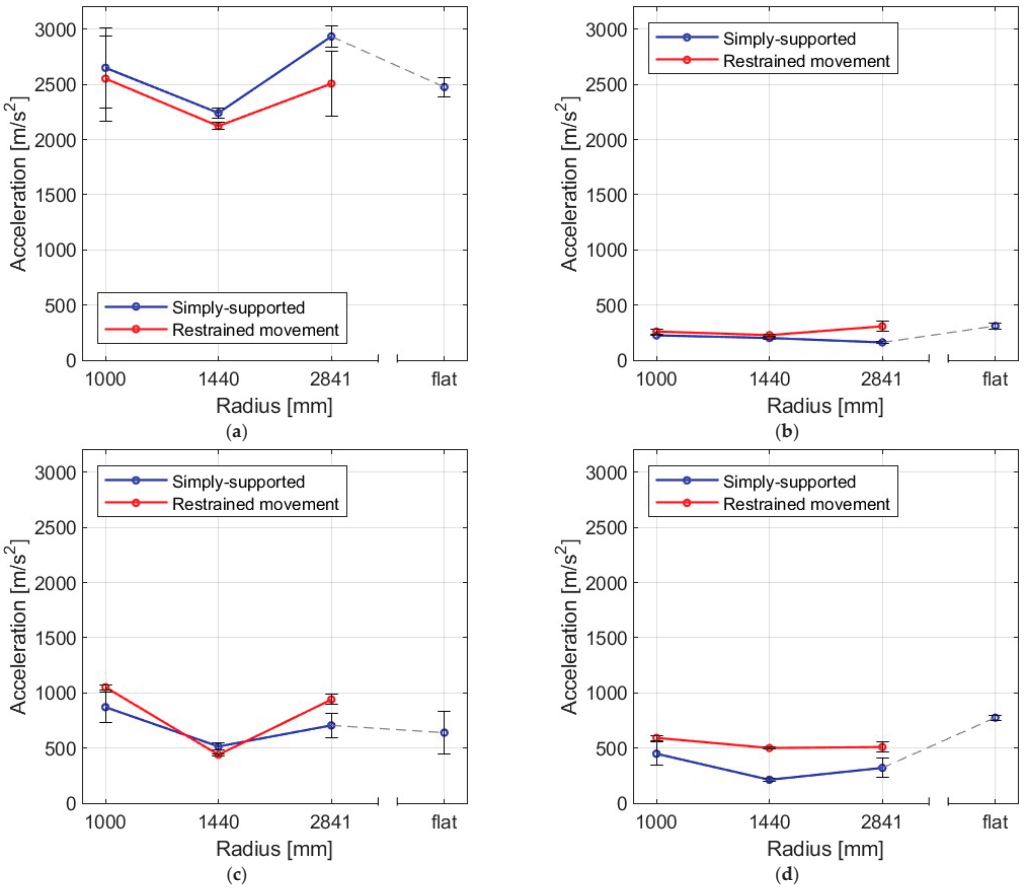

Figure 16. Mean acceleration of the panes as a result of impact by (**a**) steel ball, (**b**) rubber ball filled with sand, (**c**) elastic bag filled with peas, (**d**) basketball.

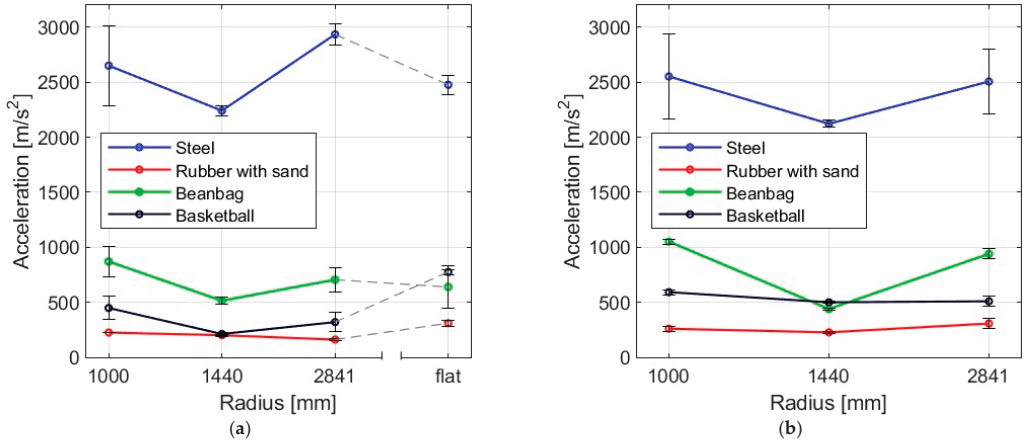

Figure 17. Mean values of acceleration for four impactors in (**a**) simply supported, (**b**) restrained movement supports.

4. Conclusions and Further Work

This paper presents the experimental results of dynamic tests of curved glass panes under low-velocity impact with simply supported and restrained boundary conditions. It investigates the variations caused by an impactor involving different parameters of stiffness, mass, and geometry. In this study, a 5 mm thick pane with a geometry of 1000×1000 mm^2 was examined.

From the experiments performed, the following conclusions were drawn.

Flat plates have a lower capacity to dampen oscillations, resulting in longer decay times compared to curved panes. Smaller bending radii in the panels lead to lower displacement values and faster dissipation of impact energy. This aligns with the observation that curved elements are generally more rigid than flat ones.

The size of the contact area plays a crucial role in determining the displacement. A smaller contact area concentrates the impact energy in a smaller point, resulting in greater displacement.

The geometry of the impactor also affects the contact area. The behavior of the glass varies depending on the type of impact body. For impactors with lower deformability, the glass panes experience uneven vibrations at the moment of impact, followed by a chaotic period of transient oscillations before reaching a stationary state. This is in contrast to bodies with greater deformability in which the main dynamic behavior shows a more predictable pattern.

Author Contributions: Conceptualization, M.K. and K.Z.; methodology, M.K. and K.Z.; formal analysis, M.K. and K.Z.; investigation, M.K. and K.Z.; data curation, M.K. and K.Z.; writing—original draft preparation, M.K. and K.Z.; writing—review and editing, M.K. and K.Z.; visualization, M.K. and K.Z.; funding acquisition, M.K. and K.Z. All authors have read and agreed to the published version of the manuscript.

Funding: This publication was supported as part of the Excellence Initiative—Research University program implemented at the Silesian University of Technology (03/060/SDU/10-21-03), Gliwice, Poland, 2021. This work was also supported by the funding provided by the Silesian University of Technology (projects BKM-630/RB6/2023 and BK-211/RB6/2023).

Institutional Review Board Statement: Not applicable.

Informed Consent Statement: Not applicable.

Data Availability Statement: Data is available on request.

Acknowledgments: The authors wish to acknowledge the assistance in conducting the experimental campaign provided by Natalia Suchecka.

Conflicts of Interest: The authors declare no conflict of interest.

References

1. Patterson, M. *Structural Glass Facades and Enclosures*; Wiley: Hoboken, NJ, USA, 2011.
2. Centelles, X.; Castro, J.R.; Cabeza, L.F. Experimental results of mechanical, adhesive, and laminated connections for laminated glass elements—A review. *Eng. Struct.* **2019**, *180*, 192–204. [CrossRef]
3. Citherlet, S.; Di Guglielmo, F.; Gay, J.-B. Window and advanced glazing systems life cycle assessment. *Energy Build.* **2000**, *32*, 225–234. [CrossRef]
4. Kosić, T.; Svetel, I.; Cekić, Z. Complexity of Curved Glass Structures. In *IOP Conference Series: Materials Science and Engineering*; IOP Publishing: Bristol, UK, 2017; Volume 262. [CrossRef]
5. Pini, V.; Ruz, J.J.; Kosaka, P.M.; Malvar, O.; Calleja, M.; Tamayo, J. How two-dimensional bending can extraordinarily stiffen thin sheets. *Sci. Rep.* **2016**, *6*, 29627. [CrossRef]
6. Aşık, M.Z.; Dural, E.; Yetmez, M.; Uzhan, T. A mathematical model for the behavior of laminated uniformly curved glass beams. *Compos. Part B Eng.* **2014**, *58*, 593–604. [CrossRef]
7. Kozłowski, M.; Respondek, Z.; Cornik, D.; Wiśniowski, M.; Zemła, K. Influence of curvature and geometrical parameters on internal pressure in cylindrical Insulating Glass Units. *Thin-Walled Struct.* **2023**, *188*, 110812. [CrossRef]
8. Kozłowski, M.; Zemła, K. Numerical Modelling of Structural Behaviour of Curved Insulating Glass Units. *Mater. Proc.* **2023**, *13*, 12. [CrossRef]

9. Kozłowski, M. Experimental and numerical assessment of structural behaviour of glass balustrade subjected to soft body impact. *Compos. Struct.* **2019**, *229*, 111380. [CrossRef]
10. Schneider, J. Impact Loading on Glass Panes by Soft Body Impact—Theoretical Analysis and Experimental Verification. *Proc. Glass Process. Days* **2001**, *5*, 682–687.
11. Kozłowski, M.; Kinsella, D.; Persson, K.; Kubica, J.; Hulimka, J. Structural Analysis of Slender Glass Panel Subjected to Static and Impact Loading. In *Challenging Glass Conference Proceedings*; Stichting: Rotterdam, NL, USA, 2018; pp. 427–434. [CrossRef]
12. Ramkumar, R.L.; Thakar, Y.R. Dynamic Response of Curved Laminated Plates Subjected to Low Velocity Impact. *J. Eng. Mater. Technol.* **1987**, *109*, 67–71. [CrossRef]
13. Christoforou, A.P.; Swanson, S.R. Analysis of Simply-Supported Orthotropic Cylindrical Shells Subject to Lateral Impact Loads. *J. Appl. Mech.* **1990**, *57*, 376–382. [CrossRef]
14. Lin, H.J.; Lee, Y.J. Impact-Induced Fracture in Laminated Plates and Shells. *J. Compos. Mater.* **1990**, *24*, 1179–1199. [CrossRef]
15. Palazotto, A.; Perry, R.; Sandhu, R. Impact response of graphite/epoxy cylindrical panels. *AIAA J.* **1992**, *30*, 1827–1832. [CrossRef]
16. Kim, S.J.; Goo, N.S.; Kim, T.W. The effect of curvature on the dynamic response and impact-induced damage in composite laminates. *Compos. Sci. Technol.* **1997**, *57*, 763–773. [CrossRef]
17. Ferreira, L.M.; Coelho, C.A.C.P.; Reis, P.N.B. Numerical Simulations of the Low-Velocity Impact Response of Semicylindrical Woven Composite Shells. *Materials* **2023**, *16*, 3442. [CrossRef] [PubMed]
18. Reis, P.N.B.; Sousa, P.; Ferreira, L.M.; Coelho, C.A.C.P. Multi-impact response of semicylindrical composite laminated shells with different thicknesses. *Compos. Struct.* **2023**, *310*, 116771. [CrossRef]
19. Sukhanova, O.; Larin, O.; Naumenko, K.; Altenbach, H. Dynamics of Curved Laminated Glass Composite Panels Under Impact Loading. In *Nonlinear Mechanics of Complex Structures, Advanced Structured Materials*; Altenbach, H., Amabili, M., Mikhlin, Y.V., Eds.; Springer International Publishing: Cham, Switzerland, 2021; pp. 91–101. [CrossRef]
20. Galuppi, L.; Royer-Carfagni, G. Analytical approach à la Newmark for curved laminated glass. *Compos. Part B Eng.* **2015**, *76*, 65–78. [CrossRef]
21. Sukhanova, O.; Larin, O. Linear dynamic properties in curved laminated glasses. *Bull. Natl. Tech. Univ. KhPI Ser. Dyn. Strength Mach.* **2021**, *1*, 44–47. [CrossRef]
22. Altec Inc. *Technical Documentation for the QACQ Family of Monitoring and Recording Modules*; Altec Inc.: Birmingham, AL, USA, 2021.
23. HBM. *Operating Manual*; QUANTUM X; HBM: Marlboro, MA, USA, 2021.
24. HBM. *Operating Manual*; Catman; HBM: Marlboro, MA, USA, 2023.
25. Altec Inc. *VIDIA Cloud. User Manual*; Altec Inc.: Birmingham, AL, USA, 2021.
26. Suchecka, N. *Analiza Odpowiedzi Dynamicznej Szklanych Tafli Płaskich i Giętych na Uderzenie Ciał o Różnych Właściwościach (Analysis of the Dynamic Response of Flat and Bent Glass Panes to the Impact of Bodies with Various Properties)*; Silesian University of Technology: Gliwice, Poland, 2023.
27. *EAD 210005-00-0505*; Internal Partition Kits for Use as Non-Load Bearing Walls. Notified Bodies for Regulation EP and Council (EC): Brussels, Belgium, 2019.
28. Diehl, T.; Carroll, D.; Nagaraj, B.K. Using Digital Signal Processing (DSP) to Significantly Improve the Interpretation of ABAQUS/Explicit Results. In Proceedings of the ABAQUS User's Conference, Chester, UK, 25–28 May 1999.

materials

MDPI

Article

A Constitutive Model for Describing the Tensile Response of Woven Polyethylene Terephthalate Geogrids after Damage

Giovani Lombardi [1,*], Margarida Pinho-Lopes [1,2], António Miguel Paula [1,2,3] and António Bastos Pereira [4,5,*]

[1] RISCO, Department of Civil Engineering, University of Aveiro, Campus Universitário de Santiago, 3810-193 Aveiro, Portugal; mlopes@ua.pt (M.P.-L.); mpaula@ipb.pt (A.M.P.)
[2] CONSTRUCT-GEO, Department of Civil Engineering, Faculty of Engineering, University of Porto, Rua Doutor Roberto Frias, s/n, 4200-465 Porto, Portugal
[3] Instituto Politécnico de Bragança, Campus de Santa Apolónia, 5300-253 Bragança, Portugal
[4] TEMA, Department of Mechanical Engineering, University of Aveiro, Campus Universitário de Santiago, 3810-193 Aveiro, Portugal
[5] LASI—Intelligent Systems Associate Laboratory, 4800-058 Guimarães, Portugal
* Correspondence: giovanilombardi@ua.pt (G.L.); abastos@ua.pt (A.B.P.)

Abstract: A constitutive model was used to describe the tensile response of two woven Polyethylene Terephthalate (PET) geogrids, before and after mechanical damage. The model parameters of undamaged and damaged specimens were estimated via numerical regressions of test results. For each sample, the experimental and fitted tensile strengths were statistically compared using hypothesis tests. For each geogrid, tensile load–strain curves of damaged samples were drawn by applying scaling factors to the plot of the undamaged sample. The curve fittings resulted in high R^2 values for undamaged and damaged specimens of the geogrids. For most samples, there was no significant mean difference between the experimental and fitted tensile strength. The model allowed us to describe the load–strain curve of a geogrid from its tensile properties: ε_{max}, T_{max} and J_i. Regardless of the type of damage (in laboratory or in situ), the model was able to describe the load–strain curves of damaged samples using data from undamaged samples and scaling factors.

Keywords: geosynthetics; constitutive models; damage; statistical analysis

Citation: Lombardi, G.; Pinho-Lopes, M.; Paula, A.M.; Pereira, A.B. A Constitutive Model for Describing the Tensile Response of Woven Polyethylene Terephthalate Geogrids after Damage. *Materials* **2023**, *16*, 5384. https://doi.org/10.3390/ma16155384

Academic Editor: Krzysztof Schabowicz

Received: 27 June 2023
Revised: 20 July 2023
Accepted: 27 July 2023
Published: 31 July 2023

1. Introduction

Geosynthetic is a generic name given to planar products, mostly composed of polymers, and used in contact with soil, rock or with any other material as part of a constructive system [1]. Most geosynthetics are composed of thermoplastic polymers, such as polypropylene, polyester, polyethylene, polyvinyl, polyamide, and polystyrene [2].

Geosynthetics have been increasingly applied in civil engineering and geotechnical works due to the advantages presented when compared to traditional solutions. Geosynthetics have several important functions and can be applied in a wide range of structures, namely, reinforced soils, support walls, very steep slopes, landfills for waste disposal, erosion control and coastal protection [2]. Geosynthetics can contribute to a more resilient and sustainable world, as they may provide quality water, protect the environment, mitigate natural disasters, use more economical solutions and connect people [3].

Among the different applications of geosynthetics, their use in roads can be highlighted. Geosynthetics are used in both paved and unpaved roads [4] to perform different functions [5]: reinforcement, stabilisation, stress-relief interlayer, separation, fluid barrier, drainage, and filtration. Roads (paved or unpaved) can be improved via mechanical means, and the relevant functions are reinforcement and stabilisation [5]; thus, the mechanical response of geosynthetics is key for the design. Similarly, there are other projects where geosynthetics act as reinforcements so that the short- and long-term mechanical responses are primary aspects in the design, such as in retaining walls and reinforced soil slopes [6–8].

Models that can realistically represent the tensile response of geosynthetics are fundamental for attaining economic solutions. In the literature, there are examples of studies using a variety of constitutive models for geosynthetics [9–12].

Different constitutive theories can form the basis of the stress–strain relation of materials, such as elasticity, plasticity, viscoelasticity and viscoplasticity [13]. The mechanical behaviour of geosynthetics is a combination of the typical response of an elastic solid, a viscous liquid, and a plastic, depending primarily on the temperature [14].

The tensile response of geosynthetics is affected by several factors, including the type and arrangement of the constituent polymer, environmental conditions, soil confinement, and loading level, rate and duration [15]. Physical models (e.g., rheological and damage models) and mathematical models (e.g., polynomial and hyperbolic models) are used to describe the tensile load–strain response of geosynthetics. Physical models are employed to account for microscopic effects, whereas mathematical models are phenomenological—they only represent experimental results and do not consider microscopic effects [16].

Hyperbolic equations to model the behaviour of geosynthetics and reinforced soil structures were reported by [17–24]. Bathurst and Naftchali [25] stated that these equations are significantly accurate for analytical and numerical modelling of geosynthetics; the authors reported that the model parameters were related to the strain rate and the curvature of the tensile load–strain plot. Ezzein et al. [26] also supported that the parameters of hyperbolic models depend on the strain rate.

In order to capture the stiffening in the tensile load–strain response of some geosynthetics, the nonlinear model given in Equation (1) combines an exponential function to fit high strains and a hyperbola to fit low strains (Figure 1). The tangent stiffness (Equation (2)) is given by the derivative of Equation (1) with respect to the tensile strain [19].

$$T = \frac{\varepsilon}{(a + 2 \cdot b \cdot \varepsilon)} + \frac{1}{2 \cdot b} \cdot e^{-c \cdot (\varepsilon - \varepsilon_{max})^2} \ (\varepsilon \geq 0) \quad (1)$$

$$J = \frac{dT}{d\varepsilon} = \frac{a}{(a + 2 \cdot b \cdot \varepsilon)^2} - \frac{c \cdot (\varepsilon - \varepsilon_{max})}{2 \cdot b} \cdot e^{-c \cdot (\varepsilon - \varepsilon_{max})^2} \ (\varepsilon \geq 0) \quad (2)$$

T: tensile load per unit width;
J: tangent stiffness;
ε: tensile strain;
a, b, and c: model parameters;
ε_{max}: strain at maximum load.

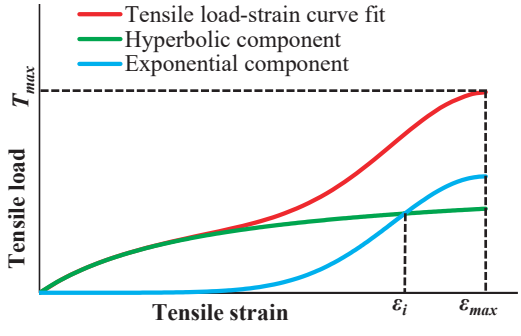

Figure 1. Typical tensile load–strain curve of a geosynthetic that presents a stiffening response. Components of the constitutive model (Equation (1)).

Geosynthetics are subjected to damage mechanisms in storage, during construction and post-installation, including weathering, chemicals, high temperatures, abrasion, creep, and oxidation. The durability of a geosynthetic depends on several factors, such as atmospheric agents, the type of polymer, its structure, and its primary function [15].

The assessment of durability is based on experimental observations and tests performed to evaluate damages expected during the design life of a geosynthetic. The lifespan of a geosynthetic is usually estimated based on gradual changes in physical and mechanical properties, increasing deformations, reductions in strength and stiffness, holes, or any other change that might compromise its performance and durability [27].

In particular, damage occurring during installation (DDI) may modify the structure of geosynthetics. Noticeable cuts and holes, detachment and disaggregation of the coating surface are typical consequences due to placement, spreading and compaction of backfill material over a geosynthetic. DDI is immediate, resulting in a rapid and irreversible reduction in stiffness and strength, thus being part of the durability assessment [27].

Bathurst and Allen [28] reported that the short-term tensile load–strain curve of a damaged geosynthetic can be described by applying scaling factors to the plot of an undamaged sample (Figure 2). In this sense, the following three scaling factors are used to characterize the tensile response after damage: peak strength retained: R_T (Equation (3)); modulus retained: R_J (Equation (4)); and peak strain retained: R_ε (Equation (5)). The authors concluded that R_T, R_J and R_ε can be used if the shape of the load–strain curve is not significantly modified after damage, and variability in the data and measurements are considered.

$$R_T = \frac{T_{max}(Y)}{T_{max}(X)} \tag{3}$$

$$R_J = \frac{J_i(Y)}{J_i(X)} \tag{4}$$

$$R_\varepsilon = \frac{\varepsilon_{max}(Y)}{\varepsilon_{max}(X)} \tag{5}$$

R_T, R_J and R_ε: scaling factors;
X: undamaged sample;
Y: damaged sample.

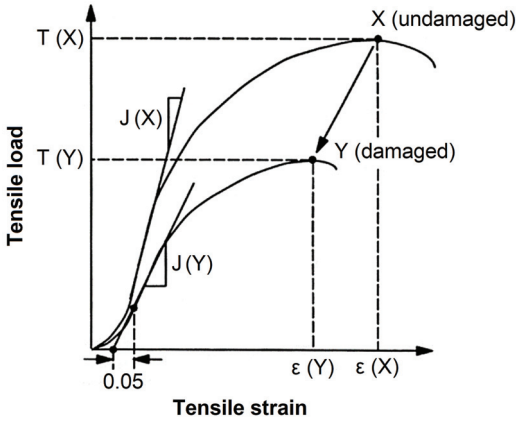

Figure 2. Changes in the short-term tensile response of a geosynthetic after damage [28]—adapted.

The objectives of this study are summarized as follows.

- Apply a constitutive model to describe the short-term tensile response of undamaged and damaged specimens of two woven Polyethylene Terephthalate (PET) geogrids;

estimate the model parameters; assess the goodness of the fits; statistically compare experimental and fitted data.
- Determine the scaling factors by relating the tensile properties of undamaged and damaged samples of the geogrids.
- For each geogrid, obtain the tensile load–strain curve of damaged samples by applying scaling factors to the plot of the undamaged sample; assess the goodness of the fits; statistically compare predicted and fitted data.

2. Materials

Data from two woven PET geogrids (Table 1) were analysed. Specimens of both geogrids were damaged in a laboratory (MEC) following EN ISO 10722 [29], in which the specimens are placed between layers of a synthetic aggregate, and then submitted to cyclic loading ranging between 5 kPa and 500 kPa, at a frequency of 1 Hz for 200 cycles. The experimental data and the procedures of damage were reported by [23,30,31].

Table 1. Nominal properties of the geosynthetics.

Geosynthetic	**GWP55**		**GWP60**	
Type	Geogrid	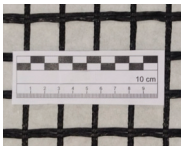	Geogrid	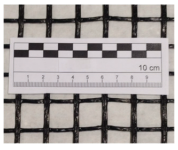
Structure	Woven		Woven	
Constituent polymer	PET		PET	
Nominal tensile strength (kN/m)	55		60	
Nominal tensile strain (%)	10.5		14.0	
Grid spacing (mm × mm)	25 × 25		20 × 20	

Specimens of the geogrid GWP60 were submitted to damage during installation: they were placed between layers of granite residual soil, and then they were subjected to two distinct levels of compaction energy as per the Proctor's test: 90% (DDI90) and 98% (DDI98). The test beds were constructed on a road-building site, over a road platform. The geosynthetics were placed on top of a 0.20 m soil lift, properly spread, levelled, and compacted. Two additional soil lifts were placed over the geosynthetics, each 0.20 m high, for a total height of 0.60 m. A vibratory roller was utilized to compress the soil. The experimental data and the procedures of damage in situ were reported by [32].

Thereafter, undamaged (UND) and damaged specimens of the geogrids were subjected to tensile tests following EN ISO 10319 [33], where the strains were measured by video extensometers at short intervals (about 0.3 s). The following tensile properties were determined from the test results: the tensile strength (T_{max}) and the strain at T_{max} (ε_{max}).

3. Methods

Although recent studies have shown a relationship between the parameters of hyperbolic models and the strain rate, the results analysed here were obtained for specimens tested at a constant strain rate: 20 ± 5%/minute, as per EN ISO 10319 [33]. Thus, the effect of the strain rate was not considered in this study. In addition, this paper reports results for geosynthetics that present a stiffening response, as shown in Figure 1.

Figure 3 illustrates the methods used to estimate the model parameters of undamaged and damaged samples, detailed in Sections 3.1–3.3. Table 2 summarizes the main terms and definitions addressed in the following topics.

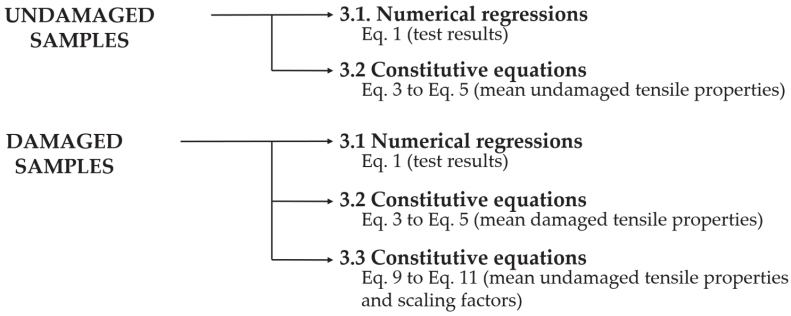

Figure 3. Methods used to estimate the model parameters, detailed in Sections 3.1–3.3.

Table 2. Main terms and definitions.

Term	Symbol	Definition
Model parameters	a, b, c	Parameters of the constitutive model (Equation (1))
Parameter estimates	–	Model parameters estimated via numerical regressions of experimental data
Mean parameter estimates	–	Mean estimates of the model parameter of a sample
Median parameter estimates	–	Median estimates of the model parameter of a sample
Tensile properties	J_i, T_{max}, ε_{max}	Tensile properties of a certain geogrid
Mean undamaged tensile properties	–	Mean experimental tensile properties of an undamaged sample
Mean damaged tensile properties	–	Mean experimental tensile properties of a damaged sample
Predicted damaged parameters	$a(Y)$, $b(Y)$, $c(Y)$	Model parameters for the response after damage predicted from undamaged data using scaling factors (Equations (3)–(5))
Representative curve:	–	Load–strain curve that best represents the trends in the data of a sample
• Mean curve [$]	–	Load–strain curve plotted using mean parameter estimates
• Median curve	–	Load–strain curve plotted using median parameter estimates
• Intermediate curve	–	Experimental load–strain curve that visually is in an intermediate position relative to the other curves of a sample

[$] mean parameter estimates were used to plot the representative curves.

3.1. Numerical Regressions (Curve Fittings)

A constitutive model (Equation (1)) was applied to describe the tensile load–strain recurves of undamaged and damaged specimens of the geogrids. The higher the sample size, the more robust the statistical analysis.

SPSS® was used to fit experimental data, and the model parameters were estimated via nonlinear regressions according to the Levenberg–Marquardt algorithm. The model parameters were estimated with confidence intervals of 95%, and the coefficient of determination (R^2 value) was used to assess the goodness of the fits.

With confidence intervals of 95%, data were statistically compared using the Student *t*-test—a hypothesis test for independent samples, applied to compare the difference in means between two samples of normally distributed data [34]. The tests of normality were performed in SPSS® using the Shapiro–Wilk method—applied to small sample sizes [35]. Levene's tests provided the homogeneity of variance.

The hypothesis tests were used to compare mean values (e.g., experimental vs. fitted T_{max}), while the R^2 values were used to assess the goodness of the fits (along the entire plot). For both undamaged and damaged samples of the geogrids, the mean estimates of model parameters were used to plot the representative tensile load–strain curve (mean curve). Other representative curves were assessed (Table 2), but the mean curve resulted in the highest R^2 values for all samples analysed.

3.2. Mathematical Relations between the Model Parameters and the Tensile Properties

The relations between the model parameters to each other and the tensile properties are mathematically determined by applying boundary conditions to Equations (1) and (2). Equation (6) is determined from Equation (2) ($\varepsilon \to 0$), and it relates the model parameter a to the initial tangent stiffness (J_i); Equation (6) was reported by [19].

Equation (7) is obtained from Equation (1) ($\varepsilon \to \varepsilon_{max}$); it relates the model parameter b to the tensile strength (T_{max}), the strain at maximum load (ε_{max}) and the model parameter a. Lastly, Equation (8) is deduced from Equation (1) ($\varepsilon \to \varepsilon_i$, Figure 1), and relates the model parameter c to ε_{max} and the parameters a and b.

$$a = \frac{1}{J_i} \ (\varepsilon \ \to \ 0) \tag{6}$$

$$b = \frac{-a \cdot T_{max} + 2 \cdot \varepsilon_{max} + \sqrt{4 \cdot {\varepsilon_{max}}^2 + a^2 \cdot {T_{max}}^2}}{4 \cdot \varepsilon_{max} \cdot T_{max}} \ (\varepsilon \ \to \ \varepsilon_{max}) \tag{7}$$

$$c = \frac{-ln\left(\frac{2 \cdot b \cdot \varepsilon_i}{a + 2 \cdot b \cdot \varepsilon_i}\right)}{\left(\varepsilon_i - \varepsilon_{max}\right)^2} \ (\varepsilon \ \to \ \varepsilon_i) \left\{ \varepsilon_i \in \mathbb{R}^+ / \varepsilon_i \neq 0, \varepsilon_i \neq \frac{-a}{2 \cdot b}, \varepsilon_i \neq \varepsilon_{max} \right\} \tag{8}$$

J_i: initial tangent stiffness;
T_{max}: tensile strength;
ε_i: strain for which the hyperbolic and exponential components intersect (Figure 1).

For each damaged and undamaged sample of the geogrids, the model parameters were determined from Equation (6) to Equation (8) using mean experimental ε_{max}, and T_{max} and J_i were fitted by the representative curve. ε_i was determined via iteration using the bisection method (there is a value of ε_i for which the components of the constitutive model intersect, as shown in Figure 1). The model parameters determined from these equations were compared to those estimated via numerical regressions of test results.

3.3. Damaged Curves Described Using Undamaged Data and Scaling Factors

For each damaged sample of the geogrids, the model parameters were predicted from undamaged data using Equations (9)–(11). These equations are analogous to Equation (6) to Equation (8), where the damaged tensile properties were determined from Equation (3) to Equation (5) (using mean undamaged tensile properties and scaling factors). The values for model parameters determined from these equations were compared to those estimated via numerical regressions of test results.

$$a(Y) = \frac{1}{J_i(Y)} \tag{9}$$

$$b(Y) = \frac{\frac{-T_{max}(Y)}{J_i(Y)} + 2 \cdot \varepsilon_{max}(Y) + \sqrt{4 \cdot [\varepsilon_{max}(Y)]^2 + \left[\frac{T_{max}(Y)}{J_i(Y)}\right]^2 \cdot [T_{max}(Y)]^2}}{4[\varepsilon_{max}(Y)] \cdot [T_{max}(Y)]} \tag{10}$$

$$c(Y) = \frac{-ln\left(\frac{2 \cdot b(Y) \cdot \varepsilon_i(Y)}{a(Y) + 2 \cdot b(Y) \cdot \varepsilon_i(Y)}\right)}{\left[\varepsilon_i(Y) - \varepsilon_{max}(Y)\right]^2} \tag{11}$$

$T_{max}(Y)$, $J_i(Y)$ and $\varepsilon_{max}(Y)$: damaged tensile properties (from Equation (3) to Equation (5)).

4. Results and Discussions

The model (Equation (1)) was able to qualitatively describe the tensile response of undamaged and damaged specimens of both geogrids, regardless of the type of damage (in laboratory or in situ). The curve fittings resulted in high R^2 values (between 0.979 and 0.997). Table 3 gives the mean experimental and fitted tensile properties. The ex-

perimental and fitted tensile load–strain curves are presented in Figure 4 (GWP55) and Figure 5 (GWP60).

Table 3. Mean experimental and fitted tensile properties.

Sample	Mean Experimental Tensile Properties		Mean Fitted Tensile Properties (Equation (1))	
	ε_{max} %	T_{max} kN/m	T_{max} kN/m	J_i kN/m
GWP55 UND	8.5	46.72	44.66	957.03
GWP55 MEC	7.8	39.80	37.88	938.93
GWP60 UND	14.0	66.84	62.70 *	734.53
GWP60 MEC	13.8	50.11	48.16	744.54
GWP60 DDI S90	14.7	63.01	59.19	708.04
GWP60 DDI S98	14.2	59.23	55.99	786.16

T_{max}: tensile strength; ε_{max}: strain at T_{max}; J_i: initial tangent stiffness; * significant mean difference.

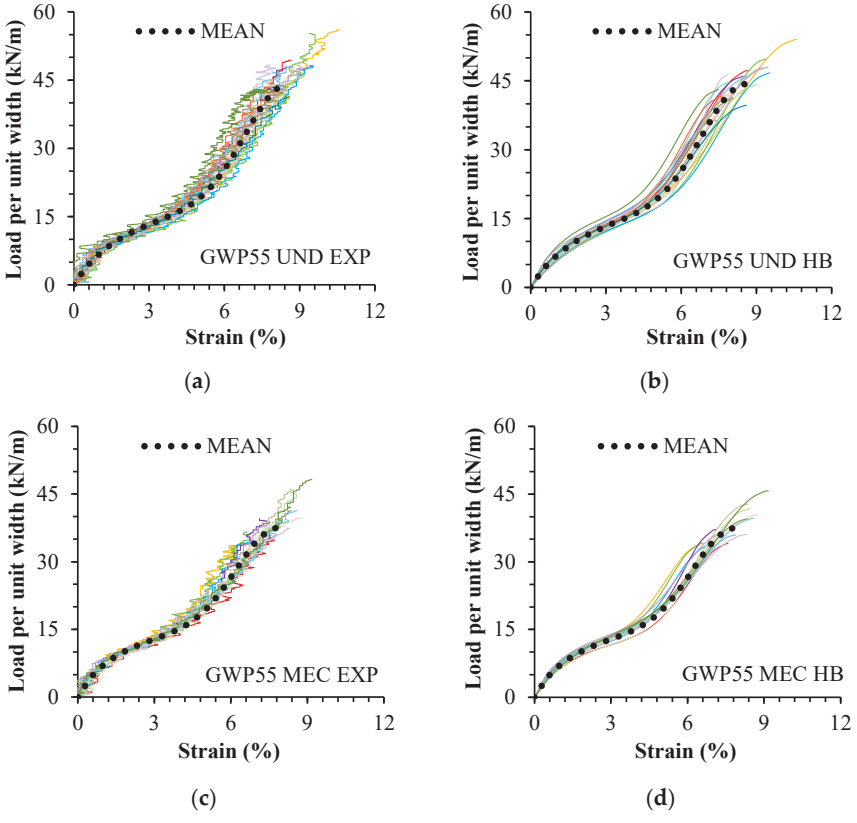

Figure 4. Geogrid GWP55. Experimental curves (EXP) and fitted curves (HB): (**a**) UND EXP; (**b**) UND HB; (**c**) MEC EXP; (**d**) MEC HB. Undamaged (UND). Damaged in laboratory (MEC). Each color represents a test.

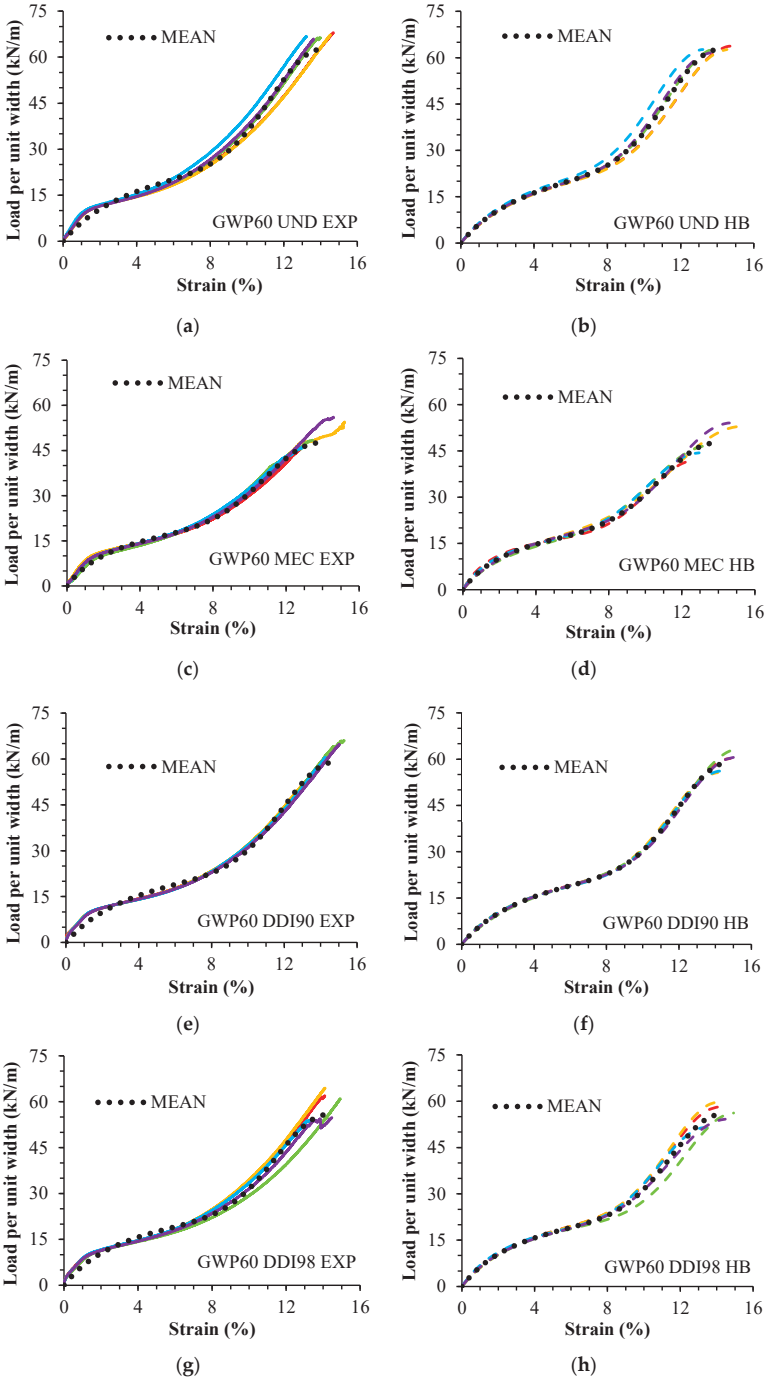

Figure 5. Geogrid GWP60. Experimental curves (EXP) and fitted curves (HB): (**a**) UND EXP; (**b**) UND HB; (**c**) MEC EXP; (**d**) MEC HB; (**e**) DDI90 EXP; (**f**) DDI90 HB; (**g**) DDI98 EXP; (**h**) DDI98 HB. Undamaged (UND). Damaged in laboratory (MEC). Damaged during installation (DDI). Each color represents a test.

Table 4 gives the sample sizes, the mean parameter estimates, the tensile properties fitted by the mean curve, and the scaling factors. All experimental and fitted data are normally distributed. The hypothesis tests indicated that there was no significant mean difference between the experimental and fitted tensile strength, except for GWP60 UND.

Table 4. Mean parameter estimates. Tensile properties fitted by the mean curve. Scaling factors.

Sample	Sample Size	Mean Parameter Estimates Equation (1) (SPSS®)			Tensile Properties Mean Curve		Scaling Factors Equation (3)	Equation (4)	Equation (5)
	N	a	b	c	T_{max}	J_i	R_T	R_J	R_ε
	–	m/kN	m/kN	–	kN/m	kN/m	–	–	–
GWP55 UND	20	0.1085	0.0198	0.1763	44.28	921.50	–	–	–
GWP55 MEC	15	0.0936	0.0240	0.1957	37.55	1068.35	0.848	1.159	0.917
GWP60 UND	5	0.1364	0.0139	0.0703	62.69	733.18	–	–	–
GWP60 MEC	5	0.1220	0.0190	0.0598	47.57	819.48	0.759	1.118	0.985
GWP60 DDI90	5	0.1418	0.0149	0.0675	59.03	705.14	0.942	0.962	1.050
GWP60 DDI98	5	0.1278	0.0159	0.0701	55.82	782.26	1.013	0.890	1.067

For undamaged and damaged samples of the geogrids, the values for model parameters determined from Equation (6) to Equation (8) were equal to those estimated via numerical regressions, which reinforces the mathematical relations between the model parameters to each other and the tensile properties, as proposed in these equations.

Table 5 gives the predicted parameters (from Equation (9) to Equation (11)), and the mean parameter estimates (from numerical regressions using Equation (1)) for damaged samples. Figure 6 shows the representative and predicted curves of damaged samples. Values for damaged parameters predicted from Equation (9) to Equation (11) were equal to those estimated via numerical regressions, which demonstrates the capacity of the model to describe damaged curves from undamaged data using scaling factors.

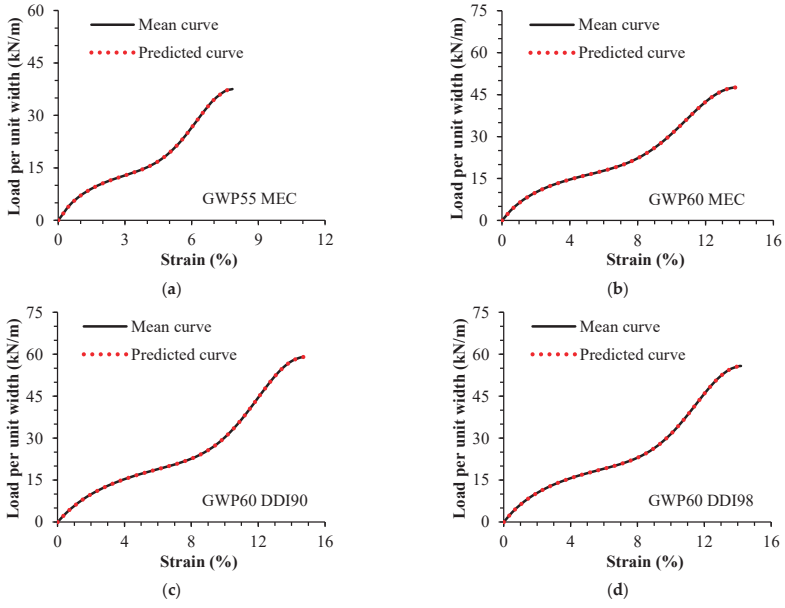

Figure 6. Damaged curves: (**a**) GWP55 MEC; (**b**) GWP60 MEC; (**c**) GWP60 DDI90; (**d**) GWP60 DDI98. Mean curve: plotted using mean parameter estimates. Predicted curve: plotted using the damaged parameters predicted from Equation (9) to Equation (11). Damaged in laboratory (MEC). Damaged during installation (DDI).

Table 5. Damaged parameters: predicted (Equations (9)–(11)) vs. estimated (Equation (1)—SPSS®).

Sample	Predicted Parameters			Mean Parameter Estimates Equation (1) (SPSS®)		
	Equation (9) $a(Y)$ m/kN	Equation (10) $b(Y)$ m/kN	Equation (11) $c(Y)$ –	a m/kN	b m/kN	c –
GWP55 MEC	0.0936	0.0240	0.1957	0.0936	0.0240	0.1957
GWP60 UND	0.1220	0.0190	0.0598	0.1220	0.0190	0.0598
GWP60 DDI90	0.1418	0.0149	0.0675	0.1418	0.0149	0.0675
GWP60 DDI98	0.1278	0.0159	0.0701	0.1278	0.0159	0.0701

5. Conclusions

In this study, a constitutive model (Equation (1)) was applied to fit the tensile response of two woven PET geogrids, before and after damage. The model parameters were estimated via numerical regressions of experimental data. Values for the model parameters were determined from Equation (6) to Equation (8) using mean tensile properties. Values for the model parameters of damaged samples were also determined from Equation (9) to Equation (11) using undamaged data and scaling factors. For each sample, hypothesis tests were used to statistically compare the experimental and fitted tensile strength (mean values). For each specimen, the R^2 value was used to assess the goodness of the fit. The main conclusions of the research are stated as follows.

- The model was able to qualitatively describe the tensile load–strain response of undamaged and damaged specimens of both geogrids (high R^2 values).
- If compared to experimental values, the model proved capable of fitting the tensile strength of most samples of the geogrids (for most samples, there was no significant mean difference between the experimental and fitted tensile strength).
- The model allowed us to describe the tensile load–strain curve of a geogrid (before and after damage) only from its tensile properties: ε_{max}, T_{max} and J_i.
- Regardless of the type of damage, the model was able to describe tensile load–strain curves of damaged samples using data from undamaged samples and scaling factors.

This paper presented a successful approach to predict the short-term tensile response of two woven geogrids after mechanical damage induced in a laboratory and after damage during installation. The estimates were based on the tensile properties of the undamaged materials and scaling factors—relating the tensile properties of the damaged samples with those of the reference material (undamaged sample). Thus, experimental data from damaged and undamaged specimens are required to determine the scaling factors.

This approach has the potential for being further extended and applied in the design of geosynthetics as the scaling factors of a geogrid could be estimated using such information—when a robust database is available for comparable conditions (geosynthetics and damage/installation conditions). Therefore, this approach could allow the prediction of the tensile load–strain curve of a damaged geogrid before test data are available.

Author Contributions: G.L.: Conceptualisation; Methodology; Validation; Formal analysis; Investigation; Data curation; Writing—original draft; Writing—review and editing; Funding acquisition. M.P.-L.: Conceptualization; Methodology; Validation; Formal analysis; Investigation; Resources; Data curation; Writing—review and editing; Supervision; Project administration; Funding acquisition. A.M.P.: Conceptualization; Methodology; Validation; Formal analysis; Investigation; Resources; Data curation; Writing—review and editing; Supervision; Project administration; Funding acquisition. A.B.P.: Validation; Investigation; Resources; Data curation; Writing—review and editing; Supervision; Funding acquisition. All authors have read and agreed to the published version of the manuscript.

Funding: This work was funded by the Foundation for Science and Technology (FCT), grant number 2020.07874.BD (doctoral scholarship), FCT/UIDB/ECI/04450/2020 (Aveiro Research Centre for Risks and Sustainability in Construction), FCT/UIDB/04708/2020 (CONSTRUCT, Instituto de I&D em Estruturas e Construções), FCT/UIDB/00481/2020, FCT/UIDP/00481/2020, and

CENTRO-01-0145-FEDER-022083 (Centre for Mechanical Technology and Automation), and by the project TRANSFORM—supported by the Portuguese Resilience Plan (PRR) and European Union (NextGenerationEU).

Institutional Review Board Statement: Not applicable.

Informed Consent Statement: Not applicable.

Data Availability Statement: The data presented in this study are available on request from the corresponding author.

Conflicts of Interest: The authors declare no conflict of interest.

References

1. *ISO 10318-1*; Geosynthetics—Part 1: Terms and Definitions. International Organization for Standardization: Geneva, Switzerland, 2015.
2. Koerner, R.M. *Designing with Geosynthetics*, 5th ed.; Pearson Prentice Hall: Upper Saddle River, NJ, USA, 2005.
3. Touze, N. Healing the World: A Geosynthetics Solution. *Geosynth. Int.* **2021**, *28*, 1–31. [CrossRef]
4. Keller, G.R. Application of Geosynthetics on Low-Volume Roads. *Transp. Geotech.* **2016**, *8*, 119–131. [CrossRef]
5. Giroud, J.P.; Han, J.; Tutumluer, E.; Dobie, M.J.D. The Use of Geosynthetics in Roads. *Geosynth. Int.* **2023**, *30*, 47–80. [CrossRef]
6. Wang, C.; Luan, M.; Zhu, Z. Model Test and Numerical Analysis on Long-Term Mechanical Properties of Stepped Reinforced Retaining Wall. *Trans. Tianjin Univ.* **2012**, *18*, 62–68. [CrossRef]
7. Zou, C.; Wang, Y.; Lin, J.; Chen, Y. Creep Behaviors and Constitutive Model for High Density Polyethylene Geogrid and Its Application to Reinforced Soil Retaining Wall on Soft Soil Foundation. *Constr. Build. Mater.* **2016**, *114*, 763–771. [CrossRef]
8. Adams, M.; Nicks, J. *Design and Construction Guidelines for Geosynthetic Reinforced Soil Abutments and Integrated Bridge Systems*; FHWA-HRT-17-080; Federal Highway Administration: St Paul, MN, USA, 2018.
9. Gao, W.; Kavazanjian, E.; Wu, X. Numerical Study of Strain Development in High-Density Polyethylene Geomembrane Liner System in Landfills Using a New Constitutive Model for Municipal Solid Waste. *Geotext. Geomembr.* **2022**, *50*, 216–230. [CrossRef]
10. Cen, W.J.; Bauer, E.; Wen, L.S.; Wang, H.; Sun, Y.J. Experimental Investigations and Constitutive Modeling of Cyclic Interface Shearing between HDPE Geomembrane and Sandy Gravel. *Geotext. Geomembr.* **2019**, *47*, 269–279. [CrossRef]
11. Bacas, B.M.; Konietzky, H.; Berini, J.C.; Sagaseta, C. A New Constitutive Model for Textured Geomembrane/Geotextile Interfaces. *Geotext. Geomembr.* **2011**, *29*, 137–148. [CrossRef]
12. Zarnani, S.; Bathurst, R.J. Influence of Constitutive Model on Numerical Simulation of EPS Seismic Buffer Shaking Table Tests. *Geotext. Geomembr.* **2009**, *27*, 308–312. [CrossRef]
13. Ottosen, N.; Ristinmaa, M. *The Mechanics of Constitutive Modeling*; Elsevier Ltd.: Edinburgh, UK, 2005; ISBN 9780080446066.
14. McGown, A.; Khan, A.J.; Kupec, J. The Isochronous Strains Energy Approach Applied to the Load-Strain-Time-Temperature Behaviour of Geosynthetics. *Geosynth. Int.* **2004**, *11*, 114–130. [CrossRef]
15. Shukla, S.K. *An Introduction to Geosynthetic Engineering*; CRC Press: Leiden, The Netherlands, 2016; ISBN 9781138027749.
16. Bathurst, R.J.; Kaliakin, V.N. Review of Numerical Models for Geosynthetics in Reinforcement Applications. In Proceedings of the 11th International Conference of the International Association for Computer Methods and Advances in Geomechanics, Torino, Italy, 19–24 June 2005; Volume 4, pp. 407–416.
17. Yogendrakumar, K.; Bathurst, R.J. Numerical Simulation of Reinforced Soil Structure During Blast Loads. *Transp. Res. Rec.* **1992**, *1336*, 1–8.
18. Ling, H.I.; Tatsuoka, F.; Tateyama, M. Simulating Performance of GRS-RW by Finite-Element Procedure. *J. Geotech. Eng.* **1995**, *121*, 330–340. [CrossRef]
19. Liu, H.; Ling, H.I. Modeling Cyclic Behavior of Geosynthetics Using Mathematical Functions Combined with Masing Rule and Bounding Surface Plasticity. *Geosynth. Int.* **2006**, *13*, 234–245. [CrossRef]
20. Zhou, Z.G.; Li, Y.Z. Creep Properties and Viscoelastic-Plastic-Damaged Constitutive Model of Geogrid. *Chin. J. Geotech. Eng.* **2011**, *33*, 1943–1949.
21. Haimin, W.; Yiming, S.; Linjun, D.; Zhaoming, T. Implementation and Verification of a Geosynthetic-Soil Interface Constitutive Model in the Geogrid Element of FLAC3D. *Acta Geotech. Slov.* **2015**, *12*, 27–35.
22. Paula, A.M.; Pinho-Lopes, M. Constitutive Modelling of Short-Term Tensile Response of Geotextile Subjected to Mechanical and Abrasion Damages. *Int. J. Geosynth. Ground Eng.* **2021**, *7*, 1–11. [CrossRef]
23. Lombardi, G.; Paula, A.M.; Pinho-Lopes, M. Constitutive Models and Statistical Analysis of the Short-Term Tensile Response of Geosynthetics after Damage. *Constr. Build. Mater.* **2022**, *317*, 125972. [CrossRef]
24. Ding, L.; Xiao, C.; Cui, F. Analytical Model for Predicting Time-Dependent Lateral Deformation of Geosynthetics-Reinforced Soil Walls with Modular Block Facing. *J. Rock Mech. Geotech. Eng.* **2023**. [CrossRef]
25. Bathurst, R.J.; Naftchali, F.M. Geosynthetic Reinforcement Stiffness for Analytical and Numerical Modelling of Reinforced Soil Structures. *Geotext. Geomembr.* **2021**, *49*, 921–940. [CrossRef]
26. Ezzein, F.M.; Bathurst, R.J.; Kongkitkul, W. Nonlinear Load–Strain Modeling of Polypropylene Geogrids during Constant Rate-of-Strain Loading. *Polym. Eng. Sci.* **2015**, *55*, 1617–1627. [CrossRef]

27. Greenwood, J.H.; Schroeder, H.F.; Voskamp, W. *Durability of Geosynthetics*; CUR Building & Infrastructure: Gouda, The Netherlands, 2012; ISBN 9789037605334.
28. Allen, T.M.; Bathurst, R.J. Characterization of Geosynthetic Load-Strain Behavior After Installation Damage. *Geosynth. Int.* **1994**, *1*, 181–199. [CrossRef]
29. *ISO 10722*; Geosynthetics—Index Test Procedure for the Evaluation of Mechanical Damage under Repeated Loading—Damage Caused by Granular Material. International Organization for Standardization: Geneva, Switzerland, 2019.
30. Rosete, A.; Mendonça Lopes, P.; Pinho-Lopes, M.; Lopes, M.L. Tensile and Hydraulic Properties of Geosynthetics after Mechanical Damage and Abrasion Laboratory Tests. *Geosynth. Int.* **2013**, *20*, 358–374. [CrossRef]
31. Pinho-Lopes, M.; Lopes, M.L. Synergisms between Laboratory Mechanical and Abrasion Damage on Mechanical and Hydraulic Properties of Geosynthetics. *Transp. Geotech.* **2015**, *4*, 50–63. [CrossRef]
32. Pinho-Lopes, M.; Recker, C.; Lopes, M.L.; Müller-Rochholz, J. Experimental Analysis of the Combined Effect of Installation Damage and Creep of Geosynthetics—New Results. In Proceedings of the 7th International Conference on Geosynthetics, Nice, France, 22–27 September 2002; Volume 4, pp. 1539–1544.
33. *ISO 10319*; Geosynthetics—Wide-Width Tensile Test. International Organization for Standardization: Geneva, Switzerland, 2015.
34. Sheskin, D.J. *Handbook of Parametric and Non Parametric Statistical Procedures*, 3rd ed.; Chapman & Hall/CRC: Boca Raton, FL, USA, 2000; ISBN 9781420036268.
35. Field, A. *Discovering Statistics Using SPSS*, 5th ed.; SAGE Publications Ltd.: London, UK, 2017; ISBN 1847879071/9781847879073.

materials

MDPI

Article

Structural Characteristics and Cementitious Behavior of Magnesium Slag in Comparison with Granulated Blast Furnace Slag

Ping Lu [1,2,3,4], Yueqi Zhao [1,2,3,4], Na Zhang [1,2,3,4,*], Yidi Wang [1,2,3,4], Jiale Zhang [1,2,3,4], Yihe Zhang [1,2,3,4] and Xiaoming Liu [5,*]

1 Engineering Research Center of Ministry of Education for Geological Carbon Storage and Low Carbon Utilization of Resources, China University of Geosciences, Beijing 100083, China
2 Beijing Key Laboratory of Materials Utilization of Nonmetallic Minerals and Solid Wastes, China University of Geosciences, Beijing 100083, China
3 National Laboratory of Mineral Materials, China University of Geosciences, Beijing 100083, China
4 School of Materials Science and Technology, China University of Geosciences, Beijing 100083, China
5 School of Metallurgical and Ecological Engineering, University of Science and Technology Beijing, Beijing 100083, China
* Correspondence: nazhang@cugb.edu.cn (N.Z.); liuxm@ustb.edu.cn (X.L.)

Abstract: Magnesium slag is a type of industrial solid waste produced during the production of magnesium metal. In order to gain a deeper understanding of the structure of magnesium slag, the composition and microstructure of magnesium slag were investigated by using characterization methods such as X-ray fluorescence, particle size analysis, X-ray diffraction, Fourier transform infrared spectroscopy and scanning electron microscopy. In addition, the state of Si occurrence in magnesium slag was analyzed using a solid-state nuclear magnetic resonance technique in comparison with granulated blast furnace slag. An inductively coupled plasma-optical emission spectrometer and scanning electron microscope with energy dispersive X-ray spectroscopy were used to characterize their cementitious behavior. The results show that the chemical composition of magnesium slag mainly includes 54.71% CaO, 28.66% SiO_2 and 11.82% MgO, and the content of Al_2O_3 is much lower than that of granulated blast furnace slag. Compared to granulated blast furnace slag, magnesium slag has a larger relative bridging oxygen number and higher [SiO_4] polymerization degree. The cementitious activity of magnesium slag is lower compared to that of granulated blast furnace slag, but it can replace part of the cement to obtain higher compressive strength. Maximum compressive strength can be obtained when the amount of magnesium slag replacing cement is 20%, where the 28-day compressive strength can be up to 45.48 MPa. This work provides a relatively comprehensive analysis of the structural characteristics and cementitious behavior of magnesium slag, which is conducive to the promotion of magnesium slag utilization.

Keywords: magnesium slag; granulated blast furnace slag; structural characterization; nuclear magnetic resonance; cementitious activity

Citation: Lu, P.; Zhao, Y.; Zhang, N.; Wang, Y.; Zhang, J.; Zhang, Y.; Liu, X. Structural Characteristics and Cementitious Behavior of Magnesium Slag in Comparison with Granulated Blast Furnace Slag. *Materials* **2024**, *17*, 360. https://doi.org/10.3390/ma17020360

Academic Editor: Krzysztof Schabowicz

Received: 29 November 2023
Revised: 28 December 2023
Accepted: 5 January 2024
Published: 11 January 2024

1. Introduction

Magnesium slag is an industrial solid waste generated during the production of magnesium metal. In China, the smelting of magnesium metal via the Pijiang method is the main commercial process for magnesium production [1,2]. More than 6 tons of magnesium slag is produced when smelting 1 ton of magnesium metal on average, and it is accompanied by nearly 30 tons of CO_2 and various types of flue gas emissions [3], which seriously pollute the environment of the area where it is located [4]. At present, there is no complete treatment technology for magnesium slag to enable its industrial utilization, which leads to massive accumulation of magnesium slag in the open air [5]. This not only

takes up considerable land resources and damages the ecological environment, but also poses a threat to human health [6–9]. Like other industrial solid wastes, if magnesium slag can be effectively utilized, this will bring great ecological and economic benefits [10–14], promoting the early realization of China's goal of "carbon peak and carbon neutrality" according to the Paris Agreement.

Magnesium slag mainly contains CaO, SiO_2 and MgO. Due to its high MgO content, expansion behavior occurs during the hydration process [15–17], and for that reason, magnesium slag is not yet used on a large scale in the construction industry. Ji et al. [18] discussed the potential of magnesium slag as a mineral admixture and found that when 30% of magnesium slag was used as a replacement for Portland cement, this was beneficial to improve the late strength of concrete and reduce drying shrinkage. Xie et al. [19] used magnesium slag as an admixture for low-carbon cement, and the prepared samples met the GB 175-2007 [20] "General Portland Cement" standard, which could reduce the production cost by more than 10%. The synthesis of porous materials from magnesium slag can have a good adsorption effect on Pb^{2+} while the materials also have high compressive strength [21]. CO_2 solidified fiber cement boards prepared with magnesium slag as a binder had high flexural strength, carbonation rate and water absorption [22]. Using the "leaching-carbonization" method, magnesium slag can be turned into two value-added products: vaterite with a purity of more than 95% and supplementary cementitious materials [23]. Magnesium slag has limited activity in its normal state, making it difficult to be applied directly. Therefore, scholars use diverse approaches to stimulate its activity and improve applicability. Lei et al. [24] proposed CO_2 activated aerated concrete with a high admixture of magnesium slag, which is capable of achieving rapid carbonation to improve compressive strength, reduce environmental pollution caused by the accumulation of magnesium slag and also facilitate the large-scale utilization of CO_2. When cured in water at 60 °C [25], a magnesium slag product treated with CO_2 activation has good volume stability and does not display excessive expansion. The effect of volumetric instability can be eliminated after carbonation for 2 h. At the same time, carbonation treatment can quickly obtain higher compressive strength, reaching 90 MPa at 24 h [26]. The incorporation of magnesium slag can improve the soil environment by granularizing the soil and providing higher cementitious activity [27–29], and also has a remediation effect on Cd- and As-contaminated paddy soils [30]. Jia et al. [31] investigated the desulfurization characteristics of magnesium slag and achieved a calcium conversion of 30.3% for samples treated with continuous hydration under optimum process parameters. In addition, magnesium slag can be used as a raw material for the preparation of phosphate adsorbents [32], with a maximum adsorption capacity of up to 50.14 mg/g. The Fe_2O_3 content in magnesium slag has a large effect on the phosphorus removal rate, which can also be enhanced after acid treatment [33]. Whilst the desulfurization performance of the original magnesium slag is poor, a calcium conversion rate of up to 73.7% can be reached after mixing with additives or modification [34]. Magnesium slag, like other solid wastes, can also be used for mine filling [5,35,36] or road base material [37–42]. Numerous studies have conducted extensive research into other industrial solid wastes, such as granulated blast furnace slag [43–45], steel slag [46], red mud [47] and so on [48–50], which provide guidance for the utilization of the corresponding tailings and slag. However, there are fewer corresponding studies on the structure and cementitious properties of magnesium slag, which is one of the reasons for its current low utilization. Accordingly, there is an urgent need to study the structural characteristics of magnesium slag and propose avenues to utilize it in an efficient and resourceful way.

This work aimed to study the structural characteristics and cementitious activity of magnesium slag in comparison with those of granulated blast furnace slag using X-ray diffraction (XRD), Fourier transform infrared spectroscopy (FTIR) and ^{29}Si solid-state nuclear magnetic resonance (NMR). The cementitious activity of magnesium slag and granulated blast furnace slag under alkaline conditions were assessed through the dissolution of Si, Al and Mg elements in alkaline solutions. Hydration behavior of magnesium slag

and granulated blast furnace slag was investigated using scanning electron microscopy and energy dispersive X-ray spectrometry (SEM-EDS), and the possibility of their replacement for cement was also discussed. The results of this study may contribute to a deeper understanding of the relationship between the microstructure and cementitious activity of magnesium slag, which will provide basic knowledge for further comprehensive utilization of magnesium slag. Additionally, this work compares the cementitious activity of magnesium slag with that of granulated blast furnace slag for the first time, which is of great reference value to the field of magnesium slag utilization.

2. Experimental Program

Details of the raw materials and related test parameters used in this work are shown below.

2.1. Raw Materials

The magnesium slag used in the experiment was provided by Dongfeng Magnesium Metal Co., Ltd. of Yulin City, Shaanxi Province, China. The 42.5 Portland cement and granulated blast furnace slag were supplied by Henan Yuanheng Environmental Protection Engineering Co., Ltd, Henan, China. The NaOH was sourced from Yili Fine Chemicals Co., Ltd., Beijing, China. The chemical compositions of magnesium slag (MS) and granulated blast furnace slag (GBFS) as determined via X-ray fluorescence spectrometry (XRF) are shown in Table 1.

Table 1. Chemical composition of raw materials.

Chemical Composition (wt%)	CaO	SiO_2	Al_2O_3	MgO	Fe_2O_3	SO_3	TiO_2	Others
MS	54.71	28.66	0.85	11.82	2.87	0.07	0.06	0.96
GBFS	42.76	27.85	15.61	7.78	0.36	2.64	1.20	2.16
Cement	71.52	15.08	3.59	1.81	3.44	3.03	0.43	1.10

2.2. Characterization Methods

2.2.1. Particle Size

The bulk magnesium slag was first crushed by a jaw crusher and then added into a ball mill and ground at 600 rpm for 2 h to obtain magnesium slag powder. The particle size of magnesium slag powder and granulated blast furnace slag powder was tested using a laser particle size analyzer (Bettersize2000, Dandong Baxter Instrument Co., Ltd., Dandong, China), where sodium hexametaphosphate was used as a dispersant.

2.2.2. X-ray Diffraction

The mineralogical components of magnesium slag were analyzed via X-ray powder diffraction (XRD) (Bruker D8 Advance Instrument, Bruker Corporation, Karlsruhe, Germany) using Cu Kα radiation (λ = 1.54056 Å) at 40 kV and 40 mA. The scanning range was 5°~90° and the scanning speed was 5°/min.

2.2.3. Nuclear Magnetic Resonance

In order to obtain more accurate solid-state NMR test results, small amounts of magnetic material were removed from the magnesium slag and granulated blast furnace slag, and then they were tested using an NMR spectrometer(AVANCE III 600M, Bruker Corporation, Karlsruhe, Germany).

2.2.4. Compressive Strength

Initially, 100 g of slag powder was added to a paste mixer, stirred, vibrated and finally poured into molds. After demolding, 20 × 20 × 20 mm paste specimens were obtained, and the compressive strength of specimens at different curing ages was tested using a

microcomputer-controlled electro-hydraulic servo universal testing machine (WAW-2000E, Jinan Kohui Testing Equipment Co., Ltd., Jinan, China).

2.2.5. Inductively Coupled Plasma-Optical Emission Spectrometer

The active element contents (Si, Al, Mg) of magnesium slag and granulated blast furnace slag dissolved in an alkaline environment, were determined using an inductively coupled plasma instrument (ICAP-7000, Thermo Fisher, Waltham, MA, USA). The specific operations were as follows: 1 g of slag powder was added to 50 mL of 1 mol/L NaOH solution, sealed and left to stand for 72 h at room temperature, after which the upper layer of clear liquid was taken following centrifugation for ICP testing.

2.2.6. Scanning Electron Microscope

The above centrifuged liquid was poured out, and anhydrous ethanol was added to terminate the hydration of the solids for 48 h, after which the solids were put into a vacuum drying oven to dry sufficiently for 24 h. The microscopic morphology of the samples was observed and analyzed using an SU 8020 field emission scanning electron microscope (SU 8020, Hitachi Ltd., Tokyo, Japan).

3. Results

3.1. Mineralogical Composition of Magnesium Slag

Figure 1 demonstrates the XRD pattern of magnesium slag. The results show that the main phases of magnesium slag are quartz (SiO_2), larnite (β-Ca_2SiO_4), calcio-olivine (γ-Ca_2SiO_4), calcium silicate (Ca_3SiO_5) and periclase (MgO). Table 2 shows the results of the quantitative XRD analysis of magnesium slag. It was found that magnesium slag contains 58.4 wt% larnite (β-Ca_2SiO_4), 27.1 wt% quartz (SiO_2) and small amounts of Ca_3SiO_5, MgO and γ-Ca_2SiO_4. Compared with γ-Ca_2SiO_4, β-Ca_2SiO_4 has higher cementitious activity, and the high content of β-Ca_2SiO_4 in magnesium slag provides great potential for its application in cementitious materials.

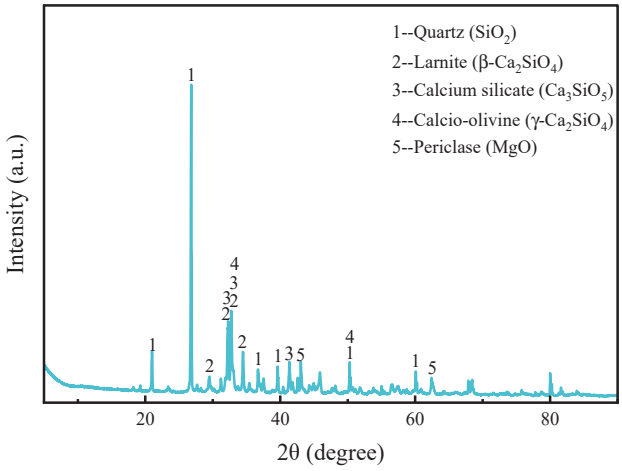

Figure 1. XRD pattern of magnesium slag.

Table 2. Quantitative XRD analysis of magnesium slag.

Mineralogical Composition (wt%)	SiO_2	β-Ca_2SiO_4	γ-Ca_2SiO_4	Ca_3SiO_5	MgO
MS	27.1	58.4	2.6	7.1	4.8

Figure 2 shows the FTIR results of magnesium slag. The main vibrational bands of magnesium slag are at 519 cm^{-1}, 846 cm^{-1}, 895 cm^{-1}, 995 cm^{-1}, 1426 cm^{-1} and 1633 cm^{-1}. Among them, the Mg-O vibrational band is at 519 cm^{-1}, and the stretching vibrational band of Si-O in SiO_2 is at 995 cm^{-1}. The bands at 846 cm^{-1}, 895 cm^{-1} and 1426 cm^{-1} are the vibrational bands of silica–aluminum matter, and the absorption band located at 1633 cm^{-1} is related to the bending vibration of the H-O-H group of bound water.

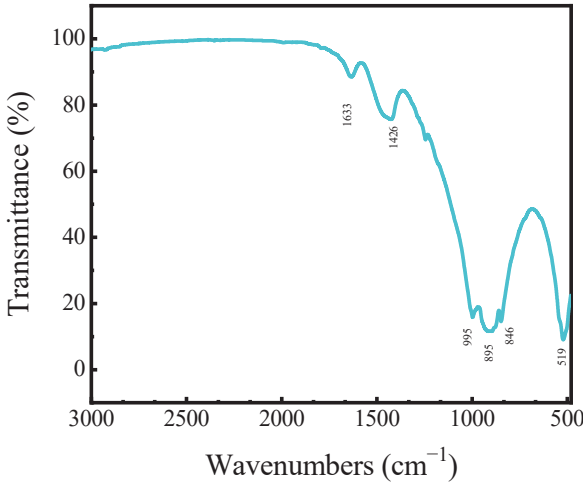

Figure 2. Infrared spectra of magnesium slag.

3.2. [SiO_4] Polymerization Degree of Magnesium Slag and Granulated Blast Furnace Slag

In order to clarify the relationship between the cementitious activity and structure of magnesium slag, solid-state ^{29}Si NMR analysis was performed to further study the [SiO_4] polymerization degree of magnesium slag in comparison with granulated blast furnace slag [51]. Figure 3 shows the NMR spectra of magnesium slag and granulated blast furnace slag. As can be seen from Figure 3, there are two main resonance peaks in the magnesium slag. According to the relationship between their chemical shifts and structures, the resonance peak at about −70 ppm belongs to SiQ^0, and the resonance peak at about −115 ppm belongs to SiQ^4. The resonance peak of granulated blast furnace slag only at about −73 ppm belongs to SiQ^0. This suggests that SiO_4 tetrahedra in magnesium slag exist as nesosilicates and framework silicate [52], which is consistent with the quantitative analysis results of XRD.

Figure 4 shows the split peak fitting results of the two main peaks in the ^{29}Si NMR spectrum of magnesium slag. Five independent resonance peaks were obtained by splitting the two main peaks of magnesium slag using PeakFit software (v4.04), and their areas were calculated separately. The resonance peaks at −66.89 ppm, −70.46 ppm and −73.40 ppm belong to SiQ^0, and the resonance peaks at −112.25 ppm and −115.77 belong to SiQ^4. The results are shown in Table 3. According to the relative bridging oxygen number (RBO) calculation formula [52],

$$RBO = \frac{1}{4}\cdot\frac{\sum n\cdot Q^n}{\sum Q^n} = \frac{1}{4}\left(1\times\frac{Q^1}{\sum Q^n} + 2\times\frac{Q^2}{\sum Q^n} + 3\times\frac{Q^3}{\sum Q^n} + 4\times\frac{Q^4}{\sum Q^n}\right)$$

$$RBO(MS) = \frac{1}{4}\cdot\frac{0\cdot Q^0 + 4\cdot Q^4}{Q^0 + Q^4}$$

it can be calculated that the RBO number of magnesium slag is 0.52. Generally speaking, the greater the relative bridging oxygen number, the higher the [SiO_4] polymerization degree and the lower the cementitious activity of the slag. Granulated blast furnace slag is mainly composed of a SiQ^0 unit with an RBO number of 0. Its [SiO_4] polymerization

degree is lower than that of magnesium slag, so the cementitious activity of granulated blast furnace slag is higher than that of magnesium slag.

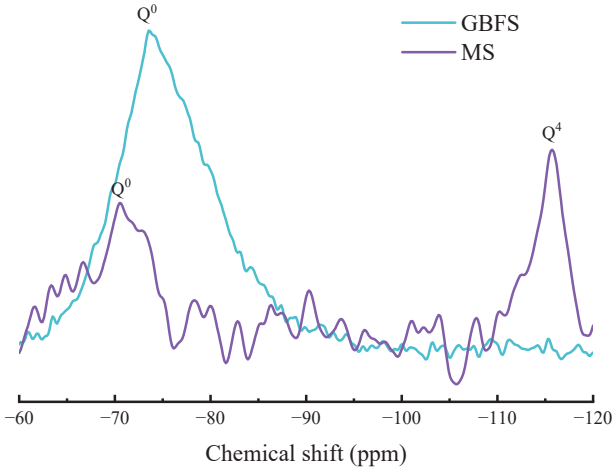

Figure 3. ^{29}Si NMR spectra of magnesium slag and granulated blast furnace slag.

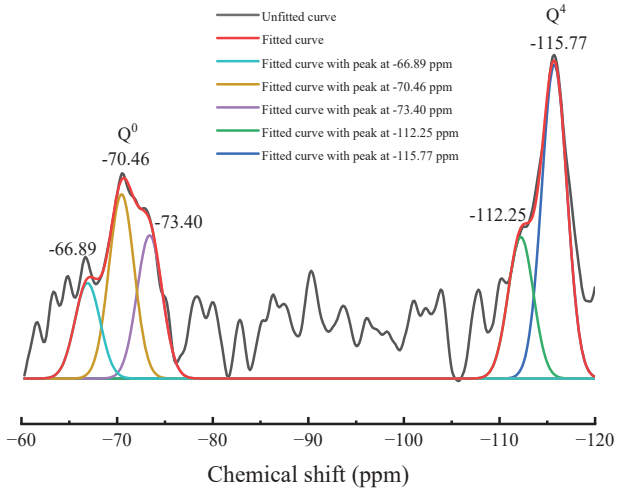

Figure 4. Peak-fitting results of ^{29}Si NMR spectrum of magnesium slag.

Table 3. RBO calculation of magnesium slag.

Structure Units	Q^0	Q^0	Q^0	Q^4	Q^4
Chemical shift (ppm)	−66.89	−70.46	−73.40	−112.25	−115.77
Relative area	30.42	58.74	45.64	45.14	100
Relative content (%)	10.87	20.98	16.30	16.13	35.72

3.3. Alkali-Activated Behavior of Magnesium Slag and Granulated Blast Furnace Slag

The ability of slag powder to release reactive ions SiO_4^{4-} and AlO_2^- in alkaline solution can reflect its cementitious activity [53]. In order to investigate the amount of active ions produced by magnesium slag in alkaline solution, magnesium slag powder and granulated blast furnace slag were activated with NaOH solution to assess any difference in cementitious activity.

The dissolution results shown in Figure 5 demonstrate both magnesium slag and granulated blast furnace slag, in which no magnesium element with cementitious activity is dissolved. Magnesium slag can dissolve a certain amount of Si and Al, while granulated blast furnace slag dissolves more. Combined with Table 1, we can surmise that the SiO_2 content in magnesium slag is slightly higher than that in granulated blast furnace slag. However, the dissolved amount of Si in granulated blast furnace slag is about six times that of magnesium slag. As the content of Al_2O_3 in granulated blast furnace slag is about twenty times higher than that in magnesium slag, the dissolved amount of Al in granulated blast furnace slag is much higher than that of magnesium slag, reaching nearly 30 times more. Figure 6 shows the particle size distribution of magnesium slag and granulated blast furnace slag. It can be found that the particle size of magnesium slag powder is smaller than that of granulated blast furnace slag. In general, a smaller particle size makes it easier for a pozzolanic reaction to occur completely. However, the results of alkali dissolution are the opposite of this. These results indicate that magnesium slag powder has a certain cementitious activity, but this is much lower than that of granulated blast furnace slag.

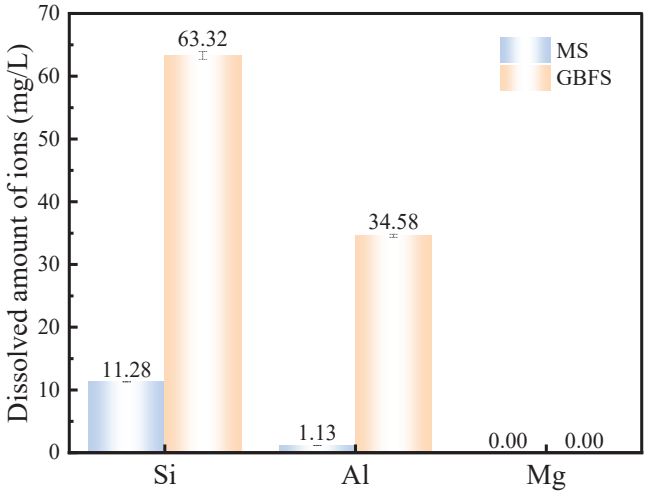

Figure 5. Dissolution content of Si, Al and Mg ions in 1 mol/L NaOH solution for magnesium slag and granulated blast furnace slag.

3.4. Microstructure of Magnesium Slag and Granulated Blast Furnace Slag

Figure 7 shows SEM images of granulated blast furnace slag and magnesium slag samples and the corresponding samples after alkali dissolution. It can be observed that both the granulated blast furnace slag and magnesium slag were in the form of flakes with a relatively smooth surface. After alkali dissolution, the morphology of slags changed from the original flake to an agglomerate, and C-A-S-H gel formed on the surface. The slags before and after alkali dissolution were analyzed using EDS, and the results are shown in Figure 8 and Table 4. The amount of each element in the granulated blast furnace slag and magnesium slag decreased significantly after alkali dissolution, except for O, which indicates that these other elements, after alkali dissolution, are involved in the formation of C-A-S-H gel. It is noted that the consumption of each element of granulated blast furnace slag is much higher than that of magnesium slag, which may indicate that granulated blast furnace slag has higher cementitious activity than magnesium slag. This is consistent with the above ICP analysis results.

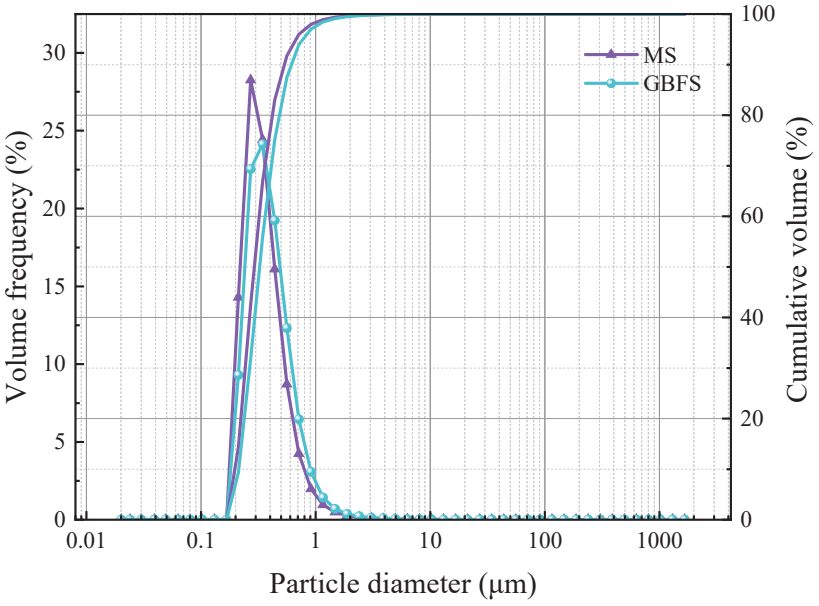

Figure 6. Particle size distribution of magnesium slag and granulated blast furnace slag.

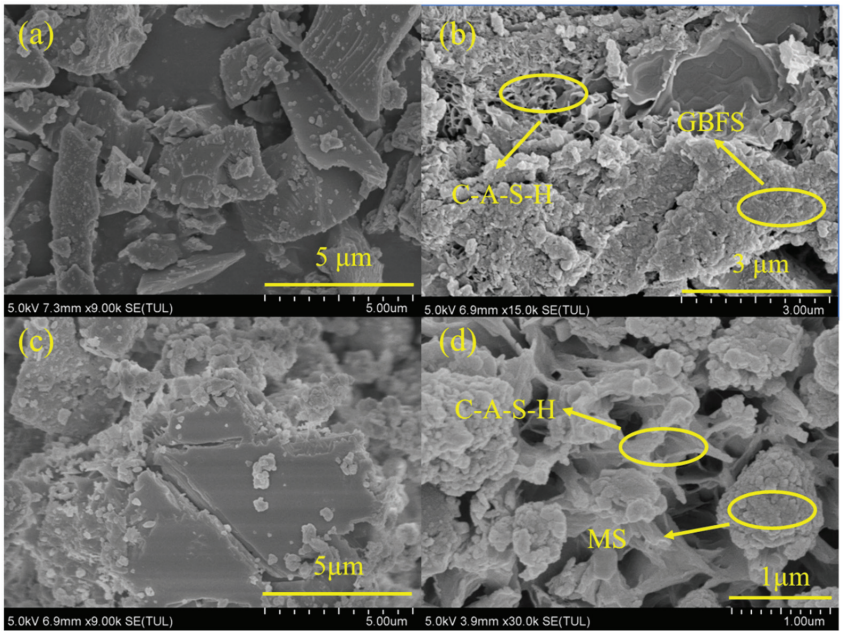

Figure 7. SEM images of GBFS (**a**) and GBFS after alkali dissolution (**b**); SEM images of MS (**c**) and MS after alkali dissolution (**d**).

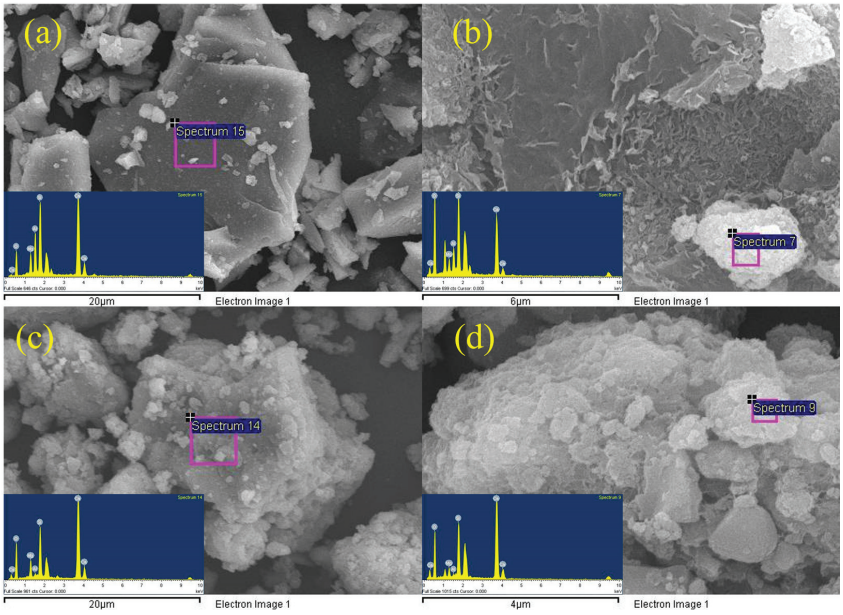

Figure 8. SEM-EDS analysis of GBFS (**a**) and GBFS after alkali dissolution (**b**); SEM-EDS analysis of MS (**c**) and MS after alkali dissolution (**d**).

Table 4. SEM-EDS analysis results.

Sample	O (Atomic%)	Mg (Atomic%)	Al (Atomic%)	Si (Atomic%)	Ca (Atomic%)
a	57.60	4.69	7.26	13.90	16.55
b	77.85	2.17	2.90	9.51	7.57
c	71.64	3.91	0.44	8.39	15.63
d	76.48	1.87	0.22	8.04	13.39

3.5. Magnesium Slag and Granulated Blast Furnace Slag as Replacements for Cement

In order to further confirm cementitious activity, magnesium slag and granulated blast furnace slag were used to replace a part of Portland cement in a paste experiment to compare the feasibility of their uses as a mineral admixture. Figure 9 shows samples of 20 × 20 × 20 mm paste prepared with reference to the literature [54] and standard [55], which were used for compressive strength testing after curing for the corresponding ages. Figures 10 and 11 show the compressive strength of blended cement after partial replacement with magnesium slag and granulated blast furnace slag, respectively. It is beneficial to increase the compressive strength when a small amount of magnesium slag is used to replace the cement. However, the compressive strength of the samples drops below that of pure cement when more than 20% of cement is replaced by magnesium slag. The main reason is that magnesium slag has limited activity in this condition without alkali activation. When the amount of magnesium slag in the system is less than 20%, $Ca(OH)_2$ produced during the hydration process of cement can play a significant role in activating the magnesium slag, so that the magnesium slag can better participate in the hydration process [56]. As a result, magnesium slag can be used to replace part of the cement within a 20% dosage whilst the compressive strength can also be improved. However, when the amount of magnesium slag continues to increase, the amount of $Ca(OH)_2$ produced through cement hydration decreases, resulting in a decrease in alkali concentration in the hydrated system, and thus the activity of magnesium slag is not well-activated. Therefore, the

compressive strength declines with increasing amounts of magnesium slag exceeding 20% addition. As shown in Figure 10, a similar phenomenon is observed when using granulated blast furnace slag to replace part of the cement. When the amount of replacement exceeds 20%, the 28-day compressive strength of the granulated blast furnace slag–cement samples gradually decreases with an increase in granulated blast furnace slag dosage. However, the compressive strength is still higher than that of the pure cement when a 50% dosage of granulated blast furnace slag is used for the replacement of cement, strongly indicating that granulated blast furnace slag is a valuable mineral admixture in cement and concrete. Moreover, due to the higher alkali activity of granulated blast furnace slag than that of the magnesium slag, it is found that the compressive strength of the granulated blast furnace slag–cement system is higher than that of the magnesium slag–cement group at the same replacement amount. These results suggest that although the cementitious activity of magnesium slag is lower than that of granulated blast furnace slag, magnesium slag can still be used as a mineral admixture for replacing a 20% amount of cement in blended cementitious materials.

Figure 9. Samples for compressive strength test.

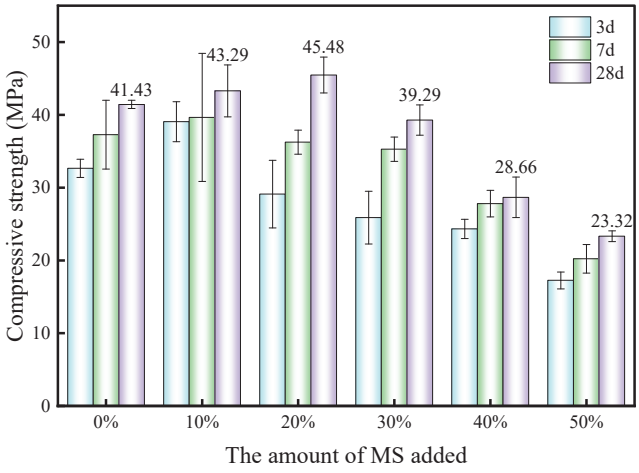

Figure 10. Compressive strengths of samples with different replacement amounts of magnesium slag.

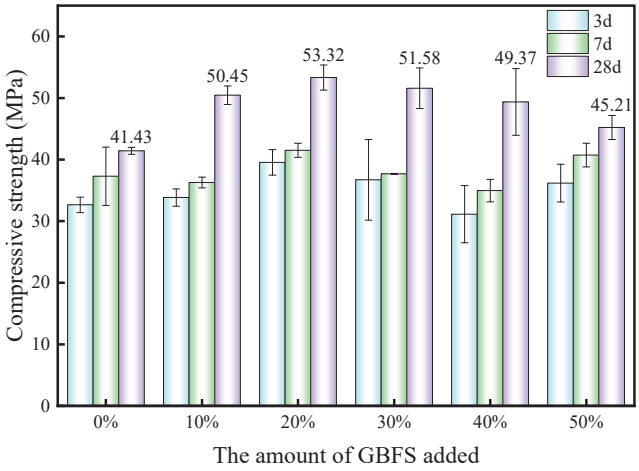

Figure 11. Compressive strengths of samples with different replacement amounts of granulated blast furnace slag.

Various methods exist to assess the cementitious activity of solid waste, such as conductivity tests, compressive strength tests, lime absorption methods and alkali dissolution methods [57–60]. Scholars have used these methods to scientifically evaluate the cementitious activity of granulated blast furnace slag [43], steel slag [46], red mud [47] and other tailings [61], but the link between the results has not been well-identified. This work investigated the structural properties and cementitious behavior of magnesium slag and granulated blast furnace slag by using NMR, compressive strength tests and alkali dissolution methods. A difference in activity between magnesium slag and granulated blast furnace slag was demonstrated in the results. These provide a reference for magnesium slag utilization as well as assessment of the cementitious activity of other tailings.

4. Conclusions

This work principally investigated the structural characteristics of magnesium slag and studied its cementitious properties in comparison with granulated blast furnace slag. The main conclusions drawn are as follows:

(1) The chemical composition of magnesium slag is mainly CaO, SiO_2, Al_2O_3, MgO and Fe_2O_3. Its main components are similar to those of granulated blast furnace slag, but it contains more MgO and less Al_2O_3 than granulated blast furnace slag. The main mineral compositions of magnesium slag are 27.1% quartz, 58.4% larnite, 7.1% calcium silicate, 4.8% periclase and 2.6% calcio-olivine.

(2) The Si in magnesium slag is mainly in the form of Q^0 and Q^4 units, which have a large relative bridging oxygen number and high [SiO_4] polymerization degree, resulting in relatively poor cementitious activity. The Si in granulated blast furnace slag is mainly in the form of Q^0 units, and the relative bridging oxygen number is close to 0. Compared with magnesium slag, the degree of [SiO_4] polymerization is lower and the cementitious activity is higher for granulated blast furnace slag. After alkali excitation, the cementitious activity of magnesium slag can be reflected, and through this approach, we found that its cementitious activity is significantly lower than that of granulated blast furnace slag.

(3) Both magnesium slag and granulated blast furnace slag can be used as mineral admixtures to replace part of cement. Higher compressive strength can be obtained after replacing cement with a small amount of magnesium slag, and the optimum replacement amount is 20%. With further increase of the replacement amount, the

compressive strength decreases, and when it exceeds 30%, the compressive strength of magnesium slag–cement samples is lower than that of pure cement.

(4) Magnesium slag has the potential to be utilized as a mineral admixture for cement, but attention should be paid to the amount of magnesium slag added, activity excitation and the expansion of magnesium hydrate products during its application in cement and concrete production. Elimination of the expansion effect caused by f-MgO in magnesium slag is an important topic for our future work.

Author Contributions: Conceptualization, Y.Z. (Yihe Zhang); data curation, P.L., N.Z., Y.W. and J.Z.; formal analysis, P.L. and Y.Z. (Yueqi Zhao); investigation, P.L., Y.Z. (Yueqi Zhao), Y.W. and J.Z.; resources, Y.Z. (Yihe Zhang) and X.L.; supervision, N.Z. and X.L.; validation, N.Z. and X.L.; writing—original draft, P.L.; writing—review and editing, N.Z. and X.L. All authors have read and agreed to the published version of the manuscript.

Funding: This research was funded by the National Natural Science Foundation of China (no. 52174388).

Institutional Review Board Statement: Not applicable.

Informed Consent Statement: Not applicable.

Data Availability Statement: Data are contained within the article.

Conflicts of Interest: The authors declare no conflicts of interest.

References

1. Abedini Najafabadi, H.; Ozalp, N.; Epstein, M.; Davis, R. Solar Carbothermic Reduction of Dolomite: Direct Method for Production of Magnesium and Calcium. *Ind. Eng. Chem. Res.* **2020**, *59*, 14717–14728. [CrossRef]
2. Telgerafchi, A.E.; Rutherford, M.; Espinosa, G.; McArthur, D.; Masse, N.; Perrin, B.; Tang, Z.; Powell, A.C. Magnesium Production by Molten Salt Electrolysis with Liquid Tin Cathode and Multiple Effect Distillation. *Front. Chem.* **2023**, *11*, 1192202. [CrossRef] [PubMed]
3. Tian, Y.; Wang, L.; Yang, B.; Dai, Y.; Xu, B.; Wang, F.; Xiong, N. Comparative Evaluation of Energy and Resource Consumption for Vacuum Carbothermal Reduction and Pidgeon Process Used in Magnesium Production. *J. Magnes. Alloys* **2022**, *10*, 697–706. [CrossRef]
4. Djokic, J.; Minic, D.; Kamberovic, Z.; Petkovic, D. Impact Analysis of Airborn Pollution Due to Magnesium Slag Deposit and Climatic Changes Condition. *Ecol. Chem. Eng. S* **2012**, *19*, 439–450. [CrossRef]
5. Ruan, S.; Liu, L.; Zhu, M.; Shao, C.; Xie, L. Development and Field Application of a Modified Magnesium Slag-Based Mine Filling Cementitious Material. *J. Clean. Prod.* **2023**, *419*, 138269. [CrossRef]
6. Webber, M.E.; Glazer, Y.R. Solid Waste, a Lever for Decarbonization. *Science* **2023**, *382*, 762–763. [CrossRef]
7. Mishra, R.; Singh, E.; Kumar, A.; Ghosh, A.; Lo, S.-L.; Kumar, S. Co-Gasification of Solid Waste and Its Impact on Final Product Yields. *J. Clean. Prod.* **2022**, *374*, 133989. [CrossRef]
8. Doorga, J.R.S.; Rughooputh, S.D.D.V.; Chung, S.Y.; McGivern, A. A Geospatial Approach for Addressing Long-Term Solid Waste Management Issues: Extracting Value from Waste. *J. Clean. Prod.* **2022**, *334*, 130282. [CrossRef]
9. Khan, H.; Baig, A.; Faisal, M.; Khan, A.; Gul, K.; Ali, N.; Ali, N.; Bilal, M. Exploration of Solid Waste Materials for Sustainable Manufacturing of Cementitious Composites. *Environ. Sci. Pollut. Res.* **2022**, *29*, 86606–86615. [CrossRef]
10. Nedunuri, A.S.S.S.; Muhammad, S. Fundamental Understanding of the Setting Behaviour of the Alkali Activated Binders Based on Ground Granulated Blast Furnace Slag and Fly Ash. *Constr. Build. Mater.* **2021**, *291*, 123243. [CrossRef]
11. Zakira, U.; Zheng, K.; Xie, N.; Birgisson, B. Development of High-Strength Geopolymers from Red Mud and Blast Furnace Slag. *J. Clean. Prod.* **2023**, *383*, 135439. [CrossRef]
12. Baalamurugan, J.; Kumar, V.G.; Padmapriya, R.; Raja, V.K.B. Recent Applications of Steel Slag in Construction Industry. *Environ. Dev. Sustain.* **2023**. [CrossRef]
13. Schatzmayr Welp Sá, T.; Oda, S.; Karla Castelo Branco Louback Machado Balthar, V.; Dias Toledo Filho, R. Use of Iron Ore Tailings and Sediments on Pavement Structure. *Constr. Build. Mater.* **2022**, *342*, 128072. [CrossRef]
14. Oprčkal, P.; Mladenovič, A.; Zupančič, N.; Ščančar, J.; Milačič, R.; Zalar Serjun, V. Remediation of Contaminated Soil by Red Mud and Paper Ash. *J. Clean. Prod.* **2020**, *256*, 120440. [CrossRef]
15. Nugmanova, A.; Shon, C.-S.; Kim, J.R.; Rossi, C.O. Characterizing Chronologically Aged Basic Oxygen Furnace Slags as Aggregates and Their Use in Asphalt Concrete Mix as Filler. *Appl. Sci.* **2023**, *13*, 10126. [CrossRef]
16. Imashuku, S.; Tsuneda, H.; Wagatsuma, K. Effects of Divalent-Cation Iron and Manganese Oxides on the Luminescence of Free Lime and Free Magnesia. *Spectrochim. Acta Part A Mol. Biomol. Spectrosc.* **2020**, *229*, 117952. [CrossRef]

17. Imashuku, S.; Wagatsuma, K. Scanning Electron Microscopy-Cathodoluminescence Imaging of Industrial Steelmaking Slag for Identifying and Determining the Free Magnesia Content. *Met. Mater Trans B* **2022**, *53*, 3459–3468. [CrossRef]
18. Ji, G.; Peng, X.; Wang, S.; Hu, C.; Ran, P.; Sun, K.; Zeng, L. Influence of Magnesium Slag as a Mineral Admixture on the Performance of Concrete. *Constr. Build. Mater.* **2021**, *295*, 123619. [CrossRef]
19. Xie, G.; Liu, L.; Suo, Y.; Zhu, M.; Yang, P.; Sun, W. High-Value Utilization of Modified Magnesium Slag Solid Waste and Its Application as a Low-Carbon Cement Admixture. *J. Environ. Manag.* **2024**, *349*, 119551. [CrossRef]
20. *GB 175-2007*; General Portland Cement. Chinese Standard Press: Beijing, China, 2007.
21. Lu, G.; Han, J.; Chen, Y.; Xue, H.; Qiu, R.; Zhou, X.; Ma, Z. Synthesis of Porous Materials Using Magnesium Slag and Their Adsorption Performance for Lead Ions in Aqueous Solution. *Materials* **2023**, *16*, 7083. [CrossRef]
22. Xie, D.; Zhang, Z.; Liu, Z.; Wang, F.; Hu, S.; Fu, J. Utilization of Magnesium Slag to Prepare CO_2 Solidified Fiber Cement Board. *Constr. Build. Mater.* **2024**, *411*, 134345. [CrossRef]
23. Lu, B.; Zhou, Y.; Jiang, L.; Liu, Z.; Hou, G. High-Purity Vaterite $CaCO_3$ Recovery through Wet Carbonation of Magnesium Slag and Leaching Residue Utilization in Cement. *Cem. Concr. Compos.* **2024**, *145*, 105353. [CrossRef]
24. Lei, M.; Deng, S.; Huang, K.; Liu, Z.; Wang, F.; Hu, S. Preparation and Characterization of a CO_2 Activated Aerated Concrete with Magnesium Slag as Carbonatable Binder. *Constr. Build. Mater.* **2022**, *353*, 129112. [CrossRef]
25. Mo, L.; Hao, Y.; Liu, Y.; Wang, F.; Deng, M. Preparation of Calcium Carbonate Binders via CO_2 Activation of Magnesium Slag. *Cem. Concr. Res.* **2019**, *121*, 81–90. [CrossRef]
26. Zhang, C.; Liu, S.; Tang, P.; Guan, X.; Shi, C. Enhancing the Hardening Properties and Microstructure of Magnesium Slag Blocks by Carbonation-Hydration Sequential Curing. *J. Build. Eng.* **2023**, *76*, 107414. [CrossRef]
27. Amini, O.; Ghasemi, M. Laboratory Study of the Effects of Using Magnesium Slag on the Geotechnical Properties of Cement Stabilized Soil. *Constr. Build. Mater.* **2019**, *223*, 409–420. [CrossRef]
28. Omid, A.; Mojtaba, G. Geotechnical Properties of Lime-Magnesium Slag Stabilized Clayey Sand: Experimental Study. *Arab. J. Sci. Eng.* **2022**, *47*, 13673–13685. [CrossRef]
29. Sipahutar, I.A.; Siregar, A.F.; Anggria, L. Husnain Magnesium and Silicon Fertilizer Application to Promote Rice Growth and Production. *IOP Conf. Ser. Earth Environ. Sci.* **2021**, *648*, 012064. [CrossRef]
30. Zhang, Y.; Tan, X.; Duan, G.; Cui, J.; Ren, M.; Cao, J.; Xu, C.; Yang, W.; Lin, A. Magnesium Slag for Remediation of Cadmium- and Arsenic-contaminated Paddy Soil: A Field Study. *Soil Use Manag.* **2022**, *38*, 1470–1480. [CrossRef]
31. Jia, L.; Fan, B.; Huo, R.; Li, B.; Yao, Y.; Han, F.; Qiao, X.; Jin, Y. Study on Quenching Hydration Reaction Kinetics and Desulfurization Characteristics of Magnesium Slag. *J. Clean. Prod.* **2018**, *190*, 12–23. [CrossRef]
32. Yang, B.; Han, F.; Li, Y.; Bai, Y.; Xie, Z.; Yang, J.; Liu, T. Phosphate Removal Mechanism of a Novel Magnesium Slag-Modified Coal Gasification Coarse Slag Adsorbent. *Environ. Sci. Pollut. Res.* **2023**, *30*, 60607–60617. [CrossRef] [PubMed]
33. Tang, X.; Li, R.; Wu, M.; Dong, L.; Wang, Z. Enhanced Phosphorus Removal Using Acid-Treated Magnesium Slag Particles. *Environ. Sci. Pollut. Res.* **2018**, *25*, 3860–3871. [CrossRef] [PubMed]
34. Fan, B.; Jia, L.; Li, B.; Huo, R.; Yao, Y.; Han, F.; Qiao, X.; Jin, Y. Study on Desulfurization Performances of Magnesium Slag with Different Hydration Modification. *J. Mater. Cycles. Waste Manag.* **2018**, *20*, 1771–1780. [CrossRef]
35. Akkaya, U.G.; Cinku, K.; Yilmaz, E. Characterization of Strength and Quality of Cemented Mine Backfill Made up of Lead-Zinc Processing Tailings. *Front. Mater.* **2021**, *8*, 740116. [CrossRef]
36. Sari, M.; Yilmaz, E.; Kasap, T.; Guner, N.U. Strength and Microstructure Evolution in Cemented Mine Backfill with Low and High pH Pyritic Tailings: Effect of Mineral Admixtures. *Constr. Build. Mater.* **2022**, *328*, 127109. [CrossRef]
37. Ramalakshmi, D.; Krishna, S.H. Study On Fly Ash as a Partial Replacement Material in Highway Embankment. *IOP Conf. Ser. Mater. Sci. Eng.* **2020**, *981*, 042094. [CrossRef]
38. Weiksnar, K.D.; Townsend, T.G. Enhancing the Chemical Performance of Phosphogypsum as a Road Base Material by Blending with Common Aggregates. *Resour. Conserv. Recycl.* **2024**, *200*, 107300. [CrossRef]
39. Al-Dossary, A.A.S.; Awed, A.M.; Gabr, A.R.; Fattah, M.Y.; El-Badawy, S.M. Performance Enhancement of Road Base Material Using Calcium Carbide Residue and Sulfonic Acid Dilution as a Geopolymer Stabilizer. *Constr. Build. Mater.* **2023**, *364*, 129959. [CrossRef]
40. Weiksnar, K.D.; Clavier, K.A.; Laux, S.J.; Townsend, T.G. Influence of Trace Chemical Constituents in Phosphogypsum for Road Base Applications: A Review. *Resour. Conserv. Recycl.* **2023**, *199*, 107237. [CrossRef]
41. Sofri, L.A.; Abdullah, M.M.A.B.; Sandu, A.V.; Imjai, T.; Vizureanu, P.; Hasan, M.R.M.; Almadani, M.; Aziz, I.H.A.; Rahman, F.A. Mechanical Performance of Fly Ash Based Geopolymer (FAG) as Road Base Stabilizer. *Materials* **2022**, *15*, 7242. [CrossRef]
42. Alzhanova, G.Z.; Aibuldinov, Y.K.; Iskakova, Z.B.; Khabidolda, S.M.; Abdiyussupov, G.G.; Omirzak, M.T.; Murali, G.; Vatin, N.I. Development of Environmentally Clean Construction Materials Using Industrial Waste. *Materials* **2022**, *15*, 5726. [CrossRef]
43. Schneider, J.; Cincotto, M.A.; Panepucci, H. 29Si and 27Al High-Resolution NMR Characterization of Calcium Silicate Hydrate Phases in Activated Blast-Furnace Slag Pastes. *Cem. Concr. Res.* **2001**, *31*, 993–1001. [CrossRef]
44. Puertas, F.; Fernández-Jiménez, A.; Blanco-Varela, M.T. Pore Solution in Alkali-Activated Slag Cement Pastes. Relation to the Composition and Structure of Calcium Silicate Hydrate. *Cem. Concr. Res.* **2004**, *34*, 139–148. [CrossRef]
45. Metlenkin, D.A.; Kiselev, N.V.; Platov, Y.T.; Khaidarov, B.B.; Khaidarov, T.B.; Kolesnikov, E.A.; Kuznetsov, D.V.; Gorokhovsky, A.V.; Offor, P.O.; Burmistrov, I.N. Identification of the Elemental Composition of Granulated Blast Furnace Slag by FTIR-Spectroscopy and Chemometrics. *Processes* **2022**, *10*, 2166. [CrossRef]

46. Zhang, N.; Wu, L.; Liu, X.; Zhang, Y. Structural Characteristics and Cementitious Behavior of Basic Oxygen Furnace Slag Mud and Electric Arc Furnace Slag. *Constr. Build. Mater.* **2019**, *219*, 11–18. [CrossRef]
47. Liu, X.; Zhang, N.; Sun, H.; Zhang, J.; Li, L. Structural Investigation Relating to the Cementitious Activity of Bauxite Residue—Red Mud. *Cem. Concr. Res.* **2011**, *41*, 847–853. [CrossRef]
48. Richardson, I.G.; Brough, A.R.; Brydson, R.; Groves, G.W.; Dobson, C.M. Location of Aluminum in Substituted Calcium Silicate Hydrate (C-S-H) Gels as Determined by 29Si and 27Al NMR and EELS. *J. Am. Ceram. Soc.* **1993**, *76*, 2285–2288. [CrossRef]
49. Bediako, M.; Kevern, J.T.; Dodoo-Arhin, D. Co-Fired Ghanaian Clay-Palm Kernel Shells Pozzolan: Thermogravimetric, 29Si and 27Al MA NMR Characteristics. *Constr. Build. Mater.* **2017**, *153*, 430–435. [CrossRef]
50. Berenguer, R.; Lima, N.; Pinto, L.; Monteiro, E.; Povoas, Y.; Oliveira, R.; Lima, N.B.D. Cement-Based Materials: Pozzolanic Activities of Mineral Additions Are Compromised by the Presence of Reactive Oxides. *J. Build. Eng.* **2021**, *41*, 102358. [CrossRef]
51. Qoku, E.; Bier, T.A.; Schmidt, G.; Skibsted, J. Impact of Sulphate Source on the Hydration of Ternary Pastes of Portland Cement, Calcium Aluminate Cement and Calcium Sulphate. *Cem. Concr. Compos.* **2022**, *131*, 104502. [CrossRef]
52. Zhang, J.; Sun, H.; Sun, Y.; Zhang, N. Correlation between 29Si Polymerization and Cementitious Activity of Coal Gangue. *J. Zhejiang Univ. Sci. A* **2009**, *10*, 1334–1340. [CrossRef]
53. Liu, X.; Liu, X.; Zhang, Z.; Wei, C.; Zeng, Q.; Li, Y.; Ma, S. Investigation of the Pozzolanic Activity Improvement of Yellow Phosphorus Slag with Thermal Activation. *Materials* **2023**, *16*, 6047. [CrossRef] [PubMed]
54. Meng, T.; Hong, Y.; Ying, K.; Wang, Z. Comparison of Technical Properties of Cement Pastes with Different Activated Recycled Powder from Construction and Demolition Waste. *Cem. Concr. Compos.* **2021**, *120*, 104065. [CrossRef]
55. *GB/T50081*; Standard for Test Method of Mechanical Properties on Ordinary Concrete. China National Standards: Beijing, China, 2002.
56. De Matos, P.R.; Andrade Neto, J.S.; Jansen, D.; De La Torre, A.G.; Kirchheim, A.P.; Campos, C.E.M. In-Situ Laboratory X-Ray Diffraction Applied to Assess Cement Hydration. *Cem. Concr. Res.* **2022**, *162*, 106988. [CrossRef]
57. Amar, M.; Benzerzour, M.; Abriak, N.-E.; Mamindy-Pajany, Y. Study of the Pozzolanic Activity of a Dredged Sediment from Dunkirk Harbour. *Powder Technol.* **2017**, *320*, 748–764. [CrossRef]
58. Martín, C.M.; Scarponi, N.B.; Villagrán, Y.A.; Manzanal, D.G.; Piqué, T.M. Pozzolanic Activity Quantification of Hollow Glass Microspheres. *Cem. Concr. Compos.* **2021**, *118*, 103981. [CrossRef]
59. Lorena Figueiredo Martins, M.; Roberto Ribeiro Soares Junior, P.; Henrique Da Silva, T.; De Souza Maciel, P.; Peixoto Pinheiro, I.; Cesar Da Silva Bezerra, A. Magnesium Industry Waste and Red Mud to Eco-Friendly Ternary Binder: Producing More Sustainable Cementitious Materials. *Constr. Build. Mater.* **2021**, *310*, 125172. [CrossRef]
60. Martins Torres, S.; Estolano de Lima, V.; de Azevedo Basto, P.; de Araújo Júnior, N.T.; de Melo Neto, A.A. Assessing the Pozzolanic Activity of Sugarcane Bagasse Ash Using X-Ray Diffraction. *Constr. Build. Mater.* **2020**, *264*, 120684. [CrossRef]
61. Rahman, S.A.; Dodd, A.; Khair, S.; Shaikh, F.U.A.; Sarker, P.K.; Hosan, A. Assessment of Lithium Slag as a Supplementary Cementitious Material: Pozzolanic Activity and Microstructure Development. *Cem. Concr. Compos.* **2023**, *143*, 105262. [CrossRef]

materials

MDPI

Article

Stiffness of Experimentally Tested Horizontally Loaded Walls and Timber-Framed Modular Building

Czesław Miedziałowski [1], Krzysztof Robert Czech [1,*], Marta Nazarczuk [2], Marta Kosior-Kazberuk [1] and Anna Żakowicz [1]

[1] Department of Building Structures and Structural Mechanics, Faculty of Civil Engineering and Environmental Sciences, Bialystok University of Technology, Wiejska 45E, 15-351 Bialystok, Poland; c.miedzialowski@pb.edu.pl (C.M.); m.kosior@pb.edu.pl (M.K.-K.); a.zakowicz@pb.edu.pl (A.Ż.)
[2] Unihouse SA, Rejonowa 5, 17-100 Bielsk Podlaski, Poland; mnazarczuk@unihouse.pl
* Correspondence: k.czech@pb.edu.pl

Abstract: This paper presents an overview of representative up-to-date research and the authors' own experimental results from tests of wall elements and a horizontally loaded timber-framed modular building. The research has been conducted in connection with the development of timber-based structures in recent years. In the present research, wall elements and modules of timber-frame construction with life-size dimensions were used. So far, these types of structures have mainly been tested in laboratories—especially with regard to anchoring and cyclic loading. An experimental testing was carried out on a natural scale in two stages based on the standard procedure described in EN 594. In the first stage, wall panels were tested. In the second stage, tests were carried out on a complete four-storey building. Dowel fasteners were used to fix the sheathing to the load-bearing wall structures. Additionally, the sheathing was glued to the timber frame of the walls. The same type of wall element was used for the construction of the tested building. Horizontal loads were applied at the height of the top of the walls in both stages. The building loads were applied in a direction perpendicular to the longitudinal axis of the modules. Based on test data, the stiffnesses of the wall panels and the whole building were derived, as well as the type of interaction between the modules and the influence of the walls on the spatial work of the building. On the basis of the conducted studies, both the stiffness of the walls in different configurations and the stiffness of the complete building were determined, as well as the nature of the interaction of neighbouring modules and the influence of wall connections on the 3D working of the building. The results show that the stiffness of the building in the horizontal plane in the direction of the applied load is almost twice as high as the sum of the stiffnesses of the building walls in the same direction.

Keywords: shear walls; spatial modules; modular building; wall stiffness; building stiffness

Citation: Miedziałowski, C.; Czech, K.R.; Nazarczuk, M.; Kosior-Kazberuk, M.; Żakowicz, A. Stiffness of Experimentally Tested Horizontally Loaded Walls and Timber-Framed Modular Building. *Materials* **2023**, *16*, 6229. https://doi.org/10.3390/ma16186229

Academic Editor: Francesca Ceroni

Received: 11 August 2023
Revised: 9 September 2023
Accepted: 11 September 2023
Published: 15 September 2023

1. Introduction

Timber-based construction is considered to be very ecological and beneficial in the current period of socio-economic development. Among the many types of timber-based construction, one of the latest trends are modular buildings. Their history dates back to the 1950s. The prototype of this type of construction was mobile transport containers. Today, timber modular buildings are made as spatial large-scale structures consisting of floor, walls and ceiling panels [1–3]. Mostly, such elements are manufactured in the factory, with external and internal surface finishes, fitted carpentry, complete sanitary and electrical installations, and even utility fittings for kitchen and bathroom modules. Modules can be of timber frame or plate structure, i.e., CLT (cross-laminated timber) [1,4,5]. The dimensions of modular elements depend on the size of the building and the transport gauge of transport routes. An example of a spatial module during its prefabrication in the factory and the assembly of modules on the construction site is shown in Figure 1.

(**a**) (**b**)

Figure 1. Example of realisation of a multi-storey building from modular elements: (**a**) prefabrication of modules in a factory and (**b**) assembly of a building from modular elements on a construction site.

One of the requirements for the exploitation of this type of building is its stiffness, especially for horizontal loads, which largely depend on the inter-module connections [6,7]. An example of the location of such inter-module connections is shown in Figure 2.

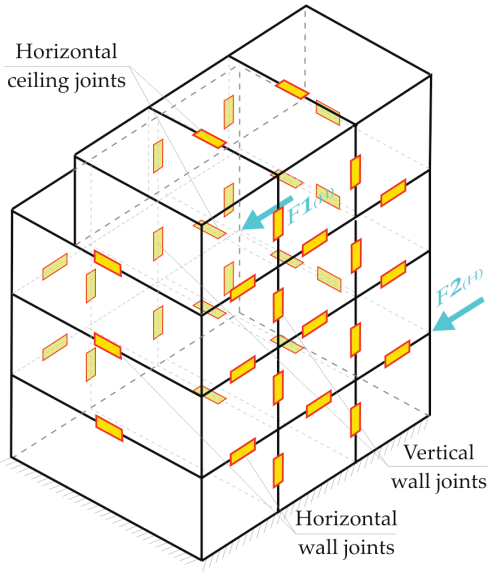

Figure 2. Types of inter-module connections in the building and the considered direction of interaction of the elements.

Buildings and their individual components are spatial structures and work in 3D static schemes. The computational and design models should also consider the 3D working of the structure. The difficulty is that these are complex systems—that is, structures made up of many different elements (columns, beams, sheathing, connectors in the elements and connections between elements). Computational models should therefore be compulsorily validated by experimental studies.

There are relatively few published experimental studies on the spatial work of buildings. Considerably more research has been caried on wall elements.

Comprehensive experimental research on walls was conducted by Kamiya F. [8], Stewart A.H. et al. [9], Sugyiama H. et al. [10] and Baszeń M. et al. [11], among others.

Recently, numerical analyses as well as experimental studies of walls with openings were carried out by Kuai L. [12].

In the studies of Martin Z.A. et al. [13], Šilih E.K. and Premrov M. [14], more attention has been paid to the study of wall elements with openings.

Parallel to experimental research on walls, studies of timber frame and sheathing connectors were conducted. In 1949, in the USA, regulations were introduced to allow the use of sheathing other than timber cladding [15].

A broad review of the literature related to the testing of walls both with and without openings was caried out in a paper by Miedzialowski Cz. and Malesza M. [16]. At present, the guidelines of the EN 594 standard of July 2011 [17] apply to testing of stiffness and load-bearing capacity of wall panels.

The first comprehensive testing of buildings started with structures erected traditionally, i.e., from linear elements. This type of research was carried out by Tuomi R.L. and McCutheon J. [18], Boughton G.N. and Reardon G.F. [19] and Boughton G.N. et al. [20], among others.

The subject of the studies by Collins et al. [21] and Malesza et al. [22] were single-family prefabricated panel buildings.

Prefabricated timber-frame modules were the object of research and numerical analyses by Smith J. et al. [23]. Experimental and numerical studies of timber-frame modules have also been carried out by Ormarsson S. et al. [24,25]. The horizontal arrangement of two modules was studied by Montaño et al. [26]. The advantages and limitations associated with modular construction of multi-family buildings are described in the work of Cameron P.J. JR and Di Carlo N.G. [1].

Popovski M. et al. [27] conducted a study of a two-storey CLT modular building. Three-storey and seven-storey buildings, also made of CLT, were the subject of laboratory tests (mainly under cyclic loading conditions) carried out by Ceccotti A. et al. [28,29]. Building tests were also analysed in the work of Li et al. [7].

An extensive review of studies of various modular building structures was performed by Lacey et al. [30].

Most recently, Cowled C. J. L. et al. [31] tested timber-frame shear walls with additional gypsum boards under monotonic loading, similarly to Valdivieso et al. [32] where they also performed cyclic loading tests. Kuai L. et al. [33] developed elasto-plastic model of timber-frame shear walls with openings and validated it by testing it under cyclic loading. Abrahamsen R. et al. [34] participated in Dyna TTB project that focused on an identification of mechanical properties of tall timber buildings by performing dynamic tests on existing objects. Amaddeo C. and Dorn M. [35] tested a timber-frame building against vibrations. As can be seen from the literature review, there is a lack of research results for modular timber-frame buildings. The paper will present both the tests of timber-frame walls, with I-joists timber studs and OSB sheathing (connected to the studs with staples and additionally glued to the timber-frame structure), and tests of a complete modular building made of the above-described frame walls. As a result of the conducted analyses, the stiffness of the walls and the building will be determined under the conditions of horizontal force applied at the top of the walls in the direction perpendicular to the length of the modules.

The study will also analyse the effect of openings in the walls and the location of particular wall types on the final stiffness of the building. The influence of module connections on the spatial behaviour of the building will also be analysed. The conclusions will indicate the possibilities of practical use of the results of the conducted research.

The aim of this paper is therefore to supplement the study of timber-frame modular buildings and to obtain experimental data to validate the numerical models. The research hypothesises that the stiffness of the building is significantly influenced by the connections between modules, the arrangement of load-bearing walls and the area and arrangement of window and door openings in the modules.

Such an experimental study of natural-scale structures will be innovative considering the current state of research in this topic and its relevance for the correct assessment of the

behaviour of timber-frame modular houses. It will be a substantive contribution to the static working theory of timber-frame modular buildings.

2. Construction of Tested Walls and Building

The building's structure was constructed using timber-frame technology. It is a four-storey building realised by Unihouse SA [36], a leading manufacturer of wooden buildings in Poland. Every storey comprises three modules. One of the modules is designed as a one-bedroom studio. Another two modules are combined to form a two-bedroom flat.

On the top floor there is one large three-room unit with a large terrace on the south side. Each unit is accessed from an external gangway. The roof is flat and made of prefabricated panels.

The single module is designed as a three-dimensional element. Its stiffness is provided by two horizontal plates (sheathed ceiling and sheathed floor), longitudinal and transverse external walls and internal walls, if possible. At the level of the ceiling and at the floor level, around the perimeter of the module, continuous timber beams were used (connected only at their corners). The individual modules are constructed from five wall types: type A external wall (marked as SZA), type B external wall (SZB), type D external wall (SZD), type M inter-module walls (SM) and type A internal walls (SA)—according to Figures 3 and 4a. Depending on the type of wall, the load-bearing structure consists of timber I-joist studs with a section hight of 300 mm or 200 mm, or 50 × 100 mm C24 or LVL timber studs different for different floors [37]. The top and bottom rails of the walls are made of LVL timber. Structural sheathing of walls is 12 mm OSB 3 boards or 12.5 mm structural gypsum boards. Internal load-bearing walls (type SA) are made of 100 mm LVL or C24 timber studs and LVL timber top and bottom rails. The sheathing of walls is made of 12.5 mm structural gypsum boards.

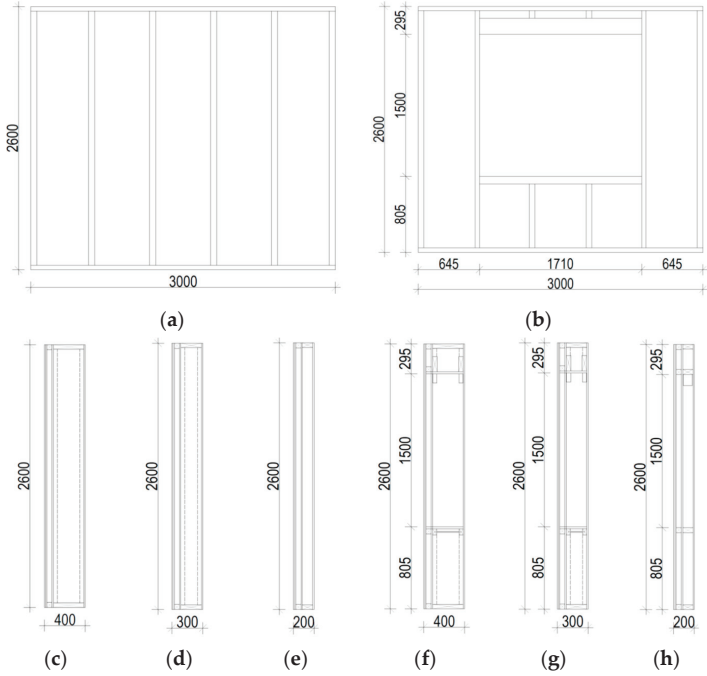

Figure 3. Tested wall panels [38]: (**a**) panel without openings, (**b**) panel with an opening, (**c**) section of the SZA wall without openings, (**d**) section of the SZB wall without openings, (**e**) section of the SZD wall without openings, (**f**) section of the SZA wall with an opening, (**g**) section of the SZB wall with an opening and (**h**) section of the SZD wall with an opening.

(**a**) (**b**)

(**c**) (**d**)

Figure 4. Plan and cross section of the tested building and module connection diagrams [39]: (**a**) ground floor plan, (**b**) vertical section, (**c**) horizontal connections between modules and (**d**) vertical connections between modules.

The structure of ceilings comprises timber joists sheathed with OSB3 boards. On the perimeter of the panel, there are continuous 150 mm LVL timber beams (connected only in corners).

The floor structure of the intermediate storey in the bathrooms is made up of 240 mm timber I-joists. In the other rooms, the heights of the joists are 300 mm. On the perimeter of panels there are LVL timber beams. Structural joists are sheathed with OSB3 boards [37].

Lintels in walls are made of timber beams.

The flat roof is ventilated, sloping in one direction. Its structure is 300 mm timber I-joists sheathed with OSB3 boards. On the perimeter of the panel there are continuous 300 mm timber beams (as before, connected only in corners).

During tests, there were no doors or windows in the building. The external staircase was designed as a steel structure.

The above-mentioned three types of walls (with or without openings) are presented in Figure 3.

The panels, depending on the type of wall, differed in the type of fasteners fixing the sheathing to the structural beams (framing):

- type 1: 1.53 × 50 mm staples, with 70 mm spacing;
- type 2: 1.53 × 50 mm staples, with 120 mm spacing;
- type 3: 3.5 × 35 mm screws, with 70 mm spacing.

Additionally, the sheathing in all walls was glued to the framing. The use of glue was intended to improve the airtightness of the building.

The form of the walls was also diversified—three panels in each group were solid, while one had an opening of 1710 × 1500 mm.

The ground floor plan and vertical section of the building under study are shown in Figure 4a,b, respectively. The connection diagrams of the modules are shown in Figure 4c,d. Between modules, board type connections of 12 mm plywood were used.

3. Experimental Research Procedures

The wall and building test methodology was adapted by analogy with the wall panel test guidelines according to EN 594 "Timber structures. Test methods. Racking strength and stiffness of timber-frame wall panels" [17].

The loading rate should ensure that 90% of the wall load-bearing capacity is achieved within 300 ± 120 s.

Wall panels' loading process ends with the collapse of the walls, according to the diagram presented in Figure 5.

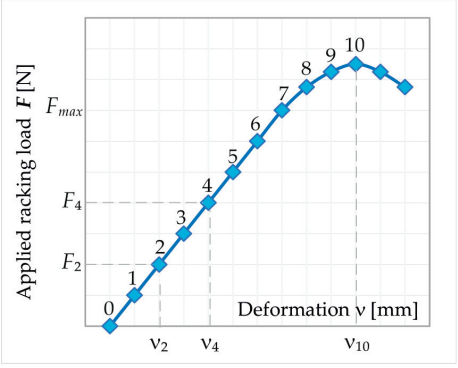

Figure 5. Wall loading process according to EN 594 [17].

According to the standard [17], the stiffness of the wall is calculated based on the formula:

$$R = \frac{F_4 - F_2}{\nu_4 - \nu_2}, \ [\mathrm{N/mm}] \quad (1)$$

where:

F_2—racking load of 0.2 F_{max};
F_4—racking load of 0.4 F_{max};
v_2, v_4—deformations corresponding to F_2 and F_4 forces.

4. Experimental Test Rig and Measuring Equipment

4.1. Wall Panels Tests

Destructive testing of wall panels was conducted in the laboratory hall of the Faculty of Civil Engineering and Environmental Sciences of Bialystok University of Technology [38]. Wall panels were fixed to the experimental test rig shown schematically in Figure 6a. A wall panel with an opening during testing is shown in Figure 6b.

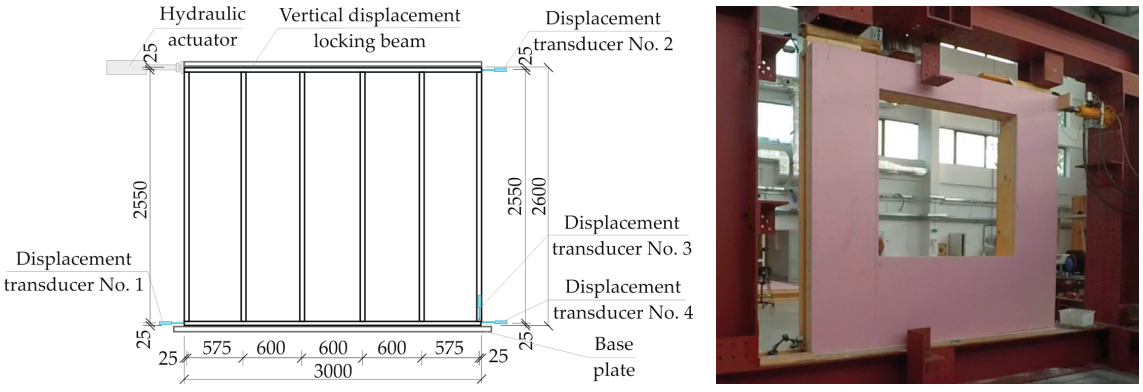

Figure 6. Experimental test rig for wall panels: (**a**) test rig scheme and (**b**) view of the test rig.

During tests, wall panels were loaded from the top with a head binder beam blocking vertical displacements. From the bottom, panels were fixed to the test rig with screws spaced at 60 cm (Figure 6a).

The load was applied in a horizontal direction with a multi-channel hydraulic system dedicated to structural loads application (HYSDOZOK). The tests used one of the available hydraulic cylinders (with a loading range of ±200 kN). The force increment during the test was 5 kN every 30 s. The loading process was continued until the wall failed (F_{max}) [38].

During the load application, the force applied to the wall panel and its displacement at selected measurement points were registered. For this purpose, a 16-channel computerised vibration analyser KSD-400 (P.U.P. SENSOR, Łódź, Poland) was used with a 12-bit AI converter card of the DAQ Card-700 type from National Instruments (Austin, TX, USA). The force and displacements were recorded at a rate of 16 samples per second.

The measurement data acquisition and recording stand is shown in Figure 7.

Figure 7. View of the data acquisition and recording station.

Displacement measurements of the wall panels were carried out using three potentiometric transducers type SPR18-50 (MEGATRON Elektronik GmbH & Co. KG,

Putzbrunn/Munich, Germany) with a 50 mm measuring base and a linearity tolerance of ±0.1% and one transducer type SPR18-75 (MEGATRON Elektronik GmbH & Co. KG, Putzbrunn/Munich, Germany) with a measuring base of 75 mm and identical linearity. The accuracy of the readings of the displacement transducers connected to the KSD-400 measurement system was verified before the measurements were carried out. A set of calibration steel plates (no. 180 492) was used for this purpose. The maximum measurement error did not exceed 3.8%. The force signal was read directly from the structural load application system (HYSDOZOK) and also recorded using the KSD-400 recorder.

As can be seen in Figure 6a, transducers No. 1, 2 and 4 were mounted to measure horizontal displacements in the plane of the wall. The task of displacement transducer No. 3 was to measure vertical displacement in the plane of the wall, taking into account the compression of the wall to the base plate.

4.2. Building Tests

When planning the experimental testing of the building, it was assumed that in order to meet the stated objective and the requirements of the company enabling the testing (Unihouse SA), the building could not be significantly damaged. The tests had to be conducted in such a way as not to cause permanent damage to the building structure. At the same time, it was desirable to obtain significant displacements of the building. This could be accompanied by minor damage to the building finishes (for example, plastering cracks) and audible crackling in the structure. Based on preliminary analyses and previous wall tests, the permissible displacement of the building in the horizontal plane was determined to be about 25 mm (ca. 1/500th of the building hight *H*) and the load-bearing capacity to be about 500 kN of force applied at the level of the ceiling above the ground floor [39].

Figure 8 schematically shows the way in which the loads were planned.

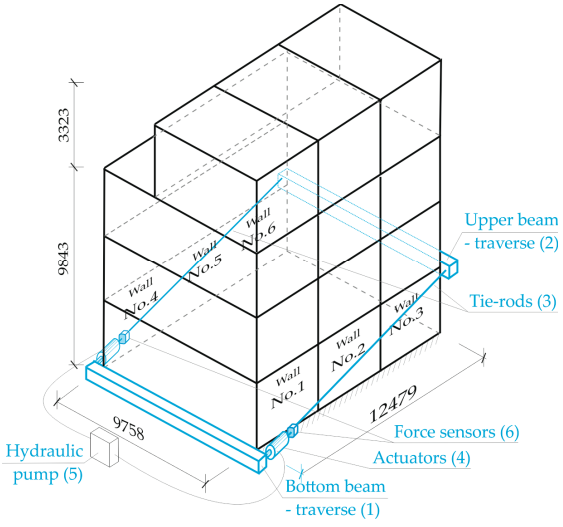

Figure 8. Schematic of the test rig for building loading.

The figure above shows external walls No. 1 to No. 3 (type SZA) and No. 4 to No. 6 (type SZB), which mainly took up the loads transmitted from the hydraulic actuators. The interior walls (type SA), which also took up part of the loads, are not visible in Figure 8. Their location in the building can be seen in Figure 4a.

The building under test and the technical instrumentation used during the measurements are shown in Figures 9 and 10.

(**a**) (**b**)

Figure 9. View of the tested building and the load application system [Fot. Unihouse SA]: (**a**) upper beam, traverse and (**b**) tie rods.

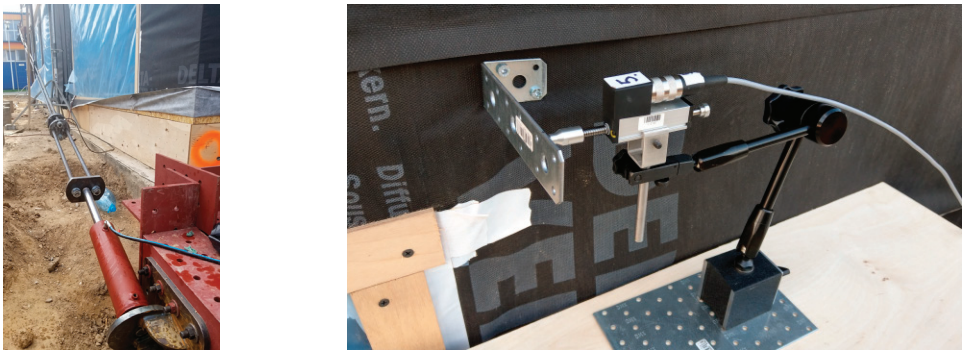

(**a**) (**b**)

Figure 10. Force application and displacement registration systems: (**a**) actuator and force sensor and (**b**) displacement transducer.

The load application system used was meant to apply horizontal loads on the building from the gable wall side and to implement assumed loading in stages (Figure 8). Loads were applied through traverse beams (1–2) placed at the level of the building foundation and at the level of ceiling above the ground floor, respectively. Traverses (1–2) were connected with tie rods (3). Loads were applied with hydraulic actuators (4) placed symmetrically on tie rods on both sides of the building. Hydraulic actuators were powered by a hydraulic pump (5).

The force values in tie rods were registered with force transducers (6), which were also mounted on the tie rods. Walls displacements were registered with displacements transducers.

The force and displacement measurements used a 16-channel KSD-400 computerised vibration analyser from P.U.P. Sensor (the same one used in the wall panel tests), two CL18-type force transducers (from ZEPWN, Marki, Poland) and a set of eight potentiometric linear displacement transducers from Megatron:

- type SPR18-25 (MEGATRON Elektronik GmbH & Co. KG, Putzbrunn/Munich, Germany) with a measurement range of 25 mm and linearity tolerance of ±0.2% (4 pieces);
- type SPR18-50 (MEGATRON Elektronik GmbH & Co. KG, Putzbrunn/Munich, Germany) with a measurement range of 50 mm and linearity tolerance of ±0.1% (4 pieces).

The measurement error for the displacement transducers wired to the KSD-400 signal recorder, was determined during tests using a set of calibration steel plates (no. 180 492). The maximum indication error of the complete measuring system did not exceed 4.3%.

Displacement transducers marked as No. 1 and No. 2 were placed directly above the foundation of the building, from the north-eastern side. Transducers No. 3 to No. 8 were placed around 30 cm above window lintels. The location of potentiometric linear transducers with its numeration (marked from No. 1 to No. 8) is shown schematically in Figure 11. In the figure below, the location of hydraulic actuators is marked as F1 and F2.

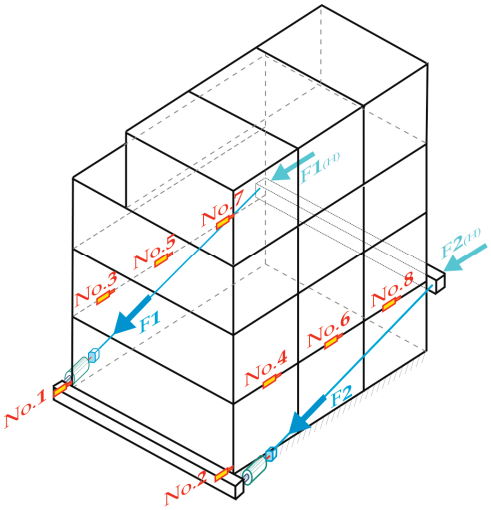

Figure 11. Schematic location plan of potentiometric linear displacement transducers and hydraulic actuators.

The tests were organized in such a way that enabled full coordination of all activities during measurements, such as implementation of load stages, forces and displacements values registration and technical state of the building supervision (displacement values, crackles, cracks).

Loads were implemented according to a static scheme shown in Figure 12.

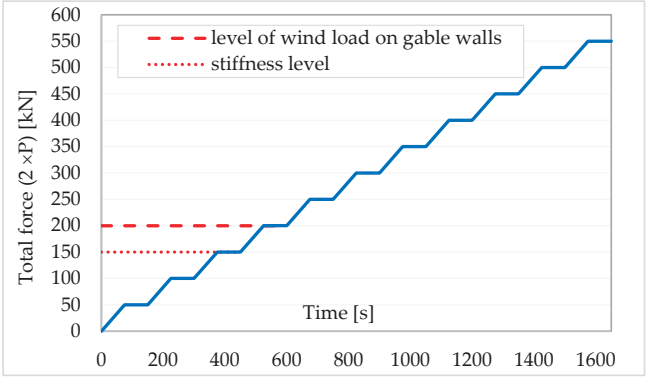

Figure 12. Assumed load implementation plan [39].

5. Test Results

5.1. Test Results for Wall Panels

Figure 13 shows an example of force–displacement diagrams obtained during testing of Type A external wall panels (designation SZA). Only the horizontal displacements in the plane of the panel recorded using displacement transducer No. 2 are summarised in the figure.

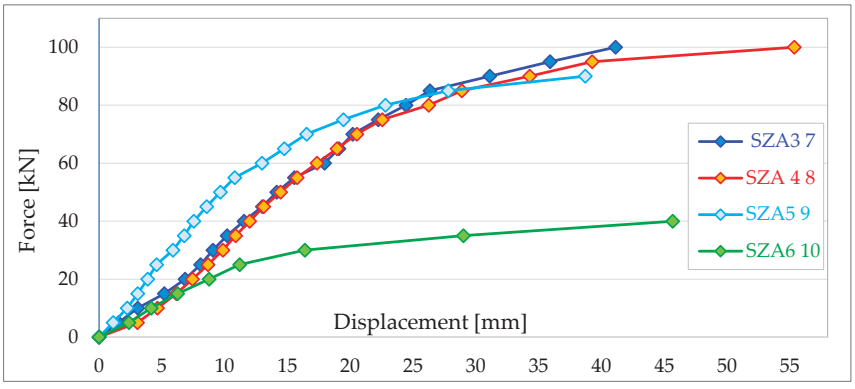

Figure 13. Force–displacement diagram for SZA-type external walls [38].

The research described in detail in [38], shows that walls with openings have only about 30–40% of the load-bearing capacity of walls without openings. These values are about 40–50 kN for each group of walls. However, the load capacity of walls without openings within all groups is similar (regardless of the type of fasteners) and does not exceed 145 kN.

External walls with structural gypsum boards sheathing (SZA type) have a lower load-bearing capacity than walls with OSB3 boards sheathing, which is quite obvious since wood-based boards have higher stiffness than gypsum boards.

The stiffness of the walls, according to the test results summarised in paper [38], ranges from 3791 N/mm to 6186 N/mm in the case of SZA-type walls, from 2316 N/mm to 4912 N/mm in the case of SZB-type walls and from 1715 N/mm to 5652 N/mm in the case of SZD-type walls.

Detailed results of stiffness calculations according to EN 594 standard [17] for selected walls used in the analysis of tested building are presented in Table 1.

Table 1. Stiffness and horizontal load-bearing capacity of the tested panels [38].

No. of Wall Panel	F_{max} [kN]	F_2 [kN]	F_4 [kN]	v_2 [mm]	v_4 [mm]	R [N/mm]
SZA3 7	100	20	40	6.85	11.54	4264
SZA6 10	40	8	16	4.15	6.26	3791
SZB6 14	55	11	22	7.60	12.35	2316
SZD4 16	120	24	48	10.52	18.76	2913
SZD5 17	145	29	58	8.99	16.67	3776

The test results confirm that the stiffness of walls significantly depends on their configuration. Panels with openings are the least rigid in each of the considered groups.

In timber-frame prefabricated modular buildings in the longitudinal direction of the building and transverse to the modules all walls usually have large door and window openings, affecting the stiffness and operation of the structure; this influences the stiffness and structural behaviour of the building, as shown in Figure 4a.

5.2. Building Test Results

A diagram of the forces in the tie rods during the building tests is shown in Figure 14 and a diagram of the displacements of individual walls is shown in Figure 15.

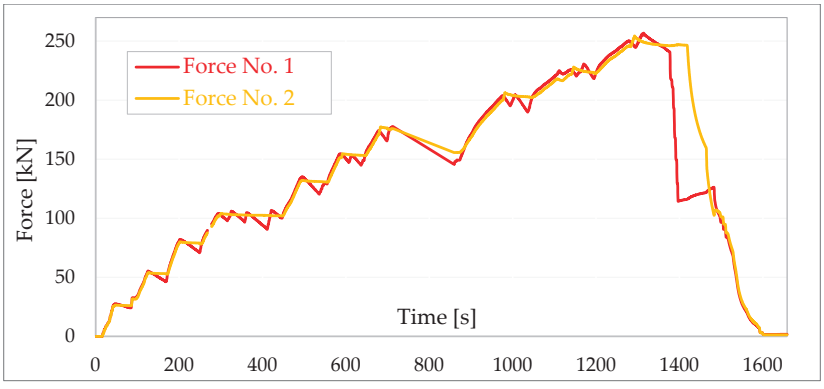

Figure 14. Diagram of forces in tie rods [39].

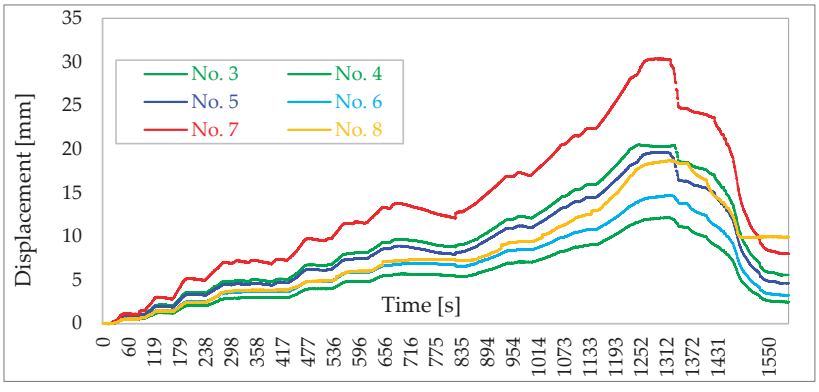

Figure 15. Diagram of wall displacements [39].

A detailed summary of the displacement values for each measurement point as a function of the applied loads is given in Tables 2 and 3 and schematically shown in Figure 16.

Table 2. Summary of the forces in the tie-rod No. 1 and the corresponding displacements of the left side of the building.

Force in Tie Rod F_1 [kN]	Horizontal Force $F_{1,H}$ [kN]	Horizontal Displacement [mm]		
		No. 3	No. 5	No. 7
0	0.0	0	0	0
26.7	25.8	0.85	0.78	1.12
53.7	51.9	2.12	1.99	3.02
79.6	76.9	3.59	3.32	5.16
102.4	99.0	4.91	4.54	7.09
131.3	126.9	6.73	6.18	9.72
153.5	148.4	8.11	7.47	11.60
176.1	170.2	9.42	8.63	13.37
204.6	197.8	12.05	11.01	16.98
225.1	217.6	15.41	13.99	21.56
246.7	238.5	20.36	19.62	29.30

Table 3. Summary of the forces in the tie rod No. 2 and the corresponding displacements of the right side of the building.

Force in Tie Rod	Horizontal Force	Horizontal Displacement [mm]		
F_2 [kN]	$F_{2,H}$ [kN]	No. 4	No. 6	No. 8
0	0.0	0	0	0
26.3	25.4	0.49	0.53	0.51
53.5	51.7	1.23	1.46	1.46
79.5	76.8	2.07	2.30	2.46
103	99.6	2.98	3.65	3.77
131.6	127.2	3.99	4.60	4.84
153.8	148.7	4.86	5.70	6.10
175.5	169.6	5.54	6.68	7.15
203.8	197.0	6.95	8.36	9.28
225.1	217.6	8.81	10.54	12.28
246.9	238.7	12.05	14.51	18.46

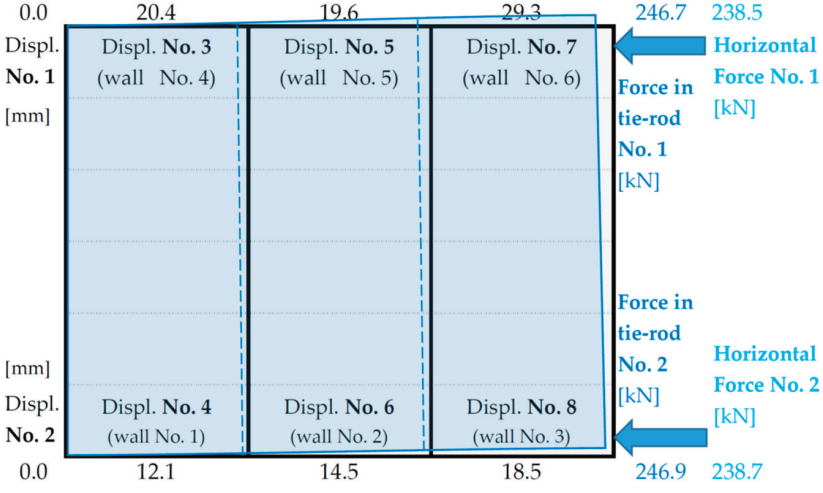

Figure 16. A schematic drawing of the displacements of the building walls corresponding to the maximum forces in the tie rods.

Displacement curves for individual measurement points as a function of applied loads in the horizontal plane (projected forces in tie rods) are shown in Figure 17.

On the basis of the results of the displacement tests, the sum of the average stiffness of the walls on the left and right sides of the building and the average total stiffness of all the walls were determined, according to the procedure specified in EN-594 [17]. The obtained results are summarised in Table 4.

Table 4. Stiffness of walls and building.

Part of the Building	F_{max} [kN]	F_2 [kN]	F_4 [kN]	v_2 [mm]	v_4 [mm]	R [N/mm]
Left side walls	238.5	51.9	99.0	2.37	5.50	15,048
Right side walls	238.7	51.7	99.6	1.40	3.50	22,810
All walls/entire building	477.2	103.6	198.6	1.88	4.50	36,530

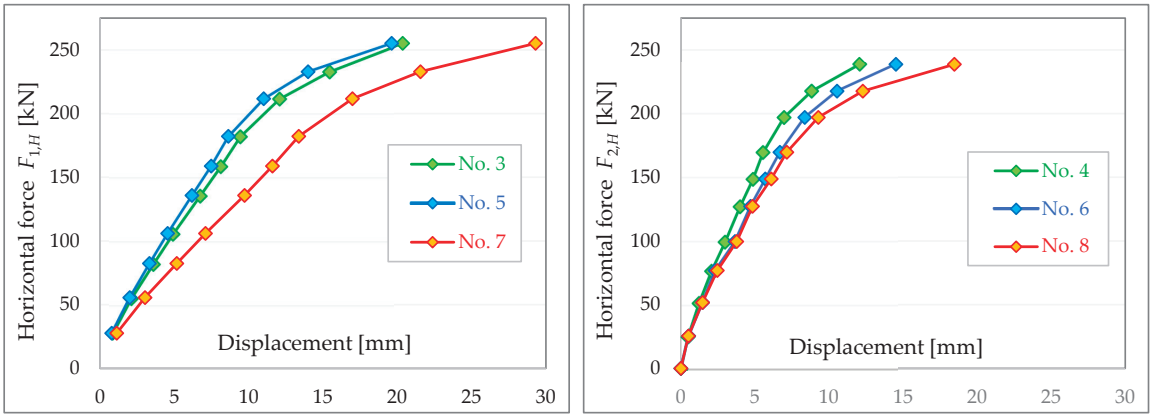

Figure 17. Displacements of the building walls in a longitudinal direction: (**a**) along the line of force F_{1H} and (**b**) along the line of force F_{2H}.

6. Discussion

The tests proved that, with increasing loads, there is a continuous increase in the displacement of all elements, in accordance with their structure and geometry.

The results presented in Table 4 show a significantly lower summed stiffness of the walls of the left side of the building with a significantly larger area of openings ($R_{W,L}$ = 15,048 N/mm) compared to the stiffness of the walls of the right side ($R_{W,R}$ = 22,810 N/mm). In the analysed case, the difference is as high as 34.0%.

The recorded building displacements confirm the significantly lower stiffness of the left side (measuring points No. 3, No. 5 and No. 7) than the right side (measuring points No. 4, No. 6 and No. 8)—as indicated by the torsion of the structure visible in Figure 16.

Deformations of timber-framed buildings, unlike traditional structures, are also highly dependent on the internal inter-elemental vertical and horizontal connections.

As conducted tests show, the horizontal displacements of individual wall panels at failure do not exceed 56 mm.

The displacements values of the tested building are not that high and range from a few to several tens of millimetres (maximum 29.3 mm). For the wind load level (according to Figure 12 approximately 75 kN), the displacement values of the walls, on the left and right sides of the building, are between 2.5 to 5.2 mm (Figure 16). At the so-called stiffness level (according to Figure 12 about 100 kN), the displacements values are around 3.8–7.1 mm (Figure 16).

The total stiffness of the walls in the building was assumed according to the tests without considering their interaction. For untested walls, the stiffness was interpolated in proportion to the stiffness of full wall segments (based on the stiffness of tested walls of the same type).

$$R_W = R_{SZB(A\text{-}B)} + 2 \cdot R_{SZB(B\text{-}C)} + 2 \cdot R_{SA} + R_{SZA(A\text{-}B)} + R_{SA(B\text{-}C)} + R_{SZA(C\text{-}D)}$$
$$= 986 + 2 \cdot 1577 + 2 \cdot 2913 + 3198 + 1866 + 4264 = 19{,}294 \text{ [N/mm]}.$$

The average stiffness of the whole building according to the data in Table 2 is R_B = 36 530 N/mm.

The first crackles in the structure were registered at loads 2·P = 100 kN load. The first drywall cracks occurred at 2·P = 150 ÷ 200 kN load.

7. Conclusions

Wall and building stiffness tests were carried out according to the methodology outlined in EN 594 standard [17]. Tests on walls were continued up to their failure, while tests on the building were carried out up to the stage of non-linear behaviour, cracking and first cracks in the finish (plaster).

As a result of the tests and comparative analyses, it should be concluded that:

- the stiffness of the walls is significantly dependent on their configuration and the surfaces of the openings, and ranges from 1715 N/mm to 6186 N/mm;
- the walls of the left side of the building with a significantly larger area of openings have a total stiffness 34.0% lower than the total stiffness of the walls of the right side (the reason for the torsion of the building visible in Figure 16);
- the total stiffness of the building walls in the direction of the applied loads (R_W = 19,294 N/mm) is 17,200 N/mm less than the spatial stiffness of the building (R_B = 36,530 N/mm)—showing how important the influence of the connections between the modules is on the overall stiffness of the building;
- the configuration and location of the walls in the modules influences the nature of the work and deformation of the building and, consequently, the distribution of horizontal loads to the individual walls.

The next stage of the research will be the development of numerical models of three-dimensional modules and entire buildings.

The results obtained are novel in terms of natural-scale testing of elements and buildings of frame and modular construction. In addition to their scientific value, the results will serve to validate three-dimensional numerical computational models—as only validated models can be used to determine reliable deformations and real internal forces in particular structural elements of buildings.

Author Contributions: Conceptualization, C.M.; methodology, C.M., K.R.C. and M.N.; software, K.R.C.; validation, K.R.C., C.M. and M.N.; formal analysis, K.R.C., C.M. and M.N.; resources, K.R.C.; data curation, K.R.C. and M.N.; writing—original draft preparation, C.M., M.N., K.R.C. and A.Ż.; writing—review and editing, C.M., K.R.C., M.N. and M.K.-K.; visualization, K.R.C., M.N. and A.Ż.; supervision, C.M., K.R.C. and M.K.-K.; project administration, C.M. and funding acquisition, C.M., M.N. and M.K.-K. All authors have read and agreed to the published version of the manuscript.

Funding: This research was carried out as part of research work No. WZ/WB-IIL/4/2023 and WZ/WB-IIL/6/2023 at the Bialystok University of Technology and financed by a subsidy provided by the Ministry of Education and Science.

Institutional Review Board Statement: Not applicable.

Informed Consent Statement: Not applicable.

Data Availability Statement: Data available on request due to privacy.

Acknowledgments: The authors would like to thank the Unihouse SA company in Bielsk Podlaski for help and making it possible to test the building described in the article.

Conflicts of Interest: The authors declare no conflict of interest.

References

1. Cameron, P.J., Jr.; Di Carlo, N.G. Piecing Together Modular: Understanding the Benefits and Limitations of Modular Construction Methods for Multifamily Development. Master's Thesis, Massachusetts Institute of Technology, Cambridge, MA, USA, September 2007.
2. Szulc, J.; Sieczkowski, J. The Future of Modular Technology in Construction, Design Guide. *Inżynier Budownictwa* **2020**, *5*, 82–86. (In Polish)
3. Malesza, J.; Miedziałowski, C. Current Directions in Development of Modern Wood-framed Houses. In Proceedings of the 12th International Conference on Modern Building Materials, Structures and Techniques (MBMST 2016), Vilnius, Lithuania, 26–27 May 2016.
4. Nazarczuk, M. Evolution of Timber Structural Systems for Multi-storey Buildings. *Civ. Environ. Eng.* **2018**, *9*, 159–166. (In Polish)

5. Malesza, J.; Baszeń, M.; Miedziałowski, C. Development Directions for Various Types of the Light Wood-Framed Structures. In Proceedings of the IOP Conference Series: Materials Science and Engineering, Tianjin, China, 22–24 September 2017; Institute of Physics Publishing Ltd.: Bristol, UK, 2017.
6. Knuppe, J. Robustness of Modular Timber Buildings: An Investigation into Alternative Load Paths in Volumetric Timber Post and Beam Modules. Master's Thesis, Delft University of Technology, Delft, The Netherlands, 2022.
7. Li, Z.; Tsavdaridis, K.D. Limited-damage 3D-printed Interlocking Connection for Timber Volumetric Structures: Experimental Validation and Computational Modeling. *J. Build. Eng.* **2023**, *63*, 105373. [CrossRef]
8. Kamiya, F. Buckling Theory of Sheathed Walls: Linear Analysis. *J. Struct. Eng.* **1987**, *9*, 2009–2022. [CrossRef]
9. Stewart, A.H.; Goodman, J.R.; Kliewer, A.; Salsbury, E.M. Full Scale Teste of Manufactured Houses under Simulated Wind Loads. In Proceedings of the Conference on Timber Engineering, Forest Products Research Society, Madison, WI, USA, 19–22 September 1988.
10. Sugyiama, H.; Andoh, N.; Uchisako, T.; Hirano, S.; Nakamura, N. Full Scale Test on Japanes Type of Two–Story Wooden–Frame House Subject to Later Load. In Proceedings of the Conference on Timber Engineering, Forest Products Research Society, Madison, WI, USA, 19–22 September 1988.
11. Baszeń, M.; Miedziałowski, C.; Malesza, M. Strength Tests of Timber Framed Walls of Buildings. In Proceedings of the XLII Scientific Conference of KILiW PAN and KN PZiTB, Krynica, Poland, 13–18 September 1999. (In Polish)
12. Kuai, L.; Ormarsson, S.; Vessby, J.; Maharjan, R. A numerical and experimental investigation of non-linear deformation behaviours in light-frame timber walls. *Eng. Struct.* **2022**, *252*, 113599. [CrossRef]
13. Martin, Z.A.; Skaggs, T.D.; Keith, E.L.; Yeh, B. Development of narrow wall bracing and effects of boundary conditions. In Proceedings of the World Conference on Timber Engineering, Portland, OR, USA, 6–10 August 2006.
14. Šilih, E.K.; Premrov, M. Analysis of timber-framed wall elements with openings. *Constr. Build. Mater.* **2010**, *24*, 1656–1663. [CrossRef]
15. *A Standard for Testing Sheathing Materials for Resistance to Racking. Technical Circular No. 12, Federal Housing Administration*; Federal Housing Administration: Washington, DC, USA, 1949.
16. Miedziałowski, C.; Malesza, M. *Timber Frame Buildings with Sheathing. Fundamentals of Structural Mechanics and Issues of Construction and Implementation*; Białystok: Warszawa, Poland, 2006. (In Polish)
17. *PN-EN 594:2011*; Timber Structures—Test Methods—Testing of Stiffness and Load-Bearing Capacity of Timber-Framed Wall Panels. PKN: Warsaw, Poland, 2011. (In Polish)
18. Tuomi, R.L.; McCutheon, J. *Testing a Full Scale House under Simulated Snow Loads and Wind Loads*; Forest Service Research Paper, FPL 234; Forest Products Laboratory: Madison, WI, USA, 1974.
19. Boughton, G.N.; Reardon, G.F. *Testing a High–Set House Designed for 42 m/s Winds*; Technical Report No. 19; Cyclone Testing Station, James Cook University: Townsville, Australia, 1983.
20. Boughton, G.N.; Parackal, K.; Satheeskumar, N.; Henderson, D.J. Development of a Full-Scale Structural Testing Program to Evaluate the Resistance of Australian Houses to Wind Loads. *Front. Built Environ.* **2017**, *3*, 21. [CrossRef]
21. Collins, M.; Kasal, B.; Paevere, P.; Foliente, G.C. Three-Dimensional Model of Light Frame Wood Buildings. Model Description. *J. Struct. Eng.* **2005**, *131*, 676–683. [CrossRef]
22. Malesza, J.; Miedziałowski, C.; Ustinovičius, L. Tests on Full-Scale and Static Analysis Models of the Wood-Framed Building Structure Horizontaly Loaded. *J. Civ. Eng. Manag.* **2017**, *23*, 814–823. [CrossRef]
23. Smith, I.; Asiz, A.; Gupta, G. *High Performance Modular Wood Construction Systems*; Final Report No UNB5, Value-to-Wood Program; Natural Resources Canada: Ottawa, ON, Canada, 2007.
24. Ormarsson, S.; Johansson, M. Finite Element Simulation of Global Structural Behaviour of Multifamily Timber Buildings Using Prefabricated Volume Modules. In Proceedings of the World Conference on Timber Engineering, Seoul, Republic of Korea, 20–23 August 2018.
25. Ormarsson, S.; Vessby, J.; Johansson, M.; Kua, L. Numerical and Experimental Study on Modular-Based Timber Structures. In Proceedings of the Modular and Offsite Construction (MOC), Banff, AB, Canada, 21–24 May 2019.
26. Montaño, J.; Almazán, J.L.; Santa María, H. Technical Feasibility Study for the Construction of Modular Light Wood-frame Prefabricated Buildings of Six-story at High Seismic Risk Regions. In Proceedings of the World Conference on Timber Engineering, Seoul, Republic of Korea, 20–23 August 2018.
27. Popovski, M.; Gavrić, I.; Schneider, J. Performance of Two-storey CLT House Subjected to Lateral Loads. In Proceedings of the 13th World Conference on Timber Engineering, Quebec, QC, Canada, 10–14 August 2014.
28. Cecotti, A. New Technologics for Construction of Medium-rise Buildings in Seismic Regions: The XLAM case. *Struct. Eng. Int.* **2008**, *18*, 156–165. [CrossRef]
29. Ceccotti, A.; Sandhaas, C.; Okabe, M.; Yasumura, M.; Minowa, C.; Kwai, N. SOFIE project-3D shaking table test on a seven-storey full-scale cross-laminated timber building. *Earthq. Eng. Struct. Dyn.* **2013**, *42*, 2003–2021. [CrossRef]
30. Lacey, A.W.; Chen, W.; Hao, H.; Bi, K. Structural response of modular buildings—An overview. *J. Build. Eng.* **2018**, *16*, 45–56. [CrossRef]
31. Cowled, C.J.L.; Slattery, T.P.; Crews, K.; Brooke, H. Influence of Plasterboard on the Structural Performance of Timber-framed Shear Walls. In Proceedings of the World Conference on Timber Engineering (WCTE 2023), Oslo, Norway, 19–22 June 2023. [CrossRef]

32. Valdivieso, D.; Lopez-Garcia, D.; Montaño, J.; Guindos, P. Testing of Strong Multi-Layered Wood Frame Shear Walls with Non-Structural Layers. In Proceedings of the World Conference on Timber Engineering (WCTE 2023), Oslo, Norway, 19–22 June 2023. [CrossRef]
33. Kuai, L.; Ormarsson, S.; Vessby, J. Nonlinear FE-analysis and Testing of Light-frame Timber Shear Walls Subjected to Cyclic Loading. *Constr Build Mater.* **2023**, *362*, 129646. [CrossRef]
34. Abrahamsen, R.; Bjertnćs, M.A.; Bouillot, J.; Brank, B.; Cabaton, L.; Crocetti, R.; Flamand, O.; Garains, F.; Gavrić, I.; Germain, O.; et al. Dynamic Response of Tall Timber Buildings Under Service Load—The DynaTTB Research Program. In Proceedings of the XI International Conference on Structural Dynamics (EURODYN 2020), Athens, Greece, 22–24 June 2020. [CrossRef]
35. Amaddeo, C.; Dorn, M. Ambient Vibration Tests and Modal Analysis of a Six-story Lightweight Timber Frame Building. In Proceedings of the World Conference on Timber Engineering (WCTE 2023), Oslo, Norway, 19–22 June 2023. [CrossRef]
36. *Designer's Guide*; Unihouse SA: Bielsk Podlaski, Poland, 2020. (In Polish)
37. Komorowski, M. *Handbook for Designing and Building in STEICO. Fundamentals. Building Physics: Implementation Recommendations*; Forest Comunication: Warszawa, Poland, 2018. (In Polish)
38. Nazarczuk, M. Testing the Stiffness and Load-bearing Capacity of Wall Panels in Timber-framed Buildings in Different Geometric and Structural Configurations. *Civ. Environ. Eng.* **2018**, *9*, 131–136. (In Polish)
39. Miedziałowski, C.; Czech, R.K.; Chyży, T.; Grygo, R.; Nazarczuk, M.; Wasilewski, A.; Żakowicz, A. *Test Report on the Transfer of Horizontal Loads in the Ceiling Segments above the Ground Floor in a Timber Frame Modular Building with an Assessment of the Degree of Horizontal Load Transfer*; Unihouse & Bialystok University of Technology: Białystok, Poland, 2018. (In Polish)

materials

MDPI

Article

Experimental Investigation on Strength and Stiffness Properties of Laminated Veneer Lumber (LVL)

Alfredo Romero * and Christoph Odenbreit

Faculty of Science Technology and Medicine (FSTM), University of Luxembourg, L-4365 Esch-sur-Alzette, Luxembourg; christoph.odenbreit@uni.lu
* Correspondence: alfredo.romero@uni.lu

Abstract: This study presents a testing campaign aimed at evaluating the strength and stiffness properties of laminated veneer lumber (LVL) specimens. LVL is an engineered wood product composed of thin glued wood veneers whose use in construction for structural applications has increased due to its sustainability and enhanced mechanical performance. Despite LVL's growing popularity, there is a lack of comprehensive information regarding stress–strain responses, failure modes, and the full set of strength and stiffness properties. These are particularly essential when LVL is employed in pure timber structures or composite systems such as steel–timber or timber–concrete load-bearing elements. This research aims to bridge this knowledge gap, focusing on crossbanded LVL panels, known as LVL-C, crafted from Scandinavian spruce wood, which is an LVL product with 20% of crossbanded veneers. The study explores LVL-C mechanical behavior in three primary orthogonal directions: longitudinal, tangential, and radial. A series of mechanical tests, including compression, tension, shear, and bending, was conducted to provide a thorough assessment of the material's performance. In compression tests, different behaviors were observed in the three directions, with the longitudinal direction exhibiting the highest stiffness and strength. Tensile tests revealed unique stress–strain responses in each direction, with gradual tension failures. Shear tests showcased varying shear stress–strain patterns and failure modes, while bending tests exhibited significant strength and stiffness values in flatwise bending parallel to the grain and flatwise bending perpendicular to the grain. This paper summarizes the comprehensive testing results and discusses the obtained strength and stiffness properties of LVL-C panels, providing valuable insights into their mechanical behavior for engineering applications.

Keywords: timber properties; laminated veneer lumber; LVL; LVL-C; spruce wood; mechanical properties; strength; stiffness

Citation: Romero, A.; Odenbreit, C. Experimental Investigation on Strength and Stiffness Properties of Laminated Veneer Lumber (LVL). *Materials* **2023**, *16*, 7194. https://doi.org/10.3390/ma16227194

Academic Editor: Krzysztof Schabowicz

Received: 27 October 2023
Revised: 13 November 2023
Accepted: 14 November 2023
Published: 16 November 2023

1. Introduction

Laminated veneer lumber (LVL) is an engineered wood product that has attracted considerable interest for its ability to harness the inherent strength and durability of wood while addressing some of the constraints related to solid timber size and natural defects. Additionally, LVL manufacturing efficiently makes use of small-diameter logs and lower-grade timber that might otherwise go to waste. LVL products are generally categorized into two main groups based on their layup: (i) those in which veneer layers are oriented with their grain parallel to each other, referred to as LVL-P, and (ii) those in which roughly 20% of the veneer layers have their grain oriented perpendicular to the rest of the veneer layers, known as LVL-C.

As the construction industry faces growing scrutiny for its environmental impact [1], engineered wood products such as CLT and LVL have emerged as a sustainable alternative to conventional materials like concrete and steel [2–5]. LVL is engineered to deliver exceptional strength and stiffness. Its composite structure, comprising 3–4 mm thick veneer layers that are pressed and bonded with phenolic adhesive, mitigates many of the natural

defects that are inherent in solid wood [6]. This leads to a highly uniform material with reduced property variations, setting it apart from traditional timber products. The appeal of LVL extends to its suitability for a wide range of structural applications, from beams and columns to slabs and shear walls. Moreover, investigations have been carried out to implement its use as slabs in conjunction with steel structural beams as steel–timber composite (STC) beams [7–9].

There are some investigations on the mechanical properties and behavior of LVL; however, none of them deal with LVL-C made from Scandinavian spruce wood. Chybinski and Polus [10] conducted compression, tension, and bending tests of LVL-P (LVL with the grain of all veneers oriented in the same direction) panels made of spruce and Scots pine; moreover, they built 2D and 3D finite element models and implemented the properties obtained in their tests, showing good agreement with the experimental observations. A comprehensive investigation on the strength and stiffness properties of Radiata pine LVL was presented by Van Beerschoten [11]. Ardalany et al. [12,13] studied the fracture energy, toughness, and strength in tension perpendicular to the grain of LVL crafted from Radiata pine. Similarly, Franke and Quenneville [14] analyzed experimentally the fracture behavior of Radiata pine LVL.

Other studies related to LVL focused on the assessment of LVL with certain variations in its standard structure and/or layup and its response under certain conditions. For example, Bal [15] determined some physical and mechanical properties of LVL reinforced with woven fibers. Sokolovic et al. [16] assessed the bending strength of flexural properties of LVL reinforced with woven carbon fibers. Bakalarz [17] studied the bending response of LVL beams reinforced with carbon-fiber-reinforced polymer (CFRP).

While there are studies that have focused on the mechanical characterization of certain LVL products and on the enhancement of their mechanical response, it is noteworthy that none of them have specifically assessed the strength and stiffness properties of crossbanded LVL derived from Scandinavian spruce wood, as far as the authors of this contribution are aware.

Despite LVL's increasing use in the construction industry, a comprehensive understanding of its mechanical behavior, including testing procedures, stress–strain responses, and failure modes, remains crucial. The technical literature lacks comprehensive insights into these aspects. The mechanical properties of this engineered timber product (e.g., strength, stiffness, stress–strain response, fracture behavior) are fundamentally important when it is used as a load-bearing structural element in pure timber, steel–timber, or timber–concrete structures. These properties are used to determine the bearing capacity of structural members, their load–deformation behavior, and potential failure modes. Additionally, the properties are essential for developing numerical models of LVL members and structures (e.g., finite element modeling). Hence, to address this existing gap of knowledge concerning the mechanical characterization of LVL-C made of Scandinavian spruce wood, this research focuses on panels made from this wood species.

This investigation studies the LVL-C in its three primary orthogonal directions: longitudinal, tangential, and radial. A series of mechanical tests of LVL-C specimens in compression, tension, shear, and bending has been conducted to comprehensively evaluate the material's performance in the three orthogonal directions. This contribution provides valuable insights concerning the testing procedures of the material along with values of strength, moduli of elasticity, and shear moduli. In addition, the stress–strain responses and load–deformation response in bending are presented.

This article is organized as follows: a description of the tested material is presented in Section 2.1, the overview of the tests is included in Section 2.2, the testing procedures, specimen characteristics, and test setups are described in Section 3, the results and the respective discussion is provided in Section 4, and, finally, the conclusions are presented in Section 5.

2. Material and Tests Overview

2.1. Material

Laminated veneer lumber is an engineered wood product made by gluing and layering wood veneers with a thickness of 3–4 mm to produce wood panels with various dimensions and layups. The maximum width (measured in the tangential direction) that can be produced is 2500 mm, and the maximum lengths range from 18 to 25 m depending on the production line. There are two standard types of layups: (i) a layup in which the veneer layers are oriented with their grain running parallel to each other, known as LVL-P; and (ii) a layup in which approximately 20% of the layers of veneer have their grain running perpendicular to the grain of the other veneers, which is known as LVL-C.

For this testing campaign, the specimens were produced from LVL-C panels with a thickness of 51 mm made of Scandinavian spruce wood (i.e., Picea abies) (see Figure 1a). This product is commercialized by Metsä Wood under the brand name of Kerto-Q. It has 17 veneers in total, each veneer with a thickness of 3 mm, where 3 of them are cross veneers distributed within the matrix of the section; hence, the layup is as follows: II-IIIII-IIIII-II, in which 'I' represents the veneers whose grain aligns with the longitudinal direction of the timber element and '-' represents the cross veneers.

Due to its nature, timber is anisotropic; however, for engineering purposes, it is considered as an orthotropic material. The three orthogonal directions are linked to the growth directions of the trees, longitudinally and transversely. The strongest and the stiffest direction is often referred to as the longitudinal direction, or grain direction, and it follows the longitudinal growth of the tree. The other two directions are the radial and the tangential direction, which follow the transversal growth of the tree. Figure 1b shows a picture of the LVL material and the definitions of the directions considered in this study for the LVL panels: the longitudinal (L), tangential (T), and radial (R) directions are defined as directions 1, 2, and 3, respectively.

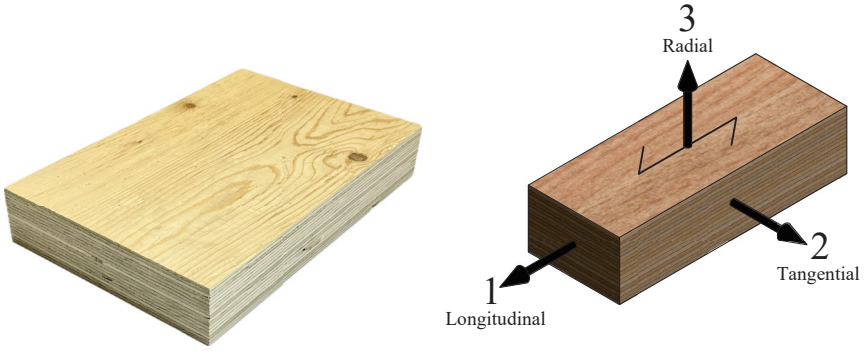

(**a**) (**b**)

Figure 1. LVL tested in this study: (**a**) picture of the material, and (**b**) directions considered.

2.2. Tests Overview

The testing campaign includes compression (C-), tension (T-), shear (S-), and bending (B-) tests to determine the stiffness and strength properties of crossbanded LVL in the three main orthogonal directions. A nomenclature was defined to label the specimens and assign IDs to the different tests; this nomenclature (see Figure 2) consists of one letter followed by two digits separated by dashes, where the letter refers to the type of test, the first digit, which is placed after the letter, refers to the direction, and the last digit refers to the specimen number within the sample. Following this nomenclature, an overview of the tests is presented in Figure 3. This figure includes the schematic representations of the specimens grain direction, the test IDs, the direction of the applied loads, and the number of specimens tested in this experimental campaign.

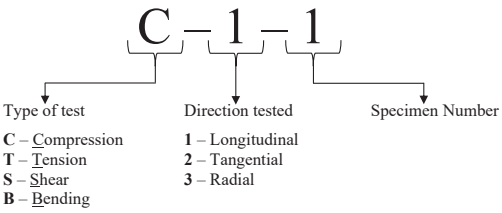

Figure 2. Nomenclature definition for test types and specimens identification.

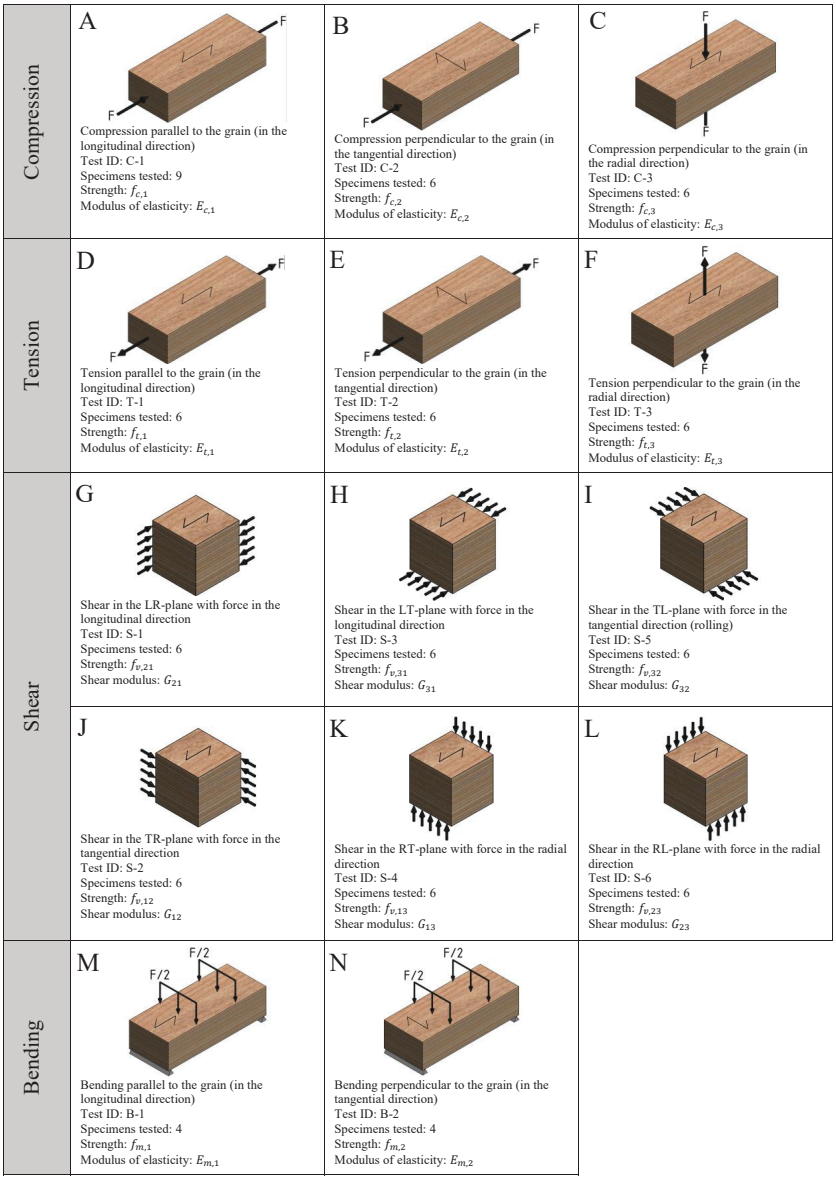

Figure 3. Overview of the tests carried out in this experimental campaign.

3. Methods

3.1. General

The tests were conducted in accordance with the standards EN 408 [18] and EN 789 [19], and the strength and stiffness values were estimated following the procedures established in these standards; further details of the calculation procedures can be found in Appendix A. The coefficient of variation and the 5-percentiles values were calculated according to EN 14358 [20].

All the tests were carried out at room temperature conditions. The moisture content of the LVL specimens was measured using a capacitive moisture sensor from ALEMO (FHA 696 MF). The air humidity and temperature were also measured using a digital sensor from ALEMO (FHAD46-Cx) (Sempeter pri Gorici, Slovenia). The average measurements recorded were as follows: moisture content at 12%, air humidity at 46%, and room temperature at 23 °C.

In accordance with standards EN 408 [18] and EN 789 [19], the loading procedures were as follows: (i) a monotonic load was applied to all specimens in displacement-controlled mode, and (ii) specific loading rates were defined for each test to ensure that specimen failure occurred within a specific time frame of 300 ± 120 s.

For the tension and shear tests, custom apparatus were designed. For tension tests, the custom apparatus consist of clamping steel plates in which bolts were used to apply pressure on the specimen; in addition, glue was applied to prevent slip, which could cause drops in forces during the tests. For shear tests, the custom apparatus consist of (i) a set of bearings that allow us to introduce the loading to the specimen with an inclination of 14° with respect to the vertical, such that shear failure is induced through the specimen, and (ii) steel plates as recommended in EN 408 [18]; these plates were glued to the specimen in two parallel faces. Further details of these devices have been included in the respective Section 3.3 Tension Tests and Section 3.4 Shear Tests.

Preliminary tests were conducted to validate the performance of the devices and to define a suitable glue for the tension and shear tests. Two types of glue were tested: (i) two-part epoxy glue (Würth ESK-50), and (ii) methylmethacrylate glue (Würth MAK 38). It was determined that the two-part epoxy glue exhibited superior resistance at the glued interface and a shorter curing time. Consequently, this glue was selected for use in both tensile and shear tests to effectively bond steel and LVL surfaces.

3.2. Compression Tests

The compression tests were performed in the longitudinal (C-1), tangential (C-2), and radial (C-3) directions. The specimens' dimensions are shown in Figure 4. In the C-1 and C-2 tests, a small preload of 5 kN and 2 kN, respectively, was applied to the specimens; then, the load was applied at a rate of 0.6 mm/min and 1.5 mm/min, respectively. In the C-3 tests, no preload was applied, and the loading rate was set to 4 mm/min.

Nine specimens were tested in C-1 tests, and six specimens in C-2 and C-3 tests. In the C-1 tests, initially, six specimens were tested and these tests were stopped at a load drop of 70 kN. However, after analyzing the results of these initial tests, it was decided to test three additional specimens up to the point of fracture to obtain more detailed information about fracture and the softening branch of the stress–strain curve in the longitudinal direction.

The test setup of the compression tests is shown in Figure 5. The C-1 and C-2 tests were carried out in a compression testing machine with a capacity of 4 MN and the C-3 tests were carried out in a compression testing machine with a capacity of 300 kN, both machines from TESTING Bluhm & Feuerherdt GmbH (Berlin, Germany).

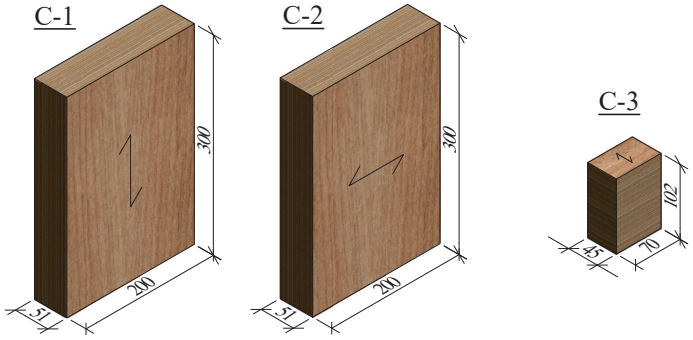

Figure 4. Dimensions in mm of the specimens tested in compression.

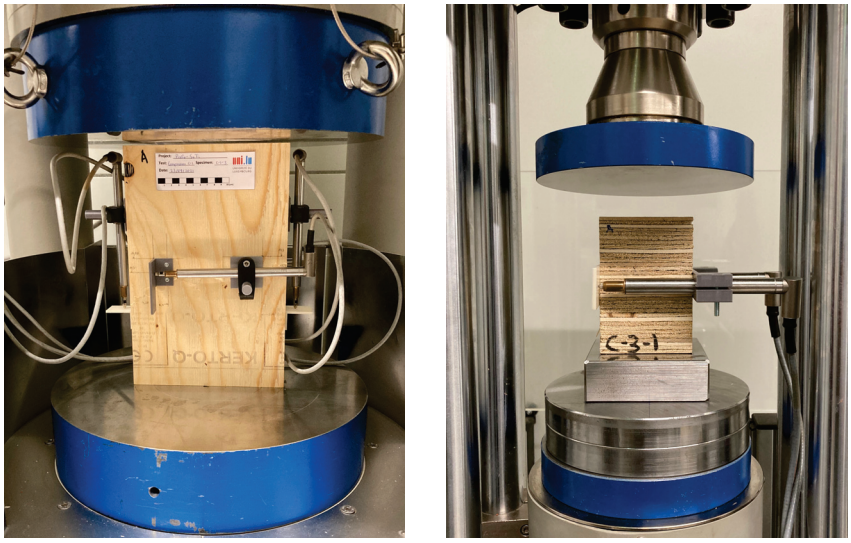

(**a**) (**b**)

Figure 5. Test setups of: (**a**) compression tests C-1 and C-2, and (**b**) tests C-3.

3.3. Tension Tests

The tension tests were performed in the three orthogonal directions: longitudinal (T-1), tangential (T-2), and radial (T-3). Six identical specimens were tested for each direction. For tests T-1 and T-2, the specimens had a coupon shape to induce failure at the central part of the specimen and to measure the local displacements within a well-defined gauge length. The T-3 tests were performed on rectangular prismatic specimens. The shapes and dimensions of the specimens tested in tension are shown in Figure 6. The tests were conducted in a universal machine for compression and tension tests Form+Test UP 500 with a capacity of 100 kN.

Custom apparatus were designed and produced to carry out these tests. The custom devices for the T-1 and T-2 tests consist of steel plates with a thickness of 20 mm with drilled holes to allow for the installation of bolts in order to apply pressure and clamp the coupon-shaped specimen from its tabs. To prevent slip and force drops due to slip of the specimen, a two-part epoxy glue was applied at the steel–timber interface of the custom griping plates. In the T-3 tests, the load was transferred to the specimen through custom grips and steel blocks that were fixed to the specimen with a two-part epoxy glue. Images of the test setup of the tension tests are shown in Figure 7.

The load was applied at rates of 0.1 mm/min, 0.3 mm/min, and 0.2 mm/min, respectively, for tests T-1, T-2, and T-3. Local displacements were measured with two LVDT sensors placed at parallel faces of the specimens. In the T-1 and T-2 tests, local displacements were measured in the gage of the specimen within a length of 100 mm. In the T-3 tests, the displacements were measured through the whole length of the specimen (i.e., 51 mm).

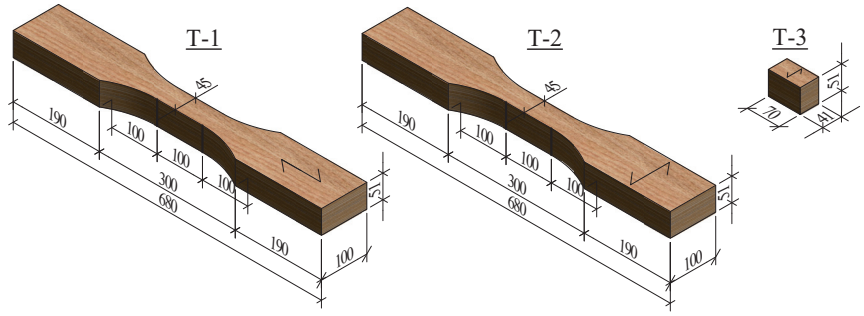

Figure 6. Dimensions in mm of the specimens tested in tension.

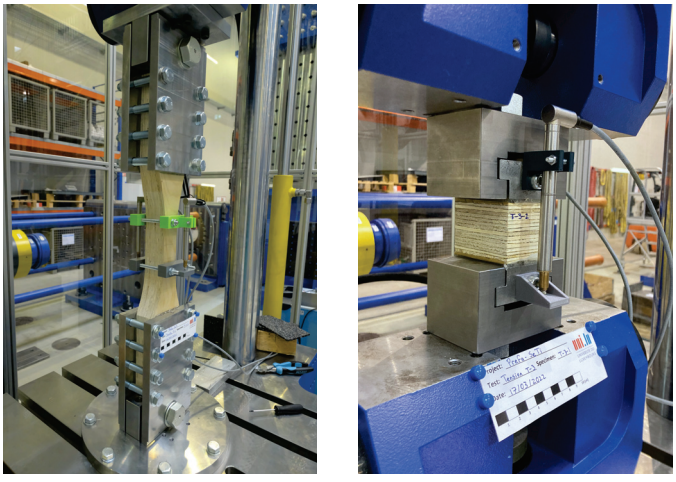

(**a**) (**b**)

Figure 7. Test setups of: (**a**) tension tests T-1 and T-2, and (**b**) tests T-3.

3.4. Shear Tests

Six different shear tests (i.e., S-1, S-2, S-3, S-4, S-5, S-6) were performed in the direction indicated in Figure 3. Six identical specimens were tested for each one of the directions; the dimensions of the specimens are shown in Figure 8. The specimens for tests S-4 and S-6 were formed by stacking and gluing 5 cubic pieces of the timber panels with dimensions 51 × 51 × 51 mm. The tests were conducted in a universal machine for compression and tension tests Form+Test UP 500 with a capacity of 100 kN.

Custom devices were designed and produced for these tests. The top and bottom bearings have a channel that allows us to place and remove a specimen at an inclination of 14° with respect to the vertical line of the applied load. Two steel plates (275 × 51 × 10 mm) with the shape recommended in EN 408 [18] were glued with two-part epoxy glue to the specimen in parallel faces of the specimen in the corresponding shear plane for each test. The differential displacement between the steel plates was measured with two LVDT sensors installed at parallel faces. The test setup is shown in Figure 9.

The loading rate for the S-1 and S-4 tests was set to 0.2 mm/min; for tests S-2 and S-3, it was set to 0.4 mm/min; for tests S-5, it was 0.5 mm/min; and for tests S-6, it was set to 0.6 mm/min.

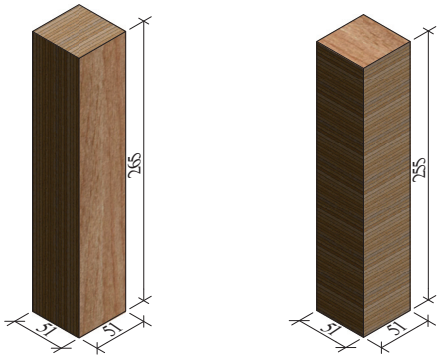

(**a**) (**b**)

Figure 8. Dimensions in mm of the shear test specimens: (**a**) S-1, S-2, S-3, S-5 and (**b**) S-4, S-6.

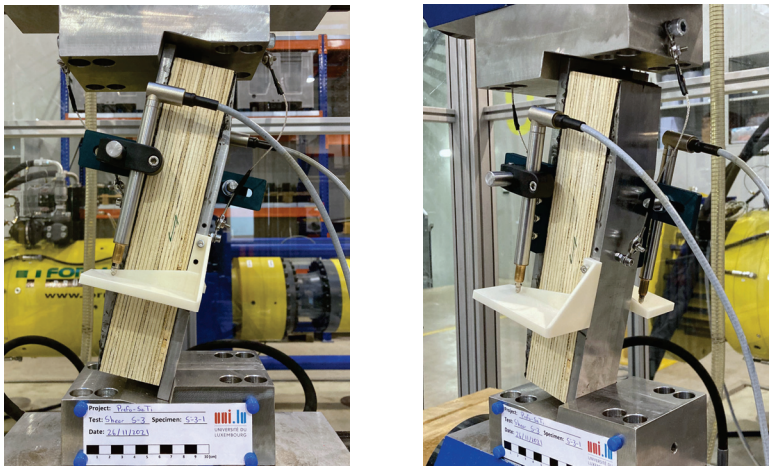

Figure 9. Shear tests setup.

3.5. Bending Tests

Simply supported panels were tested in 4-point bending. Two different bending tests were executed: flatwise bending parallel to the grain (B-1), and flatwise bending perpendicular to the grain (B-2). Four identical specimens with dimensions 1200 × 150 × 51 mm (see Figure 10) were tested for each type of test. The load was applied at rates of 4.2 mm/min and 4.8 mm/min for tests B-1 and B-2, respectively. The deflection of the panels was measured at midspan at both sides of the panels. The tests were carried out in a machine for bending tests with a capacity of 300 kN from TESTING Bluhm & Feuerherdt GmbH. The positions of the loading points and the supports are depicted in Figure 11 and the test setup is illustrated in Figure 12.

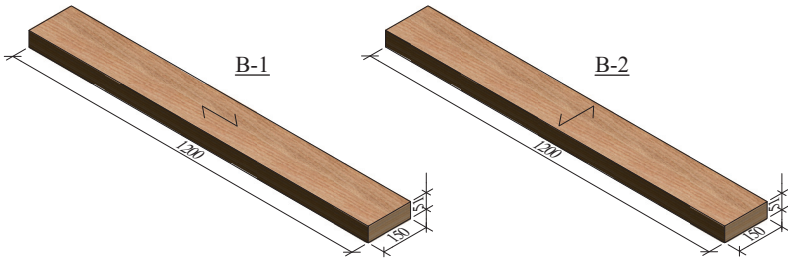

Figure 10. Dimensions in mm of the specimens tested in 4-point bending.

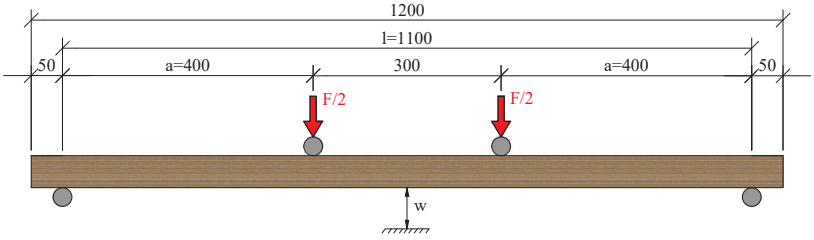

Figure 11. Side view of the position of the loading points and the supports of the bending tests (dimensions given in mm).

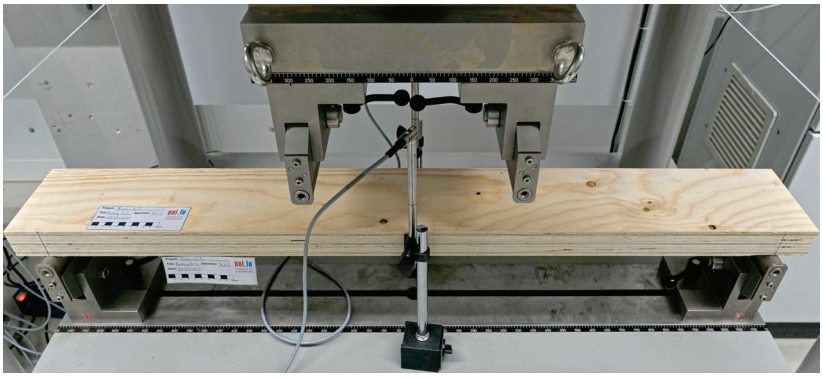

Figure 12. Test setup of the bending tests.

4. Results and Discussion

4.1. Compression Tests

The stress–strain curves of the compression tests in the three main orthogonal directions are depicted in Figure 13 and some of the tested specimens are illustrated in Figure 14. The response of the material in the longitudinal direction (tests C-1) was characterized by an initial linear monotonic increasing stress–strain relationship, followed by a non-linear response, and, after the peak, a softening branch developed. Out of the nine specimens that were tested in C-1 tests, only three were brought to rupture. After reaching the peak load, crushing of the fibers at the mid-height of the specimen, followed by delamination and opening of the veneers, was observed. In some specimens, shear failure was observed; these specimens showed an inclined crack of crushed veneers through their thickness, with an inclination of about 45°.

The specimens tested in the tangential direction (tests C-2) also exhibited an initial linear behavior followed by a hardening branch and softening after the peak. The tests were stopped before reaching the rupture. In the radial direction (tests C-3), the tested specimens

showed an initial linear behavior followed by a hardening region of increasing stress with strain. In this direction, LVL exhibited a large deformation capacity in compression.

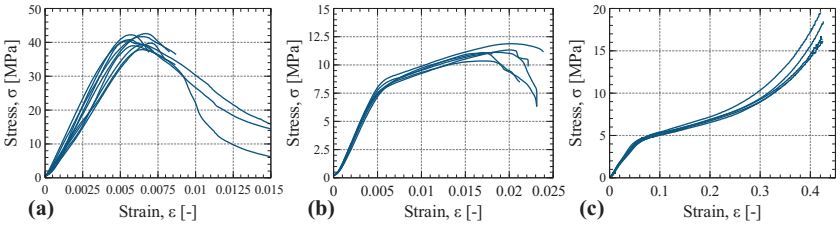

Figure 13. Stress–strain plots of the compression tests C-1 (**a**), C-2 (**b**), and C-3 (**c**).

(**a**) (**b**) (**c**)

Figure 14. Pictures of specimens tested in compression: C-1 (**a**), C-2 (**b**), and C-3 (**c**).

4.2. Tension Tests

The stress–strain plots for the tension tests conducted in the three main orthogonal directions are presented in Figure 15. In both the longitudinal (tests T-1) and tangential direction (tests T-2) tensile tests, the stress–strain curves exhibited an initial linear relationship, wherein stresses increased with strain. Subsequently, the specimens reached a maximum force, and failure of the veneers occurred. Following this peak, the stress–strain curve underwent a sharp turn, with stresses decreasing at varying rates across all specimens. Most of the specimens tested in the radial direction (tests T-3) displayed an initial linear stress–strain relationship, characterized by increasing stresses with strain. This was followed by a transition to non-linear behavior, along with a rapid force drop immediately after reaching the peak load, indicating specimen failure.

Figure 16 depicts images of specimens tested in shear at the point of failure. In the case of specimens tested in the longitudinal direction (T-1), the veneers exhibited a gradual tension failure, occurring at various locations without localization to a specific section. Consequently, in some specimens, the post-peak load drop was relatively gradual and, in others, a brief hardening branch emerged after the load drop. In contrast, during the tensile tests conducted in the tangential direction (T-2), in some specimens, the failure was concentrated in a specific section due to the tension failure of the veneers. Furthermore, in the tensile tests conducted in the radial direction (T-3), the observed failure mode was in some cases localized at a well-defined horizontal plane. At this plane, the fibers of a specific wood layer were pulled apart. In other cases, the tensile force induced shear failure through the veneers of the specimen.

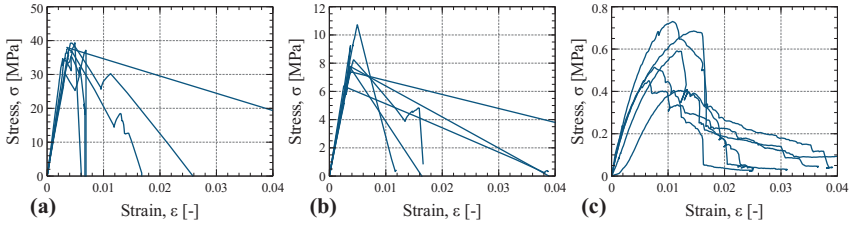

Figure 15. Stress–strain plots of the tension tests T-1 (**a**), T-2 (**b**), and T-3 (**c**).

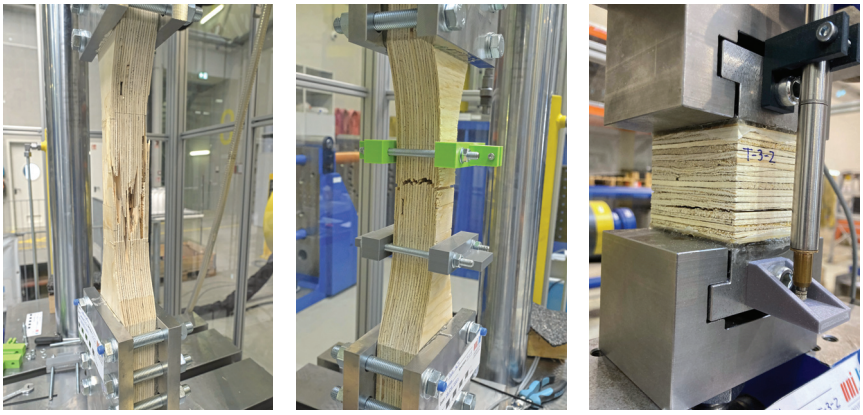

(**a**) (**b**) (**c**)

Figure 16. Pictures of specimens tested in tension: T-1 (**a**), T-2 (**b**), and T-3 (**c**).

4.3. Shear Tests

The shear stress vs. shear strain plots for the six types of shear tests conducted in this experimental study (refer to Figure 3) are presented in Figure 17. In each of the six defined types of shear tests, six specimens were tested. Nevertheless, in the case of tests S-2, two of the specimens experienced failures at the bonding steel–timber interface. Similarly, in tests S-3, one specimen exhibited glue failure. Consequently, the results of these particular tests were excluded from the calculations and were not considered in the final analysis.

Generally, the stress–strain responses of the tested samples followed a similar pattern. There was an initial linear increase in stress with increasing strain, followed by a subsequent force drop that indicated specimen failure. Notably, in tests S-1 and S-2, following this force drop, a plateau phase was observed in which there was no further increase or decrease in load with increasing strain.

Figure 18 presents images showcasing typical failure modes of the tested specimens. In the case of tests S-1, the specimens exhibited a vertical shear plane extending from the top to the bottom. However, this plane did not cut straight through the thickness of the specimen, resulting in the specimen remaining in one piece, with friction between the cut veneers preventing separation. In the S-2 tests, the shearing planes were horizontal and followed the grain direction. The failure mode observed in the S-3 tests was localized to a single veneer in the vertical direction of the specimen, with shear failure occurring along that specific wood layer. For specimens in tests S-4, the failure occurred along a cutting plane aligned horizontally with one of the LVL layers. In the case of tests S-5, the failure crack due to the induced shear propagated from one corner on the top of the specimen to the opposite corner on the bottom. Lastly, in tests S-6, cracks appeared throughout the wood veneers of the specimen, resulting in gradual softening and eventual rupture through some of the layers.

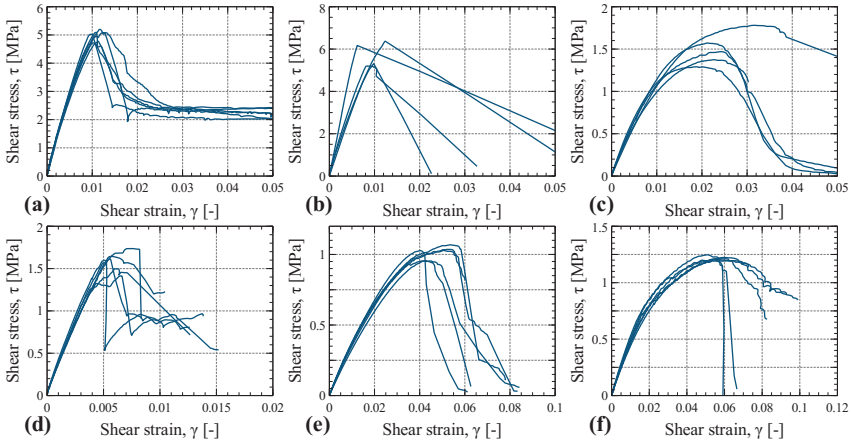

Figure 17. Shear stress vs. shear strain curves of the shear tests: S-1 (**a**), S-2 (**b**), S-3 (**c**), S-4 (**d**), S-5 (**e**), and S-6 (**f**).

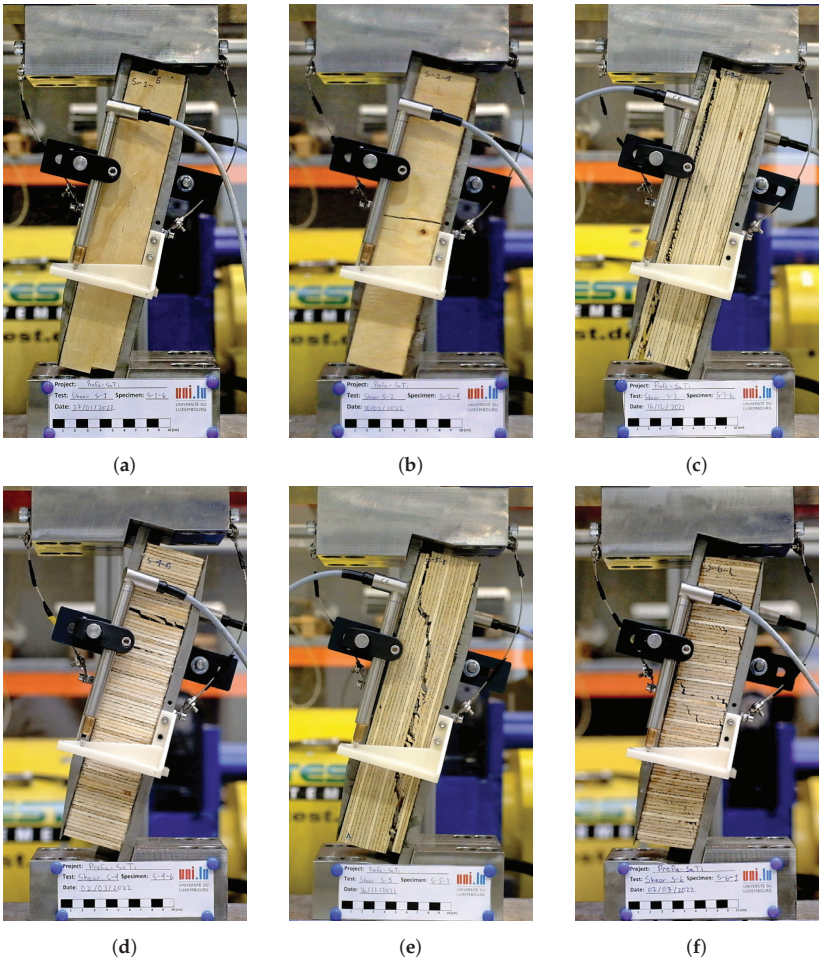

Figure 18. Pictures of specimens tested in shear: S-1 (**a**), S-2 (**b**), S-3 (**c**), S-4 (**d**), S-5 (**e**), and S-6 (**f**).

4.4. Bending Tests

The load–deflection curves (refer to Figure 19) for two types of bending tests are presented in this investigation: (i) bending flatwise parallel to the grain in the longitudinal direction (B-1 tests), and (ii) bending flatwise perpendicular to the grain in the tangential direction (B-2 tests). The peak loads achieved in these two types of tests differ significantly in magnitude, with B-1 tests reaching peak loads approximately five times greater than those observed in B-2 tests. Nevertheless, the specimens of both test types exhibited a similar load–slip response pattern. Initially, midspan deflection increased linearly up to the point of peak load, followed by a subsequent force drop attributed to the failure of some veneers.

In some specimens, following this initial drop, the panel exhibited the ability to carry additional load, resulting in a short branch where load increased in tandem with midspan deflection. Ultimately, a sudden load drop marked the failure of the specimen.

Images of some of the tested specimens are presented in Figure 20. In the bending tests in the longitudinal direction B-1, gradual failure of the bottom fibers was observed occurring at different locations within the region of the points of load application. A similar failure mode was observed in the bending tests conducted in the tangential direction, where the failure was initiated at the bottom fibers near one of the points of load application.

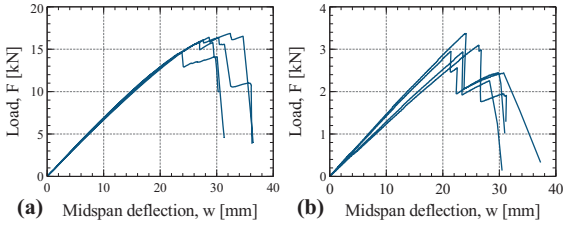

Figure 19. Load–deflection curve of tests B-1 (**a**) and B-2 (**b**).

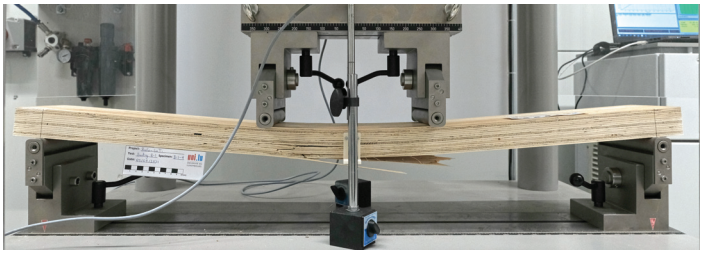

(**a**)

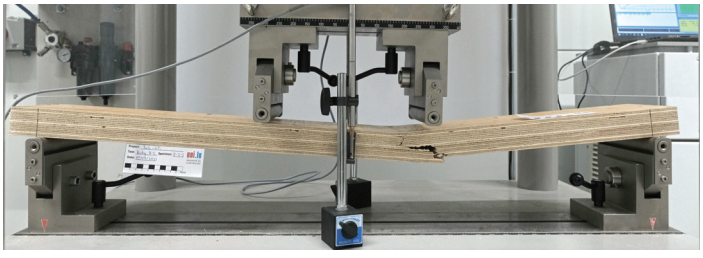

(**b**)

Figure 20. Pictures of specimens tested in bending: B-1 (**a**) and B-2 (**b**).

4.5. Summary of Strength and Stiffness Values

A summary of the calculated strength and stiffness properties is presented in Table 1 and Table 2, respectively. The values were computed according to EN 408 [18] and EN 789 [19]; more details of the calculation procedures can be found in Appendix A. The 5th percentile (5th P) values of these properties were estimated according to EN 14358 [20].

The longitudinal direction of the LVL-C tested in this study exhibited the best performance in terms of strength and stiffness for both tension and compression, followed by the tangential direction and the radial direction, which showed a very low stiffness and turned into non-linear plastic behavior at quite small stresses. Similarly, the panels tested in bending performed the best in the flatwise bending tests parallel to the grain, and the bending strength and stiffness of the panels tested in flatwise bending perpendicular to the grain were about one fifth of the values obtained in the bending parallel to the grain.

Table 1. Summary of strength properties.

Strength Property	Notation	From Figure 3	Strength [MPa]		
			Mean *	5th P *	CV * [%]
Compression strength parallel to the grain, edgewise (in the longitudinal direction)	$f_{c,1}$	A	40.41	36.11	3.91
Compression strength perpendicular to the grain, edgewise (in the tangential direction)	$f_{c,2}$	B	11.14	9.83	4.44
Compression strength perpendicular to the grain, flatwise (in the radial direction)	$f_{c,3}$	C	3.99	2.99	10.64
Tension strength parallel to the grain, edgewise (in the longitudinal direction)	$f_{t,1}$	D	37.76	34.10	4.11
Tension strength perpendicular to the grain, edgewise (in the tangential direction)	$f_{t,2}$	E	8.33	5.47	17.68
Tension strength perpendicular to the grain, flatwise (in the radial direction)	$f_{t,3}$	F	0.56	0.31	23.04
Shear in the LR-plane with force in the longitudinal direction (edgewise shear parallel to the grain)	$f_{v,21}$	G	4.98	4.40	3.79
Shear in the LT-plane with force in the longitudinal direction (flatwise shear parallel to the grain)	$f_{v,31}$	H	1.50	1.03	12.69
Shear in the TL-plane with force in the tangential direction (flatwise shear perpendicular to the grain)	$f_{v,32}$	I	1.01	0.89	4.57
Shear in the TR-plane with force in the tangential direction (edgewise shear perpendicular to the grain)	$f_{v,12}$	J	5.76	4.16	10.28
Shear in the RT-plane with force in the radial direction (edgewise shear perpendicular to the grain)	$f_{v,13}$	K	1.58	1.32	7.17
Shear in the RL-plane with force in the radial direction (edgewise shear perpendicular to the grain)	$f_{v,23}$	L	1.21	1.07	1.51
Bending parallel to the grain in the longitudinal direction (flatwise bending parallel to the grain)	$f_{m,1}$	M	49.01	40.82	6.16
Bending perpendicular to the grain in the tangential direction (flatwise bending perpendicular to the grain)	$f_{m,2}$	N	9.51	7.83	6.53

* Evaluated according to EN 14358 for the number of specimens tested in each type of test.

Table 2. Summary of stiffness properties.

Stiffness Property	Notation	From Figure 3	Stiffness [MPa]		CV * [%]
			Mean *	5th P *	
MoE in compression parallel to the grain, edgewise (in the longitudinal direction)	$E_{c,1}$	A	7 917.08	7 626.51	17.29
MoE in compression perpendicular to the grain, edgewise (in the tangential direction)	$E_{c,2}$	B	1 764.47	1 737.85	4.44
MoE in compression perpendicular to the grain, flatwise (in the radial direction)	$E_{c,3}$	C	95.49	93.83	5.74
MoE in tension parallel to the grain, edgewise (in the longitudinal direction)	$E_{t,1}$	D	10 680.01	10 174.84	15.67
MoE in tension perpendicular to the grain, edgewise (in the tangential direction)	$E_{t,2}$	E	2 199.90	2 140.77	8.91
MoE in tension perpendicular to the grain, flatwise (in the radial direction)	$E_{t,3}$	F	92.05	84.30	27.88
Shear modulus in the LR-plane with force in the longitudinal direction (edgewise shear parallel to the grain)	$G_{v,21}$	G	582.82	573.59	5.25
Shear modulus in the LT-plane with force in the longitudinal direction (flatwise shear parallel to the grain)	$G_{v,31}$	H	123.26	119.48	9.23
Shear modulus in the TL-plane with force in the tangential direction (flatwise shear perpendicular to the grain)	$G_{v,32}$	I	34.27	33.75	4.86
Shear modulus in the TR-plane with force in the tangential direction (edgewise shear perpendicular to the grain)	$G_{v,12}$	J	765.22	691.18	25.87
Shear modulus in the RT-plane with force in the radial direction (edgewise shear perpendicular to the grain)	$G_{v,13}$	K	342.96	336.90	5.86
Shear modulus in the RL-plane with force in the radial direction (edgewise shear perpendicular to the grain)	$G_{v,23}$	L	49.09	44.99	7.90
Global MoE in bending parallel to the grain in the longitudinal direction (flatwise bending parallel to the grain)	$E_{m,1}$	M	10 193.74	10 003.05	1.84
Global MoE in bending perpendicular to the grain in the tangential direction (flatwise bending perpendicular to the grain)	$E_{m,2}$	N	2 004.94	1 944.65	8.04

* Evaluated according to EN 14358 for the number of specimens tested in each type of test.

5. Conclusions

This study aimed to fill a significant knowledge gap by providing comprehensive information about the mechanical properties of laminated veneer lumber (LVL-C) made from Scandinavian spruce wood. The investigation included the determination of strength, moduli of elasticity, and shear moduli through a series of tests, including compression,

tension, shear, and bending. Additionally, the study presents the testing procedures, load–deformation responses, and descriptions of observed failure modes.

The mechanical properties obtained in this research are crucial for analyzing the load–deformation behavior and capacity of various structural components implementing LVL-C crafted from Scandinavian spruce wood, including pure timber, steel–timber, and timber–concrete load-bearing elements. These properties can be employed in analytical calculations and incorporated into numerical models, such as finite element models, to explore the deformation and failure of structural members.

In addition to the property values, stress–strain responses, and load–deformation behavior, the key findings of this study are as follows:

- In compression and tension tests, the longitudinal direction exhibits the highest strength and stiffness, followed by the tangential and radial directions.
- Stress–strain responses in compression differ among the three directions, with the longitudinal direction showing softening after reaching the peak, the tangential direction exhibiting hardening after the proportional limit, and the radial direction demonstrating significant deformation capacity and a hardening branch after the proportional limit.
- Tension tests shows a sharp transition in which the load starts to decrease, which happens when the fibers in the matrix of the specimen fail in tension; however, the failure in some cases is not sudden as the failure is not localized at a specific section but rather in an irregular pattern, and friction remains within the fractured veneers.
- Shear tests S-3 to S-6 exhibit a near-brittle post-peak response, marked by sudden load drops after reaching the peak. In contrast, shear tests S-1 and S-2 show a post-peak behavior with a gradual load decrease due to ongoing inter-layer friction.
- Bending tests reveal that failure occurs at the soffit. Gradual failure on a layer-by-layer basis is observed, with load drops occurring when the most stressed layers of the soffit fail. Ultimately, a final sudden load drop is associated with the fracture of the matrix.

These findings contribute valuable insights into the mechanical behavior of LVL-C crafted with Scandinavian spruce wood, enhancing its applicability in various engineering contexts.

Author Contributions: Conceptualization, A.R. and C.O.; Methodology, A.R. and C.O.; Validation, A.R. and C.O.; Formal analysis, A.R. and C.O.; Investigation, A.R. and C.O.; Resources, C.O.; Data curation, A.R.; Writing—original draft, A.R.; Writing—review & editing, A.R. and C.O.; Visualization, A.R.; Supervision, C.O.; Funding acquisition, C.O. and A.R. All authors have read and agreed to the published version of the manuscript.

Funding: This research and the APC were funded by Fonds National de la Recherche Luxembourg (FNR) and PREFALUX, and supported by ArcelorMittal Luxembourg, within the framework of the research project "Prefa-SeTi: Steel-Timber Composite Beams", Grant No. 15695062.

Institutional Review Board Statement: Not applicable.

Informed Consent Statement: Not applicable.

Data Availability Statement: Data are contained within the article.

Acknowledgments: The authors gratefully acknowledge the Luxembourg's National Research Fund (FNR), Prefalux, ArcelorMittal, and MetsäWood for their support in the research project Prefa-SeTi: Steel-Timber Composite Beams (PhD Industrial Fellowship Grant No. 15695062). The authors wish to also thank the laboratory team (Gilbert Klein, Marc Seil and Ed Weyer) and the former student Melis Pelivani for their support in this testing campaign.

Conflicts of Interest: The authors declare no conflict of interest.

Appendix A. Calculation Procedures of Strength and Stiffness Properties

The calculation procedures followed in this study for the computation of the presented strength and stiffness values have been taken from EN 408 [18] and EN 789 [19]. The formulas and the figures presented in this annex were reproduced from these standards.

Appendix A.1. Compression and Tension Tests

The calculation of the modulus of elasticity (E) and the strength (f) in compression and tension tests was carried out according to Formulas (A1) and (A2):

$$E = \frac{(F_2 - F_1)l}{(u_2 - u_1)A} \tag{A1}$$

$$f = \frac{F_{max}}{A} \tag{A2}$$

where:

$F_2 - F_1$ is an increment in load on the regression line with a correlation coefficient of 0.99 or better;

l is the initial gauge length;

$u_2 - u_1$ is the increment in deformation corresponding to $F_2 - F_1$;

F_{max} is the maximum force reached during the test;

A is the cross-sectional area of the specimen.

The determination of the modulus of elasticity in compression tests (C-1 and C-2) and in tension tests (T-1, T-2, and T-3) was performed by considering a load increment ($F_2 - F_1$) between 10% and 40% of the maximum applied load (F_{max}) as illustrated in Figure A1a. In compression in the radial direction (C-3), the load–deformation curves differ from the typical curves obtained in the other tests. In this case, the hardening branch increases monotonically and there is no clear turning point in which a maximum load is reached followed by softening and failure. Therefore, a different iterative procedure is defined for these tests according to EN 408 [18] as follows:

1. Using the test results, plot the load–deformation curve in the form shown in Figure A1b.
2. Calculate F_1 ($0.1F_{max}$) and F_2 ($0.4F_{max}$) and determine where these values intersect the load–deformation curve.
3. Through these two points, draw the straight line 1 as shown in Figure A1b.
4. Parallel to line 1, draw line 2 having its origin at load $F = 0$ and at a distance from it equivalent to a deformation of $0.1h_0$ as shown in Figure A1b, where h_0 is the initial height of the specimen.
5. Where line 2 intersects the curve of the test results is F_{max}. If the value of F_{max} as determined is within 5% of the initially F_{max} value estimated in step 2, then that value may be used to determine the compressive strength; otherwise, repeat the procedure until a value of F_{max} within that tolerance is obtained.

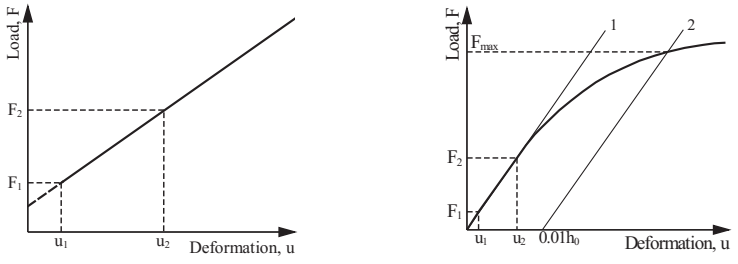

(**a**) (**b**)

Figure A1. Plots illustrating the parameters of Formulas (A1) and (A2) for (**a**) compression tests (C-1 and C-2), tension tests (T-1, T-2, and T-3), and (**b**) compression tests (C-3).

Appendix A.2. Shear Tests

The calculation of the shear modulus (G) and the shear strength (f_v) in shear tests was performed according to Formulas (A3) and (A4):

$$G = \frac{\Delta\tau}{\Delta\gamma} = \frac{(F_2 - F_1)\cdot\cos\alpha\cdot t}{l\cdot b\cdot(x_2 - x_1)} \tag{A3}$$

$$f_v = \frac{F_{max}\cdot\cos\alpha}{l\cdot b} \tag{A4}$$

where:

τ is an increment in shear stress;

γ is an increment in shear strain;

$F_2 - F_1$ is an increment in load on the regression line with a correlation coefficient of 0.99 or better;

$x_2 - x_1$ is the increment in relative displacement of the parallel steel plates corresponding to $F_2 - F_1$;

F_{max} is the maximum applied load;

α is the angle between the longitudinal direction of the specimen and the direction of the applied load;

l is the length of the specimen;

b is the width of the specimen;

t is the thickness of the specimen.

The computation of the shear modulus from shear tests (S-1 to S-6) was performed by considering a load increment ($F_2 - F_1$) between 10% and 40% of the maximum applied load (F_{max}) as illustrated in Figure A2.

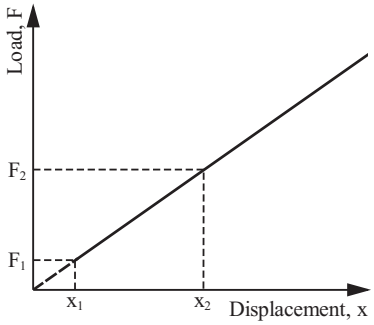

Figure A2. Plot illustrating the parameters of Formulas (A3) and (A4) for shear tests (S-1 to S-6).

Appendix A.3. Bending Tests

The calculation of the global bending modulus of elasticity (E_m) and the bending strength (f_m) in bending tests was performed according to Formulas (A5) and (A6):

$$E_m = \frac{3al^2 - 4a^3}{2bh^3\left(2\cdot\frac{w_2 - w_1}{F_2 - F_1} - \frac{6a}{5Gbh}\right)} \tag{A5}$$

$$f_m = \frac{3aF_{max}}{bh^2} \tag{A6}$$

where:

l is the distance between the two supports;

a is the distance between a loading position and the nearest support;

b is the width of the specimen;

h is the height of the specimen;

$F_2 - F_1$ is an increment in load on the regression line with a correlation coefficient of 0.99 or better;

$w_2 - w_1$ is the increment in midspan deflection corresponding to $F_2 - F_1$;

G is the shear modulus;

F_{max} is the maximum applied load.

The estimation of the global modulus of elasticity in bending was carried out by considering a load increment ($F_2 - F_1$) between 10% and 40% of the maximum applied load (F_{max}) as illustrated in Figure A3.

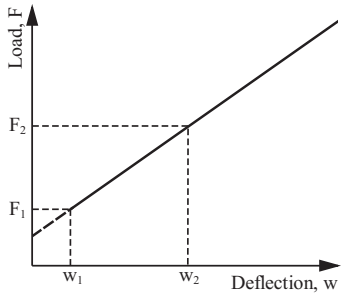

Figure A3. Plot illustrating the parameters of Formulas (A5) and (A6) for bending tests (B-1 and B-2).

References

1. OECD. *Global Material Resources Outlook to 2060: Economic Drivers and Environmental Consequences*; OECD Publishing: Paris, France, 2019. [CrossRef]
2. D'Amico, B.; Pomponi, F.; Hart, J. Global potential for material substitution in building construction: The case of cross laminated timber. *J. Clean. Prod.* **2021**, *279*, 123487. [CrossRef]
3. Kuzmanovska, I.; Gasparri, E.; Tapias Monné, D.; Aitchison, M. Tall Timber Buildings: Emerging trends and typologies. In Proceedings of the 2018 World Conference on Timber Engineering, Seoul, Republic of Korea, 20–23 August 2018.
4. Chiniforush, A.A.; Akbarnezhad, A.; Valipour, H.; Xiao, J. Energy implications of using steel-timber composite (STC) elements in buildings. *Energy Build.* **2018**, *176*, 203–215. [CrossRef]
5. Hassan, O.A.; Öberg, F.; Gezelius, E. Cross-laminated timber flooring and concrete slab flooring: A comparative study of structural design, economic and environmental consequences. *J. Build. Eng.* **2019**, *26*, 100881. [CrossRef]
6. Finnish Woodworking Industries. *LVL Handbook*; Federation of the Finish Woodworking Industries: Helsinki, Finland, 2019.
7. Hassanieh, A.; Valipour, H.; Bradford, M. Experimental and numerical study of steel-timber composite (STC) beams. *J. Constr. Steel Res.* **2016**, *122*, 367–378. [CrossRef]
8. Romero, A.; Yang, J.; Hanus, F.; Odenbreit, C. Numerical Investigation of Steel-LVL Timber Composite Beams. *ce/Papers* **2022**, *5*, 21–30. [CrossRef]
9. Romero, A.; Yang, J.; Odenbreit, C. Bending resistance of steel-timber composite (STC) beams: Analytical vs. numerical investigations. *ce/Papers* **2023**, *6*, 59–64. [CrossRef]
10. Chybinski, M.; Polus, L. Experimental and numerical investigations of laminated veneer lumber panels. *Arch. Civ. Eng.* **2021**, *67*, 351–372. [CrossRef]
11. Van Beerschoten, W.A. Structural Performance of Post-Tensioned Timber Frames under Gravity Loading. Ph.D. Thesis, University of Canterbury, Canterbury, New Zealand, 2013.
12. Ardalany, M.; Deam, B.; Fragiacomo, M. Experimental results of fracture energy and fracture toughness of Radiata Pine laminated veneer lumber (LVL) in mode I (opening). *Mater. Struct.* **2012**, *45*, 1189–1205. [CrossRef]
13. Ardalany, M.; Deam, B.; Fragiacomo, M.; Crews, K. Tension perpendicular to grain strength of wood, Laminated Veneer Lumber (LVL) and Cross-Banded LVL (LVL-C). In *Incorporating Sustainable Practice in Mechanics and Structures of Materials*; CRC Press: London, UK, 2010. [CrossRef]
14. Franke, B.; Quenneville, P. Analysis of the fracture behavior of Radiata Pine timber and Laminated Veneer Lumber. *Eng. Fract. Mech.* **2014**, *116*, 1–12. [CrossRef]
15. Bal, B.C. Some physical and mechanical properties of reinforced laminated veneer lumber. *Constr. Build. Mater.* **2014**, *68*, 120–126. [CrossRef]
16. Sokolović, N.M.; Gavrilović-Grmuša, I.; Zdravković, V.; Ivanović-Šekularac, J.; Pavićević, D.; Šekularac, N. Flexural Properties in Edgewise Bending of LVL Reinforced with Woven Carbon Fibers. *Materials* **2023**, *16*, 3346. [CrossRef] [PubMed]
17. Bakalarz, M.M.; Kossakowski, P.G. Strengthening of Full-Scale Laminated Veneer Lumber Beams with CFRP Sheets. *Materials* **2022**, *15*, 6526. [CrossRef] [PubMed]

18. *EN 408:2010*; Timbe Structures—Structural Timber and Glued Laminated Timber—Determination of Some Physical and Mechanical Properties. CEN: Brussels, Belgium, 2012.
19. *EN 789*; Timber Structures—Test Methods—Determination of Mechanical Properties of Wood Based Panels. CEN: Brussels, Belgium, 2014.
20. *EN 14358*; Timber Structures—Calculation and Verification of Characteristic Values. CEN: Brussels, Belgium, 2015.

materials

MDPI

Article

Influence of Fire Exposition of Fibre-Cement Boards on Their Microstructure

Krzysztof Schabowicz [1], Tomasz Gorzelańczyk [1], Łukasz Zawiślak [1,*] and Filip Chyliński [2]

[1] Faculty of Civil Engineering, Wrocław University of Science and Technology, Wybrzeże Wyspiańskiego 27, 50-370 Wrocław, Poland; krzysztof.schabowicz@pwr.edu.pl (K.S.); tomasz.gorzelanczyk@pwr.edu.pl (T.G.)
[2] Instytut Techniki Budowlanej, Filtrowa 1, 00-611 Warszawa, Poland; f.chylinski@itb.pl
* Correspondence: lukasz.zawislak@pwr.edu.pl

Abstract: The diagnostics of materials, elements and structures after fire exposure are very complicated. Researchers carrying out such diagnostics encounter difficulties at the very beginning, e.g., how to map fire conditions. In this publication, the authors focused on the analysis of the fibre-cement composite used as facade cladding. The fibre-cement boards are construction products used in civil engineering. The fibre-cement boards are characterised by two phases: the matrix phase and the dispersed phase. The analysis of fibre-cement composite was performed using non-destructive methods. The use of non-destructive methods in the future will allow for the analysis of facades after fires without the need to obtain large elements, which will significantly reduce costs while increasing safety. The aim of the work was to determine internal changes in the microstructure of fibre-cement boards after exposure to fire. The degraded samples were compared with reference samples in the evaluation of the microstructure. An analysis was performed using a scanning electron microscope, images of backscattered electrons (BSE) and maps obtained using Energy Dispersive X-ray Spectroscopy (EDX), which allowed conclusions to be drawn. The observed changes were presented in the form of photos showing changes in the composition of the plates, and they were commented on. It should be noted that fire temperatures act destructively, and a number of changes can be observed in the microstructure. The results of the work indicate that, in the future, the use of non-destructive methods will make it possible to assess the degree of degradation of the façade after a fire.

Keywords: fibre-cement boards; composites; exposure to fire; microstructural examination; scanning electron microscope; fibres

Citation: Schabowicz, K.; Gorzelańczyk, T.; Zawiślak, Ł.; Chyliński, F. Influence of Fire Exposition of Fibre-Cement Boards on Their Microstructure. *Materials* **2023**, *16*, 6153. https://doi.org/10.3390/ma16186153

Academic Editor: Andreas Lampropoulos

Received: 9 August 2023
Revised: 3 September 2023
Accepted: 7 September 2023
Published: 10 September 2023

1. Introduction

Fires present very dangerous situations, especially in the case of buildings used by people. They cause a lot of damage, which is also reflected in the elements, materials, structures, etc. After performing the rescue operation and extinguishing the fire, its diagnostics is important for the further survival of the building. The facades were usually completely dismantled after such an impact; the authors note that diagnostics using non-destructive methods will make it possible to determine whether these elements pose a threat. The authors focused on the analysis of fibre-cement boards using non-destructive methods which, in the future, may be used to diagnose real elements and facades.

The fibre-cement boards are construction products that have been used in civil engineering since the beginning of the 20th century. In the 1990s, the product was modified, and asbestos fibres that are dangerous to health were replaced with other fibres, mainly cellulose ones. Fibre-cement boards are composite materials consisting of two phases, including a continuous matrix phase surrounding the other phase, called a dispersed phase (strengthening elements). A schematic diagram showing the division of the phases is presented in Figure 1.

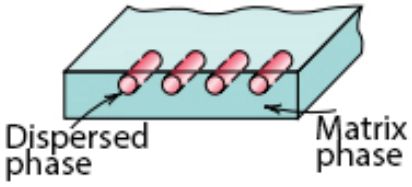

Figure 1. Two phases of composite materials [1].

Fibre-cement boards are fibre-reinforced composite materials characterised by two phases. The first one is the matrix phase which, in the referenced board's case, is a Portland-cement-based matrix responsible for matrix bonding and making it durable. The other one is a dispersed phase in the form of fibres. In addition to Portland cement, the matrix contains additional ingredients and fillers, i.e., lime flour, mica, pearlite, kaolin and microspheres [2]. The fibres in the dispersed phase are non-continuously distributed and randomly oriented. The fibres used in board manufacturing include cellulose fibres, PVA (polyvinyl alcohol) fibres and PP (polypropylene) fibres. Most manufacturers of fibre-cement boards use all the fibres mentioned above in the dispersed phase. Each fibre type fulfils a different role. Cellulose fibres form a spatial network reinforcing the whole composite, while PVA and PP fibres are added to improve the strength and durability of fibre-cement boards, especially those intended for outdoor use. Fibre-cement boards are intended for indoor and outdoor use. Outdoors, they are principally used for façade cladding and must meet the requirements set out by harmonised standards [3].

Research on fibre-cement boards in various environmental situations in the scientific literature is constantly being extended. In the field of controlling the current condition of the boards, there are many publications investigating these phenomena [4–8], but such methods cannot be applied to the analysis of burnt boards. The authors, having read the scientific literature, decided to use a non-destructive method for the diagnostics of fibre-cement boards—analysis using scanning electron microscope (SEM). The use of such a method results from the studies of other researchers who studied similar phenomena, such as Schabowicz [9], Verma [10] and Ngo [11].

High temperatures have a significantly degrading impact on most construction materials, including but not limited to fibre-reinforced composites. Scientific papers on fibre-cement boards exposed to fire focus on the evaluation of strength parameters [4].

The characteristics of fibre-reinforced composites in high-temperature conditions were investigated by references [12–16], who used stable heating as the source of fire—which does not match the testing method employed by this study's authors—but many conclusions can be drawn from them.

Szymków [17] carried out tests and evaluated the possibility of re-using fibre-cement boards after exposure to high temperatures. Fibre-cement boards were not exposed to fire (flames) but were prepared as samples and heated in a furnace for some time. The samples were tested in two temperature groups, i.e., 230 °C and 400 °C, for various heating durations in the furnace. The samples heated in the furnace at 230 °C for three hours revealed a MOR (modulus of rupture or flexural strength) that was reduced by 70–80% versus the reference sample. Among the samples exposed to 400 °C for fifteen minutes in the furnace, only one out of five was suitable for performing three-point bending and determining the MOR. The other series lost their strength parameters in a shorter time at 400 °C. One should bear in mind that the temperature inside a furnace is more stable than when façades are exposed to flames in a non-controlled or controlled fire. Szymków [17] unequivocally shows the destructive impact of fire exposure on the load capacity of fibre-cement boards. The fibre-cement boards revealed no or minimum MOR and ED modulus of elasticity up to 1.6 m above the furnace (source of fire). The façade cladding elements from the area most exposed to high temperatures degraded and came off the substrate during the test; they did

not survive the whole test, which lasted sixty minutes. Schabowicz et al. [8] analysed fibre-cement boards after exposure to fire in a real model, using a sound emission method during a three-point bending test. The samples revealed damage through high-energy brittle destruction at a low number of incidents (Nzd), which confirmed that the dispersed phase had been completely degraded.

As described above, the dispersed phase may contain cellulose, PVA and PP fibres. The following melting points characterise each fibre type: PVA (polyvinyl alcohol) fibres—ca. 200–220 °C [18,19]; PP (polypropylene) fibres—ca. 175 °C [18–20]; and cellulose fibres—260–270 °C (decomposition) [21].

In the course of assessing the macrostructure of fibre-cement composites, the work of Gou [22] should be analysed. Gou [22] performed a similar method of obtaining samples and a similar type of analysis, but their analysis did not concern fibre-cement boards, but, more broadly, cellulose fibre-reinforced concrete composites (CFRC). The final conclusions were similar to other studies, whereby the boards burst without warning and the associated structures lost their loading capacity within a short time, but it is also worth analysing all the indirect phenomena that they observe. Concrete gradually degenerates with increasing temperature. At 200 °C, a small amount of visible water vapor escaped. With constant heating, calcium hydroxide—as the main cement hydrate in the concrete—gradually decomposes. At 600 °C, the concrete was almost dehydrated. The water evaporation and decomposition of the components cause mass loss in concrete. Concrete's microstructure is damaged at high temperatures; water vapor pressure and thermal expansion inside the concrete will damage its microstructure. In addition, some cement hydrates (such as calcium silicate hydrate (C–S–H) gels) dehydrate and CH decomposes at a temperature of 800 °C. With heating at 1050 °C, rare bulk hydrates exist in the CFRC but are mainly transformed to glass; it should be noted that such temperatures do not occur on the façade.

The chemical reactions occurring in fibre-cement boards are another vital aspect related to the analysis of the boards' chemical composition. At 105 °C, the free water in the matrix phase starts to evaporate quickly; in the temperature range between 80 and 150 °C, ettringite is dehydrated. The temperatures between 150 and 170 °C represent the gypsum dehydration range [21]. The temperature of ca. 300 °C makes chemically bound water evaporate, which reduces the material's compressive strength. Portlandite decomposes between 400 °C and 540 °C. When the temperature increases over 400 °C, the cement matrix's strength drops faster and decomposes due to the degradation of calcium silicate hydrates (C–S–H), forming β-C2S (β-dicalcium silicate) [21].

Velesick [23] presented that cellulose fibres burn at temperatures of up to 400 °C while the determined endothermic effects end at 389 °C with mass loss of 71–75%, depending on the type of cellulose used for armouring. This is very significant information, but in the case of the tests [23], the course of temperatures was constant, and not variable as in the case of the fire.

For fibre-cement boards, which represent composites, the temperatures degrading the boards' structure (dispersed phase and matrix phase) and the impact of high temperatures on reducing the materials' load capacity are known. Unfortunately, the scientific literature does not mention microstructure analysis in fibre-cement boards degraded by high temperatures. In the case of degradation covered by fire, the strength parameters can be evaluated using MOR tests [4], sound emission tests [24–26] or SEM structure analysis [17].

Having identified the deficiencies in the literature, the authors attempted to determine the impact of high temperatures on the microstructure change in fibre-cement boards and explain the causes of flexural strength changes using a scanning electron microscope (SEM).

2. Materials and Methods

Microstructure tests, on fibre-cement boards degraded due to exposure to high temperatures, were performed in the study.

Samples were taken from the large scale facade model that was exposed to fire. The large scale facade model is a research platform to which the ventilated facade is attached.

The research platform is used to study the impact and development of fire, which is a very good way to study the development of fire and to assess individual elements of the façade in terms of its flammability, the behavior of individual materials in fire conditions, or the fire safety of the entire façade system. Figure 2 shows the course of the test, including the impact of flames coming out of the hearth on the façade cladding.

Figure 2. The large scale facade model during exposure to fire.

Sample D3 was taken from the large-scale facade model that was exposed to fire. The sample was taken from an element that fell off at the 34th minute of the test. The locations of the item used for making the D3 sample for further tests are presented in Figure 3. The temperature course in D3 sources was recorded by thermocouples TE3 TE7; the results of thermocouples are presented in Figure 4.

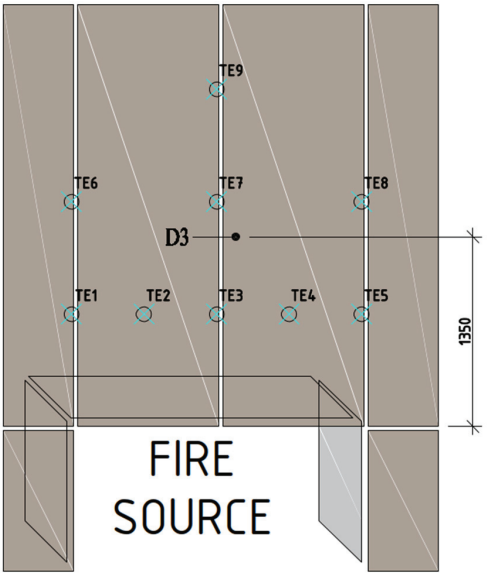

Figure 3. Diagram of external cladding board arrangement for fire impact analysis.

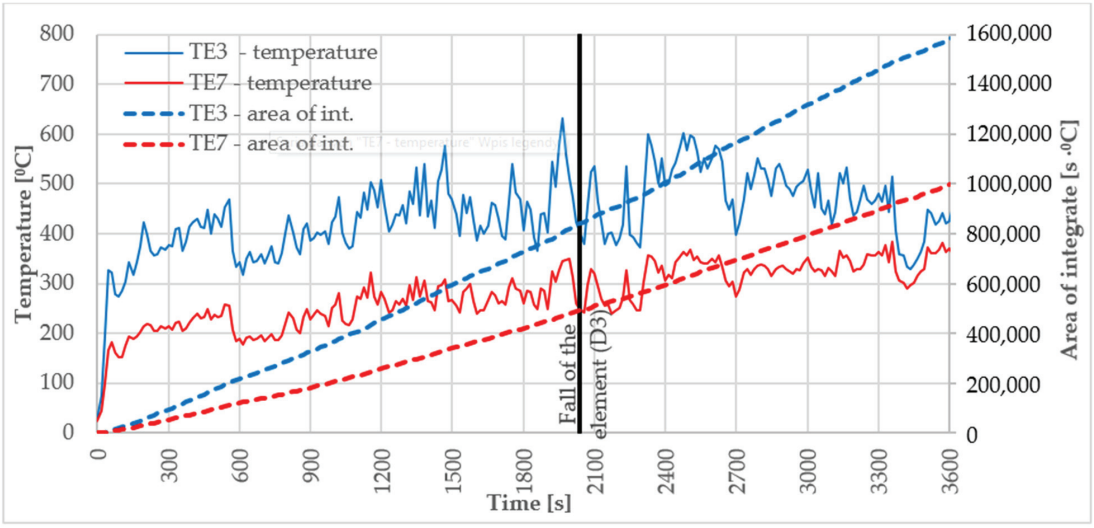

Figure 4. Temperature measurement results for TE3, TE7, thermocouples and the increasing integral for the temperature–time function, along with the determination of the fall-off time D3 element.

The degraded sample analysed in this paper was also subjected to tests using sound emission; the sample's visual assessment was presented in papers by Ngo [11] and Szymków [17], demonstrating its structural destruction.

Polished cross-sections were immersed in resin as well as elements of D.ref (reference board, not exposed to fire) and D3 fibre-cement boards. The section samples are shown in Figure 5. Before the tests, the samples were vacuum-coated with gold using a Quorum model Q 150R ES coater. The vacuum coating of non-conductive materials with gold is necessary since scanning electron microscopy requires removing the electric charge from the analysed sample's surface. Vacuum coating with gold is commonly used for analysing cement composite samples [27]. The samples were cut out from the reference board and from a façade cladding piece which came off the large scale façade model exposed to fire (shown in Figures 2 and 3).

Figure 5. Section samples for scanning microscope examination.

The examination was carried out using a Sigma 500 VP scanning electron microscope from Carl Zeiss (Jena, Germany), as shown in Figure 6. BSE images and Energy Dispersive X-ray Spectroscopy (EDX) maps were recorded during the examination. EDX works

together with SEM to provide qualitative and semi-quantitative results. Both techniques together have the potential to introduce basic information about the material composition of scanned samples, which could not be obtained by other laboratory techniques.

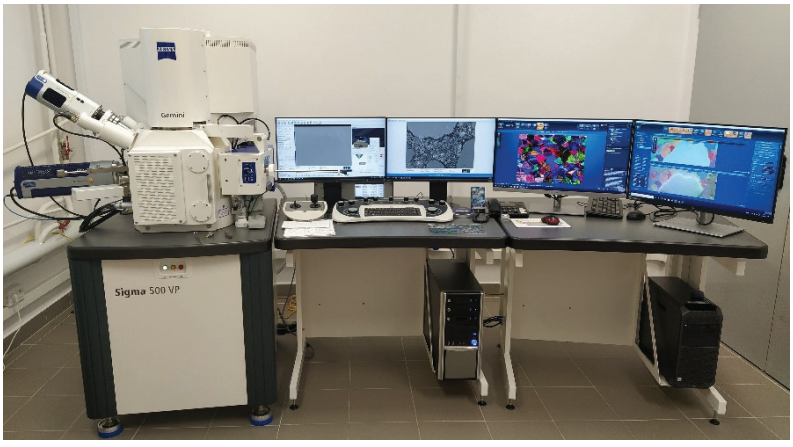

Figure 6. Scanning electron microscope from Carl Zeiss, Sigma 500 VP.

For the sake of this paper, two microscope options were used, analysing the material's microstructure and elemental composition.

The elemental composition in the micro area and mapping were performed with an EDX detector, Ultim Max 40 from Oxford Instruments (Abingdon, UK), using AztekLive software v. 6.0 SP2. The device, including the detectors and the test chamber, is shown in Figure 7.

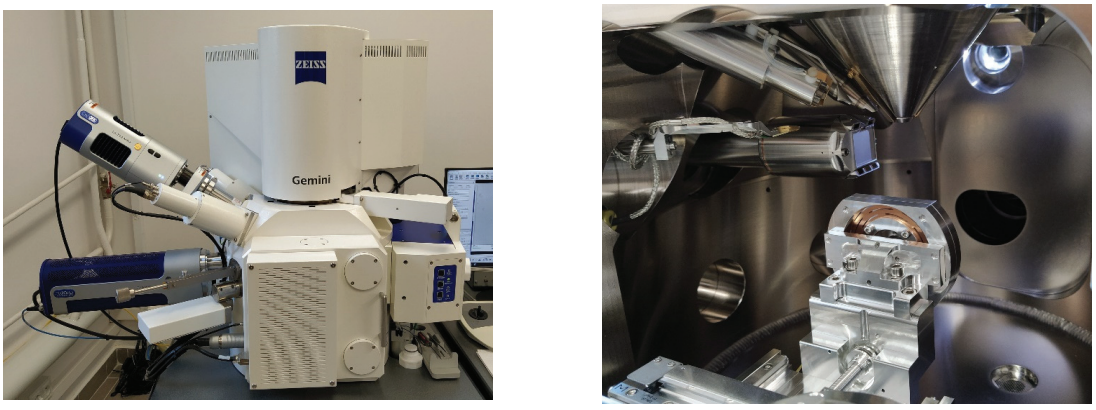

(**a**) (**b**)

Figure 7. Sigma 500 VP scanning electron microscope from Carl Zeiss: (**a**) device, (**b**) test chamber.

The item from which the D3 sample was collected came off during the test in the ca. 34th minute. The maximum temperatures in this location ranged between 300 and 400 °C.

It should be noted that the article may be an introduction to the diagnosis of façades that have been destroyed by fire.

3. Results

Figure 8 shows a summary of sample images of the D.ref and D3 samples' microstructure. The microstructure observations were carried out on the polished cross-sections' microstructure using a BSD (Backscattered Electron Detector), and mapping was performed with an EDX (Energy Dispersive Spectroscopy). The sections were observed with an SE (Secondary Electron) detector.

Figure 9 summarises the share of elements in the reference and degraded samples' structures.

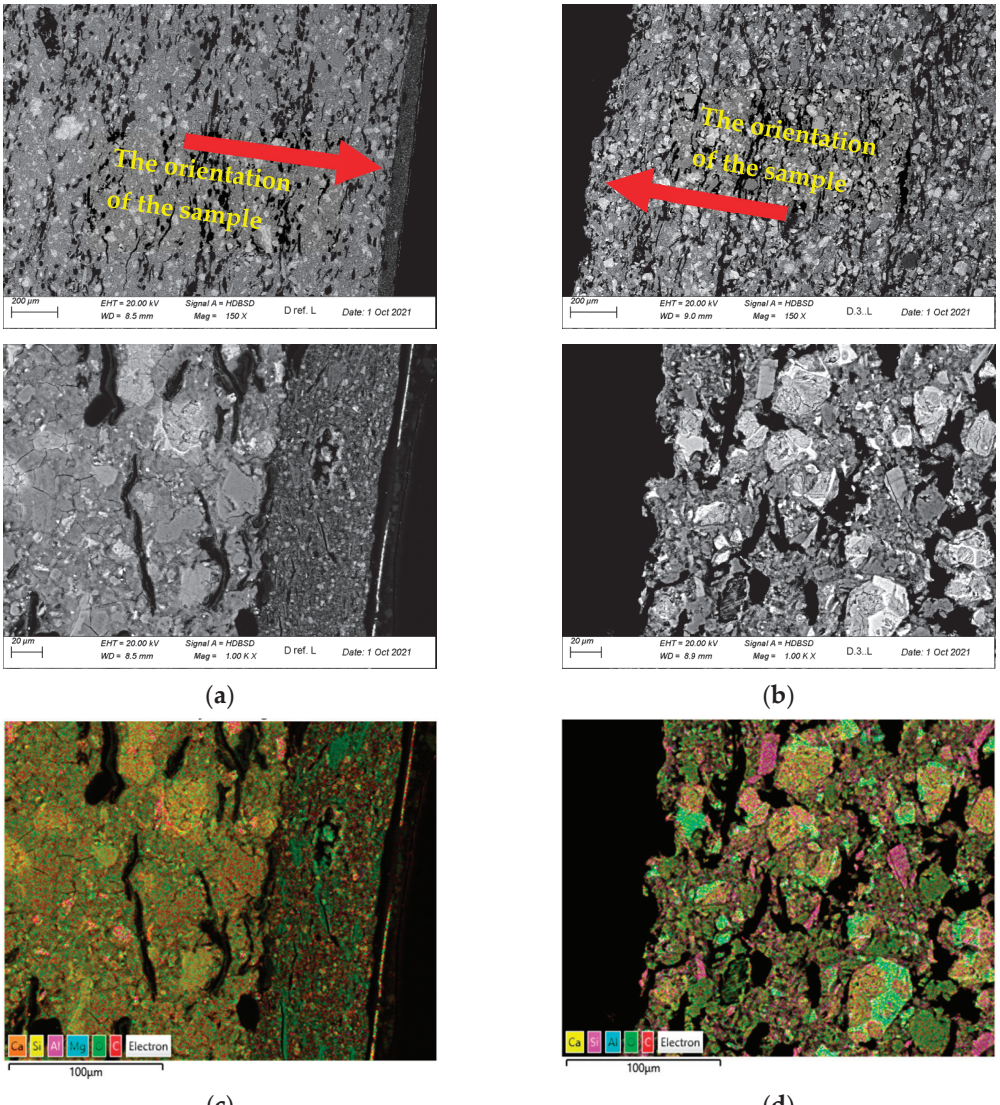

Figure 8. *Cont.*

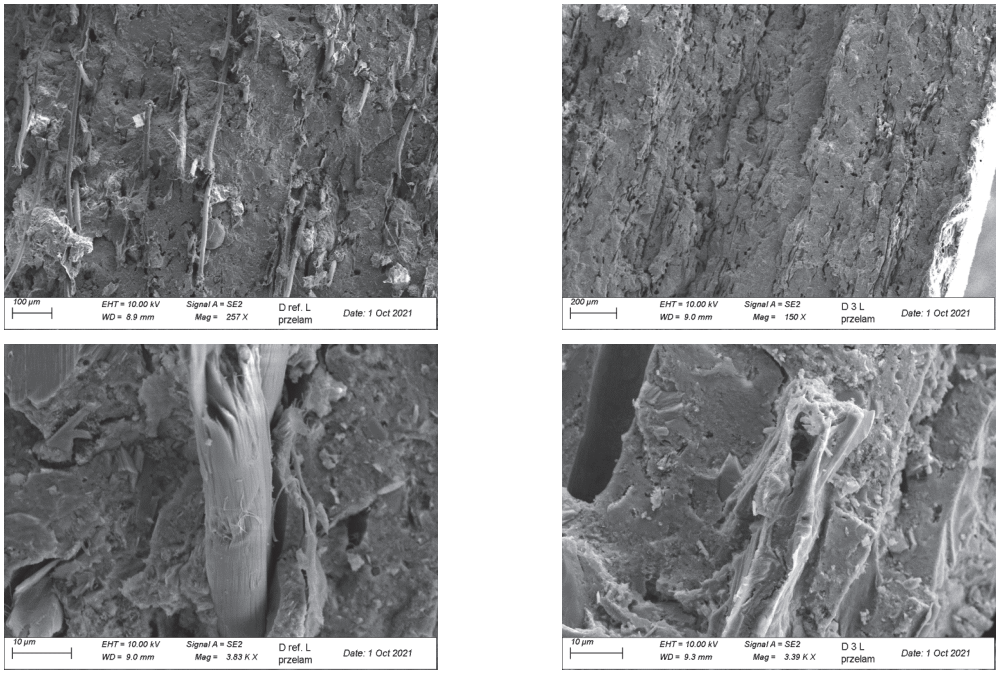

(**e**) (**f**)

Figure 8. Summary of sample images of the analysed D.ref and D3 samples' structures: (**a**) D.ref sample—section's BSD images; (**b**) D3 sample—section's BSD images; (**c**) D.ref sample—section's EDX map; (**d**) D3 sample—section's EDX map; (**e**) D.ref sample—fracture's SE images; (**f**) D3 sample—fracture's SE images.

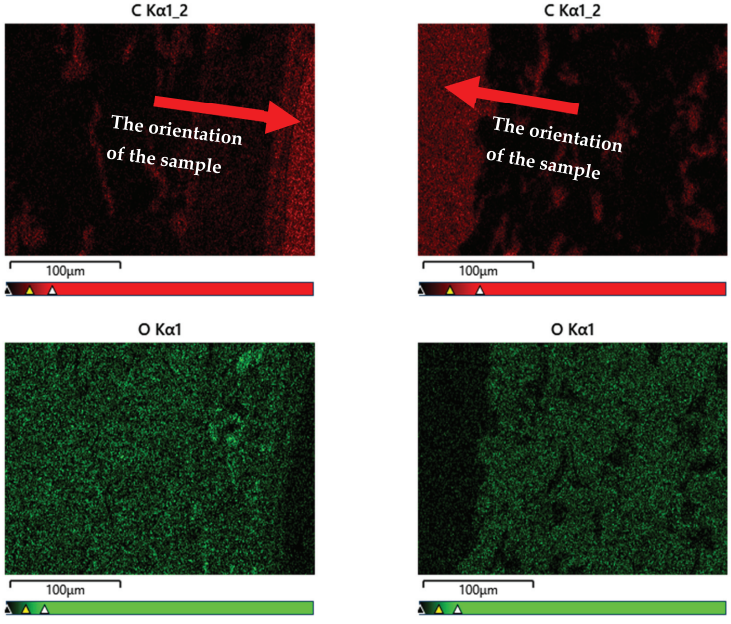

Figure 9. *Cont.*

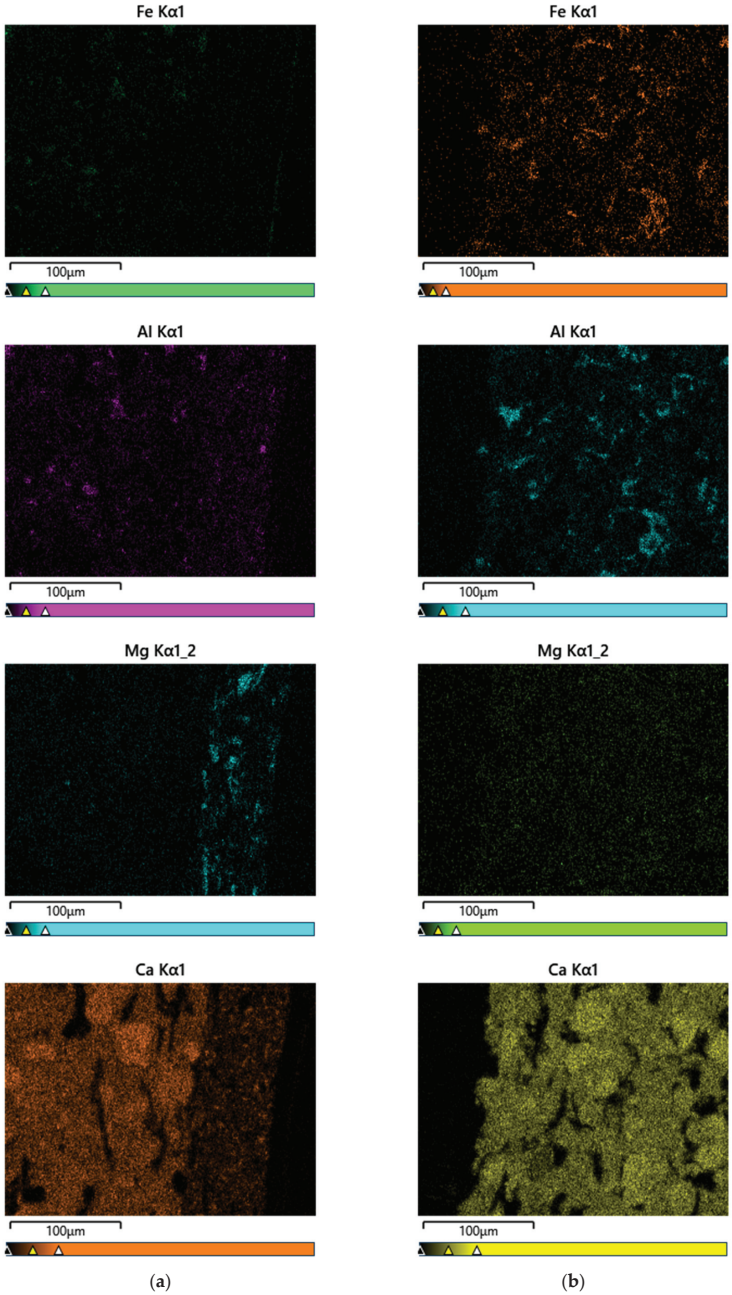

Figure 9. Summary of sample images of the analysed D.ref. and D3 samples' structures: (**a**) D.ref sample—section's BSD images; (**b**) D3 sample—section's BSD images.

An analysis of the images shown in Figure 8 revealed the board's compact structure, with visible cement binder grains on the D ref. sample's sections. Air pores elongated in the direction parallel to the boards' surface were present. The cellulose fibres present in the sample were typically parallel to the board's surface. The structure's apparent anisotropy

results directly from the manufacturing process. The fibres' arrangement in the structure favourably affects the composite's flexural strength. In the D ref. sample, the board's textured top layer was more compact than the substrate and relatively well-bound with the composite. Additionally, it was covered with a thin coat of paint on the outer side. The cellulose fibres observed on the fractures were well bound in the cement matrix and, as a result of the sample's bending, most fibres were broken and pulled out of the matrix, which is a testimony to the fact that the fibres' adhesion to the matrix fibres significantly exceeds the fibres' tensile strength.

During the tests on the real model, the D3 sample was exposed to temperatures between 300 and 400 °C for over thirty minutes. It revealed significant microstructure changes compared to the D ref. sample. The board's textured and thin paint layers were completely degraded and delaminated. The degraded sample's surface was not uniform and was characterised by protruding gaps. The tested composite's porosity increased significantly, which could have been caused by releasing thermal decomposition gas products and the pyrolysis of some of the composite's ingredients. At the temperature observed during the tests, one should expect a loss of non-bound and bound water from the C–S–H phase. Moreover, ettringite decomposition could occur, releasing significant amounts of steam. Furthermore, the portlandite contained in the structure could start to decompose, especially in the sample areas near the surface, where the temperature was higher. Cellulose fibres were subjected to pyrolysis throughout the board's observed cross-section thickness, leaving empty voids inside the structure; the voids were sometimes filled with solid decomposition products. An analysis of the sections' structures revealed no fibres that could transfer mechanical loads during bending. Only empty voids were observed in the cement matrix, left after the fibres; in a few cases, they were filled with decomposition products.

Figure 9 shows the D.ref and D3 samples that were analysed using the BSD image. In terms of the share of the carbon element (C), its significant share is visible in the near-surface zone—in the hardener layer and in the paint coating. These layers were completely degraded by the high temperature in sample D3. In the case of the element oxygen (O), due to the degradation of the near-surface zone of the D3 sample, its smaller amounts are noticeable. The share of the element oxygen (O) in the degraded sample is much smaller due to its participation in the combustion process (chemical reactions), where, as a consequence, after its participation in the chemical reaction of combustion, the sample is weakened.

The above changes in the composition of the microstructure confirm that the fibre-cement board is subject to significant degradation and its usefulness is significantly limited.

4. Discussion

The impact of high temperatures on materials is intrinsically destructive. The time in which materials or products maintain the required properties is the high-temperature impact range. The maximum values of temperatures observed in the large scale façade model were from 500 °C to 700 °C. For the degraded sample analysed in the paper, the temperatures ranged from 300 °C to 400 °C. The destructive impact of high temperature on the tested fibrous cement boards' structure becomes evident when analysing the results of a three-point bending test determining the flexural strength (MOR). Our own studies involved a composition and microstructure analysis of the reference samples and samples exposed to fire. The study was designed to explain the reasons for the observed sudden loss in the board's elasticity in the temperature range from 300 to 400 °C.

The results of fibre-cement boards' microstructural tests help explain the causes of the obtained flexural strength (MOR) values. Exposure to temperatures between 300 and 400 °C leads to irreversible microstructure changes, causing the relaxation and decomposition of cellulose fibres. Fibre decomposition directly contributes to the changes in the nature of the entire composite's mechanical properties, including but not limited to the material's response to bending force. A material deprived of fibres becomes

more brittle as it contains no ingredient that could take some of the impacting force after a scratch is formed in the composite. This is also confirmed in other studies [22,23].

The first noticeable phenomenon at the temperature observed during the tests (300 to 400 °C) is the loss of non-bound and bound water from the C–S–H phase. In the case of furnace studies, this was also the first phenomenon to occur [22].

In addition, along with the duration of the fire, an increase in the carbon element (C), and a decrease in the oxygen element (O), can be observed.

The tests unequivocally revealed that fibre degradation leads directly to the changes in the nature of the whole composite's mechanical properties, including but not limited to the material's response to the bending force. A material deprived of fibres becomes more brittle, indicating high-energy fracture as the destruction method. Moreover, it shall be underlined that a microstructural analysis of fibre-cement boards enables determining the boards' degradation rate and provides information about their re-use potential.

5. Conclusions

To conclude, the authors would like to emphasise that the tests in this study are significant from the point of view of building practice in general, as well as science, since previously, the literature made no mention of fibre-cement boards' microstructure analysis and the changes after exposure to fire. An analysis of fibre-cement board's microstructure enables the determining of the board's degradation rate. The tests can be used independently or as part of a broader test scope in order to determine the board's destruction rate. The most important conclusions are presented below:

1. Exposure to temperatures between 300 and 400 °C leads to irreversible microstructure changes, causing the relaxation and decomposition of cellulose fibres. A material deprived of fibres becomes more brittle as it contains no ingredient that could take some of the impacting force after a scratch is formed in the composite.
2. Fibre decomposition directly contributes to the changes in the nature of the entire composite's mechanical properties, including but not limited to the material's response to bending force.
3. The first changes in the microstructure appear after the loss of the paint and texture coatings.
4. Non-destructive SEM methods enable the diagnosis of fibre-cement boards after exposure to fire.

The conclusions presented above show that an analysis of the microstructure of fibre-cement boards confirms the degree of degradation of the boards, which can be used to diagnose the type after fires.

Moreover, it should be highlighted that the presented tests are a part of broader scientific research. The authors also carry out tests on fibre-cement boards exposed to fire using other methods.

Author Contributions: Conceptualisation, K.S. and F.C.; methodology, T.G. and F.C.; software, F.C. and Ł.Z.; validation, Ł.Z. and F.C.; formal analysis, Ł.Z.; investigation, T.G.; resources, Ł.Z.; data curation, Ł.Z.; writing—original draft preparation, Ł.Z. and F.C.; writing—review and editing, K.S. and T.G.; visualisation, Ł.Z.; supervision, K.S.; project administration, Ł.Z.; funding acquisition, K.S. and F.C. All authors have read and agreed to the published version of the manuscript.

Funding: This research received no external funding.

Institutional Review Board Statement: Not applicable.

Informed Consent Statement: Not applicable.

Data Availability Statement: Not applicable.

Conflicts of Interest: The authors declare no conflict of interest.

References

1. Callister, W.D.; Tethwisch, D.G. *Materials Science and Engineering: An Introduction*, 10th ed.; Wiley: Hoboken, NJ, USA, 2009; ISBN 978-1-119-40549-8.
2. Hincapié Rojas, D.F.; Pineda-Gómez, P.; Guapacha-Flores, J.F. Effect of silica nanoparticles on the mechanical and physical properties of fibercement boards. *J. Build. Eng.* **2020**, *31*, 101332. [CrossRef]
3. *EN 12467*; Fibre-cement flat sheets—Product specification and test methods. The European Standard. British Standards Institution: London, UK, 2012.
4. Pizzol, V.; Mendes, L.; Savastano, H.; Frías, M.; Davila, F.; Cincotto, M.; John, V.; Tonoli, G. Mineralogical and microstructural changes promoted by accelerated carbonation and ageing cycles of hybrid fibre–cement composites. *Constr. Build. Mater.* **2014**, *68*, 750–756. [CrossRef]
5. Adamczak-Bugno, A.; Świt, G.; Krampikowska, A. Assessment of Destruction Processes in Fibre-Cement Composites Using the Acoustic Emission Method and Wavelet Analysis. *IOP Conf. Ser. Mater. Sci. Eng.* **2019**, *471*, 032042. [CrossRef]
6. Tonoli, G.; Santos, S.; Joaquim, P.; Savastano, H. Effect of accelerated carbonation on cementitious roofing tiles reinforced with lignocellulosic fibre. *Constr. Build. Mater.* **2010**, *24*, 193–201. [CrossRef]
7. Bentchikou, B.; Guidoum, A.; Scrivener, K.; Silhadi, K.; Hanini, S. Effect of recycled cellulose fibres on the properties of lightweight cement composite matrix. *Construction* **2012**, *34*, 451–456. [CrossRef]
8. Schabowicz, K. Aging of ventilated façades made of fiber-cement panels. *Insulations* **2020**, *25*, 72–74. (In Polish)
9. Schabowicz, K.; Menéndez Orellana, A.E.; Andrianos, N. Analysis of selected non-destructive methods for diagnosis in new and old buildings. *Badania Nieniszcz. I Diagn.* **2022**, *6*, 63–70.
10. Verma, S.K.; Bhadauria, S.S.; Akhtar, S. Review of Nondestructive Testing Methods for Condition Monitoring of Concrete Structures. *J. Constr. Eng.* **2013**, *2013*, 83457. [CrossRef]
11. Ngo, T.Q.L.; Wang, Y.R.; Chiang, D. Applying Artificial Intelligence to Improve On-Site Non-Destructive Concrete Compressive Strength Tests. *Crystals* **2021**, *11*, 1157. [CrossRef]
12. Lublóy, E.; Kopecskó, K.; Balázs, G.L.; Restas, A.; Szilágyi, I.A. Improved fire resistance by using Portland-pozzolana or Portland-fly ash cement. *J. Therm. Anal. Calorim.* **2017**, *129*, 925–936. [CrossRef]
13. Xu, Y.; Wong, Y.L.; Poon, C.S.; Anson, M. Influence of PFA on cracking of concrete and cement paste after exposure to high temperatures. *Cem. Concr. Res.* **2003**, *33*, 2009–2016. [CrossRef]
14. Doleželová, M.; Scheinherrová, L.; Krejsová, J.; Vimmrová, A. Effect of high temperatures on gypsum-based composites. *Constr. Build. Mater.* **2018**, *168*, 82–90. [CrossRef]
15. Heikal, M.; El-Didamony, H.; Sokkary, T.M.; Ahmed, I.A. Behavior of composite cement pastes containing microsilica and fly ash at elevated temperature. *Constr. Build. Mater.* **2003**, *38*, 1180–1190. [CrossRef]
16. Sanchayan, S.; Foster, S.J. High temperature behaviour of hybrid steel–PVA fibre reinforced reactive powder concrete. *Mater. Struct.* **2016**, *49*, 769–782. [CrossRef]
17. Szymków, M. Identification of the Degree of Destruction of Fiber-Cement Boards under the Effects of High Temperature, Raport serii PRE nr 9/2018. Ph.D. Thesis, Wydział Budownictwa Lądowego i Wodnego, Wrocław, Poland, 2018. (In Polish).
18. Abdullah Shukry, N.; Ahmad Sekak, K.; Ahmad, M.; Bustami Effendi, T. Characteristics of Electrospun PVA-Aloe vera Nanofibres Produced via Electrospinning. In *Proceedings of the International Colloquium in Textile Engineering, Fashion, Apparel and Design 2014 (ICTEFAD 2014)*; Springe: Singapore, 2014; pp. 7–12. [CrossRef]
19. Kalifaa, P.; Chene, G.; Galle, C. High-temperature behaviour of HPC with polypropylene fibres from spalling to microstructure. *Cem. Concr. Res.* **2001**, *31*, 1487–1499. [CrossRef]
20. Schroeter, J.; Felix, F. Melting cellulose. *Cellulose* **2005**, *12*, 159–165. [CrossRef]
21. Harger, I. Behaviour of cement concrete at high temperature. *Bull. Pol. Acad. Tech. Sci.* **2013**, *61*, 145–154. [CrossRef]
22. Guo, L.; Zhang, W.; Sun, W.; Chen, B.; Liu, Y. High-Temperature Performance and Multiscale Damage Mechanisms of Hollow Cellulose Fiber-Reinforced Concrete. *Adv. Mater. Sci. Eng.* **2016**, *2016*, 2503780. [CrossRef]
23. Veliseicik, T.; Zurauskiene, R.; Valentukeviciene, M. Determining the Impact of High Temperature Fire Conditions on Fibre Cement Boards Using Thermogravimetric Analysis. *Symmetry* **2020**, *12*, 1717. [CrossRef]
24. Adamczak-Bugno, A.; Swit, G.; Krampikowska, A. Application of the Acoustic Emission Method in the Assessment of the Technical Condition of Steel Structures. *IOP Conf. Ser. Mater. Sci. Eng.* **2017**, *245*, 022031. [CrossRef]
25. Adamczak-Bugno, A.; Krampikowska, A. The Acoustic Emission Method Implementation Proposition to Confirm the Presence and Assessment of Reinforcement Quality and Strength of Fiber–Cement Composites. *Materials* **2020**, *13*, 2966. [CrossRef] [PubMed]
26. Azad, M.; Avin, A. scanning electron microscopy (sem): A review. In Proceedings of the 2018 International Conference on Hydraulics and Pneumatics—HERVEX, Băile Govora, Romania, 7–9 November 2018.
27. Chyliński, K.; Kuczyński, K. Ilmenite MUD Waste as an Additive for Frost Resistance in Sustainable Concrete. *Materials* **2020**, *13*, 2904. [CrossRef] [PubMed]

materials

MDPI

Article

Modelling of Resinous Material Filling Expansion Joints in Reinforced Concrete Structures

Krzysztof Schabowicz *, Grzegorz Waśniewski and Krzysztof Wróblewski

Faculty of Civil Engineering, Wrocław University of Science and Technology, Wybrzeże Wyspiańskiego 27, 50-370 Wrocław, Poland
* Correspondence: krzysztof.schabowicz@pwr.edu.pl

Abstract: This paper is a continuation of the research and analysis to estimate hyperelastic material constants when only uniaxial test data are available. The FEM simulation was expanded and the results obtained from three-dimensional and plane strain expansion joint models were compared and discussed. The original tests were carried out for a gap with a width of 10 mm, whereas in the case of axial stretching, the stresses and internal forces caused by the leading deformations were recorded for a smaller gap, and the axial compression was also recorded. The differences in the global response between the three- and two-dimensional models were also considered. Finally, using FEM simulations, the values of stresses and cross-sectional forces in the filling material were determined, which can be the basis for the design of expansion joints geometry. The results of these analyses could form the basis of guidelines for the design of expansion joint gaps filled with material, ensuring the waterproofing of the joint.

Keywords: reinforced concrete structure; dilatation gap; *FEM* model; hyperelasticity

Citation: Schabowicz, K.; Waśniewski, G.; Wróblewski, K. Modelling of Resinous Material Filling Expansion Joints in Reinforced Concrete Structures. *Materials* **2023**, *16*, 2011. https://doi.org/10.3390/ma16052011

Academic Editor: Angelo Marcello Tarantino

Received: 14 January 2023
Revised: 9 February 2023
Accepted: 21 February 2023
Published: 28 February 2023

1. Introduction

Building construction represents one of the largest development uses of construction chemicals. Big buildings are divided into parts that are separated by expansion joints. These are usually made during the construction and are present in every element, from the bottom slab to the roof structure [1–7].

The main problem for the system of filling the expansion joint is water, because it causes damage to internal installations and its structure. One of the most frequent problems is water leakage through expansion joints. This is a real problem in buildings under construction and during their service life [8–10]. Therefore, the material filling the expansion joint should ensure its waterproofness. In this case, application of a polyurethane-based resin is a good choice [9–12].

Within the expansion joints, section forces occur caused by, i.a., thermal deformations, concrete creep and shrinkage, and the uneven subsidence of the structural members [12,13]. Various fillings, sealing materials, and closing in the form of premoulded inserts and sealing strips are applied to ensure the expansion joints' waterproofness [11] against the above-mentioned non-mechanical excitations.

There are several products on the market for sealing expansion joints selected on the basis of "the engineering knowledge, experience and assurances of the sealing crews". One of them—the resin—becomes a permanent flexible mass after curing, which, during the cyclic excitations acting on the expansion joint, should expand or shrink depending on changes in the geometry of the expansion joint. There are no standards and guidelines that would indicate the use of a particular filler under specific conditions. There are also no standards and guidelines for surface preparation, i.e., the preparation of sidewall surfaces in an expansion joint [14,15]. For this reason, the comparison of the results of the FEM numerical analysis and the experimentally determined material strength parameters seems

to be the right direction for further research in order to correctly design the optimum width of the expansion joint.

The authors of [16] presented an interesting alternative to other ways of fixing adhesive bonded joints between glass panels and their load-bearing metal structures in façade constructions. Silicon sealants have been studied for their excellent adhesion to glass and exceptionally high resistance to environmental influences and aging. *FEM* nonlinear numerical simulations were used to verify filled joints. An overview of the available damage criteria for rubber-type materials was presented. The criteria application to silicone sealants was verified for three characteristic stress states: uniaxial tension, compression, and shearing.

A polyurethane polymer, which owing to specially selected additives providing a better damping, was analyzed in PhD thesis [17]. The efficiency of a novel material for a seismic vibration isolation bearing was carried out by experimental and detailed nonlinear numerical *FEM* analyses. Discrete models response analysis of existing steel structure with and without vibroisolation to several seismic and paraseismic excitations were performed. Laboratory tests (compression and tension) allowed the determination of the material constants for a five-parameter Mooney–Rivlin model for the analyzed polymer material.

In [18], the authors considered elastomeric tracks for industrial vehicles, in which materials are incompressible and very high deformable. The material parameters for several hyperelastic material models (Mooney–Rivlin) were determined in experiments. The parameters were used to define *FEM* discrete models for computations. Numerical results obtained for different models were compared with experiments, in which the samples were exposed to the same load.

This manuscript is a description of one of the stages, into which the authors have divided the study of the issue. The first step proposes a novel way to identify a physical model of a hyperelastic material, where only a limited set of experimental data is available. The results of these investigations were published in [19]. The next stage, presented in this manuscript, concerns the possibility of numerically determining stress distributions for typical excitations, to which the material filling the expansion joint is subjected. In this part, the authors want to assess whether, in regard to the identified material model and its previously determined physical constants, numerical simulations will give results in acceptable ranges. In the final stage, for numerically determined distributions of the stress tensor components, it is intended that various damage criteria will be applied, and attempts to verify them experimentally will be made.

2. Objectives

The aim of the development and continuation of the research is to carry out *FEM* simulations for a resin material in an expansion gap under different non-mechanical excitations: axial stretching and compression, bending, and shearing. The influence of the width of the gap on the response of the filling material in dilatated reinforced concrete beams and slabs at different levels of forcing is studied. The results are the values of stresses and cross-sectional forces in the filling material, which can be the basis for the design of expansion joints geometry.

As a material filling the expansion joint, polyurethane-based resin was considered. Its description was given in Section 3. It should be noted that during the deformation process, material can be subjected to extreme strains, even more than 100% in the case of stretching. Moreover, during laboratory tests, one observed that deformations are reversible in the whole range. For these reasons, the hyperelastic material model was adopted as the physical model of the resin. The hyperelastic material model, used in the present paper, was described in Section 4. The physical constants for the analyzed resin are presented in Section 5.

In order to describe the response of the material filling the expansion joint in the beam, a three-dimensional *FEM* model is assumed. In contrast to the surface girder, where the

dilatation gap is a long narrow structure, the plane strain problem is the most realistic physical model. Therefore, in the case of the plate, a two-dimensional model is considered.

The ABAQUS/CAE system was used for all the numerical simulations [20].

3. Description of Analyzed Material

The material analyzed in the numerical simulations was one-component resin based on polyurethane. This resin was selected because it is used for, among other things, injecting cracks and joints in reinforced concrete structures, repairing water leakages from expansion joints [9–12], the preventive sealing of structures, water infiltration control during tunnelling, curtain injections, injection repairs of concrete, and masonry underground structures (in basements, underground car parks, etc.).

The resin used in the tests is made up of two components: component A, polyurethane resin, and component B, water. The two components are mixed at the volumetric proportion of 1:1.

The components of the tested resin and its properties are presented in, respectively, Tables 1 and 2.

Table 1. Components of tested resin.

Parameter	Component A	Component B
Description	Polyurethane base	Water
Form	Liquid	Liquid
pH	Undetermined	7
Density	from 1.04 to 1.16 kg/dm^3	ca. 1.00 kg/dm^3
Viscosity	<350 mPas	ca. 1.00 mPas

Table 2. Properties of tested resin.

Property	Value
Viscosity	<200 mPas
Foam factor	>3
Tensile strength	approx. 1.3 MPa
Elongation at break	approx. 160%

4. Hyperelastic Material Model

The hyperelastic material is described by strain energy potential function U expressed per unit reference volume, enabling one to formulate a constitutive law [21,22]. For isotropic materials, the strain energy potential depends on the strain invariants only. It is possible to use different invariant sets in analytical description. The common choice is deviatoric strain invariants: $\overline{I}_1$, $\overline{I}_2$, and elastic volume ratio J_{el}, which allow definition of U components responsible for deviatoric and volumetric strain parts:

$$U = U_{dev}(\overline{I}_1,\ \overline{I}_2) + U_{vol}(J_{el}) \tag{1}$$

When thermal strains are absent, the elastic volume ratio J_{el} is equal to total volume ratio J and can be expressed by the Jacobian of the transformation between the reference $\boldsymbol{X}$ and the current $\boldsymbol{x}$ configurations:

$$\boldsymbol{F} = \frac{\partial \boldsymbol{x}}{\partial \boldsymbol{X}},\ J_{el} = J = \det(\boldsymbol{F}) = \frac{dV}{dV_0} \tag{2}$$

The deviatoric strain invariants can be expressed by deviatoric stretches $\overline{\lambda}_i$, principal stretches λ_i, or principal strains ε_i:

$$\overline{I}_1 = \overline{\lambda}_1^2 + \overline{\lambda}_2^2 + \overline{\lambda}_3^2 \tag{3}$$

$$\overline{I}_2 = \overline{\lambda}_1^{-2} + \overline{\lambda}_2^{-2} + \overline{\lambda}_3^{-2} \tag{4}$$

$$\overline{\lambda}_i = J^{-\frac{1}{3}}\lambda_i = J^{-\frac{1}{3}}(1+\varepsilon_i) \tag{5}$$

ABAQUS offers several forms of strain energy potential U. In the present work, the Ogden model was applied to describe analysed material physical properties. Strain energy potential for considered form is defined by strain invariants and material coefficients [20,23,24]:

$$U = \sum_{i=1}^{N} \frac{2\mu_i}{\alpha_i^2}\left(\overline{\lambda}_1^{\alpha_i} + \overline{\lambda}_2^{\alpha_i} + \overline{\lambda}_3^{\alpha_i} - 3\right) + \sum_{i=1}^{N} \frac{1}{D_i}(J-1)^{2i} \tag{6}$$

Material coefficients: N_i, μ_i, α_i, and D_i, which appear in the Ogden form, are related to engineering constants. The initial value of shear modulus μ_i and bulk modulus K_0 are expressed as follows:

$$\mu_0 = \sum_{i=1}^{N} \mu_i, \qquad K_0 = \frac{2}{D_1}. \tag{7}$$

5. Material Physical Constants

In paper [19], the authors described an algorithm for identifying the physical model for hyperelastic material and the decomposing of the associated physical constants. For the resin described in paragraph 3, the best compliance with the experimental results was obtained for the Ogden form for the strain energy potential order $N = 2$. The physical constants derived for the considered material are collected in Table 3.

Table 3. Material coefficients.

N	μ_1	μ_2	α_1	α_2	D_1	D_2	μ_0	K_0
[-]	[kPa]	[kPa]	[-]	[-]	[MPa^{-1}]	[MPa^{-1}]	[kPa]	[kPa]
2	410.2	3.306	1.218	−2.883	1.036	0.000	413.5	1930

The parameters listed in the table above will be used to define material physical model in examples presented in next paragraphs.

6. Dilatation Gap Simulation in Beam: Three-Dimensional Problem

6.1. Physical and Discrete Models

A rectangular beam measuring 10 × 20 cm with an expansion joint 1.0 or 2.0 cm wide is analyzed. In order to simulate an answer of the material in the dilatation gap, *FEM* discrete models were created (Figure 1). It is assumed that the concrete walls behave as perfectly rigid planes and the connection between the materials is ideal. Taking this it into account, stiff translations and rotations of the connection plane are applied as external kinematic loads. To be able to compare results for both widths, the loads ratio is the same and it is equal to 1:2.

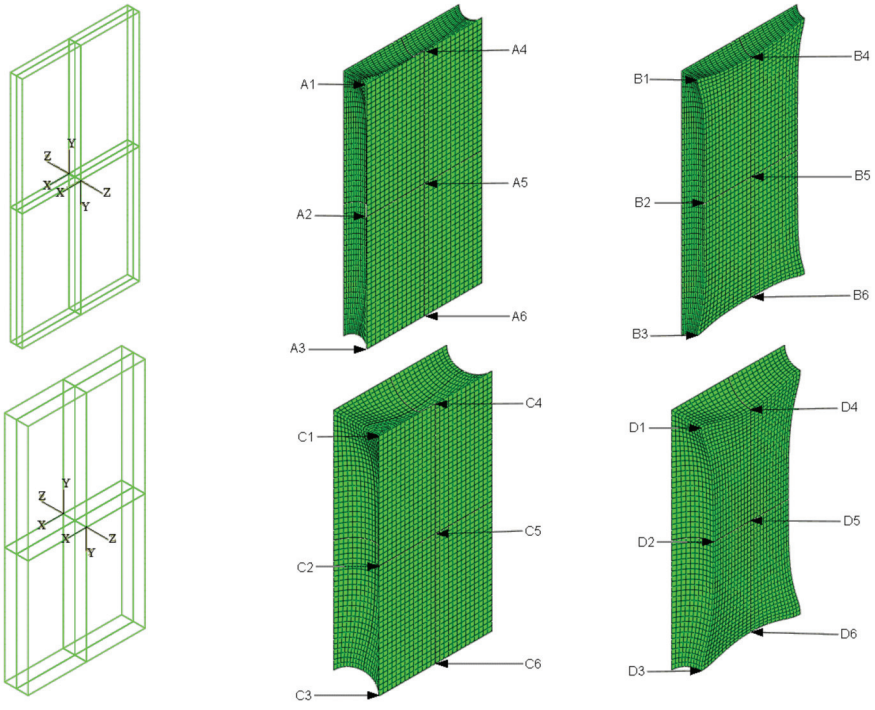

Figure 1. Material in dilatation gap numerical model. Three-dimensional problem. Expansion joint geometry and local coordinate systems on connection planes, left graphics. Selected nodes on connection plane, central graphics, and on central plane, right graphics. The width of the gap is equal to 1.0 cm, upper, and 2.0 cm, lower.

6.2. Axial Stretching

The material in the dilatation gap is analyzed under uniform stretching equal to 1.0 or 2.0 cm in the z-axis direction for widths of 1.0 or 2.0 cm, respectively. Displacements $u_z = 0.5$ or 1.0 cm, expressed in local coordinate systems of walls, are put on front and back connection planes (Figure 1). Deformation images for total load level are presented in Figure 2.

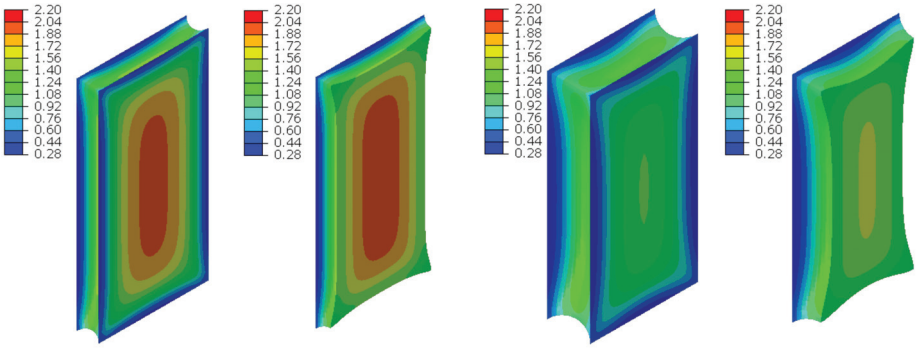

Figure 2. Deformations for scaling factor 1.0 and Cauchy stresses σ_z in MPa for total load level. The width of the gap is equal to 1.0 cm, left graphics, and 2.0 cm, right graphics. Views on connection, first and third columns, or central plane, second and fourth columns.

ABAQUS calculates Cauchy stresses (real stresses), expressed per unit deformed area. The nominal stresses, expressed per unit undeformed surface, differ significantly from the real stresses when the body in question is subjected to large deformations. In this case, the Cauchy stress values determine the stress intensity in the material. Figure 2 shows the Cauchy stresses σ_z generated in the resin for total load level for both gap widths considered.

Figure 3 presents the same stresses σ_z in selected nodes (Figure 1) versus the gap elongation for both widths considered.

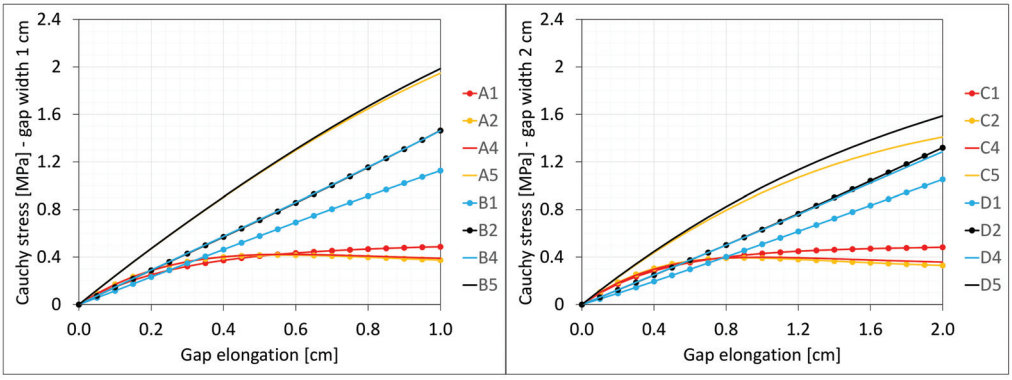

Figure 3. Equilibrium paths for stresses σ_z in selected nodes. The width of the gap is equal to 1.0 cm, left graphic, and 2.0 cm, right.

Figure 4 shows the total axial force N_z generated in the resin versus the gap elongation. The normal stresses along the direction of excitation have different values in different points of the discrete model (Figure 3). Moreover, due to the differences in deformations (Figure 2) between the considered gap widths the stress values in the same nodes of the *FEM* model differ significantly from each other. Therefore, in order to compare the results, the excitation force values are included in the charts (Figure 4).

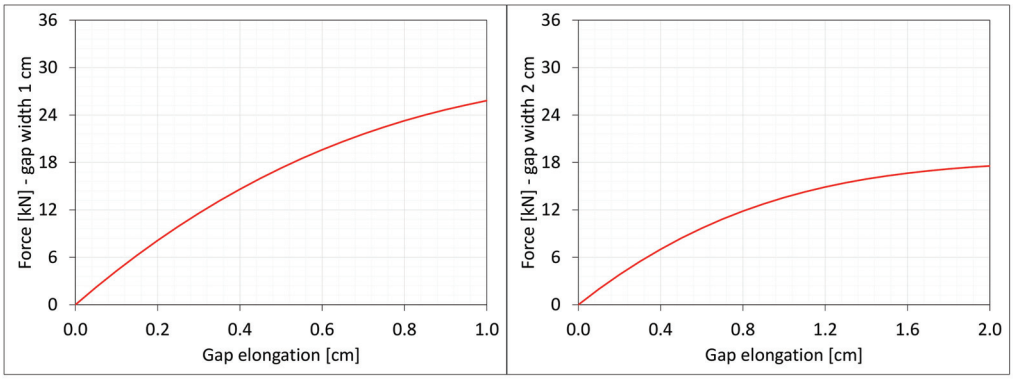

Figure 4. Equilibrium paths for excitation force σ_z The width of the gap is equal to 1.0 cm, left graphic, and 2.0 cm, right graphic.

6.3. Axial Compression

The material in the dilatation gap is analyzed under uniform compression equal to 0.5 or 1.0 cm in the *z*-axis direction. Displacements $u_z = -0.25$ or -0.5 cm, expressed in local coordinate systems of walls, are put on front and back connection planes (Figure 1). Deformation images and the Cauchy stresses σ_z generated in the resin for final load level for both gap widths considered are presented in Figure 5.

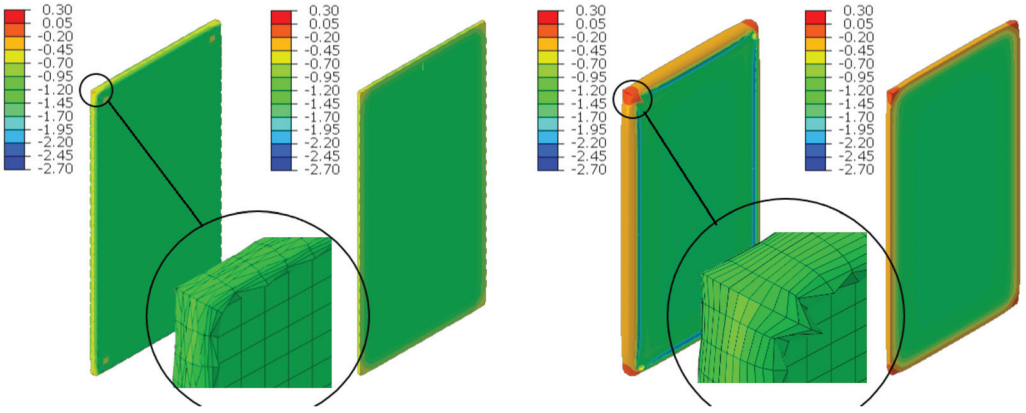

Figure 5. Deformations for scaling factor 1.0 and Cauchy stresses σ_z in MPa for final load level. The width of the gap is equal to 1.0 cm, left graphic, and 2.0 cm, right graphic. Views on connection, first and third columns, or central plane, second and fourth columns. Details of deformation are enlarged.

The incremental algorithm used to solve the nonlinear problem modelled by *FEM* loses convergence when it is impossible to satisfy the equilibrium equations in the next iteration step. In the presented examples, it was impossible to reach total declared excitations; the convergence was achieved for shortenings not greater than 0.45 and 0.95 cm. Moreover, earlier than such final load levels are achieved, non-physical deformations appear (Figure 5) for shortenings greater than 0.375 and 0.65 cm.

The Cauchy stresses σ_z in selected nodes (Figure 1) and the total axial force N_z generated in the resin versus the gap shortening are shown in the Figures 6 and 7, respectively. In the charts, the equilibrium paths parts, for which non-physical deformations appear, are displayed with thin lines.

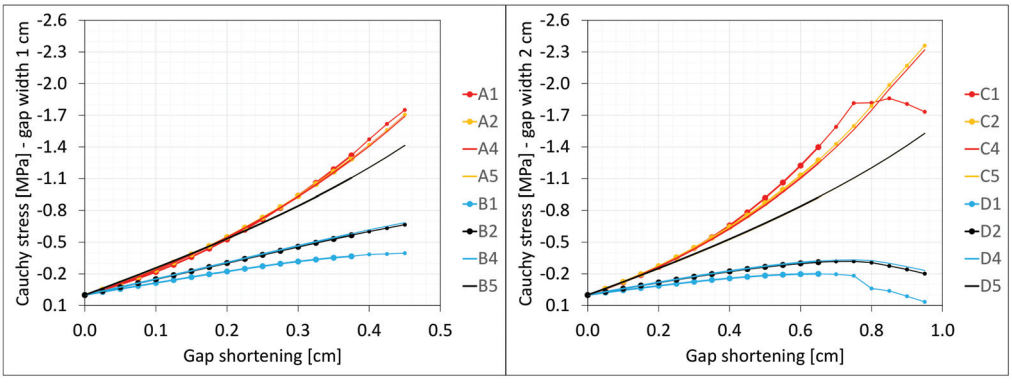

Figure 6. Equilibrium paths for stresses σ_z in selected nodes. The width of the gap is equal to 1.0 cm, left graphic, and 2.0 cm, right graphic. Parts of charts with non-physical deformations are displayed with thin lines.

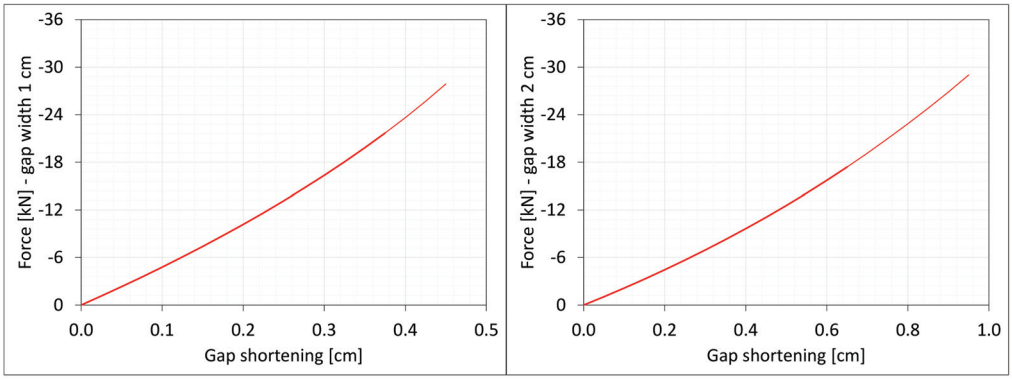

Figure 7. Equilibrium paths for excitation force N_z. The width of the gap is equal to 1.0 cm, left graphic, and 2.0 cm, right graphic. Parts of charts with non-physical deformations are displayed with thin lines.

6.4. Bending

The material in the dilatation gap exposed to bending is analyzed. Rotations around the x-axis of local walls coordinate systems of $\phi_x = -0.025$ or -0.05 rad and 0.025 or 0.05 rad are put on front and back connection planes, respectively (Figure 1). Assumed angles of rotation generate the same shortenings in beam bottom fibers, such as in the axial compression case considered. Deformation images and the Cauchy stresses σ_z generated in the resin for final load level are presented in Figure 8. The same stresses σ_z in selected nodes (Figure 1) and the total bending moment M_x generated in the resin versus mutual rotation angle of the opposite connection planes are shown in Figures 9 and 10, respectively. The stress distributions shown in Figure 8 indicate that the greatest tensile stresses will occur in different nodes than those shown in Figure 1. The equilibrium paths for these stresses are also shown in Figure 9. The convergence was achieved for mutual rotation angles not greater than 0.045 and 0.09 rad; non-physical deformations were detected for angles greater than 0.0375 and 0.06 rad.

Due to the different behavior of materials under stretching and compression (Figure 8) in the resin, which fills expansion joint, axial force is generated in addition. The equilibrium path for the force N_z is displayed in Figure 11.

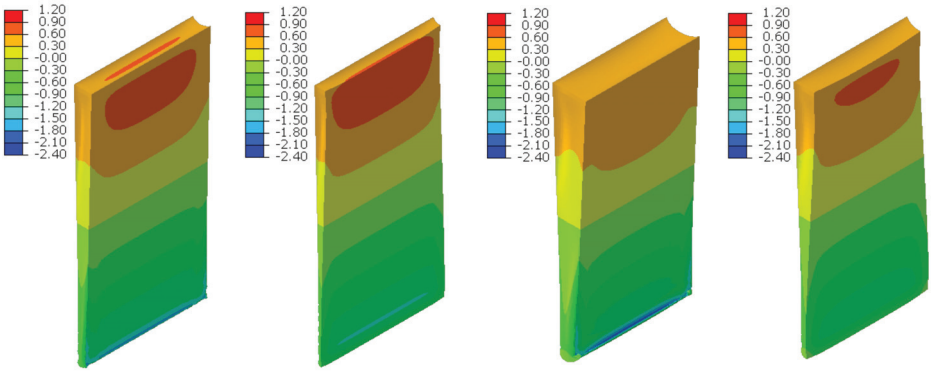

Figure 8. Deformations for scaling factor 1.0 and Cauchy stresses σ_z in MPa for final load level. The width of the gap is equal to 1.0 cm, left graphics, and 2.0 cm, right graphics. Views on connection, first and third columns, or central plane, second and fourth columns.

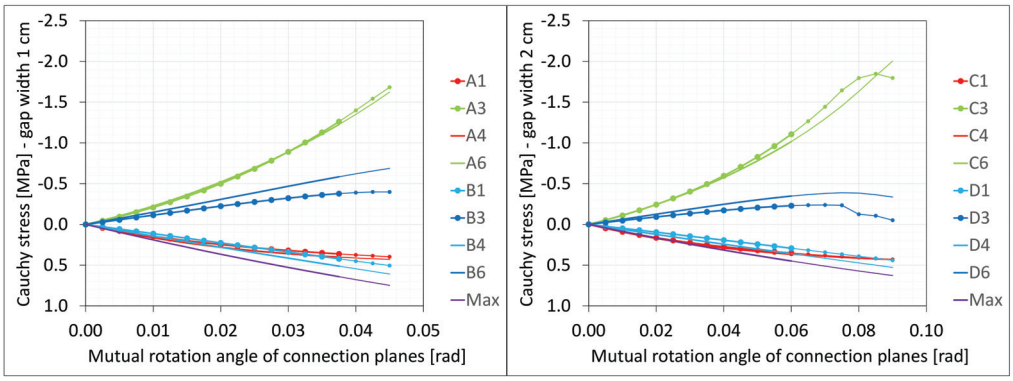

Figure 9. Equilibrium paths for stresses σ_z in selected nodes. The gap width is equal to 1.0 cm, left graphic, and 2.0 cm, right graphic. Parts of charts with non-physical deformations are displayed with thin lines.

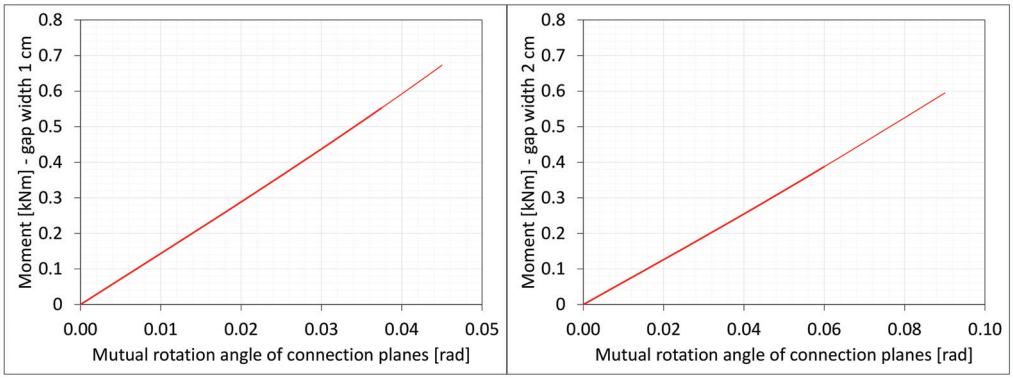

Figure 10. Equilibrium paths for excitation moment M_z. The gap width is equal to 1.0 cm, left graphic, and 2.0 cm, right graphic. Parts of charts with non-physical deformations are displayed with thin lines.

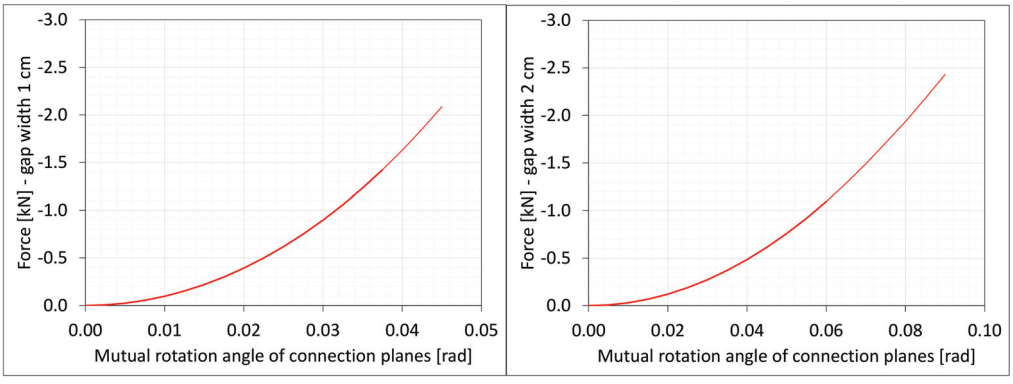

Figure 11. Equilibrium paths for excitation force N_z. The width of the gap is equal to 1.0 cm, left graphic, and 2.0 cm, right graphic. Parts of charts with non-physical deformations are displayed with thin lines.

6.5. Shearing

The material in the dilatation gap exposed to shearing is analyzed. Displacements u_y = 0.5 or 1.0 cm, expressed in local coordinate systems of walls, are put on front and back connection planes (Figure 1). Deformation images and the Cauchy stresses τ_{zy} generated in the resin for total load level are presented in Figure 12. The same stresses τ_{zy} in selected nodes (Figure 1) and the total shear force V_y generated in the resin versus mutual translation of the opposite connection planes are shown in Figures 13 and 14, respectively. The equilibrium paths for the greatest shear stresses, which occurred in different nodes than those shown in Figure 1, are also displayed in Figure 13. Additionally, the axial force N_z is generated in the resin. The equilibrium paths for these forces are displayed in Figure 15.

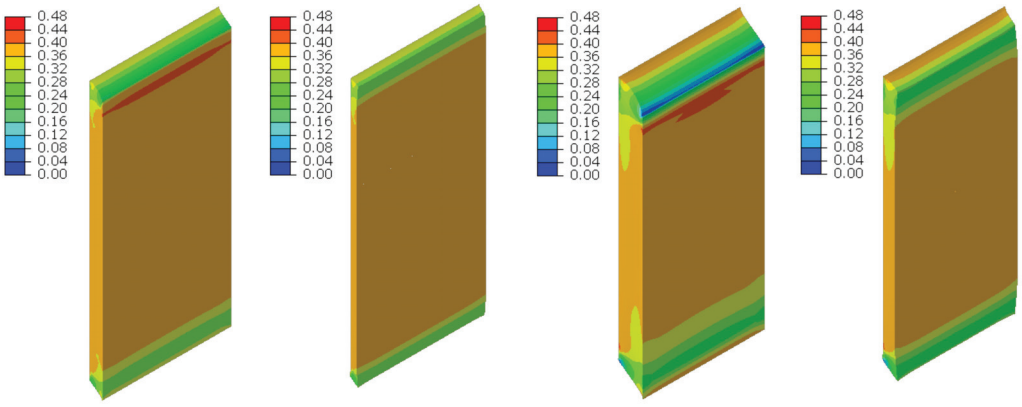

Figure 12. Deformations for scaling factor 1.0 and Cauchy stresses τ_{zy} in MPa for total load level. The width of the gap is equal to 1.0 cm, left graphics, and 2.0 cm, right graphic. Views on connection, first and third columns, or central plane, second and fourth columns.

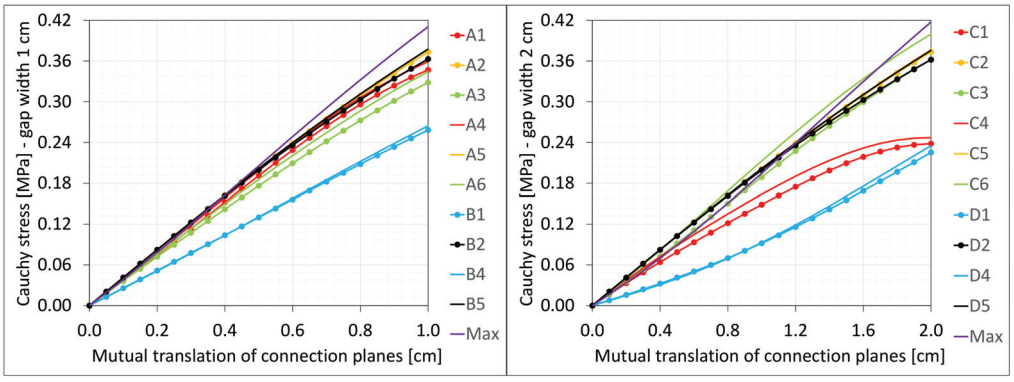

Figure 13. Equilibrium paths for stresses τ_{zy} in selected nodes. The width of the gap is equal to 1.0 cm, left graphic, and 2.0 cm, right graphic.

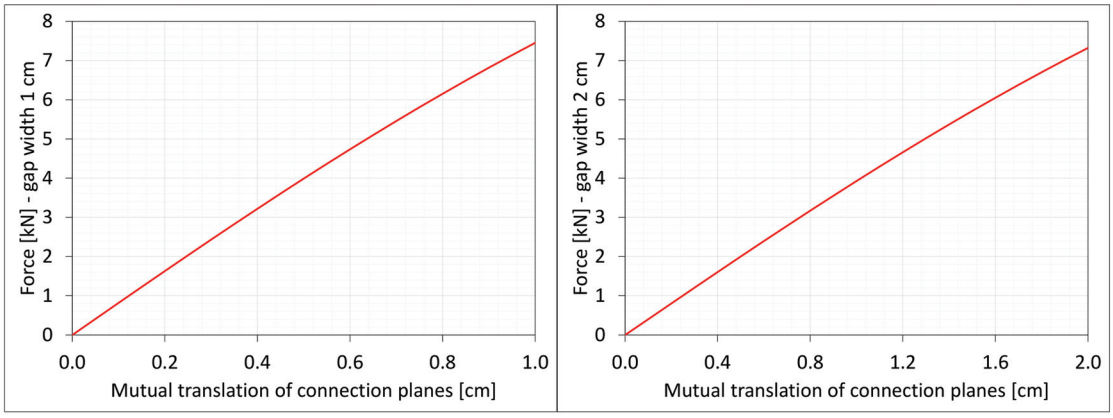

Figure 14. Equilibrium paths for shear force V_y. The width of the gap is equal to 1.0 cm, left graphic, and 2.0 cm, right graphic.

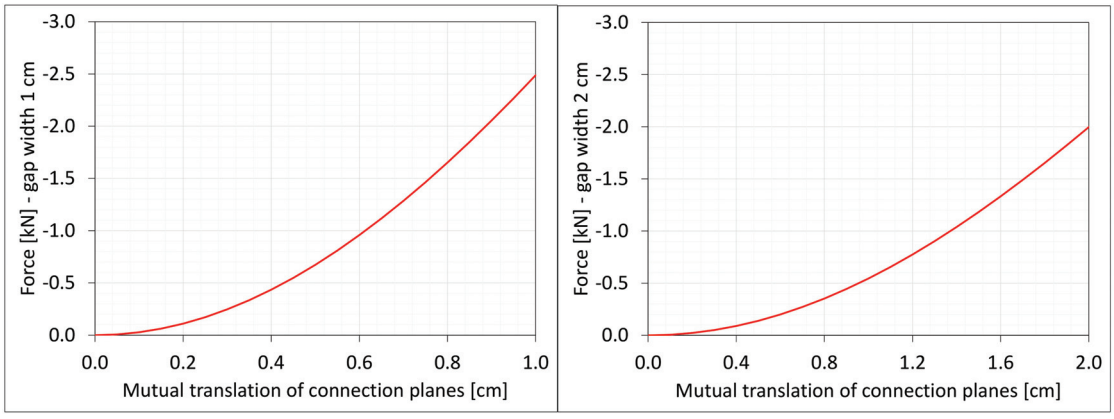

Figure 15. Equilibrium paths for axial force N_z. The width of the gap is equal to 1.0 cm, left graphic, and 2.0 cm, right graphic.

7. Dilatation Gap Simulation in Plate: Plane Strain Problem

7.1. Physical and Discrete Models

In order to compare the current results with the values obtained in paragraph 6, a plate thickness equal to the height of the analyzed beam was assumed to be 20 cm, and the same expansion joint widths equal to 1.0 or 2.0 cm were considered (Figure 16). The kinematic assumptions and load ratio for both gap widths applied for the three-dimensional discrete model are the same for the considered plane problem.

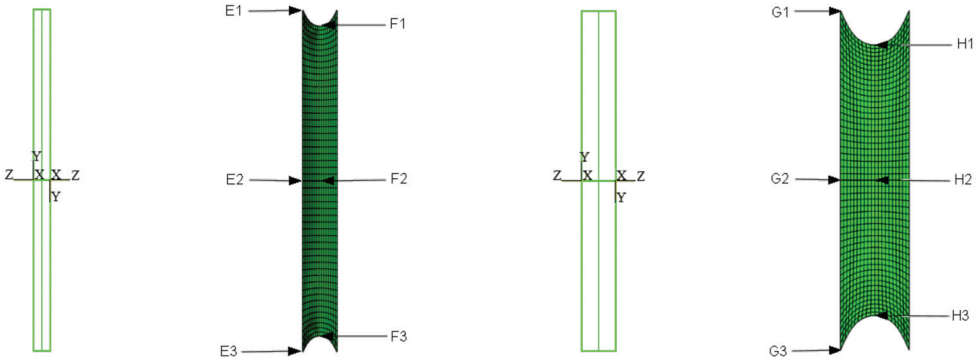

Figure 16. Material in dilatation gap numerical model. Plane strain problem. Expansion joint geometry and local coordinate systems on connection planes, first and third graphics. Selected nodes on connection and central plane, second and fourth graphics. The width of the gap is equal to 1.0 cm, left, and 2.0 cm, right.

7.2. Axial Stretching

The material in the dilatation gap is analyzed under uniform stretching equal to 1.0 or 2.0 cm in the z-axis direction. Displacements u_z= 0.5 or 1.0 cm, expressed in local coordinate systems of walls, are put on left and right connection planes (Figure 16). Deformation images and the Cauchy stresses σ_z in the resin for total load level are presented in Figure 17.

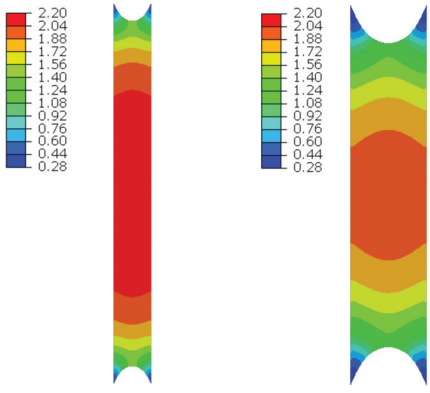

Figure 17. Deformations for scaling factor 1.0 and Cauchy stresses σ_z in MPa for total load level. The width of the gap is equal to 1.0 cm, left graphic, and 2.0 cm, right graphic.

Figures 18 and 19 present the same stresses σ_z in selected nodes (Figure 16) and the excitation force N_z versus the gap elongation, respectively. The force is from the same area as for the paths shown in Figure 4. For comparison, the results from the discrete 3D model are shown in the background. Curves for nodes lying on the same planes and with the same coordinates z are displayed in the same color (Figure 18).

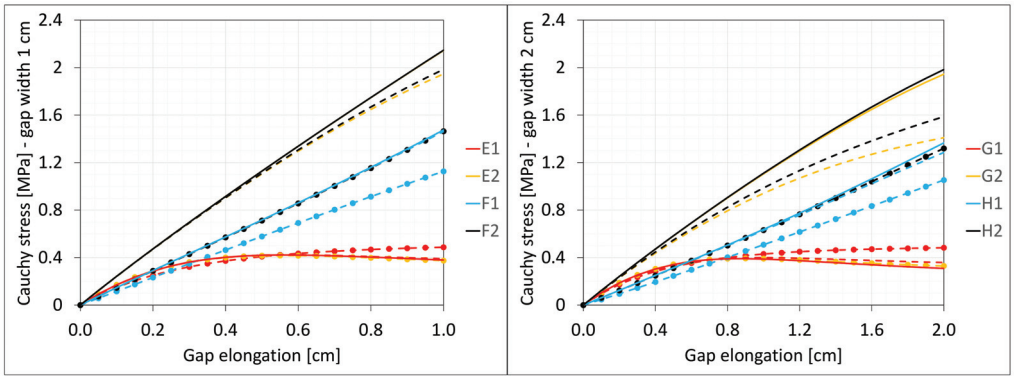

Figure 18. Equilibrium paths for stresses σ_z in selected nodes. The width of the gap is equal to 1.0 cm, left graphic, and 2.0 cm, right graphic. Plane strain models, solid lines; and 3D models, dashed lines (curves from Figure 3).

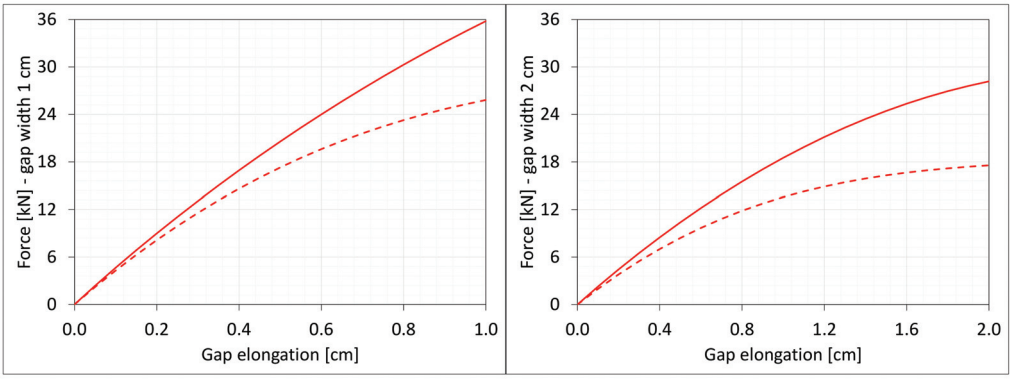

Figure 19. Equilibrium paths for excitation force N_z. The width of the gap is equal to 1.0 cm, left graphic, and 2.0 cm, right graphic. Plane strain models, solid lines; and 3D models, dashed lines (curves from Figure 4).

7.3. Axial Compression

One analyses the material in the dilatation gap under uniform compression equal to 0.5 or 1.0 cm in the z-axis direction. Displacements $u_z = -0.25$ or -0.5 cm, expressed in local coordinate systems of walls, are put on left and right connection planes (Figure 16). Deformation images and the Cauchy stresses σ_z generated in the resin for total load level are presented in Figure 20. The same stresses σ_z in selected nodes (Figure 16) and the total axial force N_z generated in the resin versus the gap shortening are shown in Figures 21 and 22, respectively. The convergence was achieved in the whole excitation ranges, and non-physical deformations (Figure 20) were detected for shortenings greater than 0.4 and 0.7 cm.

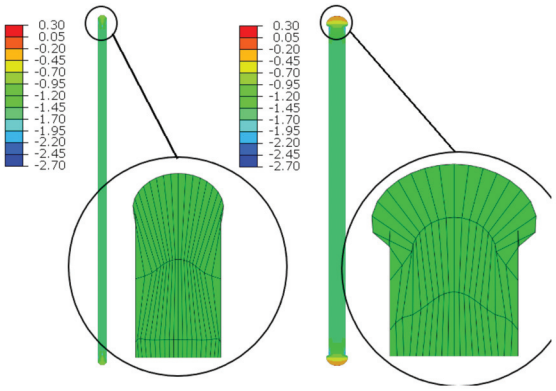

Figure 20. Deformations for scaling factor 1.0 and Cauchy stresses σ_z in MPa for total load level. The width of the gap is equal to 1.0 cm, left graphic, and 2.0 cm, right graphic. Details of deformation are enlarged.

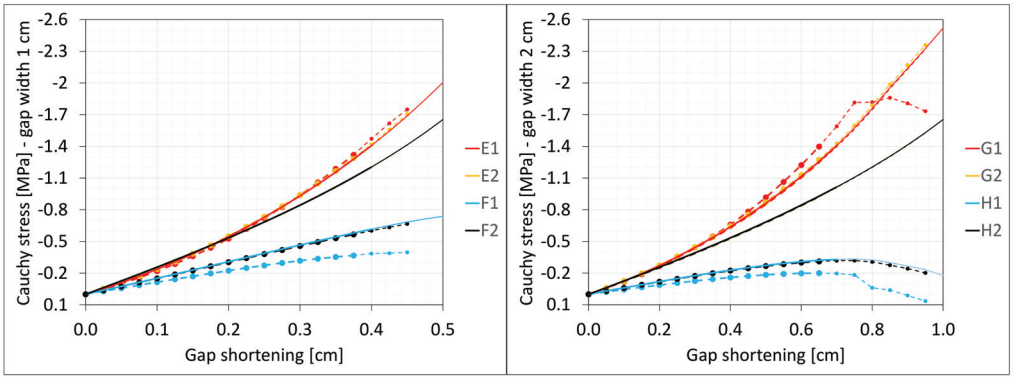

Figure 21. Equilibrium paths for stresses σ_z in selected nodes. The width of the gap is equal to 1.0 cm, left graphic, and 2.0 cm, right graphic. Plane strain models, solid lines; and 3D models, dashed lines (curves from Figure 6). Parts of charts with non-physical deformations are displayed with thin lines.

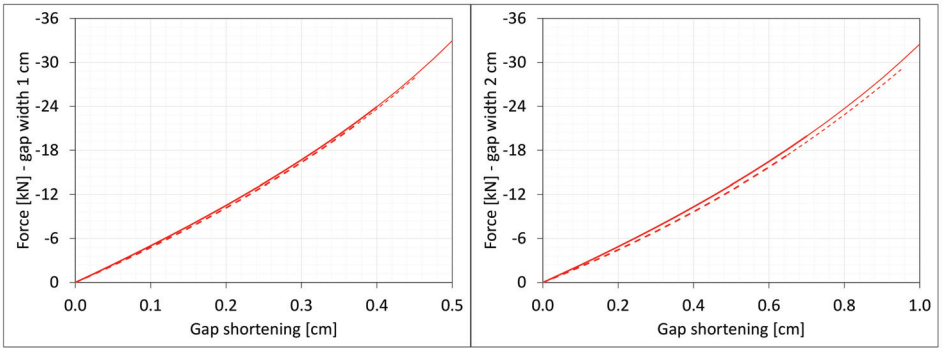

Figure 22. Equilibrium paths for excitation force N_z The width of the gap is equal to 1.0 cm, left graphic, and 2.0 cm, right. Plane strain models, solid lines; and 3D models, dashed lines (curves from Figure 7). Parts of charts with non-physical de-formations are displayed with thin lines.

7.4. Bending

The material in the dilatation gap exposed to bending are analyzed. Rotations around the x-axis of local walls coordinate systems of $\phi_x = -0.025$ or -0.05 rad and 0.025 or 0.05 rad are put on left and right connection planes, respectively (Figure 16). Deformation images and the Cauchy stresses σ_z generated in the resin for total load level are presented in Figure 23. The same stresses σ_z in selected nodes (Figure 16) and the total bending moment M_x generated in the resin versus mutual rotation angle of the opposite connection planes are shown in Figures 24 and 25, respectively. The equilibrium paths for the greatest tensile stresses, which occurred in different nodes than those shown in Figure 16, are also displayed in Figure 24. The convergence was achieved in the whole excitation range; non-physical deformations were detected for angles greater than 0.0425 and 0.075 rad. The equilibrium path for the force N_z is displayed in Figure 26.

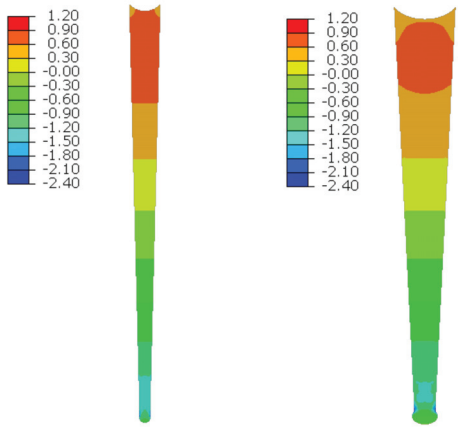

Figure 23. Deformations for scaling factor 1.0 and Cauchy stresses σ_z in MPa for total load level. The width of the gap is equal to 1.0 cm, left graphic, and 2.0 cm, right graphic.

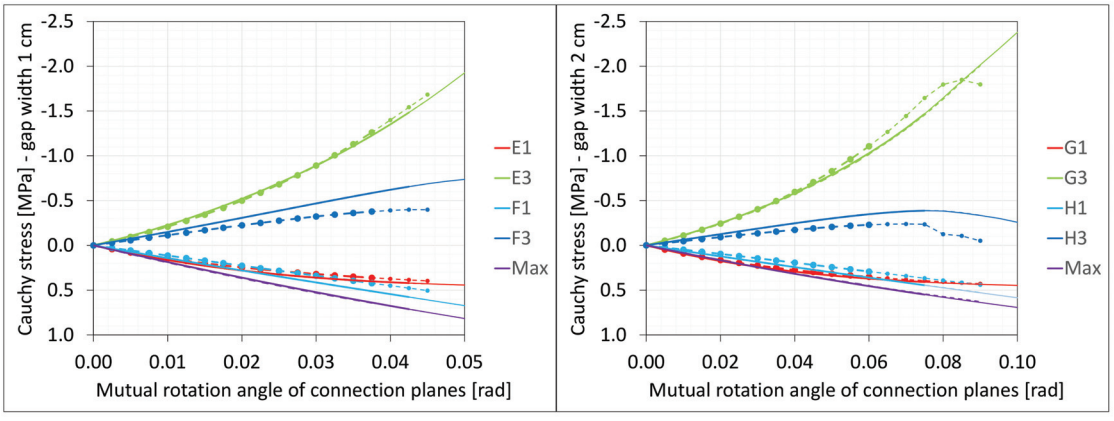

Figure 24. Equilibrium paths for stresses σ_z in selected nodes. The width of the gap is equal to 1.0 cm, left graphic, and 2.0 cm, right graphic. Plane strain models, solid lines; and 3D models, dashed lines (curves from Figure 9). Parts of charts with non-physical deformations are displayed with thin lines.

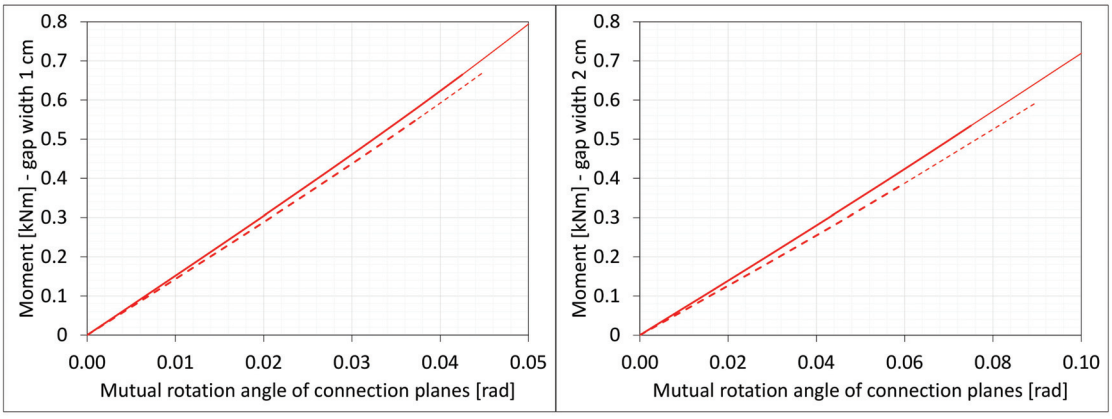

Figure 25. Equilibrium paths for excitation moment M_z. The width of the gap is equal to 1.0 cm, left graphic, and 2.0 cm, right graphic. Plane strain models, solid lines; and 3D models, dashed lines (curves from Figure 10). Parts of charts with non-physical deformations are displayed with thin lines.

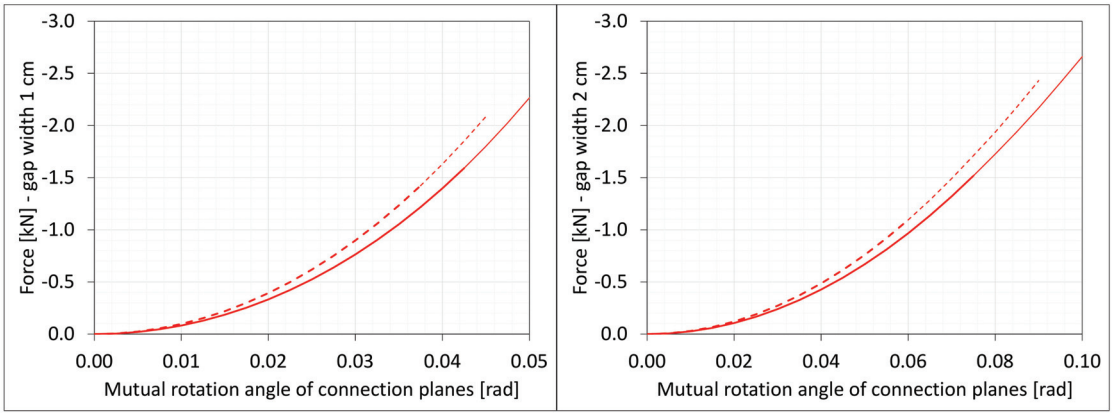

Figure 26. Equilibrium paths for axial force N_z. The width of the gap is equal to 1.0 cm, left graphic, and 2.0 cm, right graphic. Plane strain models, solid lines; and 3D models, dashed lines (curves from Figure 11). Parts of charts with non-physical deformations are displayed with thin lines.

7.5. Shearing

The material in the dilatation gap exposed to shearing is analyzed. Displacements u_y = 0.5 or 1.0 cm, expressed in local coordinate systems of walls, are put on left and right connection planes (Figure 16). Deformation images and the Cauchy stresses τ_{zy} generated in the resin for total load level are presented in Figure 27. The same stresses τ_{zy} in selected nodes (Figure 16) and the total shear force V_y generated in the resin versus mutual translation of the opposite connection planes are shown in Figures 28 and 29, respectively. The equilibrium paths for the greatest shear stresses, which occurred in different nodes than those shown in Figure 16, are also displayed in Figure 28. The equilibrium paths for the axial force N_z, which are generated in the resin, are displayed in Figure 30.

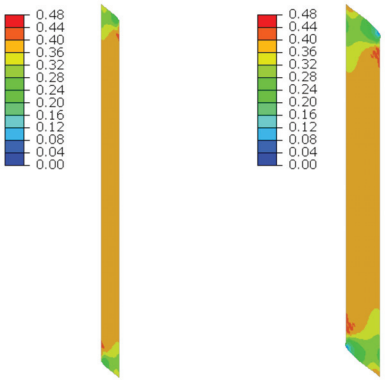

Figure 27. Deformations for scaling factor 1.0 and Cauchy stresses τ_{zy} in MPa for total load level. The width of the gap is equal to 1.0 cm, left graphic, and 2.0 cm, right graphic.

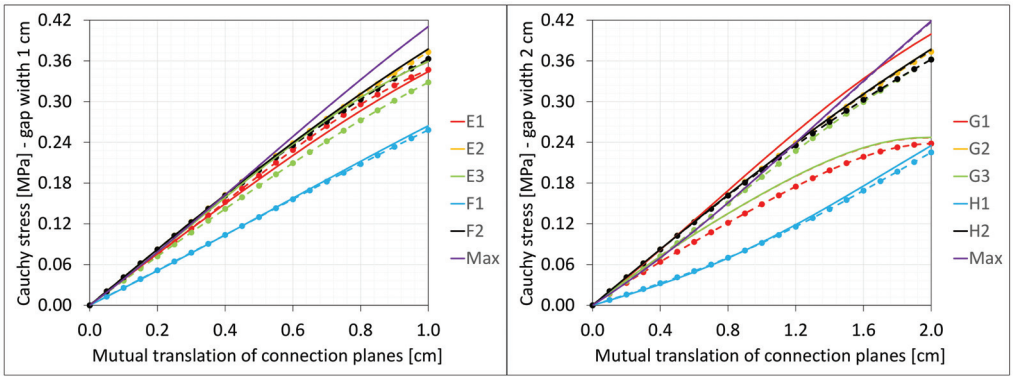

Figure 28. Equilibrium paths for stresses τ_{zy} in selected nodes. The width of the gap is equal to 1.0 cm, left graphic, and 2.0 cm, right graphic. Plane strain models, solid lines; and 3D models, dashed lines (curves from Figure 13).

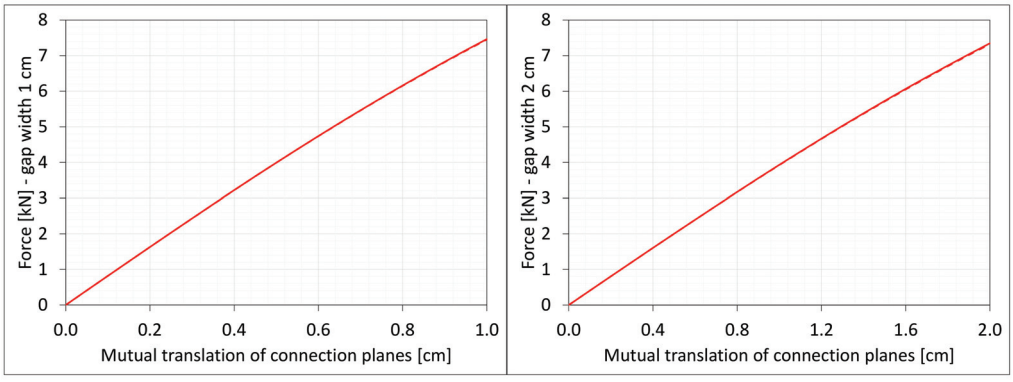

Figure 29. Equilibrium paths for shear force V_y. The width of the gap is equal to 1.0 cm, left graphic, and 2.0 cm, right graphic. Plane strain models, solid lines; and 3D models, dashed lines (curves from Figure 14).

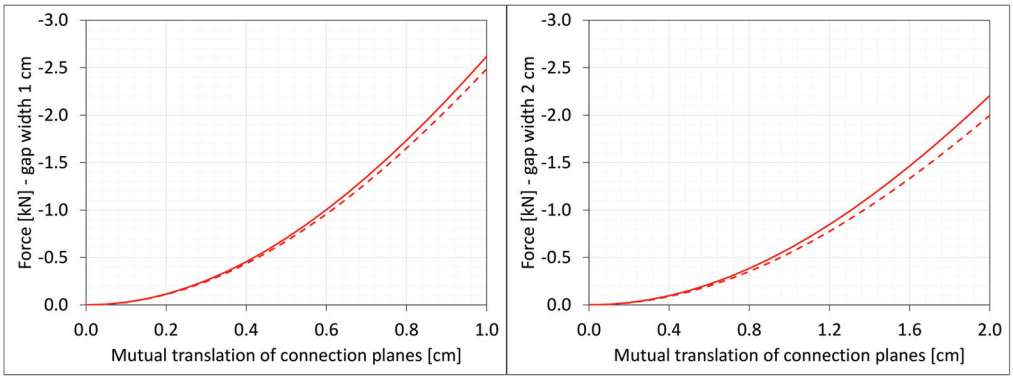

Figure 30. Equilibrium paths for axial force N_z. The width of the gap is equal to 1.0 cm, left graphic, and 2.0 cm, right graphic. Plane strain models, solid lines; and 3D models, dashed lines (curves from Figure 15).

8. Results Discussion

The results of the numerical analyses presented in the previous chapters allow for the formulation of several general observations. In the considered ranges of deformations, clearly nonlinear forms of equilibrium paths are noted. In the case of axial stretching, the stresses and internal forces caused by the leading deformation of the same value are greater in a gap of a smaller width, for axial compression they are smaller, and in other cases, no clear tendency is observed. The differences in the global response between the three- and two-dimensional models are insignificant, except in the case of axial stretching (force N_z in Figure 19).

For two-dimensional models, the *FEM* algorithm achieves convergence in a larger range of forcing, later non-physical deformations appear. The effect of non-physical deformations on the global response is not noticed, the effects of their occurrence are visible only on stress equilibrium paths in nearby nodes.

The results obtained in the numerical simulations are in expected and acceptable ranges. This suggests that physical model of the consider material, which was identified in the previous stage of investigations, is proper. A more categorical statement, however, would require empirical confirmation, which is the future intention of the authors.

9. Conclusions

Due to the physical nonlinearity and high strains, adopting a hyperelastic material model for the analyzed resin is the right choice. The experience gained during the analysis of the presented examples indicates that the results are highly sensitive to changes in the values of physical constants (Table 3). Therefore, they should be determined with high accuracy.

Using *FEM* simulations one can determine the values of stresses and cross-sectional forces in the filling material, which can be the basis for the design of expansion joints geometry. Each of the analyzed elementary deformations generates a complex stress state in the material filling the expansion joint. In the present study, the authors suggest that it is possible to determine reasonable numerical stress values for different excitations in the case of the investigated material.

As part of further research, the authors' aim will be to formulate criteria for the damage of the material and breaking its connection with the reinforced concrete structure and their experimental verification. The results of these analyses could form the basis of guidelines for the design of expansion joint gaps filled with material, ensuring the waterproofing of the joint.

Author Contributions: Conceptualization, G.W., K.S. and K.W.; methodology, G.W., K.S. and K.W.; validation, G.W. and K.S.; formal analysis, K.S.; measurements, K.W.; writing—original draft preparation, G.W.; writing—review and editing, K.S. and K.W. All authors have read and agreed to the published version of the manuscript.

Funding: This research received no external funding.

Institutional Review Board Statement: Not applicable.

Informed Consent Statement: Not applicable.

Data Availability Statement: Not applicable.

Conflicts of Interest: The authors declare no conflict of interest.

References

1. *PN-EN 1992-1-1*; Eurocode 2, Design of concrete structures, Part 1-1: General rules and rules for buildings. European Union: Brussels, Belgium, 2008. (In Polish)
2. *PN-EN 1996-2*; Eurocode 6, Design of masonry structures, Part 2: Design regulations, selection of materials and masonry structure erection. European Union: Brussels, Belgium, 2010. (In Polish)
3. Kiernożycki, W. Expansion joints in reinforced concrete structures. *Przegląd Bud.* **2006**, *12*, 33–44. (In Polish)
4. Chodor, L. Expansion Joints in Floor Slabs in Buildings. 2016. Available online: http://chodor-projekt.net/encyclopedia/dylatacje-plyt-stropowych-zelbetowych/ (accessed on 10 January 2023). (In Polish)
5. *PN-B-03264*; Concrete, Reinforced Concrete and Prestressed Structures—Static Load Calculations and Design. SBD, Sektor Budownictwa i Konstrukcji Budowlanych: Warsaw, Poland, 6 December 2002. (In Polish)
6. *PN-B-03002*; Masonry structures—Design and calculation. SBD, Sektor Budownictwa i Konstrukcji Budowlanych: Warsaw, Poland, 11 July 2007. (In Polish)
7. Hajduk, P. Expansion Joints in Industrial Flooring. HAJDUK Design and Construction Office. *Przegląd Bud.* **2014**, *7–8*, 44–49. (In Polish)
8. Schabowicz, K.; Wróblewski, K.; Sterniuk, A. Repair of structural expansion joints in parking garage. *Mater. Bud.* **2017**. (In Polish)
9. Wróblewski, K. Sealing of expansion joints in bottom slab of underground car park. *Inżynier Budownictwa* **2018**, *5*. (In Polish)
10. Rokiel, M. Sealing of expansion joints. *Inżynier Budownictwa* **2013**, *6*. (In Polish)
11. Rokiel, M. Expansion joints. Types of expansion joints. How to make expansion joints? What to fill them with? *Build. Guide*—Murator **2019**, *4*. (In Polish)
12. Pieczonka, T. *Dilatometric Method of Determining Linear Thermal Expansion Coefficient of Solids*; Department of Metals Engineering and Industrial Computing, AGH University of Science and Technology: Cracow, Poland, 2010. (In Polish)
13. Cagnona, H.; Vidala, T.; Selliera, A.; Bourbonb, X.; Campsb, G. Transient Thermal Deformation of high performance concrete in the range 20 °C–40 °C. *Cem. Concr. Res.* **2019**, *116*, 19–26. [CrossRef]
14. Available online: https://www.forbuild.eu/produkty/profile-dylatacyjne/ (accessed on 29 February 2020).
15. *PN-EN 1542:2000*; Products and Systems for Protection and Repairs of Concrete Structures—Testing Methods—Measurement of Adhesion by Pull-Off Method. SBD, Sektor Budownictwa i Konstrukcji Budowlanych: Warsaw, Poland, 25 August 2007. (In Polish)
16. Staudt, Y.; Odenbreit, C.; Schneider, J. Failure behaviour of silicone adhesive in bonded connections with simple geometry. *Int. J. Adhes. Adhes.* **2018**, *82*, 126–138. [CrossRef]
17. Falborski, T. Study on Properties of Polymer as a Material for Seismic Isolation Bearings. Ph.D. Thesis, Politechnika Gdańska, Gdańsk, Poland, 2014.
18. Czabanowski, R. Experimental identification of hyperelastic material parameters for calculations by the finite element method. *J. KONES Powertrain Transport.* **2010**, *17*, 87–92.
19. Waśniewski, G.; Schabowicz, K.; Wróblewski, K.; Kasprzak, T. Identification of physical model of resinous filling expansion joint in reinforced concrete structures. *J. Build. Eng.* **2022**, *45*, 103505. [CrossRef]
20. *ABAQUS Analysis User's Guide*; Dassault Systèmes: Providence, RI, USA, 2014.
21. Rymarz, C.Z. *Mechanics of Continuous Media*; Wydawnictwo Naukowe PWN: Warsaw, Poland, 1993. (In Polish)
22. Eringen, A.C. *Nonlinear Theory of Continuous Media*; McGraw-Hill Book Company: New York, NY, USA, 1962.
23. Ogden, R.W. Large deformation isotropic elasticity—On the correlation of theory and experiment for the incompressible rubberlike solids. *Proc. R. Soc. Lond. Ser. A Math. Phys. Sci.* **1972**, *326*, 565–584. [CrossRef]
24. Ogden, R.W. Large deformation isotropic elasticity—On the correlation of theory and experiment for the compressible rubberlike solids. *Proc. R. Soc. Lond. A* **1972**, *328*, 567–583. [CrossRef]

materials

MDPI

Article

Eco-Friendly Sustainable Concrete and Mortar Using Coal Dust Waste

Evgenii M. Shcherban' [1], Sergey A. Stel'makh [2], Alexey N. Beskopylny [3,*], Levon R. Mailyan [2], Besarion Meskhi [4], Diana Elshaeva [2], Andrei Chernil'nik [2], Alexander L. Mailyan [5] and Oxana Ananova [6]

[1] Department of Engineering Geology, Bases and Foundations, Don State Technical University, 344003 Rostov-on-Don, Russia; au-geen@mail.ru
[2] Department of Unique Buildings and Constructions Engineering, Don State Technical University, 344003 Rostov-on-Don, Russia; sergej.stelmax@mail.ru (S.A.S.); lrm@aaanet.ru (L.R.M.); diana.elshaeva@yandex.ru (D.E.); chernila_a@mail.ru (A.C.)
[3] Department of Transport Systems, Faculty of Roads and Transport Systems, Don State Technical University, 344003 Rostov-on-Don, Russia
[4] Department of Life Safety and Environmental Protection, Faculty of Life Safety and Environmental Engineering, Don State Technical University, 344003 Rostov-on-Don, Russia; spu-02@donstu.ru
[5] Department of Urban Construction and Economy, Don State Technical University, 344003 Rostov-on-Don, Russia; mailyan_a@sroufo.ru
[6] Department of Marketing and Engineering Economics, Faculty of Innovative Business and Management, Don State Technical University, 344003 Rostov-on-Don, Russia; o_ananova@mail.ru
* Correspondence: besk-an@yandex.ru; Tel.: +78-632-738-454

Abstract: Finding the solution to the problem of the accumulating waste from the mining and processing industries, as well as reducing their carbon footprint, is among the most important tasks today. Within the construction industry, in the field of the production of building materials such as concrete, these problems may be solved through the use of waste and by saving the binder component. The purpose of this study is to substantiate the feasibility of using waste coal dust (CD) in concrete and cement–sand mortars as a partial replacement for cement. Test samples were made by partially replacing cement with CD in an amount from 0% to 10% in increments of 2% by weight. The following main characteristics were studied: mobility and density of mixtures, as well as density, compressive strength, bending strength and water absorption of concrete and mortars. X-ray diffraction and microscopic analysis methods were used in this work. The introduction of CD to replace part of the cement, up to 10%, did not have a significant effect on the density of concrete and mortar mixtures but reduced their workability. The best values of physical and mechanical characteristics were recorded for concrete and mortar with 4% CD. The increases in the compressive strength of concrete and mortars were 6.6% and 5.7%, and in flexural strength 6.1% and 5.6%, respectively. Water absorption decreased by 9.7% for concrete and by 9.3% for mortar.

Keywords: coal dust; concrete; mortar; compressive strength; bending strength; water absorption

Citation: Shcherban', E.M.; Stel'makh, S.A.; Beskopylny, A.N.; Mailyan, L.R.; Meskhi, B.; Elshaeva, D.; Chernil'nik, A.; Mailyan, A.L.; Ananova, O. Eco-Friendly Sustainable Concrete and Mortar Using Coal Dust Waste. *Materials* **2023**, *16*, 6604. https://doi.org/10.3390/ma16196604

Academic Editor: Pizhong Qiao

Received: 16 September 2023
Revised: 2 October 2023
Accepted: 4 October 2023
Published: 9 October 2023

1. Introduction

Currently, in many countries of the world, there is a big problem associated with the accumulation of waste from the mining and processing industries [1–5], in particular, for industrial mining purposes. For example, in coal mines and related industries, a huge amount of by-material of coal products is formed that is not used for its intended purpose [6,7]. One of the most typical representatives of this waste group is coal dust. This problem is inherent in many countries and regions of the world where the mining industry is well developed. Enterprises and scientific institutes in such countries face a serious challenge in developing proposals at the fundamental and applied levels to study the possibility of using such coal dust [8–10].

Coal dust can be classified as an inert mineral additive that does not fully react with the binder component in the concrete mixture. The main purpose of using additives of this type in concrete technology is the additional compaction of cement composites achieved by reducing porosity [11,12]. These types of additives include clay, metakaolin, electric arc furnace dust waste, various types of rock dust and finely ground calcium powders from aquaculture waste. For example, in the study [13], compositions of self-compacting concrete mixtures were developed in which part of the cement was replaced by calcined clay. It was found that when replacing up to 20% by volume, the fluidity of the mixture, compressive strength and durability of the developed composites did not change much and were comparable to the control composition. There is known work using the addition of metakaolin in self-compacting concrete (SCC) compositions [14]. As a result, it was found that with the optimal replacement of 10% of cement with metakaolin, SCC has good resistance to magnesium sulfate solution, chloride diffusion and water absorption, and the microstructure of these composites is characterized by a smaller amount of ettringite. A similar study was carried out in [15]. It was established that metakaolin in SCC at a rational quantity also has a positive effect on the strength, water absorption and porosity. The use of metakaolin as a partial replacement for cement in concrete technology was also studied in detail in [16–19]. It is noted that the use of this additive in rational quantities makes it possible to improve the strength characteristics and durability of composites and reduce their porosity and water absorption.

In studies [20–28], the use of various types of dust was investigated. The use of electric arc furnace dust in [20] when replacing part of the cement in an amount of 2% helped to improve the strength characteristics. In the study [21], the most effective concrete compositions were obtained by replacing part of the cement with freshly homogenized electric arc furnace dust in an amount of 4%. In [22], in addition to improving the mechanical properties of the composites, the results of SEM analysis showed that the introduction of electric arc furnace dust led to a noticeable decrease in ettringite crystals. The use of marble dust as a partial replacement for cement [23] in an amount of 10% increased the compressive, tensile and flexural strength by 12.68%, 21.71% and 16.73%, respectively, compared to the control mixture. Similarly, in [24], cement composites with 10% replacement of part of the binder with marble dust showed good results. In general, the effectiveness of using stone dust in concrete as a partial replacement for binders was also confirmed by the following works [25–27]. Powders from aquaculture waste are often used as a replacement for cement. For example, in [29], the use of finely ground oyster shell powder in an amount of 3% helped improve the properties of cement composites. And in work [30], when replacing part of the cement with seashell powder in an amount of 5–15%, the concrete had less porosity compared to control compositions. The positive effects of using finely ground powders of various types of shells as a replacement for part of the cement in concrete are also described in a number of the following studies [31–33].

The use of coal dust in building materials and in particular in cement composites was considered in works [8–10,34]. Overall, the addition of coal dust in certain quantities can facilitate its efficient use in the production of cement and concrete and thus make a significant contribution to the sustainable development of the construction industry in terms of long-term energy savings, a reduction in greenhouse gas emissions and the mitigation of global climate change [8]. These few studies made it possible to conduct a more accurate analysis of the current existing gaps in the study of the use of coal dust in concrete.

The relevance of the research being carried out is confirmed by the high degree of risk of violating the environmental agenda due to the accumulation of coal dust. Such dust has a direct impact on the creation of a carbon footprint and the risk of not achieving sustainable development goals. As for the relevance of the scientific research of this work, it should be noted that the natural mechanism for the formation of concrete based on coal dust is complex [34]. Coal dust, as a fine powdery material, has a certain chemical composition that must be carefully taken into account when integrating such a powdered

material into the composition of a concrete conglomerate. In particular, it is necessary to clearly understand the physicochemical processes that occur during the formation of the structure of concrete based on coal dust and to evaluate the compatibility of coal dust with other components in the concrete [9,35]. In this case, one needs to clearly understand which component or additional component this powder material is replacing. The shape of these particles plays a significant role, as does their size and distribution, according to fractional analysis. X-ray phase analysis, carried out before using such coal dust in concrete, is important. Eliminating such scientific deficiencies will help to better assess the fundamental relationship between the composition, structure and properties of new concretes [36]. One way or another, any composite that uses a new, uncharacteristic component will be a rather unpredictable or hard-to-predict material. It is necessary to take into account not only the chemical, physical–mechanical and other characteristics of the raw materials but also aspects of concrete mixing and aspects of the distribution of coal dust in the concrete body in order to achieve maximum uniformity of particle distribution in combination with other components [37,38]. It is important to have a clear understanding of the role of these particles. This is necessary to prevent the creation of harmful clusters in which particles stick to each other and to strive for a uniform distribution of coal dust particles mixed with other components. That is why it is important to understand what the rational amount of coal dust in the body of the concrete is and how the required percentage of coal dust relates to the amount of other powdered materials, for example, cement or other fillers used simultaneously with coal dust. The compatibility of coal dust with fillers and concrete aggregates is important, for which the shape, development of the grain surface and other aspects that can affect the achievement or nonachievement of specified characteristics also play an important role [9,39]. Restrictions on the use of coal dust are regulated by technological and regulatory requirements. In terms of technology, the limitations arise from the need to comply with technological processes and rely on the requirements of standards. In the regulatory and technical sphere, limitations are determined by the lack of a systematized base of regulatory and technical documents, which gives such composites the character of experimental ones, requiring more serious justification and testing [40].

The purpose of this study is to substantiate the feasibility of using waste coal dust (CD) in concrete and cement–sand mortars as a partial replacement for cement. It is important to prevent a decrease in the characteristics of concrete when using coal dust compared to control samples. This effect can definitely be called positive and, based on this, our scientific hypothesis is formulated as follows. Provided that optimal recipe–technological factors and parameters are observed when achieving the compatibility of the components of concrete containing coal dust and the conditions for the formation of a rational structure, it is possible to achieve high-performance indicators of concrete that are at least not inferior to analogous concrete made without the use of such dust. The environmental effect of this development is achieved by creating ways to dispose of waste such as coal dust. In the same context, there is also an economic effect that makes it possible to reduce the cost of concrete by saving an expensive component—cement. The technological effect should be to prevent a decrease in the technological properties of the created carbon–concrete mixture. The scientific novelty of the ongoing research is the acquisition of new fundamental and applied knowledge about the patterns of formation of the structure and properties of concrete based on coal dust, depending on rational recipe–technological factors and parameters, as well as the achievement of empirical values within certain limits and ranges for the specified parameters.

2. Materials and Methods

In order to structure this research and present it in the form of a program, we first list the most key objects and parameters to be studied in order to study the effect of coal dust on cement composites. Based on the fact that coal dust is a finely dispersed modifier for cement composites, we will focus on such composites as cement mortars and heavy concrete. The choice of these research objects was made because these composites cover the widest

field of application in modern construction. And in particular, in those areas where the extraction of the corresponding raw materials in the form of coal dust occurs, it is advisable to study these types of composites. At the same time, it is important to understand that it is not only hardened composites in finished form that are subject to research but also their fresh mixtures, which have a number of rheological and other technological characteristics. Thus, the experimental research program will include the most important and indicative properties and characteristics of mortar mixtures, cement mortars and concrete mixtures, that is, fresh concrete and hardened concrete. The parameters that determine the most important aspects of the influence of the addition of coal dust on the properties of all these mixtures and composites will be those properties that are strictly regulated in the regulatory and technical documentation and are the most important. These are the mobility of fresh composites and the mechanical strength characteristics of hardened composites.

2.1. Materials

The following raw materials were used as components for the manufacture of the experimental samples:

- Portland cement CEM I 52.5N (C) (CEMROS, Stary Oskol, Russia) [41];
- Crushed sandstone (CS) (RostMed, Kamensk, Russia);
- Quartz sand (S) (RostStroyMix, Rostov-on-Don, Russia);
- Coal dust (CD) (IMPEX-GROUP, Krasny Sulin, Russia).

The characteristics of the raw materials are presented in Table 1.

Table 1. Characteristics of raw materials.

Property					**Value**	
Portland cement CEM I 52.5N						
Specific surface area (m^2/kg)					339	
Soundness (mm)					0.5	
Fineness, passage through sieve No. 008 (%)					97.5	
Setting times (min): - Start - End					 170 240	
Compressive strength (MPa): - 2 days - 28 days					 25.7 58.5	
Crushed sandstone						
Particle size (mm)					5–20	
Bulk density (kg/m^3)					1429	
Apparent density (kg/m^3)					2553	
Resistance to fragmentation (wt %)					11.8	
Content of lamellar and acicular grains (wt %)					9.7	
Quartz sand						
Sieve diameter (mm)					Content (% by weight) of grains with a particle size of less than 0.16 mm	Fineness modulus
Partial residues on sieves (%)						
Total residues on sieves (%)						
2.5	1.25	0.63	0.315	0.16		
3.2	10.1	14.3	16.6	54.7	1.0	1.87
3.2	13.3	27.6	44.2	99.0		

Table 1. *Cont.*

Property	Value
Quartz sand	
Bulk density (kg/m^3)	1255
The content of dust and clay particles (%)	0.09
Content of clay in lumps (%)	0.12
Organic and contaminant content (%)	No
Coal dust (CD)	
Bulk density (kg/m^3)	345
Loss on ignition (%)	37.34
Silicon oxide SiO_2 (%)	30.83
Aluminum oxide Al_2O_3 (%)	15.74
Iron oxide Fe_2O_3 total (%)	6.22
Calcium oxide CaO (%)	2.92
Magnesium oxide MgO (%)	3.43
Titanium oxide TiO_2 (%)	0.64
Phosphorus oxide P_2O_5 (%)	0.07
Total sulfur oxide SO_3 (%)	2.81

The plasticizer Sikament® BV 3M (P) (Zika, Lobnya, Russia) was used as an additive to regulate the workability of the concrete and mortar mixtures.

The grain composition and X-ray diffraction pattern of coal dust are presented in Figures 1 and 2.

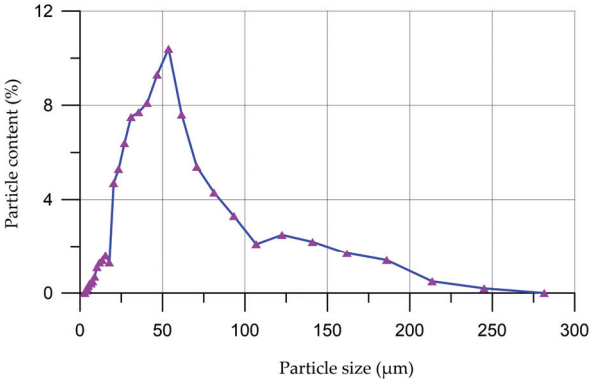

Figure 1. Distribution curve of coal dust particles.

According to the granulometric curve presented in Figure 1, the largest proportion of coal dust particles, 67%, have sizes from 20 μm to 70 μm, the proportion of particles with a size of less than 20 μm is 9.4% and particles with a size of more than 70 μm is 23.6%.

Based on the results of XRD analysis of coal dust, we identified muscovite, quartz and chlorite phases, and an amorphous carbon phase was also present.

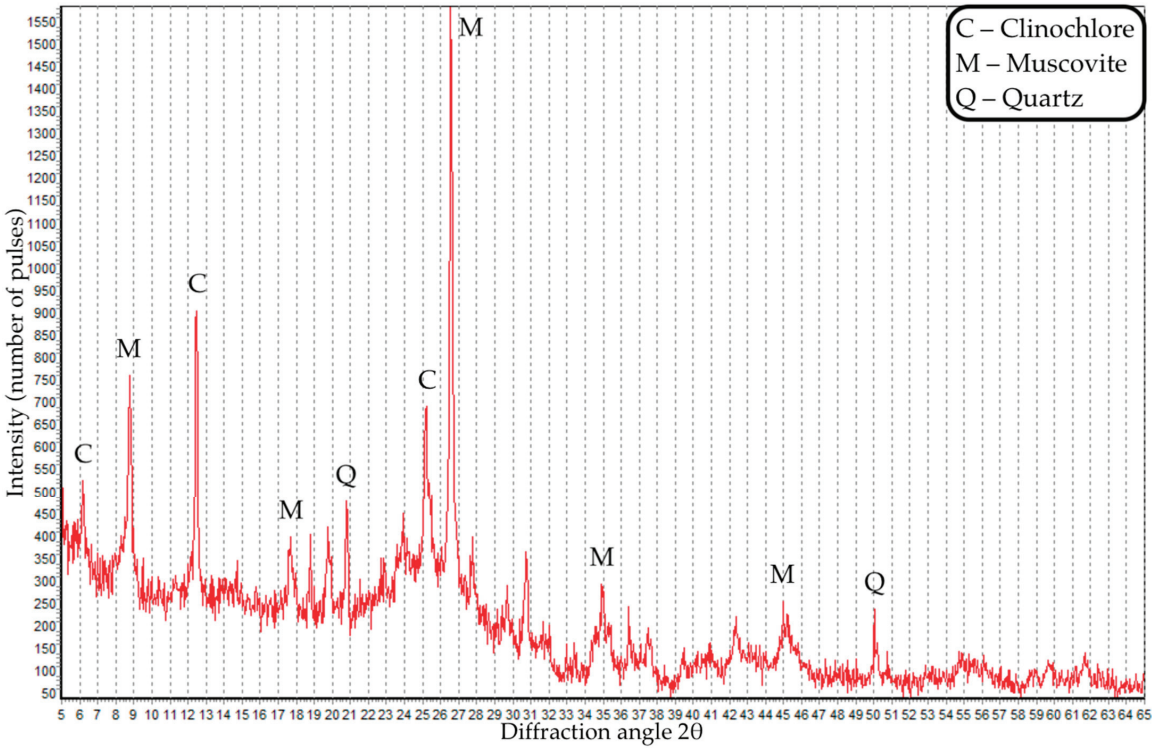

Figure 2. X-ray pattern of coal dust.

2.2. Methods

The compositions of experimental concrete mixtures and mortars are presented in Tables 2 and 3.

Table 2. Concrete mix designs.

Mixture Type	Concrete Mixture Proportion per 1 m^3					
	C (kg/m^3)	W (L/m^3)	CS (kg/m^3)	S (kg/m^3)	CD (kg/m^3)	P (% by Weight of Cement)
0CD/C	353	199	936	711	0	0
2CD/C	345.9	199	936	711	7.1	1.0
4CD/C	338.9	199	936	711	14.1	1.5
6CD/C	331.8	199	936	711	21.2	1.5
8CD/C	324.8	199	936	711	28.2	2.0
10CD/C	317.7	199	936	711	35.3	2.5

The production of concrete and mortar samples included the following main technological steps. First, all raw materials were measured in accordance with the recipe. The production of concrete mixtures was carried out in a laboratory concrete mixer. All raw materials were premixed in dry form, and then mixing water with a plasticizing additive was introduced. Next, the concrete mixture was mixed until homogeneous and placed into molds, which were then additionally vibrated for 60 s.

Table 3. Mortar mix designs.

Mixture Type	Mortar Mixture Proportion per 1 m^3				
	C (kg/m^3)	W (L/m^3)	S (kg/m^3)	CD (kg/m^3)	P (% by Weight of Cement)
0CD/M	346	214	1481	0	0
2CD/M	339.1	214	1481	6.9	1.0
4CD/M	332.2	214	1481	13.8	1.5
6CD/M	325.2	214	1481	20.8	1.5
8CD/M	318.3	214	1481	27.7	2.0
10CD/M	311.4	214	1481	34.6	2.0

Note: C—cement, W—water, CS—crushed stone, S—sand, CD—coal dust, P—plasticizer.

A day later, all samples were removed from the molds and placed in a normal hardening chamber for 27 days at a temperature of 20 ± 2 °C and a relative humidity of 95%. The preparation of mortar samples was carried out in a similar way. After production, the mortar samples were stored in a normal hardening chamber for 27 days.

No differences were observed in the quality or macrostructure of the two types of concrete samples and mortar. The only striking difference was the color of the samples. Samples with coal dust had a pronounced black color.

The main technological equipment for the production of the concrete and mortar samples was as follows:

- Laboratory concrete mixer BL-10 (ZZBO, Zlatoust, Russia);
- Forms 2FK-100, 3FK-70, FB-400, 3FB40 (RNPO RusPribor, St. Petersburg, Russia);
- Normal curing chamber KNT-1 (RNPO RusPribor, St. Petersburg, Russia);
- Laboratory vibration platform (IMash, Armavir, Russia).

The experimental program is presented in Figure 3.

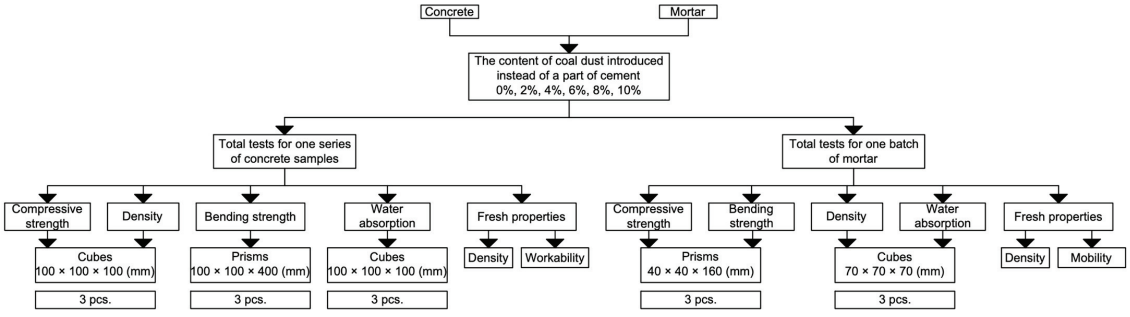

Figure 3. Experimental program.

A total of 36 cubes and 18 prisms of concrete as well as 18 cubes and 18 prisms of mortar were produced.

The fresh properties of the concrete mixture, such as density and workability, were determined in accordance with the methods of [42,43]. The concrete mixture was compacted in a rigid waterproof container with a known volume and mass and then weighed. Density was calculated using the formula

$$D = \frac{m_1 - m_2}{V}$$

where D is the density of the concrete mixture (kg/m^3); m_1—mass of the container filled with compacted concrete (kg); m_2—empty container mass (kg); V—capacity volume (m^3).

The essence of the method for determining the settlement of a cone when testing a concrete mixture for mobility was to compact the prepared concrete mixture in the form of a truncated cone, and the measured distance to which the concrete mixture settled after removing the cone indicated the mobility of the concrete mixture.

Determination of the compressive strength of concrete was carried out in accordance with the methods in [44–49] using a Press P-50 installation (PKC ZIM, Armavir, Russia).

The density of hardened concrete was determined according to the method [50,51] as the ratio of the mass of concrete (sample) in a state of normal humidity, when the samples were stored for 28 days in a normal hardening chamber at a relative air humidity of at least 95% and a temperature of 18 to 22 °C, to its total volume.

The determination of water absorption of concrete samples was carried out in accordance with the requirements of regulatory documents [52,53]. The samples were placed in a container filled with water in such a way that the water level in the container was approximately 50 mm above the top level of the stacked samples. The water temperature in the container was (20 ± 2) °C. The samples were weighed every 24 h during water absorption with an error of no more than 0.1%. The mass of water flowing out of the pores of the sample onto the scale was included in the mass of the saturated sample. The test was carried out until the results of two consecutive weighings differed by no more than 0.1%. The samples were tested in a state of natural humidity. The water absorption of concrete of each sample (wt.%) was calculated with an error of up to 0.1% using the formula:

$$W = \frac{m_w - m_d}{m_d} \times 100$$

where m_w is the mass of the sample saturated with water (g); m_d is the mass of the dry sample (g).

The determination of the fresh properties of mortar mixtures, as well as the density of the hardened mortar, their compressive strength, bending strength and water absorption was carried out in accordance following the requirements of [54,55].

The mobility of the mortar mixture was characterized by the depth of immersion of the reference cone into it, measured in centimeters. The immersion depth of the cone was estimated based on the results of the arithmetic average of two tests on different samples of the mortar mixture from one batch.

The density of the mortar mixture was characterized by the ratio of the mass of the compacted mortar mixture to its volume and was expressed in kg/m^3.

The strength of the hardened solution was determined using prism samples (bending strength) and then using half-prism samples obtained after destruction (compressive strength). The bending strength was calculated as the arithmetic mean of the two highest test results of three samples. The six prism halves obtained after the bending test were immediately subjected to a compression test. One half of the prism was placed between two plates in such a way that the side faces, which, during manufacturing, were adjacent to the walls of the mold, were on the planes of the plates, and the stops of the plates were tightly adjacent to the smooth end plane of the sample. The sample, together with the plates, was centered on the press base plate. The average rate of load increase during testing was (2.0 ± 0.5) MPa/s. The compressive strength of an individual sample was calculated as the quotient of the breaking load divided by the working area of the plate. The compressive strength was calculated as the arithmetic mean of the four highest test results of six samples.

The density of the solution was determined by testing cube samples with an edge of 70 mm. The samples were stored for 28 days in a normal hardening chamber at a relative air humidity of at least 95% and a temperature of (20 ± 2) °C.

The water absorption of the solution was determined using samples that were placed in a container filled with water in such a way that the water level was approximately 50 mm above the top level of the laid samples. Samples were weighed after every 24 h of water absorption. In general, the test parameters were the same as when determining the water absorption of concrete samples [54].

Particle size gradations of components of concrete and mortar were determined using a Microsizer model 201C (VA Insalt, St. Petersburg, Russia).

The chemical composition of fine coal dust was determined in accordance with the requirements of GOST R 55661-2013: Solid mineral fuel. Determination of ash content followed method NSAM 138-X: Chemical methods, Method of quantitative chemical analysis. Accelerated methods for determining rock-forming elements in rocks and ores followed NSAM 3-X methodology. Determination of the total sulfur content in rocks, ores and products of their processing was completed using the gravimetric method. For this purpose, the following equipment was used: analytical balance CAS CAUX-220 (Seoul, Republic of Korea), muffle furnace LOIP (St. Petersburg, Russia), low-temperature furnace SNOL (AB "UMEGA GROUP", Utena, Lithuania) and spectrophotometer UNICO 2100 (Dayton, NJ, USA).

X-ray diffraction analysis was performed on an ARLX'TRA diffractometer using the characteristic radiation of a copper anode (wavelength CuKα11.5406 Å, CuKα21.5444 Å). The PDF-2 X-ray database was used to identify serpentinite phases and minor minerals.

Cured concrete and mortar samples retained a significant difference in color between the control composition and the CD composition. The appearance of the samples did not differ significantly, but in the control mortar samples, there were quite large surface pores.

3. Results

The results of this study of fresh properties of concrete and mortar mixtures are presented in Figures 4–7.

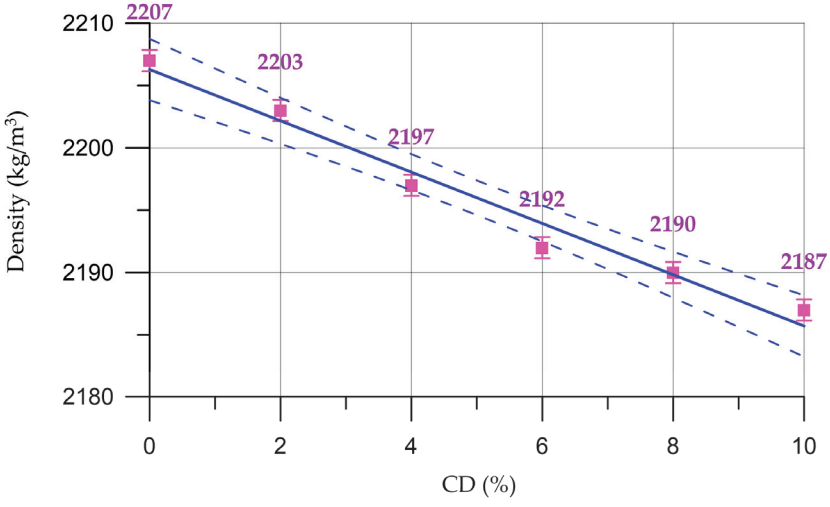

Figure 4. Dependence of the density of the concrete mixture on the CD content (the dashed line shows confidence limits with a level of 0.95).

The dependence of the density of the concrete mixture on the CD content (x in equation) presented in Figure 4 is described by a linear equation with a coefficient of determination R^2:

$$D_{cm} = 2206.2 - 2.057\,x, \quad R^2 = 0.975 \tag{1}$$

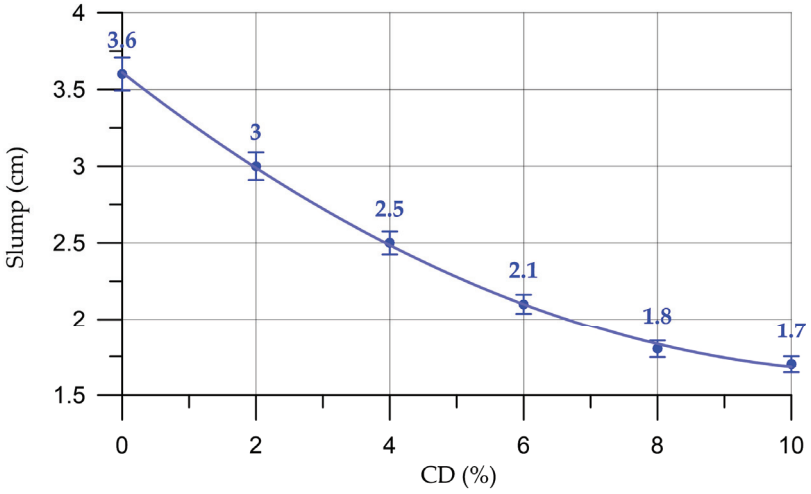

Figure 5. Dependence of mobility of concrete mixture on CD content.

The dependence of the mobility of the concrete mixture on the CD content (%) presented in Figure 5 is described by a second-degree equation:

$$M_{cm} = 3.61 - 0.34\,x + 0.0147\,x, \quad R^2 = 0.99 \tag{2}$$

According to the results of the fresh properties of concrete mixtures, it was found that the density of concrete mixtures with an increase in the percentage of replacing part of the cement with coal dust decreases slightly and varies from 2207 kg/m^3 to 2187 kg/m^3. As for workability, according to [56], it varies within one brand; however, with an increase in the percentage of replacement of part of the cement with coal dust, its decrease is observed. When the replacement value is from 4 to 6%, the consumption of the plasticizing additive increases from 1% to 1.5%; when replacing 8%, the additive consumption increases to 2%; and at 10% CD, it increases to 2.5%.

The results of studying the fresh properties of mortar mixtures are presented in Figures 6 and 7.

The dependence of the density of the mortar on the CD content (%) presented in Figure 6 is described by the linear equation:

$$D_M = 2046.7 - 1.585\,x, \quad R^2 = 0.984 \tag{3}$$

The dependence of mortar mobility on CD content (%) presented in Figure 7 is described by the linear equation:

$$M_M = 7.44 - 0.218\,x, \quad R^2 = 0.99 \tag{4}$$

For the properties of fresh mortar, a similar situation is observed here as with concrete mixtures, namely, with an increase in the percentage of replacing part of the cement with coal dust, the density of the mortar mixtures also decreases slightly. The workability parameter of mortar mixtures also decreases but is within the same brand [57]. When the cement replacement rate is from 4% to 6%, the plasticizer consumption increases from 1% to 1.5%; when replacing from 8% to 10%, the additive consumption is 2%.

A decrease in the mobility of concrete and mortar mixtures when replacing part of the cement with coal dust is associated with increasing water demand. Fine particles of coal dust in concrete and mortar mixtures act as a filler. And as is known, finely dispersed mineral filler additives in cement composites can significantly increase the water–cement ratio of the mixture, which will subsequently lead to a decrease in strength characteristics.

However, the use of these types of mineral additives in combination with a plasticizer will eliminate this problem and maintain the water–cement ratio and workability characteristics of the mixtures within the required limits [9]. Thus, the introduction of the plasticizing additive Sikament® BV 3M into concrete mixtures and mortars with coal dust allows them to maintain their workability within the same grade.

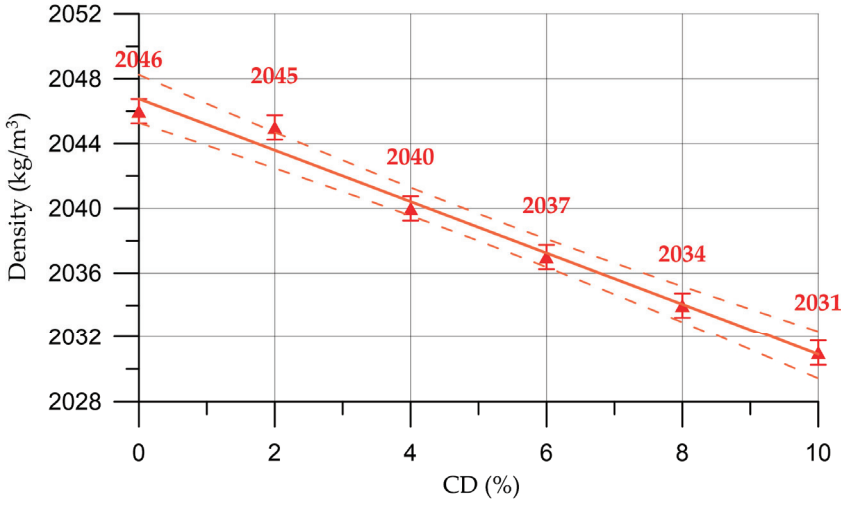

Figure 6. Change in mortar density depending on CD content (the dashed line shows confidence limits with a level of 0.95).

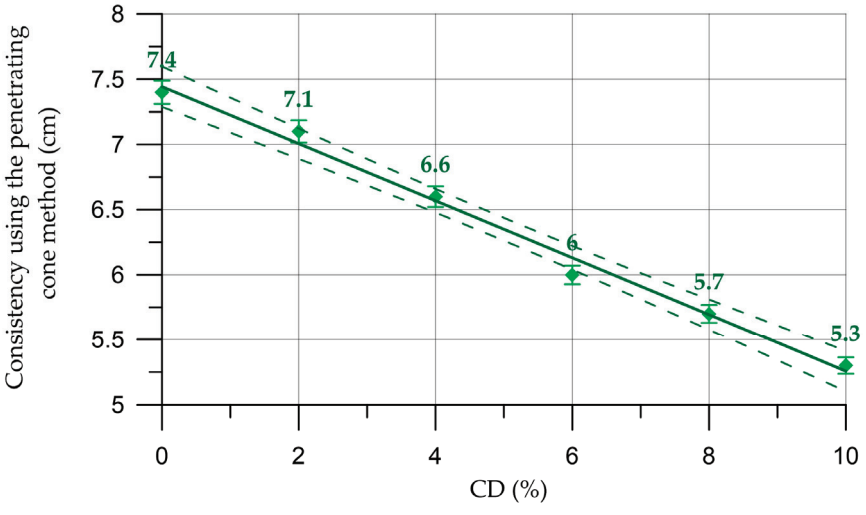

Figure 7. Change in mortar mobility depending on CD content (the dashed line shows confidence limits with a level of 0.95).

The results of determining the physical and mechanical characteristics of concrete and mortars are shown in Figures 8–13. The dependence of concrete density on the content of coal dust is presented in Figure 8.

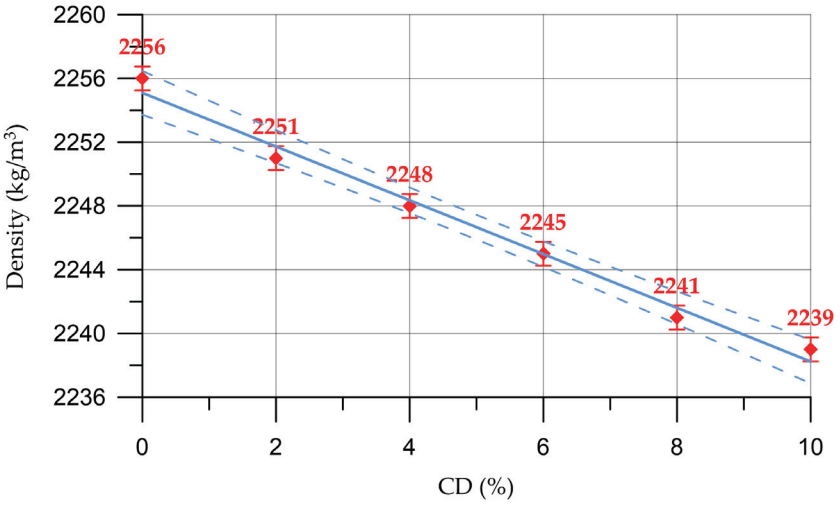

Figure 8. Dependence of concrete density on CD content (the dashed line shows confidence limits with a level of 0.95).

The dependence of concrete density on CD content (%) presented in Figure 8 is described by the linear equation:

$$D_C = 2255 - 1.68\,x, \quad R^2 = 0.987 \tag{5}$$

Figure 9 shows the dependence of the density of the mortar on the content of coal dust.

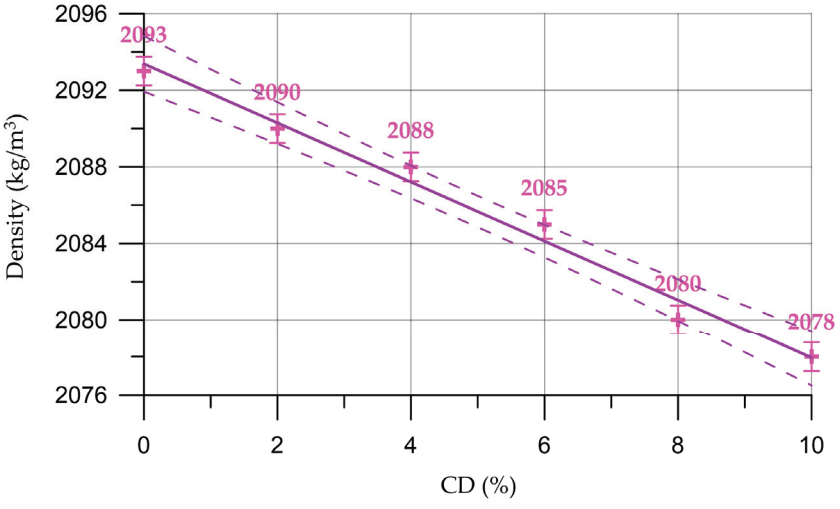

Figure 9. Change in mortar density depending on CD content (the dashed line shows confidence limits with a level of 0.95).

The dependence of the density of the cement mortar on the CD content (%) presented in Figure 9 is described by the linear equation:

$$D_M = 2093 - 1.543\,x, \qquad R^2 = 0.984 \tag{6}$$

From Figures 8 and 9, it can be seen that the density of concrete and mortar decreases slightly with the increasing percentage of the replacement of part of the cement with coal dust. This can be explained by the fact that CD has a lower density compared to cement. However, due to small quantities, CD does not have a significant effect on the change in density of cementitious composites. Thus, the density of concrete varied from 2239 kg/m^3 to 2256 kg/m^3, and the density of the mortar from 2078 kg/m^3 to 2093 kg/m^3.

Figure 10 shows a graph of the dependence of the compressive strength of concrete on the content of coal dust in it.

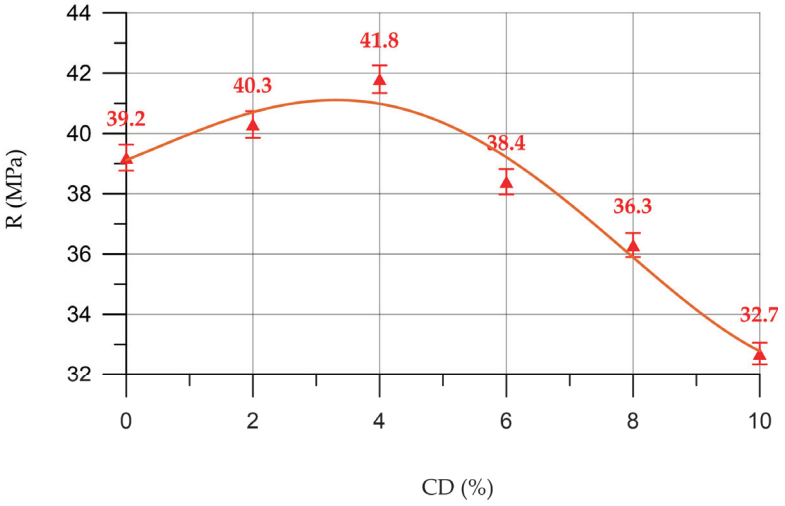

Figure 10. Change in compressive strength (R) of concrete depending on CD content.

To distinguish between the properties of concrete and mortar, the symbols C (for concrete) and M (for mortar) were added to the designations for equations.

The dependence of the compressive strength of concrete (R_C) on CD content (%) presented in Figure 10 is described by a polynomial of the fourth degree

$$R_C == 39.11 + 0.84\,x + 0.0727\,x^2 - 0.0545\,x^3 + 0.00325\,x^4, \quad R^2 = 0.968 \qquad (7)$$

According to the results of determining the compressive strength, presented in Figure 10, it was found that when replacing part of the cement with CD in the amounts of 2% and 4%, small increases in strength are observed up to 2.8% and 6.6%, respectively. However, with a further increase in the amount of CD, a negative effect is observed. At 6% CD, there is a slight loss in the compressive strength of 2% compared to the control composition. However, at CD quantities of 8% and 10%, significant losses in compressive strength were already recorded, which amounted to 7.4% and 16.6%, respectively.

The dependence of the compressive strength of the mortar on the content of coal dust in it is presented in Figure 11.

The dependence of the compressive strength of the mortar (R_M) on CD content (%) presented in Figure 11 is described by a fourth-degree polynomial:

$$R_M == 12.27 + 0.041\,x + 0.1192\,x^2 - 0.0314\,x^3 + 0.00169\,x^4, \quad R^2 = 0.976 \qquad (8)$$

The dependence of the compressive strength of mortar with different CD contents is similar to the change in the compressive strength of concrete. When replacing part of the cement with CD in amounts of 2% and 4%, small increases in compressive strength are observed up to 1.6% and 5.7%, respectively. At a CD quantity of 6%, a drop in compressive

strength is observed by 2.4%, and at 8% and 10% CD, the compressive strength decreases by 8.9% and 17.9%, respectively.

Figure 12 shows a graph of the flexural strength of concrete.

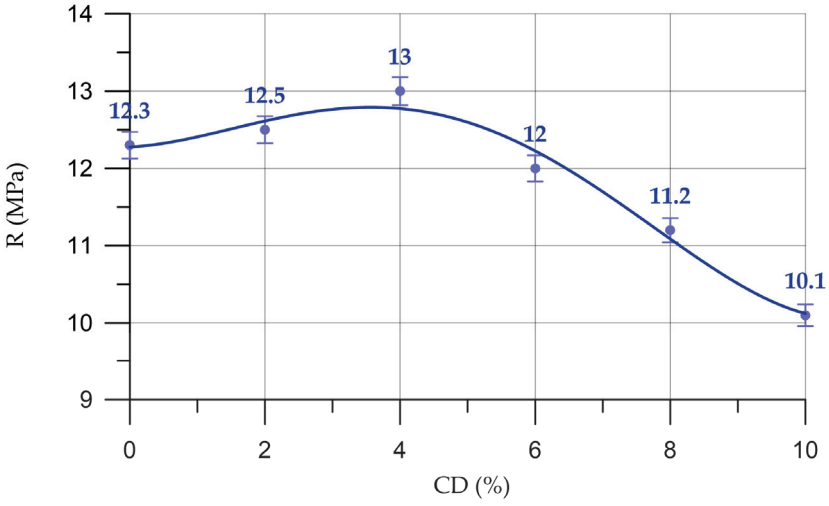

Figure 11. Change in compressive strength (R) of the mortar depending on the CD content.

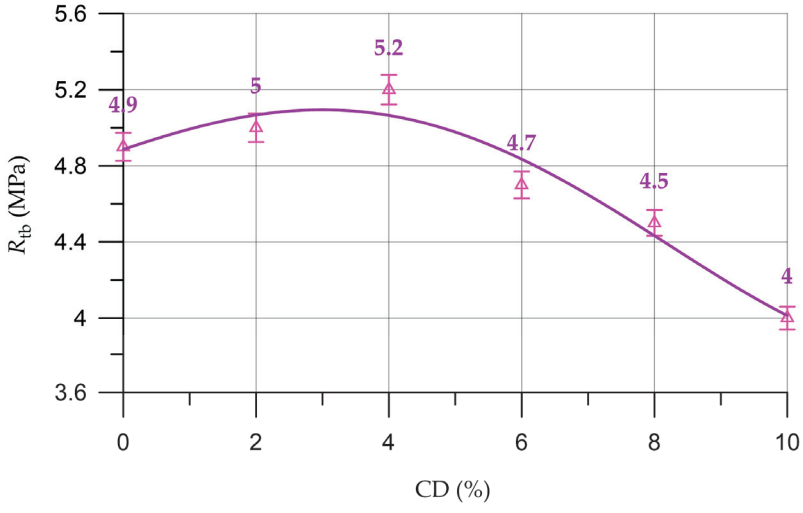

Figure 12. Dependence of concrete flexural strength (R_{tb}) on CD content.

The dependence of concrete flexural strength (R_{tb}^{C}) on CD content (%) presented in Figure 12 is described by a polynomial of the fourth degree:

$$R_{tb}^{C} == 4.88 + 0.1164\,x - 0.0059\,x^2 - 0.00405\,x^3 + 0.0002604\,x^4, \quad R^2 = 0.95 \qquad (9)$$

The dependence of the flexural strength of concrete on the amount of CD has a similar character as the compressive strength. At a CD quantity of 2% to 4%, increases in concrete flexural strength of up to 2.0% and 6.1%, respectively, are observed, and at 6%, 8% and 10% CD, the strength decreased by 4.1%, 8.2% and 18.4%, respectively, compared to the control composition.

The dependence of the flexural strength of the mortar on the amount of coal dust is shown in Figure 13.

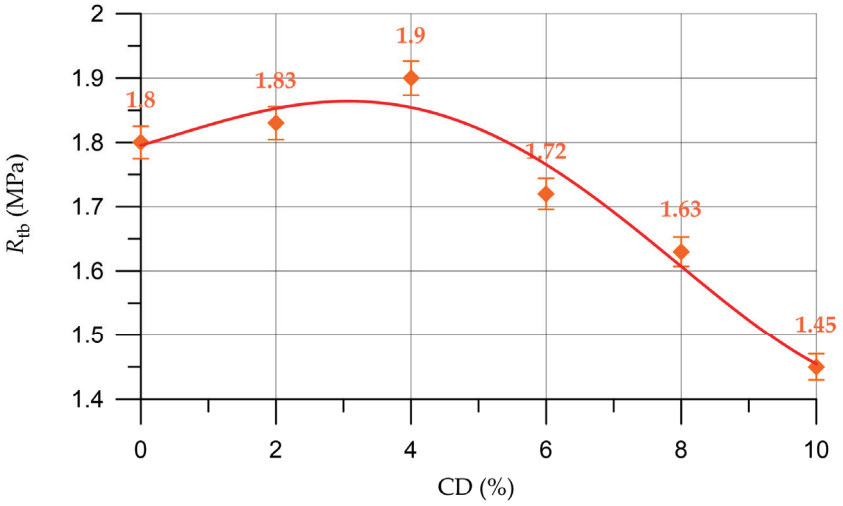

Figure 13. Change in the flexural strength of the mortar depending on the CD content.

The dependence of the flexural strength of the mortar (R_{tb}^{M}) on the content of CD (%) presented in Figure 13 is described by a polynomial of the 4th degree:

$$R_{tb}^{M} == 1.79 + 0.0300\,x - 0.0036\,x^2 - 0.00243\,x^3 + 0.0001432\,x^4, \quad R^2 = 0.96 \qquad (10)$$

When replacing part of the cement in the mortar with CD in an amount of 2%, the flexural strength increases by 1.7%; when replacing 4%, it increases by 5.6%; and with 6%, 8% and 10% CD, the flexural strength decreases compared to the control composition by 4.4%, 9.4% and 19.4%, respectively.

Thus, based on the results of a study of the strength characteristics of concrete and mortar with different CD contents, the following can be noted. This type of finely dispersed additive can be used as a partial replacement for cement up to 6% without a significant loss of strength characteristics. With a larger replacement of cement with coal dust, a deterioration in the strength characteristics of the composites is observed. But it is worth noting that with a quantity of coal dust from 2% to 4%, there is an increase in compressive and bending strength. This result is explained by the fact that replacing cement with 2–4% fine coal dust and adding a plasticizing additive can increase the efficiency of using CD in cement composites. Strength increases because a more dense structure of the hardened cement paste is obtained; this is achieved by increasing the volume concentration of cementing products of binder hydration and by reducing pore volume [9]. The increase in the volume concentration of cementing products of binder hydration is directly related to the chemical composition of CD, presented in Table 2. Coal dust contains 30.83% SiO_2. The available part of silicon dioxide reacts with the hydration of the binder and promotes the formation of additional hydrosilicates [58].

Next, Figures 14 and 15 present the results of determining the water absorption of concrete and mortar with different CD contents.

Figure 14 shows the dependence of the water absorption of concrete on the CD content.

The dependence of the water absorption of concrete on CD content (%) presented in Figure 14 is described by a fourth-degree polynomial:

$$W_C == 5.14 - 0.0794\,x - 0.0604\,x^2 + 0.0188\,x^3 - 0.001119\,x^4, \quad R^2 = 0.95 \qquad (11)$$

According to Figure 14, the lowest water absorption values were recorded for concrete compositions with 2% and 4% CD, introduced to replace part of the cement. At these percentages of CD content, water absorption decreased by 3.5% and 9.7%, respectively. And with a CD content of 6%, 8% and 10%, the water absorption values increased by 2.3%, 9.4% and 15.6%, respectively.

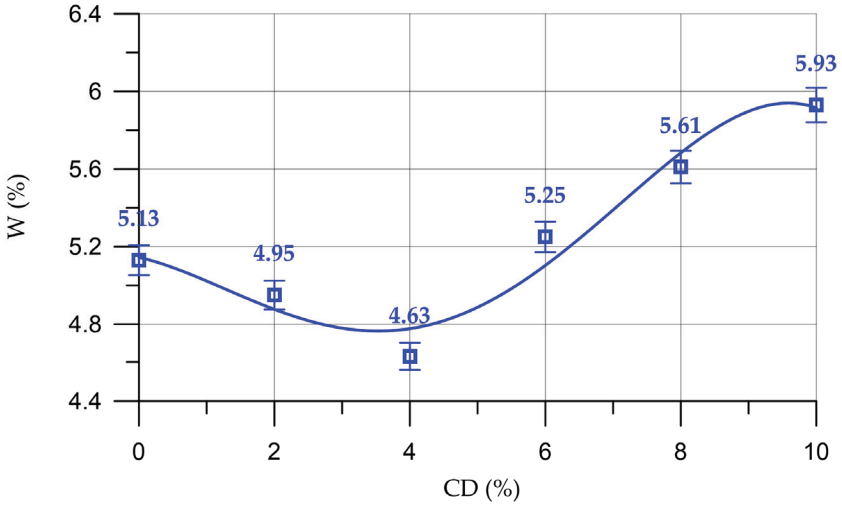

Figure 14. Change in water absorption of concrete depending on CD content.

Figure 15 shows a graph of the dependence of the water absorption of the mortar on the CD content in it.

The dependence of water absorption of the mortar on the content of CD (%) presented in Figure 15 is described by a polynomial of the fourth degree:

$$W_M == 6.58 - 0.0982\,x - 0.0811\,x^2 + 0.0246\,x^3 - 0.001458\,x^4, \quad R^2 = 0.95 \qquad (12)$$

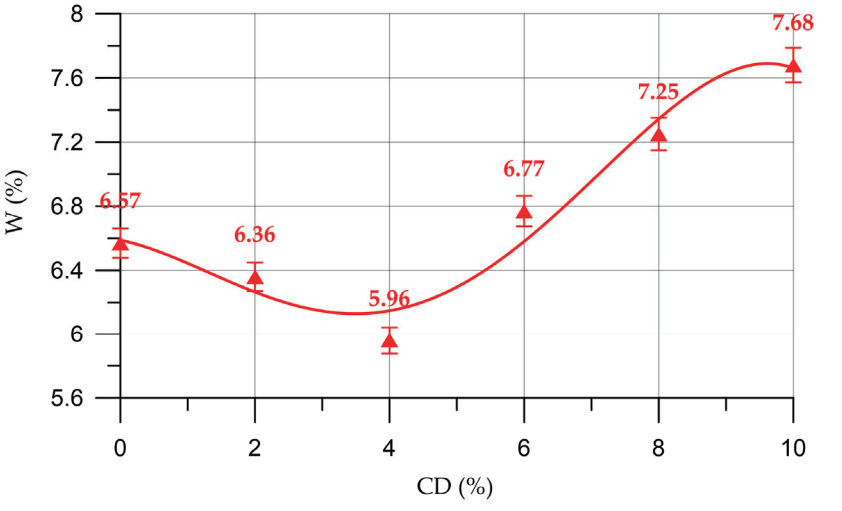

Figure 15. Change in water absorption of the mortar depending on the CD content.

The dependence of the water absorption of the mortar on the CD content has a similar trend as the dependence of the change in water absorption of concrete. At CD quantities of 2% and 4%, the water absorption of the mortar decreased by 3.2% and 9.3%, respectively. At quantities of 6%, 8% and 10%, coal dust negatively affected the water absorption of the mortar. At 6% CD, water absorption increased by 3.0%, at 8% CD by 10.4%; and at 10% CD by 16.9%. The decrease in water absorption is associated with compaction of the structure of the hardened cement paste due to an increase in the volume concentration of cementing products of binder hydration and a decrease in pore volume [9].

Changes in the physical and mechanical characteristics of concrete and mortar with different CD contents are presented as a percentage compared to the control composition in Table 4.

Table 4. Changes in the physical and mechanical characteristics of concrete and mortar with different CD contents.

Characteristics	Δ (%) with CD Content Introduced Instead of Part of the Cement (%)					
	0	**2**	**4**	**6**	**8**	**10**
Concrete						
Density (kg/m^3)	0	−0.2	−0.4	−0.5	−0.7	−0.8
R (MPa)	0	2.8	6.6	−2.0	−7.4	−16.6
R_{tb} (MPa)	0	2.0	6.1	−4.1	−8.2	−18.4
W (%)	0	−3.5	−9.7	2.3	9.4	15.6
Mortar						
Density (kg/m^3)	0	−0.1	−0.2	−0.4	−0.6	−0.7
R (MPa)	0	1.6	5.7	−2.4	−8.9	−17.9
R_{tb} (MPa)	0	1.7	5.6	−4.4	−9.4	−19.4
W (%)	0	−3.2	−9.3	3.0	10.4	16.9

XRD analysis of concrete with control composition and concrete with 4% CD was also carried out. X-ray diffraction analysis of the composites is presented in Figures 16 and 17.

Based on the results of XRD analysis of concrete of the control composition, the phases of portlandite, illite, anorite, calcite and quartz were identified. XRD analysis of concrete with 4% CD identified phases such as larite, albite, portlandite, calcite and quartz. Thus, the introduction of coal dust into concrete contributes to a change in its phase composition and the appearance of such phases as larite and albite.

The results obtained during this study indicate a number of achievements and need to be compared with the results of other authors obtained earlier in order to clarify the scientific novelty and scientific and practical value of this study.

So, in the course of this study, the relationships between the composition and properties of concrete and mortars based on coal dust waste were determined. The structure formation of such concrete largely depends on the following aspects. It is important to understand the role of the carbon modifier in the composition of the cement composite. If the applied carbon modifier is intended to replace part of the binder component, then, on the one hand, there is a risk of not achieving the required strength in such aspects as a decrease in the amount of binder that forms the cement coating of inert particles; an increase in fine components in the material, which additionally require wetting with water; and an increase in the wetting surface, which, in turn, leads to the risk of undercompaction and underformation of the composite structure.

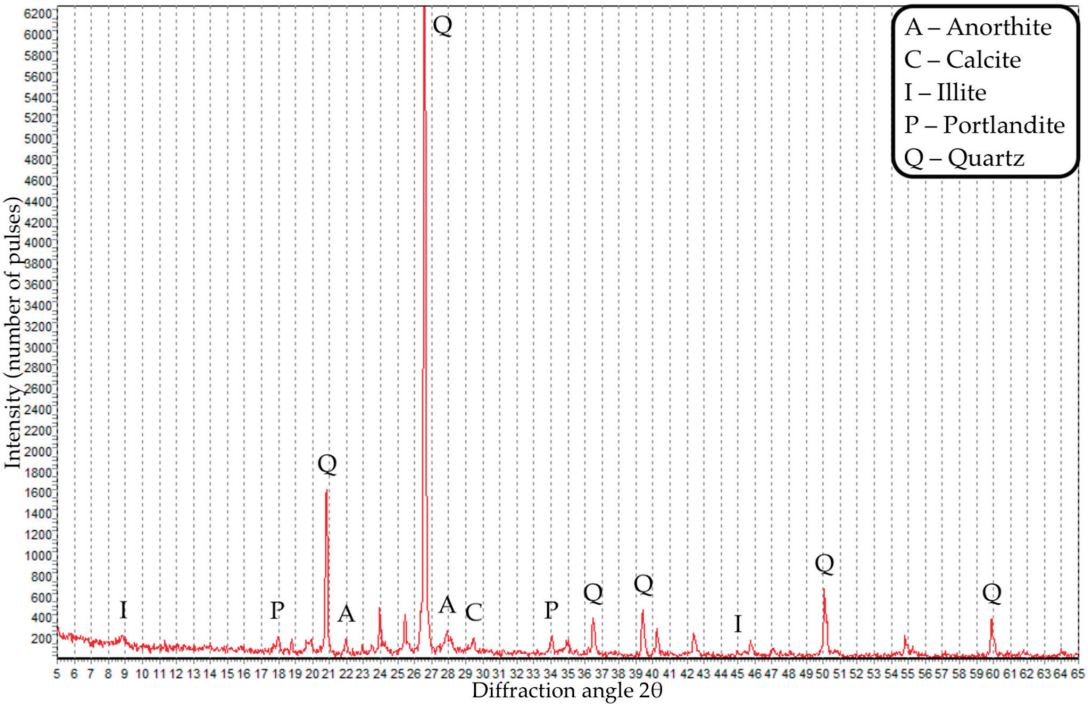

Figure 16. X-ray image of concrete of the control composition.

Based on the results of experimental studies, it was established that with the optimal amount of replacement of part of the cement with coal dust, it is possible to obtain high-quality and environmentally efficient concrete and mortars. It should be noted that, based on the results of the literature review, no studies were found on the use of coal dust with a similar chemical composition as a partial replacement for binders in the technology of cement composites. However, there are a number of studies [13–27] where the use of inert mineral additives, namely, clay, metakaolin, electric arc furnace dust, stone dust and finely ground sea shell powders, as a partial replacement for cement allows in rational amounts the improvement of the physical and mechanical characteristics of the composite and at the same time an increase in its environmental friendliness. The optimal percentages for replacing part of the cement with these types of additives varied from 2% to 20%, while improvements in the strength characteristics, water absorption and porosity of experimental cement composites were observed. In this study, the optimal value for replacing part of the cement with coal dust was 4%. At the same time, the increases in compressive and bending strength were 6.6% and 6.1% for concrete and 5.7% and 5.6% for mortar compared to samples of the control composition. And the water absorption of concrete decreased by 9.7%, and for mortar it decreased by 9.3%. This is in good agreement with the works of a number of authors, in particular with the works [13–19] devoted to the processes of structure formation of concrete composites using coal dust and the works of the authors [20–27] devoted to the physical and mechanical characteristics of concrete modified with coal dust.

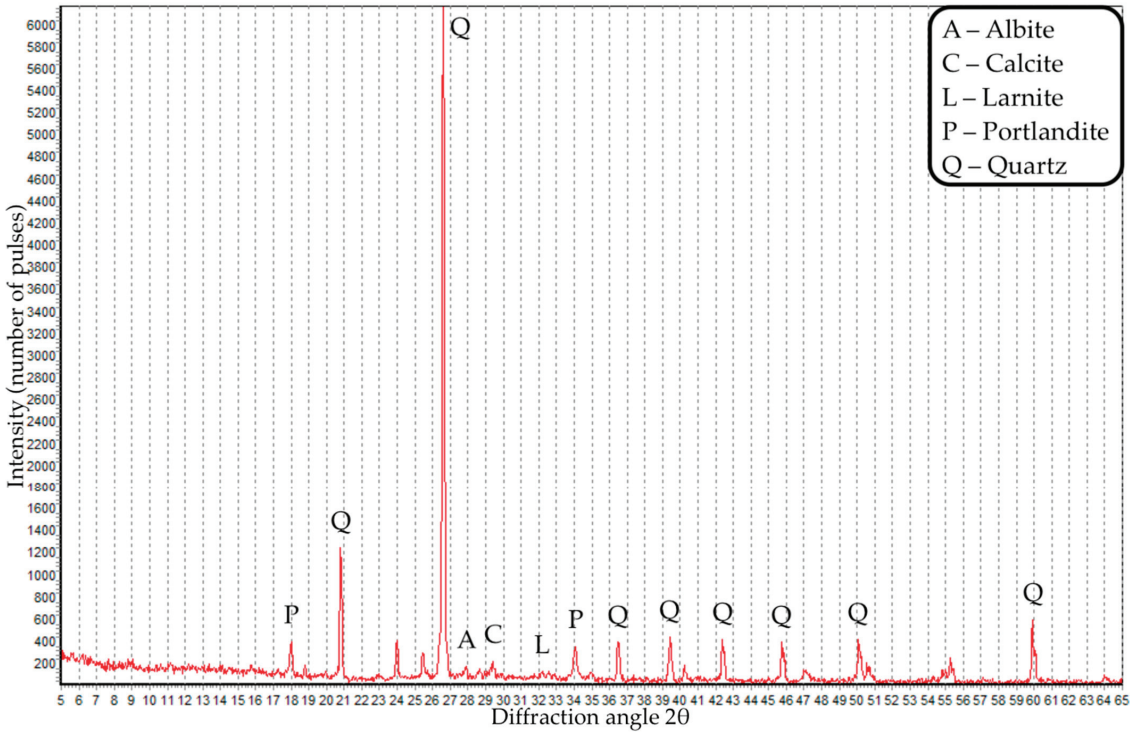

Figure 17. X-ray diffraction pattern of concrete with a CD content of 4%.

The use of coal dust of similar origin in the study [8] in small quantities—up to 2.5 wt.% of ordinary Portland cement—made it possible to improve the mechanical strength of cement composites by reducing open porosity and increased formation of hydration products compared to the reference ones. The prospect of the effective use of coal dust in appropriate, rationally selected quantities in the production of concrete was noted [8]. That study is in excellent agreement with the results presented above. In addition, the use of coal industry waste is potentially effective in the construction sector due to its mineral activity and geographical availability. Thus, separating generated waste into different fractions depending on its origin and production characteristics will be one of the innovations in the search for cleaner production and a more circular economy [10], which fits well with the points presented in this study.

Thus, in terms of replacing the binder, there are two types of risk: the risk of failure to achieve strength indicators and the risk of insufficient wetting of the inert components and hence failure to achieve uniformity of the structure [59–61], which affects the coefficient of structural quality [62]. As for the risks when using coal dust as a modifier in addition to the applied coarse and fine aggregates, the important role of achieving the goal of creating additional crystallization centers should be noted here. That is, coal dust in itself does not contribute to a significant improvement in the processes of structure formation, but, nevertheless, in the case of rationally selected recipe–technological parameters, it can help achieve the goal of denser packing of particles. The structural analysis, XRD analysis and confirmation of these theses by the results of laboratory physical and mechanical tests showed that the problem of determining the rational recipe and technological parameters was solved for a specific type of concrete composite using coal dust. Thus, the scientific hypothesis of this study can be considered confirmed and is in good agreement with the results previously achieved by other authors. The main value of the conducted research in a practical sense is to obtain applied experimental relationships between the composition,

structure and properties of cement mortars and readymade concrete, including a large crushed stone fraction. In this regard, important parameters are the properties of cement mortars, since it is often the mortar component that is the basis for creating new types of concrete or the use of this mortar for other purposes, for example, in masonry or plastering. With all other parameters, the most important property of solutions based on coal dust is the achievement of a rational structure in order to prevent the subsequent occurrence of cracks, peeling and mechanical damage. Thus, the conducted research, in addition to its experimental value for scientific purposes, is important for the applied industry.

4. Conclusions

The rheological and physical–mechanical characteristics of concrete and mortar with different contents of coal dust were developed and studied. This study used normative tests and X-ray diffraction analysis. Based on the results obtained in this study, the following conclusions were drawn:

(1) It was established that coal dust, introduced to replace part of the cement, negatively affects the mobility of concrete and mortar mixtures. However, the introduction of a plasticizing additive allows one to adjust the mobility value of concrete and mortar mixtures and maintain it within the same brand.
(2) Replacing part of the cement with coal dust by up to 10% does not have a significant effect on the change in the density of concrete and mortar mixtures or in hardened composites.
(3) Compared to the control composition, concrete samples with 4% coal dust showed greater efficiency: increases in compressive and flexural strength were 6.6% and 6.1%, and water absorption decreased by 9.7%.
(4) The increases in compressive and flexural strength of the mortar with 4% coal dust content compared to control samples were 5.7% and 5.6%, and water absorption decreased by 9.3%.
(5) The most effective amount of coal dust, introduced instead of part of the cement, was 4%. It was possible to use coal dust in an amount of 6% without a significant loss of strength characteristics for both concrete and mortars.
(6) The use of coal industry waste is potentially effective in the construction sector due to its mineral activity and geographical accessibility. The prospect of effective use of coal dust in appropriate, rationally selected quantities in concrete production was confirmed.

Author Contributions: Conceptualization, S.A.S., E.M.S., A.N.B. and D.E.; methodology, S.A.S., E.M.S. and A.C.; software, O.A., S.A.S., E.M.S., A.N.B. and A.C.; validation, D.E., S.A.S., E.M.S. and A.L.M.; formal analysis, A.C., S.A.S. and E.M.S.; investigation, O.A., D.E., L.R.M., S.A.S., E.M.S., A.N.B. and B.M.; resources, B.M. and A.L.M.; data curation, S.A.S., E.M.S. and A.C.; writing—original draft preparation, S.A.S., E.M.S. and A.N.B.; writing—review and editing, S.A.S., E.M.S. and A.N.B.; visualization, O.A., S.A.S., E.M.S. and A.N.B.; supervision, L.R.M. and B.M.; project administration, L.R.M. and B.M.; funding acquisition, O.A. and B.M. All authors have read and agreed to the published version of the manuscript.

Funding: This research received no external funding.

Institutional Review Board Statement: Not applicable.

Informed Consent Statement: Not applicable.

Data Availability Statement: The study did not report any data.

Acknowledgments: The authors would like to acknowledge the administration of Don State Technical University for their resources and financial support.

Conflicts of Interest: The authors declare no conflict of interest.

References

1. Kumar, R.; Srivastava, A.; Lakhani, R. Industrial Wastes-Cum-Strength Enhancing Additives Incorporated Lightweight Aggregate Concrete (LWAC) for Energy Efficient Building: A Comprehensive Review. *Sustainability* **2022**, *14*, 331. [CrossRef]
2. Li, J. Municipal Solid Waste Incineration Ash-Incorporated Concrete: One Step towards Environmental Justice. *Buildings* **2021**, *11*, 495. [CrossRef]
3. Ribeiro, M.C.S.; Fiúza, A.; Ferreira, A.; Dinis, M.D.L.; Meira Castro, A.C.; Meixedo, J.P.; Alvim, M.R. Recycling Approach towards Sustainability Advance of Composite Materials' Industry. *Recycling* **2016**, *1*, 178–193. [CrossRef]
4. Stel'makh, S.A.; Shcherban', E.M.; Beskopylny, A.N.; Mailyan, L.R.; Meskhi, B.; Shilov, A.A.; Evtushenko, A.; Chernil'nik, A.; El'shaeva, D.; Karalar, M.; et al. Physical, Mechanical and Structural Characteristics of Sulfur Concrete with Bitumen Modified Sulfur and Fly Ash. *J. Compos. Sci.* **2023**, *7*, 356. [CrossRef]
5. Meskhi, B.; Beskopylny, A.N.; Stel'makh, S.A.; Shcherban', E.M.; Mailyan, L.R.; Shilov, A.A.; El'shaeva, D.; Shilova, K.; Karalar, M.; Aksoylu, C.; et al. Analytical Review of Geopolymer Concrete: Retrospective and Current Issues. *Materials* **2023**, *16*, 3792. [CrossRef]
6. Du, J.; Ma, A.; Wang, X.; Zheng, X. Review of the Preparation and Application of Porous Materials for Typical Coal-Based Solid Waste. *Materials* **2023**, *16*, 5434. [CrossRef]
7. Liu, Z.; Ao, Z.; Zhou, W.; Zhang, B.; Niu, J.; Wang, Z.; Liu, L.; Yang, Z.; Xu, K.; Lu, W.; et al. Research on the Physical and Chemical Characteristics of Dust in Open Pit Coal Mine Crushing Stations and Closed Dust Reduction Methods. *Sustainability* **2023**, *15*, 12202. [CrossRef]
8. Pokorný, J.; Ševčík, R.; Zárybnická, L.; Podolka, L. The Role of High Carbon Additives on Physical–Mechanical Characteristics and Microstructure of Cement-Based Composites. *Buildings* **2023**, *13*, 1585. [CrossRef]
9. Caneda-Martínez, L.; Kunther, W.; Medina, C.; Sánchez de Rojas, M.I.; Frías, M. Exploring sulphate resistance of coal mining waste blended cements through experiments and thermodynamic modelling. *Cem. Concr. Compos.* **2021**, *121*, 104086. [CrossRef]
10. Simão, L.; Faraco, M.N.S.; Borgert, C.H.; Olivo, E.; Montedo, O.R.K.; Raupp-Pereira, F. Waste valorization of coal mining waste from a circular economy perspective: A Brazilian case study based on environmental and physicochemical features. *Resour. Policy* **2023**, *80*, 103243. [CrossRef]
11. Beskopylny, A.N.; Stel'makh, S.A.; Shcherban', E.M.; Mailyan, L.R.; Meskhi, B.; Varavka, V.; Beskopylny, N.; El'shaeva, D. A Study on the Cement Gel Formation Process during the Creation of Nanomodified High-Performance Concrete Based on Nanosilica. *Gels* **2022**, *8*, 346. [CrossRef] [PubMed]
12. Korovkin, M.O.; Grintsov, D.M.; Eroshkina, N.A. Rational Use of Inert Mineral Additives in Concrete Technology. *Eng. Bull. Don* **2017**, *3*, 115. Available online: ivdon.ru/ru/magazine/archive/n3y2017/4361 (accessed on 6 October 2023).
13. Muhammad, A.; Thienel, K.-C. Properties of Self-Compacting Concrete Produced with Optimized Volumes of Calcined Clay and Rice Husk Ash—Emphasis on Rheology, Flowability Retention and Durability. *Materials* **2023**, *16*, 5513. [CrossRef] [PubMed]
14. Kavithaa, O.R.; Shanthib, V.M.; Prince Arulraja, G.; Sivakumar, V.R. Microstructural studies on eco-friendly and durable Self-compacting concrete blended with metakaolin. *Appl. Clay Sci.* **2016**, *124–125*, 143–149. [CrossRef]
15. Gill, A.S.; Siddique, R. Durability properties of self-compacting concrete incorporating metakaolin and rice husk ash. *Constr. Build. Mater.* **2018**, *176*, 323–332. [CrossRef]
16. Abdul Sahib, M.Q.; Farzam, M.; Sukkar, K.A. Development and Performance Evaluation of UHPC and HPC Using Eco-Friendly Additions as Substitute Cementitious Materials with Low Cost. *Buildings* **2023**, *13*, 2078. [CrossRef]
17. Hasan, N.M.S.; Shaurdho, N.M.N.; Sobuz, M.H.R.; Meraz, M.M.; Islam, M.S.; Miah, M.J. Utilization of Waste Glass Cullet as Partial Substitutions of Coarse Aggregate to Produce Eco-Friendly Concrete: Role of Metakaolin as Cement Replacement. *Sustainability* **2023**, *15*, 11254. [CrossRef]
18. Elkerany, A.M.; Keshta, M.M.; Elshikh, M.M.Y.; Elshami, A.A.; Youssf, O. Characteristics of Sustainable Concrete Containing Metakaolin and Magnetized Water. *Buildings* **2023**, *13*, 1430. [CrossRef]
19. Selvaraj, T.; Kaliyavaradhan, S.K.; Kakria, K.; Malladi, R.C. Use of E-Waste in Metakaolin Blended Cement Concrete for Sustainable Construction. *Sustainability* **2022**, *14*, 16661. [CrossRef]
20. Saeb, S.; Capitán, J.A.; Cobo, A. The Effect of Electric Arc Furnace Dust (EAFD) on Improving Characteristics of Conventional Concrete. *Buildings* **2023**, *13*, 1526. [CrossRef]
21. Fares, G.; Al-Negheimish, A.I.; Al-Mutlaq, F.M.; Alhozaimy, A.M.; Iqbal Khan, M. Effect of freshly produced electric arc-furnace dust and chloride-free chemical accelerators on concrete performance. *Construct. Build. Mater.* **2021**, *274*, 121832. [CrossRef]
22. Fares, G.; Al-Zaid, R.Z.; Fauzi, A.; Alhozaimy, A.M.; Al-Negheimish, A.I.; Iqbal Khan, M. Performance of optimized electric arc furnace dust-based cementitious matrix compared to conventional supplementary cementitious materials. *Constr. Build. Mater.* **2016**, *112*, 210–221. [CrossRef]
23. Singh, P.; Yee, N.C.; Mohammed, B.S. Utilizing Stearic-Acid-Coated Marble Dust for the Production of Eco-Friendly Self-Cleaning Concrete: RSM Modeling and Optimization. *Sustainability* **2023**, *15*, 8635. [CrossRef]
24. Vardhan, K.; Goyal, S.; Siddique, R.; Singh, M. Mechanical properties and microstructural analysis of cement mortar incorporating marble powder as partial replacement of cement. *Constr. Build. Mater.* **2015**, *96*, 615–621. [CrossRef]
25. Ansari, Y.; Husain, D.; Das, U.K.; Haloi, J.; Khan, N.A.; Prakash, R.; Husain, M. Ecological Footprint Assessment of Concrete: Partial Replacement of Cement by Water Treatment Sludge and Stone Dust. *Sustainability* **2023**, *15*, 7512. [CrossRef]

26. Zamir Hashmi, S.R.; Khan, M.I.; Khahro, S.H.; Zaid, O.; Shahid Siddique, M.; Md Yusoff, N.I. Prediction of Strength Properties of Concrete Containing Waste Marble Aggregate and Stone Dust—Modeling and Optimization Using RSM. *Materials* **2022**, *15*, 8024. [CrossRef]
27. Rana, A.; Kalla, P.; Csetenyi, L.J. Sustainable use of marble slurry in concrete. *J. Clean. Prod.* **2015**, *94*, 304–311. [CrossRef]
28. Shcherban', E.M.; Beskopylny, A.N.; Stel'makh, S.A.; Mailyan, L.R.; Meskhi, B.; Shilov, A.A.; Pimenova, E.; El'shaeva, D. Combined Effect of Ceramic Waste Powder Additives and PVA on the Structure and Properties of Geopolymer Concrete Used for Finishing Facades of Buildings. *Materials* **2023**, *16*, 3259. [CrossRef]
29. Seo, J.H.; Park, S.M.; Yang, B.J.; Jang, J.G. Calcined Oyster Shell Powder as an Expansive Additive in Cement Mortar. *Materials* **2019**, *12*, 1322. [CrossRef]
30. Bamigboye, G.O.; Nworg, A.T.; Odetoyan, A.O.; Kareem, M.; Enabulele, D.O.; Bassey, D.E. Sustainable use of seashells as binder in concrete production: Prospect and challenges. *J. Build. Eng.* **2021**, *34*, 101864. [CrossRef]
31. Stel'makh, S.A.; Shcherban', E.M.; Beskopylny, A.N.; Mailyan, L.R.; Meskhi, B.; Beskopylny, N.; Dotsenko, N.; Kotenko, M. Nanomodified Concrete with Enhanced Characteristics Based on River Snail Shell Powder. *Appl. Sci.* **2022**, *12*, 7839. [CrossRef]
32. Stel'makh, S.A.; Shcherban', E.M.; Beskopylny, A.N.; Mailyan, L.R.; Meskhi, B.; Tashpulatov, S.S.; Chernil'nik, A.; Shcherban', N.; Tyutina, A. Composition, Technological, and Microstructural Aspects of Concrete Modified with Finely Ground Mussel Shell Powder. *Materials* **2023**, *16*, 82. [CrossRef] [PubMed]
33. Shetty, P.P.; Rao, A.U.; Pai, B.H.V.; Kamath, M.V. Performance of High-Strength Concrete with the Effects of Seashell Powder as Binder Replacement and Waste Glass Powder as Fine Aggregate. *J. Compos. Sci.* **2023**, *7*, 92. [CrossRef]
34. Zhang, H.; Liao, W.; Chen, G.; Ma, H. Development and Characterization of Coal-Based Thermoplastic Composite Material for Sustainable Construction. *Sustainability* **2023**, *15*, 12446. [CrossRef]
35. Arogundade, S.; Dulaimi, M.; Ajayi, S. Holistic Review of Construction Process Carbon-Reduction Measures: A Systematic Literature Review Approach. *Buildings* **2023**, *13*, 1780. [CrossRef]
36. Mostafaei, H.; Badarloo, B.; Chamasemani, N.F.; Rostampour, M.A.; Lehner, P. Investigating the Effects of Concrete Mix Design on the Environmental Impacts of Reinforced Concrete Structures. *Buildings* **2023**, *13*, 1313. [CrossRef]
37. Digulla, F.-E.; Bringezu, S. Comparative Life Cycle Assessment of Carbon Dioxide Mineralization Using Industrial Waste as Feedstock to Produce Cement Substitutes. *Energies* **2023**, *16*, 4118. [CrossRef]
38. Gurvich, A.; Creamer, G.G. Overallocation and Correction of Carbon Emissions in the Evaluation of Carbon Footprint. *Sustainability* **2021**, *13*, 13613. [CrossRef]
39. Sizirici, B.; Fseha, Y.; Cho, C.-S.; Yildiz, I.; Byon, Y.-J. A Review of Carbon Footprint Reduction in Construction Industry, from Design to Operation. *Materials* **2021**, *14*, 6094. [CrossRef]
40. Mačiūnas, D.; Nosewicz, S.; Kačianauskas, R.; Boris, R.; Stonys, R. Numerical Simulation of Thermal Conductivity and Thermal Stress in Lightweight Refractory Concrete with Cenospheres. *Materials* **2023**, *16*, 190. [CrossRef]
41. *GOST 31108-2020*; Common Cements. Specifications. Available online: https://docs.cntd.ru/document/1200174658 (accessed on 25 September 2023).
42. *GOST R 57813-2017/EN 12350-6:2009*; Testing Fresh Concrete. Part 6. Density. Available online: https://docs.cntd.ru/document/1200157335 (accessed on 15 September 2023).
43. *GOST R 57809-2017/EN 12350-2:2009*; Testing Fresh Concrete. Part 2. Slump Test. Available online: https://docs.cntd.ru/document/1200157288 (accessed on 15 September 2023).
44. *GOST 10180-2012*; Concretes. Methods for Strength Determination Using Reference Specimens. Gost Standard: Moscow, Russia, 2012. Available online: http://docs.cntd.ru/document/1200100908 (accessed on 15 September 2023).
45. *EN 12390-1:2021*; Testing Hardened Concrete—Part 1: Shape, Dimensions and Other Requirements of Specimens and Moulds. iTeh Standards: Etobicoke, ON, Canada, 2021. Available online: https://standards.iteh.ai/catalog/standards/cen/d1c9ccee-2e5a-425e-a964-961da95d2f99/en-12390-1-2021 (accessed on 15 September 2023).
46. *EN 12390-2:2019*; Testing Hardened Concrete—Part 2: Making and Curing Specimens for Strength Tests. iTeh Standards: Etobicoke, ON, Canada, 2019. Available online: https://standards.iteh.ai/catalog/standards/cen/ae7e6a86-1cbc-455e-8b2a-8964be9087f9/en-12390-2-2019 (accessed on 15 September 2023).
47. *EN 12390-3:2019*; Testing Hardened Concrete—Part 3: Compressive Strength of Test Specimens. iTeh Standards: Etobicoke, ON, Canada, 2019. Available online: https://standards.iteh.ai/catalog/standards/cen/7eb738ef-44af-436c-ab8e-e6561571302c/en-12390-3-2019 (accessed on 15 September 2023).
48. *EN 12390-4:2019*; Testing Hardened Concrete—Part 4: Compressive Strength—Specification for Testing Machines. iTeh Standards: Etobicoke, ON, Canada, 2019. Available online: https://standards.iteh.ai/catalog/standards/cen/10b1c613-819b-42d7-8f94-480cd37a666a/en-12390-4-2019 (accessed on 15 September 2023).
49. *EN 12390-5:2019*; Testing Hardened Concrete—Part 5: Flexural Strength of Test Specimens. iTeh Standards: Etobicoke, ON, Canada, 2019. Available online: https://standards.iteh.ai/catalog/standards/cen/5653c2c7-55a9-4bcb-8e13-5b1dfb0e3baf/en-12390-5-2019 (accessed on 15 September 2023).
50. *GOST 12730.1-2020*; Concretes. Methods of Determination of Density. Gost Standard: Moscow, Russia, 2020. Available online: https://docs.cntd.ru/document/1200177299 (accessed on 15 September 2023).

51. *EN 12390-7:2019*; Testing Hardened Concrete—Part 7: Density of Hardened Concrete. iTeh Standards: Etobicoke, ON, Canada, 2019. Available online: https://standards.iteh.ai/catalog/standards/cen/811a0cf3-55e3-495a-b06e-5c302d5f2806/en-12390-7-2019 (accessed on 15 September 2023).
52. *GOST 12730.3-2020*; Concretes. Method of Determination of Water Absorption. Gost Standard: Moscow, Russia, 2020. Available online: https://docs.cntd.ru/document/1200177301 (accessed on 15 September 2023).
53. *BS 1881-122:2011+A1:2020*; Testing Concrete Method for Determination of Water Absorption. European Standards: Plzen, Czech Republic, 2020. Available online: https://www.en-standard.eu/bs-1881-122-2011-a1-2020-testing-concrete-method-for-determination-of-water-absorption/ (accessed on 15 September 2023).
54. *GOST 5802-86*; Mortars. Test Methods. Gost Standard: Moscow, Russia, 1986. Available online: https://docs.cntd.ru/document/901710699 (accessed on 15 September 2023).
55. *ISO 13765-1:2004*; Refractory mortars—Part 1: Determination of Consistency Using the Penetrating Cone Method. International Standard: Geneva, Switzerland, 2004. Available online: https://www.iso.org/standard/35314.html (accessed on 15 September 2023).
56. *GOST 7473-2010*; Fresh Concrete. Specifications. Gost Standard: Moscow, Russia, 2010. Available online: https://docs.cntd.ru/document/1200085075 (accessed on 15 September 2023).
57. *GOST 28013-98*; Mortars. General Specifications. Gost Standard: Moscow, Russia, 1998. Available online: https://docs.cntd.ru/document/1200003926 (accessed on 15 September 2023).
58. Babkov, V.V.; Gabitov, A.I.; Sakhibgareev, R.R.; Sakhibgareev, R.R. Amorphous microsilica in structurization and hardening of a cement stone processes. *Bashkir Chem. J.* **2010**, *17*, 206–210.
59. Shcherban', E.M.; Stel'makh, S.A.; Beskopylny, A.N.; Mailyan, L.R.; Meskhi, B.; Varavka, V.; Beskopylny, N.; El'shaeva, D. Enhanced Eco-Friendly Concrete Nano-Change with Eggshell Powder. *Appl. Sci.* **2022**, *12*, 6606. [CrossRef]
60. Beskopylny, A.N.; Shcherban', E.M.; Stel'makh, S.A.; Mailyan, L.R.; Meskhi, B.; Evtushenko, A.; Varavka, V.; Beskopylny, N. Nano-Modified Vibrocentrifuged Concrete with Granulated Blast Slag: The Relationship between Mechanical Properties and Micro-Structural Analysis. *Materials* **2022**, *15*, 4254. [CrossRef] [PubMed]
61. Stel'makh, S.A.; Shcherban', E.M.; Beskopylny, A.N.; Mailyan, L.R.; Meskhi, B.; Butko, D.; Smolyanichenko, A.S. Influence of Composition and Technological Factors on Variatropic Efficiency and Constructive Quality Coefficients of Lightweight Vibro-Centrifuged Concrete with Alkalized Mixing Water. *Appl. Sci.* **2021**, *11*, 9293. [CrossRef]
62. Stel'makh, S.A.; Shcherban', E.M.; Beskopylny, A.; Mailyan, L.R.; Meskhi, B.; Varavka, V. Quantitative and Qualitative Aspects of Composite Action of Concrete and Dispersion-Reinforcing Fiber. *Polymers* **2022**, *14*, 682. [CrossRef] [PubMed]

materials

MDPI

Article

Dynamic Diagnostic Tests and Numerical Analysis of the Foundations for Turbine Sets

Jerzy Szolomicki [1,*], Grzegorz Dmochowski [1] and Maciej Roskosz [2]

[1] Faculty of Civil Engineering, Wroclaw University of Science and Technology, 50-370 Wroclaw, Poland
[2] Faculty of Mechanical Engineering and Robotics, AGH University of Science and Technology, 30-059 Krakow, Poland
* Correspondence: jerzy.szolomicki@pwr.edu.pl; Tel.: +48-505-995-008; Fax: +48-71-320-36-45

Abstract: This paper shows current trends in testing and numerical analysis of dynamic loading in relation to a real frame foundation for a turbogenerator set. The analysis of the machine's foundations, which are subjected to static and dynamic loads, is a complex problem combining the issues of geotechnics, structural engineering, and vibration theory. The authors present a case study of the assessment of the foundation's technical condition. The main objective of this study is to perform and compare experimental and numerical dynamic analysis which includes the measurement of the acceleration, speed, and amplitude of the natural vibrations of the foundation during the operational speed of the turbogenerator. In addition, auxiliary material tests were carried out to fully diagnose the foundation and obtain the material properties required for the numerical analysis. They included both destructive and non-destructive of concrete strength, the evaluation of the degree of its carbonation, and the scanning of the reinforcement distribution. The research presented in the paper is intended to facilitate the preparation of appropriate data for the design of the foundation renovation and strengthening.

Keywords: machine foundations; FEM static and dynamic analysis; concrete testing; modelling structural elements

Citation: Szolomicki, J.; Dmochowski, G.; Roskosz, M. Dynamic Diagnostic Tests and Numerical Analysis of the Foundations for Turbine Sets. *Materials* **2023**, *16*, 1421. https://doi.org/10.3390/ma16041421

Academic Editor: Oldrich Sucharda

Received: 16 January 2023
Revised: 3 February 2023
Accepted: 7 February 2023
Published: 8 February 2023

1. Introduction

The foundations of turbine sets are, in most cases, reinforced concrete supporting structures. The turbine sets consist of a synchronous generator that produces electricity, and a steam or gas turbine in which the enthalpy of the medium is transformed into mechanical energy of rotary motion [1]. In Poland, turbine sets are the most common energy sets that operate with the combustion of coal dust. The newer structures are gas or gas steam sets with a heat recovery steam generator. In such cases, the structure of the turbo set can be a multi-shaft and multi-body structure supported by metal foundation plates attached to a concrete foundation.

The shape of the foundation structure is mainly the result of the technical solution of the turbine set [2]. Foundations for turbine sets can be divided into two main types, depending on the shape of the structure: block foundations and frame foundations.

The block foundations are made up of a single-body reinforced concrete structure with numerous cutouts, which is placed on the ground or on piles. The basic feature of block foundations is their high stiffness, which allows them to be classified as non-deformable structures that are placed on elastic subsoil.

A variation of block foundations are:

- open box foundations,
- or closed box foundations.

The second type are frame foundations that consist of an upper plate or upper grate, columns or walls, and a raft plate set on the ground or on piles. The base raft plate, with

a thickness selected to ensure the adequate stiffness and non-deformation of the entire foundation structure, is also intended to create conditions for the full restraint of the columns in the frame part. In frame foundations, vibrations are the result of the elasticity of the structure itself and, moreover, of the ground elasticity on which the bottom raft plate is placed.

Frame foundations are the basic type of supporting structure for high-speed machines that give lower inertia forces than reciprocating machines.

The main source of the dynamic forces in a turbine generator set are interactions that are related to the occurrence of vibrations with the frequency of the first and second harmonics and also those caused by its normal operation.

The loads from the turbine set to the foundation structure are transferred through the foundation bolts that fasten its individual parts. These bolts are screwed onto the recessed parts to the top plate of the foundation.

Foundations for turbine sets work mainly under dynamic load, and therefore high-quality materials with an appropriate strength and durability should be used for their construction. Due to the nature of the load and the need to maintain a rigid and homogeneous concrete structure with the same material properties, it is very important to ensure the homogeneity of the concrete in the entire foundation [3].

There are many scientific problems concerning the dynamics of foundations for turbine sets, which not only concern the structure itself, its geometric shape, material parameters, and boundary and initial conditions, but also those issues related to the identification of the place, value, and precise characteristics of the dynamic forces that originate from the rotating parts of the turbine set acting on the foundation structure [4,5]. The dynamic properties that characterise machines are the frequencies and forms of natural vibrations. In each rotor bearing (in the turbine and generator), the harmonic forces in the direction perpendicular to the longitudinal axis of rotation can be defined as:

$$F_i(t) = P_i \sin(\omega t), \tag{1}$$

$$P_i = m_i e \omega^2, \tag{2}$$

where:

m_i—the proportional part of the rotating mass supported by the i-th bearing,
e—the eccentricity of the mass,
$\omega = 2\pi f$—the cyclic frequency of the turbogenerator's operation,
f—the operating frequency (f_0 = 50 Hz at the nominal speed of the turbine).

The harmonic analysis of the foundation is performed for frequencies in the range of $0.8 f_0 \leq f \leq 1.2 f_0$ between 40 and 60 Hz [6].

Diagnostics of the structure of foundations for a turbogenerator (Figure 1) is one of the most complicated [7–9]. It includes tests, calculations, and analyses that take into account the actual state of the structure and the occurring loads and operational factors, and which also require the adoption of an adequate model that shows the behaviour of the structure [10,11]. Therefore, structural diagnostics often require the use of the most modern research methods, as well as complex variants of analytical methods that use elaborate computer simulations [12–16]. The main objective of this study is to perform and compare experimental and numerical dynamic analysis which includes the measurement of the acceleration, speed, and amplitude of the natural vibrations of the foundation during the operational speed of the turbogenerator. In addition, verification of resonance conditions and weather vibration magnitude must satisfy code limits. Results of the experimental tests in situ enable one to design foundation structure strengthening and update structural models for numerical analysis. The research presented in the paper is intended to facilitate the preparation of appropriate data for the design of the renovation and strengthening of the foundation.

Figure 1. General view of a turbogenerator.

2. Materials and Methods

The authors analysed the existing turbogenerator foundation for a combined heat and power plant. The following experimental dynamic tests were used to verify the resonance conditions and magnitude of vibrations:

- measurement of the acceleration, speed, and natural vibration amplitude of the foundation during the normal operation of the turbogenerator.

In addition, the following material tests were carried out to fully diagnose the foundation and obtain the material properties required for the numerical analysis:

- destructive tests of cores cut from the structure in order to assess the compressive strength of concrete;
- investigations concerning the homogeneity of strength characteristics, and the estimation of the concrete's strength grade on the basis of sclerometer tests [17,18];
- measurements of the extent and intensity of the carbonation process of the subsurface concrete layer conducted on the cut cores using the rainbow test [19,20];
- localisation of the concrete's reinforcement and the determination of its arrangement, its diameters, and the thickness of the concrete's cover using a non-destructive electromagnetic method [21], followed by the comparison of the obtained results with archival documentation. Figure 2 shows a general flow chart of the analysis performed.

The experimental tests were carried out with direct access to the structure and the use of test equipment that met all the necessary technical requirements for this type of measurement. After the experimental analysis of the foundation, the next step of research was numerical modelling with parametric study. It included its structure, which was considered as a reinforced concrete frame system founded on the ground through the raft plate. Dynamic numerical analysis was carried out using AxisVM X6 software. The calculation of the natural frequencies and the appropriate mode shapes is the basis for determining the dynamic parameters of the foundation. The numerical determination of the eigenfrequencies and the form of vibrations of the foundation TG is quite difficult in this

case and, therefore, was verified by experimental measurements. Results of experimental analysis were utilised for creating a numerical model.

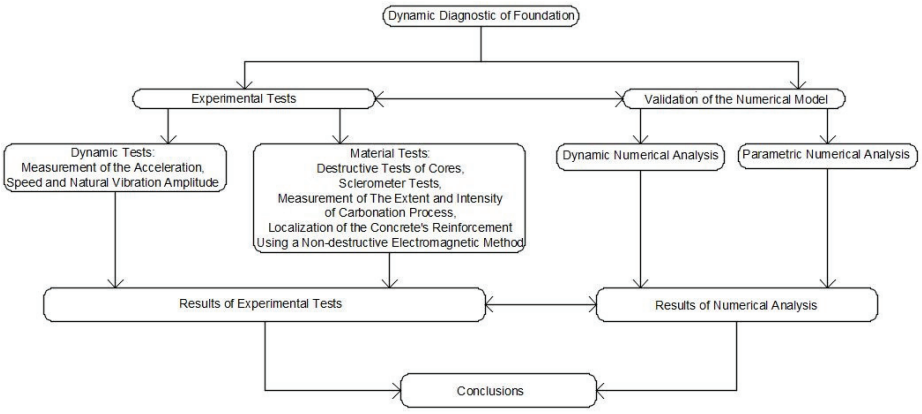

Figure 2. Flow chart of the analysis performed.

3. Dynamic Actions—A Literature Review

Dynamic actions are additional loads on the foundation that must be taken into account in strength calculations. In the dynamic analysis of the foundation, the natural frequencies are determined (there should be a 20% difference compared to the operating frequency of the machine [22]) to check the possibility of the occurrence of resonance. It is also checked if the vibration amplitude resulting from the operation of the turbogenerator is within the acceptable standard limits. In addition, the calculations include the determination of stresses in various structural elements of the foundation (columns, beams, top plate, and base raft plate in the case of a frame foundation) and the checking of their load-bearing capacity.

The scientific literature contains many research results that concern a wide spectrum of machine foundation analysis. The main purpose of the research is to identify the dynamic parameters that are extremely important in the diagnosis of this type of structure. Among the various analyses available in the literature, the following can be distinguished:

- research on the interaction between the foundation and the soil with the determination of the displacements and internal forces of the foundation using three-dimensional viscoelastic boundary elements for the model of the upper plate of the frame foundation [23];
- estimating the foundation parameters in the event of failure, using the inherent unbalance of the rotor and developments in modelling for improved balancing [24–26];
- simulation analysis for asynchronous operation capacity of the turbogenerator under excitation loss [27];
- study of the superposition of vibrations and analysis of ground sensitivity [16];
- numerical analysis with the use of FEM programs (ANSYS, SAP, STAAD) in order to carry out a modal analysis to determine the frequency and amplitude of the vibrations of the foundation [28–30];
- studies of the effects of seismic interactions and the structural configuration for the natural vibrational frequencies of the structures and seismic resistance estimation of existing turbogenerator foundation by a non-linear static method [31,32];
- field tests of frame foundations in terms of settlement and resistance to temperature load [33];
- an investigation of the influence of the supporting structure on the dynamics of the rotor system [34]

- an investigation of stiffness, damping value, natural frequencies, and vibration mode shapes by modelling the soil–foundation system using the FEM [35–39];
- tests of the damping coefficient conducted on the basis of the analysis of the measuring signal using the wavelet transform [40,41];
- analysis of multi-criteria optimisation with regards to the foundations for the turbogenerators [42,43];
- dynamic analysis of a thin and narrow turbogenerator foundation on piles with differentiation of frequency, shear wave velocity, and mode shape [44] and determination procedure of load-bearing capacity [45];
- the estimation of multiple fault parameters of a fully assembled turbogenerator system based on the least squares technique requires forced response information [46].

4. Case Study—A Foundation for a Turbogenerator in a Combined Heat and Power Plant

This paper analyses an existing foundation for a turbogenerator directly coupled to a steam turbine with a rotational speed of 3000 rpm. The turbine is an axial single body and has four vents and two steam outlets for heaters. Steam from the first vent is taken for technological and heating purposes, and from the remaining three, it is directed to low-pressure regenerative exchangers. The turbine set is supported by three bearings, one of which is the load bearing.

The analysed foundation is a reinforced concrete frame structure that consists of a raft plate, columns, and a top plate, as shown in Figure 3. The raft plate of the foundation is set directly on the ground. The part of the reinforced concrete frame of the foundation is supported on this plate. The top plate is supported by three pairs of columns. The basic thickness of the top plate in the generator section is 2.50 m. All columns have cross-sectional dimensions equal to 1000 mm × 1000 mm.

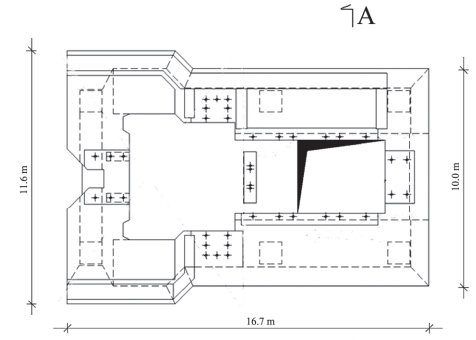

(a) PLAN

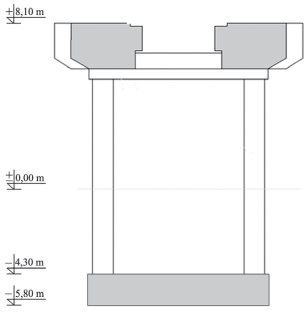

(b) SECTION A - A

Figure 3. Foundation structure: (**a**) plan; (**b**) section.

To diagnose the foundation (Figure 4), dynamic and material and numerical analyses using the results of the experimental tests were carried out.

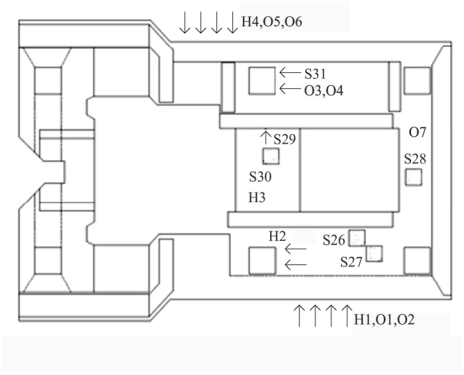

H_i - the place of sampling for the chemical test

O_i - the place of control the drilling samples for the strength tests

S_i - the place of scanning the reinforcement

Figure 4. Localisation of measurement sites on the surface of the tested foundation.

4.1. Dynamic Experimental Test

Dynamic tests were performed with impulse forced vibration of the foundation structure to determine the basic foundation parameters.

Measurement of the Amplitude of Foundation Forced Vibrations

At the level of the floor slab, the measurements of vibrations at the operating speed of the turbine set were conducted in eight points of the foundation's top plate using a piezoelectric accelerometer (Figure 5). As a result of the research, the following root mean square (RMS) values of the acceleration of vibrations, the velocity of vibrations, and the displacement of the foundation are presented in Table 1. Figure 6 illustrates the frequencies of forced vibrations determined on the basis of the measurements. The measured values of the average displacement amplitudes are between 1 and 5 μm, which is much lower than the permissible amplitude for the foundations of turbogenerators.

Figure 5. Measurement of vibrations at the operating speed of the turbine placed on the top plate of the foundation using a piezoelectric accelerometer.

Table 1. Results of the vibration acceleration measurement, vibration velocity, and foundation displacement (average value).

Measurement No.	Amplitude Spectrum RMS m/s^2			Amplitude Spectrum RMS mm/s			Amplitude Spectrum RMS mm		
	X	Y	Z	X	Y	Z	X	Y	Z
1	0.027–24	0.08	0.061	0.18	0.57	0.4	0.002	0.046	0.003
2	0.016–25	0.0058	0.05	0.11–12	0.032	0.4	0.002	0.0024	0.005
3	0.014–32	0.019	0.003	0.11	0.10	0.09	0.002	0.002	0.005
4	0.014–50	0.063	0.03	0.05	0.085	0.095	0.001	0.005	0.002
5	0.006–50	0.003	0.006	0.04	0.025	0.02	0.002	0.001	0.001
6	0.0022–18	0.0045	0.016	0.03	0.03	0.09	0.002	0.002	0.005
7	0.038–50	0.025–23	0.04	0.11	0.16	0.25–25	0.004	0.002	0.004
8	0.017–22	0.022	0.35–17	0.12	0.15	0.33–18	0.002	0.001	0.003

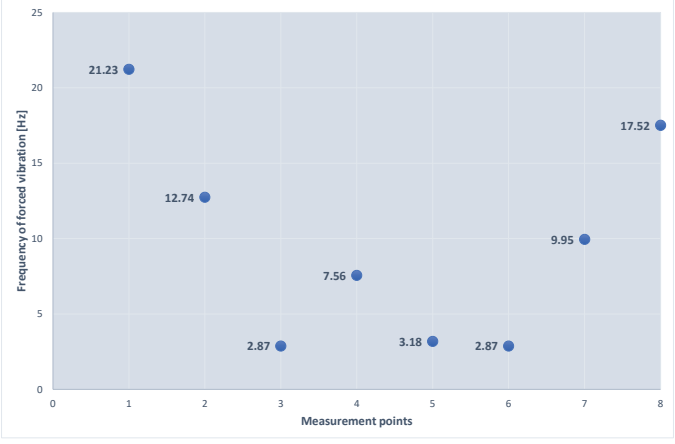

Figure 6. Forced vibration frequency diagram for individual measurements points.

4.2. Auxiliary Material Experimental Tests

4.2.1. Assessment of the Compressive Strength of Concrete

The compressive strength of concrete was determined on the basis of core samples $\phi \times h = 100 \times 100$ mm that were cut from the elements of the tested structure, as shown in Figure 7. The measurement site was previously scanned with a reinforcement detector to avoid cutting the rebars when drilling the core samples. The test was carried out with a BOSCH drilling set in accordance with the procedures specified in standards EN 12504:1:2009 and EN 12390-3:2009.

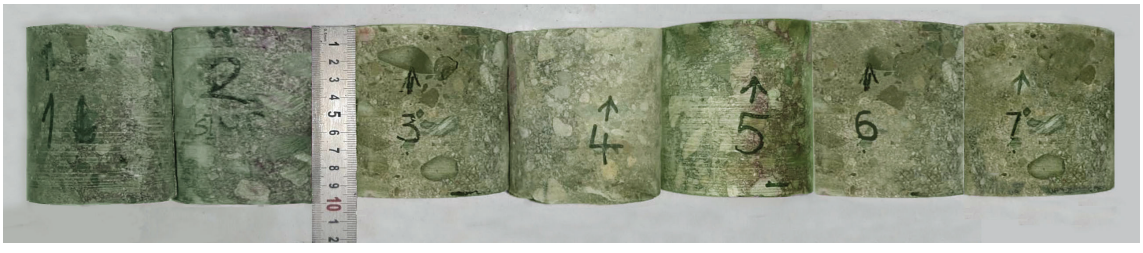

Figure 7. The control drilling samples cut from the tested fragments of the foundation structure.

The sampled drillings were compressed in a testing machine. The strength grade of the concrete was determined on the basis of the results of the destructive tests of the core samples (Table 2). It was determined in relation to standard EN 13791:2019-12.

Table 2. Summary of concrete the results of compressive strength tests.

Localisation	Measurement Point	Drilling Diameter [mm]	Compressive Strength [MPa]
Foundation	O1 (F1)	100	34.00
	O2 (F2)	100	34.60
	O3 (F3)	100	43.20
	O4 (F4)	100	37.50
	O5 (F5)	100	32.20
	O6 (F6)	100	29.50
	O7 (F7)	100	34.40

As a result of the calculations, the following were obtained:

- the average value of the concrete's compressive strength $f_{m(n),is} = 35.06$ MPa,
- the minimum value of the concrete's compressive strength $f_{is,lowest} = 29.5$ MPa,
- standard deviation $s_R = 4.34$.

According to the standard EN 13791:2019-12, it was assumed that the characteristic strength of concrete in the tested elements is the lower of the following two values:

$$f_{ck,is,cube} = f_{m(n),is} - k_n * s \text{ or } f_{ck,is,cube} = f_{is,lowest} + \mathrm{M} \quad (3)$$

where:

$f_{ck,is,cube}$—characteristic compressive strength of the concrete in the structure, which corresponds to the strength of the concrete determined on cubic samples with a side length of 150 mm;
$f_{m(n),is}$—the average value of the concrete's compressive strength in the structure obtained from n measurement results;
$f_{is,lowest}$—the lowest of the determined values of the compressive strength of the concrete in the structure;
k_n—coefficient that depends on the number of samples $n = 7$, $k = 2$.

After the calculation, the following was obtained:

$$f_{ck,is,cube} = 35.06 - 2 \times 4.34 = 26.38 \text{ MPa} \quad (4)$$

or

$$f_{ck,is,cube} = 29.5 + 4 = 33.50 \text{ MPa} \quad (5)$$

Based on the results of the tests obtained, it can be assumed that the value of the characteristic strength of the concrete tested in the foundation structure is not higher than 26.38 MPa and, according to the EN 13791:2019-12 standard, it is assumed that its strength grade corresponds to the archival documentation.

4.2.2. Sclerometer Test of Concrete

Concrete homogeneity tests were carried out using a Schmidt "N" sclerometer according to the procedures specified in the standard PN-EN 12504-2:2021-12. Measurement locations were assumed in the following foundation elements: a horizontal longitudinal beam, an outer column, and a middle column. The results of the sclerometer measurements presented in Tables 3 and 4 were correlated at the drilling sites. Sclerometer measurements were used to assess the quality of the concrete on the basis of the homogeneity of its strength properties.

$$L_{av} = \sum L_i \, / n = 48.22 \text{ MPa} \quad (6)$$

$$s_L = \sqrt{\frac{\sum(L_i - L_{av})^2}{n-1}} = 2.06 \text{ MPa} \quad (7)$$

$$n_L = \frac{s_L}{L_{av}} \cdot 100\% = 4.28\% \quad (8)$$

Table 3. Summary of sclerometer test results for the horizontal beam.

Site	Angle [Deg]	Readings	L_i	$L_i - L_{av}$	$(L_i - L_{av})^2$
1	90	45 44 47 47 44 44 46 46 47	45.6	−2.67	7.11
2	90	52 52 49 49 51 50 49 49 49	50	1.78	3.16
3	90	48 47 47 48 47 48 48 49 49	47.9	−0.33	0.11
4	90	50 52 52 49 49 50 52 52 52	50.9	2.67	7.11
5	90	44 44 46 46 48 46 47 48 48	46.3	−1.89	3.57
6	90	48 49 50 49 48 48 48 49 49	48.7	0.44	0.2

n = 6—number of readings.

Table 4. Summary of sclerometer test results for the middle column.

Site	Angle [Deg]	Readings	L_i	$L_i - L_{av}$	$(L_i - L_{av})^2$
1	90	51 51 50 52 50 50 51 50 52	50.8	−1.35	1.83
2	90	52 52 52 50 51 52 52 50 52	51.4	−0.69	0.47
3	90	51 52 54 54 52 54 52 52 52	52.6	0.43	0.18
4	90	54 52 54 54 52 53 53 54 52	53.1	0.98	0.96
5	90	54 54 52 52 52 52 54 53 53	52.9	0.76	0.58
6	90	52 52 52 52 54 51 52 51 52	52	−0.13	0.02

n = 6—number of readings.

The following equation was adopted as the hypothetical regression equation:

$$R_{av} = L_{av} \cdot (0.0356 * L_{av} * \left(\left(\frac{n_L}{100} \right)^2 + 1 \right) - 0.795 + \frac{6.4}{L_{av}} = 51.00 \text{ MPa} \quad (9)$$

$$s_R = L_{av} \cdot \left(\frac{n_L}{100} \right) \cdot \sqrt{0.00254 \cdot L_{av}^2 \cdot \left(\left(\frac{n_L}{100} \right)^2 + 2 \right) - 0.1134 \cdot L_{av} + 0.633} = 5.45 \text{ MPa} \quad (10)$$

$$n_R = \frac{s_R}{R_r} \cdot 100\% = 10.69\% \quad (11)$$

$$R_{min} = R_r - 1.64 \cdot s_R = 42.06 \text{ MPa} \quad (12)$$

Correction coefficients that depend on the concrete age α = 0.6 and the dry air state β = 1 were adopted in the analysis.

$$R_b^G = \alpha \cdot \beta \cdot R_{min} = 25.24 \text{ MPa} \quad (13)$$

$$L_{av} = \sum L_i \, / n = 52.13 \text{ MPa} \quad (14)$$

$$s_L = \sqrt{\frac{\sum(L_i - L_{av})^2}{n-1}} = 0.90 \text{ MPa} \quad (15)$$

$$n_L = \frac{s_L}{L_{av}} \cdot 100\% = 1.72\% \quad (16)$$

The following equation was adopted as the hypothetical regression equation:

$$R_{av} = L_{av} \cdot (0.0356 * L_{av} * \left(\left(\frac{n_L}{100} \right)^2 + 1 \right) - 0.795 + \frac{6.4}{L_{av}} = 61.73 \text{ MPa} \quad (17)$$

$$s_R = L_{av} \cdot \left(\frac{n_L}{100}\right) \cdot \sqrt{0.00254 \cdot L_{av}^2 \cdot \left(\left(\frac{n_L}{100}\right)^2 + 2\right) - 0.1134 \cdot L_{av} + 0.633} = 2.62 \text{ MPa} \quad (18)$$

$$n_R = \frac{s_R}{R_r} \cdot 100\% = 4.25\% \quad (19)$$

$$R_{min} = R_r - 1.64 \cdot s_R = 57.43 \text{ MPa} \quad (20)$$

The analysis adopted correction coefficients that depend on the concrete age $\alpha = 0.6$ and the dry air state $\beta = 1$. Finally, the guaranteed concrete strength is:

$$R_b^G = \alpha \cdot \beta \cdot R_{min} = 34.46 \text{ MPa} \quad (21)$$

Based on the sclerometer tests, the concrete strength grade in the horizontal beams was estimated as C20/25 and in the columns as C25/C30. Finally, concrete was adopted for the entire structure according to the C20/C25 class. It is one class weaker than was assumed in the archival project.

4.2.3. Measurement of the Intensity of the Carbonation Process of the Subsurface Concrete Layer

Under the influence of the carbon dioxide contained in the atmosphere (CO_2), and the moisture in the pores of the concrete, the subsurface concrete layer undergoes a gradual process of carbonation. The carbonation front gradually moves deeper into the concrete, with the main reaction in this process being the reaction of carbon dioxide with calcium hydroxide. As a result of this reaction, calcium carbonate ($CaCO_3$) is formed. This lowers the reaction of the concrete, which in turn leads to a gradual loss of the protective properties of the concrete against steel. The pH of fresh concrete is 11.8–12.6. It is assumed that a decrease in the concrete's pH to about 10.0–11.8 causes the loss of stability of the protective passive layer on the steel. Within the performed research, the scope and intensity of the carbonation process were assessed using the rainbow test. This test allows the pH distribution profile to be determined within the range of 5.0–13.0 (with gradation every two pH degrees). Measurement involved spraying the surface of the fresh fracture of the tested element with the indicator and then determining the pH distribution based on the colour table, as shown in Figure 8. The tests were carried out according to the procedures specified in the standard PN-EN 12390-12:2020-06.

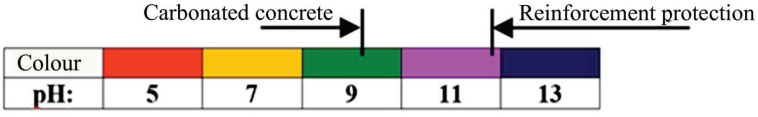

Figure 8. A colour template for assessing the depth and intensity of the carbonation process for the rainbow test.

Measurement of the carbonation intensity was carried out on four drilling core samples from the foundation columns and beams, as shown in Figure 9. No carbonation was found in these samples. The main reinforcement bars have a cover of 2.5–3.0 cm. No corrosion was found in the uncovering of the main reinforcement (made of Ø32 bars) in either the beams or columns.

4.2.4. Investigation of the Thickness of the Concrete's Cover and the Location and Diameter of the Reinforcement

Measurements were carried out in a non-destructive manner with the use of specialised Hilti Ferroscan instruments that are intended for locating the reinforcing bars and for measuring the thickness of the concrete's cover [47]. The measurements used the electromagnetic method of excitation of currents in the reinforcement. The instruments

automatically calculate the cover thickness as the smallest distance between the bar side and the concrete surface for a given bar diameter. The electromagnetic method is a research method that uses the phenomenon of induction of a current in an electric circuit that is caused by the electromagnetic field of the circuit being disturbed. Testings of reinforced concrete structures with the use of the electromagnetic method involve successive scanning of concrete surfaces with a measuring probe to locate the reinforcing bars, followed by the determination of their diameter and thickness. Before measuring the thickness of the cover, the diameters of the reference bars, determined on the basis of the technical documentation or during a micro-uncovering, are entered into the device. The tests were carried out at six foundation measurement sites (S26–S31) on an area of 60 cm × 60 cm, as shown in Figures 10 and 11.

Figure 9. Test of the extension of concrete carbonation.

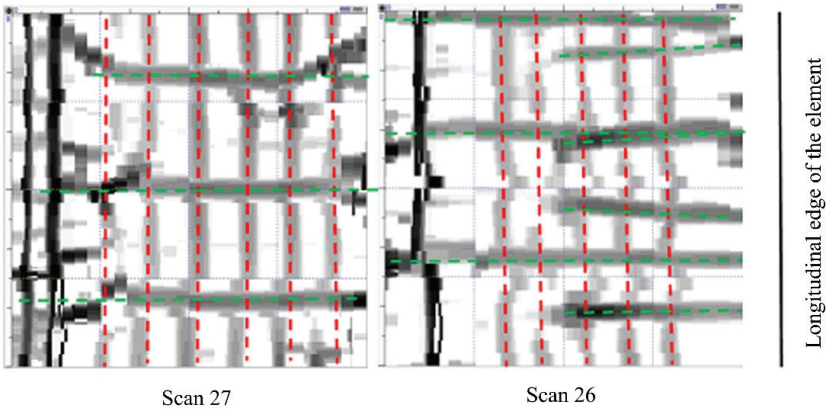

Figure 10. The image of reinforcement scanning at the S26 and S27 measurement sites (at the bottom of the foundation body); red means bars of the main reinforcement; green means cross-bars.

The scanning of the reinforcing bars confirmed that their actual distribution is similar to that presented in the technical documentation. On the basis of the performed uncoverings, it was found, in the case of the columns and beams, that the main reinforcement is consistent with the archival documentation, has a diameter of 32, is made of 18G2 steel, and that the stirrup spacing in the beams is equal to 20 cm.

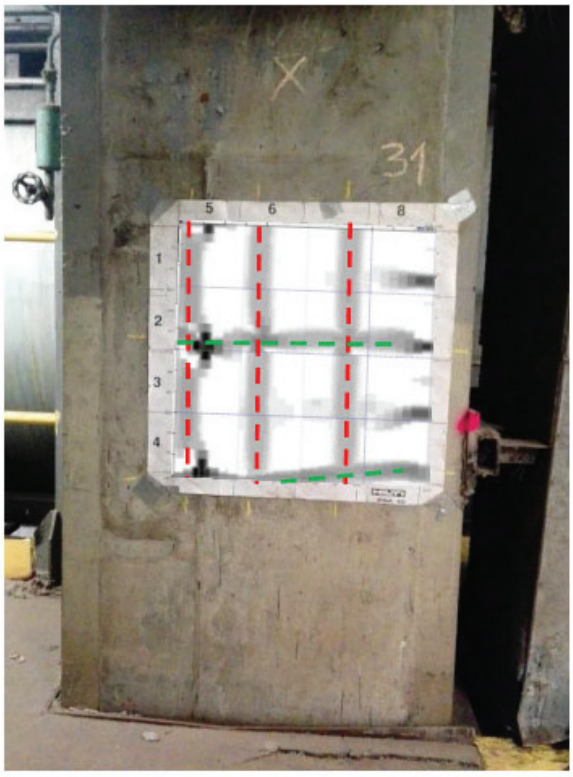

Figure 11. The image of reinforcement scanning at the S31 measurement site (column area under the foundation body) superimposed on the tested element.

4.3. Numerical Analysis of the Foundation

On the basis of the experimental tests and the archival technical documentation, a numerical analysis was performed using the FEM, as shown in Figure 12. The analysis involved the verification of the conditions of the ultimate and serviceability limit states of the foundation, and the performing of tests of forced vibrations. Dynamic numerical analysis was carried out using AxisVM software. The permanent load was defined as the self-weight of the foundation's structure and the weight of the turbine set. In the numerical model, it was modelled as a concentrated mass that is connected, using rigid elements, to the turbine set's fastening points in the foundation, as can be seen in Figure 13. The analysis assumed an elastic ground, the characteristics of which were determined on the basis of archival research.

The self-weight was determined on the basis of the foundation's dimensions, while the weight of the turbine set was assumed according to the technical documentation. For a generator with a stator, the weight is 169.5 t, and for a turbine, it is 66.7 t.

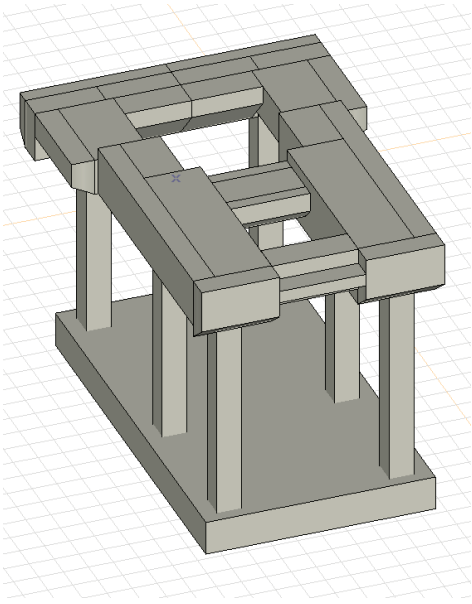

Figure 12. Numerical FEA model of the foundation's geometry.

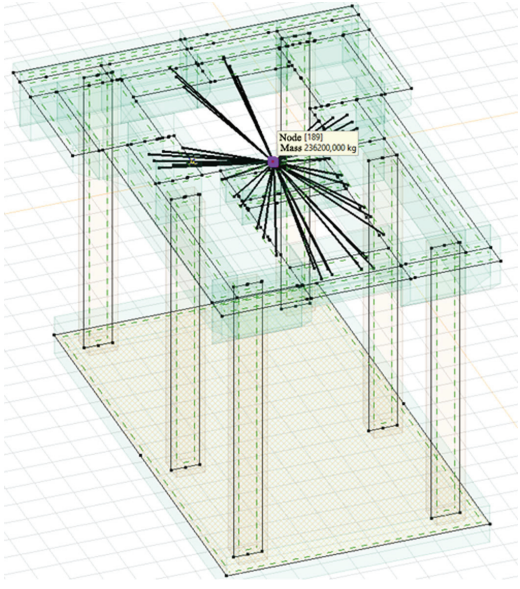

Figure 13. FEA model of the foundation's load.

4.3.1. Analysis of the Amplitude of the Foundation's Vibration

In the dynamic calculations, the load from misalignment of the rotating parts of the turbogenerator, i.e., the stator rotor and the turbine rotor, was taken into account. This load is assumed based on the equation:

$$F_s = M_w \cdot g \cdot n \cdot 0.2 \quad (22)$$

where:

M_W—the mass of the rotating part: stator rotor: 30,150 kg, turbine rotor 17,000 kg,
g—acceleration due to gravity,
n = 1.2.
Finally assumed:
$F_{s,stator} = 70.96$ kN,
$F_{s,rotor} = 40.34$ kN.

On the basis of the technical documentation, it was assumed that the foundation raft plate is set on subsoil that consists of gravel mix with the degree of compaction $I_D = 0.5$. Therefore, the following elasticity coefficients of the subsoil were adopted for foundations with an area greater than 50 m^2:

$$C_z = 50 \text{ MPa/m},$$

$$C_x = C_y = 0.7 \cdot C_z = 35 \text{ MPa/m}.$$

The calculated natural frequencies of the foundation do not indicate the presence of a resonance state with any mode shape, as shown in Figure 14. The natural frequencies obtained, which are closest to the frequency of the reactive force, are the frequencies for the 26 and 27 mode shapes (44.01 Hz, 56.23 Hz). The exciting forces were applied at the places where the rotor and stator are fastened. For the load scheme adopted in this way, the forced vibration amplitudes were calculated for individual values of transient resonances. The amplitude of the vertical forced vibrations of the top foundation plate, both at the operating rotational speed of the machine and during transient resonances, does not exceed 9 μm (Figure 15). This is much lower than the permissible vibration amplitude for turbogenerator foundations, which is 20 μm [48]. The calculated theoretical vibration amplitude of the foundation corresponds well with the actual measured vibration amplitude of the foundation during normal operation of the turbogenerator, which is equal to 3 μm (the measured vibration amplitude was classified as not degrading the foundation).

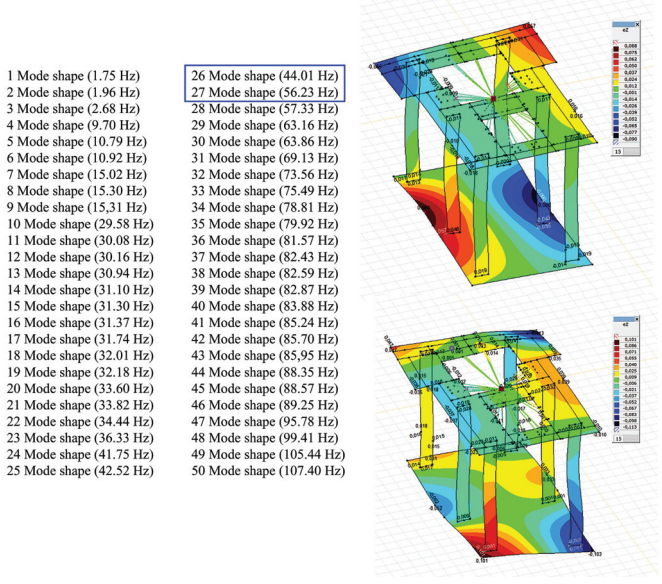

Figure 14. Calculation results of the foundation's natural frequency obtained by AxisVM software: (**a**) amplitude of foundation displacement for 26 mode shapes of frequency (44.01 Hz); (**b**) amplitude of foundation displacement for 27 mode shapes of frequency (56.23 Hz).

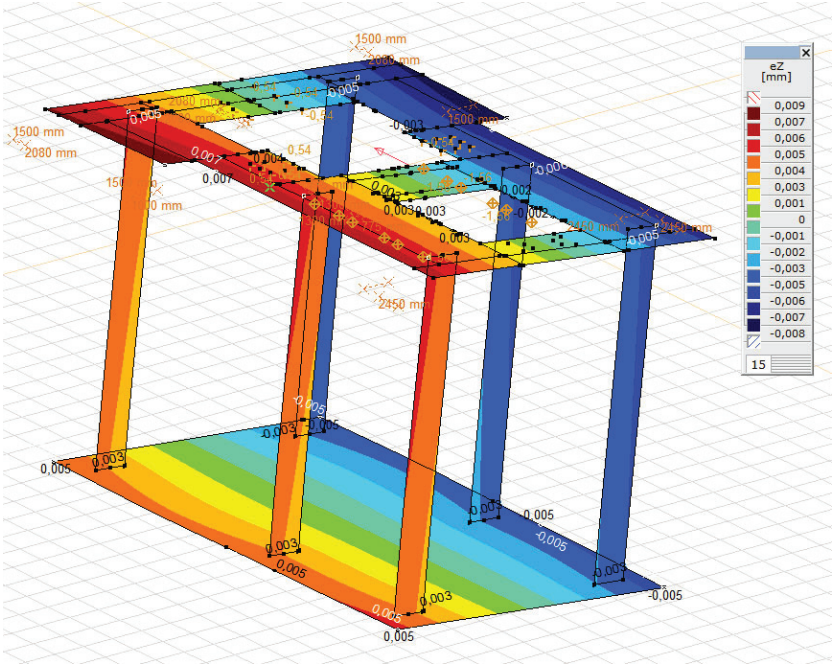

Figure 15. Maximum amplitude of foundation displacement for forced vertical vibrations obtained by the AxisVM software.

4.3.2. Analysis of the Load-Bearing Capacity of the Foundation

The EN 1991-3 standard was used to calculate the dynamic forces caused by rotation. The interaction effect which results from the excitation of the machine with the rotating masses and the dynamic behaviour of the structure can be expressed by an equivalent static force defined as:

$$F_{eg} = F_s \cdot \varphi_M, \tag{23}$$

where:

F_s—the centrifugal force of the rotating part equal to 111.3 kN,
φ_M—the dynamic coefficient which depends on the ratio of the natural frequency n_e to the frequency of the excitation forces n_s:

$$\varphi_M = \left[\left(1 - \frac{n_s^2}{n_e^2} \right)^2 + \left(\frac{2\varsigma n_s}{n_e} \right)^2 \right]^{,0.5} \tag{24}$$

where:

ζ—the damping coefficient, n_s = 50 Hz—frequency of the exciting force.

According to [24], for turbogenerators on RC frame foundations, the damping coefficient is defined as:

$$\zeta = \Delta / 2\pi, \tag{25}$$

where:

Δ—the logarithmic damping decrement of the foundation, which is equal to approx. 0.4 for RC frame foundations.
After inserting n_e = 44.01 Hz,
φ_{M1} = 3.1.

After inserting n_e = 56.23 Hz,
φ_{M2} = 4.2.
Finally, the following was assumed:
φ_M = 4.2.

According to [24], the computational value of the forces, which replaces the impact of dynamic loads on the foundation, is obtained from the following formula:

$$P_d = \varphi M \, \mu \, \gamma \, Pc \tag{26}$$

where:

φ_M—dynamic coefficient (as above),
μ—fatigue factor equal to 2,
γ—calculation factor equal to 5.

The centrifugal force of a rotating part F_s = 111.3 kN.

For the purposes of the calculations, this force was divided into the force from the stator rotor and the turbine rotor:

$F_{s,stator}$ = 70.96 kN, adjusted to the value of 71.0 kN,
$F_{s,turbine}$ = 40.34 kN, adjusted to a value of 40.3 kN.

The design value is as follows:

$F_{s,stator,eq} = 4.2 \cdot 2 \cdot 5 \cdot 71 = 2982$ kN,
$F_{s,turbine,eq} = 4.2 \cdot 2 \cdot 5 \cdot 40.3 = 1693$ kN.

The forces determined in this way were loaded on the turbogenerator's foundation. Additionally, the exceptional moment derived from the start up and stop run up loads was considered in the calculations. According to the EN 1991-3 standard, for this moment, the equivalent static moment can be calculated in the following way:

$$Mk, eq = 1.7 \, Mk, max, \tag{27}$$

where:

$M_{k,max}$—the peak value of the moment derived from the start up and stop run up loads according to the archival documentation:

$$Mk, max = Fzw \cdot a, \tag{28}$$

where:

F_{zw} = 876.3 kN—start up and stop run up load,
a = 3.69 m (spacing of fastening bolts),
$M_{k,max}$ = 3233.55 kNm,
$M_{k,eq} = 1.7 \cdot 3233.55 = 5497.03$ kNm.

For such loads, the required main reinforcement was calculated, as can be seen in Figures 16 and 17. The obtained values of the reinforcement area do not exceed the value of the reinforcement applied in the foundation, that is, min. 5 × ϕ 32 per 1 m = 4020 mm^2/m. The execution of the numerical calculations of the natural frequencies and mode shapes of the foundation construction was possible thanks to the research and measurements conducted. The theoretical vibration amplitude of the foundation is greater than that measured during normal operation of the turbogenerator; however, both are lower than the permissible value. The calculated values of the stresses in the concrete and reinforcing bars are lower than the permissible values.

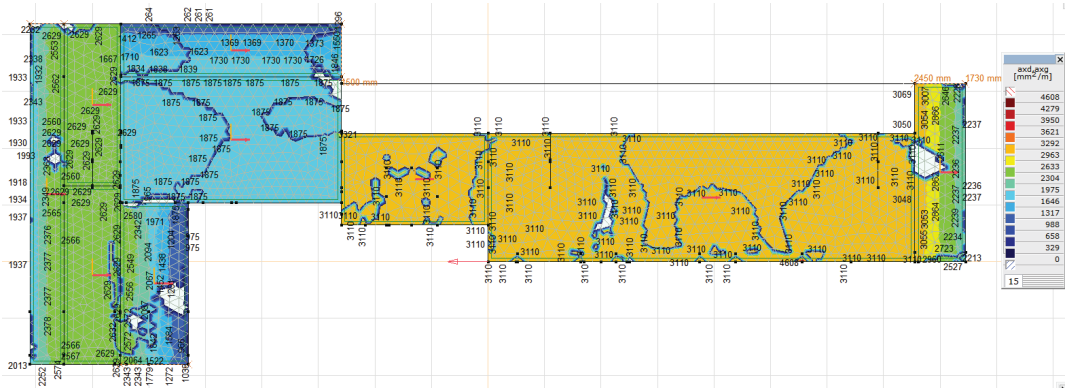

Figure 16. Bottom and top reinforcement of the top plate in the horizontal direction (main direction) obtained by the AxisVM software.

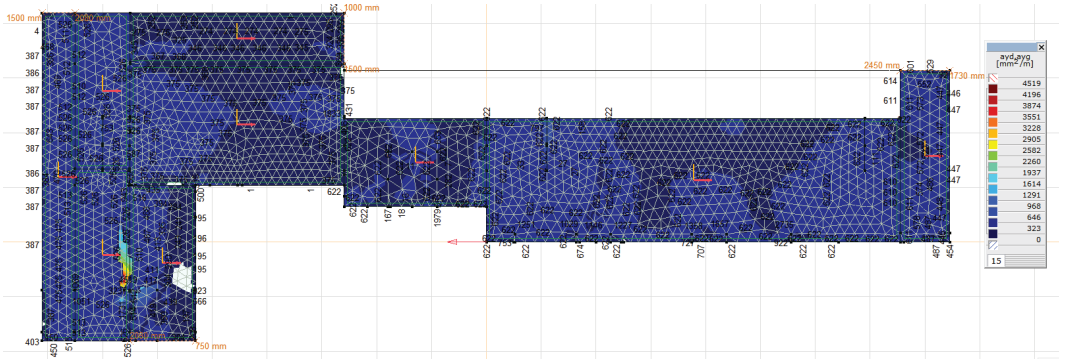

Figure 17. Bottom and top reinforcement of the top plate in the vertical direction (main direction) obtained by the AxisVM software.

5. Discussion

The performed dynamic analyses show the great possibilities of using the FEM in the diagnostic process of foundation structures for turbogenerators. Due to the enormous cost of such objects, the use of FEM allows one to accurately verify the entire structure not only for the dynamic behaviour of the object but also for the structural strength and resistance to earthquake-type excitations. The complexity of such an object requires a very accurate reconstruction of the whole structure, together with taking into account the correct material parameters and dynamic characteristics. Therefore, the creation of a proper numerical model required conducting experimental dynamic and material tests of the foundation. The results of the experimental tests, especially in situ, enable the design of the existing foundation structure strengthening for future performance and update the initial foundation structural model for final numerical analysis. It can be stated that numerical analysis allows for better recognition of foundation properties, dynamic damping characteristics, fatigue, rheological changes, corrosion, and the degree of efficiency due to exploitation. The research presented in this paper was based on a limited amount of data. This problem, which affects the effectiveness of numerical analysis, can be solved in the future by using artificial neural networks. The ANN represents an artificial system based on mathematical models similar to biological nervous systems and is capable of intelligently processing simulated information. Currently, ANNs are used for the diagnostics and

monitoring of shafts in turbines [49]. The benefits of the use of neural networks can exceed many times the work required for diagnostics of the foundation for turbogenerators implemented to date.

6. Conclusions

The turbine set has a value that is on average 20 times higher than the cost of its foundation. The foundation, together with the turbine set and the adjacent devices, must ensure safe use in continuous operation conditions, where the turbine set shaft rotates at 3000/3600 rpm (which corresponds to a frequency of 50/60 Hz). During operation, the dynamic condition of the turbine set usually deteriorates as a result of the ongoing wear and tear processes. Changes in harmonic values in the analysis of the vibrations' spectrum (e.g., fast Fourier transformation) affect the harmonically variable load in both the horizontal and vertical directions. The main design goal for a machine's foundation is to limit its movement to amplitudes that do not endanger the proper operation of the machine. In the case of high-speed machines, it is desirable to design the foundation to be low tuned, with the value of the vertical natural frequency below the operating speed of the machine.

The article presents the dynamic analysis and diagnostics of reinforced concrete foundations for machines, which are very important in terms of ensuring the proper safety, reliability, and durability of these very expensive machines. The design of a frame foundation for a turbogenerator is the most difficult task when compared to designing any other foundation. There are many parameters that influence the foundation's response. The rigidity of the frame structure plays a key role. The individual vibration characteristics of individual elements, such as columns and beams, are very important in determining the behaviour of the foundation [50].

A real foundation of a turbogenerator in a CHP plant is presented as the case study. The dynamic analytical and experimental analysis method presented in the paper turned out to be a good tool to verify the foundation structure, making it possible to perform a sensitivity analysis of the impact of changes in various parameters. A numerical analysis (AxisVM software) was carried out using experimental data in which the bearing capacity of the foundation was determined and the natural frequencies and maximum amplitude were checked. In the analysis process, the auxiliary material tests were also very important. The experimental material tests performed were related to the strength of the concrete and the identification of reinforcement. The numerical analysis was positively verified using experimental tests. Comparison of analytical and experimental results allows optimising the calculation model of the foundation structure, as well as determining the dynamic parameters of the existing foundation structure. It also enables the behaviour of the foundation after reconstruction and strengthening of its structure, as well as the damage or remaining service time to be determined. A key factor in the successful design of the foundation of a turbogenerator is a precise engineering analysis of the foundation response to dynamic loads caused by the machine operation.

Author Contributions: Conceptualisation, J.S., G.D. and M.R., methodology, J.S., G.D. and M.R., validation, G.D. and M.R., investigation, J.S. and G.D., writing—original draft preparation, J.S., G.D. and M.R., writing—review and editing, J.S., G.D. and M.R., visualisation, J.S. and G.D., supervision, M.R. All authors have read and agreed to the published version of the manuscript.

Funding: This research received no external funding.

Institutional Review Board Statement: Not applicable.

Informed Consent Statement: Not applicable.

Data Availability Statement: Not applicable.

Conflicts of Interest: The authors declare no conflict of interest.

References

1. Sołbut, A. *Maszyny Synchroniczne—Budowa*; Internetowa Encyklopedia PWN: Białystok, Poland, 2016; pp. 1–7. Available online: https://we.pb.edu.pl/keeie/wp-content/uploads/sites/7/2020/09/as-me-synchro_budowa.pdf (accessed on 15 January 2021). (In Polish)
2. Liu, H. *Concrete Foundations for Turbine Generators. Analysis, Design, and Construction*; American Society of Civil Engineers: Reston, VA, USA, 2018; p. 245.
3. Krasowski, C.; Walkowiak, R. Experience in Placing the Concrete of Massive Concrete Construction Foundations of Recuperator Furnace and 460 MW Steam and Gas Turbine Set at PKN Orlen SA in Włocławek, Poland. 2014, pp. 3–10. Available online: https://www.dnibetonu.com/wp-content/pdfs/2014/Krasowski_Walkowiak.pdf (accessed on 10 January 2021). (In Polish)
4. Fidali, M. Badania własności dynamicznych maszyn. *Utrzymanie Ruchu* **2019**, *2*, 38–45.
5. Nawrotzki, P. Static and Dynamic Analysis of Concrete Turbine. *Struct. Eng. Int.* **2008**, *18*, 265–270.
6. Livshits, A. Dynamic Analysis and Structural Design of Turbine Generator Foundations. In Proceedings of the European Built Environment CAE Conference, London, UK, 5–6 June 2008; pp. 1–12. Available online: https://www.iec.co.il/engprojects/Documents/Dynamicanalysisandstructuraldesignofturbinegeneratorfoundations.pdf (accessed on 20 December 2020).
7. Zhivaev, A.A. Machine Foundation Monitoring. In Proceedings of the Fifth International Conference on Experimental Vibration Analysis for Civil Engineering EVACES'13, Ouro Preto, Brazil, 28–30 October 2013; pp. 1–5. Available online: https://www.researchgate.net/publication/282646878_MACHINE_FOUNDATION_MONITORING/link/561523ad08ae4ce3cc651fdb/download (accessed on 10 January 2021).
8. Mitchell, J.S. *An Introduction to Machinery Analysis and Monitoring*; Pennwell Corp.: Tulsa, OK, USA, 1993.
9. Edwards, S.; Lees, A.W.; Friswell, M.I. Fault diagnosis of rotating machinery. *Shock Vib. Dig.* **1998**, *30*, 4–13.
10. Kassem, A.T. Displacement Analysis of Turbo-generator's raft foundations resting on Friction Piles. *J. Am. Sci.* **2018**, *14*, 1–7. Available online: http://www.jofamericanscience.org/journals/am-sci/am140418/01_33542jas140418_1_7.pdf (accessed on 10 December 2020).
11. Benčat, J.; Tomko, M.; Lukač, M. Dynamic analysis of the turbo—Generator foundation structure. *MATEC Web Conf.* **2020**, *310*, 00035.
12. Qi, H.; Renpeng, C.; Yunmin, C. Optimization Design of Foundations of Large Steam Turbine-Generator Sets. *J. Power Eng.* **2007**, *27*, 327–331.
13. Hongxia, L.; Xu, F.; Minjie, W. Dynamic characteristics analysis and optimization for stream turbine generator foundation. *Chin. J. Appl. Mech.* **2018**, *35*, 178–184.
14. Bendat, J.S.; Piersol, A.G. *Engineering Applications of Correlation and Spectral Analysis*, 2nd ed.; Wiley: Hoboken, NJ, USA, 2013; p. 472.
15. Tang, M.; Wenqi, E.; Zeng, C. Analysis of Mechanical Properties of Turbogenerator Foundation Based on ANSYS. In *Lecture Notes in Civil Engineering, Proceedings of the International Conference on Green Building, Civil Engineering and Smart City*; Springer: Singapore, 2022; pp. 926–933.
16. Wang, B.; Cao, D.; Yang, Y.; Xu, C.; Qian, H. Numerical Analysis and Optimization on Dynamic Performance of Large Turbo Generator Frame Foundation. *Appl. Mech. Mater.* **2012**, *166–169*, 720–724. [CrossRef]
17. Kowalski, R.; Wróblewska, J. Application of a sclerometer to the preliminary assessment of concrete quality in structures after fire. *Arch. Civ. Eng.* **2018**, *64*, 171–186.
18. Jedidi, M. Evaluation of the concrete quality using destructive and non-destructive tests. *MOJ Civ. Eng.* **2018**, *4*, 219–223.
19. Rathinarajan, S.; Pillai, R. Carbonation rate and service life of reinforced concrete systems with mineral admixtures and special cements. In Proceedings of the CORCON, Mumbai, India, 17–20 September 2017; pp. 1–8. Available online: https://www.researchgate.net/publication/324137411_Carbonation_rate_and_service_life_of_reinforced_concrete_systems_with_mineral_admixtures_and_special_cements (accessed on 15 December 2020).
20. Czarnecki, L.P. Prediction of the reinforced concrete structure durability under the risk of carbonation and chloride aggression. *Bull. Pol. Acad. Sci.* **2013**, *61*, 173–181.
21. Hüblova, S.; Cikrle, P.; Karel, O.; Kocab, D. Experimental measurement of the diameter and cover depth of steel reinforcement using an electromagnetic concrete cover meter. In Proceedings of the XXV International Conference and Meeting of Departments, Zuberec, Slovakia, 29–31 May 2019; Volume 549, pp. 1–7. [CrossRef]
22. Puttatt, J. Dynamic Analysis of Turbo-generator Machine Foundations. *J. Civ. Eng. Environ. Technol.* **2014**, *1*, 30–35.
23. Fang, M.; Wang, T.; Li, H. Dynamic behavior of turbine foundation considering full interaction among facility, structure and soil. In Proceedings of the 15th World Conference on Earthquake Engineering, Lisbon, Portugal, 24–28 September 2012; Volume 23, pp. 18256–18265.
24. Smart, M.G.; Friswell, M.I.; Lees, A.W. Estimating turbogenerator foundation parameters: Model selection and regularization. *Proc. R. Soc. A Math. Phys. Eng. Sci.* **2008**, *456*, 1583–1607.
25. Sinha, J.K.; Friswell, M.I.; Lees, A.W. The Identification of the Unbalance and the Foundation Model of a Flexible Rotating Machine from a Single Run-Down. *Mech. Syst. Signal Process.* **2002**, *16*, 255–271. [CrossRef]
26. Chen, P.Y.P.; Feng, N.; Hu, W. Recent Developments in Turbomachinery Modeling for Improved Balancing and Vibration Response Analysis. *J. Eng. Gas Turbines Power* **2005**, *127*, 646–653.

27. Jin-Yao, H.; Yan-Ping, L.; Jing, C.; Hao, H. Simulation analysis for asynchronous operation capacity of turbogenerator under excitation-loss. In Proceedings of the 6th International Forum on Strategic Technology, Harbin, China, 22–24 August 2011; Volume 1, pp. 529–532. [CrossRef]
28. Musiał, M. Models for Calculating Dynamic Characteristics of Frame Foundation Under the Turbine Set. *Tech. Trans. Civ. Eng.* **2016**, *2016*, 133–144.
29. Jayarajan, P.; Kouzer, K.M. Dynamic Analysis of Turbogenerator Machine Foundations. *J. Civ. Eng. Environ. Technol.* **2014**, *1*, 30–35. Available online: https://www.researchgate.net/profile/Jayarajan_Puttatt/publication/334732195_Dynamic_Analysis_of_Turbo-generator_Machine_Foundations/links/5d3dce9e4585153e59294379/Dynamic-Analysis-of-Turbo-generator-Machine-Foundations.pdf (accessed on 10 November 2020).
30. Naik, M.; Tande, S.N. Analysis and Design of Steam Turbine Generator Building with R.C.C. Deck. *Int. J. Innov. Res. Sci. Eng. Technol.* **2016**, *5*, 5633–5641. Available online: https://www.ijirset.com/upload/2016/april/73_6_Analysis.pdf (accessed on 10 January 2021).
31. Thakare, A.U.; Rangari, S.M. Effect of Seismic Parameters on Analysis of Turbo-Generator Foundation. *Int. J. Eng. Res. Technol.* **2015**, *4*, 393–398. Available online: https://www.ijert.org/research/effect-of-seismic-parameters-on-analysis-of-turbo-generator-foundation-IJERTV4IS050554.pdf (accessed on 15 December 2020).
32. Baesler, H.; Cruz, E.; Enriquez, P. Improving Seismic Performance of Modular Turbo-Generator Equipment. In Proceedings of the 8th US National Conference on Earthquake Engineering, San Francisco, CA, USA, 18–22 April 2006; pp. 9275–9285. Available online: http://toc.proceedings.com/05301webtoc.pdf (accessed on 10 December 2022).
33. Barkan, D.D. *Dynamics of Bases and Foundations*; McGraw-Hill: New York, NY, USA, 1962; p. 478.
34. Cavalca, K.L.; Cavalcante, P.; Okabe, E. An investigation on the influence of the supporting structure on the dynamics of the rotor system. *Mech. Syst. Signal Process.* **2005**, *19*, 157–174. [CrossRef]
35. Jiang, P. Modal Analysis for Steam Turbine/Generator Machine Table-Top Foundation. In Proceedings of the Structures Congress ASCE, Orlando, FL, USA, 12–15 May 2010; pp. 2684–2691. Available online: https://vdocuments.mx/ping-jiang-modal-analysis-for-steam-turbine-generator-machine-table-top-foundation.html (accessed on 10 December 2020).
36. Novak, M. Dynamic Stifness and Damping of Piles. *Can. Geotech. J.* **1974**, *11*, 574–598.
37. Song, S.H.; Lee, S.S. Finite Element Steady-State Vibration Analysis Considering Frequency- Dependent Soil-Pile Interaction. *Appl. Sci.* **2019**, *9*, 5371.
38. Roesset, J.M. Stiffness and Damping Coefficients of Foundations. In Proceedings of the APEC Session on Dynamic Response of Pile Foundation: Analytical Aspects, New York, NY, USA, 30 October 1980; pp. 1–10.
39. Adel, M.; Alzeni, Y.; Ghalab, A. Structural Dynamic Behavior of Turbo Generator Foundation Connected with Passive Supplemental Damping Devices. *Int. Res. J. Innov. Eng. Technol.* **2019**, *3*, 42–52.
40. Kim, H.; Melhem, H. Damage detection of structures by wavelet analysis. *Eng. Struct.* **2004**, *26*, 347–362.
41. Hans, S.; Ibraime, E.; Pernost, S.; Boutin, C.; Lamarque, C.H. Damping Identification in MDOF systems via a wavelet logarithmic decrement—Part II: Study of a civil engineering building. *J. Sound Vib.* **2000**, *253*, 375–403.
42. Jun, Y.; Jing, L.; Youqiang, H. Research on techniques for optimizing design of 1000 MW turbo-generator foundation. *Eng. J. Wuhan Univ.* **2009**, *42*, 474–477.
43. Zhaojun, L.; Zheng, L.; Xicheng, W. A parallel multi-objective optimization method for turbine foundation. *J. Dalian Univ. Technol.* **2015**, *55*, 229–235.
44. Virdi, K.S.; Matthews, R.; Clarke, L.; Garas, F. *Abnormal Loading on Structures—Chapter: Dynamic Analysis of a Narrow Turbogenerator Foundation on Piles*; Taylor & Francis Group: Oxfordshire, UK, 2000; p. 12.
45. Taranov, V.G.; Shvetz, N.S.; Shvetz, V.B. Some problems of the founding of the powerful turbogenerator sets. In Proceedings of the 16th International Conference on Soil Mechanics and Geotechnical Engineering, Osaka, Japan, 12–16 September 2005; pp. 1567–1570.
46. Lal, M. Multiple Fault Parameter Estimation of a Fully Assembled Turbogenerator System. *Arch. Mech. Eng.* **2018**, *LXV*, 233–252.
47. Ebensperger, L.; Donoso, J.P. New methodology for assessment of reinforced concrete structures with non-destructive testing. *Rev. Ing. Constr.* **2021**, *36*, 233–250.
48. Lipiński, J. *Fundamenty pod Maszyny*; Arkady: Warsaw, Poland, 1985; p. 687. (In Polish)
49. Rahmoune, M.B.; Hafaifa, A.; Abdellah, K.; Chen, X.Q. Monitoring of high-speed shaft of gas turbine using artificial neural networks: Predictive model application. *Diagnostyka* **2017**, *18*, 3–10.
50. Adel, M.; Alzeni, Y.; Ghalab, A. Modelling of Turbo-Generator Foundation Using FEM to Study the Isolation Effect on the System. *Int. J. Innov. Eng. Technol.* **2019**, *3*, 31–41.

materials

MDPI

Article

Diagnostics of Large-Panel Buildings—An Attempt to Reduce the Number of Destructive Tests

Maciej Wardach * and Janusz Ryszard Krentowski

Faculty of Civil Engineering and Environmental Sciences, Bialystok University of Technology, Wiejska 45E, 15-351 Bialystok, Poland; janusz@delta-av.com.pl
* Correspondence: m.wardach@doktoranci.pb.edu.pl

Abstract: Structural condition diagnostics provides the basis for decision making regarding the possibility of continued safe operation, necessary reinforcement, repair work, and in extreme cases, dismantling of the structure. The most reliable results concerning the condition and strength of materials are provided by destructive testing. However, these tests are very time-consuming, costly, and difficult to perform on in-service facilities. In addition, they involve the need to obtain the consent of the occupants of the premises and subsequent renovations. This article focuses on presenting an opportunity to reduce the number of destructive tests necessary to reliably assess the condition of large-panel structures, which constitute a significant housing stock in Europe. Based on tests carried out on a real building, the risk factors associated with obtaining reliable results by non-destructive methods were determined. Areas where destructive testing is necessary were identified. In addition, reference was made to standard recommendations and guidelines from a reputable research institution. Practical guidelines were formulated regarding the diagnostics of large-panel structures, resulting in a reduction in the number of destructive tests required.

Keywords: condition assessment; prefabricated buildings; large-panel; destructive testing; NDT

Citation: Wardach, M.; Krentowski, J.R. Diagnostics of Large-Panel Buildings—An Attempt to Reduce the Number of Destructive Tests. *Materials* **2024**, *17*, 18. https://doi.org/10.3390/ma17010018

Academic Editor: Oldrich Sucharda

Received: 28 November 2023
Revised: 11 December 2023
Accepted: 18 December 2023
Published: 20 December 2023

1. Introduction

During the building design process, the architects work with the client to define the form of the building and adjust the layout of the rooms to suit the intended use. The designers then select structural solutions so that all the limit state conditions are met. This involves selecting materials with suitable strength properties, adopting and verifying optimum cross-sections of structural elements, and correctly designing their connections. In the case of prefabricated system buildings, the process of manufacturing and completing the elements begins once the design documentation has been approved. The last stage is the erection (assembly) phase, which continues until the building is handed over for use. Each of these phases of construction is subject to the risk of errors that may affect the durability of the completed building. Structures that have been in use for several decades are subject to a process of ageing of materials, as well as degradation resulting from improper use, environmental impact, or exposure to exceptional loads. Errors occurring during both the execution of the building and external factors occurring during operation create a risk of structural failure. In order to avoid undesirable phenomena associated with the failure of a structure or to identify ways of strengthening it should they occur, it is necessary to diagnose the actual condition of the building.

This article considers the research methodology for large-panel structures, which represent a significant proportion of Europe's housing stock. Tens of millions of people live in these buildings, which makes ensuring safe and comfortable operation a matter of great social concern. During routine inspections, visual examinations are the most common practice, as they do not interfere with the structure of the building and are the least labour-intensive, but at the same time have the highest risk of error. If these inspections

do not identify any signs of structural or component degradation, the inspections can be considered reliable and sufficient. However, if symptoms characteristic of structural degradation are present, or if an upgrade/reconstruction of the structure is planned, the condition assessment should be more precise. To this aim, tests should be carried out using methods that allow the strength parameters of the building materials to be determined. Destructive testing and excavation provide the most reliable data on the strength and condition of individual materials and structural elements. Performing destructive testing involves interfering with the structure of the building, which is highly undesirable in residential buildings due to the potential need for subsequent repairs to the premises. This factor poses problems for both the tenants and facility manager, who is burdened with covering the cost of the repair work.

Large-panel structures were erected in many countries, primarily in Central and Eastern Europe [1]. After many years of use, typically around 40–50 years, scientific and professional evaluation should focus on their potential for modernisation [2–4], analysis of occurring failures [5–8], and solutions aimed at enhancing their architectural qualities and energy efficiency by altering the facades [9,10]. All of these aspects are interconnected with the necessity of conducting a diagnostic assessment of the structure. Given the quantity of buildings, diagnostics should be carried out in an efficient manner, providing both rapid and reliable results.

This paper focuses on presenting the possibilities of reducing the number of destructive tests for assessing the condition of large-panel structures. Based on the conducted research, risk factors related to obtaining reliable results through non-destructive methods were identified, and areas where destructive tests are necessary were pinpointed. A selected large-panel structure located in Poland, constructed using the regional OWT system, was chosen for the study. The structure was in use for 33 years since 1978, decommissioned, and after another 10 years, a decision was made to dismantle it (Figure 1).

(**a**) (**b**) (**c**)

Figure 1. Examined large-panel building: (**a**) east side; (**b**) north side; (**c**) west side.

The analysed large-panel system was characterised by a structural module of 4.80 m × 5.40 m and a height of 2.70 m [11]. The 0.14 m thick prefabricated floor slabs were supported by walls, also 0.14 m thick, and on an external beam-wall. The edges of the wall slabs were dowelled at the prefabrication plant, and the spaces between adjacent walls were filled with concrete on site to form vertical concrete joints working in shear. Walls, floors, and beam-walls were connected during assembly by steel welded joints. The gable walls and beam-walls that formed the facade of the building were made of three layers. The facade layer was suspended on steel hangers to the bearing layer, and insulation in the form of wool or polystyrene was placed between these layers.

Performing structural diagnostics enables the selection of appropriate strengthening and repair methods. The tests are intended to provide both information about the strength

parameters of the material being tested and the type and extent of deterioration. An example of the use of non-destructive testing to determine repair and rehabilitation strategies for a reinforced concrete structure is presented in [12]. Researchers have been working on methods of strengthening large-panel buildings for years. An extensive analysis in terms of the work required to increase the durability of these buildings and improve the comfort of their use is described in [13]. In [14], the author presents the possibilities of reinforcing vertical joints with a new steel connection system. The method of strengthening the connections of gable and beam-wall facade layers is presented in [15].

Widely practised methods of strengthening various types of concrete structures include reinforcement with composite tape [16,17] and repair mortar [18]. The repair materials used are extensively tested to determine their structural properties, their effect on the working of the structure, and their resistance to environmental influences. A very important issue is to subject the structure to testing after the strengthening work has been carried out. This is to determine the actual adhesion of the repair layer with the damaged structural elements. Correct adhesion is essential for the correct interaction of the old concrete with the newly added layer. An example of the use of the ultrasonic method to determine the adhesion of a repair layer is presented in [19]. To ensure proper adhesion to the concrete substrate, a suitable curing method is also required. In [20], the use of semi-destructive methods to test repair mortars applied using different curing methods is presented. The authors in [21] describe a repair material for which ohmic heat curing was used to obtain strength in a very low temperature environment. Interesting analyses are been presented in [22], wherein the effect of surface preparation on the adhesion of concrete for underwater structural repairs is been analysed. Researchers have also addressed the issue of self-healing cracks in concrete, as extensively discussed in [23]. Researchers have also been involved in analyses related to determining the influence of the external environment on the self-healing effect of concrete cracks [24].

Methods of strengthening structures that are located in seismically active zones have also been analysed. In [25], studies related to the placement of inter-storey seismic isolation in a wall-frame building are presented to determine the best location of the isolation at the height of the structure, which can significantly contribute to the durability of seismically exposed structures. Analyses related to the design of earthquake-resistant structures are also described in [26], wherein a seismic design concept is presented in which a building is divided into several segments, connected to one another by additional vibration isolation systems.

As presented in [27–29], large-panel buildings are characterised by numerous errors arising during production and installation, as well as degradation resulting from use often extending over 50 years. A number of papers can be found in the literature in which studies of large-panel buildings are presented [30–34]. Despite the development of non-destructive testing apparatus and its increased availability, there are still doubts about the effectiveness and validity of its use in practice. The main problem is the lack of testing methodologies. These should concern specific types of structures, characterised by their typical structural solutions and defects, and take into account the possibility of using various testing methods, including non-destructive ones. This article is a continuation of the analyses related to the improvement of testing methodology for large-panel structures and the implementation of modern non-destructive testing methods in engineering practice. The authors described their earlier analyses in detail [35–39], wherein they presented a wide range of tests using different methods. The research results presented in this article are novel and have not been taken from other sources. The development of technology allows for a change in the techniques/methods used in the assessment of structures, which can speed up diagnostic processes and reduce the number of destructive tests. The authors have attempted to answer the research question of whether a large number of destructive tests are necessary to diagnose structures and in which areas destructive testing is necessary to carry out a reliable assessment of the building's condition.

The body of knowledge on non-destructive methods is very broad, as exemplified by the numerous papers on the subject [40–44]. This article is a continuation of the extensive literature on non-destructive testing, but focuses strictly on the specificity of large-panel buildings. Thus, it tries to respond to the need to develop dedicated and precise research methodologies for system structures. The manuscript concentrates on the aspect of using non-destructive methods that can improve the diagnostic processes of thousands of large-panel structures. With regard to the application of the testing methods used, reference was made to standard recommendations and guidelines from a reputable research institution. Based on the performed research, practical guidelines were formulated with a view to reduce the number of destructive tests and increase the efficiency of conducted structural condition assessments. The unique opportunity to carry out such extensive tests on a large-panel object provides a unique opportunity to improve diagnostic techniques.

2. Structural Diagnostics—Own Research

In large-panel construction, two main structural materials were traditionally used: concrete and steel. Load-bearing elements, such as wall panels, floor slabs, beams, beam-walls, stairs, and foundations, were made of reinforced concrete with steel rebars. Steel was also used in constructing joints connecting the prefabricated elements. The condition of structural elements is influenced by the degree of degradation in both concrete and steel. Due to the intended demolition of the building, the authors were not restricted in the number and scope of conducted destructive tests. Hence, dozens (about 80 units) of core drillings and numerous excavations were carried out, along with cutting reinforcement bars and connection plates for subsequent laboratory strength tests (Figure 2). The unique opportunity to obtain such a large number of samples enabled the discovery of empirical relationships between results obtained from various methods.

Figure 2. Destructive testing: (**a**) Core sampling from the wall panel; (**b**) core sampling from the floor tie beam; (**c**) excavation in the beam-wall; (**d**) image of some of the samples taken.

2.1. Methods of Assesing the Quality and Strength of Concrete

Concrete, as a material consisting of aggregate, cement, water, and various admixtures and additives, is characterised by different physical and strength properties. The properties of concrete depend on both the composition and environmental conditions in which it is formed/bonded, as well as the method of placement and compaction itself. In addition, concrete elements are exposed to environmental influences that can significantly affect their strength properties, as well as their ability to protect reinforcing steel from corrosion.

Many test methods dedicated to the assessment of concrete quality have been described in the literature [45–50]. Many of the modern techniques are usually applied under laboratory conditions [51–53]. In construction practice, a visual method is first used to assess the condition of reinforced concrete structures, allowing cracks and scratches to be observed, which can provide a basis for deciding whether more thorough testing is

necessary. Subsequently, sclerometric, ultrasonic, and destructive testing methods are used to assess the condition of concrete and reinforced concrete elements. As these three methods are the most commonly used, the authors have selected them for analysis with the aim of reducing the number of destructive tests in construction practice.

By using samples obtained by core drilling, we can acquire many parameters, such as compressive strength, tensile strength, Young's modulus, water resistance, information on the extent of carbonation, the composition of the concrete mix, and many others. The basic question is which parameters are necessary to assess the condition of a building that has been in service for several decades. Many times such buildings do not show any symptoms indicating that their durability is at risk. It is therefore reasonable to determine the purpose of the diagnosis to be carried out. A thorough analysis, including the composition of the mixture, may be necessary in exceptional situations, such as a building catastrophe, to verify that the structure was designed and constructed in accordance with the applicable standards. For regular condition monitoring, or to perform an expert assessment prior to retrofitting works, basic strength parameters and identification of degradation processes may be sufficient to determine. Large-panel structures often maintain a technical state that does not pose a threat of failure, partly due to latent safety reserves, so analyses of the condition of reinforced concrete elements can be simplified to some extent in many cases.

In residential buildings, floor slabs are covered with floor layers, while walls are usually plastered and painted or wallpapered. For non-destructive testing, it is often required to remove unnecessary layers from the walls, whereas in the case of the floor slabs, it is reasonable to test from underneath, eliminating the need to remove the floor layers. When collecting samples for destructive testing, drilling rigs are used, which are usually water-cooled. Water degrades large areas of the finish layers, including those of the flats on the storey below, and it is additionally necessary to mask the entire newly created cavity. The common opinion perceiving destructive surveys as the most problematic and labour-intensive, both at the time they are carried out and in order to bring the flats to a condition equivalent to before they were started, is justified.

In order to determine the strength of the concrete, the authors carried out numerous tests using sclerometric (Figure 3a) and ultrasonic methods (Figure 3b), followed by core drilling samples (Figure 3c) at the same locations for destructive strength tests. In order to check the suitability of the individual testing techniques, the results obtained using destructive and non-destructive methods were correlated according to the procedures described in the standard [54] and its previous version [55], which described some aspects of the testing in more detail. The analyses were also based on recommendations (instructions) of the Building Research Institute (in Polish: 'Instytut Techniki Budowalnej'—'ITB') [56–58], a leading research institution in Poland, which are very often practised by engineers. European standards and the guidelines of national research institutes are the most reliable source of knowledge for building surveyors, so the authors focused on assessing the suitability of their recommendations for the diagnosis of large-panel structures.

The regression curves were determined based on the correlations obtained between samples collected from core drillings made on the 4 interior walls of the 5th floor of the building under analysis. Three core drillings were made on each wall (with a diameter of d = 10 cm, which were cut to obtain l/d = 1). Before core drilling, the number of rebounds was read 10 times at each measuring point to determine the median. At the same locations, the ultrasonic wave velocity was measured using the direct method, i.e., by placing transducers on 2 sides of the walls.

(**a**) (**b**) (**c**)

Figure 3. Concrete testing: (**a**) sclerometric method; (**b**) ultrasonic method; (**c**) drilling core sampling.

2.1.1. Concrete Compressive Strength Testing by Sclerometric Method

The first of the methods analysed for testing the compressive strength of concrete was the sclerometric method. This method is distinguished by its low effort, simplicity, and availability of equipment. This makes it an attractive and widely used technique. The results obtained using the testing machine and sclerometer are presented in Table 1, which also includes the differences between the obtained values (Δf). Both the most common regression curves proposed by the standard [55] (denoted by $f_{R,EN}$) and the ITB instructions [56,57] ($f_{R,ITB}$) were used for the analyses. Using the data from the destructive tests (f_{is}), empirical relationships were determined and corrected curves were determined—both with the approximate method ($f_{R,EN,scaled}$) according to [55], and with the exact method, i.e., the least squares method ($f_{R,accurate}$). In addition, a regression curve with strength reduction factors due to the age of the concrete was determined according to the recommendations of the ITB instructions [56,57] ($f_{R,ITB,reduced}$). All curves are presented in Figure 4.

Table 1. Compressive strength results from core drilling and based on empirical relationships obtained.

f_{is} [MPa]	Rebound Median [-]	$f_{R,ITB}$ [MPa]	Δf [%]	$f_{R,EN}$ [MPa]	Δf [%]	$f_{R,ITB,reduced}$ [MPa]	Δf [%]	$f_{R,EN,scaled}$ [MPa]	Δf [%]	$f_{R,accurate}$ [MPa]	Δf [%]
20.10	36.50	28.62	−30%	28.65	−30%	17.17	17%	18.87	7%	20.02	0%
20.83	37.00	29.67	−30%	29.51	−29%	17.80	17%	19.73	6%	20.66	1%
21.00	37.00	29.67	−29%	29.51	−29%	17.80	18%	19.73	6%	20.66	2%
21.17	37.50	30.74	−31%	30.38	−30%	18.45	15%	20.60	3%	21.30	−1%
21.80	38.00	31.83	−32%	31.24	−30%	19.10	14%	21.46	2%	21.94	−1%
22.49	38.50	32.94	−32%	32.11	−30%	19.77	14%	22.33	1%	22.58	0%
23.50	39.00	34.08	−31%	32.97	−29%	20.45	15%	23.19	1%	23.21	1%
23.60	39.00	34.08	−31%	32.97	−28%	20.45	15%	23.19	2%	23.21	2%
23.80	39.50	35.23	−32%	33.84	−30%	21.14	13%	24.06	−1%	23.85	0%
24.50	40.00	36.40	−33%	34.70	−29%	21.84	12%	24.92	−2%	24.49	0%
25.20	40.50	37.59	−33%	35.57	−29%	22.56	12%	25.79	−2%	25.13	0%
25.93	41.00	38.81	−33%	36.43	−29%	23.28	11%	26.65	−3%	25.77	1%

The obtained results showed that, in the case of concrete made more than 40 years ago, the compressive strength calculated on the basis of the regression curves proposed in [55] and refs. [56,57] was significantly higher (by about 30%) than the actual values. This fact can be explained by the phenomenon of concrete carbonatisation (overestimating the reflection number), which, when measured with phenolphthalein solution, ranged from 1 to 3.7 cm deep in the tested walls. The smallest differences between the obtained results were represented by the equation of the curve determined using the exact method (difference of an average of 1%). The equation determined using the approximate method produced results that deviated from the actual results by an average of 3%. The regression curve recommended by the ITB instructions, which takes into account the reduction in strength of the concrete due to its age, underestimated the results by 14% on average.

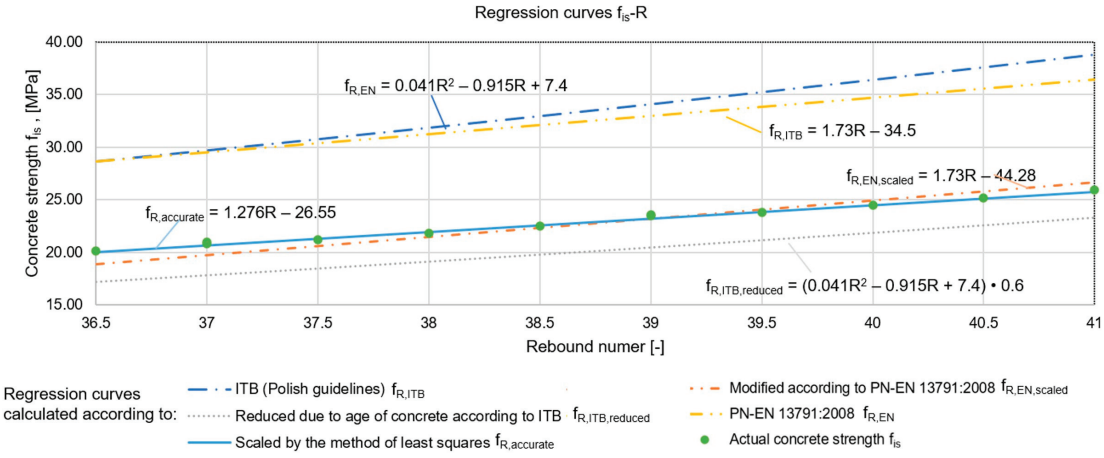

Figure 4. Regression curves for estimating the compressive strength of concrete using the scleroemtric method and results of destructive strength tests.

For further analyses, curves described by two equations were selected, i.e., the regression curves $f_{R,accurate}$ and $f_{R,ITB,reduced}$. The choice was based on the fact that the results obtained with the curve obtained using the exact method were the most precise, while the second equation underestimated the strength of the concrete, but this curve did not need to be scaled, which is a huge convenience for the diagnostician in practice. In addition, obtaining lower results than the actual values is safer from the point of view of the structural surveyor because the difference creates a hidden safety reserve. However, the caveat is that if the analysis carried out on the basis of the results obtained in this way indicates that the limit states are not met, it is imperative that the parameters should be confirmed by a destructive method before a reinforcement decision is taken. This is to avoid unnecessary expense on works to increase the strength of the structure.

Large-panel buildings were assembled from prefabricated elements which, for a particular structure, were most often made in a single factory using the same concrete mix. Hence, it can be assumed that the concrete quality and strength of the elements located on different storeys should be similar. In order to verify that the selected curves were applicable to the determination of the compressive strength of the other building elements, a comparison was made between the results obtained from 12 core drillings (f_{is}) taken from the walls and floors of storeys 1, 3, 7, and 10. The results are presented in Table 2 and Figure 5. The difference between the obtained strength values is denoted as Δf.

Table 2. Compressive strength results from the core drillings and based on the empirical relationships obtained from the different structural elements located on storeys 1, 3, 7, and 10 (using the sclerometric method).

Element	Median Number of Rebounds [-]	f_{is} [MPa]	$f_{R,accurate}$ [MPa]	Δf [%]	$f_{R,reduced}$ [MPa]	Δf [%]
Interior wall storey 7	38.5	23.56	22.58	4%	19.77	19%
Gable wall storey 10	39	23.81	23.21	3%	20.45	16%
Floor slab storey 3	39	23.79	23.21	2%	20.45	16%
Gable wall storey 7	39.5	25.71	23.85	8%	21.14	22%
Interior wall storey 1	40	24.23	24.49	−1%	21.84	11%
Floor slab storey 7	40	27	24.49	10%	21.84	24%
Interior wall storey 3	40.5	25.11	25.13	0%	22.56	11%
Floor slab storey 10	40.5	23.51	25.13	−6%	22.56	4%
Gable wall storey 3	41	24.61	25.77	−4%	23.28	6%
Floor slab storey 1	41.5	25.87	26.40	−2%	24.02	8%
Gable wall storey 1	42	23.7	27.04	−12%	24.78	−4%
Interior wall storey 10	42.5	26.11	27.68	−6%	25.54	2%

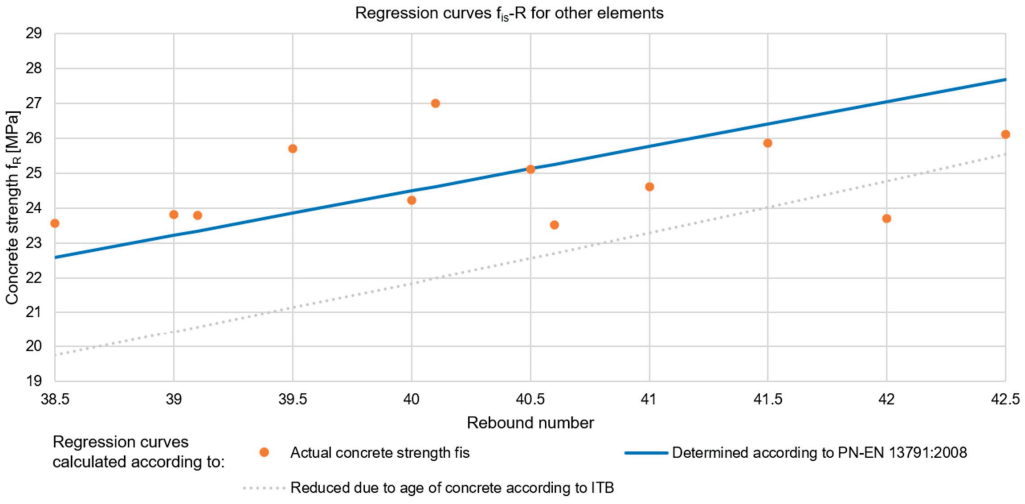

Figure 5. Regression curves and results of destructive strength tests for various structural elements located on storeys 1, 3, 7, and 10 (using the sclerometric method).

Based on the obtained results, it can be concluded that the compressive strength of the concrete calculated using the equation determined from the empirical relationships established for the walls of the 5th floor was very close to the actual compressive strengths of the concrete of the other prefabricated elements located on storeys 1, 3, 7, and 10. The maximum overestimation of the concrete strength was 12%, while the underestimation was 10%. When the regression curve recommended by the Building Research Institute (ITB) was applied (i.e., strength reduced due to the age of the concrete), the concrete strength was slightly (by 4%) overestimated only for one sample. In the remaining cases, the maximum underestimation was 24%. The above analysis confirmed that the concrete used throughout the building was characterised by similar strengths, irrespective of the storey or type of structural element. The above relationship may be a typical feature of buildings constructed using large-panel technology.

The current standard [54] indicates that, for the purpose of assessing an existing structure, an estimate of the compressive strength should be based on at least 8 or 12 valid measurement values, depending on the diameter of the core. On the other hand, for a small measurement site that contains 1 to 3 structural elements, the total volume of which does not exceed 10 m^3, a minimum of 3 drillings should be made. The standard also indicates that the calibration of results obtained using indirect methods (non-destructive methods) should include at least 10 pairs of results. It is also permissible to use indirect methods without calibration to locate sites of questionable quality, after which a minimum of 3 core drillings should be carried out. This method is limited to measurement locations where there is no doubt about the compressive strength of the concrete and the total volume of the elements does not exceed 30 m^3.

The authors, based on their professional experience, their knowledge of large-panel buildings (especially those constructed in OWT system), and the studies carried out, recommend that the concrete throughout the structure should be assumed to represent the same compressive strength class. This makes it possible to adopt, as shown in the flowchart proposed in the standard [54], a procedure that allows the structure to be treated as a single measuring site. It is therefore suggested to take core drilling samples from different structural elements located on different storeys, instead of taking several cores from one/multiple elements located on one storey. In this way, the structural surveyor can obtain information about the condition of the concrete in the entire structure without performing a large number of destructive tests. In a further step, empirical relationships

should be determined with the results obtained using the sclerometric method. Subsequent elements are suggested to be tested exclusively using the sclerometric method to estimate the concrete compressive strength. In the case of locating areas with an extremely different number of rebounds, a core drilling should be carried out in this location. In situations where drilling is not possible, it is not suggested to use the curve recommended by the standard [55] without calibration. Instead, it is recommended to use the curve proposed by ITB [56,57], taking into account the reduction in compressive strength of the concrete due to age. The results may deviate considerably from the actual results, but it should be assumed that it is better to estimate the result than to not to have it at all in such a case.

2.1.2. Concrete Compressive Strength Testing by Ultrasonic Method

Another method to be analysed for estimating the compressive strength of concrete was the ultrasonic method. There is no direct correlation between strength and ultrasonic wave speed. The relationship should be established for a specific concrete mix recipe. The results are also influenced by factors such as the moisture content and temperature of the concrete, the location of the reinforcement, as well as cracks and voids. The moisture content of the concrete and its temperature affect the velocity of wave propagation. Wave propagation can be faster in wet concrete. The temperature of the concrete under normal conditions does not significantly affect the velocity and attenuation of waves, except when the concrete is subjected to freezing. All elements were tested a few days apart, during the summer season, where the outside temperature did not exceed 25 °C in the day and did not drop below 10 °C at night. There was also no precipitation at that time. According to the test equipment producer's instructions [59], no correction factors were implemented for concrete at temperatures between 10 °C and 30 °C, regardless of the degree of moisture in the material. As the measuring conditions were the same throughout the test period, and following the producer's instructions, the influence of temperature and moisture was neglected. Another factor is the influence of the location of the reinforcement. The velocity of the ultrasonic wave through rebar is much higher than in concrete. Measurement locations through which the reinforcement passes should therefore be avoided. For the purposes of this study, scanning of the tested elements using the electromagnetic method was carried out in order to locate the rebars. Measurement locations without reinforcement were then determined. In this way, the influence of the reinforcement on the results was avoided. The last factor mentioned above is the presence of cracks and voids. Cracks and voids with a length greater than the diameter of the transducer or the wavelength in the path of the ultrasonic pulse present an obstacle that causes the wave energy to dissipate. This causes the wave transit time to be extended. In the tested elements, the ultrasonic wave velocity and rebound number qualified the concrete mix as homogeneous and of relatively good quality. In addition, visual examinations were carried out after the core drilling, confirming the good quality of the concrete, with no internal cracks or voids at the designated measuring points.

Testing the speed of the wave propagation is recommended for locating areas of varying quality.

Both the standard [55] and ITB instructions [58] provide the equations of the basic regression curves, the shapes of which are shown in Figure 6. On the basis of the obtained results of our own tests (Table 3) and using the producer's software, the empirical relationships and equation of the curve were determined ($f_{V,accurate}$), which are also shown in Figure 6. The compressive strength of concrete determined using the destructive method is denoted by the symbol f_{is}.

As can be seen in Figure 6, the shapes of the curves are quite different, so estimating the compressive strength of concrete without determining empirical relationships is unreliable. Therefore, standard curves should not be adopted without scaling, and if this is not possible, the use of the ultrasonic method should be limited to locating areas of poorer quality.

Similar to the sclerometric method, the authors verified that the determined curve was applicable to the reliable determination of the strength of other structural elements.

The relationships were verified for the same measurement points as in the analyses of the sclerometric method. The results are presented in Table 4 and Figure 7.

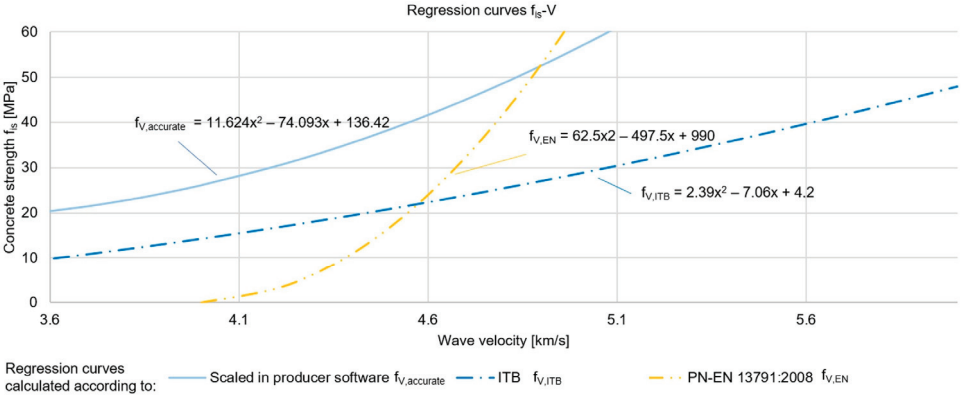

Figure 6. Regression curves for estimating the compressive strength of concrete using the ultrasonic method.

Table 3. Compressive strength results from core drilling and longitudinal wave velocities at the surveyed measurement points.

Wave Velocity [km/s]	f_{is} [MPa]
3.572	20.10
3.630	20.83
3.679	21.00
3.709	21.17
3.739	21.80
3.785	22.49
3.815	23.50
3.845	23.60
3.891	23.80
3.922	24.50
3.967	25.20
3.981	25.93

Table 4. Compressive strength results from the core drilling and from the empirical relationships obtained from the various structural elements located on storeys 1, 3, 7, and 10 (using the ultrasonic method).

Vp [km/s]	$f_{V,accurate}$ [MPa]	f_{is} [MPa]	Δf [%]
3.721	21.66	23.56	9%
3.788	22.55	23.79	6%
3.833	23.20	24.23	4%
3.872	23.80	23.7	0%
3.885	24.01	25.11	5%
3.891	24.11	23.51	−2%
3.898	24.23	23.81	−2%
3.899	24.24	24.61	2%
3.952	25.15	25.71	2%
3.964	25.37	26.11	3%
3.991	25.86	25.87	0%
3.998	25.99	27	4%

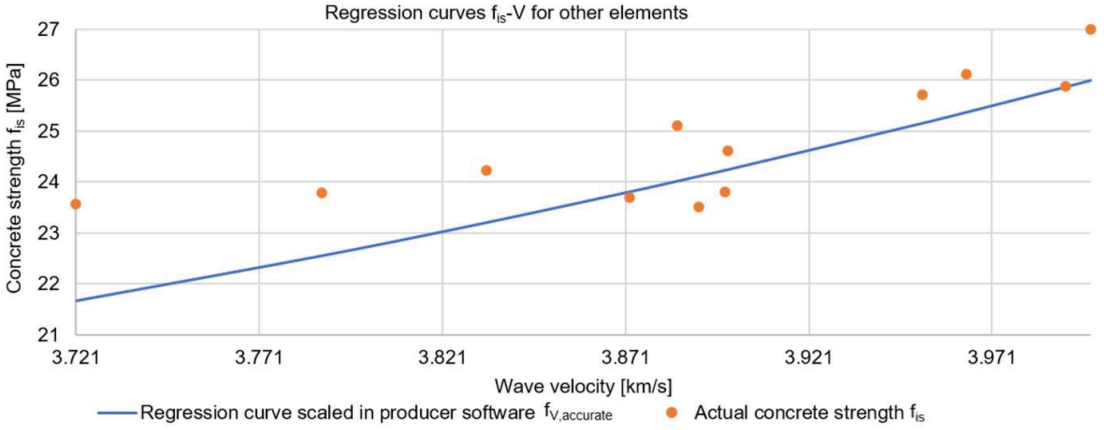

Figure 7. Regression curve and results of destructive strength tests for various structural elements located on storeys 1, 3, 7, and 10 (using the ultrasonic method).

The maximum difference in the compressive strength of the concrete was 9%, demonstrating that the selected regression curve was applicable for reliable estimation of concrete strength in the whole tested structure, without differentiation by storey and type of prefabricated elements. This demonstrated the use of a concrete mix of the same, or very similar, composition for the prefabricated elements, as well as the same standards of workmanship of the elements at the prefabrication plant.

2.1.3. Testing the Quality/Homogeneity of Concrete Using Sclerometric and Ultrasonic Methods

Both the sclerometric and ultrasonic methods are commonly used to estimate the quality/homogeneity of a concrete mix. The guidelines contained in ITB [56] enable the homogeneity of concrete to be assessed on the basis of the calculated coefficient of variation of concrete compressive strength (v_f), which is determined using the sclerometric method. By contrast, ref. [60] presents a classification of concrete quality based on the velocity of longitudinal wave propagation in the element. The authors decided to compare the results of the two methods using their own tests carried out on 5 internal walls, for which the mean velocity from 10 longitudinal wave readings and the median from 10 reflection number readings were obtained. The results are presented in Table 5. The calculated coefficient of variation of concrete compressive strength was calculated according to the guidelines in [56].

Table 5. Assessment of concrete quality based on longitudinal wave velocity and homogeneity based on reflection number.

Element No.	Average P-Wave Velocity [m/s]	Concrete Quality According to [60]	Median Rebound Number	Calculated Coefficient of Variation of Concrete Compressive Strength v_f	Concrete Homogeneity According to [56]
Wall 1	3816	Good	39	9%	Very good
Wall 2	3726	Good	40	11%	Good
Wall 3	3988	Good	38.5	14%	Medium
Wall 4	3765	Good	38	11%	Good
Wall 5	3811	Good	39.5	12%	Good

Based on the presented results, it can be concluded that the tested concrete was of good quality. The range of longitudinal wave velocity values contained in [60] was quite wide,

resulting in all of the elements tested being assigned to one quality category. When the sclerometric method was used, the homogeneity of the concrete was classified as medium, good, or very good. In the case of assessing the homogeneity as 'medium', a value of 14% was the lower limit of this category; hence, taking into account the other results, the concrete could be considered homogeneous. Analysing the above table, it was concluded that both methods converged and could be successfully used to assess the quality and homogeneity of concrete. However, it is recommended to compare the results obtained using the two methods. Using only surface methods (e.g., the sclerometric method) runs the risk of not identifying some areas of poorer quality, which can be successfully detected by ultrasonic methods, as described in [36].

2.2. Methods of Assessing the Condition and Strength of Steel

In large-panel buildings, steel is present in structural elements in the form of reinforcement bars and welded joints of prefabricated elements. Degradation of this material is difficult to identify due to it being covered in concrete. The reinforcing bars are wrapped in the concrete mixture forming an integral whole, while the steel connections are hidden under other reinforced concrete elements, i.e., walls, floors, and beam-walls.

Corrosion of the reinforcement leads both to a reduction in the load-bearing capacity of the reinforced concrete elements (e.g., through a reduction in rebar cross-section, loss of adhesion to the concrete, or loss of ductility). In order to assess the quality of the reinforcement works, electromagnetic methods are most often used or excavations are carried out. Modern measuring equipment makes it possible to determine the diameters and spacing of the reinforcement without the need to remove finish layers. Carrying out a series of tests in a building which has been used for its intended purpose for several decades and also exposed to a more aggressive environment for a short period of time (as a result of being taken out of service and not being heated) can provide a reference for an approximate assessment of the condition of the reinforcement of the load-bearing elements in other large-panel buildings. In order to determine the strength parameters and quality of the reinforcement works, a dozen excavations were carried out, several dozen rebars (more than 100) were cut for destructive testing, and tests were carried out using the electromagnetic method. Comparison of the test results obtained using the electromagnetic method and destructive methods made it possible to determine the accuracy of the non-destructive method in relation to the actual state and to locate sensitive areas where special care should be taken when taking measurements and interpreting the data. Precise determination of the strength parameters of the reinforcing bars using destructive testing allowed visualisation of the expected state of rebar degradation in a large-panel building more than 40 years after installation. Strength tests were also carried out on the steel connections of the prefabricated elements, which are responsible for the proper redistribution of internal forces in the structure.

2.2.1. Testing the Quality of Reinforcement Works and Strength of Bars

The authors first carried out electromagnetic measurements (Figure 8a) of the walls, floors, and beam-walls to determine the location of rebars and quality of the reinforcement works. Several of these locations were marked for excavation and sampling for laboratory testing (Figure 8b,c). The diameter measurement made with the apparatus, according to the manufacturer's specifications [59], can be subject to an error of ± 2 mm. It should be noted that in the case of ribbed bars, a distinction was made between the basic diameter of the core and height of the ribs, and the declared diameter was a dimension defined in product-specific standards. The measuring device did not distinguish between smooth and ribbed rebars, hence it was necessary to be careful in interpreting the results. The authors measured the actual diameters of the bars after excavation using a calliper and micrometer and then determined their declared diameter, taking into account the dimensional tolerances given in refs. [61,62], i.e., the local standards in use at the time when the structure was erected. Based on the ribbing, the steel grades were identified, which are presented in Table 6. The

Φ8 diameter bars were smooth reinforcement, while the bars of the other diameters were ribbed. Examples of the values obtained were compared with the electromagnetic test results, as shown in Table 6.

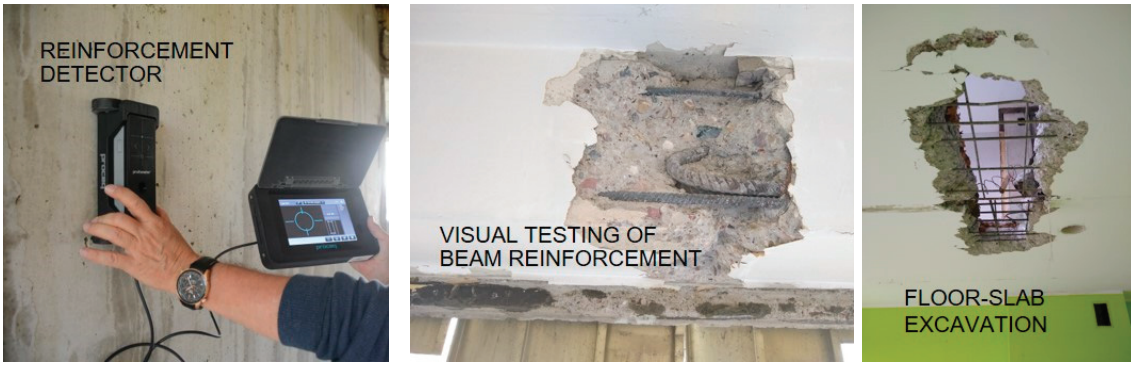

(**a**) (**b**) (**c**)

Figure 8. Reinforcement work quality assessment: (**a**) electromagnetic method; (**b**,**c**) excavations.

Table 6. Results of rebar diameters.

Identified Steel Grade	Ideal Diameter of Bars with Ribs [mm] [61,62]	Actual Diameter with Ribs [mm]	Design Diameter [mm]	Diameter Obtained Using the Electromagnetic Method [mm]
St3SX	8 (no ribs)	8.62	Φ8	8
		8.67	Φ8	8
		8.68	Φ8	8
		8.87	Φ8	9
		8.79	Φ8	9
18G2	10.3	11.33	Φ10	11
		11.11	Φ10	10
		11.63	Φ10	12
		11.22	Φ10	10
		11.15	Φ10	10
34GS	12.6	13.79	Φ12	14
		13.32	Φ12	12
		13.37	Φ12	12
		13.60	Φ12	14
		12.58	Φ12	12
34GS	14.6	15.00	Φ14	14
		14.88	Φ14	14
		14.98	Φ14	15
		15.04	Φ14	15
		14.73	Φ14	14

The obtained results supported the conclusion that the deviations in the measurement of diameter using the electromagnetic method were within the range declared by the device manufacturer. In addition, the most frequent reading for each diameter type indicated the design value, which made it easier to interpret the results. However, it should be noted that the identification of the correct diameter should also be based on the diagnostician's experience and knowledge of design solutions. For example, bars with a nominal (design) diameter of Φ15 were not used in Poland. If the readings at a given location were Φ14 or Φ15, it should be assumed that Φ14 bars were used in the construction. It is worth mentioning that all of the measured bar diameters were within the upper limits of the

dimensional tolerances, which is beneficial for the load-bearing capacity of reinforced concrete elements.

Dozens of rebars (10 to 20 for each diameter type) were tested in a machine to determine their yield (f_y) and tensile strength (f_u) (Figure 9). The specimens were machine-cut to obtain a full cross-sectional area (without ribbing) in order to precisely determine the strength parameters tested. The results are presented in Table 7.

Figure 9. Testing of reinforcing bars: (**a**) rebars before tests; (**b**) testing in the machine; (**c**,**d**) rebars after testing with visible constriction.

Table 7. Results of the rebar strength tests.

Design Diameter [mm]	Identified Steel Grade	Average Measured Yield Strength f_y [MPa]	Minimum Yield Strength $f_{y,min}$ [MPa] [63]	Δf_y [%]	Average Measured Tensile Strength f_u [MPa]
Φ8	St3SX	395.68	240.00	65%	475.01
Φ10	18G2	458.52	360.00	27%	660.93
Φ12	34GS	475.77	420.00	13%	713.16
Φ14	34GS	470.83	420.00	12%	693.02

The actual yield strength values were between 12 and 65% higher than the minimum values for the identified steel grades specified in the standard [63] in use at the time when the facility was designed. None of the individual specimen results indicated that the yield strength value was too low—all rebars met the standard strength requirements.

2.2.2. Concrete Resistivity Testing—Estimating the Risk of Reinforcement Corrosion Processes

At the same measuring points, a resistivity test of the concrete was also carried out prior to the excavations. This test is especially useful for assessing the resistance of concrete to the ingress of chloride ions, which cause corrosion of the steel. The chlorides that initiate steel degradation processes come primarily from de-icing salts to which car parks and underground garages are exposed, as well as chlorides from seawater and air. In the case of large-panel structures, the danger of chloride aggression occurs on coastal shores in the form of wind-borne aerosol and in areas of large industrial districts. The resistivity test method is also used to estimate the corrosion rate of already-depassed steel. A classification of the corrosion intensity, divided into chloride-induced and general corrosion depending on the resistivity of the concrete, is presented in [64]. The results obtained using Wenner probe measurement are presented in Figure 10 and the test equipment is shown in Figure 11a.

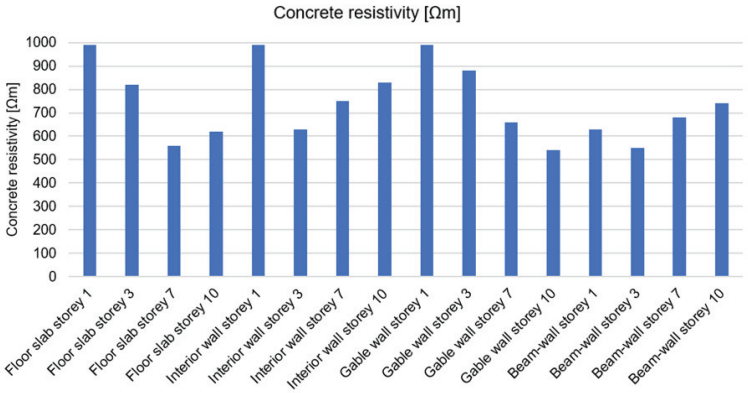

Figure 10. Resistivity of the concrete at the test points read with a Wenner probe.

The obtained results indicated that, in a facility not located by the sea and not in the zone of a large industrial district, the probability of chloride corrosion was assessed as very low. The results (>500 Ωm) also indicated that the conditions in the concrete cover were not conducive to rapid corrosion of the reinforcing steel. The absence of corrosion signs of the rebars was confirmed by visual inspection of the cut specimens (Figure 11b). However, corrosion of the reinforcement was identified in the area of the window joinery (Figure 11c), which occurred as a result of the bars being exposed by inadequate dismantling of the joinery, and in the facade hangers of the textured (facade) layers, the concrete resistivity of which was not tested due to lack of access.

(**a**) (**b**) (**c**)

Figure 11. Corrosion investigation of reinforcing steel: (**a**) Wenner probe test; (**b**) visual inspection of rebars from excavations; (**c**) exposed corroded beam-wall rebar.

2.2.3. Testing the Strength of Steel Connections

The most difficult places to carry out condition assessments are the steel connections of prefabricated elements. As described in [35], in order to reduce nuisance to residents, it is recommended that joints should be tested in stairwell areas. By assessing the condition of several such connections, including the conformity of their workmanship with catalogue solutions, it is possible to determine with what care the connections were made and whether degradation processes (e.g., in the form of corrosion) are occurring. If the connections in a stairwell are identified as being in poor condition, it is highly likely that the connections throughout the building are in a similar state. When exposing a steel joint, it is highly desirable to determine the condition without cutting it out, which would result in a loss of load-bearing capacity. To do this, the surfaces should be brushed out using power

tools, and then non-destructive testing should be carried out. Ultrasonic hardness tests are helpful for estimating the strength of steel, while plate thickness can be successfully read using ultrasonic thickness gauges. The number of destructive tests should be limited to as few as possible. In order to check whether the results for the tensile strength of the steel obtained by correlation with its hardness were reliable, the authors cut several plates of the connections (Figure 12), which were tested in a testing machine. From the results, the differences (Δf) between the values obtained using the destructive ($f_{u,is}$) and non-destructive methods (f_u) were determined, as shown in Table 8.

(**a**) (**b**) (**c**)

Figure 12. Steel joints (plates) tests: (**a**,**b**) cut-out plates with brushed elements for destructive testing; (**c**) example fragments of torn plates.

Table 8. Tensile strength test results of connection plates.

Sample Number	Strength Test Determined by Destructive Method	Strength Test Determined by Hardness Test	Δf [%]
	$f_{u\cdot is}$ [MPa]	f_u [MPa]	
1	351	355	−1.1%
2	362	369	−1.9%
3	372	394	−5.6%
4	375	371	1.1%
5	376	399	−5.8%
6	379	360	5.3%
7	400	382	4.7%
8	409	413	−1.0%
9	409	402	1.7%
10	421	424	−0.7%
11	422	424	−0.5%
12	425	427	−0.5%
13	430	442	−2.7%
14	449	462	−2.8%
15	455	482	−5.6%

The obtained results allowed the tested steel to be classified as St3SX with a minimum tensile strength f_u = 360 MPa [65], which was in accordance with the design assumptions. This grade was most similar to the currently used equivalent with the symbol S235. The tensile strength values obtained using the non-destructive method and in the testing machine were very similar, and the maximum difference in strength was less than 6%. The clear correlation between the steel's hardness and its strength made it possible to reduce destructive testing to the necessary minimum. The authors recommend that only part of the section (e.g., a section of angle) should be cut out in order to minimise the loss

of load-bearing capacity due to damage of the joint. Therefore, it is suggested to avoid cutting whole flat bars connecting precast elements. In the case of similar results for the hardness of steel on different types of joint, the minimum number of destructive tests is recommended to determine the average tensile strength, i.e., 3 specimens. In the event of large discrepancies, areas of lower hardness should be identified using a non-destructive method, after which a sample should be taken for strength testing.

3. Discussion—Practical Aspects of Diagnostics

Using specialised measuring equipment to determine the actual strength characteristics, followed by FEA calculation software, it is possible to determine when a component under analysis will be destroyed with a high degree of accuracy. Non-destructive testing is always subject to the risk of error, whether this is caused by failure to take into account the influence of any of the factors affecting the measuring equipment, incorrect use of the equipment, or misinterpretation of the results. Destructive testing provides the most reliable results and a basis for confirming the reliability of data obtained using other methods. Extensive tests carried out on the analysed large-panel object enabled the identification of differences between the results obtained using destructive methods and the most commonly used non-destructive methods.

The obtained results showed a convergence of the concrete compressive strengths of the different types of precast elements and their good quality. The prefabricated elements were made in factories in which care was taken to maintain the technological regime, which may have had a positive effect on their quality and durability. In the authors' opinion, for the diagnosis of large-panel structures where visual inspection does not indicate disturbing degradation processes and the buildings are not located in highly chemically contaminated zones, the number of destructive tests can be reduced to the necessary minimum. Standard recommendations for obtaining the required number of pairs of results obtained using destructive and non-destructive methods may not be possible in some cases. In such situations, building surveyors should base their decisions on their own experience and the recommendations given in articles such as this paper. In the authors' opinion, with the knowledge of the specifics of the construction of a given building (the knowledge that the elements may be made of the same class of concrete) and the convergence of results obtained using non-destructive methods indicating good concrete quality, the number of drillings can be limited to a few per whole object. The number of drillings should be adequate to the number of storeys and the sampling locations should be on different structural elements and storeys. In this way, the results obtained using non-destructive methods can be confirmed with a minimum workload. It should be noted that when carrying out non-destructive testing, both the equipment producers' recommendations and applicable standards should be strictly respected. Otherwise, the results obtained may be falsified, which may lead to wrong decisions being taken regarding the condition of the structure.

Tests related to the determination of the quality of the reinforcement works can be successfully carried out using non-destructive methods. A comparison of the results in terms of rebar spacing and diameter showed no significant differences between the readings obtained using the electromagnetic method and the measurements from the excavations. Resistivity measurements have also been shown to be helpful in determining whether the environment is conducive to the formation of corrosion processes. However, it is not possible to determine the strength parameters of the reinforcement using non-destructive methods. Tests carried out on dozens of rebars in the testing machine made it possible to conclude unequivocally that the reinforcing steel in the investigated object had not been subjected to degradation related to the long period of exploitation (ageing processes) and the influence of factors in the form of moisture from the premises and external environment, temperature, and atmospheric pollutants. It is noteworthy that the degradation processes of the reinforcing steel did not occur despite the fact that the building was out of use for a decade, which was associated with non-heating of the object in winter conditions and

acts of vandalism in the form of broken glass in the windows. The authors recommend performing a minimum number of openings in selected structural elements and taking a few rebars in order to obtain certainty about the absence of corrosion processes and the preservation of the strength parameters of the steel. It is reasonable to excavate the gable walls, which are also bathroom walls, and basement walls. These are the elements most exposed to moisture from both inside and outside the building. Rebars passing through retrieved reinforced concrete cores can also be used for testing, which in some cases can eliminate the need for excavations.

Despite the absence of any mention in the literature regarding the identification of symptoms indicative of advanced degradation processes in large-panel structures in service, regular assessment of their technical condition is very important. In addition to the degradation processes associated with material ageing and inappropriate use, climate change and the strong industrialisation of urban regions are a threat. The changes taking place in the environment result in atmospheric factors (snow, wind, rain, and temperature) of a different intensity than was expected when the facilities were designed. Industrialisation, meanwhile, causes air and water pollution, which can contribute to the degradation of construction materials. These factors make it necessary to monitor the conditions of structures to ensure their safe operation.

4. Conclusions

In conclusion, on the basis of professional experience, previous research, and the analyses presented in this article, conclusions have been made regarding the diagnosis of large-panel structures aimed at reducing the number of destructive tests.

A number of research limitations were identified in the area of testing systemic prefabricated objects, resulting in recommendations to improve the diagnostic process:

- Problems associated with determining the location and number of survey points. The authors recommend starting the survey by performing a visual inspection to assess the condition of the object and identify degraded areas. Then, carry out non-destructive tests to provide a basis for selecting sites for taking cores in areas of questionable quality.
- Lack of access to archival documentation of the investigated building. This makes it difficult to identify the original structural assumptions and solutions. In the absence of such documentation, it is recommended to make an initial assumption that all main structural elements were made of the same class of concrete.
- Uncertainty of results obtained using non-destructive methods. The results obtained using these methods are influenced by many factors, including moisture content, temperature, carbonisation processes, reinforcement, cracking and voids. In order to minimise the risk of obtaining an incorrect result, it is recommended to carry out comparative tests with two non-destructive methods. The results need to be confirmed by data obtained from destructive testing. These data should form the basis for finding empirical relationships between the destructive method and non-destructive methods: ultrasonic and sclerometric. When estimating the strength of concrete in subsequent structural elements already without confirming the results with cores, measurement by two non-destructive methods increases confidence in the data obtained. It also makes it possible to locate questionable areas in the event of differing values being obtained at the measuring point under examination, which provides an indication of the need for further destructive testing.
- Lack of possibility for destructive testing. In the absence of core drilling, estimating the compressive strength of concrete based solely on non-destructive methods is subject to a high risk of error. However, based on professional experience, the authors have sometimes found themselves in situations in which they have been forced to suggest only the results obtained using non-destructive methods. At that time, the guiding principle was that it was better to have estimates as a basis for any analysis than to be based only on visual assessment.

The analyses carried out also allowed conclusions to be drawn regarding the application of various test methods for assessing the condition of large-panel structures and the formulation of guidelines to reduce the workload involved in carrying out the tests:

- The assessment of the compressive strength of concrete, when core drilling is not possible, should be based on the use of the sclerometric method and regression curves that take into account the age of the concrete. The ultrasonic method is then proposed to assess the quality of the concrete and locate areas of questionable quality.
- Determination of the cover thickness and spacing of the reinforcement can be successfully carried out using the electromagnetic method. However, the sensitive data are the rebar diameters, as it is necessary to take into account the measuring accuracy of the instrument and type of rebar (ribbed/smooth).
- In most cases, it may not be necessary to assess the tensile strength of the reinforcing steel. However, if it is required to assess the strength parameters of the steel, it is recommended to identify the area where the rebars run and then to drill a core. This core can be used in two ways: first to determine the strength of the concrete and then, after breaking, to obtain a sample of the reinforcement. The rebar can be visually examined to assess corrosion processes and then be tested in a machine. According to the authors' numerous experiences, the effect of the reinforcement placed transverse to the drill axis on the compressive strength of the concrete can be neglected in most cases. This reduces the need for performing additional excavations.
- A concrete resistivity test can be helpful to assess whether the concrete cover is conducive to corrosion processes of the reinforcing steel. This test is recommended to be carried out in the area of planned excavations or drillings in order to be able to confirm the results.
- The tensile strength of steel connection plates can be successfully determined by correlation with its hardness, using ultrasonic hardness testers. Destructive tests can be reduced to the minimum number necessary to confirm the parameters obtained using non-destructive methods.

Improving the methodology for assessing the condition of large-panel buildings contributes to reducing the labour intensity and, at the same time, the costs associated with carrying out surveys. This is particularly important for property managers who, due to the age of the buildings, will increasingly be obliged to carry out repairs, modernisations, or strengthening of the structures and thus perform condition assessments.

The authors also identified the following research gaps related to non-destructive testing of large-panel structures:

- Lack of equipment to identify degradation of steel joints without performing excavations.
- Lack of research methodologies related to the assessment of the degradation status of facade layer connections in gable walls and beam-walls in modernised buildings.

A potential technique that can contribute to solving these research problems is computed tomography, the use of which will be an area of the authors' future research.

Author Contributions: Conceptualization, M.W.; methodology, M.W.; formal analysis, J.R.K.; investigation, M.W.; resources, M.W. and J.R.K.; writing—original draft preparation, M.W.; writing—review and editing, J.R.K.; visualization, M.W.; supervision, J.R.K.; project administration, J.R.K.; funding acquisition, M.W. All authors have read and agreed to the published version of the manuscript.

Funding: The research was carried out within the scope of work no. WI/WB-IIL/2/2021 and no. WZ/WB-IIL/4/2023 and financed by the resources for science of the Ministry of Education and Science of Poland.

Institutional Review Board Statement: Not applicable.

Informed Consent Statement: Not applicable.

Data Availability Statement: The data presented in this study are available upon request from the corresponding author.

Conflicts of Interest: The authors declare no conflict of interest.

References

1. Folic, R.; Laban, M.; Milanko, V. Reliability and Sustainability Analysis of Large Panel Residential Buildings in Sofia, Skopje and Novi Sad. *Facta Univ.-Ser. Archit. Civ. Eng.* **2011**, *9*, 161–176. [CrossRef]
2. Radziejowska, A.; Sobotka, A. Assessment of Large-Panel Prefabricated Buildings in the Social Aspect of Sustainable Construction | Ocena Budynków z Wielkiej Płyty w Aspekcie Socjalnym Zrównoważonego Budownictwa. *Arch. Civ. Eng.* **2021**, *67*, 93–108.
3. Rák, O.; Borsos, Á.; Iványi, P. Examination of Large-Panel Building Apartments Renovation. *Pollack Period.* **2021**, *16*, 143–149. [CrossRef]
4. Onyszkiewicz, J.; Sadowski, K. Proposals for the Revitalization of Prefabricated Building Facades in Terms of the Principles of Sustainable Development and Social Participation. *J. Build. Eng.* **2022**, *46*, 103713. [CrossRef]
5. Kadela, M.; Cincio, A.; Fedorowicz, J.; Gerylo, R. Attempt at Numerical Representation of Gas Explosion in a Large Panel Building. In Proceedings of the IOP Conference Series: Materials Science and Engineering, Prague, Czech Republic, 17–21 June 2019; Volume 603. [CrossRef]
6. Hryhorovskyi, P.; Osadcha, I.; Jurelionis, A.; Basanskyi, V.; Hryhorovskyi, A. A BIM-Based Method for Structural Stability Assessment and Emergency Repairs of Large-Panel Buildings Damaged by Military Actions and Explosions: Evidence from Ukraine. *Buildings* **2022**, *12*, 1817. [CrossRef]
7. Guri, M.; Brzev, S.; Lluka, D. Performance of Prefabricated Large Panel Reinforced Concrete Buildings in the November 2019 Albania Earthquake. *J. Earthq. Eng.* **2022**, *26*, 5799–5825. [CrossRef]
8. Jędrzejczyk, A.; Byrdy, A.; Firek, K.; Rusek, J. Partial Least Squares Regression Approach in the Analysis of Damage Intensity Changes to Prefabricated RC Buildings during the Long Term of Mining Activity. *Appl. Sci.* **2022**, *12*, 467. [CrossRef]
9. Ghazi Wakili, K.; Dworatzyk, C.; Sanner, M.; Sengespeick, A.; Paronen, M.; Stahl, T. Energy Efficient Retrofit of a Prefabricated Concrete Panel Building (Plattenbau) in Berlin by Applying an Aerogel Based Rendering to Its Façades. *Energy Build.* **2018**, *165*, 293–300. [CrossRef]
10. Ilomets, S.; Kalamees, T. Evaluation of the Criticality of Thermal Bridges. *J. Build. Pathol. Rehabil.* **2016**, *1*, 11. [CrossRef]
11. Dzierżewicz, Z.; Starosolski, W. *Large Panel Systems in Poland in Years 1970–1985*; Oficyna A Wolters Kluwer Business: Warsaw, Poland, 2010. (In Polish)
12. Harish Kumar, K.; Veerendra Babu, N.; Lingeshwaran, N. A Study on Repair of Concrete Structure Using Non Destructive Tests. *Mater. Today Proc.* **2021**, *47*, 5439–5446. [CrossRef]
13. Tofiluk, A.; Knyziak, P.; Krentowski, J. Revitalization of Twentieth-Century Prefabricated Housing Estates as Interdisciplinary Issue. In Proceedings of the IOP Conference Series: Materials Science and Engineering, Prague, Czech Republic, 18–22 June 2018; Volume 471. [CrossRef]
14. Ligęza, W. Renovation of Large-Panel Buildings in Context of Urban Renewal. *Civ. Environ. Eng. Rep.* **2015**, *17*, 83–95. [CrossRef]
15. Krentowski, J.R.; Knyziak, P.; Mackiewicz, M. Durability of Interlayer Connections in External Walls in Precast Residential Buildings. *Eng. Fail. Anal.* **2021**, *121*, 105059. [CrossRef]
16. Kałuża, M.; Ajdukiewicz, A. Comparison of Behaviour of Concrete Beams with Passive and Active Strengthening by Means of CFRP Strips. *Archit. Civ. Eng. Environ.* **2008**, *1*, 51–64.
17. Kotynia, R.; Oller, E.; Marí, A.; Kaszubska, M. Efficiency of Shear Strengthening of RC Beams with Externally Bonded FRP Materials—State-of-the-Art in the Experimental Tests. *Compos. Struct.* **2021**, *267*, 113891. [CrossRef]
18. Cai, G.; Zhao, J. Application of Sulphoaluminate Cement to Repair Deteriorated Concrete Members in Chloride Ion Rich Environment-A Basic Experimental Investigation of Durability Properties. *KSCE J. Civ. Eng.* **2016**, *20*, 2832–2841. [CrossRef]
19. Czarnecki, S. Ultrasonic Evaluation of the Pull-Off Adhesion between Added Repair Layer and a Concrete Substrate. *IOP Conf. Ser. Mater. Sci. Eng.* **2017**, *245*, 032037. [CrossRef]
20. Varzaneh, A.S.; Naderi, M. Determination of Shrinkage, Tensile and Compressive Strength of Repair Mortars and Their Adhesion on the Concrete Substrate Using "Twist-off" and "Pull-off" Methods. *Iran. J. Sci. Technol. Trans. Civ. Eng.* **2021**, *45*, 2377–2395. [CrossRef]
21. Liu, Y.; Wang, M.; Tian, W.; Qi, B.; Lei, Z.; Wang, W. Ohmic Heating Curing of Carbon Fiber/Carbon Nanofiber Synergistically Strengthening Cement-Based Composites as Repair/Reinforcement Materials Used in Ultra-Low Temperature Environment. *Compos. Part A Appl. Sci. Manuf.* **2019**, *125*, 105570. [CrossRef]
22. Brzozowski, P.; Horszczaruk, E. Influence of Surface Preparation on Adhesion of Underwater Repair Concretes under Hydrostatic Pressure. *Constr. Build. Mater.* **2021**, *310*, 125153. [CrossRef]
23. Gupta, S.; Pang, S.D.; Kua, H.W. Autonomous Healing in Concrete by Bio-Based Healing Agents—A Review. *Constr. Build. Mater.* **2017**, *146*, 419–428. [CrossRef]
24. Jiang, L.; Han, Q.; Wang, W.; Zhang, Y.; Lu, W.; Li, Z. A Sugar-Coated Microbial Agent for Self-Healing Cracks in Concrete. *J. Build. Eng.* **2023**, *66*, 105890. [CrossRef]

25. Forcellini, D.; Kalfas, K.N. Inter-Story Seismic Isolation for High-Rise Buildings. *Eng. Struct.* **2023**, *275*, 115175. [CrossRef]
26. Amit, R.D.; Gajjar, R. Structural Control System for Mid-Rise Building. *Int. J. Adv. Eng. Technol.* **2012**, *3*, 30–33.
27. Knyziak, P. The Impact of Construction Quality on the Safety of Prefabricated Multi-Family Dwellings. *Eng. Fail. Anal.* **2019**, *100*, 37–48. [CrossRef]
28. Knyziak, P.; Bieranowski, P.; Krentowski, J.R. Impact of Corrosion Processes in the Basement Level on the Durability of the Construction of Large-Panel Buildings. In Proceedings of the MATEC Web of Conferences, Warsaw, Poland, 21–25 August 2017; Volume 117. [CrossRef]
29. Mackiewicz, M.; Krentowski, J.R.; Knyziak, P.; Wardach, M. Consequences of Excessive Deformation of Structural Elements in Precast Buildings. *Eng. Fail. Anal.* **2022**, *137*, 106261. [CrossRef]
30. Baszeń, M.; Miedziałowski, C. An Environmental Impact on the Condition of an Unfinished Building in the OWT Technology. In Proceedings of the E3S Web of Conferences, Polańczyk, Poland, 19–23 June 2018; Volume 49. [CrossRef]
31. Knyziak, P. The Quality and Reliability in the Structural Design, Production, Execution and Maintenance of the Precast Residential Buildings in Poland in the Past and Now. *Key Eng. Mater.* **2016**, *691*, 420–431. [CrossRef]
32. Szulc, J.; Piekarczuk, A. Diagnostics and Technical Condition Assessment of Large-Panel Residential Buildings in Poland. *J. Build. Eng.* **2022**, *50*, 104144. [CrossRef]
33. Górski, W. Problems of Early Large Panel Structures in Poland. *Acta Sci. Pol.–Archit. Bud.* **2001**, *20*, 45–53. [CrossRef]
34. Kalamees, T.; Õiger, K.; Kõiv, T.; Liias, R.; Kallavus, U.; Mikli, L.; Lehtla, A.; Kodi, G.; Arumägi, E. Technical Condition of Prefabricated Concrete Large Panel Apartment Buildings in Estonia. In Proceedings of the 12DBMC–International Conference on Durability of Building Materials and Components, Porto, Portugal, 12–15 April 2011; pp. 1–9.
35. Wardach, M. Assessment of the Degradation State of Joints in Large-Panel Buildings. *Eng. Fail. Anal.* **2023**, *145*, 107020. [CrossRef]
36. Wardach, M. Assessing the Technical Condition of Unfinished or Temporarily Out-of-Service Large-Panel Buildings. *Mater. Bud.* **2022**, *1*, 108–111. [CrossRef]
37. Wardach, M.; Krentowski, J.R.; Knyziak, P. Degradation Analyses of Systemic Large-Panel Buildings Using Comparative Testing during Demolition. *Materials* **2022**, *15*, 3770. [CrossRef] [PubMed]
38. Wardach, M.; Krentowski, J.R.; Mackiewicz, M. Evaluation of Precast Beam Deflections Resulting in Cracks in Curtain Walls. *Eng. Fail. Anal.* **2022**, *140*, 106568. [CrossRef]
39. Wardach, M.; Pawłowicz, J.A.; Kosior-Kazberuk, M.; Krentowski, J.R. The Diagnostics of the Condition and Management of Large-Panel Buildings Using Point Clouds and Building Information Modelling (BIM). *Buildings* **2023**, *13*, 2089. [CrossRef]
40. Abdallah, W.; Sbartaï, Z.-M.; Saliba, J.; Elachachi, S.M.; Hage Chehade, F.; Sadek, M. Assessment of the Reliability of Concrete Evaluation by Multi-Physical Inversion of NDT Measurements—A Probabilistic Approach. *Constr. Build. Mater.* **2021**, *300*, 124371. [CrossRef]
41. Kouddane, B.; Sbartaï, Z.M.; Alwash, M.; Ali-Benyahia, K.; Elachachi, S.M.; Lamdouar, N.; Kenai, S. Assessment of Concrete Strength Using the Combination of NDT—Review and Performance Analysis. *Appl. Sci.* **2022**, *12*, 12190. [CrossRef]
42. Pallarés, F.J.; Betti, M.; Bartoli, G.; Pallarés, L. Structural Health Monitoring (SHM) and Nondestructive Testing (NDT) of Slender Masonry Structures: A Practical Review. *Constr. Build. Mater.* **2021**, *297*, 123768. [CrossRef]
43. Yuva, Y. Low-Strength Concrete Properties in Existing Structures Using NDT and Core Test Results. *J. Build. Eng.* **2023**, *76*, 107281. [CrossRef]
44. Dey, A.; Miyani, G.; Debroy, S.; Sil, A. In-Situ NDT Investigation to Estimate Degraded Quality of Concrete on Existing Structure Considering Time-Variant Uncertainties. *J. Build. Eng.* **2020**, *27*, 101001. [CrossRef]
45. Kazemi, M.; Madandoust, R.; de Brito, J. Compressive Strength Assessment of Recycled Aggregate Concrete Using Schmidt Rebound Hammer and Core Testing. *Constr. Build. Mater.* **2019**, *224*, 630–638. [CrossRef]
46. Stawiski, B.; Kania, T. Tests of Concrete Strength across the Thickness of Industrial Floor Using the Ultrasonic Method with Exponential Spot Heads. *Materials* **2020**, *13*, 2118. [CrossRef]
47. Bacharz, K.; Raczkiewicz, W.; Bacharz, M.; Grzmil, W. Manufacturing Errors of Concrete Cover as a Reason of Reinforcement Corrosion in a Precast Element—Case Study. *Coatings* **2019**, *9*, 702. [CrossRef]
48. Park, J.Y.; Yoon, Y.G.; Oh, T.K. Prediction of Concrete Strength with P-, S-, R-Wave Velocities by Support Vector Machine (SVM) and Artificial Neural Network (ANN). *Appl. Sci.* **2019**, *9*, 4053. [CrossRef]
49. Kovler, K.; Wang, F.; Muravin, B. Testing of Concrete by Rebound Method: Leeb versus Schmidt Hammers. *Mater. Struct.* **2018**, *51*, 138. [CrossRef]
50. Maj, M.; Ubysz, A.; Hammadeh, H.; Askifi, F. Non-Destructive Testing of Technical Conditions of RC Industrial Tall Chimneys Subjected to High Temperature. *Materials* **2019**, *12*, 2027. [CrossRef] [PubMed]
51. Golewski, G.L. Evaluation of Fracture Processes under Shear with the Use of DIC Technique in Fly Ash Concrete and Accurate Measurement of Crack Path Lengths with the Use of a New Crack Tip Tracking Method. *Measurement* **2021**, *181*, 109632. [CrossRef]
52. Golewski, G.L. Measurement of Fracture Mechanics Parameters of Concrete Containing Fly Ash Thanks to Use of Digital Image Correlation (DIC) Method. *Measurement* **2019**, *135*, 96–105. [CrossRef]
53. Meyer, D.M.; Combrinck, R. Utilising MicroCT Scanning Technology as a Method for Testing and Analysing Plastic Shrinkage Cracks in Concrete. *Constr. Build. Mater.* **2022**, *317*, 125895. [CrossRef]
54. *EN 13791:2019-12*; Assessment of In-Situ Compressive Strength in Structures and Precast Concrete Components. PKN: Warsaw, Poland, 2019.

55. *EN 13791:2008*; Assessment of In-Situ Compressive Strength in Structures and Precast Concrete Components. PKN: Warsaw, Poland, 2008.
56. Runkiewicz, L.; Sieczkowski, J. *Ocena Wytrzymałości Betonu w Konstrukcjach Na Podstawie Badań Sklerometrycznych*; Instytut Techniki Budowlanej: Warsaw, Poland, 2022. (In Polish)
57. Runkiewicz, L.; Brunarski, L. *Instrukcja Stosowania Młotków Schmidta Do Nieniszczącej Kontroli Jakości Betonu w Konstrukcji. Instrukcja Nr 210*; Instytut Techniki Budowlanej: Warsaw, Poland, 1977. (In Polsih)
58. Brunarski, L.; Runkiewicz, L. *Instrukcja Stosowania Metody Ultradźwiękowej Do Nieniszczącej Kontroli Jakości Betonu w Konstrukcji*; Instytut Techniki Budowlanej: Warsaw, Poland, 1977. (In Polish)
59. Proceq, S.A. *Profometer. Operating Instructions*; Proceq SA: Schwerzenbach, Switzerland, 2014.
60. Dermawan, A.S.; Dewi, S.M.; Wisnumurti; Wibowo, A. Performance Evaluation and Crack Repair in Building Infrastructure. *IOP Conf. Ser. Earth Env. Sci.* **2019**, *328*, 012007. [CrossRef]
61. *PN-H-93215:1969*; Walcówka Pręty Stalowe Do Zbrojenia Betonu. PKN: Warsaw, Poland, 1969. (In Polish)
62. *PN-H-93243:1970*; Walcówka i Pręty Ze Stali Klasy A-O, A-I i A-II Do Zbrojenia Betonu. PKN: Warsaw, Poland, 1970. (In Polish)
63. *PN-B-03260:1956*; Konstrukcje Żelbetowe—Obliczenia Statyczne i Projektowanie. PKN: Warsaw, Poland, 1956. (In Polish)
64. Hornbostel, K.; Larsen, C.K.; Geiker, M.R. Relationship between Concrete Resistivity and Corrosion Rate—A Literature Review. *Cem. Concr. Compos.* **2013**, *39*, 60–72. [CrossRef]
65. *PN-88-H-84020*; Stal Niestopowa Konstrukcyjna Ogólnego Przeznaczenia–Gatunki. PKN: Warsaw, Poland, 1988. (In Polish)

materials

MDPI

Article

Application of Composite Bars in Wooden, Full-Scale, Innovative Engineering Products—Experimental and Numerical Study

Agnieszka Wdowiak-Postulak [1,*], Grzegorz Świt [1] and Ilona Dziedzic-Jagocka [2]

[1] Department of Strength of Materials and Building Structures, Faculty of Civil Engineering and Architecture, Kielce University of Technology, al. Tysiąclecia Państwa Polskiego 7, 25-314 Kielce, Poland; gswit@tu.kielce.pl
[2] Department of Quality Management and Intellectual Property, Faculty of Management and Computer Modeling, Kielce University of Technology, al. Tysiąclecia Państwa Polskiego 7, 25-314 Kielce, Poland; i.dziedzic@tu.kielce.pl
* Correspondence: awdowiak@tu.kielce.pl; Tel.: +48-41-34-24-398

Abstract: The commercialization of modular timber products as cost-effective and lightweight components has resulted in innovative engineering products, e.g., glued laminated timber, laminated veneer lumber, I-beams, cross-laminated timber and solid timber joined with wedge joints. With the passage of time, timber structures can deteriorate, or new structural elements are required to increase the stiffness or load-bearing capacity in newly built structures, e.g., lintels over large-scale glazing or garages, or to reduce cross-sectional dimensions or save costly timber material while still achieving low weight. It is in such cases that repair or correct reinforcement is required. In this experimental and numerical study, the static performance of flexural timber beams reinforced with prestressed basalt BFRP, glass GFRP and hybrid glass–basalt fiber bars is shown. The experimental tests resulted in an increase in the load-carrying capacity of BFRP (44%), GFRP (33%) and hybrid bars (43%) and an increase in the stiffness of BFRP (28%), GFRP (24%) and hybrid bars (25%). In addition to this, glued laminated timber beams reinforced with prestressed basalt rods subjected to biological degradation, 7 years of weathering and prolonged exposure to various environmental conditions were examined, and an increase in the load-bearing capacity of 27% and an increase in stiffness of 28% were obtained. In addition, full-size laminated timber beams reinforced with prestressed basalt bars were investigated in the field as an exploratory test under fire conditions at elevated temperatures, and the effect of the physical–mechanical properties during the fire was examined via an analysis of these properties after the fire. In addition, a satisfactory correlation of the numerical simulations with the experimental studies was obtained. The differences were between 1.1% and 5.5%. The concordance was due to the fact that, in this study, the Young, Poisson and shear moduli were determined for all quality classes of sawn timber. Only a significant difference resulted in the numerical analysis for the beams exposed to fire under fire conditions. The experimental, theoretical and numerical analyses in this research were exploratory and will be expanded as directions for future research.

Keywords: reinforcement; timber structures; bars; BFRP; GFRP; hybrid bars; flexural behavior; fire; environmental conditions; biological degradation; increased temperature; prestressing; FEM

Citation: Wdowiak-Postulak, A.; Świt, G.; Dziedzic-Jagocka, I. Application of Composite Bars in Wooden, Full-Scale, Innovative Engineering Products—Experimental and Numerical Study. *Materials* **2024**, *17*, 730. https://doi.org/10.3390/ma17030730

Academic Editor: Giovanni Garcea

Received: 28 December 2023
Revised: 26 January 2024
Accepted: 29 January 2024
Published: 3 February 2024

1. Introduction

The use of wood is currently increasing significantly, and it is a popular building material due to the fact that it has a wide range of lightweight construction applications. It is also characterized by its ease of production, its very good physical and mechanical properties and its low density. Environmental protection and low energy requirements are also among its advantages. This is why wood is increasingly being used as a construction material. Taking into account the orthotropic nature of wood, it is a complex material.

The presence of knots, cracks or grain inclination, especially in the tension zone, has a significant influence on the behavior of a wooden member. Also, the properties of wood vary within the same species, and a description of many parameters is necessary to fully describe models of the behavior of wood.

It should be noted that fiber-reinforced polymer (FRP) materials are synthetic composites made from either high-strength fibers based on chemical synthesis (typically glass, carbon, aramid and basalt) or natural fiber-reinforced polymer (NFRP) composites, as well as hybrid fibers (a blend of synthetic and natural fibers) embedded in an adhesive matrix, e.g., epoxy, polyester and polyolefin.

The reinforcement elements can be available in various shapes and sizes. They are characterized by a very high strength and rigidity. It is worth considering that the repair of damaged timber is usually more cost-effective or less time-consuming, and it is FRP composite materials that have a high modulus of elasticity, strength or corrosion resistance [1–4].

It should be noted that composite materials have consistently played a significant role in construction, from the early civilizations to the present day. Above all, the main task has been to increase the strength, corrosion resistance and durability and to obtain a better strength-to-weight ratio [5–9]. Therefore, important and significant improvements in mechanical or thermal properties can be achieved by integrating reinforcements characterized by a high modulus and tensile strength into polymers [9,10]. FRPs are composed primarily of glass (GFRP), basalt (BFRP), carbon (CFRP) and aramid fibers incorporated into polymer matrix resins such as epoxy, polyester and vinyl ester resins. Typically, GFRP is mainly used because of its ability to achieve effective tensile strength compared to steel and its better cost-effectiveness than CFRP and BFRP. Unfortunately, a limitation of GFRP is its elastic modulus, which is significantly lower than that of structural steel, leading to an increased deformation of GFRP-reinforced components [11,12]. Much research has also been carried out using CFRP, BFRP, GFRP or steel fibers in various forms, including in tapes, mats and rods or in various other forms and characteristics of FRP, such as in construction, structures, reinforcing solid wood beams, wedge-jointed solid beams, laminated veneer lumber (LVL), cross-laminated timber (CLT) and glued laminated timber (GLT) beams—see [13–20].

Modern solutions also include engineered products such as glulam, formed from layers of graded structural lumber [13–20]. The advantages of these products include the use of shorter pieces of timber to form full-length laths using structural adhesives. They can then produce structural elements with different shapes and sizes with greater strength than their individual layers. Unfortunately, over time, timber structures deteriorate due to factors such as increased service loads, aging or biological degradation [21]. In this case, the use of repair or reinforcement instead of replacement is more beneficial. Traditional reinforcement techniques include the use of steel plates, aluminum plates or timber battens, but these may incur additional dead loads or reinforcement costs. In addition, steel components corrode under thermal stress. For this reason, FRP composites are an excellent solution for reinforcing timber structures, primarily due to their lightweight properties, while they can also achieve an increased stiffness or load-bearing capacity. Glued laminated timber beams are therefore excellent structural elements that are used in sports halls, swimming pools and public buildings. In modular timber frame construction, I-beams with laminated veneer lumber flanges are ideal because of their lightness, low cost and considerable load-bearing capacity or stiffness or due to the possibility of routing installation cables. On the other hand, beams made entirely of glued veneer, due to their higher cost, are only used as lintels for large areas of glazed windows, in openings above garages or as columns or foundations. But you cannot see them because they are placed inside, whereas glued laminated beams are visible. The GIROD (European glued-in rods) project involved several European countries with the aim of developing an acceptable standard, including fatigue testing, for connections based on glued-in rods in the context of Eurocode 5 [22]. The use of such connections has many advantages in obtaining high stiffness under axial loads, as well as excellent fire resistance, as a wood substance protects the bar and provides a good aesthetic

appearance. Nowadays, glued-in rods are usually used, and several configurations of these connections can be found. They can also be used to repair rotten beam ends in traditional buildings [19]. In a research paper by Bengtsson and Johansson [23], structural applications of steel glued-in bars can be found. On the other hand, studies of laminated veneer beams reinforced with FRP and steel under different forms were shown in [24–28]. For example, Harvey and Ansell [24] from the University of Bath found that glass-fiber-reinforced plastic (GFRP) bars could be used as an alternative to steel bars. This is because GFRP pultruded bars have better compatibility with resin and wood, higher resistance to wet or acidic environments and better performance due to better bonding and weight reduction. Based on research, it was determined that the most suitable resin for bonding rods in laminated veneered wood (LVL) was an epoxy resin applied with a minimum glue joint thickness of 2 mm. It was also recommended that the surfaces of GFRP pultruded rods should first be treated by sandblasting or solvent wiping [24,25]. In addition, it was recommended that the minimum thickness of the adhesive bond should be 2 mm, to obtain the optimum static tensile strength of GFRP pultrusion in LVL. However, above this thickness, the strength does not change much. Broughton and Hutchinson [26] found that thicker bond lines between LVL steel bars increased the strength up to a thickness of 6 mm. In [27], the bond quality and joint performance between laminated veneer lumber (LVL) and metal panels were determined. Excellent results were obtained for specimens bonded to galvanized sheets and ChT and R plates. It should be noted that timber structures subjected to cyclic loading are now more commonly used in timber bridges, high-rise buildings or wind turbine towers. Unfortunately, however, no normative regulations are yet available for the fatigue of glued rods, resulting in incomplete or completely missing experimental data. Therefore, the author is currently researching glued laminated timber beams, solid beams, solid beams connected with wedge joints, cross-laminated timber beams, I-beams also with laminated veneer lumber, laminated veneer lumber beams reinforced with FRP materials, and steel in various forms and sizes and with different characteristics and structures, including in the form of rods made of various artificial fibers and natural fibers under cyclic load. In a study [28], it was found that low-cycle fatigue (LCF) resulted in wood and glue fracture, while rod failure was the limiting factor in high-cycle fatigue (HCF). Gentile et al. [29] investigated reinforced wooden beams with GFRP bars using the NSM technique. In their study, they obtained an increase in the flexural strength of the beam in the range of 18–46% with a percentage of reinforcement equal to 0.27–0.82% compared to unreinforced bars [29]. Raftery and Kelly [30] studied laminated timber beams reinforced with basalt FRP bars in the tension zone. Based on the results, the average increase in load-carrying capacity was 23%, and stiffness increased in the range of 8.4–10.3% [31]. Yang et al. [31] studied the reinforcement of glulam beams with steel, FRP bars and plates. They evaluated significant flexural strength and structural stiffness improvements, averaging up to 56.3 and 27.5%, respectively. In an experimental study [29], the flexural behavior of creosote-impregnated Douglas fir beams reinforced with glass-fiber-reinforced polymer (GFRP) rods was determined. Twenty-two half-scale and four full-scale GFRP-reinforced timber beams with reinforcement percentages ranging from 0.27 to 0.82% were tested for failure. The use of this reinforcement changed the mode of failure from brittle tensile failure to compressive failure, and the bending strength increased by 18 to 46%, eliminating the effect of local wood defects and increasing the bending strength of the elements. In a study [32], the impact of bonding different types of glass fiber reinforcement—in particular in the form of glass fiber fabric laminates—on the bending behavior of different compositions of timber elements—in particular sawn timber and glulam beams, consisting of spruce, pine and fir (SPF) No. 2, with dimensions of 140 mm × 140 mm × 2025 mm and 110 mm × 140 mm × 2025 mm, respectively—was determined. It was found that FRP fabric laminates increased the strength of lumber and glulam beams by up to 52% and 36%. Also, timber defects using FRP resulted in a change in the failure modes of unreinforced beams. In post-loading, the stresses were then transferred to the FRP bars. In subsequent research [33], it was determined whether using composites in the form of carbon fabric reinforcement or laminate

strips for wooden beams would increase the load-bearing capacity of beams in bridges. Ten solid Douglas fir beams were taken from a timber stringer bridge in Yuma, Arizona, which was replaced in 1999. After testing, it was found that using carbon fabric on the timber beams provided a significant increase in flexural and shear strength and a nominal increase in beam stiffness. Another study [34] focused on four-point bending, where five beams were unreinforced and three were reinforced with two or four layers of straight and U-shaped FRP stressing threats. An additional load was created with a different maximum displacement with respect to the unreinforced beams. Results for simple pretensioned beams and reinforced U-shaped glulam beams showed increased strength and stiffness compared to unreinforced members [35]. However, the combination of span-to-depth ratio and insufficient development length resulted in shear failure. Inferior failure results were obtained by using transversely applied FRP sheets. Entirely confined beams were also the subject of this study in order to better understand the effect of the amount of reinforcement and to make a comparison with unreinforced beams. It was shown that the material model used to generate resistance curves achieved a model-to-experimental strength ratio of 0.92. In another study [36], the fiber reinforcement (FRP) of glulam beams subjected to simulated explosion loads was experimentally investigated. The strength and maximum deflection increases were in the ranges of 1.35–1.66 and 1.3–1.62, respectively. Likewise, the addition of FRP contributed to an increase in the tensile strain at break by 1.17 compared to the unreinforced beams.

It should also be noted that in European countries, such as Poland, due to the regulations in force here regarding reaction to fire and the spread of fire in multi-family buildings and public buildings such as offices, wood has been eliminated in structural form. But as mentioned above, in countries that pay special attention to the so-called "green" construction, in recent times, we have noticed an increasing use of wood in projects. However, the European leaders in this respect are Germany and the Scandinavian countries; e.g., in Norway, in 2015, a 14-story apartment building with a wooden structure was built, and in 2019, the construction of the highest (84.5 m) Mjøstårnet hotel on Lake Mjøsa was completed. In Canada, an 18-story wooden structure building was built on the campus of the University of British Columbia (excluding the cores of staircases, elevator shafts and the lowest floor, mainly made of reinforced concrete) [37]. In Polish regulations related to fire safety, specified in regulations [37–39], the key terms are as follows: fire resistance (properly made wooden elements usually achieve), fire spread (requires special treatment or protection from wooden elements), flammability (a feature related to the reaction to fire, which wood, even fire-retardant, is not able to achieve). When it comes to the scope of fire resistance, wooden elements are among the most complex and difficult to verify. Certain types of structures, such as beams and columns, can be calculated using the provisions of the standard [37,40]. Surface elements, e.g., walls and ceilings, are more difficult because the number of available solutions, e.g., cladding, is so large. Their impact is so different that work is still ongoing to select the appropriate calculation method beyond that described in ref. [40]. However, solutions where wood is used as a structure for other elements, e.g., partition walls, skylights, doors, and windows, which have a significant impact on fire resistance, pose even greater problems [37]. Then, it is very important to perform full-scale research. Therefore, as already written in published works [16,41–43], the next stage of these experimental, theoretical and numerical studies will be the study of the fire resistance of small-sized wooden elements (solid wood, laminated timber, cross-laminated timber, glued laminated timber beams, solid timber joined with glued joints, I-beams, laminated veneer lumber) reinforced with steel and FRP materials in various forms and structures, including different artificial fibers, natural fibers, etc. (FRP composite materials will be the external reinforcement; additionally, they will also constitute the internal reinforcement of the cross-section, so the same chopped fibers will be used and placed inside the cross-section as well as outside the cross-section); fire resistance of full-size wooden elements, including in the form of beams (solid wood, laminated wood, cross-laminated timber, solid wood joined with glued joints, glued laminated timber beams, I-beams, laminated veneer

lumber) reinforced with steel and FRP materials in various forms and structures, including different artificial fibers and natural fibers (FRP composite materials will be the external reinforcement; additionally, they will also constitute the internal reinforcement of the cross-section, so the same chopped fibers will be used and placed inside the cross-section as well as outside the cross-section); and the impact of elevated temperatures on physical and mechanical properties—the behavior in the event of fire, as well as the physical and mechanical properties after fire of small- and full-size wooden elements will be examined, including in the form of beams (solid wood, laminated wood, glued laminated timber beams, cross-laminated timber, solid wood joined with glued joints, I-beams, laminated veneer lumber) reinforced with steel and FRP materials in various forms and structures, including different artificial fibers and natural fibers (FRP composite materials will be the external reinforcement; additionally, they will also constitute the internal reinforcement of the cross-section, so the same chopped fibers will be used and placed inside the cross-section as well as outside the cross-section). All these features will also be considered depending on the direction of fiber arrangement, structure of the wood element and reinforcement, as well as reinforced at individual technological stages of the production of wooden structural elements (solid wood, laminated wood, glued laminated timber beams, cross-laminated timber, solid wood joined with glued joints, I-beams, laminated veneer lumber) among others for fire protection and protection against long-term exposure to various environmental conditions. Research on the impact of biological degradation and 5-year exposure to atmospheric influences on reinforced wooden beams using composite and steel bars has been conducted for a long time and has long been demonstrated in published works [42,43]. In the works [42,43], apart from wooden beams, composite and steel bars were also subjected to long-term atmospheric influences in various weather and environmental conditions. In this study, the economic aspect was considered, and cheaper FRP materials such as basalt and glass were used. After innovative scientific, practical, economical and environmentally friendly was conducted research, satisfactory results were obtained. The full range of results of the used wooden beams subjected to 5 years of weathering and biological degradation as well as long-term operation in various environmental conditions and FRP materials subjected to long-term operation in different environmental conditions, their operation, and analysis are presented in the doctoral thesis [43].

These experimental, theoretical and numerical studies will be continued and will also be extended in the field of reinforced wooden beams for long-term operation in various environmental conditions of wood and reinforcement and their impact on the final result of combining reinforced structural beams (made of solid wood, glued laminated wood, glued laminated timber beams, cross-laminated timber, solid wood joined with glued joints, I-beams, laminated veneer lumber) as well as FRP reinforcements in various forms and structures as composite materials and chopped fibers, including different artificial fibers and natural fibers and steel (in various forms and structures and chopped fibers). These experimental, theoretical and numerical studies are also carried out under monotonic, static, dynamic, cyclic and repeatedly variable loads; long-term loads; environmentally variable loads; and exceptional loads on reinforced structural beams (made of solid wood, glued laminated wood, glued laminated timber beams, cross-laminated timber, solid wood joined with glued joints, I-beams, laminated veneer lumber) and FRP reinforcements in various forms and structures as composite materials and chopped fibers, including different artificial fibers and natural fibers and steel in various forms.

This paper investigates the behavior of reinforced bonded beams in the tension and compression zone under static loading with glued-in BFRP and GFRP bars. An identical degree of reinforcement for the bars used was assumed specifically for comparison purposes. Glass fibers have the advantage of being very well wettable by polymers, so the resin adheres easily to them. At the same time, the number of air voids at the interface is reduced to a minimum. This allows for high adhesion between the fibers and the surrounding polymer and an adhesive force between the two, ensuring a better bond. Glass fibers are characterized by their high tensile strength, lack of electrical conductivity and low thermal

expansion. Their disadvantages include their tensile strength and modulus of elasticity decreasing at elevated temperatures. Glass fibers also creep under long-term loading. Their strength decreases over time, and they have less corrosion resistance than other fiber types. Basalt fibers are single-component materials obtained by melting solidified volcanic lava. It is important to consider that they are relatively inexpensive and have better physical and mechanical properties than glass fibers. Therefore, in addition to innovative and economical as well as practical and scientific research on glulam beams reinforced with prestressed composite bars as very cheap and easy-to-use materials in existing structures, the durability of wooden elements such as these bars was also shown. Moreover, due to the existing fire problem in wooden structures, especially multi-story ones, preliminary exploratory tests of reinforced beams in fire and post-fire conditions were presented. This is a very important study of the current legal and standard regulations. As mentioned above, the reinforcement application shown is practical, fast, easy and effective. All you need to do is make the grooves, prestress them, especially in the anchorage area, and then fill them with epoxy glue. Liquid epoxy glue is recommended to increase the adhesion of the ribbed bar and the wood, as it can penetrate into the wood's pores.

Therefore, along with E-glass fibers, basalt fibers are the most widely used raw materials for composite bars. The main advantages of basalt fibers include fire resistance, the ability to damp internal vibrations, high sound insulation, high fatigue strength, a fiber service temperature of 982 °C, a fiber melting point of 1450 °C, high hardness and resistance to corrosion (including acid and alkaline corrosion).

Fibers also form the basis of the entire composite. Their characteristic properties include high strength and stiffness as well as low weight and size. This is due to the highly organized internal structure and the low probability of structural defects. The fibers used to construct FRP rods are glass, carbon, aramid and basalt fibers. Therefore, FRP rods with the appropriate type of fibers are used as reinforcement depending on the structural requirements (e.g., high strength, low deflection limit) or environmental requirements (e.g., chloride corrosion, high fire protection requirements). Fibers also differ in many properties, dependent on their production process or the types of particles they are made of. Aramid fibers are the lightest, carbon fibers are the most durable, glass fibers are the cheapest and basalt fibers are the most resistant to high temperatures. Also, all fibers are characterized by a typically linear stress–strain relationship. The modulus of elasticity depends not only on the diameter of a rod of one type (scale effect), the type of fibers used and the type of resin used, but also on the number and arrangement of fibers in the core, the physical and chemical match between the component materials of the rod and the production process and quality control carried out during production of composite bars. It should be noted that fibers and resin are quite resistant to creep in composite bars. For example, at elevated temperatures, reaching approximately 40% of the melting temperature of the polymer resin, thermosetting resins exhibit significant creep deformations under constant load. A very dangerous phenomenon is the sudden rupture of the composite reinforcement under the influence of creep deformations. This is related to the rod type; the direction, number and arrangement of fibers in the core; the fiber strength; and environmental conditions. However, the resin has much worse properties than the fibers. Conditions unfavorable for creep resistance include high temperature, exposure to ultraviolet rays, high alkalinity and cycles of moisture and drying, as well as freezing and melting. It was also found that rapid rupture will not occur when long-term stresses are limited to 60% of the early strength of FRP rod-reinforced elements. It should be noted that the phenomenon of rupture due to creep has not yet been fully investigated. There are no relevant conclusions yet regarding the behavior of structures reinforced with FRP bars for less than 100 h. Due to the insufficient understanding of the behavior of composite bars under long-term loading, it is often the high safety factors for creep that determine the size and amount of reinforcement needed (not the ultimate limit state). Therefore, further experimental, theoretical and numerical studies in this area will be continued, including testing of reinforced wooden beams, e.g., with composite and steel bars, under

long-term loads, including the creep effect—the phenomenon of rupture. However, fatigue in composite materials is very complex because various fatigue effects may appear in the cross-section of the rod, such as resin cracks, fiber breaks, crack merging and component delamination. It should be noted that composite bars have relatively high fatigue strength. Moreover, the fibers themselves have virtually no fatigue resistance, but due to the good wettability of the polymers, the fiber–resin connection is strong enough to cope with load change cycles very well. However, the fatigue strength of composite bars is determined by the type of fibers and resin used, whether they are matched to each other, the adhesion between them, the number of fibers in the cross-section and environmental factors occurring during fatigue. It should be noted that the fatigue strength decreases with a decrease in the coefficient comparing the minimum stress with the maximum stress. Important issues are the limitation of cyclical displacements of the rod by the surrounding concrete or wood and the adhesion of the rod to concrete or wood. It should be noted that any embossments, recesses or other types of surface deformations improve adhesion but, at the same time, become places of stress concentration during fatigue loads. Also, fatigue is not yet fully understood because it depends on many factors in composite bars. It should be noted that the current design is based on components that rely on the production process, the environmental conditions in which the element will operate and the type of fatigue load to which it will be subjected. Therefore, experimental, theoretical and numerical research on wooden beams (made of solid wood, glued laminated wood, glued laminated timber beams, cross-laminated timber, solid wood joined with glued joints, I-beams, laminated veneer lumber) reinforced with FRP and steel and cyclical loads also continues. The issue of fatigue is also not fully understood yet because composite rods depend on many factors. Now, it is designed on components that rely on the production process, the environmental conditions in which the analyzed element will work and the type of fatigue load to which it will also be subjected. According to the ACI 440.1R-06 [44] standard, the thermal expansion coefficients of GFRP bars are as follows: linear: 6–10 $\times$ $10^{-6}/^{\circ}$C; lateral: 21–23 $\times$ $10^{-6}/^{\circ}$C. It should be noted that the standard does not provide thermal expansion coefficients for BFRP bars. It is assumed that they have similar properties, and we think expansion coefficients for BFRP rods are as follows: linear: 9–12 $\times$ $10^{-6}/^{\circ}$C; transverse: 21–23 $\times$ $10^{-6}/^{\circ}$C. The fire protection requirements for composite bars must be different in closed spaces, such as buildings, and in open spaces, such as bridges [45]. Likewise, it should be taken into account that using FRP bars to reinforce structures with high resistance to elevated temperatures is conditional on maintaining the structural integrity of the structure and is not advisable. The reason is the softening of the polymer material constituting the matrix and the outer cover of the rod under the influence of high temperature. This reduces the mechanical properties of the resin and increases its susceptibility to moisture absorption. It should be noted that irreversible changes in the internal structure due to particle movement occur after the glass transition temperature is exceeded. The value of the glass transition temperature depends on the type of resin. In composite materials, the fibers have much better resistance to high temperatures than the resin surrounding them. Therefore, they can carry significant longitudinal loads (tension). However, when the cooperation of individual fibers constituting the core of the bar is necessary—e.g., during bending and shearing—the load capacity reduction is much greater. Based on the research, it was found that due to the much greater resistance to high temperatures of fibers compared to resin, beams under long-term loads subjected to tests were destroyed when the composite reinforcement reached a temperature of 250–350 °C. It should be noted that the threshold temperature for fiber operation is approximately 880 °C for glass fibers and approximately 1250 °C for basalt fibers. Long-term exposure to negative temperatures may cause the matrix to harden, cause microcracks and microscratches and reduce the adhesion between the matrix and individual composite fibers. Likewise, freeze–thaw cycles combined with the action of salt may also result in the deterioration of the resin properties in the form of swelling of the polymer on the surface of the rod [45]. Likewise, changes over time in composite rods' strength properties and stiffness depend on the environment in which

they work. Different environmental conditions affect the bars before they are incorporated into the structure, during installation and after installation. It should be taken into account that the aggressiveness of the environment varies depending on the location of the element reinforced with FRP rods. Likewise, the properties of the bars may deteriorate, improve or remain unchanged. The environmental factors that affect the durability of FRP bars include water, heating and cooling cycles, freezing and thawing cycles, UV, higher temperature, acid solutions, alkali solutions, salt solutions and stresses in the rod. Therefore, composite bars' durability is greater than steel's, mainly due to the polymer resin constituting the surface layer of the bar, as it is in direct contact with the external environment. The composite rod must not degrade, and its three components must be sufficiently durable and interact appropriately with each other; these are the fibers, resin and cooperation surface between fibers and resin [45]. These are the factors that determine the susceptibility of a structure reinforced with FRP bars to degradation. These factors include covering of fibers by resin (wettability of fibers by resin), no scratches on the surface or in the cross-section of the rod, no air voids (smaller voids and larger spacing being better), internal solid bonds in the polymer structure of the resin (the production process must be properly controlled for the resin to achieve its strength properties) and strong adhesion between the fibers and the matrix (selecting the type of resin based on the type of rod so that the adhesion between the materials is as high as possible). Thus, the ends of the composite rod are a vulnerable place. If the bars are cut lengthwise, composite fibers will be visible in the final cross-section. Therefore, in this place, aggressive environmental factors can freely penetrate the rod along its length. It is equally important to properly seal the end sections of the FRP rods. Therefore, basalt rods are the most durable, while glass rods are the least durable. Therefore, the types of fibers differ in their resistance to environmental factors. At the same time, the disproportions in the longevity of composite rods are further deepened by the fact that polymer resins also react unequally to environmental aggressions depending on their composition. Moist and alkaline environments are unfavorable. However, this type of rod can also be made resistant by using appropriately shaped fibers, appropriate resin and an improved production process [45].

2. Materials and Methods

2.1. Materials

The following materials were used in the experimental and numerical work:

Glued laminated timber: Twenty-eight beams made of glued laminated wood coming from the Małopolska Region Nature and Forest of Poland and from the beginning and end of the growing season were used, with final dimensions 82 mm × 162 mm × 3650 mm according to PN-EN 14080:2013-07 [46] class GL24c (external laths class T14, internal laths class T9), bending strength 24 MPa, shear strength 3.5 MPa, modulus of elasticity 11,000 MPa, shear modulus 650 MPa. The laths for testing were visually sorted, and all structural and geometric characteristics of the structural lumber were determined; KS—medium quality class of structural lumber; KG—lower quality class of structural lumber, Figure 1 [47], pine, spruce and fir species from Scandinavian countries. In addition, glued laminated timber beams subjected to biological degradation, 7 years of atmospheric influences and long-term exposure to various environmental conditions were used.

Reinforcing bars: BFRP basalt bars, GFRP glass bars, and glass–basalt hybrid bars were 10 mm in diameter and were introduced as reinforcement in the tension and compression zones for glued laminated beams. BFRP—experimentally determined elastic modulus 81.2 GPa, failure force 65,244 N, tensile strength 1521.3 MPa; GFRP—experimentally determined elastic modulus 62.3 GPa, failure force 51,312 N, tensile strength 1311.9 MPa; GFRP and BFRP hybrid bar—experimentally determined elastic modulus 77.1 GPa, failure force 52,675 N, tensile strength 1434.6 MPa. In addition, prestressed bars subjected to biological degradation, 7-year atmospheric influences and long-term exposure to various environmental conditions were used.

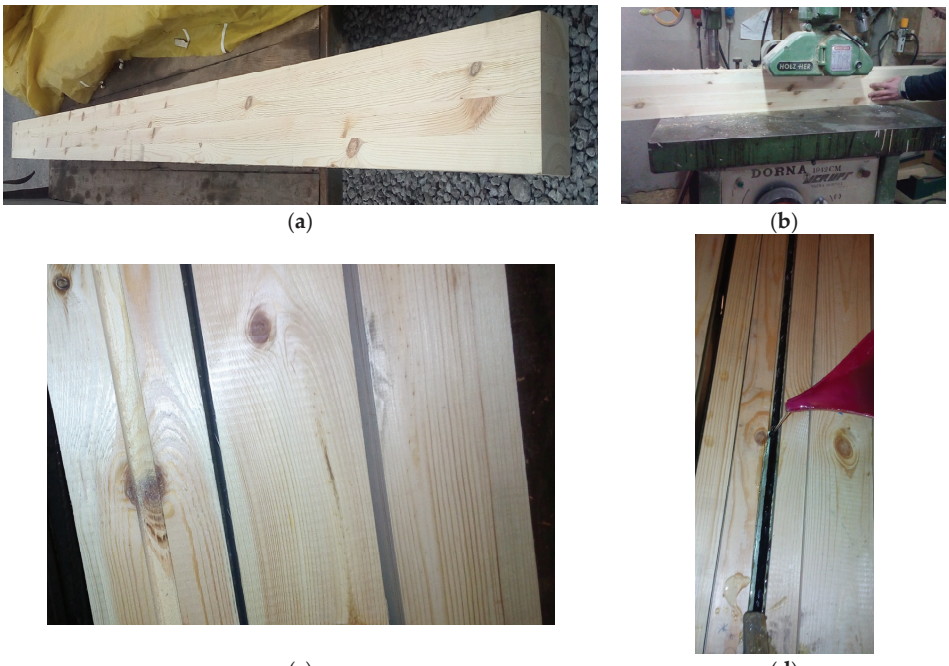

(**a**) (**b**)

(**c**) (**d**)

Figure 1. Production of 14 mm × 14 mm grooves for composite bar reinforcements: (**a**) glued laminated timber beam; (**b**) slot milling; (**c**) preparation of grooves to be filled with reinforcement; (**d**) filling prestressed basalt rods with glue.

The epoxy resin for reinforced rods in the groove of glued beams was MapeWrap 31 [48]. It is a resin used to impregnate MapeWrap mats when reinforcing or repairing concrete structures, reinforced concrete or masonry elements using the dry method. MapeWrap 31 is a solvent-free epoxy resin with a gel consistency. Its parameters are as follows [48]: tensile strength ≥40 N/mm^2, compressive strength ≥70 N/mm^2, flexural strength ≥70 N/mm^2, tensile modulus ≥2600 N/mm^2. In addition, after gluing, the epoxy resin was subjected to biological degradation, seven years of atmospheric influences, and long-term exposure to various environmental conditions.

Figure 1 shows the preparation of glued laminated timber beams. The moisture content of artificially dried sawn timber was tested in industrial conditions at a sawmill. The humidity was 11.78%. The moisture content of the assortment was measured using a moisture meter type HT 65, manufactured by GANN (Gerlingen, Germany). The measurement was taken in the middle of the board width, at a distance of not less than 0.5 m from the face. The measurement sites were selected randomly. Measurements were not performed in places where defects and contamination occurred. The number of measurement places was three on each side of the sawn timber; in each place, the number of measurements was not less than three. The distance between individual measurement places was 10–15 mm. The measurement result was taken as the arithmetic mean of three measurements with the most similar values.

Then, the structural timber was sorted visually according to the PN-D-94021:2013-10 standard [47]. The sawn timber's thickness, width and length were measured during sorting. During the inspection of each piece of sawn timber, all structural and geometric features present in a given piece of sawn timber were measured, such as knots, fiber twist, cracks, resin blisters, plugs and fasteners, rot, insect spots, blue stain, hardwood, graininess, density, veneer, longitudinal curvatures of planes and sides, twist about width,

transverse curvatures in relation to width, scratches, waviness of the cut, non-parallelism of planes and sides and non-perpendicularity of ends. In general, the most common indicator determining the quality class of sawn timber was knots, primarily their size and location on the cross-section of the sorted piece of sawn timber. The classes obtained were KS, a medium quality class, and KG, a lower quality class.

Later, the slats were glued. Each beam contained four layers, and the thickness of each layer after planing was approximately 40 mm, giving a total beam height of approximately 162 mm. Each lamella was cut from 4000 mm long timber. The slats were glued using D4 polyvinyl acetate glue. The gluing time was less than two hours. The slats were arranged so that the core was directed towards the upper part of the beam, according to PN-EN 14080:2013-07 [46].

The placing of the reinforcement was preceded by the milling of square grooves. The groove depth was 14 mm. The reinforcement in all grooves had a cover of approximately 2 mm and was connected to the wood using epoxy glue. The composite materials were cleaned with "Acetone" solvent before the glue was applied. It should be noted that the composite bars were fixed and prestressed (5 mm thick sheets and nuts were attached to the supports), and then epoxy glue was applied, filling the square grooves along the entire beam length. A minimum of 7 days was waited before laboratory tests to obtain the full strength of the reinforcement used.

2.2. Experimental Study

In the experimental part of the study, 28 full-size laminated beams in six groups were used for comparison with unreinforced beams. Five unreinforced beams were made as group B1; five reinforced beams prestressed with three basalt bars in the tension and compression zone with initial stress of 10 MPa were made as group B2; five reinforced beams prestressed with three glass rods in the tension and compression zone with a pretension of 10 MPa, as group B3; five reinforced beams prestressed with three glass–basalt rods in the tension and compression zone with a pretension of 10 MPa, as group B4; see Figure 2. In addition, five beams were made of glued laminated wood reinforced with prestressed basalt rods subjected to biological degradation, seven years of atmospheric influences and long-term operation in various environmental conditions, as B2* beams. Three glulam beams reinforced with prestressed bars were exposed to fire, and the reinforced beams were tested at elevated temperatures in fire and post-fire conditions to determine the physico-mechanical properties of their static work. The deformation of the bars was first examined before the bars were prestressed with a 'Demec' extensometer (Mayes $ Son, Vansittart Estate, Windsor, England, UK), and then, after the bars were prestressed, the deformation of the bars was again examined along the length of the bars with the extensometer, especially in the middle of the beam span, to analyze the elongation along the length of the beam. The groove was then filled with epoxy adhesive. Prestressing of the bars was carried out to give them straightness and better interaction with the wood and epoxy glue. Making the holes and filling them with bars alone without prestressing, filling them with bars with prestressing and epoxy glue, and fixing them at the ends of the beams on supports does not give an increase in reinforcement and reinforcement efficiency.

The experimental beams were tested in accordance with EN 408 + A1:2012 [49] using a bending test under static loading. Each beam was 3.65 m long with a rectangular cross-section of 82 mm $\times$ 162 mm. The percentage of reinforcement was 2.6 percent. The dimensions of the glued laminated beams were adapted to the static scheme according to EN 408 + A1:2012 [49]. The choice of this dimension was determined by the availability of timber in the local construction market. In these test models, it was important to use the top bars to reinforce the compressive stresses, for the reason that there is no significant difference between the compressive and tensile strengths.

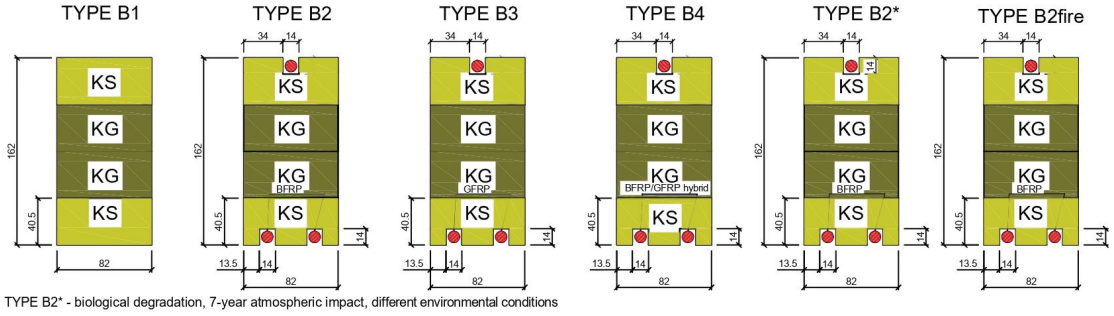

Figure 2. Reinforcement configurations of composite bars in glued laminated beams.

All prestressed full-size reinforced wooden beams with dimensions of 82 × 162 × 3650 mm^3 were tested for four-point bending. To determine the bending mechanical properties in reinforced and unreinforced beams, the 4-point loading method was used. The tests were carried out on samples conditioned in air with a temperature of 20 ± 2 °C and relative humidity of 65 ± 5%. The load was applied at a constant feed rate and thrust to reach the maximum load after 300 ± 120 s. The loading force was tested; deformations over the entire surface of the beams over a length of 3000 mm between supports on two sides of the beams (which is very precise, considering there are usually tests in the literature only in the middle of the beam span) were tested using a Demec (Mayes $ Son, Vansittart Estate, Windsor, England, UK), 8-inch mechanical extensometer and 3 mechanical dial gauges over a length of 810 mm. All tests were carried out on a mechanically loaded testing machine. The test specimens were loaded to failure; all specimen elements were tested using a hydraulic machine with a capacity of 100 kN per actuator. During testing, the distance between supports was 3000 mm, and the distance between the loading forces and supports was 1000 mm. The experimental layout is shown in Figure 3.

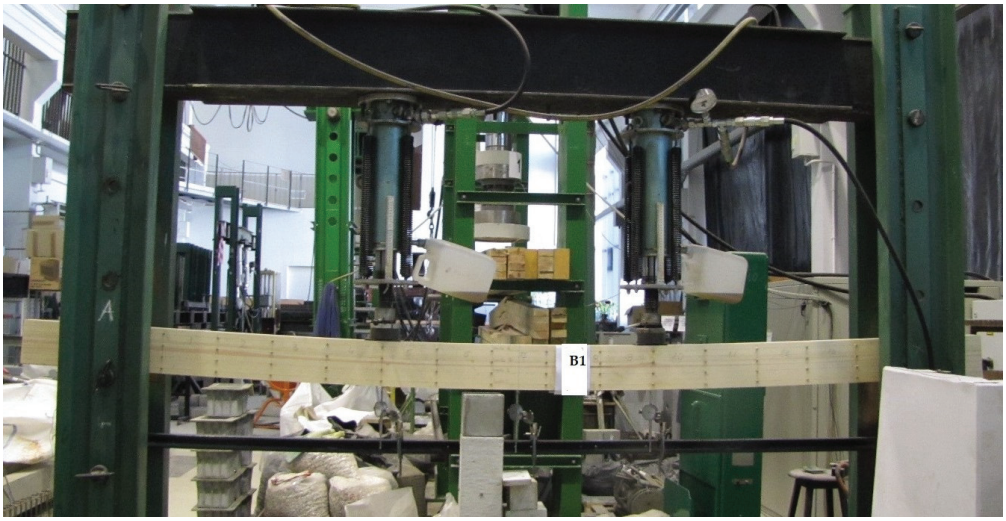

Figure 3. Schematic of the actual beams under test.

In addition, the thermal properties of three reinforced B2 beams were examined at elevated temperatures as an exploratory determination of heat propagation and fire spread in reinforced wooden beams. The grooves and holes in the beams were filled only every 50 cm with epoxy glue and at the ends in the anchorage during prestressing. To ensure the

safety of the experiment, experimental, theoretical and numerical tests were carried out in field conditions. Beams were placed on supports (aerated concrete bricks) and mechanically loaded, mechanical clock sensors were placed under the beam and the temperature inside the beams was measured. In field tests, the tested beams were surrounded by insulating material on the rear, left and right sides to reduce lateral heat flows during the heating process. Aerated concrete bricks were placed on the front surface of the beam, on which ten type K thermocouples were mounted at regular intervals of 30 cm. The temperatures ranged from 15 °C to 850 °C. Then, for safety reasons, the test prototype was turned off (Figure 4). Further research consisted of preliminary exploratory research aimed at determining the impact of increased temperature in fire conditions and physical and mechanical properties during and after the fire as a long-term action in various environmental conditions. Another aim was to determine whether the reinforcement protects the wooden element as internal reinforcement against fire. Therefore, the next stage will be research on small- and full-size elements with different arrangements of the wood structure as well as external or internal reinforcements such as FRP and steel, as well as chopped fiber. In the next laboratory stage, in addition to full-size wooden elements, it is planned to test small-size reinforced wooden elements in a chamber furnace with a very high operating temperature. After the reinforced samples are heated to specified temperatures, they will be tested statically and cyclically.

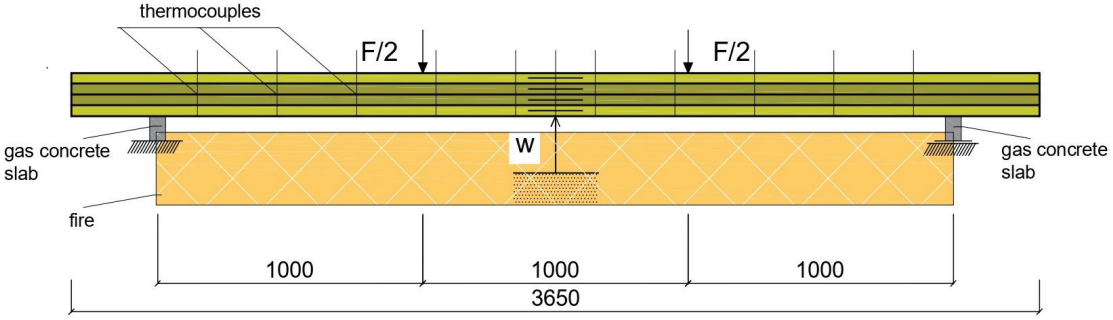

Figure 4. Test system for full-size reinforced beam type B2 at elevated fire temperatures.

Additionally, for the B2 configuration, tests were carried out using wooden beams, subjected to biological degradation and seven years of weathering (e.g., water, snow, wind, temperature drop and rise), that were reinforced with basalt bars, which were also exposed to biological degradation and long-term operation in various environmental conditions. Therefore, the wood and the bars were subjected to biological degradation, seven years of atmospheric influences and long-term exposure to different environmental conditions. Environmental factors include water, ultraviolet radiation, elevated temperature, acid solutions, alkali solutions, salt solutions, heating and cooling cycles, freezing and thawing cycles and stresses in the rod.

2.3. Numerical Study

Numerical modeling was performed with ANSYS 16.0, using the Static Structural module. Geometrical models of the beams were made using CATIA V5 and the finite element method. In the numerical studies, geometry was introduced for unreinforced as well as reinforced beams, so that the oriented geometry and reinforcement configurations identically reflect the beams tested experimentally. Also, boundary conditions were established using pinned or roller supports to eliminate vertical movement of the beams. The finite element mesh consisted of hexagonal and tetragonal elements. Hexagonal elements with a dimension equal to 10 mm were used on the lamella and support geometries. Tetragonal elements with a dimension equal to 5 mm were used on the rods and the glue area as hole filling and glue joints between the lamellas. The proposed finite element model is shown in Figure 5. The boundary conditions assumed in the numerical analysis were intended to

reproduce a four-point beam's bending faithfully. For this purpose, two concentrated forces of the same values were applied to the upper surfaces of the blocks. The supports were the lower blocks, placed at a greater distance between each other. One of the supports served as a fixed support, and the other served as a movable support. These assumptions were implemented using the Fixed Support function for the fixed support and Displacement for the movable one. Thermal analyses, including a temperature study, were designed for the reinforced beam. The numerical analysis also used the temperature in the experimental research to check the possibility of fire spreading over the entire surface of the beam and inside the beam. In the finite element method, the thermal analysis was performed in ANSYS in the Mechanical APDL module. Also, thermal visualizations were carried out and checked using the 'Nodal temperature' option. To determine the heat flow, the thermal properties of materials, namely the specific heat, thermal conductivity and density, must be given as a function of temperature, which is enabled by the Ansys program. The numerical model was also modeled in ANSYS. The finite element analysis involved heat flow in places exposed to fire and simulations in other places. This was a preliminary exploratory analysis as a direction for further research. Simulation fire action was modeled using preliminary experimental tests. To model beams loaded with fire, finite elements for thermal analysis were used as above. The dimensions of the finite element mesh were 10 mm and 5 mm. As mentioned, these were preliminary, exploratory studies and will be continued as directions for further research. The material data entered into the program are shown in Tables 1 and 2.

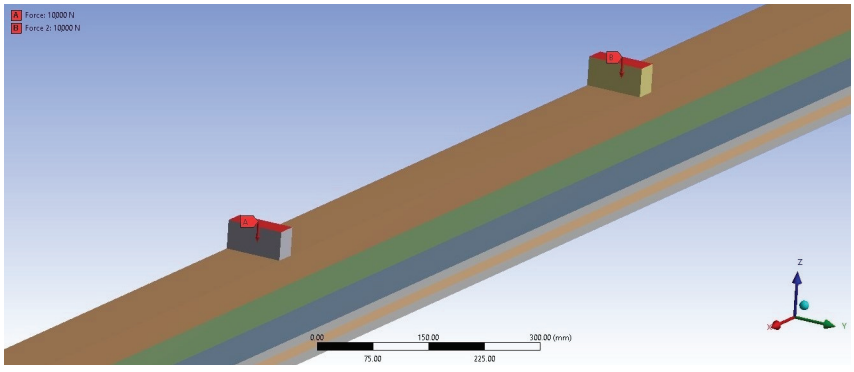

Figure 5. Finite element model—lamella geometry—various quality classes, glue between lamellas and rods, and rods.

Table 1. The material data for the reinforcing elements.

Material	MOE (MPa)			Poisson's Ratio			Shear Modulus (MPa)		
	L	R	T	L	R	T	LR	RT	LT
Epoxy resin	2600	78	78	0.3	0.015	0.3	-	-	-
GFRP	62,300	1880	1880	0.25	0.0125	0.25	-	-	-
BFRP/GFRP	77,100	2327	2327	0.22	0.011	0.22	-	-	-
BFRP	81,200	2451	2451	0.19	0.0095	0.19			

Table 2. The material data for the lamellas of the glued laminated beam.

Quality Class for Structural Sawn Timber	Young's Modulus (MPa)			Poisson Modulus						Shear Modulus (MPa)		
	L	R	T	LR	LT	RT	TR	RL	TL	LR	LT	RT
KG	9130	3013	3013	0.45	0.49	0.56	0.35	0.044	0.018	550	550	55
KS	11700	386	386	0.48	0.51	0.60	0.37	0.048	0.019	880	880	88

3. Results

The results from experimental and numerical studies of the flexural properties of glued beams reinforced with prestressed FRP rods are shown. The experimental results of laminated beams are shown in terms of load-carrying capacity, failure mode, load–deflection and deformation.

3.1. Load–Deflection

Based on the experimental bending tests, Figure 6 shows the load–deflection curves at the center of the beam span compared to unreinforced beams. From the tests, it was found that the use of reinforcing bars in the tension and compression zones of bonded beams improved the flexural strength and reduced the deflection values compared to the behavior of unreinforced beams in the range of 23.81–28.35%, improving the flexural stiffness. It is noted in the graph that the load–displacement curve for unreinforced B1 beams is linear, behaving in a virtually linear manner. It should also be noted that any deviation is due to the fact that the glued beams consist of different glued lamellas, which contain natural defects such as knots. However, in the case of biologically degraded wooden beams, subjected to seven years of atmospheric influences and long-term exposure to various environmental conditions (type B2*), the increase in stiffness was comparable to that for beams without degradation, without atmospheric influences and various environmental conditions (type B2), and amounted to 28.09% (F/2 = 7.5 kN). In the case of reinforced beams exposed to fire at initial loads (up to F/2 = 4 kN), the stiffness increased compared to unreinforced beams and amounted to approximately 21.68%. Then, at higher loads, deflections increased. For F/2 = 7.5 kN, the increase in beam stiffness at elevated temperature was 11.25% compared to unstrengthened beams without fire exposure. As mentioned, these were preliminary reconnaissance tests (field and outdoor tests); subsequent tests included laboratory tests of fire resistance, as well as the impact of elevated temperatures and checking the physico-mechanical properties after fire and in fire conditions.

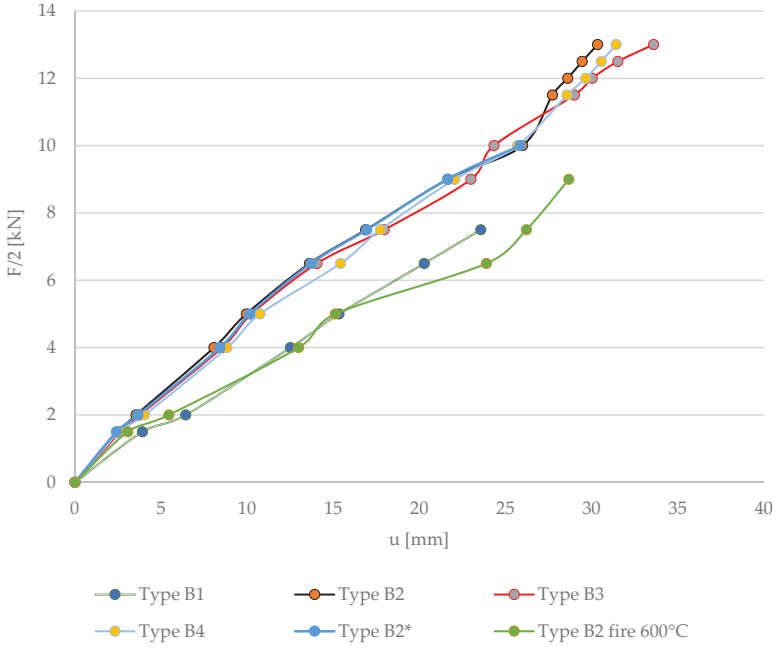

Figure 6. Load–displacement for all tested beams.

3.2. The Maximum Bending Moment

In Table 3 below, the maximum bending moment results for beams unreinforced and reinforced with prestressed FRP basalt bars are shown.

Table 3. The bending moments (M_{max}) for beam types "B1", "B2", "B3", "B4","B2*", "B2fire".

BEAM B1	M_{max} [kNm]	BEAM B2	M_{max} [kNm]	BEAM B3	Mmax [kNm]	BEAM B4	Mmax [kNm]	BEAM B2*	Mmax [kNm]	BEAM B2fire	Mmax [kNm]
B1-1	18.50	B2-1	27.00	B3-1	22.50	B4-1	24.00	B2-1*	19.50	B2fire-1	18.00
B1-2	16.50	B2-2	22.00	B3-2	24.00	B4-2	22.50	B2-2*	24.00	B2fire-2	16.50
B1-3	17.00	B2-3	25.50	B3-3	21.00	B4-3	28.00	B2-3*	21.00	B2fire-3	17.00
B1-4	15.50	B2-4	26.00	B3-4	24.50	B4-4	24.50	B2-4*	23.50		
B1-5	18.00	B2-5	23.00	B3-5	22.00	B4-5	23.00	B2-5*	20.50		
Average	17.10	Average	24.70	Average	22.80	Average	24.40	Average	21.70	Average	17.17
Increase [%]	-	Increase [%]	44.44	Increase [%]	33.33	Increase [%]	42.69	Increase [%]	26.90	Increase [%]	0.39

The applied reinforcement in most glued laminated beams stiffened the beams, allowing them to carry higher loads. Therefore, the applied reinforcement leads to a combination of resulting horizontal shear and tensile failures, in contrast to unreinforced beams. The same satisfactory results were obtained for beams with biological degradation, atmospheric influences and long-term operation in various environmental conditions, as much as a 26.90 increase in load-bearing capacity. However, when it comes to field tests as reconnaissance tests on the effects of fire, the impact of increased temperatures on reinforced beam elements as well as the wood materials themselves and the reinforcement used, searching for appropriate protective and fire-retardant reinforcement, maintaining appropriate fire resistance, obtaining the assumed reaction to fire, examining the spread of fire and then conducting theoretical and numerical analyses, as well as analysis of physicomechanical properties after fire and in fire conditions, they will be extended as directions for further research.

3.3. The Image of the Destruction of the Beams

The failure pattern of the glued beams varied for each beam type. This was due to the loading system, the timber material's heterogeneity, the structural and geometric features' magnitude and knots. Therefore, the basic stages of failure included the following:

- Rapid failure in the tension zone in the unreinforced element due to the presence of knots; the tensile stress in the extreme tensile fibers exceeded the tensile strength limit of the timber.
- Usually, in elements reinforced with prestressed composite rods in the tension and compression zones, rapid and sudden shear failure occurred along the wood fibers after the glulam shear strength limit was exceeded; see Figure 7.

In most of the reinforced beams, there was shear damage, sometimes delamination, and cracks in the epoxy resin appeared. It was also noted that the reinforcement also prevented damage and inhibited crack propagation in the timber.

3.4. Deformation of Wood at the Height of the Beam Section

Unreinforced type B1 beams showed tensile strains (with normal stresses) greater than those for unreinforced type B2, B3, B4, B2* and B2fire beams. Below is a graph of the wood deformation at the height of the beam section in a beam reinforced with prestressed basalt bars, B2-3; see Figure 8. The application of reinforcement significantly reduced the tensile stresses by up to 22% and the compressive stresses by 15%. In the areas of wood defects (knots, fiber twists, cracks, resin blisters, etc.), increases in the deformation and stresses of the wood and fiber composite were noted.

Figure 7. An image of the destruction of the reinforced beams—B3-4.

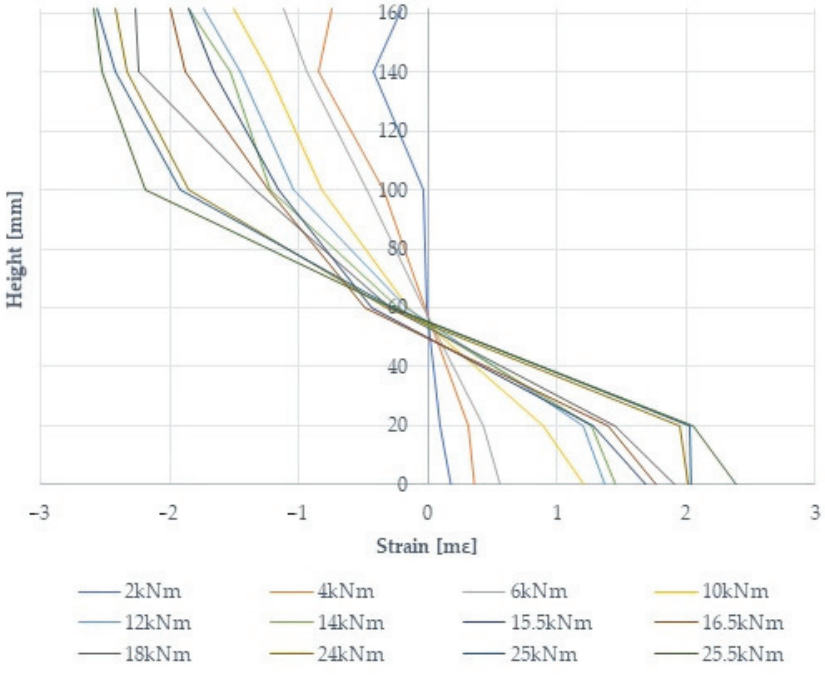

Figure 8. A diagram of timber deformation at the height of the timber section at the center of the B2-3 beam span.

3.5. Experimental and Numerical Studies

In the numerical study, a three-dimensional finite element model was defined to determine the behavior of unreinforced and reinforced beams, made with different configurations of wood quality classes, reinforced with composite bars. Numerical investigations included checking and comparing the results of unreinforced beam elements with rein-

forced elements in the laboratory and numerical analysis. The experimental and numerical results obtained were compared to verify the accuracy of the finite element models for a force F/2 equal to 5 kN; see Tables 4 and 5. Figure 9 shows an example of a finite element numerical displacement analysis for beam B1, while the finite element normal stresses are shown in Figure 10.

Table 4. The comparison of laboratory and numerical results of the tested beams; displacements—F/2 = 5 kN.

Type	Experimental Study—Deflection [mm]	Numerical Study—Deflection [mm]	Difference [%]
B1	15.33	15.5	1.1
B2	9.95	10.5	5.5
B3	10.26	10.7	4.3
B4	10.75	11.3	5.1
B2*	10.15	10.7	5.4
B2fire	15.12	16.9	11.8

Table 5. The comparison of laboratory and numerical results of the tested beams; tensile stresses—F/2 = 5 kN.

Type	Experimental Study—Normal Stress [MPa]	Numerical Study—Normal Stress [MPa]	Difference [%]
B1	36.11	40.0	1.1
B2	31.15	37.4	2.0
B3	33.07	38.9	1.8
B4	32.51	37.8	1.6
B2*	33.12	-	-

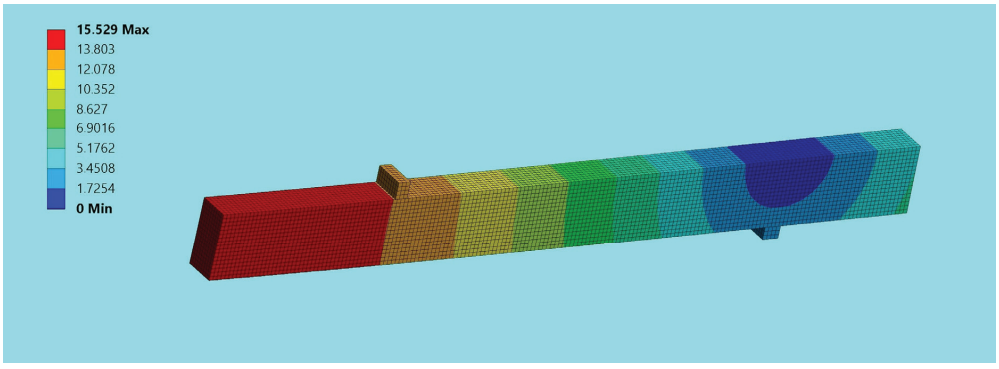

Figure 9. Displacement image using the finite element method for beam B1—Ansys.

Based on the results obtained, it was concluded that numerical analysis can be applied to reinforced elements to design different reinforcement schemes with particular attention to the configuration of wood quality classes. In the above study, a three-dimensional finite element model was defined that determined the stiffness of unreinforced and reinforced beams with reasonable accuracy. The model obtained was consistent with experimental studies; the stiffness of reinforced beams can be increased by using different configurations of lamella quality classes and composite bar placement. In the numerical studies, a satisfactory agreement was obtained in the materials tested, in the timber and the composite bar, and in particular, in the consistency of the results. This is because Young's modulus, Poisson's modulus and the shear modulus for all quality classes of structural lumber were determined experimentally for the numerical analysis. The only significant difference

resulted in beams at increased fire temperature, but these numerical tests will also be further extended.

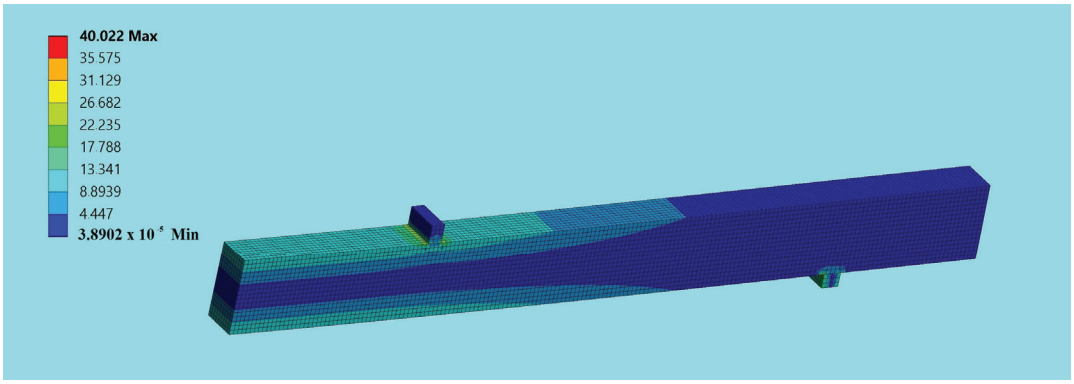

Figure 10. Normal stress image using the finite element method for beam B1—Ansys.

4. Discussion

Experimental and numerical studies show the static behavior of beams reinforced with various prestressed BFRP fibers. Additionally, the tests used beams and bars subjected to biological degradation, seven years of atmospheric influences and various long-term environmental conditions. The next part also presents experimental research in field conditions as an exploratory study of exposure to fire at elevated temperatures in fire and post-fire conditions. The force–deflection diagram shows that most of the beams show a linear relationship, which means that the deformations in prestressed bars increase linearly for the most part. Composite rods, however, do not have the ability, of course, after exceeding certain stresses, to strengthen plastically or to redistribute internal forces. It should be noted that this is different from steel. Based on the research, it can be concluded that the reinforcement with prestressed composite bars does not show any increase in plastic deformation, which would indicate an impending disaster. As you can see, the deformation increases until it exceeds a certain value, and then brittle failure of the structural element occurs. Therefore, in the process of designing structures, it also happens that it is not the criteria of the limit state of stresses and strains but the fatigue resistance and the resistance to sudden breakage of the bar—creep—that are determining factors [45].

It should also be remembered that using FRP bars to reinforce structures, where high resistance to elevated temperatures is a necessary condition for maintaining the structural integrity of the structure, is not recommended. Similarly, in the tests, because the fibers themselves in composite materials have much better resistance to high temperatures than the resin surrounding them, in the case of fire-reinforced beams, attempts were made to fill only the holes every 50 cm and at the anchor point with epoxy glue. In future research, it is also planned to investigate, in addition, only composite staple fibers used in the internal and external cross-section of the wooden element, in addition to other FRP materials and steel. Then, they can carry significant longitudinal loads (tension). In tests on beams made of wood laminated with prestressed basalt rods, the epoxy glue determined the adhesion of the rod to the wood. But when the basalt bar's temperature limit was reached, the epoxy adhesive was no longer able to transfer the stresses from the wood to the bar's core. It was noticeable that when the temperature was above 200 degrees Celsius, the adhesion decreased by up to 65%. Here, we can extend the tests under long-term load by acting on fiber-reinforced beams, and then we will obtain a higher temperature threshold and a decrease in adhesion, even assuming 400 degrees Celsius. These were reconnaissance tests, as mentioned, and a sudden increase in deflections occurred starting from F/2 = 4 kN. Then, there was a decrease in the adhesion of the bars to the wood, but the limit temperature of the glued wood was still reached at 600 degrees Celsius, for a time of approximately

one hour. It was still possible to test the sample, but for safety reasons, everything was dismantled and secured; only then were the physical and mechanical properties after the fire additionally tested. These were exploratory studies; subsequent extended studies were designated as directions for further research. Also, during these experimental tests, it was observed that excessive beam deflections and significant cracks suddenly occurred due to the deterioration of the anchoring quality as the temperature increased. It was also noticed that the physical and mechanical properties of the composite rods deteriorated with increasing temperature, but if they did not exceed the glass transition temperature of the fibers, they returned almost completely to their initial values [45].

It should also be remembered that in prestressed structures, additional stresses occurred at the bar–wood interface in these tests due to the relatively high coefficient of transverse thermal expansion. Similarly, during a fire, the flame had access to the rod and caused the formation of toxic fumes when burning the polymer resin. But then gases were released, which insulated the rod and made it difficult for the flame to penetrate deeper into its structure. If a cover is made, there is no access to oxygen needed for oxidation, and therefore, the structure does not burn despite high temperatures. Similarly, it was noticed that long-term exposure to negative temperature may also cause hardening of the matrix, microscratches, microcracks or reduced adhesion between the matrix and individual FRP fibers. Freeze–thaw cycles during various long-term environmental conditions and the effect of salt also manifested themselves in the deterioration of the resin properties as the polymer swelled on the rod surface—but this was only observed in two rods.

Therefore, to prevent the reduction in adhesion between FRP rods and wood as a result of the expansion and contraction of the rods under the influence of temperature cycles and degradation, e.g., resulting from frost, the rod cover and composite building blocks should be selected appropriately depending on the type of rod and the element's operating environment. In the case of securing the structure at elevated temperatures, it is necessary to select a cover that protects the rod against the influence of high temperatures. Likewise, the type of polymer resin material and the type and size of fibers in the rods must be sufficiently known because, of course, the critical temperatures of the materials—the glass transition temperature of the resin and the threshold temperature at which the fibers lose their strength properties— are decisive here, affecting the designed operating temperature of the structure and its fire resistance [45].

5. Conclusions

On the basis of the results of the experimental and numerical tests and analyses of static work efficiency, load capacity, stiffness, deformations at average and elevated temperatures and various environmental conditions carried out on beams glued in layers with prestressed composite bars, the following conclusions were drawn:

- The use of prestressed composite bars to reinforce timber beams is an effective way of increasing the load-bearing capacity and stiffness of members used in both existing and newly designed structures.
- The highest load-bearing capacity and stiffness increases were obtained for beams reinforced with prestressed basalt bars. The increase in load capacity was 44%, and that in stiffness was 28%. It should also be noted that comparable efficiencies were obtained for glued laminated beams reinforced with prestressed glass–basalt bars, so-called hybrid bars (increase in load capacity—43%; stiffness—25%). Therefore, it is possible to reduce the production costs of basalt bars by producing hybrid bars using winding, ribbed basalt fibers wound on glass fiber.
- A decrease in compressive and tensile strains was observed in all types of reinforced bonded beams. Reinforcement significantly reduced tensile stresses by 19–22% and compressive stresses by 11–15%. The presence of composite bars inhibits or limits crack propagation.
- For reinforced beam elements made of glued laminated timber of classes KS and KG, the most common form of failure was shearing of the timber along the fibers. For

unreinforced beams, the failure usually occurred in the tension zone as a result of the fracturing of the timber fibers near timber defects or hidden defects—knots. Therefore, it was observed that prestressed composite bars improved the interaction between the cracking knot and the stiffening 'glue-bar' joint.

- In the above study, a three-dimensional finite element model was defined which determined the stiffness of unreinforced and reinforced beams with reasonable accuracy. The model obtained was consistent with the experimental studies. The differences were at the level of 1.1–5.5%. Among other things, satisfactory agreement was obtained by using experimental tests to determine the Young's modulus, Poisson's modulus and shear modulus for the KS and KG classes of structural lumber quality forming the laths of the laminated beams. A significant difference of as much as 11.8% concerned only beams at elevated temperatures in fire conditions. These were only exploratory tests. They will be extended as directions for further experimental, theoretical and numerical research on small-size and full-size wooden beams (including solid beams, solid ones joined with glued joints, glued laminated timber, laminated veneer lumber, I-beams (with laminated veneer lumber and also solid wood), glued laminated beams, cross-laminated timber) reinforced in various forms at every production and technological stage with different FRP fibers (including various artificial and natural fibers) and steel as external and internal reinforcement or as staple fibers, at elevated temperatures, in fire conditions, after fire, under the influence of fire, reacting to fire, in fire spread and standard fire resistance tests, in long-term operation in various environmental conditions (to study their load-bearing capacity, stiffness, deformability and acoustic emission) and as structural elements of various structures with various fiber shapes subjected to static, cyclic, long-term and variable loads—bending, shear, compression, tension.
- FRP-reinforced timber beams subjected to tension zone stress at elevated temperatures typically failed through anchorage degradation. This was due to the loss of their properties due to exposure to high temperatures or to the basalt polymer, e.g., softening, or due to the basalt fibers exceeding the threshold temperatures for fibers. Therefore, due to the deterioration of anchoring quality as the temperature increased, excessive beam deflections and crack widths that exceeded the norm possibly occurred.
- In prestressed structures, it should also be considered that the high coefficient of transverse thermal expansion causes additional stresses at the rod–adhesive and rod–wood interfaces. Then, during a fire, the flame that has access to the rod causes the formation of toxic fumes while burning the polymer resin. But it should also be noted that gases may then be released, insulating the rod and preventing the flame from penetrating deeper into its structure. But the bars in the structures are also located inside the wood—there is no access to oxygen needed for oxidation, and they do not burn despite the high temperature.
- It should be noted that despite biological degradation, atmospheric influences and long-term exposure to various environmental conditions, very satisfactory load-bearing capacity (27%) and stiffness (28%) results were obtained. Therefore, the durability of composite bars is greater than the durability of steel. This is because the polymer resin, as the surface layer of the rod, does not allow aggressive factors to penetrate into the composite. This research program was planned to be expanded as a direction for further research, taking into account various long-term atmospheric influences and environmental conditions of the beams and the reinforcement used.
- It should also be taken into account that in numerical modeling, we treat wood as an orthotropic material; in reality, it is a heterogeneous material—anisotropic. Therefore, any defects in the wood are very much 'averaged out'. And yet, wood defects, especially knots and defects occurring in the tension zone, primarily determine the load-bearing capacity or stiffness of the flexural member.
- Thus, the applied reinforcement technique can be useful in innovative wood products and engineering for reinforcement system analysis and repair.

- Analytical methods for predicting the strength of reinforced beams are imprecise due to the very high heterogeneity of natural wood material, indicating the need to use more full-size technical-scale elements per trial to reduce the error tolerance. Also, due to the significant heterogeneity of wood materials, full-size elements should be examined on a technical scale; the scale effect in wood materials is unreliable.

Author Contributions: Conceptualization, A.W.-P.; methodology, A.W.-P.; software, A.W.-P.; validation, A.W.-P.; formal analysis, A.W.-P.; investigation, A.W.-P. and G.Ś.; resources, A.W.-P.; data curation, A.W.-P.; writing—original draft preparation, A.W.-P.; writing—review and editing, A.W.-P., G.Ś. and I.D.-J.; visualization, A.W.-P., G.Ś. and I.D.-J.; supervision, A.W.-P. and G.Ś.; project administration, A.W.-P. and G.Ś.; funding acquisition, A.W.-P. and G.Ś. All authors have read and agreed to the published version of the manuscript.

Funding: The APC was funded by 02.0.18.00/1.02.001, SUBB.BKWK.23.001.

Institutional Review Board Statement: Not applicable.

Informed Consent Statement: Not applicable.

Data Availability Statement: Data are contained within the article.

Acknowledgments: We would like to thank KONSBUD and Tartak OLCZYK for the wood materials provided. In addition, we would like to thank the companies MAPEI Polska Sp. z o. o., Tatran 3R Sp. z o. o. and GRM Systems s.r.o. for the materials provided to strengthen wooden beams.

Conflicts of Interest: The authors declare no conflicts of interest.

References

1. Khaled, S. Finite Element Modelling for Timber Beams Reinforced with Carbon Fibre Reinforced Polymers (CFRP). A PHD Dissertation Submitted to the Faculty of Civil Engineering in Candidacy for the Degree of Doctor of Philosophy. BUDAPEST. 2023. Available online: https://repozitorium.omikk.bme.hu/items/9a7c910f-257e-4643-8f63-2c6be3a6de74 (accessed on 23 January 2024).
2. Sathishkumar, T.P.; Naveen, J.; Satheeshkumar, S. Hybrid fiber reinforced polymer composites—A review. *J. Reinf. Plast. Compos.* **2014**, *33*, 454–471. [CrossRef]
3. Unterweger, C.; Bruggemann, O.; Furst, C. Synthetic fibers and thermoplastic short-fiber-reinforced polymers: Properties and characterization. *Polym. Compos.* **2014**, *35*, 227–236. [CrossRef]
4. Ramesh, M.; Bhoopathi, R.; Deepa, C.; Sasikal, G. Experimental investigation on morphological, physical and shear properties of hybrid composite laminates reinforced with flax and carbon fibers. *J. Chin. Adv. Mater. Soc.* **2018**, *6*, 640–654. [CrossRef]
5. Kilinçarslan, S.; Türker, Y.S.; Avcar, M. Numerical and Experimental Evaluation of the Mechanical Behavior of FRP-Strengthened Solid and Glulam Timber Beams. *J. Eng. Manag. Syst. Eng.* **2023**, *2*, 158–169. [CrossRef]
6. Singh, S.; Uddin, M.; Prakash, C. *Introduction, History, and Origin of Composite Materials*; CRC Press: Boca Raton, FL, USA, 2022. [CrossRef]
7. Van Vinh, P.; Avcar, M.; Belarbi, M.O.; Tounsi, A.; Lê, H.Q. A new higher-order mixed four-node quadrilateral finite element for static bending analysis of functionally graded plates. *Structures* **2023**, *47*, 1612–2023. [CrossRef]
8. Tong-de, Z.; Li, Q.; Yu, B.; Huang, C.; Gao, Z.; Wang, K. Experimental study on dynamic mechanical properties of mortar-sandstone composite under impact load. *Structures* **2023**, *51*, 1070–2023. [CrossRef]
9. Amrollahi, S.; Ramezanzadeh, B.; Yari, H.; Ramezanzadeh, M.; Mahdavian, M. Synthesis of polyaniline-modified graphene oxide for obtaining a high performance epoxy nanocomposite film with excellent UV blocking/anti-oxidant/anti-corrosion capabilities. *Compos. Part B Eng.* **2019**, *173*, 106804. [CrossRef]
10. Rod, K.A.; Nguyen, M.T.; Elbakhshwan, M.; Gills, S.; Kutchko, B.; Varga, T.; McKinney, A.M.; Roosendaal, T.J.; Childers, M.I.; Zhao, C.; et al. Insights into the physical and chemical properties of a cement-polymer composite developed for geothermal wellbore applications. *Cem. Concr. Compos.* **2019**, *97*, 287–2019. [CrossRef]
11. Farhad, A.; Shojaei, A.; Dordanihaghighi, S.; Jafarpour, E.; Mohammadi, S.; Arjmand, M. Effects of hybrid carbon-aramid fiber on performance of non-asbestos organic brake friction composites. *Wear* **2020**, *452–453*, 203280. [CrossRef]
12. Atefeh, A.; Shockravi, A.; Rezania, H.; Farahati, R. Investigation of anticorrosive properties of novel silane-functionalized polyamide/GO nanocomposite as steel coatings. *Surf. Interfaces* **2020**, *18*, 100453. [CrossRef]
13. Wdowiak-Postulak, A. Ductility load capacity and bending stiffness of Scandinavian pine beams from waste timber strengthened with jute fibres. *Drewno* **2022**, 65. [CrossRef]
14. Wdowiak-Postulak, A. Numerical, theoretical and experimental models of the static performance of timber beams reinforced with steel, basalt and glass pre-stressed bars. *Compos. Struct.* **2023**, *305*, 116479. [CrossRef]

15. Wdowiak-Postulak, A.; Bahleda, F.; Prokop, J. An Experimental and Numerical Analysis of Glued Laminated Beams Strengthened by Pre-Stressed Basalt Fibre-Reinforced Polymer Bars. *Materials* **2023**, *16*, 2776. [CrossRef] [PubMed]
16. Wdowiak-Postulak, A.; Wieruszewski, M.; Bahleda, F.; Prokop, J.; Brol, J. Fibre-Reinforced Polymers and Steel for the Reinforcement of Wooden Elements—Experimental and Numerical Analysis. *Polymers* **2023**, *15*, 2062. [CrossRef]
17. Chybiński, M.; Polus, Ł. Experimental and numerical investigations of aluminium-timber composite beams with bolted connections. *Structures* **2021**, *34*, 1942–1960. [CrossRef]
18. Ozcifci, A. Effects of scarf joints on bending strength and modulus of elasticity to laminated veneer lumber (LVL). *Build. Environ.* **2007**, *42*, 1510–1514. [CrossRef]
19. Madhoushi, M.; Ansell, M.P. Experimental study of static and fatigue strengths of pultruded GFRP rods bonded into LVL and glulam. *Int. J. Adhes. Adhes.* **2004**, *24*, 319–325. [CrossRef]
20. Bednarek, Z.; Pieniak, D.; Ogrodnik, P. Wytrzymałość na Zginanie i Niezawodność Kompozytu Drewnianego LVL w Warunkach Podwyższonych Temperatur. Zeszyty Naukowe SGSP 40/2010. Available online: http://yadda.icm.edu.pl/baztech/element/bwmeta1.element.baztech-4f6852a4-1b30-4cf5-b814-b5bef9e9b6c0 (accessed on 31 December 2010).
21. Pallab, D.; Tiwari, P. Thermal degradation study of waste polyethylene terephthalate (PET) under inert and oxidative environments. *Thermochim. Acta* **2019**, *679*, 178340. [CrossRef]
22. *PN-EN 1995-1-1:2010*; Eurokod 5—Projektowanie Konstrukcji Drewnianych—Część 1-1: Postanowienia Ogólne—Reguły Ogólne i Reguły Dotyczące Budynków. Polish Committee for Standardization: Warsaw, Poland, 2010.
23. Bengtsson, C.; Johansson, C.J. Test methods for glued-in rods for timber structures. In Proceedings of the 33th Conference of CIB-W18, Delft, The Netherlands, 2000. Paper 33-7-8.
24. Harvey, K.; Ansell, M.P. Improved timber connections using bonded-in GFRP rods. In Proceedings of the World Conference of Timber Engineering, Whistler Resort, BC, Canada, 31 July–3 August 2000.
25. Hunger, F.; Stepinac, M.; Rajčić, V.; van de Kuilen, J.W.G. Pull-compression tests on glued-in metric thread rods parallel to grain in glulam and laminated veneer lumber of different timber species. *Eur. J. Wood Prod.* **2016**, *74*, 379–391. [CrossRef]
26. Broughton, J.; Hutchinson, A. Pull-out behaviour of steel rods bonded into timber. *Mater. Struct.* **2001**, *34*, 100–109. [CrossRef]
27. Pîrvu, C.; Yoshida, H.; Taki, K. Development of LVL frame structures using glued metal plate joints I: Bond quality and joint performance of LVL-metal joints using epoxy resins. *J. Wood Sci.* **1999**, *45*, 284–290. [CrossRef]
28. Myslicki, S.; Bletz-Mühldorfer, O.; Diehl, F.; Lavarec, C. Fatigue of glued-in rods in engineered hardwood products—Part I: Experimental results. *J. Adhes.* **2019**, *95*, 675–701. [CrossRef]
29. Gentile, C.; Svecova, D.; Rizkalla, S.H. Timber beams strengthened with GFRP bars: Development and Applications. *J. Compos. Construction* **2002**, *6*, 11–20. [CrossRef]
30. Raftery, G.M.; Kelly, F. Basalt FRP rods for reinforcement and repair of timber. *Comps. B Eng.* **2015**, *70*, 9–19. [CrossRef]
31. Yang, H.; Liu, W.; Lu, W.; Zhu, S.; Geng, Q. Flexural behavior of FRP and steel reinforced glulam beams: Experimental and theoretical evaluation. *Constr. Build. Mater.* **2016**, *106*, 550–563. [CrossRef]
32. Che, C. Investigating the Effects of Glass-Fibre-Reinforced Polymer Fabrics and Bars on the Flexural Behaviour of Sawn Timber and Glulam Beams. Master's Thesis, University of Waterloo, Waterloo, ON, Canada, 2023.
33. Buell, T.W.; Saadatmanesh, H. Strengthening timber bridge beams using carbon fiber. *J. Struct. Eng.* **2005**, *131*, 173–187. [CrossRef]
34. Shrimpton, C.; Siciliano, S.; Chen, H.; Vetter, Y.; Lacroix, D. An Experimental Investigation of Failure Modes in Short-Span FRP Reinforced Glulam Beams. In Proceedings of the World Conference on Timber Engineering, Oslo, Norway, 19–22 June 2023; pp. 1–7.
35. Vetter, Y. Investigating the Behaviour of Short-Span FRP-Reinforced Glulam Beams. 2022. Available online: http://hdl.handle.net/10012/18457 (accessed on 20 July 2022).
36. Lacroix, D.; Doudak, G. Experimental and analytical investigation of FRP retrofitted glued-laminated beams subjected to simulated blast loading. *J. Struct. Eng.* **2018**, 144. [CrossRef]
37. Sulik, P.; Sędłak, B. General Rules for Research of Fire Resistance of Wooden Components [Ogólne Zasady Dotyczące Badań Odporności Ogniowej Elementów Drewnianych]. IZOLACJE 10/2019. Available online: https://www.izolacje.com.pl/artykul/sciany-stropy/193406,ogolne-zasady-dotyczace-badan-odpornosci-ogniowej-elementow-drewnianych (accessed on 18 November 2019).
38. Rozporządzenie Ministra Infrastruktry z Dnia 12 Kwietnia 2002 r. w Sprawie Warunków Technicznych, Jakim Powinny Odpowiadać Budynki i ich Usytuowanie. (DzU Nr 75 poz. 690) z Późniejszymi Zmianami (DzU 2015 poz. 1422 t.j.). Available online: https://isap.sejm.gov.pl/isap.nsf/DocDetails.xsp?id=wdu20020750690 (accessed on 15 June 2002).
39. Obwieszczenie Ministra Rozwoju i Technologii z Dnia 15 Kwietnia 2022 r. w Sprawie Ogłoszenia Jednolitego Tekstu Rozporządzenia Ministra Infrastruktury w Sprawie Warunków Technicznych, Jakim Powinny Odpowiadać Budynki i Ich Usytuowanie. Available online: https://isap.sejm.gov.pl/isap.nsf/DocDetails.xsp?id=WDU20220001225 (accessed on 9 June 2022).
40. *PN-EN 1995-1-2:2008*; Projektowanie Konstrukcji Drewnianych. Cz. 1–2: Postanowienia Ogólne—Projektowania Konstrukcji z Uwagi na Warunki Pożarowe. Polish Committee for Standardization: Warsaw, Poland, 2008.
41. Wdowiak-Postulak, A.; Gocál, J.; Bahleda, F.; Prokop, J. Load and Deformation Analysis in Experimental and Numerical Studies of Full-Size Wooden Beams Reinforced with Prestressed FRP and Steel Bars. *Appl. Sci.* **2023**, *13*, 13178. [CrossRef]
42. Wdowiak-Postulak, A. Natural Fibre as Reinforcement for Vintage Wood. *Materials* **2020**, *13*, 4799. [CrossRef]

43. Wdowiak, A. Structural and Strength Properties of Bended Wooden Beams Reinforced with Fiber Composites. Ph.D. Thesis, Kielce University of Technology, Kielce, Poland, 12 April 2019.
44. *ACI 440.1R-06*; Guide for the Design and Construction of Structural Concrete Reinforced with FRP Bars. American Concrete Institute: Farmington Hills, MI, USA, 2006.
45. Catalog—POLPREK Composite Bars for Concrete Reinforcement, Part II—Guide for Designers. Available online: https://www.firmybudowlane.pl/firma/polprek-sp-z-oo,d8zdb.html (accessed on 16 March 2016).
46. *PN-EN 14080:2013-07*; Konstrukcje Drewniane—Drewno Klejone Warstwowo i Konstrukcyjne Sklejone Drewno Lite—Wymagania. Polish Committee for Standardization: Warsaw, Poland, 2013.
47. *PN-D-94021:2013-10*; Coniferous Construction Timber Sorted by Strength Methods. Polish Committee for Standardization: Warsaw, Poland, 2013.
48. Available online: https://www.mapei.com/pl/pl/produkty-i-rozwiazania/lista-produktow/informacje-o-produktach/mapewrap-31 (accessed on 22 November 2023).
49. *PN-EN 408+A1:2012*; Timber Structures—Structural Timber and Glued Laminated Timber—Determination of Some Physical and Mechanical Properties. Polish Committee for Standardization: Warsaw, Poland, 2012.

materials

MDPI

Article

Computational Complexity and Its Influence on Predictive Capabilities of Machine Learning Models for Concrete Mix Design

Patryk Ziolkowski

Faculty of Civil and Environmental Engineering, Gdansk University of Technology, Gabriela Narutowicza 11/12, 80-233 Gdansk, Poland; patziolk@pg.edu.pl; Tel.: +48-58-347-2385

Abstract: The design of concrete mixtures is crucial in concrete technology, aiming to produce concrete that meets specific quality and performance criteria. Modern standards require not only strength but also eco-friendliness and production efficiency. Based on the Three Equation Method, conventional mix design methods involve analytical and laboratory procedures but are insufficient for contemporary concrete technology, leading to overengineering and difficulty predicting concrete properties. Machine learning-based methods offer a solution, as they have proven effective in predicting concrete compressive strength for concrete mix design. This paper scrutinises the association between the computational complexity of machine learning models and their proficiency in predicting the compressive strength of concrete. This study evaluates five deep neural network models of varying computational complexity in three series. Each model is trained and tested in three series with a vast database of concrete mix recipes and associated destructive tests. The findings suggest a positive correlation between increased computational complexity and the model's predictive ability. This correlation is evidenced by an increment in the coefficient of determination (R^2) and a decrease in error metrics (mean squared error, Minkowski error, normalized squared error, root mean squared error, and sum squared error) as the complexity of the model increases. The research findings provide valuable insights for increasing the performance of concrete technical feature prediction models while acknowledging this study's limitations and suggesting potential future research directions. This research paves the way for further refinement of AI-driven methods in concrete mix design, enhancing the efficiency and precision of the concrete mix design process.

Keywords: applied machine learning; buildings; cement; concrete mix design; concrete strength prediction; concrete; construction industry; data mining; green building; innovation; sustainability; sustainable development; sustainable

Citation: Ziolkowski, P. Computational Complexity and Its Influence on Predictive Capabilities of Machine Learning Models for Concrete Mix Design. *Materials* **2023**, *16*, 5956. https://doi.org/10.3390/ma16175956

Academic Editors: Krzysztof Schabowicz and Eddie Koenders

Received: 18 July 2023
Revised: 24 August 2023
Accepted: 25 August 2023
Published: 30 August 2023

1. Introduction

The field of concrete mix design has seen significant advancements in recent years with the integration of machine learning techniques. The ability of these models to predict the compressive strength of concrete has the potential to revolutionise the construction industry by providing more efficient and accurate methods for mix design. However, the prediction accuracy of these models depends on many factors, including the computational complexity of the model itself. This study aims to investigate the influence of computational complexity on the prediction accuracy of concrete compressive strength in machine learning models for concrete mix design. The findings of this research will provide insights into the trade-off between model accuracy and computational efficiency and will guide the development of more effective machine learning models for concrete mix design in the future. The concrete mix composition consists of cement, water, a combination of fine and coarse aggregates, and supplementary materials referred to as additives and admixtures, where additives are incorporated during the cement manufacturing stage, whereas admixtures are introduced during concrete mix preparation. These substances are formulated to enhance the chemical

properties and performance of concrete, specifically with regard to compressive strength, durability, and workability. There are various types of additives and admixtures [1–4], including accelerators, substances that improve fresh concrete properties [5], materials that enhance durability, fibres that reinforce concrete [6], set-retarding admixtures, and water-reducing agents.

Properly designing a concrete mixture is a crucial aspect of the construction process, with multiple factors to consider. It should be designed with economy in mind, ensuring that the desired properties can be achieved using the most cost-effective raw materials. The mixture must also be optimised for the specific technology used in the construction process, considering elements such as workability and setting speed. Environmental conditions, such as temperature [7,8], precipitation, distance away from the construction area, as well as the volume of traffic, must also be considered when designing the concrete mix. The final composition of the mix is determined by construction specifications, such as the desired compressive strength or resistance to environmental elements such as chloride ingression and, increasingly, ecological considerations, such as low emissivity. To address environmental concerns, various solutions exist to reduce concrete carbonation, including admixtures of graphene nanoparticles. Designing a concrete mix involves selecting the proper proportions of primary and secondary components to achieve the desired properties. Once the mix is prepared, it is conveyed to the construction location and poured into the formwork, where it undergoes the progression of hardening and increasing strength. The hardening process is initiated by the cement's hydration, which involves a heat-releasing chemical reaction that occurs upon contact between cement and water [9]. The reaction initiates the formation of various components, such as tobermorite gel [10], hydroxide, as well as additional components, which improve the bonding between coarse and fine aggregates. During this procedure, the hydration products steadily accumulate on the cement grains and replace the water in the mixture. The ultimate hydration stage occurs when all the water molecules are fully integrated, or no unreacted cement is left in the mixture. After the hydration process begins, hardened concrete acquires some of its compressive strength within a few days, and most of its compressive strength is attained after roughly 28 days (although some types of concrete may take longer to reach their full strength). The quantity of water required to hydrate the cement completely ranges from 20% to 25% of its weight, excluding water trapped in pores. However, specific models suggest that 42% of the cement's weight is needed for proper hydration [11]. The design methods for concrete mixtures currently employed in engineering practice have been derived from solutions developed more than a decade ago and rely on estimating the bending strength of the concrete mortar. Implementing these techniques in practice might be a tedious and inefficient process that does not consider the intricate chemical composition and variability of modern concrete mixes. The current challenges in the field at hand necessitate novel technological solutions. Machine learning-based methods could offer a promising avenue, as they have demonstrated varying degrees of success in predicting concrete compressive strength.

Machine learning, a prominent subfield of artificial intelligence, has garnered significant attention in recent years due to its vast applications and transformative potential across various domains. The fundamental concept behind machine learning involves empowering computers to acquire knowledge from data, recognize patterns, and arrive at informed choices while minimizing the need for extensive human involvement. By utilising algorithms and statistical models, machine learning systems can adapt and improve their performance over time, making them valuable tools for a multitude of tasks, ranging from natural language processing [12] and image recognition [13] to real estate value forecasting [14–17] and medical purposes [18]. The foundation of machine learning lies in its ability to extract knowledge from data, which is achieved by employing various learning paradigms. These paradigms include supervised, unsupervised, and reinforcement learning, each catering to different problem domains. Supervised learning, the most common approach, involves training a model using labelled data with known outcomes, while unsupervised learning deals with discovering hidden structures in unlabelled data [19].

Reinforcement learning, on the other hand, focuses on learning through trial and error, with a model receiving feedback in the form of rewards or penalties [20,21]. A plethora of algorithms have been developed for each learning paradigm, and the choice of the algorithm largely depends on the specific problem and the available data. Popular algorithms include linear regression, decision trees, support vector machines, neural networks, and clustering algorithms. These algorithms often involve tuning various parameters, known as hyperparameters, to optimise the model's performance. Machine learning has proven particularly effective in addressing complex problems with high-dimensional data. This has been facilitated by the advent of deep learning, a subset of machine learning that relies on artificial neural networks with multiple layers. These networks, drawing inspiration from the organization and operation of the human brain, excel in acquiring complex patterns and representations from extensive datasets, making them suitable for a diverse array of uses, including natural language processing and computer vision. The success of machine learning in diverse fields has prompted researchers to investigate its potential for predicting and optimising properties of materials, such as concrete.

In this paper, the influence of computational complexity on the performance of machine learning models used for predicting the compressive strength of concrete is explored. This research assessed three sets of five deep neural network models (MLM1, MLM2, MLM3, MLM4, MLM5), each with differing levels of computational complexity. Through an examination of various machine learning models, the goal is to identify the trade-offs between accuracy and computational efficiency. This could provide valuable insights into the development of robust and cost-effective models for concrete mix design.

2. Concrete Mix Design and Machine Learning

2.1. Prediction of Concrete Technical Properties in Concrete Mix Design

Designing an optimal concrete mix is a multifaceted challenge requiring a comprehensive understanding of concrete technology and significant practical experience. The primary objective of the design process is to determine suitable material compositions to achieve the desired properties in fresh concrete during transportation and placement and in hardened concrete. Distinct mechanical properties are anticipated at each stage of the concrete fabrication process. Various characteristics influence concrete performance, including plasticity, durability, compressive strength, and modulus of elasticity. The significance of these properties may vary at different stages, for instance, adequate compressive strength is crucial for the designed ultimate limit state, whereas sufficient durability is critical in aggressive environments. Designing a mix with inappropriate specifications can result in severe consequences. Therefore, fearing noncompliance with the necessary criteria, concrete mix manufacturers often intentionally exceed the designed parameters [22].

Global corporate engineering practices related to concrete technology exhibit considerable variation and notable commonalities. Within the European Union, the primary standard governing concrete technology issues is EN 206 Concrete: Specification, Performance, Production, and Conformity [23], while EN 1992-1-1: Eurocode 2: Design of Concrete Structures [24] provides guidelines for the design of concrete structures. Both standards have national equivalents and appendices, such as DIN EN 206 [25] in Germany and PN-EN 206 + A1: 2016-12 in Poland. Member states of the European Union employ diverse methods for designing concrete mixes. In Poland, the Bukowski, Eyman, Klaus, Kopycinski, and Paszkowski methods are predominantly used alongside the double-coating method. Conversely, the Bolomey, Fuller, and 0.45 power gradation chart methods are more prevalent in the United States. Most of these approaches are derived from the "three equations method" representing a combined experimental-analytical strategy for concrete mix design.

The approach that combines experimental and analytical methods involves determining the required quantity of ingredients through analytical calculations and confirming its accuracy through destructive lab testing. This technique enables the researchers to establish the proportions of cement, water, and aggregate by weight for a given volume, employing three formulas related to consistency (1), strength (2), and impermeability (3). The con-

sistency formula (1) is integrated into the water requirement equation, which assists in identifying the optimal consistency. The demand for water in cement and aggregate relies on factors such as particle size, form, texture, ratio within the mixture, and the desired consistency of the concrete blend. To account for the water needs of concrete additives and admixtures, they are added to the aggregate or cement based on the particle dimensions. Factors such as grain size, shape, surface roughness, composition proportion, and the concrete mix's required consistency influence the cement–water and aggregate–water demand indices created by Bolomey and Stern [26].

$$W = \mathrm{C}\cdot w_c + \mathrm{K}\cdot w_k, \tag{1}$$

$$f_{cm} = A\left[\left(\frac{\mathrm{C}}{W} + p\right) - a\right], \tag{2}$$

$$f_{cm} = A_{1,2}\left(\frac{\mathrm{C}}{W} \pm a\right), \tag{3}$$

$$\frac{\mathrm{C}}{\rho_c} + \frac{\mathrm{K}}{\rho_k} + W = 1000, \tag{4}$$

In Equation (1), W denotes the volume of water (in litres) present in one cubic meter of concrete. The weight of cement in one cubic meter of concrete is represented by C (in kilograms). The cement–water demand index w_c, indicates the volume of water (in litres per kilogram) required to be combined with one kilogram of a specific cement class in one decimetre cubed. K represents aggregate weight in one cubic meter of concrete, measured in kilograms. Lastly, the aggregate–water demand index w_k, signifies the volume of water (in litres per kilogram) needed to be added to one kilogram of a certain dry aggregate fraction to achieve the desired consistency. The subsequent formula, called the concrete compressive strength formula, exists in two variations: Bolomey and Feret. This formula illustrates the connection between concrete compressive strength and factors such as water–cement ratio, cement grade, and aggregate grade. The Feret and Bolomey versions of the formula are represented by Equations (2) and (3), respectively. In these equations, f_{cm} denotes the average concrete compressive strength in MPa, while A, A_1, and A_2 are coefficients contingent upon the aggregate's type and strength class and the cement's strength class. A_1 is utilised when the cement-to-water ratio (C/W) is less than 2.5, and A_2 is employed when the ratio exceeds 2.5. In the equations, C signifies the cement weight in 1 cubic meter of concrete (measured in kg), W represents the water quantity in 1 cubic meter of concrete (measured in L), p is the air content in one cubic meter of concrete (measured in dm^3), and a is a numeric value that depends on cement and aggregate quality, typically considered constant equal to 0.5. The a value is positive for water–cement ratios greater than or equal to 2.5, while it is negative for ratios below 2.5. The Feret equation is applicable when the aggregate strength is inferior to the grout strength, specifically in the case of porous concrete. The water-tightness equation, designated as Equation (4), asserts that the total volume of individual components in a concrete mix is equivalent to the mix's overall volume. In this equation, W signifies the water content in litres per cubic meter (m^3) of concrete, while C stands for the cement weight in kilograms per cubic meter (m^3) of concrete. Additionally, ρ_c represents the density of cement in kg/dm^3, K denotes the weight of cement in kg per cubic meter (m^3) of concrete, and ρ_k refers to the aggregate density in kg/dm^3. Using the equations mentioned above, one can determine the quantitative composition of a concrete mix, which consists of the quantities of cement, water, and aggregate in a cubic meter (m^3) of the mixture. The three equations method does have specific boundary constraints, for instance, the porosity of the concrete mix must not surpass 0.002 of the mix volume without air-entraining additives or 0.008 of the mix volume when incorporating air-entraining additives.

The process of creating a concrete mix design incorporates several steps such as formulating initial suppositions, defining the necessary characteristics of both the fresh and cured

concrete, selecting and assessing the components of the mix, crafting the blend, testing its properties in a lab setting, and finally devising a workable formula. In formulating initial suppositions, key considerations include the concrete's intended application and the specific traits of the new structure. These factors include location, degree of reinforcement, and the structural cross-section's geometric properties. The primary attributes of interest for fresh concrete are its bulk density, consistency, and air content. As for the hardened concrete, we look at its frost and fire resistance and the grade of its compressive strength. It is essential to scrutinise the technological process and evaluate the conditions under which the concrete matures and the method used for compacting the fresh mix. The concrete exposure class is a significant parameter, defining the level and nature of environmental stress the material can withstand. Further specifications such as the concrete's impermeability need to be established. Parameters such as maximum aggregate size and mix workability also need determination. The components of the concrete mix, including the appropriate type of cement, water, and aggregate quality, should be selected and appraised as per relevant standards. Following the mix design and lab tests, the final stage involves creating a functional formula for one cubic meter of the concrete mix. One should also anticipate potential recipe modifications due to the aggregate's moisture content and adjust it according to specific circumstances, such as the transportation vehicle's capacity [27,28].

2.2. Machine Learning in Prediction of Concrete Technical Properties

Machine learning has permeated numerous scientific domains, showcasing its versatility and potency. It has a particularly large number of applications in the field of structural and material engineering. Machine learning has found use within this branch of science in areas such as structural health monitoring, crack detection, life-cycle cost assessment, or prediction of diffusivity [29]. Particular interest has been shown in predicting technical properties [30], most of which were devoted to concrete compressive strength prediction.

The complexities of predicting concrete strength through machine learning were first articulated by Yeh et al. [31] in 1998. They experimented with seven input variables using artificial neural networks (ANN) and linear regression to forecast the strength of high-strength concrete. While their model was trained on a vast array of concrete samples, these were not scrutinised for content. Their study considered concrete samples in the maturing phase, including those as young as three days old, which may have led to skewed results.

In 2003, this subject was further refined by Seung-Chang Lee [32], who employed a unique, modular network architecture consisting of five ANNs. Each ANN represented concrete at various stages of maturation up to its maximum strength. Lee used the parameter condensation technique to ascertain the number of neurons in the input layer. Despite claiming his condensation and weighing techniques as beneficial for optimal network performance, the practicality of his ANN model, which illustrates the maturation process from pouring to full strength, is questionable. From an engineering perspective, attention should be devoted to concrete that has achieved full or near-full strength.

In 2005, Hola, J. and Schabowicz, K. [33,34] introduced a novel nondestructive approach for assessing concrete strength. Rather than relying on the concrete mix composition, they trained their ANN model on data obtained from nondestructive concrete testing tools. Their database incorporated ultrasonic wave velocity, reflection number, hardness, pull-out strength, concrete age, and bulk density. To evaluate their lab results, they experimented on concrete compressive strength samples with a 28-day strength ranging from 24 to 105 MPa. Using the Levenberg–Marquardt training method, they developed the ANN with eight hidden neurons within one layer. The authors posited that the average compressive strength comparison between the ANN and nondestructive tests was comparable.

In 2006, a neural-expert system for predicting the compressive strength of high-performance concrete was proposed by Gupta et al. [35]. They focused on training the algorithm through example inferences, employing a multilayer ANN trained with generalised backpropagation for interval training patterns. They also used input variables from unrelated metrics, such as curing time, that were unrelated to the recipe. However,

these strategies may lead to algorithm training based on insignificant patterns and unclear results. The use of a neural-expert system for concrete compressive strength prediction was also explored by Dac-Khuong Bui et al. [36] with a focus on the practical application of this method.

The advent of deep learning in this field was introduced by Fangming Deng et al. [37] in 2018. They prepared a database of recycled concrete samples for algorithm training. They chose not to train the algorithm on the concrete mix composition with direct amounts of individual components, but they called deep features on several ratios. This approach was emulated in the current study with the inclusion of feature scaling. Deng and his team used Softmax regression to identify a suitable prediction model. They claimed that deep learning compared to ANN, provided better generalisation capabilities, superior efficiency, and greater precision. However, these claims were not definitive and warranted further research. Given that convolution neural networks are computationally costly, the authors used a limited database of 74 samples compared to 741 in the current study. This limited sample size might lead to underfitting, implying a model that does not fully capture the modelled phenomenon. A comparable level of accuracy between artificial neural networks and deep neural networks was reported by Hosein Naderpour et al. [38] in 2018.

Ziolkowski, P. et al. [39] introduced an algorithm in 2019 that assists in designing a concrete mix by predicting the strength based on the mix composition. While this algorithm accurately predicted the strength of the concrete mix, it underperformed in the high-strength spectrum of 40 MPa and beyond and was insufficient in predicting the properties of mixtures with additives and admixtures. Furthermore, it neglected other essential parameters that contribute to concrete's performance, such as durability, which is essential for maintaining structural service quality over time [40].

In a publication from 2020, Nunez, I. and his team [41] shared insights on using machine learning to accurately forecast the compressive strength of recycled aggregate concrete, consequently refining the concrete mix design process. The researchers recognised the critical importance of an effective optimisation method for concrete mix design in light of the inherent variability and the absence of reliable compressive strength prediction formulae for recycled aggregate concrete. Three innovative machine learning models were developed in their study, specifically the Gaussian process model, the recurrent neural network model, and the gradient-boosted regression tree model. Based on their findings, they reported superior predictive outcomes, particularly with the gradient-boosted regression trees model.

Another noteworthy contribution from the same year is a study by Marani, A. and his colleagues [42], who explored the use of machine learning to forecast the compressive strength of ultra-high-performance concrete. Their algorithm was trained on a comprehensive dataset of 810 samples from freely accessible resources, encompassing 15 variables as input data. Rather uniquely, they capitalised on their dataset to generate 6513 records, a substantial number of synthetic data samples, using tabular generative adversarial networks. The wealth of data facilitated a more robust training of their machine learning model. Upon evaluation, the model trained with synthetic data yielded exceptional predictive performance when assessed with the primary dataset.

In 2021 Ziolkowski, P. et al. [43] introduced a new adaptive machine learning method that more precisely estimates the compressive strength of concrete based on the composition of its primary ingredients. Unlike previous models that had mixed success in forecasting concrete strength and struggled to encapsulate the variability inherent in current concrete mixes, this method incorporated two observations for each concrete batch in the model. The authors built this machine learning model using a deep neural network architecture and trained it on a comprehensive database of concrete recipes before translating it into a mathematical formula. The algorithm was tested on four concrete mix recipes calculated using contemporary design methods such as Bolomey and Fuller, with the findings revealing that this new algorithm outperformed nonadaptive models trained on the same dataset.

Adil, M. et al. [44] investigated the effect of the number of neurons and layers in ANN for generalised concrete mix design. They developed an ANN with 17 inputs and five outputs related to the concrete mix's composition and properties. The authors proposed optimising the network with one or two hidden layers. It represented a significant departure from previous work, where concrete's technical parameters were predicted based on the composition ratio.

Feng, W., in their paper [45] explores the mechanical characteristics of rubber-modified recycled aggregate concrete (RRAC). The authors utilised machine learning (ML) models to predict these thermomechanical properties of RRAC, employing a unique algorithm called the beetle antennae search (BAS) to tune the hyperparameters of these models. Four ML models were tested: random forest, logistic regression, multiple linear regression, and back-propagation neural network (BPNN). Among them, BPNN yielded the most accurate and reliable UCS and peak strain predictions, suggesting that ML models, particularly BPNN, can serve as robust tools for predicting the properties of sustainable construction materials such as RRAC. This study highlights the potential of RRAC in sustainable construction and the effective use of ML models in predicting its performance.

Tavares, C. et al., in their two-part study [46,47], proposed an innovative method that utilises machine learning (ML) for the optimised mixture design of ultra-high-performance concrete (UHPC). This methodology presents an attractive alternative to resource-consuming experimental runs by employing orthogonal arrays for data collection, which could enable ML design optimisation. The researchers used an ensemble of ML techniques, specifically random forest and k-nearest neighbours, to create performance density diagrams (PDDs). These diagrams serve as an intuitive tool to demonstrate the trade-offs between mix proportions and mechanical performance of UHPC, providing practical assistance to designers in the construction industry. Their research has shown promising results, where the PDDs effectively predicted the behaviour of most mixtures in the test set. This method facilitated the design of a UHPC mixture averaging 155 MPa at age 56 days, maintaining the fine-aggregate-to-cementitious-material ratio above the unit. It represents a substantial advancement in developing mix design tools for UHPC, leading to cost and eco-efficiency improvements. Notably, this methodology was further extended in the second part of their study to allow simultaneous evaluation of performance, cost, and carbon footprint. This approach lays a foundation for the broader adoption of ML techniques in sustainable construction and the development of mix designs for UHPC.

Endzhievskaya, I.G. et al. [48] presented a study on road concrete's physical and mechanical characteristics. The authors employed machine learning techniques, specifically a random forest and decision trees. These methods were advantageous due to their ease of use, minimum hyperparameters for tuning, and the ability to predict with low errors. Their findings indicate that components such as air-entraining additives and specific sizes of crushed stone contribute significantly to improving compressive and bending strengths. Machine learning's predictive accuracy demonstrated its potential in optimising road concrete mixtures, enhancing road surfaces' quality and service life.

The study presented by Taffese, W.Z. and Espinosa-Leal, L. [49] stands out in concrete properties prediction. Their research leverages machine learning, specifically decision tree-based ensemble methods, to develop multitarget models predicting compressive strength and nonsteady-state chloride migration coefficients (D_{nssm}) of concrete. This work's novelty lies in developing a single model that simultaneously predicts two crucial concrete properties, compressive strength and D_{nssm}. The gradient boosting model demonstrated the most impressive prediction accuracy, yielding the mean absolute error (MAE) of 6.683 and 1.363, mean squared error (MSE) of 83.369 and 3.712, and root mean squared error (RMSE) of 9.131 and 1.927 for compressive strength and D_{nssm}, respectively. The authors stress the necessity to expand the model with comprehensive datasets encompassing a wider range of concrete properties to improve its versatility.

3. Materials and Methods

3.1. Essentials

Machine learning models can be used to predict concrete's technical properties based on the mix composition. This study tries to determine the impact of increasing the computational complexity of the artificial neural network on the model's performance. The quantity of layers is one of the deep neural network (DNN)'s [50,51] features that represents a critical determinant of model complexity and its inherent capability to discern and replicate complex patterns embedded in the data. This aspect forms the basis of the term "deep" within deep learning, where an increased number of layers, representing greater depth, facilitates the modelling of progressively intricate and abstract features. Each layer within a DNN can be conceptualised as performing successive transformations of the raw input into higher-level, abstract features. For instance, in applying convolutional neural networks (CNNs) [52–54], commonly used for image recognition tasks, initial layers may decipher basic, low-level features such as edges and colours. As the depth of the network increases, subsequent layers amalgamate these rudimentary features to detect more abstract patterns, encompassing shapes and, ultimately, entire objects or scenes.

However, while an increased depth can enable a model to learn more complex representations, it poses new challenges. The augmentation in the number of layers directly expands the model's parameters, thereby escalating the risk of overfitting. Overfitting manifests when a model excessively adapts to the training data, compromising its ability to generalise to unseen data effectively [55–57]. This becomes particularly problematic when the volume of available training data is limited compared to the complexity of the model. Furthermore, training highly deep networks introduces additional technical difficulties. One notable issue is vanishing or exploding gradients, which can decelerate training or result in suboptimal solutions [58,59]. Techniques such as parameter initialisation, batch normalisation, and incorporating residual connections have been suggested to alleviate these concerns. Consequently, the selection of an optimal layer quantity necessitates a delicate balancing act, taking into account the trade-off between a network's capacity to model intricate patterns (which tends to increase with depth) and the potential challenges associated with overfitting and training difficulties. Strategies such as early stopping, dropout, and using validation sets can help to manage the risks inherent to increased depth [60–62]. Despite these challenges, the capacity to train deep networks remains a pivotal factor propelling recent advancements in artificial intelligence and machine learning.

The analysis adopted a classical approach involving the construction of a model that will estimate the concrete compressive strength determined by the quantitative concrete mix composition. The prepared analysis used a database from previous studies [39,43], which contains several hundred records of concrete recipes, along with corresponding destructive compressive strength tests on normalised samples in the laboratory. The number of records has been increased by using a dedicated AI model to generate reliable synthetic data [63–65]. The database used contains recipes for the concrete mix composition, which were designed as intended for incorporation into various concrete elements. At the same time, differentiation of dimensions, functions, and purpose is assumed here. Some recipes contained admixtures for various purposes, such as workability improvers, plasticisers or setting retarders. It is taken for granted that the concrete production process employed met the necessary quality standards. However, due to varying design requirements and the use of different admixtures, some differences between formulations may be difficult to quantify. Therefore, the procedure of removing univariate outliers as multiples of the standard deviation was used, described in detail later in the paper. Individual components of concrete mixes and the water–cement ratio were assigned input variables, while the concrete compressive strength was treated as the output variable. The presented study, along with many studies in the literature, focuses on predicting one of the main technical properties of concrete, which is concrete compressive strength. However, it should be noted that many other technical properties affect the final behaviour of concrete, especially at various stages of the technological production process. The quality of this process is also

essential, which is influenced by factors such as the curing process [66,67] or the concrete pouring temperature [68]. Figure 1 shows a flowchart illustrating the research procedures outlined in this investigation.

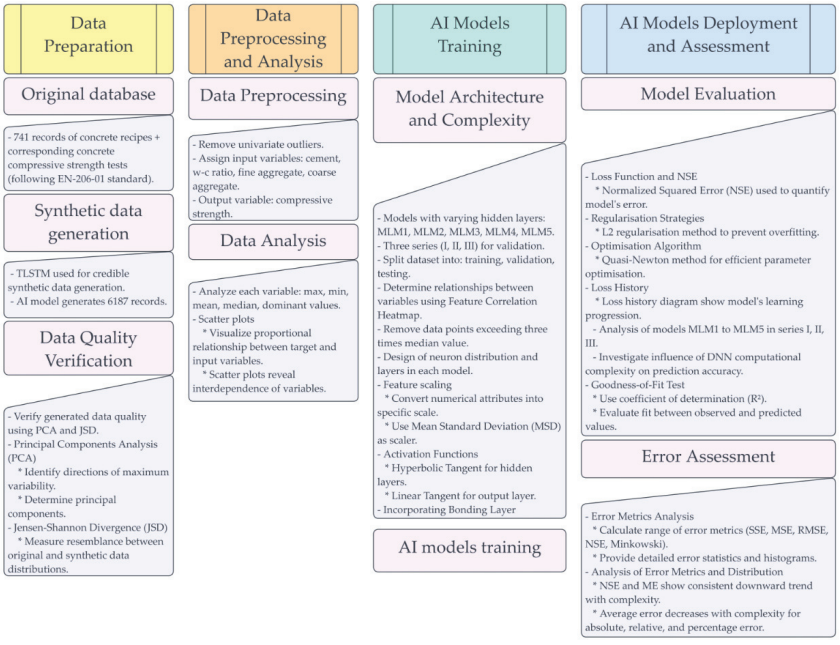

Figure 1. Flowchart showing the procedures described in this study.

3.2. Data Processing

The database used in this research contains 6187 records, generated using a dedicated AI model from the original database that contained 741 records of concrete recipes [39,43], along with corresponding compressive strength tests conducted under laboratory conditions on standard samples according to PN-EN: 206 [23]. This set has six variables, as follows: f_{ck}—concrete compressive strength (MPa), C—cement (kg/m^3), W—water–cement ratio (-), FA—fine aggregate (kg/m^3), CA—coarse aggregate (kg/m^3). These synthetic data do not create new knowledge but helps to achieve better robustness of the AI model. The parameters utilized have been showcased in Table 1. A fundamental statistical analysis was prepared for each variable in the analysed dataset. Table 2 shows each variable's maximal, minimal, mean, median, and dominant values.

Table 1. The parameters utilized within the dataset.

Parameter	Concrete Compressive Strength	Cement	Water–Cement Ratio	Fine Aggregate	Coarse Aggregate
Type	Target	Input	Input	Input	Input
Description	The 28-day compressive strength of concrete that is considered to have most of its strength (MPa).	Content of cement added to the mixture (kg/m^3).	Water-to-cement ratio (-).	Content of fine aggregate added to the mixture (kg/m^3).	Content of coarse aggregate added to the mixture (kg/m^3).

Table 2. Ranges of input variables for the database.

Input Variable	Minimum	Maximum	Mean	Median	Dominant
Cement	87.00 kg/m^3	540.00 kg/m^3	322.15 kg/m^3	312.45 kg/m^3	380.00 kg/m^3
Water–cement ratio	0.30	0.80	0.58	0.58	0.58
Fine aggregate	472.00 kg/m^3	995.60 kg/m^3	767.96 kg/m^3	774.00 kg/m^3	594.00 kg/m^3
Coarse aggregate	687.80 kg/m^3	1198.00 kg/m^3	969.92 kg/m^3	963.00 kg/m^3	932.00 kg/m^3

The tabular long short-term memory (TLSTM) model [69,70] was used to generate credible synthetic data. The experiments were carried out to validate the excellence of the produced data, specifically a principal components analysis (PCA) [71,72] and Jensen–Shannon divergence (JSD) [73–76]. In order to verify the statistical integrity of deeper, multifield distributions and correlations, a comparative analysis was performed using PCA computed first on the original data, then on the synthetic data. The basis of PCA lies in capturing the essential shape of all the features in a few key features, referred to as the principal components. Consider a dataset with just two columns, as graphed below for illustrative purposes. PCA can be visualised as an exercise in fitting an ellipsoid to the data, where the axis of the ellipsoid, signifying the directions of maximum variability in the data, represents the principal components. In a more complex multidimensional scenario, the objective of PCA becomes analogous to rotating an object in hand to achieve a view of maximal width, which is then determined to be the first principal component. Subsequent rotations, while maintaining horizontal steadiness, aim to achieve the view of maximal height, thus determining the second principal component. The approach is structured around identifying the axis with maximum variability, always maintaining perpendicularity to the previously chosen axis. Consequently, the newly created dimensions encapsulate the essence of the fundamental shape of the data. The quality of synthetic data can be assessed by evaluating the distributional distance between the principal components in the original data and those in the synthetic data. The proximity of the principal components directly influences the quality of synthetic data, with closer principal components yielding better quality. Given the ubiquity of PCA in machine learning for dimensionality reduction and visualisation, this score provides an immediate assessment of the utility of the obtained synthetic data for machine learning applications. The approach hence aims to measure the statistical integrity of the synthetic data by evaluating its conformance to the structure encapsulated in the principal components of the original data. The results of PCA are presented in Figure 2.

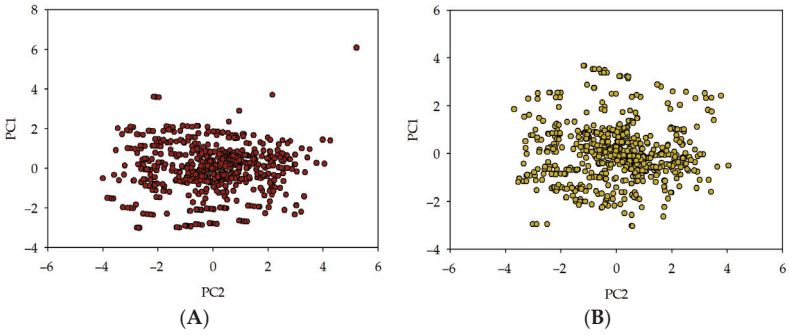

Figure 2. Principal component analysis: training data (**A**), synthetic data (**B**). Training data are the data used to generate synthetic data.

JSD represents the degree of resemblance between the field distributions of the original and synthetic data. It is a method commonly applied for comparing two distributions. The average Jensen–Shannon divergence value across all fields inversely correlates with the

data quality, with lower value indicating higher quality. A visual comparison of the original and synthetic field distributions is facilitated by presenting bar charts in Figure 3.

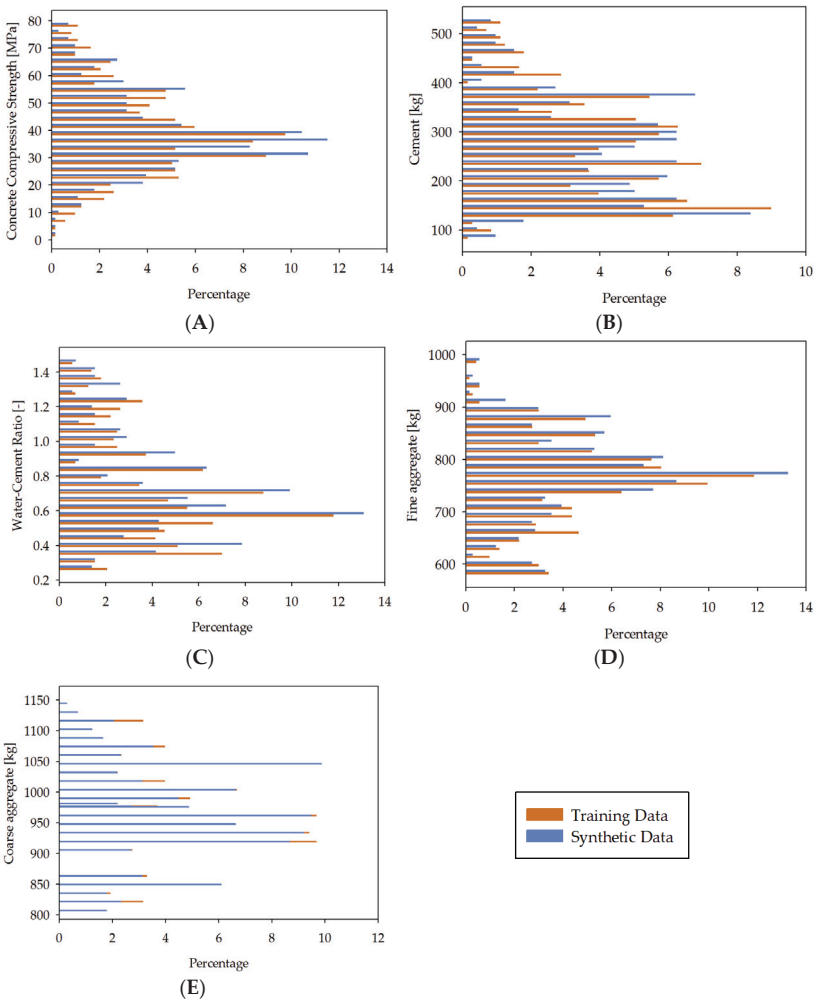

Figure 3. Field distribution comparisons: concrete compressive strength (**A**), cement (**B**), water–cement ratio (**C**), fine aggregate (**D**), coarse aggregate (**E**). Purple bars correspond to training data. Green bars correspond to synthetic data. Vertical axes are percentages.

The compressive strength of concrete was assessed in a laboratory setting utilising standardised samples under the EN-206-01 standard [77]. The samples in question, standardised as per the specifications, were cylinders with a diameter of 15 cm and a hight of 30 cm and cubes with a side length of 15 cm. The results were presented as the compressive strength of cylindrical samples, while the results from the cubic samples were converted according to the standard mentioned above [77] to represent the strengths obtainable from cylindrical samples. The samples were fabricated using ordinary portland cement, and the sand employed was free from clay contamination. As per the EN-206-01 standard [77], the strength was examined after 28 days, generally when the concrete attained full strength. It should be emphasised that the time required for concrete to achieve full strength mainly depends on the type of cement used, and for some types of cement, this period may be

longer or shorter. However, it was assumed that the cement used in the mixture did not result in any reduction or extension of the time to achieve strength. To standardise the investigation, samples without full strength were excluded from the dataset. The quantity of records mentioned above is devoid of such samples. Due to the fact that all ANN has been trained on specific datasets, it is advisable to operate within the maximum values of the model's input parameters and preferably avoid deviant areas. In some cases, input parameters that fall outside the maximum values of the model can lead to unreliable or inaccurate results.

Figure 4 displays scatter plots that elucidate the proportional relationship between targeted and input variables. The utility of scatter plots as a comprehensive method for scrutinising the interdependence of variables is well-established [78]. It is a visually striking demonstration of the nexus between these two variable categories. Owing to the many possible combinations, only a select number of examples involving target variables were furnished for illustrative purposes. The said plots specifically cater to the objective variable corresponding to the concrete compressive strength.

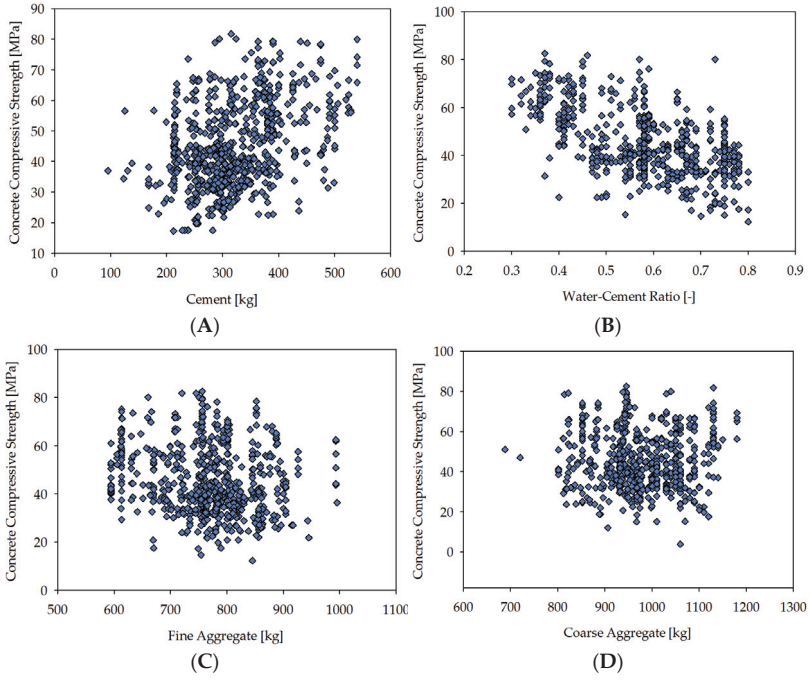

Figure 4. The scatter plots depict the relationship between the input variables and the target variable. The vertical axis represents the compressive strength of concrete in MPa, while the horizontal axis represents input variables: (**A**) cement (kg/m^3), (**B**) water–cement ratio (-), (**C**) fine aggregate (kg/m^3), (**D**) coarse aggregate (kg/m^3).

3.3. Training, Testing, and Model Selection

The above database was used to train a series of deep artificial neural network models. The goal of the analysis is to investigate the influence of the computational complexity of DNNs on the accuracy of predicting technical parameters of concrete. Created models, given the quantitative composition, can estimate the compressive strength of concrete. In the analysis below, five neural network models of varying computational complexity, differentiated by the number of hidden layers (MLM1, MLM2, MLM3, MLM4, MLM5), were compared, repeating the entire process in three series (I, II, III) for validation purposes. From the least complex model, MLM1 has two hidden layers, to MLM5, which has

six hidden layers. The number of neurons in a typical hidden layer is four. Each model has five parameters, four input variables, and one output variable. For effective training of deep neural networks, the dataset is typically divided into three independent parts: training, validation (or selection), and testing. This is a standard procedure applied in deep learning [79,80]. The training set is used to optimise the parameters of the neural network. The validation set allows its effectiveness to be assessed during the learning process and to choose the best model, while the test set is used to evaluate the final performance of the model. An outlier elimination procedure was implemented in the datasets under investigation where any data point exceeding three times the median value of each variable, calculated from the dataset's centre, was excluded. These exclusion criteria, formulated to target univariate outliers, were employed to safeguard the precision and dependability of the subsequent statistical analyses [81,82]. Due to the influential effect of univariate outliers, the potential distortion of results could yield a misinterpretation of the dataset's actual characteristics. Thus, outlier removal enhances the sample's representativeness, contributing to more robust and reliable results. It is essential to acknowledge that this procedure, despite potentially impacting the sample size, is essential in affirming this study's validity. The applied process ensures the statistical integrity of the analyses, reinforcing the reliability of this study's conclusions. The used dataset was allocated as follows: 59.6% of the records (3689) were assigned to the training set, 19.9% (1229 records) to the selection set, 19.9% (1231 records) to the test set, and 0.6% (38 records) were unused. The number of input, target, and unused variables in the final models and the division of subsets are presented in Figure 5.

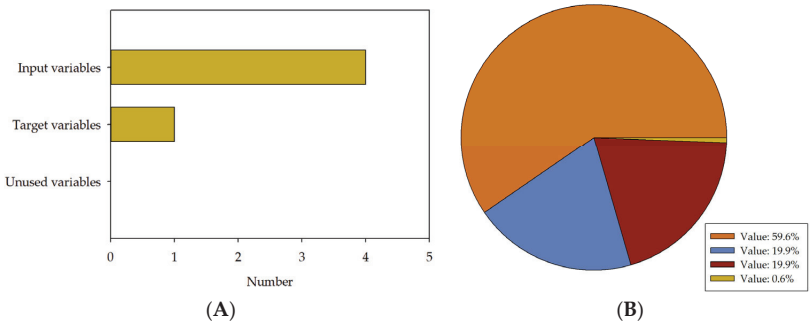

(**A**) (**B**)

Figure 5. Number of input, target, and unused variables in final models and division of subsets. The diagram includes a variable bar chart (**A**) and a sample pie chart (**B**).

The architecture of the first model, MLM1, consists of 20 neurons, including four input neurons, nine neurons spread over two hidden layers, with four neurons in one scaling layer, one neuron in the descaling layer, one neuron in the bonding layer, and one neuron in the output layer. The architecture of the second model, MLM2, consists of 28 neurons, including four input neurons, 17 neurons spread over three hidden layers, with four neurons in one scaling layer, one neuron in the descaling layer, one neuron in the bonding layer, and one neuron in the output layer. The architecture of the third model, MLM3, consists of 36 neurons, including four input neurons, 25 neurons spread over four hidden layers, with four neurons in one scaling layer, one neuron in the descaling layer, one neuron in the bonding layer, and one neuron in the output layer. The architecture of the fourth model, MLM4, consists of 44 neurons, including four input neurons, 33 neurons spread over five hidden layers, with four neurons in one scaling layer, one neuron in the descaling layer, one neuron in the bonding layer, and one neuron in the output layer. The architecture of the fifth model, MLM5, consists of 52 neurons, including four input neurons, 41 neurons spread over six hidden layers, with four neurons in one scaling layer, one neuron in the descaling layer, one neuron in the bonding layer, and one neuron in the output layer. Figure 6 shows the architectures of the models analysed in this research.

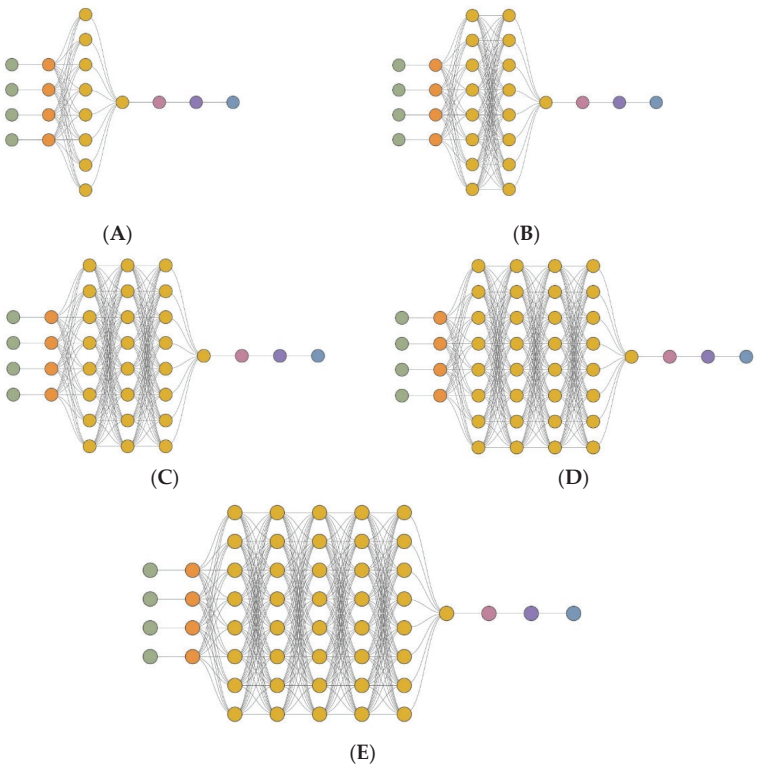

Figure 6. The topology of the deep neural network (DNN) for each model is presented as follows: MLM1 (**A**)**,** MLM2 (**B**), MLM3 (**C**), MLM4 (**D**), and MLM5 (**E**). The figure shows the DNN architecture, which includes input neurons (green), scaling neurons (orange), hidden neurons (yellow), descaling neurons (red), bonding neurons (purple), and output neurons (blue).

The data features, represented as input variables, are assigned to the input neurons of the neural network structure, while the output neuron is connected to the target variables. To enhance the model's effectiveness, a method known as feature scaling was implemented across all models. This process entails converting the numerical attributes of the data into a specific scale [83]. This scaling and the subsequent descaling were carried out using the mean standard deviation (MSD) as a scaler [84]. The models maintain consistent activation functions, with the hyperbolic tangent [85–87] being used for the hidden layers and the linear tangent [87] for the output layer. A bonding layer was also incorporated into the models. The constructed models were meticulously calibrated to minimise the associated loss function. The quantification of the model's error in computing the index loss was executed utilising the normalized squared error (NSE). It is to be noted that lower NSE values are indicative of a model's superior predictive capabilities. Conversely, values tending towards one highlight the model's weaker predictive potential, while values close to zero signify a commendable predictive performance. To further enhance the performance of our model and inhibit the potential for overfitting or underfitting, the adoption of regularisation strategies was necessitated. Specifically, the L2 method [88–90] was instituted as our chosen regularisation function. This regularisation phase is instrumental in tuning the model by minimising the adjusted loss function. It contributes towards mitigating biases and, consequently, facilitates more precise predictions. It is pertinent to underscore the importance of the regularisation step in the model-building process, as it aids in ensuring that the model is absorbing the intrinsic patterns and relationships within the data instead of merely reproducing the training data. In successfully preventing overfitting

and underfitting, a model is deemed accurate and generalisable, rendering it suitable for application to novel, unseen data. In this context, the efficacy of the L2 regularisation method [88–90] is particularly pronounced. It appends a penalty term to the loss function proportional to the square of the magnitude of the network parameters' weights. As a result, the weights are driven towards zero, facilitating the generation of smaller, simpler models less susceptible to overfitting.

The quasi-Newton method [91,92] was employed as the optimisation algorithm in the present study. The quasi-Newton method is a popular choice for optimisation algorithms due to its efficiency and effectiveness in tackling large-scale optimisation problems [92]. It does so by using first-order derivative information to build up an approximation of the Hessian matrix [93], which represents the second-order partial derivatives of the objective function [91]. This method has shown substantial success in solving nonlinear optimisation problems that arise in diverse applications, thanks to its robustness and ability to converge to the solution more quickly than traditional gradient descent algorithms. The quasi-Newton method's effectiveness is enhanced by its ability to handle functions that are not necessarily smooth, making it a versatile tool in optimisation [94]. Employing this algorithm in the current study was an integral part of the process, allowing for the efficient optimisation of the model's parameters. The resulting loss history for the model and series are presented in Figure 7A–C (for series I, II, and III, respectively), illustrating the model's learning progression throughout the training process. The loss history represents how the loss function of a machine learning model changes over the course of its training and selection process. The loss function quantifies the discrepancy between the predicted outputs of the model and the actual target values, and the goal of training is to minimize this loss. The adopted training strategy proved to be highly effective in optimising the model's performance, providing the desired level of accuracy while minimising computational resources.

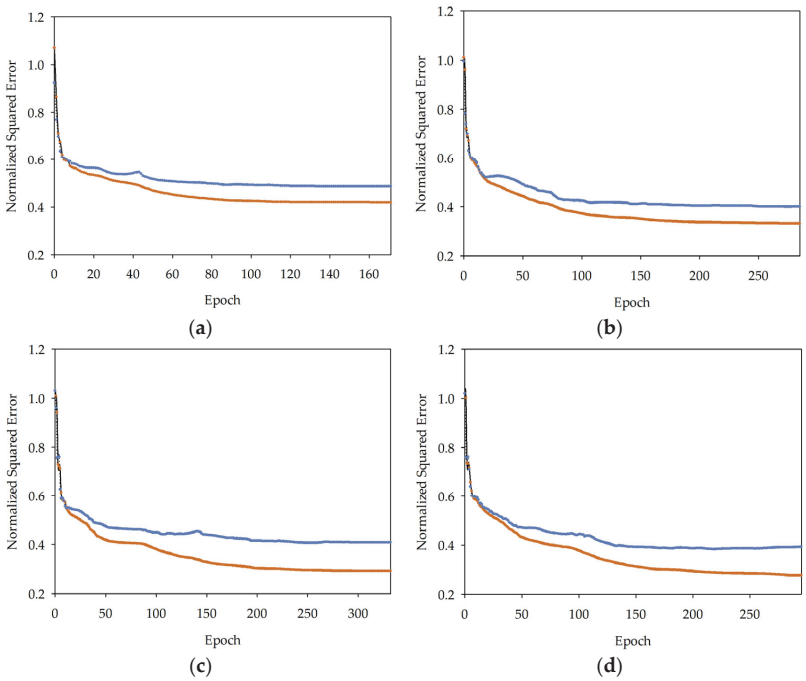

Figure 7. *Cont.*

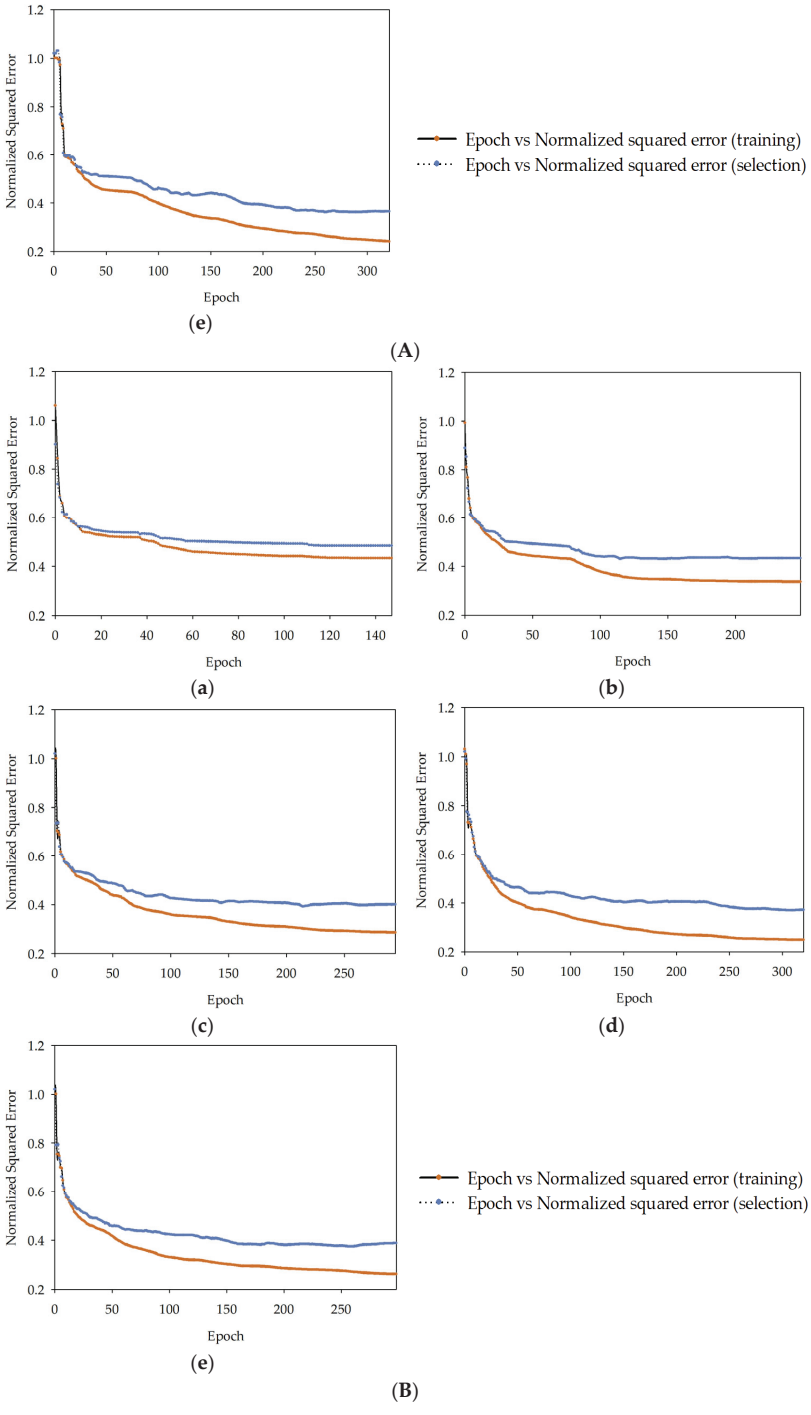

Figure 7. *Cont.*

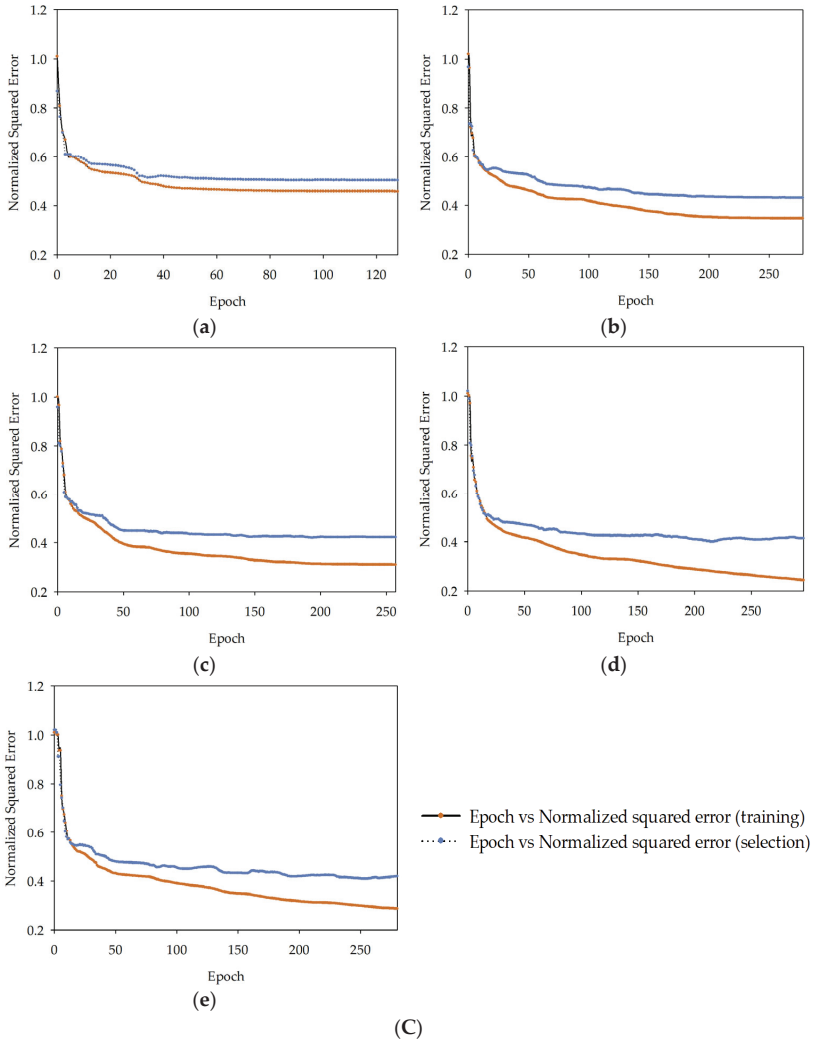

Figure 7. (**A**) Loss history diagram for specific models in series I: MLM1 (epoch from 1 to 171) (**a**), MLM2 (epoch from 1 to 285) (**b**), MLM3 (epoch from 1 to 332) (**c**), MLM4 (epoch from 1 to 295) (**d**), MLM5 (epoch from 1 to 321) (**e**). (**B**) Loss history diagram for specific models in series II: MLM1 (epoch from 1 to 147) (**a**), MLM2 (epoch from 1 to 248) (**b**), MLM3 (epoch from 1 to 294) (**c**), MLM4 (epoch from 1 to 320) (**d**), MLM5 (epoch from 1 to 298) (**e**). (**C**) Loss history diagram for specific models in series III: MLM1 (epoch from 1 to 128) (**a**), MLM2 (epoch from 1 to 278) (**b**), MLM3 (epoch from 1 to 257) (**c**), MLM4 (epoch from 1 to 296) (**d**), MLM5 (epoch from 1 to 280) (**e**).

It should be noted that the models were trained on a specific set of data. Therefore, when using the models, one should operate within the values indicated in Table 2 as minimal and maximal. The following research does not consider the impact of using additives and admixtures on concrete. The usable range for the water–cement ratio extends from approximately 0.3 to beyond 0.8. A proportion of 0.3 results in highly rigid consistency (unless superplasticisers are employed), while a ratio of 0.8 yields concrete that is damp and lacking in strength [95,96]. All records outside the range water–cement 0.3–0.8 have been removed from the dataset.

3.4. Results and Discussion

In the following study, five models of deep artificial neural networks with varying degrees of computational complexity were analysed, named consecutively MLM1, MLM2, MLM3, MLM4, and MLM5, starting from the least complex network to the most complex, in three series I, II, III. First, a feature correlation analysis was prepared to determine precise relationships between individual variables. The result of the analysis is a feature correlation heatmap visible in Figure 8.

	Cement	Fine Aggregate	Coarse Aggregate	WC
Cement	1	−0.321	−0.054	−0.793
Fine Aggregate	−0.321	1	−0.351	0.196
Coarse Aggregate	−0.054	−0.351	1	−0.088
WC	−0.793	0.196	−0.088	1

Figure 8. Feature correlation heatmap.

The feature correlation heatmap reveals the relationships of individual variables, where a value closer to 1.0 indicates a stronger correlation [97]. One can notice that the input variables related to the water–cement ratio and the cement content have the strongest association with the output variable. The relationships of other input variables with the output variable are much weaker, with the amount of fine aggregate having a more significant impact than water content and water content having a greater impact than the amount of coarse aggregate. It can be observed that the impact of the water–cement ratio and the quantity of cement on the strength of concrete is evident. Several research papers in the literature have affirmed the crucial role of these factors in determining the compressive strength of concrete [98].

Each of the models was subjected to a goodness-of-fit test [99–103]. This assessment provides a means to quantify the discrepancy between observed values and those predicted by the model. A standard metric used to gauge the goodness-of-fit in scientific investigations is the coefficient of determination, denoted as R^2 [104,105]. This parameter is utilized to measure the extent of disparity between observed values and projected predictions. More specifically, R^2 determines the fraction of this discrepancy that can be accounted for by the model. In a scenario where the model fit is ideal, resulting in output values perfectly matching the target values, the R^2 coefficient would equate to one. Figure 9A–C provide a detailed visual representation of a goodness-of-fit analysis for series I, II, and III, utilising the statistical measure known as the coefficient of determination (R^2).

In the considered issue, a series of R^2 values were calculated for the target variable f_{ck} in the individual models and series. In series I, it was 0.5691 for MLM1, 0.6268 for MLM2, 0.6053 for MLM3, 0.6438 for MLM4, and 0.6453 for MLM5. In series II, it was 0.5467 for MLM1, 0.6017 for MLM2, 0.6227 for MLM3, 0.6285 for MLM4, and 0.6514 for MLM5. In series III, it was 0.5272 for MLM1, 0.5959 for MLM2, 0.6136 for MLM3, 0.6337 for MLM4, and 0.6571 for MLM5. The values of the coefficient of determination (R^2) for each model are shown in Figure 10.

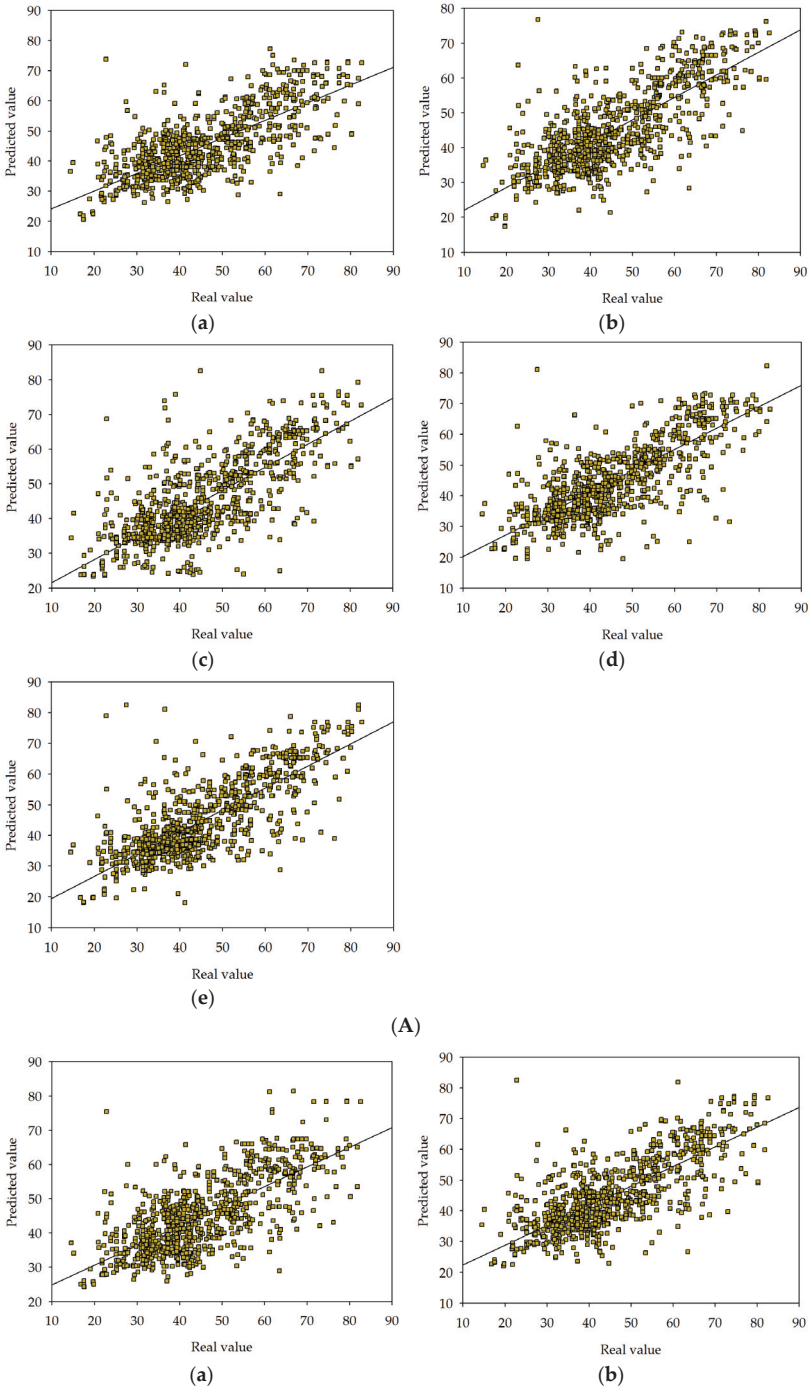

Figure 9. *Cont.*

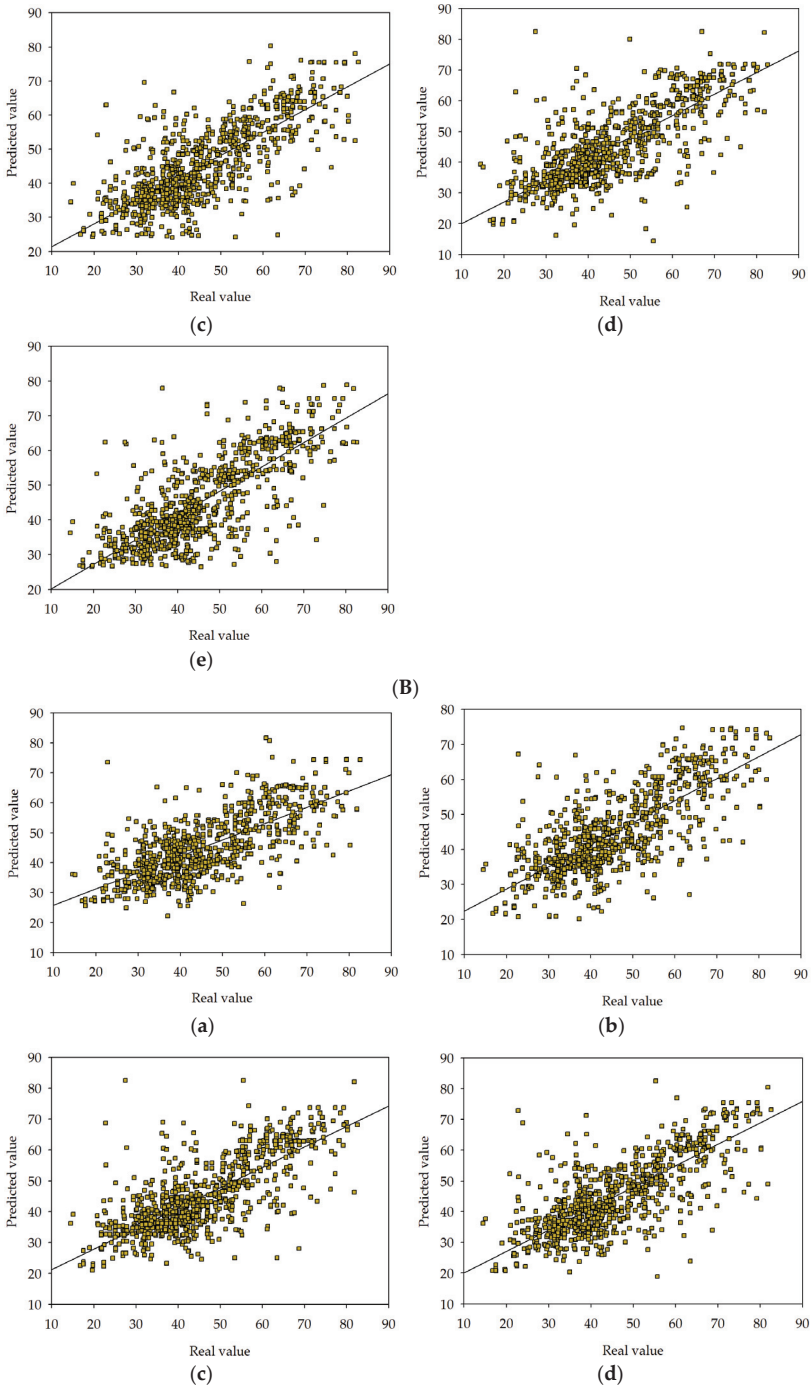

Figure 9. *Cont.*

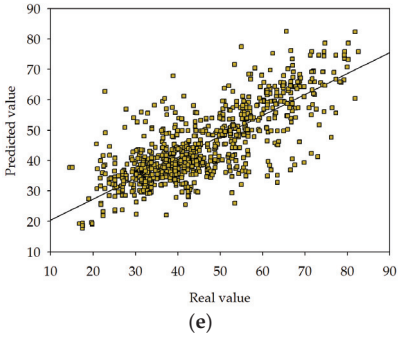

(**e**)

(**C**)

Figure 9. (**A**) Goodness-of-fit chart for MLM1 (**a**), MLM2 (**b**), MLM3 (**c**), MLM4 (**d**), MLM5 (**e**) in series I. The chart shows predicted value of target variable versus real one. (**B**) Goodness-of-fit chart for MLM1 (**a**), MLM2 (**b**), MLM3 (**c**), MLM4 (**d**), MLM5 (**e**) in series II. The chart shows predicted value of target variable versus real one. (**C**) Goodness-of-fit chart for MLM1 (**a**), MLM2 (**b**), MLM3 (**c**), MLM4 (**d**), MLM5 (**e**) in series III. The chart shows predicted value of target variable versus real one.

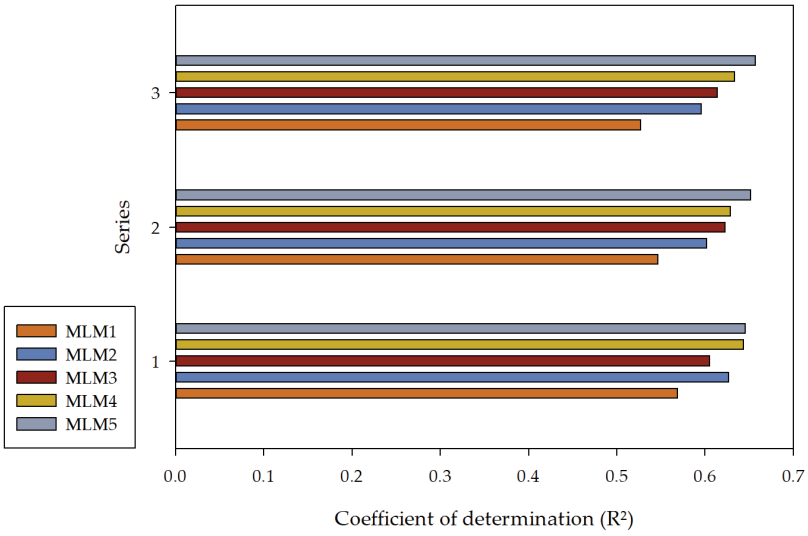

Figure 10. The coefficient of determination (R^2) values for MLM1, MLM2, MLM3, MLM4, and MLM5 in series I, II, and III.

It can be observed that a reasonably good performance of the created models was achieved. Simultaneously, with the increased computational complexity, a higher R^2 value can be noticed in more complex models, suggesting that these models exhibit better predictive capabilities than less complex models. This observation is evident in three series, except for series I, where the MLM2 model has a higher R^2 coefficient value than the MLM3 model. This deviation was not observed in the remaining series and may result from various reasons. An exhaustive analysis of the model's errors was performed by computing a range of error metrics across each series. This analysis included metrics such as mean squared error, Minkowski error, normalized squared error, root mean squared error, sum squared error [106–109]. Furthermore, a detailed report outlining the minimum and maximum values and the mean and standard deviation for absolute, relative, and percentage errors of the model concerning the test data was provided. Histograms were constructed for

the test subset to obtain a more tangible understanding of the distribution of errors in the model. The outcomes of this analysis provide a rigorous evaluation of the model's accuracy and precision, illuminating potential avenues for further refinement. Table 3 and Figure 11 present individual error metrics for each model, divided into respective subsets, for series I, II, and III.

Table 3. Error metrics for various data subsets.

Series I			
MLM1			
	Training	Selection	Testing
Sum squared error	550.201	342.198	317.183
Mean squared error	0.149	0.278	0.258
Root mean squared error	0.386	0.528	0.508
Normalised squared error	0.416	0.479	0.432
Minkowski error	1893.670	975.049	911.882
MLM2			
	Training	Selection	Testing
Sum squared error	489.493	310.386	295.271
Mean squared error	0.133	0.253	0.240
Root mean squared error	0.364	0.503	0.490
Normalised squared error	0.330	0.394	0.374
Minkowski error	1680.550	876.432	842.034
MLM3			
	Training	Selection	Testing
Sum squared error	458.547	313.610	305.511
Mean squared error	0.124	0.255	0.248
Root mean squared error	0.353	0.505	0.498
Normalised squared error	0.289	0.402	0.400
Minkowski error	1561.140	865.786	860.635
MLM4			
	Training	Selection	Testing
Sum squared error	447.218	307.594	290.030
Mean squared error	0.121	0.250	0.236
Root mean squared error	0.348	0.500	0.485
Normalised squared error	0.275	0.387	0.361
Minkowski error	1510.870	842.743	807.330
MLM5			
	Training	Selection	Testing
Sum squared error	416.643	296.432	291.111
Mean squared error	0.113	0.241	0.236
Root mean squared error	0.336	0.491	0.486
Normalised squared error	0.239	0.359	0.364
Minkowski error	1403.290	810.031	798.990
Series II			
MLM1			
	Training	Selection	Testing
Sum squared error	559.448	340.780	325.536
Mean squared error	0.152	0.277	0.264
Root mean squared error	0.389	0.527	0.514
Normalised squared error	0.431	0.475	0.455
Minkowski error	1944.850	974.611	947.078

Table 3. *Cont.*

MLM2			
	Training	Selection	Testing
Sum squared error	493.298	322.494	305.668
Mean squared error	0.134	0.262	0.248
Root mean squared error	0.366	0.512	0.498
Normalised squared error	0.335	0.425	0.401
Minkowski error	1687.480	905.087	867.447
MLM3			
	Training	Selection	Testing
Sum squared error	454.568	310.576	297.960
Mean squared error	0.123	0.253	0.242
Root mean squared error	0.351	0.503	0.492
Normalised squared error	0.284	0.394	0.381
Minkowski error	1539.040	852.571	837.393
MLM4			
	Training	Selection	Testing
Sum squared error	423.191	298.929	297.827
Mean squared error	0.115	0.243	0.242
Root mean squared error	0.339	0.493	0.492
Normalised squared error	0.246	0.365	0.381
Minkowski error	1431.560	823.304	820.941
MLM5			
	Training	Selection	Testing
Sum squared error	435.508	304.092	286.750
Mean squared error	0.118	0.247	0.233
Root mean squared error	0.344	0.497	0.483
Normalised squared error	0.261	0.378	0.353
Minkowski error	1458.890	834.351	799.642
Series III			
MLM1			
	Training	Selection	Testing
Sum squared error	575.272	347.520	332.199
Mean squared error	0.156	0.283	0.270
Root mean squared error	0.395	0.532	0.519
Normalised squared error	0.455	0.494	0.473
Minkowski error	2007.800	1004.980	969.083
MLM2			
	Training	Selection	Testing
Sum squared error	500.105	321.972	307.902
Mean squared error	0.136	0.262	0.250
Root mean squared error	0.368	0.512	0.500
Normalised squared error	0.344	0.424	0.407
Minkowski error	1706.130	905.095	879.370
MLM3			
	Training	Selection	Testing
Sum squared error	473.081	318.669	301.983
Mean squared error	0.128	0.259	0.245
Root mean squared error	0.358	0.509	0.495
Normalised squared error	0.308	0.415	0.391
Minkowski error	1608.550	889.350	844.676

Table 3. *Cont.*

MLM4			
	Training	Selection	Testing
Sum squared error	419.356	315.651	295.121
Mean squared error	0.114	0.257	0.240
Root mean squared error	0.337	0.507	0.490
Normalised squared error	0.242	0.407	0.374
Minkowski error	1407.230	862.350	814.506
MLM5			
	Training	Selection	Testing
Sum squared error	455.535	317.058	283.630
Mean squared error	0.123	0.258	0.230
Root mean squared error	0.351	0.508	0.480
Normalised squared error	0.286	0.411	0.345
Minkowski error	1529.650	866.807	798.284

In Figure 11, a clear error downward trend can be noticed for the NSE metric in the training, selection, and testing sections and for the ME metric in the training section in all three series, with the increase in computational complexity. Simultaneously, a milder error downward trend can be observed in the remaining metrics, along with the increase in computational complexity. Statistical calculations were conducted for individual target variables, presented in Table 4. Table 4 provides minimums, maximums, averages, and standard deviations of absolute and percentage errors of the model for the test data. Figure 12 shows the values of mean error (absolute error, relative error, percentage error) for every model in series I, II, and III.

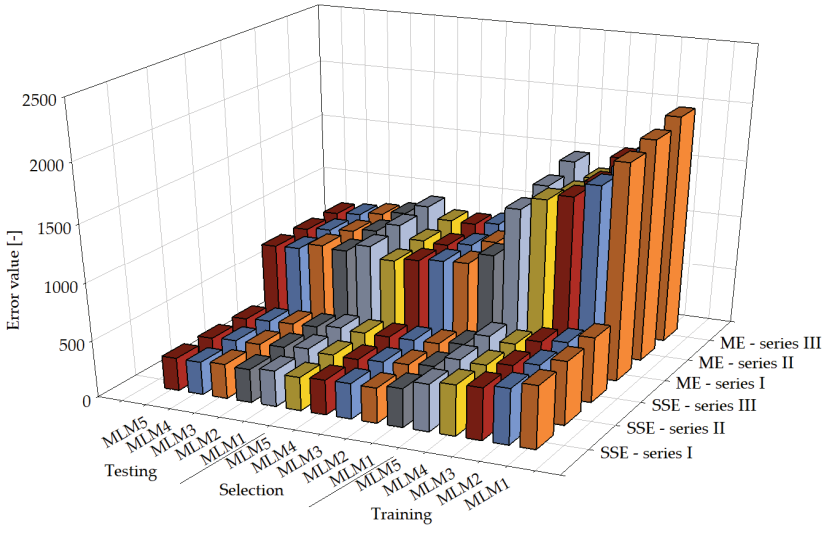

(**A**)

Figure 11. *Cont.*

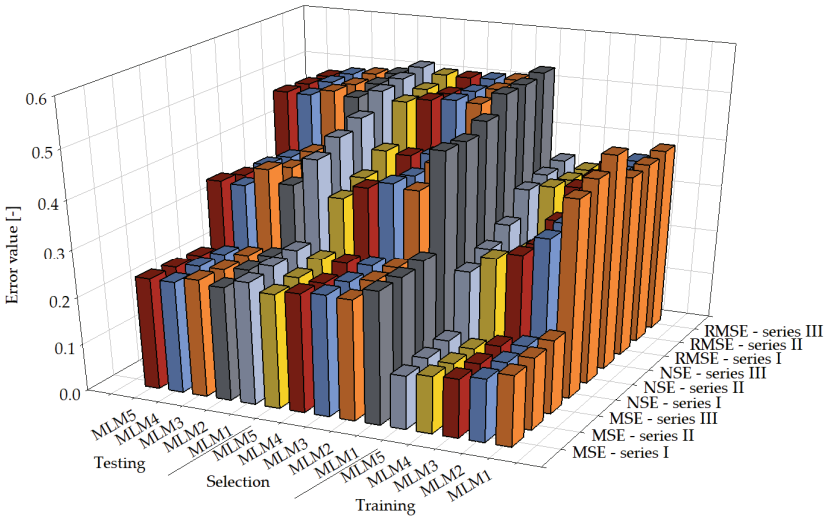

(**B**)

Figure 11. Error metrics for MLM1, MLM2, MLM3, MLM4, MLM5 in series I, II, and III. Error metrics used: mean squared error (MSE) (**B**), Minkowski error (ME) (**A**), normalized squared error (NSE) (**B**), root mean squared error (RMSE) (**B**), sum squared error (SSE) (**A**).

Table 4. Error statistics for calculation of target value f_{ck}.

Series I				
	Minimum	Maximum	Mean	Deviation
Absolute error				
MLM1	0.00000119209	0.0695368	0.00936655	0.00818558
MLM2	0.00000104308	0.0120825	0.00145332	0.00118896
MLM3	0.000000119209	0.0879388	0.00273278	0.0041617
MLM4	0.00000119209	0.148637	0.00331478	0.00663424
MLM5	0.00000119209	0.148637	0.00331478	0.00663424
Relative error				
MLM1	0.0000011413	0.0665743	0.00896749	0.00783684
MLM2	0.00000851071	0.0985832	0.011858	0.009701
MLM3	0.000000296304	0.218579	0.00679255	0.0103442
MLM4	0.00000213266	0.265913	0.00593016	0.0118687
MLM5	0.00000119209	0.148637	0.00331478	0.00663424
Percentage error				
MLM1	0.00011413	6.65743	0.896749	0.783684
MLM2	0.000851071	9.85832	1.1858	0.9701
MLM3	0.0000296304	21.8579	0.679255	1.03442
MLM4	0.000213266	26.5913	0.593016	1.18687
MLM5	0.00000119209	0.148637	0.00331478	0.00663424
Series II				
	Minimum	Maximum	Mean	Deviation
Absolute error				
MLM1	0.00000119209	0.0695368	0.00936655	0.00818558
MLM2	0.00000104308	0.0120825	0.00145332	0.00118896
MLM3	0.000000119209	0.0879388	0.00273278	0.0041617

Table 4. *Cont.*

MLM4	0.00000119209	0.148637	0.00331478	0.00663424
MLM5	0.00000119209	0.148637	0.00331478	0.00663424
		Relative error		
MLM1	0.0000011413	0.0665743	0.00896749	0.00783684
MLM2	0.00000851071	0.0985832	0.011858	0.009701
MLM3	0.000000296304	0.218579	0.00679255	0.0103442
MLM4	0.00000213266	0.265913	0.00593016	0.0118687
MLM5	0.00000119209	0.148637	0.00331478	0.00663424
		Percentage error		
MLM1	0.00011413	6.65743	0.896749	0.783684
MLM2	0.000851071	9.85832	1.1858	0.9701
MLM3	0.0000296304	21.8579	0.679255	1.03442
MLM4	0.000213266	26.5913	0.593016	1.18687
MLM5	0.00000119209	0.148637	0.00331478	0.00663424
		Series III		
	Minimum	Maximum	Mean	Deviation
		Absolute error		
MLM1	0.00000119209	0.0695368	0.00936655	0.00818558
MLM2	0.00000104308	0.0120825	0.00145332	0.00118896
MLM3	0.000000119209	0.0879388	0.00273278	0.0041617
MLM4	0.00000119209	0.148637	0.00331478	0.00663424
MLM5	0.00000119209	0.148637	0.00331478	0.00663424
		Relative error		
MLM1	0.0000011413	0.0665743	0.00896749	0.00783684
MLM2	0.00000851071	0.0985832	0.011858	0.009701
MLM3	0.000000296304	0.218579	0.00679255	0.0103442
MLM4	0.00000213266	0.265913	0.00593016	0.0118687
MLM5	0.00000119209	0.148637	0.00331478	0.00663424
		Percentage error		
MLM1	0.00011413	6.65743	0.896749	0.783684
MLM2	0.000851071	9.85832	1.1858	0.9701
MLM3	0.0000296304	21.8579	0.679255	1.03442
MLM4	0.000213266	26.5913	0.593016	1.18687
MLM5	0.00000119209	0.148637	0.00331478	0.00663424

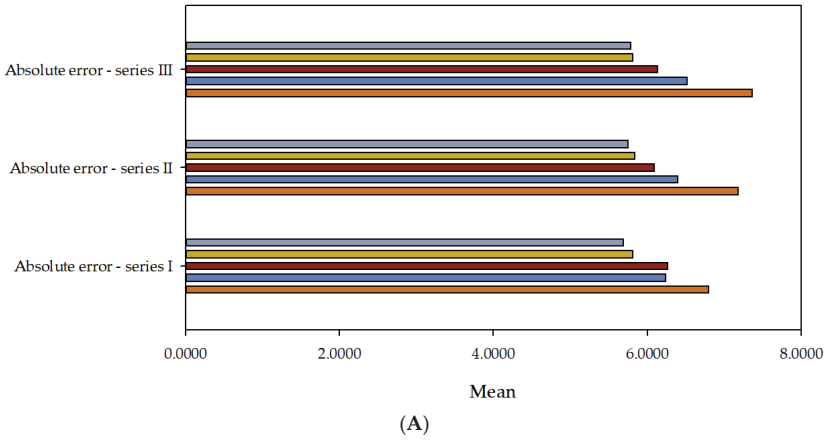

(**A**)

Figure 12. *Cont.*

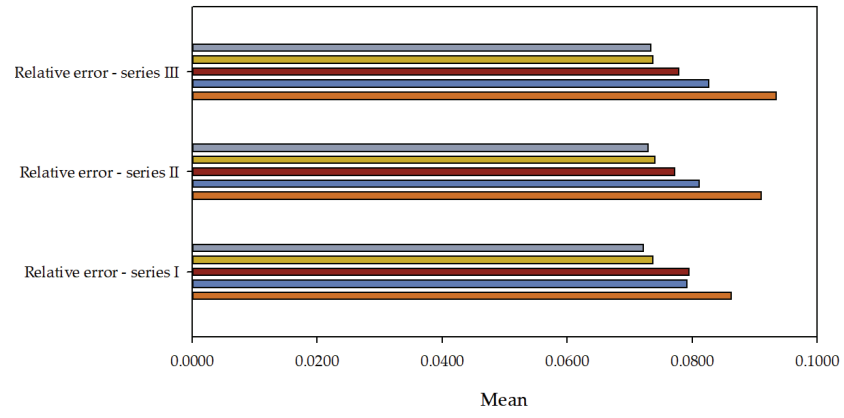

(**B**)

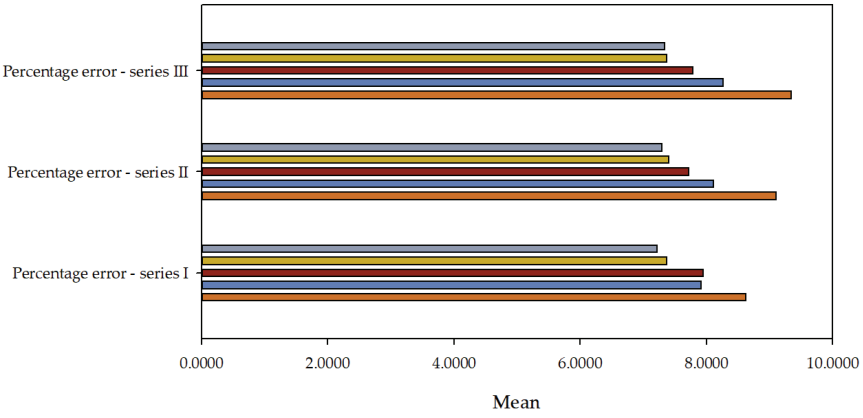

(**C**)

Figure 12. The values of mean error (absolute error (**A**), relative error (**B**), percentage error (**C**)) for MLM1 , MLM2 , MLM3 , MLM4 , MLM5 in series I, II, and III.

Analysing Table 4 and Figure 12A–C, one can observe that the average error decreases with the increase in the model's computational complexity for absolute error, relative error, and percentage error. Figures 13–15 represent the distribution of the relative error for the target variable f_{ck}. The abscissa represents the centres of the containers, and the ordinate represents their corresponding frequencies. Error histograms show the distribution of errors from the model for the test subset. A normal distribution for the target variable is expected. For Figure 13A, the maximum frequency is 36.75%, which corresponds to the bin centred at 0%. The minimum frequency is 0.2%, which corresponds to the bins with centres at −48.277%. For Figure 13B, the maximum frequency is 39%, corresponding to the bin centred at 0%. The minimum frequency is 0.12%, corresponding to the bins with centres at −47.614%. For Figure 13C, the maximum frequency is 38.76%, which corresponds to the bin centred at 0%. The minimum frequency is 0.28%, which corresponds to the bins with centres at 47.656%. For Figure 13D, the maximum frequency is 42.11%, corresponding to the bin centred at 0%. The minimum frequency is 0.04%, corresponding to the bins with centres at −53.646%. For Figure 13E, the maximum frequency is 42.37%, which corresponds to the bin centred at 0%. The minimum frequency is 0.12%, which corresponds to the bins with centres at −52.676%.

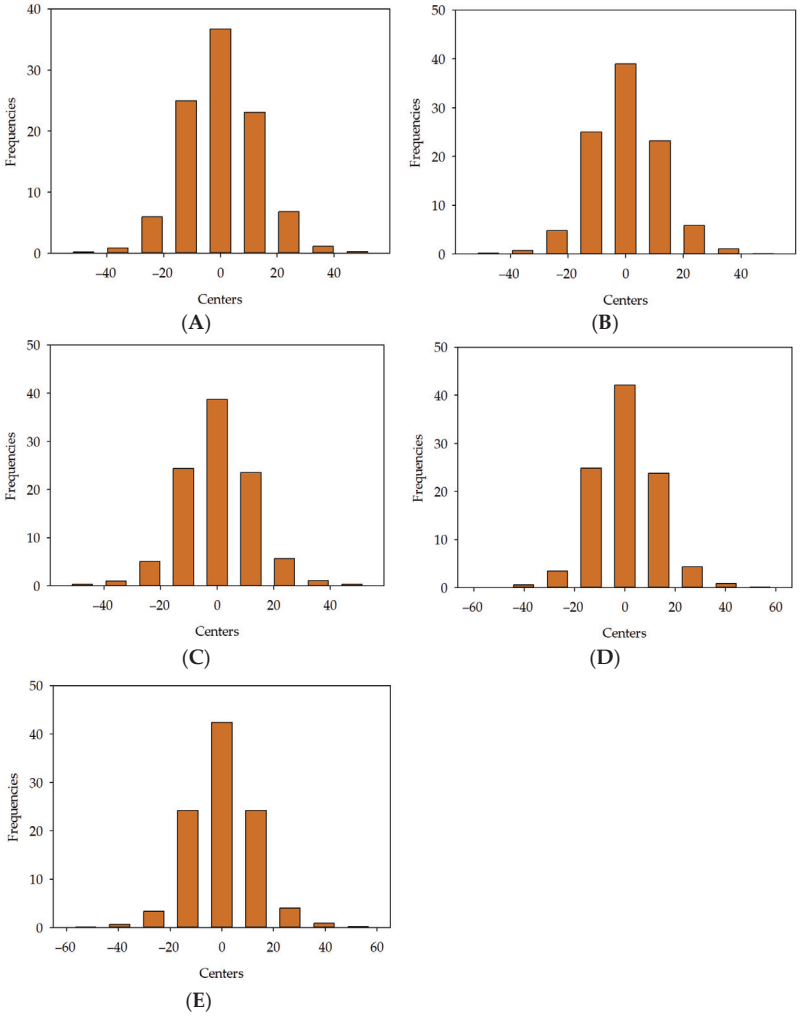

Figure 13. Error histogram for developed models in series I: MLM1 (**A**), MLM2 (**B**), MLM3 (**C**), MLM4 (**D**), MLM5 (**E**).

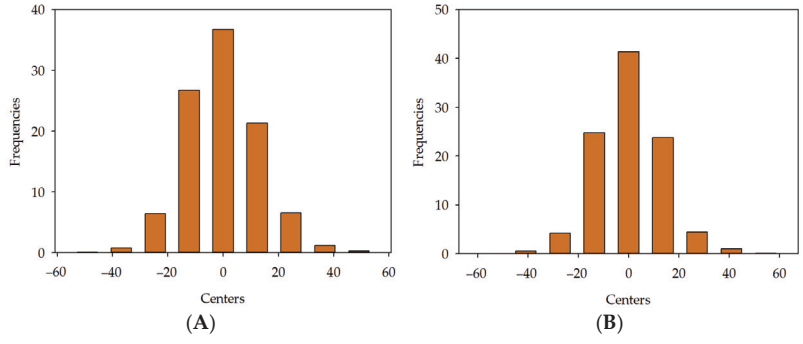

Figure 14. *Cont.*

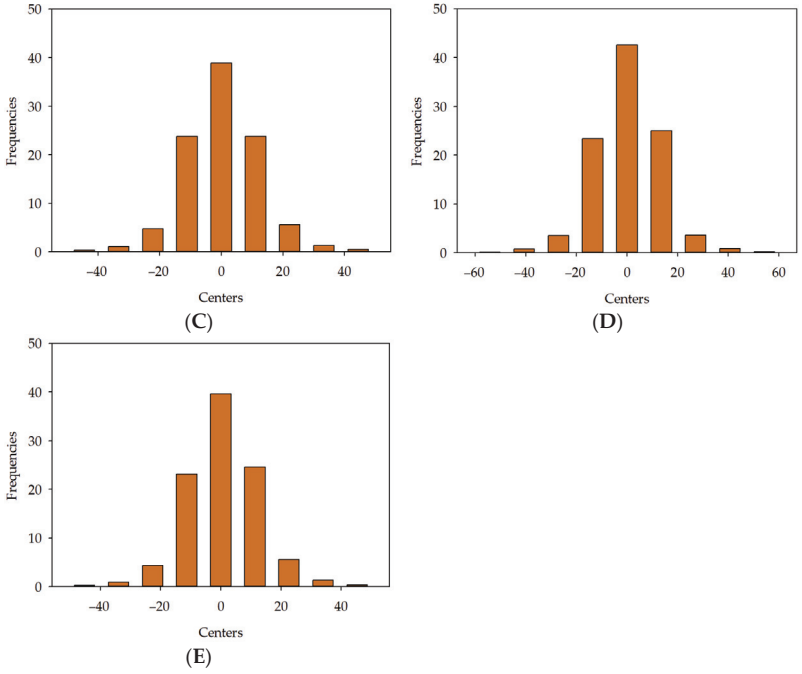

Figure 14. Error histogram for developed models in series II: MLM1 (**A**), MLM2 (**B**), MLM3 (**C**), MLM4 (**D**), MLM5 (**E**).

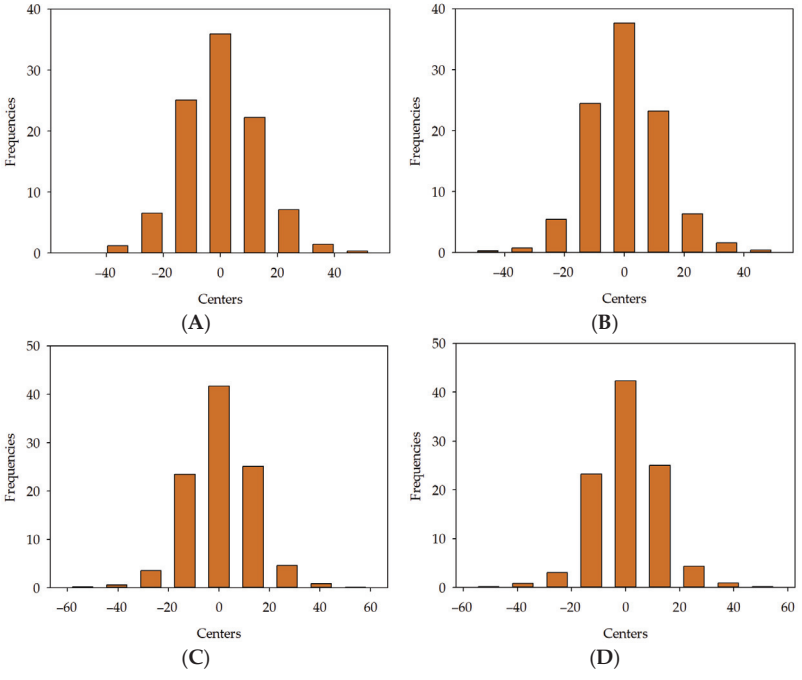

Figure 15. *Cont.*

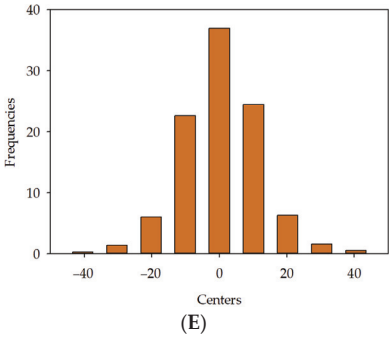

Figure 15. Error histogram for developed models in series III: MLM1 (**A**), MLM2 (**B**), MLM3 (**C**), MLM4 (**D**), MLM5 (**E**).

For Figure 14A, the maximum frequency is 36.75%, which corresponds to the bin centred at 0%. The minimum frequency is 0.08%, which corresponds to the bins with centres at −49.165%. For Figure 14B, the maximum frequency is 41.3%, corresponding to the bin centred at 0%. The minimum frequency is 0.04%, corresponding to the bins with centres at −54.49%. For Figure 14C, the maximum frequency is 38.93%, which corresponds to the bin centred at 0%. The minimum frequency is 0.33%, which corresponds to the bins with centres at −44.438%. For Figure 14D, the maximum frequency is 42.6%, corresponding to the bin centred at 0%. The minimum frequency is 0.12%, corresponding to the bins with centres at −54.26%. For Figure 14E, the maximum frequency is 39.65%, which corresponds to the bin centred at 0%. The minimum frequency is 0.24%, which corresponds to the bins with centres at −45.284%.

For Figure 15A, the maximum frequency is 35.93%, which corresponds to the bin centred at 0%. The minimum frequency is 0.04%, which corresponds to the bins with centres at −48.049%. For Figure 15B, the maximum frequency is 37.62%, corresponding to the bin centred at 0%. The minimum frequency is 0.24%, corresponding to the bins with centres at −45.596%. For Figure 15C, the maximum frequency is 41.64%, which corresponds to the bin centred at 0%. The minimum frequency is 0.12%, which corresponds to the bins with centres at −54.004%. For Figure 15D, the maximum frequency is 42.29%, corresponding to the bin centred at 0%. The minimum frequency is 0.2%, corresponding to the bins with centres at −50.63%. For Figure 15E, the maximum frequency is 36.95%, which corresponds to the bin centred at 0%. The minimum frequency is 0.24%, which corresponds to the bins with centres at −40.473%.

It should be noted that all error histograms presented in Figures 13–15 have a bell shape, which indicates a correctly obtained normal distribution [108,109]. The models are designed to estimate concrete compressive strength as determined by the composition of the concrete mixture. It is important to bear in mind that numerous additional elements, primarily linked to the technological process of concrete production and environmental conditions, exert influence over the concrete's strength. The initial critical aspect involves the proper maintenance of concrete after the setting process. Incorrect handling of concrete can lead to a substantial deterioration its attributes, particularly its durability. Taking environmental aspects into account, it is essential to consider the effect of environmental aggression [110] that detrimentally affect concrete quality, such as frost action or exposure large amounts of alkalis. One of pivotal concern is pouring concrete under unfavourable weather conditions, particularly subjecting it to excessive shrinkage due to rapid drying under high temperatures or freezing early in the setting process. The arrangement and size distribution of the aggregates dictate the requirements for an appropriately workable concrete paste as well as the source, shape, and texture of aggregates. It impact especially the workability and durability of the concrete [111,112]. Admixtures and additives are also important in whole process, especially those that profoundly affect the chemical properties

of the mixture. This assessment has omitted several factors, including environmental elements, technological processes, and properties of raw materials. It is assumed that the quality of the produced concrete samples met acceptable standards. The source code of all AI models presented in this research is available in an open repository [113].

4. Summary and Conclusions

In concrete structure production technology, a key challenge lies in ensuring predictable characteristics in the raw concrete mix and the hardened end product. Concrete mix manufacturers are responsible for guaranteeing that the concrete they deliver to construction sites meets the desired standards. However, achieving these standards consistently throughout the manufacturing process can prove daunting. Reliable prediction of concrete technical parameters is intricate, and most current solutions in the engineering field are estimations, which have increasingly become obsolete due to rapid advancements in material engineering. Predictive analytics dedicated to forecasting various phenomena, attributes, and patterns based on machine learning holds the potential to enhance the methodology behind concrete mix design substantially. The paper analyses the impact of computational complexity on the effectiveness of predicting the compressive strength of concrete using machine learning models. This study focuses on the growing interest in applying machine learning algorithms in material engineering, specifically in predicting the compressive strength of concrete, a key indicator of its quality. Computational complexity in this research refers to the number of hidden layers in the neural network architecture. In the context of machine learning models, computational complexity is essential, as it can influence the speed and effectiveness of the model's training and its ability to generalise to new data. This study evaluated five deep neural network models (MLM1, MLM2, MLM3, MLM4, MLM5) of varying computational complexity in three series. Each of the MLM1-MLM5 models underwent training, selection, and testing in each three series. The crux of this research was to establish an ideal deep neural network structure and train it using a vast database of concrete mix recipes and their associated laboratory-based destructive tests.

Presented machine learning models predicts the compressive strength of the concrete mix based on its unique composition. Based on the obtained results, the following conclusions can be formulated. There is a relationship between the computational complexity of deep neural network models and their ability to predict the compressive strength of concrete. The conducted analyses showed that as the computational complexity of the model increases, so does its predictive ability. This means that the more complex the neural network architecture, the more effective it is in predicting the compressive strength of concrete within the conducted analyses. Several parameters point to the above conclusion. In all three series, the coefficient of determination (R^2) increase was observed along with the increase in the model's computational complexity. The smallest value of R^2 was captured for model MLM1 and the largest for MLM5. It can be observed that errors in the five analysed metrics, namely mean squared error (MSE), Minkowski error (ME), normalized squared error (NSE), root mean squared error (RMSE), sum squared error (SSE), in training, selection, and testing decrease with the increase in the model's computational complexity, with the greatest error decrease observable for the NSE metric in training, selection, and testing and the ME metric in training. Furthermore, it is worth examining the mean values of absolute error, relative error, and percentage error, which tend to decrease as the computational complexity of the model increases. The error histograms for all analysed models in all series have a normal distribution. While the proposed method offers a promising solution, it possesses certain limitations and does not comprehensively encapsulate all the interactions between concrete mix components and their resulting properties. This is a research gap that necessitates further exploration. Nonetheless, the outcomes of this paper inspire optimism for this method's expanded application in practical engineering settings.

Future investigations should aim to broaden this method's utility in the concrete mix design process by predicting additional fresh and hardened concrete properties such

as durability, workability, air entrainment, and reliability. A more holistic strategy for optimising concrete mix design is also essential to development. The findings from this research lay a robust groundwork for further refinement and application of the proposed AI-driven method in concrete mix design. AI-driven methods automate the traditionally labour-intensive tasks, granting civil and structural engineers the liberty to tackle more intricate and inventive challenges. It is anticipated that this method will improve both the efficiency and precision of the design process, particularly in an era where advancements in hardware are accelerating the computational capabilities of AI.

Funding: The funding for these studies was obtained from the Faculty of Civil and Environmental Engineering at Gdansk University of Technology (Gdansk Tech) through the Grants for Young Scientists program.

Institutional Review Board Statement: Not applicable.

Informed Consent Statement: Not applicable.

Data Availability Statement: Not applicable.

Conflicts of Interest: The author declares no conflict of interest.

References

1. Suchorzewski, J.; Prieto, M.; Mueller, U. An Experimental Study of Self-Sensing Concrete Enhanced with Multi-Wall Carbon Nanotubes in Wedge Splitting Test and DIC. *Constr. Build. Mater.* **2020**, *262*, 120871. [CrossRef]
2. Nowek, A.; Kaszubski, P.; Abdelgader, H.S.; Górski, J. Effect of Admixtures on Fresh Grout and Two-Stage (Pre-Placed Aggregate) Concrete. *Struct. Concr.* **2007**, *8*, 17–23. [CrossRef]
3. Kujawa, W.; Olewnik-Kruszkowska, E.; Nowaczyk, J. Concrete Strengthening by Introducing Polymer-Based Additives into the Cement Matrix-a Mini Review. *Materials* **2021**, *14*, 6071. [CrossRef]
4. Suchorzewski, J.; Chitvoranund, N.; Srivastava, S.; Prieto, M.; Malaga, K. Recycling Potential of Cellular Lightweight Concrete Insulation as Supplementary Cementitious Material. In *Proceedings of the RILEM Bookseries*; Springer: Berlin/Heidelberg, Germany, 2023; Volume 44, pp. 133–141.
5. Liu, G.; Cheng, W.; Chen, L.; Pan, G.; Liu, Z. Rheological Properties of Fresh Concrete and Its Application on Shotcrete. *Constr. Build. Mater.* **2020**, *243*, 118180. [CrossRef]
6. McNamee, R.; Sjöström, J.; Boström, L. Reduction of Fire Spalling of Concrete with Small Doses of Polypropylene Fibres. *Fire Mater.* **2021**, *45*, 943–951. [CrossRef]
7. Cos-Gayón López, F.; Benlloch Marco, J.; Calvet Rodríguez, V. Influence of High Temperatures on the Bond between Carbon Fibre-Reinforced Polymer Bars and Concrete. *Constr. Build. Mater.* **2021**, *309*, 124967. [CrossRef]
8. Gupta, S.; Kua, H.W.; Pang, S.D. Effect of Biochar on Mechanical and Permeability Properties of Concrete Exposed to Elevated Temperature. *Constr. Build. Mater.* **2020**, *234*, 117338. [CrossRef]
9. Marchon, D.; Flatt, R.J. Mechanisms of Cement Hydration. *Sci. Technol. Concr. Admix.* **2016**, *41*, 129–145. [CrossRef]
10. Liu, Y.; Kumar, D.; Lim, K.H.; Lai, Y.L.; Hu, Z.; Ambikakumari Sanalkumar, K.U.; Yang, E.H. Efficient Utilization of Municipal Solid Waste Incinerator Bottom Ash for Autoclaved Aerated Concrete Formulation. *J. Build. Eng.* **2023**, *71*, 106463. [CrossRef]
11. Kocaba, V.; Gallucci, E.; Scrivener, K.L. Methods for Determination of Degree of Reaction of Slag in Blended Cement Pastes. *Cem. Concr. Res.* **2012**, *42*, 511–525. [CrossRef]
12. Boinski, T.; Chojnowski, A. Towards Facts Extraction from Text in Polish Language. In Proceedings of the 2017 IEEE International Conference on INnovations in Intelligent SysTems and Applications, INISTA 2017, Gdynia, Poland, 3–5 July 2017; IEEE: Piscataway, NJ, USA, 2017; pp. 13–17.
13. Pawlicki, M.; Marchewka, A.; Choraś, M.; Kozik, R. Gated Recurrent Units for Intrusion Detection. In *Proceedings of the Advances in Intelligent Systems and Computing*; Springer: Cham, Switzerland, 2020; Volume 1062, pp. 142–148.
14. Renigier-Biłozor, M.; Janowski, A.; d'Amato, M. Automated Valuation Model Based on Fuzzy and Rough Set Theory for Real Estate Market with Insufficient Source Data. *Land Use Policy* **2019**, *87*, 104021. [CrossRef]
15. Renigier-Biłozor, M.; Chmielewska, A.; Walacik, M.; Janowski, A.; Lepkova, N. Genetic Algorithm Application for Real Estate Market Analysis in the Uncertainty Conditions. *J. Hous. Built Environ.* **2021**, *36*, 1629–1670. [CrossRef]
16. Renigier-Biłozor, M.; Janowski, A.; Walacik, M.; Chmielewska, A. Modern Challenges of Property Market Analysis-Homogeneous Areas Determination. *Land Use Policy* **2022**, *119*, 106209. [CrossRef]
17. Chmielewska, A.; Renigier-Biłozor, M.; Janowski, A. Representative Residential Property Model—Soft Computing Solution. *Int. J. Environ. Res. Public Health* **2022**, *19*, 15114. [CrossRef]
18. De Prado, R.P.; García-Galán, S.; Muñoz-Expósito, J.E.; Marchewka, A. Acceleration of Genome Sequencing with Intelligent Cloud Brokers. In *Proceedings of the Advances in Intelligent Systems and Computing*; Springer: Cham, Switzerland, 2018; Volume 681, pp. 133–140.

19. Van Engelen, J.E.; Hoos, H.H. A Survey on Semi-Supervised Learning. *Mach. Learn.* **2020**, *109*, 373–440.
20. Sutton, R.S.; Barto, A.G. *Reinforcement Learning: An Introduction*; MIT Press: Cambridge, MA, USA, 2018; ISBN 0262352702.
21. Li, Y. Deep Reinforcement Learning: An Overview. *arXiv* **2017**, arXiv:1701.07274.
22. Ambroziak, A.; Ziolkowski, P. Concrete Compressive Strength under Changing Environmental Conditions during Placement Processes. *Materials* **2020**, *13*, 4577. [CrossRef] [PubMed]
23. Tam, C.T.; Babu, D.S.; Li, W. EN 206 Conformity Testing for Concrete Strength in Compression. *Procedia Eng.* **2017**, *171*, 227–237. [CrossRef]
24. *EN 1992-1-1: 2004*; Eurocode 2: Design of Concrete Structures. British Standards Institution: London, UK, 2004.
25. *DIN EN 206-1:2001-07*; Beton–Teil 1: Festlegung, Eigenschaften, Herstellung Und Konformität; Deutsche Fassung EN 206-1:2000. German Institute for Standardisation: Berlin, Germany, 2001.
26. Abdelgader, H.S.; El-Baden, A.S.; Shilstone, J.M. Bolomeya Model for Normal Concrete Mix Design. *J. Concr. Plant Int.* **2012**, *2*, 68–74.
27. Zhang, C.; Nerella, V.N.; Krishna, A.; Wang, S.; Zhang, Y.; Mechtcherine, V.; Banthia, N. Mix Design Concepts for 3D Printable Concrete: A Review. *Cem. Concr. Compos.* **2021**, *122*, 104155. [CrossRef]
28. Li, N.; Shi, C.; Zhang, Z.; Wang, H.; Liu, Y. A Review on Mixture Design Methods for Geopolymer Concrete. *Compos. Part B Eng.* **2019**, *178*, 107490. [CrossRef]
29. Liu, Q.F.; Iqbal, M.F.; Yang, J.; Lu, X.Y.; Zhang, P.; Rauf, M. Prediction of Chloride Diffusivity in Concrete Using Artificial Neural Network: Modelling and Performance Evaluation. *Constr. Build. Mater.* **2021**, *268*, 121082. [CrossRef]
30. Iqbal, M.F.; Liu, Q.F.; Azim, I.; Zhu, X.; Yang, J.; Javed, M.F.; Rauf, M. Prediction of Mechanical Properties of Green Concrete Incorporating Waste Foundry Sand Based on Gene Expression Programming. *J. Hazard. Mater.* **2020**, *384*, 121322. [CrossRef] [PubMed]
31. Yeh, I.C. Modeling of Strength of High-Performance Concrete Using Artificial Neural Networks. *Cem. Concr. Res.* **1998**, *28*, 1797–1808. [CrossRef]
32. Lee, S.C. Prediction of Concrete Strength Using Artificial Neural Networks. *Eng. Struct.* **2003**, *25*, 849–857. [CrossRef]
33. Hola, J.; Schabowicz, K. Application of Artificial Neural Networks to Determine Concrete Compressive Strength Based on Non-Destructive Tests. *J. Civ. Eng. Manag.* **2005**, *11*, 23–32. [CrossRef]
34. Hola, J.; Schabowicz, K. New Technique of Nondestructive Assessment of Concrete Strength Using Artificial Intelligence. *NDT E Int.* **2005**, *38*, 251–259. [CrossRef]
35. Gupta, R.; Kewalramani, M.A.; Goel, A. Prediction of Concrete Strength Using Neural-Expert System. *J. Mater. Civ. Eng.* **2006**, *18*, 462–466. [CrossRef]
36. Bui, D.K.; Nguyen, T.; Chou, J.S.; Nguyen-Xuan, H.; Ngo, T.D. A Modified Firefly Algorithm-Artificial Neural Network Expert System for Predicting Compressive and Tensile Strength of High-Performance Concrete. *Constr. Build. Mater.* **2018**, *180*, 320–333. [CrossRef]
37. Deng, F.; He, Y.; Zhou, S.; Yu, Y.; Cheng, H.; Wu, X. Compressive Strength Prediction of Recycled Concrete Based on Deep Learning. *Constr. Build. Mater.* **2018**, *175*, 562–569. [CrossRef]
38. Naderpour, H.; Rafiean, A.H.; Fakharian, P. Compressive Strength Prediction of Environmentally Friendly Concrete Using Artificial Neural Networks. *J. Build. Eng.* **2018**, *16*, 213–219. [CrossRef]
39. Ziolkowski, P.; Niedostatkiewicz, M. Machine Learning Techniques in Concrete Mix Design. *Materials* **2019**, *12*, 1256. [CrossRef] [PubMed]
40. McCormac, J.C.; Brown, R.H. *Design of Reinforced Concrete*; John Wiley & Sons: Hoboken, NJ, USA, 2015; ISBN 1118879104.
41. Nunez, I.; Marani, A.; Nehdi, M.L. Mixture Optimization of Recycled Aggregate Concrete Using Hybrid Machine Learning Model. *Materials* **2020**, *13*, 4331. [CrossRef] [PubMed]
42. Marani, A.; Jamali, A.; Nehdi, M.L. Predicting Ultra-High-Performance Concrete Compressive Strength Using Tabular Generative Adversarial Networks. *Materials* **2020**, *13*, 4757. [CrossRef] [PubMed]
43. Ziolkowski, P.; Niedostatkiewicz, M.; Kang, S.B. Model-Based Adaptive Machine Learning Approach in Concrete Mix Design. *Materials* **2021**, *14*, 1661. [CrossRef]
44. Adil, M.; Ullah, R.; Noor, S.; Gohar, N. Effect of Number of Neurons and Layers in an Artificial Neural Network for Generalized Concrete Mix Design. *Neural Comput. Appl.* **2022**, *34*, 8355–8363. [CrossRef]
45. Feng, W.; Wang, Y.; Sun, J.; Tang, Y.; Wu, D.; Jiang, Z.; Wang, J.; Wang, X. Prediction of Thermo-Mechanical Properties of Rubber-Modified Recycled Aggregate Concrete. *Constr. Build. Mater.* **2022**, *318*, 125970. [CrossRef]
46. Tavares, C.; Wang, X.; Saha, S.; Grasley, Z. Machine Learning-Based Mix Design Tools to Minimize Carbon Footprint and Cost of UHPC. Part 1: Efficient Data Collection and Modeling. *Clean. Mater.* **2022**, *4*, 100082. [CrossRef]
47. Tavares, C.; Grasley, Z. Machine Learning-Based Mix Design Tools to Minimize Carbon Footprint and Cost of UHPC. Part 2: Cost and Eco-Efficiency Density Diagrams. *Clean. Mater.* **2022**, *4*, 100094. [CrossRef]
48. Endzhievskaya, I.G.; Endzhievskiy, A.S.; Galkin, M.A.; Molokeev, M.S. Machine Learning Methods in Assessing the Effect of Mixture Composition on the Physical and Mechanical Characteristics of Road Concrete. *J. Build. Eng.* **2023**, *76*, 107248. [CrossRef]
49. Taffese, W.Z.; Espinosa-Leal, L. Multitarget Regression Models for Predicting Compressive Strength and Chloride Resistance of Concrete. *J. Build. Eng.* **2023**, *72*, 106523. [CrossRef]

50. Gulli, A.; Pal, S. *Deep Learning with Keras: Beginners Guide to Deep Learning with Keras*; Packt Publishing Ltd.: Birmingham, UK, 2017; ISBN 9781787128422.
51. Cichy, R.M.; Kaiser, D. Deep Neural Networks as Scientific Models. *Trends Cogn. Sci.* **2019**, *23*, 305–317. [CrossRef]
52. Saxena, A. An Introduction to Convolutional Neural Networks. *Int. J. Res. Appl. Sci. Eng. Technol.* **2022**, *10*, 943–947. [CrossRef]
53. Li, Z.; Liu, F.; Yang, W.; Peng, S.; Zhou, J. A Survey of Convolutional Neural Networks: Analysis, Applications, and Prospects. *IEEE Trans. Neural Netw. Learn. Syst.* **2022**, *33*, 6999–7019. [CrossRef]
54. Zhang, Q.; Zhang, M.; Chen, T.; Sun, Z.; Ma, Y.; Yu, B. Recent Advances in Convolutional Neural Network Acceleration. *Neurocomputing* **2019**, *323*, 37–51. [CrossRef]
55. Li, H.; Li, J.; Guan, X.; Liang, B.; Lai, Y.; Luo, X. Research on Overfitting of Deep Learning. In Proceedings of the 2019 15th International Conference on Computational Intelligence and Security, CIS 2019, Macau, China, 13–16 December 2019; IEEE: Piscataway, NJ, USA, 2019; pp. 78–81.
56. Salman, S.; Liu, X. Overfitting Mechanism and Avoidance in Deep Neural Networks. *arXiv* **2019**, arXiv:1901.06566.
57. Bejani, M.M.; Ghatee, M. A Systematic Review on Overfitting Control in Shallow and Deep Neural Networks. *Artif. Intell. Rev.* **2021**, *54*, 6391–6438. [CrossRef]
58. Liu, M.; Chen, L.; Du, X.; Jin, L.; Shang, M. Activated Gradients for Deep Neural Networks. *IEEE Trans. Neural Netw. Learn. Syst.* **2023**, *34*, 2156–2168. [CrossRef]
59. Rehmer, A.; Kroll, A. On the Vanishing and Exploding Gradient Problem in Gated Recurrent Units. *IFAC-PapersOnLine* **2020**, *53*, 1243–1248. [CrossRef]
60. Garbin, C.; Zhu, X.; Marques, O. Dropout vs. Batch Normalization: An Empirical Study of Their Impact to Deep Learning. *Multimed. Tools Appl.* **2020**, *79*, 12777–12815. [CrossRef]
61. Salehinejad, H.; Valaee, S. Ising-Dropout: A Regularization Method for Training and Compression of Deep Neural Networks. In Proceedings of the ICASSP, IEEE International Conference on Acoustics, Speech and Signal Processing-Proceedings, Brighton, UK, 12–17 May 2019; IEEE: Piscataway, NJ, USA, 2019; pp. 3602–3606.
62. Piotrowski, A.P.; Napiorkowski, J.J.; Piotrowska, A.E. Impact of Deep Learning-Based Dropout on Shallow Neural Networks Applied to Stream Temperature Modelling. *Earth-Sci. Rev.* **2020**, *201*, 103076. [CrossRef]
63. Tjoa, E.; Cuntai, G. Quantifying Explainability of Saliency Methods in Deep Neural Networks With a Synthetic Dataset. *IEEE Trans. Artif. Intell.* **2022**, *4*, 858–870. [CrossRef]
64. Hernandez, M.; Epelde, G.; Alberdi, A.; Cilla, R.; Rankin, D. Synthetic Data Generation for Tabular Health Records: A Systematic Review. *Neurocomputing* **2022**, *493*, 28–45. [CrossRef]
65. Juneja, T.; Bajaj, S.B.; Sethi, N. Synthetic Time Series Data Generation Using Time GAN with Synthetic and Real-Time Data Analysis. In *Proceedings of the Lecture Notes in Electrical Engineering*; Springer: Berlin/Heidelberg, Germany, 2023; Volume 1011 LNEE, pp. 657–667.
66. Ravikumar, D.; Zhang, D.; Keoleian, G.; Miller, S.; Sick, V.; Li, V. Carbon Dioxide Utilization in Concrete Curing or Mixing Might Not Produce a Net Climate Benefit. *Nat. Commun.* **2021**, *12*, 855. [CrossRef]
67. Shi, J.; Liu, B.; Wu, X.; Qin, J.; Jiang, J.; He, Z. Evolution of Mechanical Properties and Permeability of Concrete during Steam Curing Process. *J. Build. Eng.* **2020**, *32*, 101796. [CrossRef]
68. Li, Y.; Nie, L.; Wang, B. A Numerical Simulation of the Temperature Cracking Propagation Process When Pouring Mass Concrete. *Autom. Constr.* **2014**, *37*, 203–210. [CrossRef]
69. Patel, S.K.; Parmar, J.; Katkar, V. Graphene-Based Multilayer Metasurface Solar Absorber with Parameter Optimization and Behavior Prediction Using Long Short-Term Memory Model. *Renew. Energy* **2022**, *191*, 47–58. [CrossRef]
70. Zhou, X.; Lin, W.; Kumar, R.; Cui, P.; Ma, Z. A Data-Driven Strategy Using Long Short Term Memory Models and Reinforcement Learning to Predict Building Electricity Consumption. *Appl. Energy* **2022**, *306*, 118078. [CrossRef]
71. Wold, S. Principal Component Analysis Why Principal Component Analysis? In *IEEE Signal Processing Letters*; Elsevier: Amsterdam, The Netherlands, 2002; Volume 9, pp. 40–42; ISBN 0-387-95442-2.
72. Vidal, R.; Ma, Y.; Sastry, S. Principal Component Analysis. In *Interdisciplinary Applied Mathematics*; Springer: New York, NY, USA, 2016; Volume 40, pp. 25–62. [CrossRef]
73. Thiyagalingam, J.; Shankar, M.; Fox, G.; Hey, T. Scientific Machine Learning Benchmarks. *Nat. Rev. Phys.* **2022**, *4*, 413–420. [CrossRef]
74. Menéndez, M.L.; Pardo, J.A.; Pardo, L.; Pardo, M.C. The Jensen-Shannon Divergence. *J. Frankl. Inst.* **1997**, *334*, 307–318. [CrossRef]
75. Fuglede, B.; Topsoe, F. Jensen-Shannon Divergence and Hilbert Space Embedding. In Proceedings of the International symposium on Information theory, 2004. ISIT 2004. Proceedings, Chicago, IL, USA, 27 June–2 July 2004; IEEE: Piscataway, NJ, USA, 2004; p. 31.
76. Nielsen, F. On a Generalization of the Jensen-Shannon Divergence and the Jensen-Shannon Centroid. *Entropy* **2020**, *22*, 221. [CrossRef] [PubMed]
77. Toniolo, G.; Di Prisco, M. *Reinforced Concrete Design to Eurocode 2*; Springer Tracts in Civil Engineering; Springer International Publishing: Berlin/Heidelberg, Germany, 2017; pp. 1–836.
78. Keim, D.A.; Hao, M.C.; Dayal, U.; Janetzko, H.; Bak, P. Generalized Scatter Plots. *Inf. Vis.* **2010**, *9*, 301–311. [CrossRef]
79. Larochelle, H.; Bengio, Y.; Louradour, J.; Lamblin, P. Exploring Strategies for Training Deep Neural Networks. *J. Mach. Learn. Res.* **2009**, *10*, 1–40.

80. Zhu, H.; Akrout, M.; Zheng, B.; Pelegris, A.; Jayarajan, A.; Phanishayee, A.; Schroeder, B.; Pekhimenko, G. Benchmarking and Analyzing Deep Neural Network Training. In Proceedings of the 2018 IEEE International Symposium on Workload Characterization, IISWC 2018, Raleigh, NC, USA, 30 September–2 October 2018; IEEE: Piscataway, NJ, USA, 2018; pp. 88–100.
81. Banerjee, S.; Iglewicz, B. A Simple Univariate Outlier Identification Procedure Designed for Large Samples. *Commun. Stat. Simul. Comput.* **2007**, *36*, 249–263. [CrossRef]
82. Seo, S.; Gary, M.; Marsh, P.D. A Review and Comparison of Methods for Detecting Outliersin Univariate Data Sets. *Dep. Biostat. Grad. Sch. Public Health* **2006**, 1–53.
83. Wan, X. Influence of Feature Scaling on Convergence of Gradient Iterative Algorithm. In *Proceedings of the Journal of Physics: Conference Series*; IOP Publishing: Bristol, UK, 2019; Volume 1213, p. 32021.
84. Zheng, A.; Casari, A. *Feature Engineering for Machine Learning: Principles and Techniques for Data Scientists*; O'Reilly Media, Inc.: Sevastopol, CA, USA, 2018; ISBN 978-1491953242.
85. Namin, A.H.; Leboeuf, K.; Muscedere, R.; Wu, H.; Ahmadi, M. Efficient Hardware Implementation of the Hyperbolic Tangent Sigmoid Function. In Proceedings of the IEEE International Symposium on Circuits and Systems, Taipei, Taiwan, 24–27 May 2009; IEEE: Piscataway, NJ, USA, 2009; pp. 2117–2120.
86. Zamanlooy, B.; Mirhassani, M. Efficient VLSI Implementation of Neural Networks with Hyperbolic Tangent Activation Function. *IEEE Trans. Very Large Scale Integr. Syst.* **2013**, *22*, 39–48. [CrossRef]
87. Rasamoelina, A.D.; Adjailia, F.; Sincak, P. A Review of Activation Function for Artificial Neural Network. In Proceedings of the SAMI 2020-IEEE 18th World Symposium on Applied Machine Intelligence and Informatics, Herl'any, Slovakia, 23–25 January 2020; IEEE: Piscataway, NJ, USA, 2020; pp. 281–286.
88. Van Laarhoven, T. L2 Regularization versus Batch and Weight Normalization. *arXiv* **2017**, arXiv:1706.05350.
89. Cortes, C.; Mohri, M.; Rostamizadeh, A. L2 Regularization for Learning Kernels. In Proceedings of the 25th Conference on Uncertainty in Artificial Intelligence UAI 2009, Montreal, QC, Canada, 18–21 June 2009; pp. 109–116.
90. Moore, R.C.; DeNero, J. L1 and L2 Regularization for Multiclass Hinge Loss Models. In Proceedings of the Symposium on Machine Learning in Speech and Natural Language Processing, Bellevue, WA, USA, 27 June 2011.
91. Goldfarb, D.; Ren, Y.; Bahamou, A. Practical Quasi-Newton Methods for Training Deep Neural Networks. *Adv. Neural Inf. Process. Syst.* **2020**, *33*, 2386–2396.
92. Byrd, R.H.; Hansen, S.L.; Nocedal, J.; Singer, Y. A Stochastic Quasi-Newton Method for Large-Scale Optimization. *SIAM J. Optim.* **2016**, *26*, 1008–1031. [CrossRef]
93. Nilsen, G.K.; Munthe-Kaas, A.Z.; Skaug, H.J.; Brun, M. Efficient Computation of Hessian Matrices in TensorFlow. *arXiv* **2019**, arXiv:1905.05559.
94. Keskar, N.; Wächter, A. A Limited-Memory Quasi-Newton Algorithm for Bound-Constrained Non-Smooth Optimization. *Optim. Methods Softw.* **2019**, *34*, 150–171. [CrossRef]
95. Ayanlere, S.A.; Ajamu, S.O.; Odeyemi, S.O.; Ajayi, O.E.; Kareem, M.A. Effects of Water-Cement Ratio on Bond Strength of Concrete. *Mater. Today Proc.* **2023**, *86*, 134–139. [CrossRef]
96. Almusallam, A.A.; Maslehuddin, M.; Waris, M.A.; Al-Amoudi, O.S.B.; Al-Gahtani, A.S. Plastic Shrinkage Cracking of Concrete in Hot-Arid Environments. *Arab. J. Sci. Eng.* **1998**, *23*, 57–71.
97. Wilkinson, L.; Friendly, M. History Corner the History of the Cluster Heat Map. *Am. Stat.* **2009**, *63*, 179–184. [CrossRef]
98. Argiz, C.; Menéndez, E.; Sanjuán, M.A. Efecto de La Adición de Mezclas de Ceniza Volante y Ceniza de Fondo Procedentes Del Carbón En La Resistencia Mecánica y Porosidad de Cementos Portland. *Mater. Constr.* **2013**, *63*, 49–64. [CrossRef]
99. Berk, R.H.; Jones, D.H. Goodness-of-Fit Test Statistics That Dominate the Kolmogorov Statistics. *Z. Wahrscheinlichkeitstheorie Verwandte Geb.* **1979**, *47*, 47–59. [CrossRef]
100. Larntz, K.; Read, T.R.C.; Cressie, N.A.C. *Goodness-of-Fit Statistics for Discrete Multivariate Data*; Springer Science & Business Media: Berlin/Heidelberg, Germany, 1989; Volume 84; ISBN 1461245788.
101. Mckinley, R.L.; Mills, C.N. A Comparison of Several Goodness-of-Fit Statistics. *Appl. Psychol. Meas.* **1985**, *9*, 49–57. [CrossRef]
102. Lospinoso, J.; Snijders, T.A.B. Goodness of Fit for Stochastic Actor-Oriented Models. *Methodol. Innov.* **2019**, *12*, 2059799119884282. [CrossRef]
103. Baum, J.; Kanagawa, H.; Gretton, A. A Kernel Stein Test of Goodness of Fit for Sequential Models. In Proceedings of the International Conference on Machine Learning, PMLR, Honolulu, HI, USA, 23–29 July 2023; pp. 1936–1953.
104. Piepho, H.P. A Coefficient of Determination (R2) for Generalized Linear Mixed Models. *Biom. J.* **2019**, *61*, 860–872. [CrossRef] [PubMed]
105. Camirand Lemyre, F.; Chalifoux, K.; Desharnais, B.; Mireault, P. Squaring Things Up with R2: What It Is and What It Can (and Cannot) Tell You. *J. Anal. Toxicol.* **2022**, *46*, 443–448. [CrossRef] [PubMed]
106. Botchkarev, A. A New Typology Design of Performance Metrics to Measure Errors in Machine Learning Regression Algorithms. *Interdiscip. J. Inf. Knowl. Manag.* **2019**, *14*, 45–76. [CrossRef]
107. Naser, M.Z.; Alavi, A.H. Error Metrics and Performance Fitness Indicators for Artificial Intelligence and Machine Learning in Engineering and Sciences. *Archit. Struct. Constr.* **2021**, 1–19. [CrossRef]
108. Michael, W.; Berry, A.M. *Supervised and Unsupervised Learning for Data Science*; Springer: Berlin/Heidelberg, Germany, 2020; ISBN 978-3-030-22474-5.
109. Kubat, M. *An Introduction to Machine Learning*; Springer: Berlin/Heidelberg, Germany, 2021; ISBN 9783030819354.

110. Sanjuán, M.Á.; Estévez, E.; Argiz, C.; del Barrio, D. Effect of Curing Time on Granulated Blast-Furnace Slag Cement Mortars Carbonation. *Cem. Concr. Compos.* **2018**, *90*, 257–265. [CrossRef]
111. Poloju, K.K.; Anil, V.; Manchiryal, R.K. Properties of Concrete as Influenced by Shape and Texture of Fine Aggregate. *Am. J. Appl. Sci. Res.* **2017**, *3*, 28–36.
112. Chinchillas-Chinchillas, M.J.; Corral-Higuera, R.; Gómez-Soberón, J.M.; Arredondo-Rea, S.P.; Alamaral-Sánchez, J.L.; Acuña-Aguero, O.H.; Rosas-Casarez, C.A. Influence of the Shape of the Natural Aggregates, Recycled and Silica Fume on the Mechanical Properties of Pervious Concrete. *Int. J. Adv. Comput. Sci. Its Appl.* **2014**, *4*, 216–220.
113. Ziolkowski, P. *Source Code – AI Models (MLM1-5-series I–III-QNM opt)*; Gdansk University of Technology: Gdańsk, Poland, 2023. [CrossRef]

MDPI
St. Alban-Anlage 66
4052 Basel
Switzerland
www.mdpi.com

Materials Editorial Office
E-mail: materials@mdpi.com
www.mdpi.com/journal/materials

Academic Open
Access Publishing

mdpi.com

ISBN 978-3-7258-0382-8